Investigation of High Temperature Polymer Electrolyte Membrane Fuel Cells

Newcastle University

A Thesis Submitted By

MOHAMED MAMLOUK

For the Degree of Doctor of Philosophy

School of Chemical Engineering & Advanced Materials
University of Newcastle upon Tyne

August 2008

Abstract

One of the major issues limiting the introduction of polymer electrolyte membrane fuel cells (PEMFC) is the low temperature of operation which makes platinum-based anode catalysts susceptible to poisoning by trace amounts of CO, typically present in reformed fuel. In order to alleviate the problem of CO poisoning and improve the power density of the cell, operating at temperature above 100 °C is preferred. Nafion® type perfluorosulphonated polymers have been typically used for PEMFC but cannot function at temperatures above 100 °C. In addition, higher temperatures will enable more effective cooling of the cell stacks and provide a means for combined electrical and heat energy generation.

The solution to improved PEMFCs technology is to develop a new polymer electrolyte membrane which exhibits stability and high conductivity in the absence of liquid water. A High-Temperature PEMFC based on a Phosphoric acid (H_3PO_4) doped Polybenzimidazole poly[2,2-(m-phenylene)-5,5 bibenzimidazole] (PBI) membrane has been developed and demonstrated as an alternative to Nafion® for operation at temperatures up to 200 °C. PBI membranes, when doped with phosphoric acid, do not rely on hydration for conductivity; a significantly lower water content of the membrane, compared to Nafion, is required for proton transport. The resulting system improvements include; high CO tolerance, simple thermal and water management, excellent oxidative and thermal stability, and good proton conductivity at elevated temperatures. Two issues associated with phosphoric acid in the PBI based fuel cell are the lower activity of the electrocatalysts and the potential loss of the acid into the fuel cell gas/vapour exhaust streams. The limited oxygen permeability and slow oxygen reduction kinetics in phosphoric acid is a major limitation for the performance of PBI based PEMFCs.

The kinetics of oxygen reduction in PBI/H_3PO_4 has been studied in electrochemical single electrode cells. Several Membrane Electrode Assemblies (MEAs) have been manufactured to allow optimisation of the electrode performance. Various electrochemical techniques such as chronoamperometry, polarisation curves and Frequency Response Analysis (FRA) were used to study and separate the effects of the various phenomena taking place at the electrode surface: IR losses, mass transport and kinetics. A new Electrode structure utilizing PTFE has been developed

allowing higher oxygen permeability and therefore enhanced performance of 0.55 W cm^{-2} with oxygen and 0.27 W cm^{-2} with air (atm) at temperature as low as 120 °C. The Platinum loading was reduced to 0.4 mg_{Pt} cm^{-2} at the cathode and 0.2 mg_{Pt} cm^{-2} at the anode. Further reduction of cathode platinum loading to 0.2 mg_{Pt} cm^{-2} was achieved without dramatic drop in the performance by utilising Pt based binary alloy catalyst (Pt-Co/C).

A simplified thin film steady-state, isothermal, one dimensional model of a proton exchange membrane fuel cell (PEMFC), with a polybenzimidazole (PBI) membrane, was developed. The electrode kinetics were represented by the Butler-Volmer equation, mass transport was described by the multi-component Stefan Maxwell equations and Fick's law, and the ionic and electronic resistances described by Ohm's law. The model incorporated the effects of temperature and pressure on the open circuit potential, the exchange current density and diffusion coefficients, together with the effect of water on the acid concentration and ionic conductivity. The polarisation curves predicted by the model were validated against experimental data for a PEMFC which included the effect of temperature and oxygen/air pressure on cell performance.

An additional problem which faces the introduction of PEMFC technology is that of supplying or storing hydrogen for cell operation, especially for vehicular applications. Consequently the use of alternative fuels such as methanol and ethanol is of interest, especially if this can be used directly in the fuel cell, without reformation to hydrogen. A limitation of the direct use of alcohol is the lower activity of oxidation in comparison to hydrogen, and hence to improve activity and power output higher temperatures of operation are preferable. The performance of a high temperature direct methanol fuel cell (DMFC) using PBI based electrode assemblies was investigated. The performance of the system was limited by poor methanol oxidation kinetics in a phosphoric acid environment and consequently power performance was inferior to that achieved with low temperature DMFCs based on Nafion membranes.

Acknowledgements

Over the last four years I have been blessed with the opportunity to work with a body of people who have been a source of guidance, friendship and support. I would like to take this occasion to thank and acknowledge a few key individuals who especially stood out.

First and foremost thank you, Keith, or rather Professor Scott, for the opportunity to work on this project and for many great opportunities you offered me. Your patience, guidance, constant encouragement and support, both technical and moral, were motivating and inspiring. What I have got from you is invaluable and unparallel and for that I'm truly grateful.

In the first year of this project, I had the chance to work in conjunction with Dr Dave Hall and Mr Jose Linares, through which we shared ideas and had fruitful discussions for this I am very thankful.

Of my friends and colleagues in "the lab", there are a few of you who have especially contributed to my time there. Aris, (or Georgios if you like) your friendship and company helped me to overcome some difficult times both in the lab and also in my personal life. Nuri, thank you for your help in the preparation of some of the methanol work. Ruth, Stephen, Georgina, Tiago, Jang and all the graduate students and post-docs of the Electrochem Lab, I shall miss you all and hope our paths cross in the future.

Our friendly CEAMs technical support team: Stu, Iain, Brian, Simon, Jimmy, Rob and Paul. I would like to thank you all for your valuable suggestions and advice as well as the friendly chats. I also appreciate the technical support of John Marshall for his proficient glass work.

I would like to thank the European commission for their financial support through the FURIM project "Further Improvement and System Integration of High Temperature Polymer Electrolyte Fuel Cells" under frame work 6. FURIM partners: Technical University of Denmark, Volvo Technology Corporation, Norwegian University of Science and Technology, Danish Power Systems, Case Western Reserve University, University of Stuttgart, HyGear, Freudenberg

FCCT, IRD Fuel Cells, ICE/HT-FORTH & Between Lizenz GmbH, it has been a great pleasure to work with you all on such interesting project.

My gratitude to RAPRA (U.K) technologies, for their help in characterising polymer's molecular weight distribution, DTU for their supply of some of the PBI membrane materials and Freudenberg (FCCT) for their generous supply of gas diffusion electrodes used in this work.

I would like to dedicate my work to my parents, who valued science above all treasures. Parents, brother and sisters, thank you for your love and continual support and encouragement over the past years.

Finally, thanks to you Eve, because you were always there for me.

Table of Contents

List of Figures

Chapter Two

Chapter Three

Chapter Four

Chapter Five

Chapter Six

Chapter Seven

Appendix: A

List of Tables

Chapter Seven

Nomenclature

A	pre-exponential factor the geometric area (flux) / cm^2 constant related to the standard free energy of adsorption at zero coverage θ_0
AR	amplitude ratio: the impedance magnitude is given by $\|Z\|$ / ohm
a	constant 0.0002745 for di-atomic gases and 0.000364 for water vapour Mark-Houwink equation constant
a_c	the catalyst specific (electrochemical surface area) / $m^2\ g^{-1}$
B	activation energy for proton conductivity / kJ $mole^{-1}$
b	Tafel slope / mV dec^{-1} constant 1.832 for di-atomic gases and 2.334 for water vapour
C_A, C_B	methanol concentration in compartment A & B / M
C_{Pt} or C_{O2}	oxygen concentration in the thin film at platinum-electrolyte boundary / mole cm^3
$C_{dissolve}$	oxygen concentration in the thin film at gas pore-electrolyte boundary / mole cm^3
C^0_{H2}	the reference standard H_2 concentration (expressed as 1/RT) / mol cm^{-3} atm^{-1}
C^0_{O2}	the reference standard O_2 concentration (expressed as 1/RT) / mol cm^{-3} atm^{-1}
C_0	the reactant reference concentration where i_0 is measured (O.C.P) / mol cm^{-3} the initial uniform concentration within the membrane / mol cm^{-3}
C_{ref}	reference concentration where i_0^{ref} is measured / mol cm^{-3}
C	the surface concentration at current i ($i > i_0$ & $C < C_0$) / mol cm^{-3} the adsorbed species surface concentration / mol cm^{-3} capacity of capacitor / F
C_1	the constant (O_2) species concentration at the membrane boundary / mol cm^{-3}
C_2	the constant (O_2) species concentration at the electrode boundary / mol cm^{-3}
$C_{channnel}$	oxygen concentration at the gas pore-ionomer interface / mol cm^{-3}
C_{load}	the capacity of the capacitance to be charged / F
C_Δ	the surface concentration at current $i+\Delta i$ / mol cm^{-3}
C_{ads}	adsorption capacitor / F
C_d	diffusion capacitor / F
C_{mass}	diffusion capacitor / F
C_g	geometric impedance (capacitor) / F
C_{dl}	double layer capacitance / F
C_{tot}	total equivalent capacitance / F

$C_{lf\,low}$	low frequency capacitor / F
C_{eq}	equivalent capacitor / F
CL	catalyst layer
D	diffusion coefficient through the polymer membrane / $cm^2\ s^{-1}$
$D_{O2}^{PBI\text{-}H3PO4}$	oxygen diffusion through ionomer / $cm^2\ s^{-1}$
D_{ij}^{eff}	the effective binary diffusion / $cm^2\ s^{-1}$
D_{ij}	binary diffusion / $cm^2\ s^{-1}$
DS	degree of sulfonation / %
$D`_{O2}$	oxygen diffusion through porous structure / $cm^2\ s^{-1}$
D_{O2}	oxygen diffusion through electrolyte thin film / $cm^2\ s^{-1}$
D_F	the fractal dimension
E_c or E_a	activation energy / kJ $mole^{-1}$
E^0_{rev}	standard cell reversal potential / V
E_{rev}	cell reversal potential / V
ESA	Electrochemical surface area / $m^2\ g^{-1}$
F	Faraday constant / coulomb $mole^{-1}$
f	frequency / Hz
f	the heterogeneity factor
ΔG^0	standard Gibbs free energy of a reaction / kJ the Gibbs free energy for O_2H radicals adsorption at coverage θ / kJ
ΔG_θ	the Gibbs free energy for O_2H radicals adsorption at zero coverage / kJ
GDL	gas diffusion electrode
H	Henry's constant for oxygen solubility in the electrolyte m^3 atm $mole^{-1}$
ΔH^0	standard enthalpy of a reaction / kJ enthalpy of adsorption at zero coverage / kJ
ΔH_l^f	the enthalpy of water formation in liquid phase / kJ
ΔH_l^f	the enthalpy of vapour water formation / kJ
ΔH_T^{Vap}	the heat of liquid water vaporisation / kJ
$[H^+]$	(ionized) proton concentration / M
I or i	current / A
I_{charge}	the maximum amount of current available for the charging process / A
i_0	the exchange current density / A $cm^{-2}{}_{Pt}$ (ESA)

i_0^{ref}	the exchange current density at reference temperature / A cm^{-2}_{Pt}
$i_{cross-over}$	cross-over current (rate) / A cm^{-2} (geometric)
i_0^{CO}	the exchange current density for hydrogen oxidation after CO poisoning / A cm^{-2}_{Pt}
Δi	perturbation of current / A (AC)
j_{lim}	limiting current density / A cm^{-2} (geometric)
j	current density / A cm^2 (geometric) the imaginary number
j_0	the reference current density /A cm^{-2} (geometric) current density at time zero (transient) /A cm^{-2} (geometric)
K	Partition coefficient Mark-Houwink equation constant current-time transient response gain, is equal to j_0-j_L /A cm^{-2} (geometric) constant (0.85) relates to change of coverage with pH and potential / V^{-1}
K_{a1}	equilibrium constant of first proton ionization (acid)
K_0	the adsorption equilibrium constant of adsorption at zero coverage
k_2	reaction rate constant / mol dm^{-3} s^{-1}
k	the adsorption rate constant / mol dm^{-3} s^{-1}
L_c	the catalyst loading, weight of platinum per unit area / g cm^{-2}
L	membrane thickness / m length of electrolyte thin film / m inductance / Henry capacitor electrodes separation distance / m
M	the molecular weight of the gas / g $mole^{-1}$
M_n	number average molecular weight
M_w	weight average molecular weight / Da
M_i	molecular weight of polymer molecule/ Da
M_{H3PO4}	the mass of acid per unit area / mg cm^2 (geometric)
M_{PBI}	the mass of PBI per unit area (PBI loading) / mg cm^2 (geometric)
MPL	micro porous layer
N_i	the molar flux of species i / mole s^{-1} cm^{-2} (geometric) numbers of polymer molecules with molecular weight M_i
N_{O2}	oxygen flux (per unit area) / mole s^{-1} cm^{-2}
n	number of electrons involved in the reaction
P_{O2}	oxygen partial pressure / atm

P_{Cat}	oxygen partial pressure at the catalyst surface / atm
$P_{channel}$	oxygen partial pressure at the channel / atm
P_c	the gas critical temperature and pressure / atm
P^0_{O2}	the reference standard oxygen partial pressure (unity) / atm
P^0_{H2}	the reference standard hydrogen partial pressure (unity) / atm
P^*_{H2O}	the saturation vapour pressure of pure water at given temperature / atm
PRU	number of doped acid molecules per repeat polymer unit
Q_H	charge associated with under potential hydrogen adsorption-desorption / coulomb
Q_t	the total amount of diffusing species through unit area / mole s^{-1} cm^{-2}
Q_{mass}	diffusion capacitor / F
q	the rate of change (decrease) of free energy of adsorption with coverage
R	gas constant / J K^{-1} mol^{-1}
R^{Δ}_{ac}	kinetic activation loss resistor / ohm
R^{Δ}_{mass}	mass transport losses resistor / ohm
RH	relative humidity / %
R_{tot}	total equivalent resistor / ohm
R_s	Electron/proton transport resistance / ohm
R_{ads}	adsorption losses resistor / ohm
R_d	mass transport losses resistor / ohm
r	the numbers of electrons transferred in the rate-determining step
S	membrane area (for methanol flux) / cm^2 (geometric)
S_c	the specific surface area of carbon per unit area / dimensionless
S_{Pt}	the specific surface area of Platinum per unit area / dimensionless
S_A	the surface area / m^2 g^{-1}
ΔS^0	the standard entropy of a reaction / J K^{-1} entropy of adsorption at zero coverage / J K^{-1}
s	the numbers of electrons transferred in steps preceding the rate-determining step
T	temperature / K
T_C	the time required to charge the double layer / s
T_c	gas critical temperature / K
T_{ref}	the reference temperature where i_0^{ref} is measured / K

t_0	permeability time lag / s
t	time / s
U_{cell}	cell potential / V
V	potential versus SHE / V
V_{charge}	the amplitude of a voltage step (charge capacitor) / V
W	phosphoric acid weight concentration / wt %
X_i	the molar fraction of species i
X	phosphoric acid molar concentration / mole %
Y_0	the admittance / F s^{n-1}(or ohm^{-1})
Z'	the real part of the impedance / ohm
Z''	the imaginary part of the impedance / ohm
Z_d	diffusion impedance / ohm
Z_{polar}	the resistor used to polarise the cell / ohm
$Z_{observed}$	the observed (measured) impedance by the instrument (due to perturbation) / ohm
z	number of electrons involved in a reaction

Greek Symbols

α	transfer coefficient diffusion current decay time-dependence ($t^{-\alpha}$)
α_a& α_c	transfer coefficient for anodic and cathodic reactions
α_{H2O}	the water activity
α^0_{H2O}	the reference standard water activity (unity)
β	symmetry factor
β_H	the enthalpic components of the overall symmetry factor
β_S	the entropic components of the overall symmetry factor
γ	the pressure coefficient or the reaction order geometrical factor
δ	average ionomer film thickness covering a catalyst particle / m
δ`	length of the porous path / m
ε	the porosity / % the dielectric constant of the electrolyte / F m^{-1}

ε_0	the dielectric constant of the vacuum / F m^{-1}
η	overpotential / V
η_a	anode overpotential / V
η_c	cathode overpotential / V
$\eta_{cross\text{-}over}$	cross over potential loss / V
η_{ac}	kinetics overpotential loss / V
η_{mass}	mass transport overpotential loss / V
$\Delta\eta$	perturbation of potential / V (AC)
$\eta_{inherent}$	inherent viscosity / dl g^{-1}
$[\eta]$	intrinsic viscosity / dl g^{-1}
θ	the total coverage of all O_2H radicals the phase angel between voltage and current / °
θ_{CO}	the surface coverage by CO
θ_0	constant (0.65) intercept at zero coverage
θ_T	coverage of all adsorbed specie (impurities & O_2H radicals)
λ	geometrical factor
υ	the stoichiometric coefficient (or number)
ρ	the density / g cm^3
σ	conductivity / S cm^{-1} mass transfer coefficient / m s^{-1}
τ	the tortuosity the response time constant / s
τ_c	the charge transfer time constant / s
τ_d	diffusion time constant / s
φ	the volume fraction
ω	the angular frequency / s^{-1} (rad s^{-1})
ω_{max}	angular frequency corresponds to max of impedance arc / s^{-1} (rad s^{-1})

1 Introduction and objectives

1.1 Overview

Proton exchange membrane Fuel Cells (PEMFC) have been considered as a suitable alternative to internal combustion engines because of their high power density, high-energy conversion efficiency and low emission level. However the current Proton Exchange Membrane Fuel Cell technology suffers several limitations. These limitations are due to the inherent difficulties of hydrogen production, purity, distribution and storage, and secondly a function of the membrane upon which the technology has been based thus far. For membrane materials such as Nafion®, and similar to perform as highly effective proton conducting materials, they need to be fully hydrated during operation and therefore operate at temperatures lower than 80 °C. Such a limitation in operating temperature results in several technical problems, which have delayed commercialization and require costly solutions.

With current PEMFCs; decreased catalytic activity and increased sensitivity to poisonous species such as sulphur and carbon monoxide [1], capable of deactivating catalyst materials, are significant at low temperatures. The operating conditions dictate that noble metal catalysts and high cost polymer membranes are required [2], along with complex system construction and operation with respect to water and thermal management [3]. Further challenges for technology development include: fuel supply, low value of heat energy [4], low overall efficiency (~30%), limited co-generation of heat and power for stationary applications and poor integration with hydrogen fuel supply systems (reformers) [5].

Developments of High Temperature PEMFC technology will doubtless aid in the rapidly growing area of alternative fuels for fuel cells [6]. Direct use of methanol and ethanol is an option for many fuel cell applications, since elimination of the fuel pre-processors for reforming and CO removal is desirable [7]. However, direct ethanol fuel cell technology is far from satisfactory as anode catalysis is not sufficiently active at temperatures below 100 °C. High temperature operation will improve the overall fuel cell performance and allow the use of renewable and sustainable carbon neutral fuels.

The solution to improved PEMFCs technology is to develop a new polymer electrolyte membrane which exhibits stability and high conductivity in the absence of liquid water. Many different types of alternative high-temperature polymer electrolyte membranes have been studied [8-10]. One of the most promising is acid-doped poly [2,2-(m-phenylene)-5,5 bibenzimidazole] known as PBI. Polybenzimidazole (PBI) is a relatively low cost ($70-100/lb) non-perfluorinated basic polymer (pK_a = 5.5) easily doped with strong acids to form single phase polymer electrolyte [11, 12]. PBI was firstly proposed by Aharoni and Litt [13] and later demonstrated by Savinell, Wainright et al [14, 15] as a polymer electrolyte in its acid doped form.

Savadogo and Xing [16] compared the conductivity of PBI membranes doped in various acids, and found that the conductivity changes are in the order of H_2SO_4 >H_3PO_4 > $HClO_4$ > HNO_3 > HCl for high doping levels. While PBI films are not stable (dissolve) in hot concentrated sulphuric acid, phosphoric acid offers many advantages over the other studied acids at elevated temperature, including: excellent thermal, chemical and electrochemical stability at the operating conditions of fuel cells [17] and low volatility at temperatures above 150°C.

PBI membranes, when doped with phosphoric acid, do not rely on hydration for conductivity; a significantly lower water content of the membrane, compared to Nafion, is required for proton transport. The resulting system improvements include:

- High CO tolerance: Li et al [1] report a CO tolerance of 3% CO in hydrogen at current densities of 0.8 A cm^{-2} at 200 °C and 0.1% CO in hydrogen at 125 °C and current densities lower than 0.3 A cm^{-2}, where CO tolerance is defined by a voltage loss less than 10 mV. Samms et al [3] similarly reported CO tolerance of 1% at 170 °C.
- Simple thermal and water management, excellent oxidative and thermal stability [11].
- Good proton conductivity at elevated temperatures: Acid-doped PBI has a very good proton conductivity and thermal stability at temperatures up to 200 °C [5, 15, 18-20].
- Near zero electro-osmotic drag [21]: which means that the proton transport through the PBI membrane does not involve water transport.
- Low gas permeability [22] and methanol crossover [23, 24].

- Excellent oxidative and thermal stability and good mechanical flexibility at elevated temperature up to 200 °C [25].
- More effective cooling of the cell stacks and provides a means for combined electrical and heat energy generation [4].

1.2 Limitations

Two issues associated with phosphoric acid in the PBI based fuel cell are the lower activity of the electrocatalysts and the potential loss of the acid into the fuel cell gas/vapour exhaust streams. The limited oxygen permeability and slow oxygen reduction kinetics in phosphoric acid (phosphates and impurities within adsorb on platinum) is a major limitation for the performance of PBI based PEMFCs.

1.3 Project Objective

The aim of this research is the design, fabrication, electrochemical testing and evaluation of electrodes for phosphoric acid doped PBI high temperature PEMFCs.

The research program was comprised of the following goals:

- Synthesis and characterisation of PBI polymer and films, as they are no longer available commercially for fuel cell research.
- Obtain kinetic and mass transport information on oxygen reduction at PBI/H_3PO_4 interface by testing several electrodes' performance in three-electrode cell.
- Fabricate HT-PEMFCs membrane electrode assemblies and compare and optimise their performances from the collected polarisation curves.
- Utilise other electrochemical techniques such as frequency response analysis and chronoamperometry to provide further information about electrode performance.
- Test system tolerances to CO/CO_2 in order to estimate the system performance under reformate.

- Investigation of methanol as an alternative anode fuel for HT-PEMFCs.
- Development of a simple one dimensional model for PBI fuel cell allowing increase understanding of their behaviour, enable prediction of their performance and assist with their operational control.

This thesis is divided into eight chapters.
In Chapter 1, an overview of high temperature fuel cell with a focus on PBI based is presented.

Chapter 2, describes PBI and other high temperature polymers synthesise and characterisation in terms of proton conductivity, methanol cross-over and mechanical properties.

Chapter 3, describes half cell tests (three electrode cell) used to obtain kinetics information regarding oxygen reduction reaction in PBI/phosphoric acid interface. The three phase boundaries are also discussed and the effect of ionomer properties (permeability, density & conductivity) and content in the catalyst layer are investigated.

Chapter 4, data from several fuel cells is presented and discussed. The effects of catalyst thickness (Pt:C ratio), PBI, acid & catalyst loading, and binder/electrolyte materials; for both anode and cathodes are investigated along with CO/CO_2 tolerance.

In Chapter 5, data from a three electrode cell is discussed for methanol oxidation in phosphoric acid/PBI interface. High temperature direct methanol fuel cells are also fabricated and analysed.

In Chapter 6, chronoamperometry data is presented to establish the contribution of mass transport on system performance. EIS (electrochemical impedance spectroscopy) is also used to provide further information about electrodes structure and effect on the overall cell performance. A simplified circuit model is built and an attempt is made to relate the circuit components to the physical phenomenon taking place at the electrode surface in terms of kinetics, mass transport and IR losses.

In Chapter 7, one dimensional isothermal fuel cell model is developed. The model is used to simulate the influence of operating condition, cell parameters and different fuel gas compositions on the cell voltage current density characteristics.

In Chapter 8, conclusions of the study are presented which form the basis for the recommendations for future work.

Due to the diversity of the chapters' topics, the relevant literature reviews are provided separately for each chapter.

1.4 References

1. Li, Q.F., R.H. He, J.A. Gao, J.O. Jensen, and N.J. Bjerrum, *The CO poisoning effect in PEMFCs operational at temperatures up to 200 degrees C.* Journal of the Electrochemical Society, 2003. **150**(12): p. A1599-A1605.
2. Li, Q., J.O. Jensen, R. He, G. Xiao, J.A. Gao, R.W. Berg, H.A. Hjuler, H. Hennesoe, and N.J. Bjerrum, *Acid-Doped Polybenzimidazole Membranes as Electrolyte for Fuel Cells Operating Above 100 °C.* Recent Research Developments in Electrochemistry, 2003. **6**: p. 1-26.
3. Samms, S.R. and R.F. Savinell, *Kinetics of methanol-steam reformation in an internal reforming fuel cell.* Journal of Power Sources, 2002. **112**(1): p. 13-29.
4. Li, Q.F., R.H. He, J.O. Jensen, and N.J. Bjerrum, *Approaches and recent development of polymer electrolyte membranes for fuel cells operating above 100 degrees C.* Chemistry of Materials, 2003. **15**(26): p. 4896-4915.
5. Li, Q.F., R.H. He, R.W. Berg, H.A. Hjuler, and N.J. Bjerrum, *Water uptake and acid doping of polybenzimidazoles as electrolyte membranes for fuel cells.* Solid State Ionics, 2004. **168**(1-2): p. 177-185.
6. Scott, K. and A.K. Shukla, *Direct Methanol Fuel Cells: Fundamentals, Problems and Perspectives.*, in *Modern aspects of electrochemistry V.40*, R.E. White, Editor. 2007, Springer: New York.
7. Scott, K., A.K. Shukla, C.L. Jackson, and W.R.A. Meuleman, *A mixed-reactants solid-polymer-electrolyte direct methanol fuel cell.* Journal of Power Sources, 2004. **126**(1-2): p. 67-75.
8. Jones, D.J. and J. Roziere, *Recent advances in the functionalisation of polybenzimidazole and polyetherketone for fuel cell applications.* Journal of Membrane Science, 2001. **185**(1): p. 41-58.
9. Savadogo, O., *Emerging membranes for electrochemical systems - Part II. High temperature composite membranes for polymer electrolyte fuel cell (PEFC) applications.* Journal of Power Sources, 2004. **127**(1-2): p. 135-161.
10. Roziere, J. and D.J. Jones, *Non-fluorinated polymer materials for proton exchange membrane fuel cells.* Annual Review of Materials Research, 2003. **33**: p. 503-555.
11. Wang, J.T., R.F. Savinell, J. Wainright, M. Litt, and H. Yu, *A H-2/O-2 fuel cell using acid doped polybenzimidazole as polymer electrolyte.* Electrochimica Acta, 1996. **41**(2): p. 193-197.
12. Fontanella, J.J., M.C. Wintersgill, J.S. Wainright, R.F. Savinell, and M. Litt, *High pressure electrical conductivity studies of acid doped polybenzimidazole.* Electrochimica Acta, 1998. **43**(10-11): p. 1289-1294.
13. Aharoni, S.M. and M.H. Litt, *Synthesis and some properties of poly-(2,5-trimethylene benzimidazole) and poly-(2,5-trimethylene benzimidazole hydrochloride.* Journal of Polymer Science: Part A, 1973. **12**(3): p. 639 - 650.
14. Wainright, J.S., J.T. Wang, R.F. Savinell, M. Litt, H. Moaddel, and C. Rogers. *Acid doped polybenzimidazoles, a new polymer electrolyte.* in *Proc. Electrochem. Soc.* 1994.
15. Wainright, J.S., J.T. Wang, D. Weng, R.F. Savinell, and M. Litt, *Acid-Doped Polybenzimidazoles - a New Polymer Electrolyte.* Journal of the Electrochemical Society, 1995. **142**(7): p. L121-L123.

16. Xing, B.Z. and O. Savadogo, *The effect of acid doping on the conductivity of polybenzimidazole (PBI).* Journal of New Materials for Electrochemical Systems, 1999. **2**(2): p. 95-101.
17. Kinoshita, K., *Electrochemical oxygen technology* 1992, New York: Wiley.
18. Ma, Y.L., J.S. Wainright, M.H. Litt, and R.F. Savinell, *Conductivity of PBI membranes for high-temperature polymer electrolyte fuel cells.* Journal of the Electrochemical Society, 2004. **151**(1): p. A8-A16.
19. Samms, S.R., S. Wasmus, and R.F. Savinell, *Thermal stability of proton conducting acid doped polybenzimidazole in simulated fuel cell environments.* Journal of the Electrochemical Society, 1996. **143**(4): p. 1225-1232.
20. Scott, K. and M. Mamlouk, *High temperature polymer electrolyte membrane fuel cell.* Battery Bimonthly, 2006. **36**(5): p. 11.
21. Weng, D., J.S. Wainright, U. Landau, and R.F. Savinell, *Electro-osmotic drag coefficient of water and methanol in polymer electrolytes at elevated temperatures.* Journal of the Electrochemical Society, 1996. **143**(4): p. 1260-1263.
22. Li, Q.F., H.A. Hjuler, and N.J. Bjerrum, *Phosphoric acid doped polybenzimidazole membranes: Physiochemical characterization and fuel cell applications.* Journal of Applied Electrochemistry, 2001. **31**(7): p. 773-779.
23. Pu, H.T. and Q.Z. Liu, *Methanol permeability and proton conductivity of polybenzimidazole and sulfonated polybenzimidazole.* Polymer International, 2004. **53**(10): p. 1512-1516.
24. Wang, J.T., S. Wasmus, and R.F. Savinell, *Real-time mass spectrometric study of the methanal crossover in a direct methanol fuel cell.* Journal of the Electrochemical Society, 1996. **143**(4): p. 1233-1239.
25. Wang, J.T., W.F. Lin, M. Weber, S. Wasmus, and R.F. Savinell, *Trimethoxymethane as an alternative fuel for a direct oxidation PBI polymer electrolyte fuel cell.* Electrochimica Acta, 1998. **43**(24): p. 3821-3828.

2 Preparation of High Temperature Membranes

In this chapter, PBI and SPEEK polymers were synthesized and characterized in terms of degree of sulfonation using ^{1}H-NMR (SPEEK), molecular weight distribution, using GPC (PBI) and chemical structure using FTIR (PBI).

Membranes were later prepared either directly from the synthesised polymers or with composite materials (TiO_2). The prepared membranes were characterized in terms of their mechanical properties (tensile stress), methanol permeability and proton conductivity.

2.1 Introduction

In the recent years research has been carried out trying to develop ionically conducting polymer electrolyte membranes that operate at temperatures above 100 °C. According to the proton conduction mechanism, these membranes can be classified in to three main groups [1]:

Sulfonated polymers: where the polymer is modified by bonding acidic groups (such as sulfonic group SO^{-3}) onto the backbone as side chain, making it exhibit ionic conductivity. Most common candidates that exhibit good thermal and chemical stability are: flouropolymers (Nafion), silicon-based (polysiloxanes) or aromatic hydrocarbons such as polybenzimidazoles (PBI), polyetheretherketone(PEEK) and polysulfones (PSF).

Inorganic-organic composite: this is usually obtained by incorporating solid inorganic proton conductors such as zirconium phosphates or hetropolyacids into a polymer matrix, which can be functionalised (ionic conductive) or not. Incorporating hygroscopic nano-crystalline oxides such as TiO_2 or SiO_2 into functionalized polymer matrix, helps in retaining water, increasing the operating temperate limit.

Acid-base polymer complexes: polymers (amide, ether or alcohol) have basic properties (hold basic sites) and as such can easily react with strong acids by establishing hydrogen bonds in acid-

base complex systems, this in some cases can lead to the formation of blend membranes between a polymer, exhibiting acidic properties, and another exhibiting basic properties, such as polybenzimidazole (basic)-sulfonated polyetheretherketone (acidic) blend [2]. Another good example of acid-base complexes is phosphoric acid doped PBI; PBI exhibits good thermal and mechanical properties arising from the presence of three benzene rings in the polymer backbone while phosphoric acid offers excellent thermal, chemical and electrochemical stability accompanied by low volatility under fuel cell operating conditions, at temperatures above 150 °C.

Among the three main groups, three candidates were selected for investigation in this research:

i. Sulfonated polyetheretherketone, a much cheaper to produce polymer compared to solfonated flouro polymers.
ii. Phosphoric acid doped polybenzimidazole, a promising acid-base complex that exhibits good proton conductivity at elevated temperatures.
iii. Titania based composite membranes using SPEEK, acid doped PBI and Nafion as polymer materials.

2.2 Polymers Synthesis

2.2.1 Sulfonated polyether-ether-ketone (S-PEEK) polymer synthesis

Polyether-ether-ketone is a class of polymers consisting of sequences of ether and carbonyl linkages between phenyl rings. PEEK is commercially available under the name of Victrex® PEEK™ (ICI advanced materials, U.K). PEEK is a high performance thermoplastic material with excellent friction and wear properties, high stability at elevated temperatures (T_g 143-145 °C and T_m 340 °C), excellent resistance to wide range of chemical environment and good electrical properties over wide range of frequency and temperature. However, PEEK is similar to PBI in the fact that its proton conductivity as pristine materials is very low (less than 10^{-4} S cm^{-1}) and requires function groups to facilitate proton conduction. While in the case of PBI, there is a

maximum of two sites available for the acid to bond to, any excess acid will be mobile in the polymer matrix; Poly-aryl-ether-ketones can be sulfonated directly by reacting it with concentrated sulphuric acid [3], or prepared indirectly from sulfonated monomers [4]. The level of sulfonation is dependant on the number of aromatic rings bridged by oxygen atoms (Fig. 2-1), as only O-phenyl-O units can be sulfonated, while O-phenyl-CO groups remains un-sulfonated. Therefore, increasing the number of ether groups relative to carbonyl groups leads to an increase in the available number of sulfonation sites on the polymer backbone.

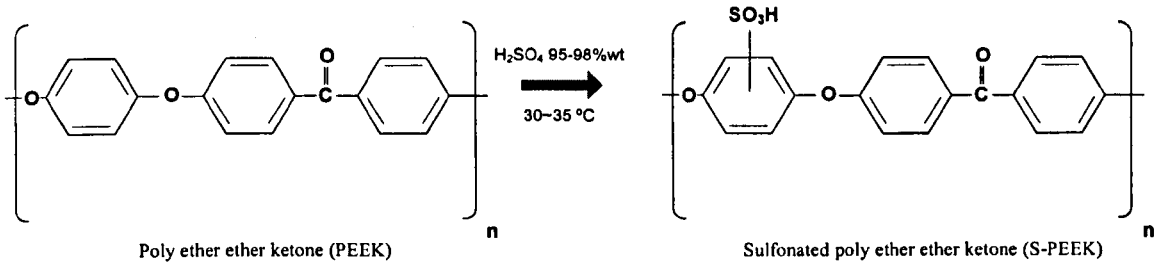

Figure 2-1. Direct synthesis of polyetheretherketone.

A wide range of equivalent weights can be obtained from the direct sulfonation of PEEK depending on the reaction conditions; the substitution with sulfonic groups is Ortho directed due to the high activity of the four equivalent sites [5] in the hydroquinone unit between the ether segments. The extent of sulfonation is a function of:

Temperature: At room temperature (22 °C), the IEC increases slowly with sulfonation time and almost reaches a plateau at about 1.7 (mEq g^{-1}), at higher temperature (e.g., 55 °C), the IEC increases sharply, the first-type substitution (2.56 mEq g^{-1}) nearly comes to an end in about 5 hrs, then surpasses this value, which corresponds to 100% Ortho substitution. This implies that another type of substitution has been initiated at higher temperature (55 °C), in other words, more than one sulfonic group has been attached to one repeating unit of PEEK [6].

Sulphuric acid concentration: increasing the concentration above 98% (100%) leads to cross-linking due to sulphone formation [7].

Reaction time: as mentioned above the reaction time affects the sulfonation degree, depending on the reaction temperature. To achieve 100% Ortho substitution can take up to 700 hrs at room temperature [8] and 5 hrs at 55 °C [6]. However the initial PEEK to acid ratio does not affect the progress of the reaction [9].

2.2.2 Polybenzimidazole polymer synthesis

Brinker and Robinson disclosed the synthesis of aliphatic polybenzimidazole in 1959 [10]. Two years later, Vogel and Marvel [11] were the first to prepare poly[2,2'-m-(phenylene)-5,5'-bibenzimidazole] from 3-3'-diaminobenzidine and aromatic dibasic acids at temperatures 200-350 °C.

Iwakura et al [12] prepared polybenzimidazoles from 3-3'-diaminobenzidine hydrochloride (DAB) and isophthalic acid (IPA) in poly-phosphoric acid (PPA) by solution poly-condensation at temperatures between 170-200 °C, according to the reaction below (Fig. 2-2). Offering lower reaction temperature and homogeneous solution polymerization, however, the proposed reaction has a major disadvantage arising from the necessity of working at low solid content (3-5 %) and therefore the recovery and re-use of Poly-phosphoric acid.

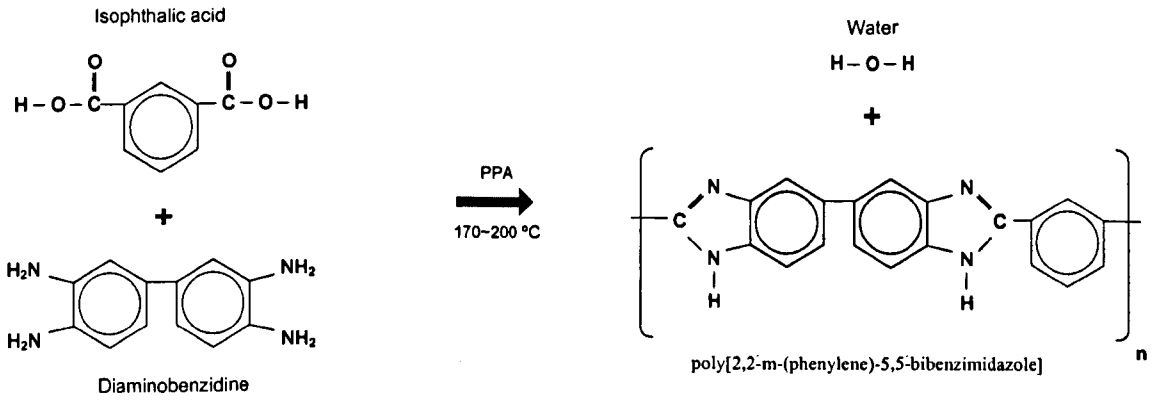

Figure 2-2. Synthesis of polybenzimidazole using solution poly-condensation route.

The most practical process for an engineering scale is the solid-state polymerization. Plummer and Marvel used melt polymerization to produce Polybenzimidazoles [13] following pioneering work by Vogel and Marvel [14], starting from diaminobenzidine (DAB) and diphenyl isophthalate (DPIP) according to the reaction below (Fig. 2-3):

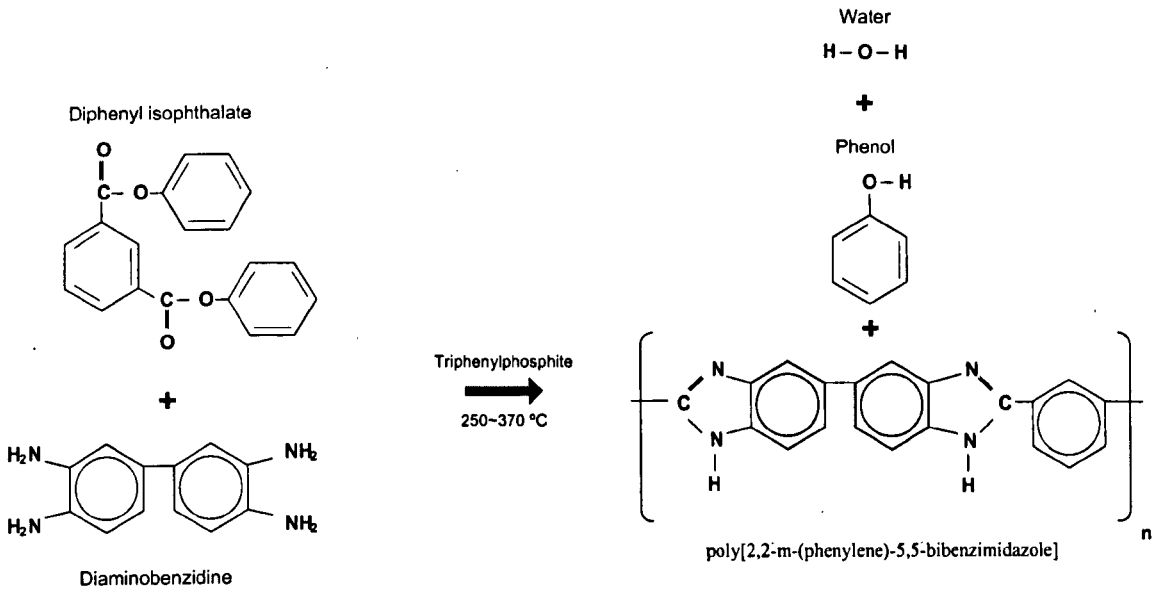

Figure 2-3. Synthesis of polybenzimidazole using melt polymerisation route.

The synthesis typically involves two stages: Initial heating:, melt polymerization at temperatures 200-300 °C until a pre-polymer with inherent viscosity of 0.13-0.3 dl g^{-1}, on average takes 0.5 to 3 hours [15]. This is followed by a second step, where the polymer is powdered and reheated to 390-400 °C for a period 1.5-3 hours increasing the molecular weight of the polymer and consequently its inherent viscosity [16].

Hedberg and Marvel [17] demonstrated a single stage reaction similar to the poly-condensation reaction; however, they have substituted PPA with sulfolane, which is easily recovered by distillation.

Foster and Marvel [18] suggested replacing DAB with Benzophenone-3,3',4,4'-tetracarboxylic dianhydride (BTDA) to obtain more soluble polymeric products.

Recently, Kim et al [19] and Shin et al [20], prepared a new precursor to prepare polybenzimidazoles utilizing a new synthesis route at low temperatures.

Polymer prepared with both methods exhibit inherent viscosities in the range of 0.6-0.8 dl g^{-1} when measured as 0.4 g of PBI in 100 cm^3 of 97 % sulphuric acid at 25 °C in glass capillary viscometer.

$$\eta_{inherent} = I.V. = \frac{Ln[flow\,time\,of\,solution / flow\,time\,of\,solvent]}{Solution\,concentration\,in\,(g\,dl^{-1})} \qquad [1]$$

To be able to obtain membranes with good mechanical properties from polybenzimidazole (PBI) polymer, the polymer should have an inherent viscosity from 0.8 to 1.1 dl g^{-1} [21].
The intrinsic viscosity is obtained from the inherent viscosity [22] using the equation:

$$[\eta] = 1.0585\eta_{inherent} \qquad [2]$$

The intrinsic viscosity directly depends on the molecular weight of the studied polymer [22, 23]; the Mark-Houwink equation describes this dependence:

$$[\eta] = K M_w^a \qquad [3]$$

Where [η] is the intrinsic viscosity, K and a are constants the values of which depend on the nature of the polymer and solvent as well as on temperature and M_w is the average molecular mass.
Values for $K = 1.35326 \times 10^{-4}$ & $a = 0.73287$ were given [22, 23] for a molecular weight range of 2.1 to 1800 kDa. Other value for $K = 3 \times 10^{-4}$ & $a = 0.75$ were given [24] over a narrower range of 7 to 51 kDa (Fig. 2-4). The erliear values from [22, 23] were used in this study due to their validity over wider range of molecular weight and the good agreement with the values obtained using Gel Permeation Chromatography (GPC) for molecular weight distribution analysis.

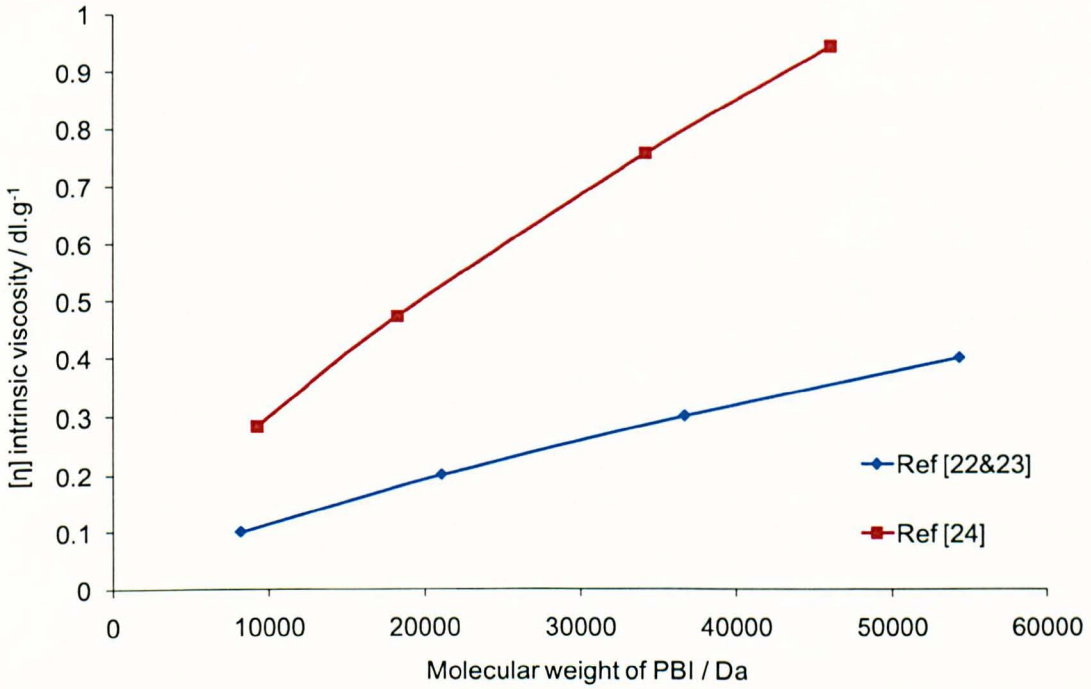

Figure 2-4. Molecular weight & intrinsic viscosity relation using Mark-Houwink equation.

Polymer with higher molecular weights can be achieved, by either altering the reaction conditions, such as the monomer ratio or addition of catalyst or by extracting high molecular weight material from the polymer using an appropriate solvent (fractionating) [25]. The latest was used by Case Western University to obtain high molecular weight PBI from commercial powder [26]. Several catalysts have been suggested for PBI synthesis, most of which are phosphorus based [27, 28]; such a catalyst was used for the melt polymerization route with one stage or two stages [15, 22]. Similarly, in the poly-condensation route, poly-phosphoric acid is used as solvent, with or without the addition of P_2O_5 as catalyst.

Other suggested catalysts are arylhalo phosphorus based [23], organosilicon halide based [29], tin based [30] and aryl phosphonic based [31].

More recently, Choe [32] studied several phosphorus based catalyst and monomers for PBI production using melt polymerization; among several catalysts studied, dichlorophenylphosphine gave superior results, leading to PBI with an inherent viscosity of 1.5

dl g^{-1} with an optimum concentration around ~1% wt based on the weight of DPIP or IPA depending on which monomer was used for the synthesis.

For the lab scale production in this research, the poly-condensation route using PPA was more favourable over the solid state route, due to the following difficulties encountered in the solid state reaction:

- Monomers used in solid-state reactions are very sensitive to oxygen, so the reactor has to be degassed several times and purged continuously with nitrogen during the reaction, or operated under high vacuum conditions.
- Adhesion of polymer product to the reactor walls.
- Melted ionomers without solvent have very high viscosity make the mixing very difficult.
- Poor thermal conductivity of the ionomers and the polymer product, lead to slow heat transfer from reactor walls to the reacting core.

In order to enhance the molecular weight of the prepared polymer a small quantity of dichlorophenylphosphine (1.5%wt of IPA) can be added as catalyst during the synthesis process [32]. Even though the suggested catalyst proved to be useful in the melt polymerisation route, no information is available on its effects on the adopted poly-condensation method.

2.3 Experimental

2.3.1 PBI polymer preparation

In the procedure for preparation of PBI, 0.025 moles (5.36 g) of 3-3'-diaminobenzidine (99% Aldrich) was reacted with 0.025 moles (4.15 g) of isophthalic acid ((99% Aldrich) in 311.85 g of poly-phosphoric acid (Aldrich) by solution poly-condensation at temperature of 200 °C.

DAB was first added to PPA, at room temperature, while stirring and purging with nitrogen and 0.063 g (1.5% wt of IPA) of the catalyst dichlorophenylphosphine (97% Aldrich) was then injected. The mixture was then heated to 200 °C under nitrogen, and the IPA was introduced. Initially the mixture colour turned to dark blue/green and after ~30 mins the mixture became purple. This was accompanied by an increase in volume due to formation of bubbles (foam). Even though water vapour (bubbles) formation was rapid, PBI synthesis requires much longer

times as the water evolution is the second most rapid reaction in the condensation after the amine reaction [33]. After 9 hrs the mixture was poured into cold de-ionised water to stop the reaction. PBI was obtained as a yellow precipitate; the precipitate was washed with sodium hydroxide solution, until neutralisation. Further washing with dilute hydrochloric acid was introduced to remove un-reacted monomers. The powder was then immersed in a saturated solution of sodium bicarbonate overnight. Finally, PBI powder was boiled, rinsed thoroughly with de-ionised water, dried and pulverized.

During the synthesis of PBI, addition of catalyst increased the inherent viscosity of the polymer product from 0.8 to 2.4 dl g^{-1}, corresponding to an increase in average molecular weight from 17 to 62 kDa, but also broadened its polydispersity (MWD). For example, when the concentration of dichlorophenylphosphine was increased from 0 to 0.57 to 0.86 %wt (of DPIP) the polydispersity increased from 2.56 to 3 to 3.3, respectively [32]; comparable results were obtained experimentally. Increasing the dichlorophenylphosphine concentration from 0 to 1.5 %wt (of IPA) lead to MWD increase from 2.8 to 4.6.

Two samples from the same PBI batch (using dichlorophenylphosphine as catalyst) were dissolved in DMAc, one at room temperature and the other at 250 °C and their molecular weight distributions were determined. The sample dissolved at room temperature was 100 % soluble, whilst the sample dissolved at 250 °C required filtration to remove approximately 10 %wt of a non-soluble part. The resulting molecular weight distributions are given in Table 2-1 and compared with those of a commercially available PBI and PBI synthesised without catalyst. PBI synthesised using catalyst had a much higher molecular weight. The polymer obtained after dissolving in DMAc at low temperature had a higher molecular weight than that dissolved at 250 °C. The observed reduction in the average molecular weight and narrowed polydispersity, after heat treatment, can be attributed to cross-linking occurring during heat treatment with DMAc, where 10 wt% of the polymer become insoluble. Plummer and Marvel [13] found that polybenzimidazoles prepared from DAB underwent cross-linking when heated above 350 °C where they became insoluble in all known solvents. Similarly, Colson et al [34] prepared polybenzimidazole films starting from DAB, and found that the prepared polymers became

insoluble in common organic solvents after heating above 140 °C (cross linking), especially those exhibiting high inherent viscosity (1 – 1.5 dl g^{-1}).

2.3.2 SPEEK polymer preparation procedure

In the preparation of the polymer, 30 g of oven dried PEEK 450P M_w~39000 Da (Victrex, U.K) was added to 1.5 dm^3 of 95-98% sulphuric acid (Aldrich) in a water jacketed flask under vigorous stirring at room temperature. The temperature was then increased rapidly to 35 °C and after 3 hrs the solution colour became reddish-brown and all the PEEK pellets were dissolved. The temperature was maintained with a water bath equipped with heating/cooling controller (Grant) until the desired reaction time was reached.

To terminate the sulfonation reaction, the solution was poured gently into a large access of ice-cold water under continues mechanical agitation. The creamy-white coloured precipitate (SPEEK) formed was a difficult to filter colloid, which was then separated with centrifuge. The obtained polymer was washed and centrifuged several times until the pH was close to neutral. Finally, the powder was filtered using a 0.2 μm pore size cellulose acetate membrane and dried at 100 °C under vacuum.

2.4 Polymer Characterisations

2.4.1 Sulfonation degree determination using ^{1}H-NMR

The sulfonation degree is given by:

$$DS = \frac{sulfonated\ repeating\ units}{total\ number\ of\ repeating\ units} \times 100\% \qquad [4]$$

^{1}H NMR spectra of SPEEK was used to determine the degree of sulfonation (DS). A 2-5 wt% solution of the SPEEK in DMSO-d_6 (Aldrich) was prepared and measurements were obtained using a Bruker NMR spectroscope.

The presence of sulfonic group causes 0.25 ppm down-field shift in the hydrogen H_E signal (~ 7.5ppm) compared with that of H_C and H_D of the same hydroquinone ring. All the four H_A's signals appear at low field (to the left of H_E) due to the de-shielding effect of the carbonyl group [35]. The intensity of the H_E signal is directly related to the H_E content in the polymer and therefore the degree of sulfonation per repeat unit.

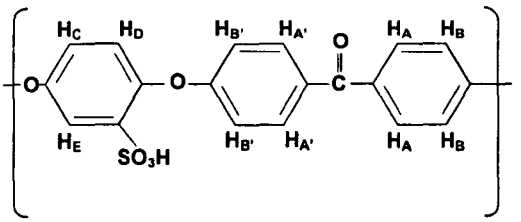

Sulfonated poly ether ether ketone (S-PEEK)

The DS can be derived from the ratio of the area under the H_E peak (AH_E) and sum of the areas of the all the other aromatic hydrogen peaks ($AH_{A,A',B,B',C,D}$) using the equation below [36]:

$$\frac{DS}{12-2DS} = \frac{AH_E}{\sum AH_{A,A',B,B',C,D}} \qquad [5]$$

For example, for an integrated areas (A) under the peak of $H_{A,A'}$, H_E and $H_{B,B',C,D}$ of 5.97, 1 and 9.915, respectively, a sulfonation degree of 67.1% was determined.

Figure 2-5 shows the typical NMR spectra for SPEEK, the increase in the peak intensities can be easily seen with an increase in the sulfonation degree (DS) from 29.05, 49.08, 70.79 & 89.87, respectively.

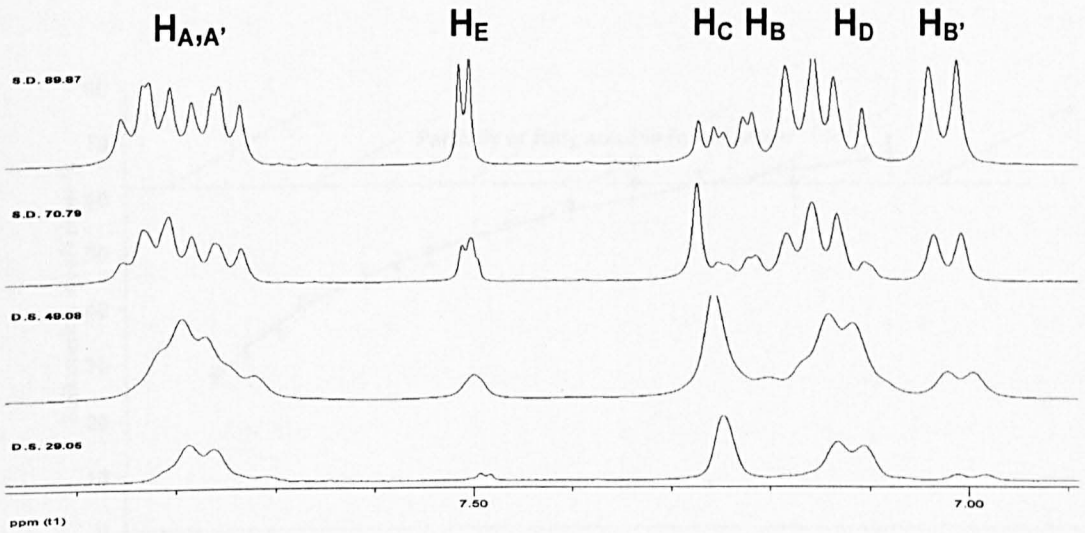

Figure 2-5. ^{1}H-NMR spectra of SPEEK at various sulfonation degrees.

Alternatively, the DS was determined by titration: 1-2 g of SPEEK was placed in 0.5 M sodium hydroxide and left for a day to fully react, the solution was then back titrated using 0.5 M HCl and phenolphthalein as indicator [37]. The titration method was only used to confirm the results obtained from NMR spectroscopy, as it requires large amounts of polymer to carry out the titrations with reasonable accuracy (error ~20%).

Figure 2-6 shows the effect of reaction time on sulfonation degree at the studied reaction temperature of 35 °C, where it can be seen that the sulfonation degree exhibited a logarithmic dependence with reaction time.

Increasing the sulfonation degree lead to an increase in conductivity and on the other hand greater swelling and brittleness. For sulfonation degrees < 30%, SPEEK is insoluble in most organic solvents or water, while for sulfonation degree above 70% the polymer become soluble in methanol and partially soluble in hot water. The complete sulfonation of PEEK leads to fully water soluble polymer [38]. A sulfonation degree around 60% was found to be a good compromise between conductivity and mechanical properties (brittleness and swelling) [39].

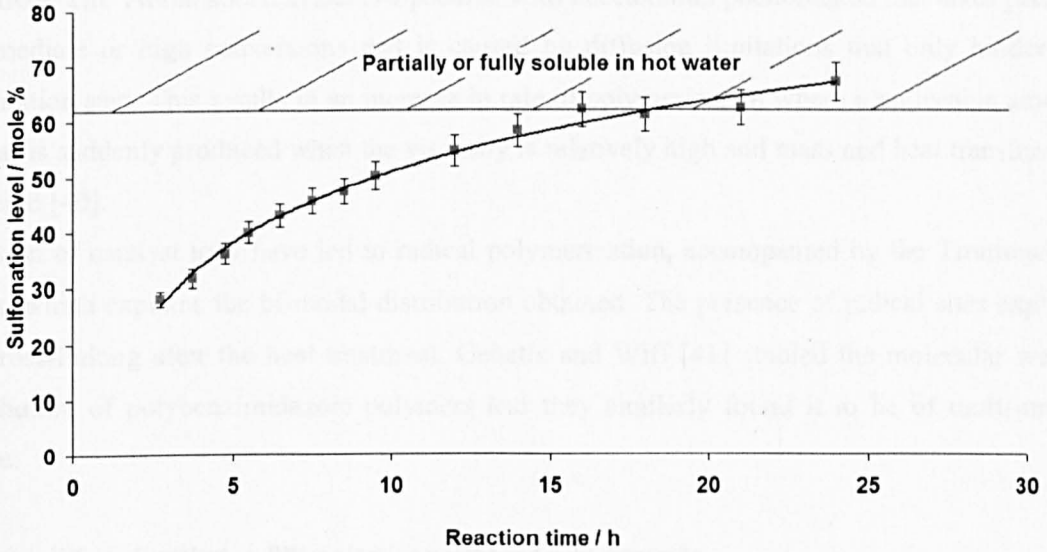

Figure 2-6. Effect of reaction time on sulfonation degree as measured by ^{1}H-NMR.

2.4.2 PBI Molecular weight distribution using GPC

Gel Permeation Chromatography (GPC) was carried out by RAPRA technologies (U.K) using HPLC (Waters model 150C, U.S.A) equipped with PLgel guard plus 2 mixed bed-B columns (30 cm, 10 μm). Prior to tests the system was calibrated with narrow distribution poly(methyl methacrylate) calibrants. The solvent used (for measurements and calibration) was dimethylacetamide (DMAc) with 1 % added lithium chloride as stabilizer.

The nominal flow-rate used was 1.0 mL min^{-1} at operating temperature of 80°C. Refractive index was used as the detection method. Data capture and subsequent data handling was carried out using Viscotek 'Trisec' 3.0 software.

The obtained PBI distribution from GPC with no added catalyst showed a Gaussian normal distribution for narrow distributed batches, whilst with catalyst addition a wide bi-modal or multi-modal distribution (polydispersity) was observed (Fig. 2-7). This behaviour is normally

observed in polymers and particularly in radical polymerization. Either there are two different reaction routes leading to bi-modal distribution or this is a consequence of the Trommsdorff or gel effect. The Trommsdorff effect is a peculiar auto-acceleration phenomenon that takes place at intermediate or high conversions and is caused by diffusion limitations that only hinder the termination step. This results in an increase in rate of polymerization where a noticeable amount of heat is suddenly produced when the viscosity is relatively high and mass and heat transfers are hindered [40].

Addition of catalyst may have led to radical polymerization, accompanied by the Trommsdorff effect, which explains the bi-modal distribution obtained. The presence of radical sites explains the cross-linking after the heat treatment. Gehatia and Wiff [41] studied the molecular weight distribution of polybenzimidazole polymers and they similarly found it to be of multi-modal nature.

Table 2-1. Effect of catalyst on PBI molecular weight and poly-dispersity.

Sample	Mw	Mn	Mw/Mn
Commercial (dissolved)	170,000	65,700	2.6
Liquid form (Aldrich)	171,000	65,400	2.6
Synthesised	186,000	66,500	2.8
without catalyst	179,000	63,000	2.8
Synthesised with catalyst dissolved at	415,000	88,100	4.7
250 °C	412,000	91,900	4.5
Commercial	158,000	57,300	2.6
Powder form (Aldrich)	154,000	58,300	2.6
Synthesised with catalyst dissolved at	623,000	116,000	5.4
room temperature	609,000	112,000	5.4

In Table 2-1 the M_w is the weight average molecular weight given by:

$$M_w = \frac{\sum_i N_i M_i^2}{\sum_i N_i M_i} \qquad [6]$$

M_n is the number average molecular weight given by:

$$M_n = \frac{\sum_i N_i M_i}{\sum_i N_i} \qquad [7]$$

N_i is the number of molecules of molecular weight M_i.

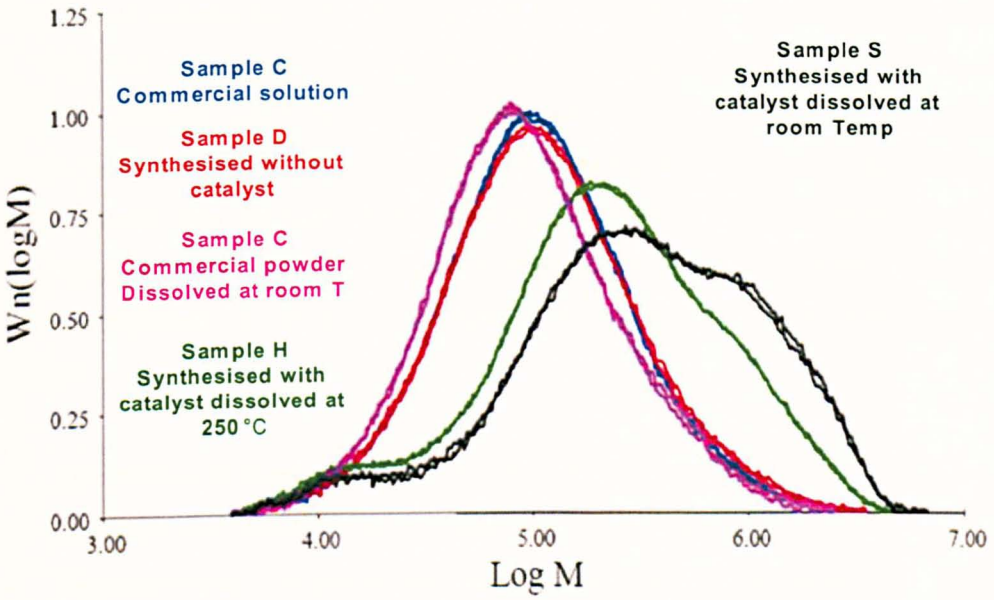

Figure 2-7. Molecular weight distribution using gel permeation chromatography.

2.4.3 PBI Chemical structure using Fourier transforms infrared spectroscopy (FTIR)

The main infrared spectra of PBI have been discussed previously in several publications [42-47]. In this study, the focus was in the range of 2000 to 4000 cm^{-1} where most of the informative N-H stretching modes occur in order to confirm the chemical structure of the synthesised polymer. Below 2000 cm^{-1} the spectrum is characterized by some narrow peaks attributed to localized normal vibrations of the phenyl groups (pristine PBI) [44] and hydrogen bonds between acid anions and the polymer (doped PBI) [48].

The spectra of commercial PBI (Aldrich) and home-made PBI are compared in both film form (Fig. 2-9) and in powder form mixed with KBr (Fig. 2-8). The obtained spectra of the synthesised polymer match that of the commercial material very closely. The results obtained from the powder samples were sharper, with clearer peaks, unlike the spectra from the film samples. Spectra from the KBr/powder mixture disc shown in Figure 8 did not contain a medium peak at 3615-3618 cm^{-1} corresponding to the stretching of the O-H bond from the absorbed water [46] by the polymer. By observing the spectra in figures 2-8&2-9, the following bands can be identified:

- Isolated free N-H stretching at 3395-3414 cm^{-1}(strong) [44].
- Imidazole and benzene rings overtone at 3185 cm^{-1}(weak) [47].
- Ring associated C-H groups stretching at 3050-3065 cm^{-1}(medium).
- C=C and C=N stretching at 1624-1629 cm^{-1}(very strong).
- Vibration of the Imidazole ring at 1282-1287 cm^{-1}(very strong).
- No DMAc traces were found (no C-H stretching from CH_3 in DMAc at 2940 cm^{-1}).

The bands obtained above confirm the structure of PBI and confirm the presence of the imidazole ring and the three N-H distinguishable bands at 3410, 3145 and 3065 cm^{-1}, which is in very good agreement with the previous reported work on PBI spectra [42-47].

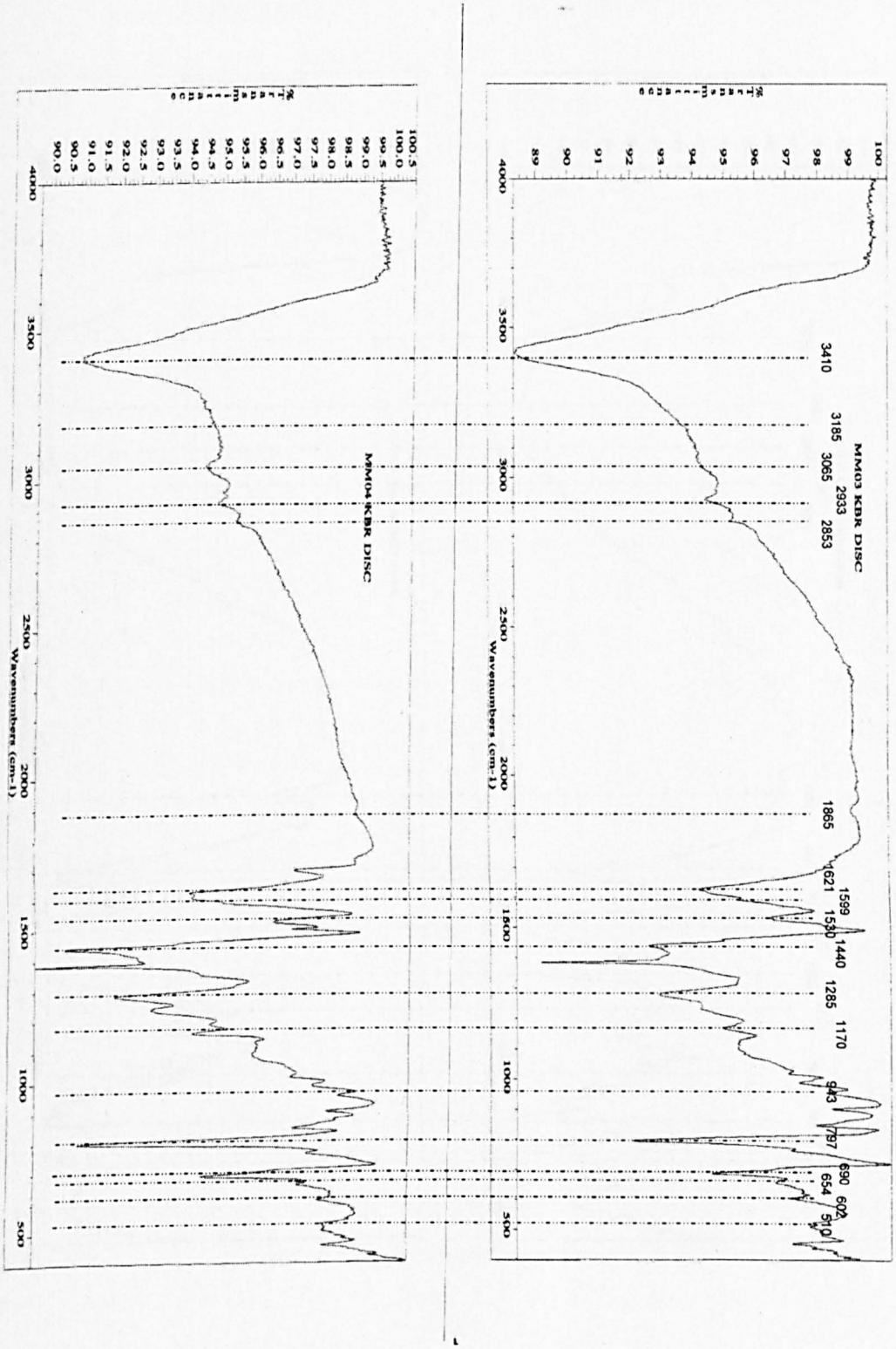

Figure 2-8. FT-IR spectroscopy of PBI KBr discs, MM03 commercial&MM04 home-made.

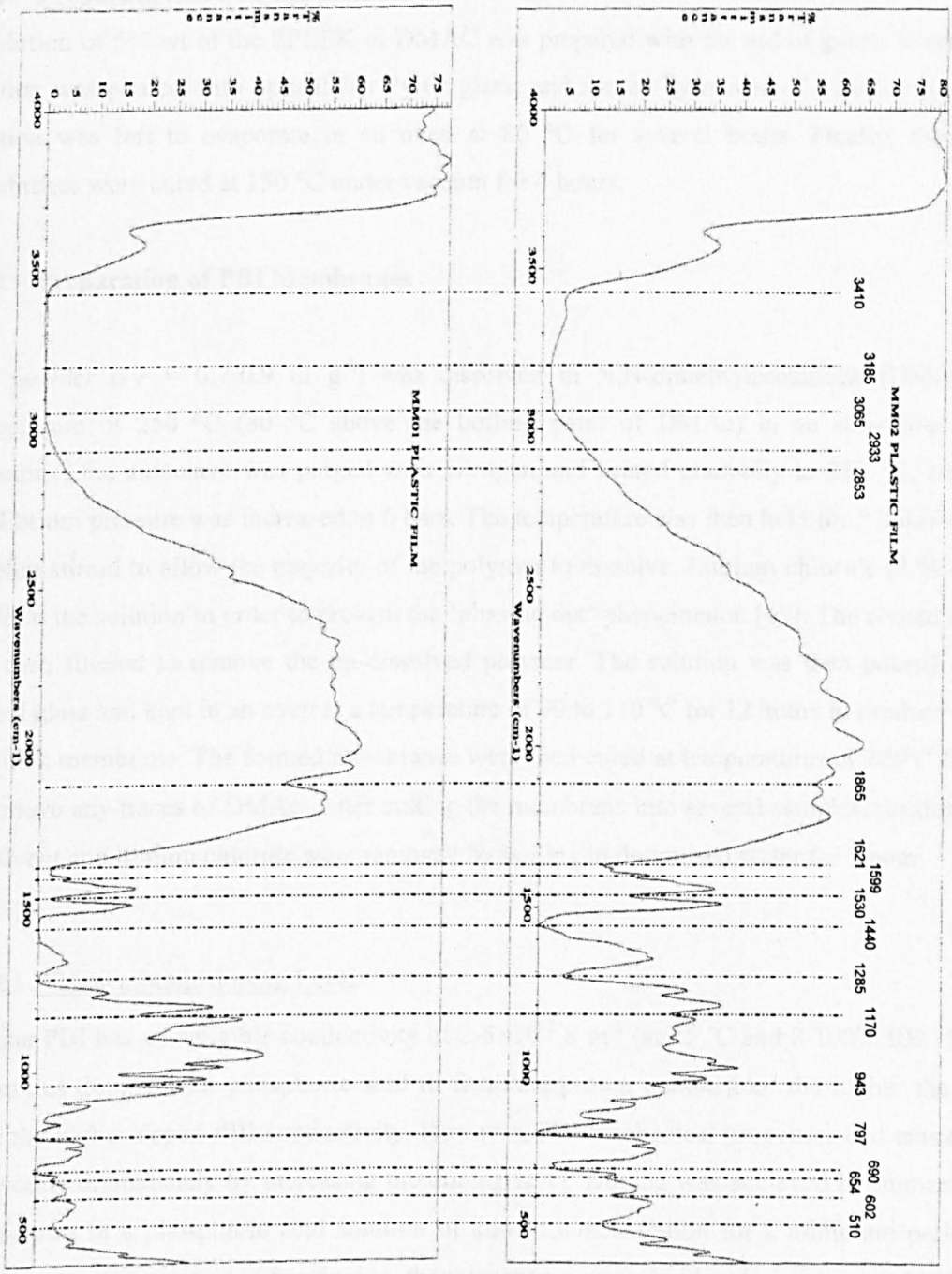

Figure 2-9. FT-IR spectroscopy of PBI films, MM01 commercial and MM02 home-made.

2.5 Membrane preparations

2.5.1 Preparation of SPEEK membranes

A solution of 5% wt of the SPEEK in DMAC was prepared with the aid of gentle heating. The solution was poured onto optical flat Pyrex glass, and spread by means of a doctor blade. The solution was left to evaporate in an oven at 80 °C for several hours. Finally, the formed membranes were cured at 150 °C under vacuum for 4 hours.

2.5.2 Preparation of PBI Membranes

PBI powder (IV = 0.7-0.9 dl g^{-1}) was dissolved in N,N-dimethylacetamide (DMAc) at a temperature of 250 °C (80 °C above the boiling point of DMAc) in an autoclave. In this procedure, the autoclave was purged with nitrogen and heated gradually to 250 °C, whilst the equilibrium pressure was increased to 6 bars. The temperature was then held for 5 hours with the solution stirred to allow the majority of the polymer to dissolve. Lithium chloride (2 % wt) was added to the solution in order to prevent the 'phasing out' phenomenon [49]. The cooled solution was then filtered to remove the un-dissolved polymer. The solution was then poured onto an optical glass and kept in an oven at a temperature of 90 to 110 °C for 12 hours to produce a 40-60 μm thick membrane. The formed membranes were then cured at temperatures of 200°C for 2 hrs to remove any traces of DMAc. After cutting the membrane into several samples, residual traces of solvent and lithium chloride were removed by boiling in de-ionised water for 1 hour.

2.5.2.1 PBI membrane doping Level

Pristine PBI has a negligible conductivity of $2\text{-}8\times10^{-2}$ S m^{-1} (at 25 °C and 0-100% RH [50]) and it requires doping with phosphoric acid to facilitate proton conduction: the higher the doping level the higher doped-PBI conductivity. However, PBI mechanical properties and tensile stress deteriorate dramatically by increasing the doping level. Doping was achieved by immersing the membranes in a phosphoric acid solution of known concentration for a minimum period of 4 days at room temperature. After doping, the membranes were dried under vacuum at 110 °C until a constant weight was achieved [51]. The doping level was calculated from the membrane weight gain before and after doping [52].

The effects of doping level on membrane tensile stress and proton conductivity were previously studied by Li et al [52]; they found that for PBI membranes with medium molecular weights, i.e. IV between 0.6 and 0.9 dL g^{-1}, the optimum doping level was around 5 moles H_3PO_4 per PBI repeat unit where a compromise between conductivity and mechanical properties was achieved. The doping level was affected by the following factors:

Acid concentration: increasing acid concentration increased the doping level or acid uptake. Figure 10 shows this dependency at room temperature for a membrane with thickness in the range of 40 μm to 60 μm. Whilst the maximum amount of bonded acid to polymer backbone (imidazole ring) is 2 moles per mole polymer (2 PRU), the rest of the acid is freely mobile in the polymer matrix and held by hydrogen bonds.

Doping temperature: increasing the temperature will enhance acid diffusion to/within the polymer film, for example increasing the temperature from 20 to 60 °C (at fixed concentration of 11 M) increased the doping level from 4.5 to 6.8 per repeat unit.

Membrane thickness: the thicker the polymer film the larger the film equilibrium acid uptake, however, such equilibrium might take longer to achieve. For example, for a fixed 85% wt/wt H_3PO_4 (14.7 M) concentration, membrane films with thickness of 40 μm to 60 μm achieved doping level of ~9.8 per repeat unit, whilst a doping level of 14 per repeat unit was achieved when the thickness of the membrane films was in the range of 90 μm to 110 μm.

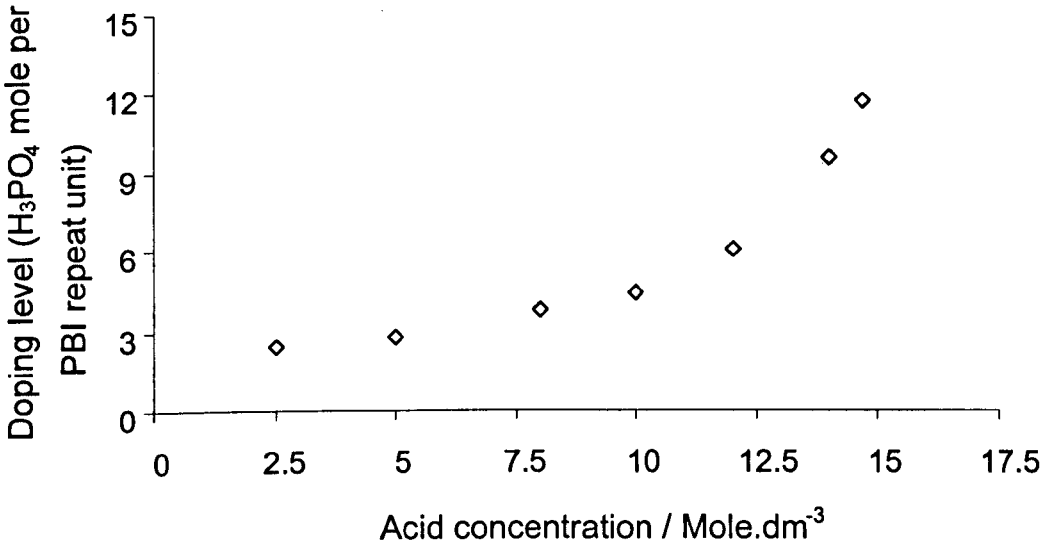

Figure 2-10. Variation of PBI doping level with phosphoric acid concentration.

2.5.3 Preparation of nano-composites membranes

Watanabe et al [53, 54] proposed a self humidifying composite membrane with highly dispersed nano-size metal oxides with or without the addition of nano-size (1-2 nm) platinum. The nano-crystalline platinum inside the membrane will catalyse the reaction between H_2 which had diffused through the membrane (crossover) and oxidant (O_2), generating water inside the membrane. This makes it possible for water dependant membranes to operate at low humidity or without external humidification [55]. However, the addition of Platinum to the membrane is an expensive solution accompanied by the increasing risk of hot spots generation. On the other hand, hygroscopic nano-crystalline oxides such as TiO_2 or SiO_2 will retain some of the produced water within the composite membrane. In the preparation of the membrane, titania can be mixed directly with an appropriate solution of the ionomers and cast on flat surface [56, 57], or impregnated as titanium alk-oxide into the membrane which is hydrolysed to form titanium

dioxide [58]. However, when using the latter technique only low percentages (~2%) of TiO_2 can be achieved.

In this work the recast from solution technique was chosen to prepare composite membranes of 5 %wt TiO_2 in Nafion®, SPEEK and PBI, due to the ease and precision in controlling the amount of TiO_2 added. Starting from solutions of 5% wt of Nafion 117 in low aliphatic alcohols (Aldrich), 5% wt of SPEEK in DMAc (home-made) and 5% wt PBI in DMAc (home-made), an appropriate amount (5%wt of dry composite polymer) of nano-metric size (<25 nm) titanium dioxide (99.7% Aldrich) was added and dispersed by means of ultrasonic bath. After reaching a suitable viscosity, the solution was cast on an optical flat Pyrex glass at 80 °C, and then thermally treated at 150 °C for PBI & SPEEK and 110 °C for Nafion. For comparisons the following membranes were used: commercial Nafion 117 (184 μm) and in-house casted Nafion, SPEEK and PBI membranes of similar thicknesses 70, 50 & 50 μm, respectively, using the above procedure without the addition of titania.

The prepared membranes were evaluated in terms of methanol cross-over and conductivity. SEM images of the cross-section of the composite membranes (by fracturing them in liquid nitrogen) are shown in figure 2-11. A homogenous distribution of titania in the polymer matrices can be seen, despite this, large agglomerates of titania (300-800 nm) were observed.

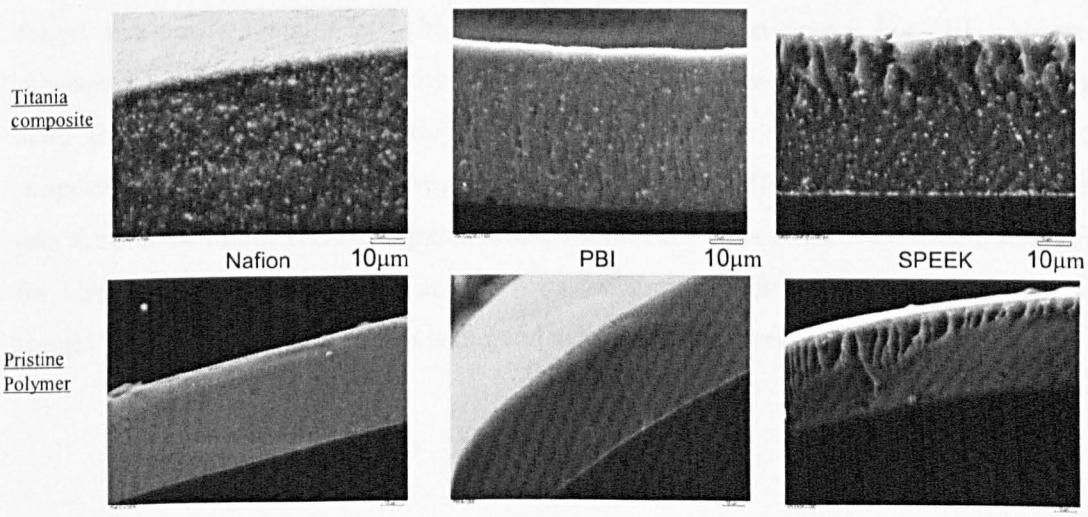

Figure 2-11. SEM images of pristine and titania composite PBI, SPEEK and Nafion membranes.

2.6 Mechanical properties

Several factors affect the mechanical properties of a polymer film including: molecular weight, composition, solvent used for casting and uniformity of the membrane (amorphous or crystalline structure). The glass transition temperature of SPEEK is about 50 °C higher than that of PEEK (T_g 143 °C) and increases slightly with an increase of sulfonation [59]. For PBI (T_g 425-436 °C) it decreases sharply with increase in the doping level [60].

Table 2-2 summarise the tensile stress results and accordingly the elongation at break values measured at ambient conditions (temperature and humidity) for the prepared PBI, doped PBI, S-PEEK and compared with Nafion® 117. It can be concluded that Nafion® 117 with the lowest glass transition temperature (T_g 132 °C) exhibited high elasticity (elongation at break ~150 %) compared to doped PBI and SPEEK. SPEEK on the other hand exhibited good mechanical properties (high tensile strength) superior to that of Nafion, which made it a good candidate for membranes in PEMFC applications. The tensile strength values of SPEEK was in the range of 57-69 MPa which is in very good agreement with the values obtained by Li et al [61].

The relationship between sulfonation degree and tensile stress was also examined, and it was found that tensile strength fell with increasing the sulfonation degree. For PBI, a severe loss in mechanical properties and elasticity was observed when the polymer was doped with phosphoric acid. Even at a relatively low doping levels (5.6 PRU), a compromise between mechanical properties and conductivity was suggested by Li et al [52]. The tensile strength fell to less than one third of its initial value compared with pristine PBI. Li et al reported tensile strength values for non doped PBI of 107 MPa and 20 MPa for similar doping level (4 PRU) and molecular weight (i.v. ~0.7 $dL.g^{-1}$)[1] which is in good agreement with results of this work.

Table 2-2. Summary of tensile stress and elongation at break measurements for PBI, doped PBI, SPEEK & Nafion 117.

Room Temp	Tensile strength (Mpa)	Elongation at break (%)	Thickness (μm)
NAFION 117 Du Pont	20.4 ± 2.68	145.87 ± 28.55	184
SPEEK (DS 45.6 %)	69.13 ± 13.68	31.74 ± 8.63	55, 120
SPEEK (DS 47.3 %)	61.55 ± 1.60	35.86 ± 1.07	90
SPEEK (DS 67.1 %)	57.84 ± 13.29	31.13 ±7.77	80, 115
Non-doped PBI I.V ~0.8 $dL.g^{-1}$	113.90 ± 11.3	81.79 ± 8.3	35
Doped PBI (5.6 PRU)	34.43 ± 3.4	32.96 ± 4.3	45

2.7 Methanol permeability measurements

A two-compartment glass cell was utilised for permeability tests. One compartment (V_A = 75 mL) was filled with pure methanol and the other (V_B = 75 mL) was filled with deionised water. The membrane (area 4.9 cm^2) was clamped between the two compartments and both solutions were stirred continuously during the experiment. Methanol concentrations were measured continuously during experiments. The methanol concentrations were obtained by measuring the refractive index for 0.5 ml sample from each compartment at fixed time intervals and compared the corresponding value with the calibration curve.

The variation of methanol concentration in the receiving compartment with time is obtained from Fick's first law (assuming $C_B << C_A$):

$$V_B \frac{dC_B(t)}{dt} = S \cdot \frac{D \cdot K}{L} \cdot C_A \qquad [8]$$

Where C_A and C_B are methanol concentrations in compartment A and B, respectively, S and L are the membrane area and thickness respectively; D and K are the methanol diffusivity and partition coefficient between the membrane and the adjacent solution respectively.

The membrane permeability, P, is defined as the product of D and K. The time lag, t_0, is explicitly related to the diffusivity:

$$t_0 = \frac{2L}{6D} \qquad [9]$$

Figure 2-12 shows a comparison of methanol permeability at room temperature for Nafion117, cast Nafion (~70 μm), SPEEK (~50 μm) and PBI (~50 μm) films, and the influence of 5% wt TiO_2 in the composite membranes.

Polybenzimidazole films had lower permeabilities, i.e. superior methanol barrier, with values of 7×10^{-8} cm^2 s^{-1} for pristine films and 2×10^{-8} cm^2 s^{-1} for PBI/TiO_2 composite, these values are in good agreement with reported values for PBI in the range of 10^{-8} -10^{-9} cm^2 s^{-1} at room temperature [62-64]. SPEEK had a permeability of 9×10^{-7} cm^2 s^{-1} and 8×10^{-7} cm^2 s^{-1} with TiO_2 in close agreement with reported values for SPEEK in the range of 10^{-7} cm^2 s^{-1}[65]. Nafion had the highest permeability of 4, 5.2 & 5 $\times10^{-6}$ cm^2 s^{-1} for Nafion 117, cast Nafion & cast Nafion with TiO_2, respectively. Reported values for Nafion in the literature are in a similar range of 10^{-6} cm^2 s^{-1} [65].

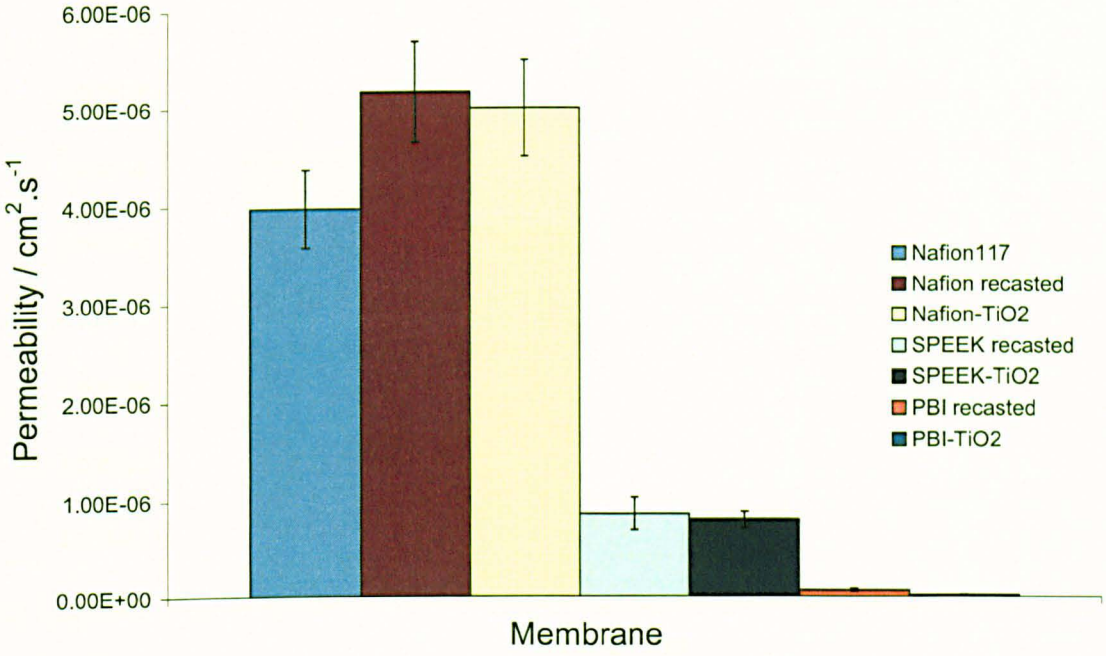

Figure 2-12. Methanol permeability for PBI, SPEEK & Nafion and their titania composite.

A minor increase in methanol cross-over was noticed with the cast Nafion compared with the commercial N117, which can be attributed to different casting conditions and different solvent used [66]. Nafion cast from low aliphatic alcohols solution containing water produces porous membranes, due to the low volatility of water compared to alcohols, a solid film will be formed on the surface of the membrane restricting water removal from the membrane and forming trapped bubbles in the polymer matrix. Sacca et al [67] and Baglio et al [56] suggested a method to resolve this problem by using a dry residue of Nafion, from the low aliphatic alcohols solution, and then dissolving it in appropriate solvent like DMAc or DMSO, followed by hot pressing the membrane above its glass transition temperature at 160 °C for 10 mins [56].

Figure 2-13 shows water permeabilities for the studied films at room temperature (from compartment B to compartment A). Values for water permeability across Nafion, SPEEK and PBI were in the same range as methanol permeability i.e. 10^{-6}, 10^{-7}& 10^{-8} $cm^2.s^{-1}$, respectively.

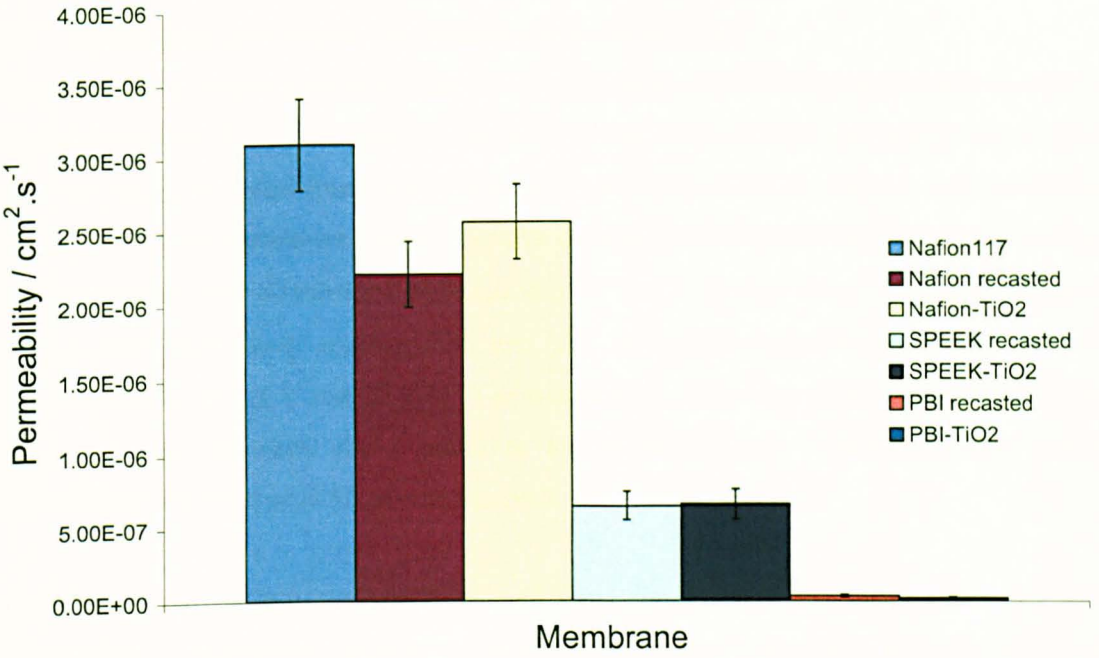

Figure 2-13. Water permeability for PBI, SPEEK & Nafion and their titania composite.

Small reductions in MEOH cross-over were obtained when adding 5% wt of TiO_2 to membranes. Further reductions can be obtained by using higher percentages of TiO_2 and new methods to prepare the composite, such as sol gel, in order to obtain more homogeneous structures in the membrane/fillers interface, as large agglomerates (300-800 nm) were observed using the commercial materials (Aldrich).

To avoid precipitation of the inorganic composites during the preparation, a chelating agent such as acetyl acetone can be added [68]. Otherwise, membranes with non-homogeneous distribution will be obtained, with one (dull) side completely covered with titania agglomerates and the other (shiney) side dominated by the polymer matrix [69].

2.8 Conductivity measurements

2.8.1 Phosphoric acid doped PBI membrane's conductivity

To assess the acid doped PBI membranes for high temperature PEMFC, their conductivities were measured using the four point probe technique, by frequency response analysis (Voltech TF2000, UK). The technique used four equally spaced probes (Fig. 2-14) in contact with the measured material; two of the probes were used to source current while the other two were used to measure the voltage drop. The membranes were cut into 10 mm × 50 mm strips and placed across four platinum foils with equal spacing of 5 mm. AC impedance measurements were carried out between frequencies of 1 and 20 kHz. The membranes were held at the desired conditions of temperature and humidity for 3 hours to ensure steady state equilibrium was achieved, measurements were taken at 30 minute intervals.

The effect of relative humidity (RH) on membrane conductivity was investigated in a test rig incorporating a humidifier capable of supplying a water saturated nitrogen stream to a membrane conductivity test cell, and a humidity analyser. For measurements, the membrane was maintained at the desired temperature in the test cell and the relative humidity was changed by varying the humidifier temperature (low to high), whilst maintaining the nitrogen flow rate at 1.2 $dm^3\ min^{-1}$. Relative humidity was measured using a Vaisala HUMICAP® (Finland) intrinsically safe humidity and temperature transmitter.

PBI conductivity strongly depends on three main factors: acid doping level, temperature and relative humidity. During conductivity measurements the temperature and the relative humidity were varied using two doping levels: 5 moles of H_3PO_4 per PBI repeat unit for composite PBI study & 5.6 moles of H_3PO_4 per PBI repeat unit for standard PBI study. The values of conductivities obtained are shown in Figure 2-15. Conductivity increased with an increase in humidity and temperature. However, at a similar relative humidity, no significant gain in proton conductivity was obtained by increasing the temperature above 175 °C. This effect was a result of water lost by phosphoric acid dimerisation [70]. It is known that, at elevated temperatures, phosphoric acid starts to dehydrate; this process occurs in many stages, the first two of which are shown below:

First stage: $2H_3PO_4 \leftrightarrow H_4P_2O_7 + H_2O\uparrow$

Second stage: $H_4P_2O_7 + H_3PO_4 \leftrightarrow H_5P_3O_{10} + H_2O\uparrow$

The equilibrium concentrations of these reversible reactions depend on temperature and relative humidity and the dimerised products have lower proton conductivity than phosphoric acid [71]. This explains the observed increase in dependency of conductivity on humidity at elevated temperatures, above 170 °C [64].

PBI with phosphoric acid doping level of 5.6 per repeat unit had a conductivity between 2 and 6 S m^{-1} in the temperature range 120 to 200 °C under very low humidity (1-7%). These results agree very closely with results obtained by He et al [72] and Ma [73].

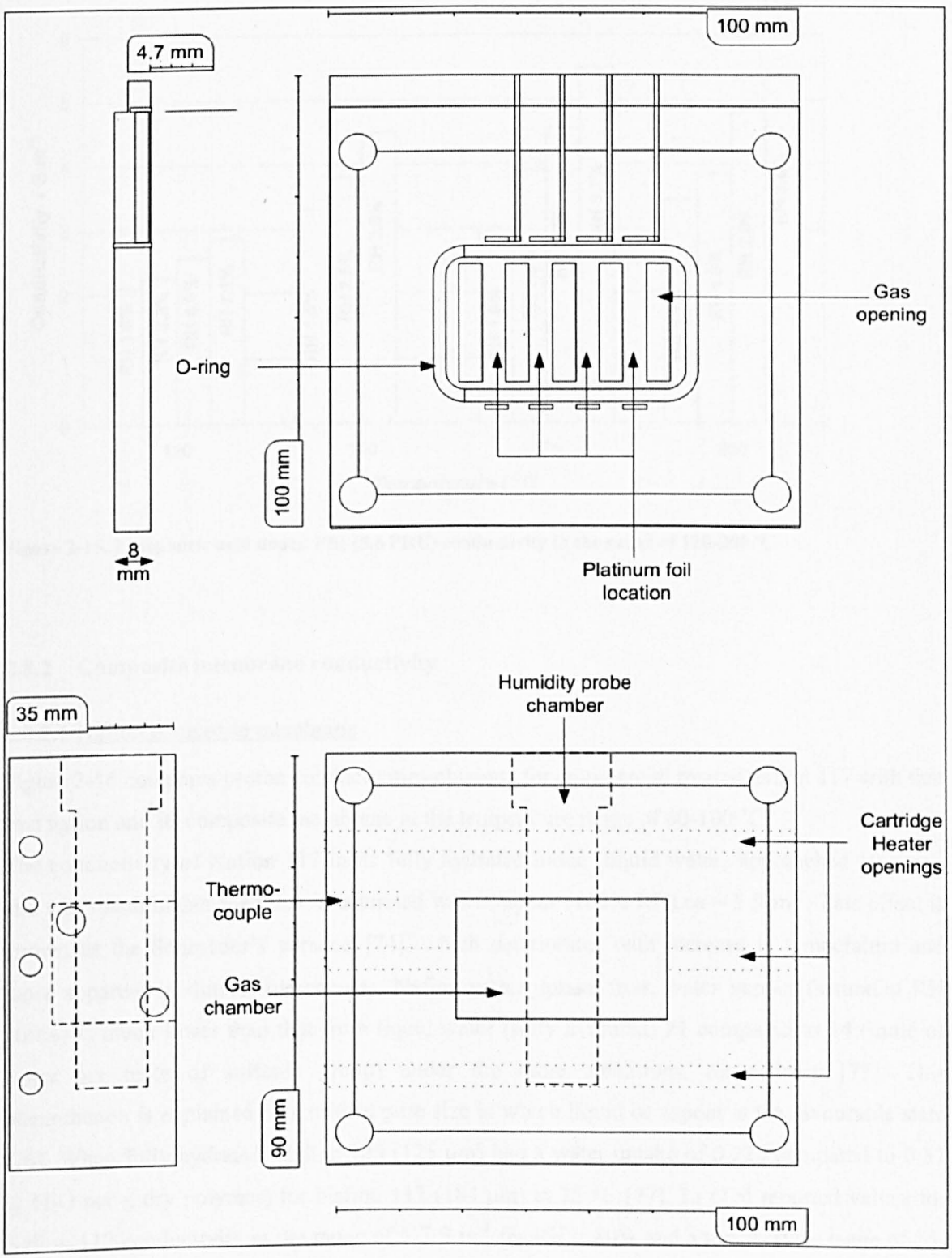

Figure 2-14. Schematic drawing of proton conductivity measurement cell.

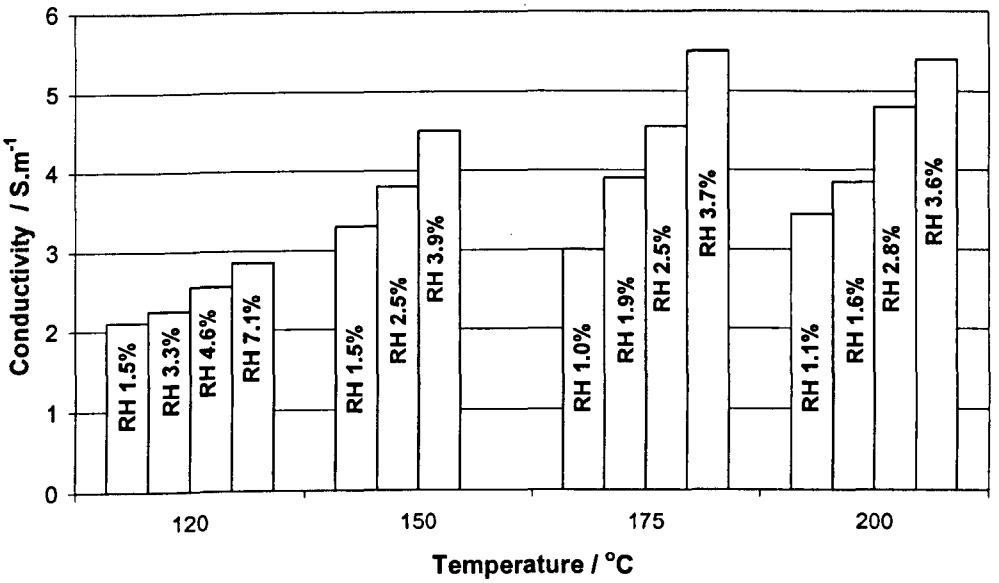

Figure 2-15. Phosphoric acid doped PBI (5.6 PRU) conductivity in the range of 120-200 °C.

2.8.2 Composite membrane conductivity

2.8.2.1 Nafion composite membrane

Figure 2-16 compares proton conductivities obtained for commercial treated nafion 117 with that cast nafion and its composite membrane in the temperature range of 60-100 °C.

The conductivity of Nafion 117 in its fully hydrated mode (liquid water) approached 10 S m^{-1} and was much higher than that in saturated water vapour (100% RH) ca ~ 5 S m^{-1}. This effect is known as the Schroeder's paradox [74], which deteriorates with increase in temperature and more apparent in thinner membranes. Nafion water uptake from water vapour (saturated RH 100%) is much lower than that from liquid water (fully hydrated) 21 compared to 14 (mole of water per mole of sulfonic group) under the same conditions, respectively [75]. This phenomenon is explained by a critical pore size in which liquid or vapour is the favourable state [76]. When fully hydrated, Nafion 125 (125 μm) had a water uptake of 0.225 compared to 0.37 (g H_2O per g dry polymer) for Nafion 117 (184 μm) at 25 °C [77]. Li et al reported values for Nafion 117 conductivity in the range of 5-7 S m^{-1} for RH = 80% and a temperature range of 25-80 °C [24].

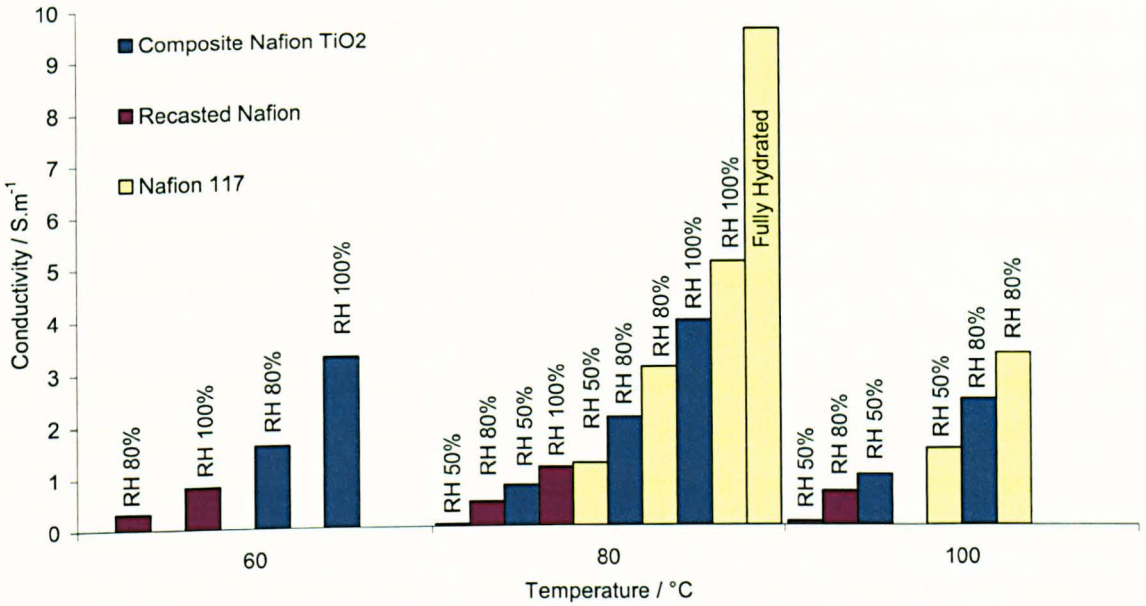

Figure 2-16. Proton conductivity of Nafion 117, re-casted Nafion & titania composite Nafion.

The conductivity of re-casted Nafion films is an order of magnitude lower than that of commercial Nafion 117, which is attributed to the following three reasons:

I. Membrane thickness: Nafion 117 has thickness of 184 μm compared to that of re-casted Nafion of ~70μm. The effect of membrane thickness causing non-linearity in water content under the same conditions should always be carefully considered when comparing performances of PEFCs [78]. For thinner membranes, such as Nafion 115 (127 μm) less water is held by the membrane (uptake) and therefore a lower conductivity is expected: values of 1 to 3 S m^{-1} were reported for the temperature range between 20 and 100 °C under 100 % relative humidity [65]. Higher values were reported by Yang et al for Nafion 115 in the range of 4 to 6.7 S m^{-1} at 80 °C and relative humidity from 60 to 80% [79]. However, all the reported values are much lower than that of Nafion 117.

II. Effect of drying at 105 °C during the re-casting procedure: Nafion exhibits an irreversible conductivity decay (almost an order of magnitude) at temperatures of 120 °C and above;

even at very high relative humidity RH 95% [80]. When Nafion is dried at a temperature of 105 °C its water uptake drops dramatically. Hinatsu et al noticed a fall from 0.37 to 0.18 (g H_2O per g dry polymer) [77], while Zawodzinski et al reported a fall from 21 to 12 (mole of water per mole of sulfonic group) [75]. As a consequence of the fall in water uptake, drop in conductivity is observed under similar conditions. Sone et al [81] reported an order of magnitude fall in the conductivity of Nafion 117 after heat treatment at 105 °C; conductivity values before the heat treatment were 1, 3 and 7.8 S m^{-1} dropping to 0.1, 1 and 2 at relative humidity of 40, 80 and 100%, respectively.

III. Effect of Solvent: The solvent used during membrane preparation can have a severe effect on the cast membrane's conductivity. For example using DMF instead of DMAc to prepare SPEEK (60% DS) membranes resulted in an order of magnitude fall in conductivity from 1 to 0.1 S m^{-1} (at room temperature and 100% RH) [59]. Similarly, acid doped PBI prepared using trifluoroacetic acid (TFA) had a better proton conductivity and poorer mechanical properties (more crystalline) than that prepared using DMAc [71]. Sacca et al [67] and Baglio et al [56] suggested using a dry residue of Nafion (from the low aliphatic alcohols solution) and then dissolving it in an appropriate solvent like DMAc or DMSO to improve membrane characteristics. Moore and Martin [66] reported large differences in physical properties of Nafion membranes prepared using different solvents.

Zawodzinski et al [75] studied the relation between water content and water permeability through Nafion 117 membranes; they reported values of 4 to 5 (moles of water per mole of sulfonic group) at 30 °C and corresponding conductivities in the range of 1 to 2 S m^{-1} at 30 °C for similar water permeabilities to that obtained in this work, in the range of 2-3 × 10^{-6} cm^2 s^{-1}.

Good water retention (uptake) is achieved with the addition of titania nano-particles. This is reflected by enhanced conductivity of the composite films at similar relative humidity, from 1.3 to 3.92 S m^{-1} at 80 °C and 100% RH, in comparison to that of pristine materials. However, even with the enhancement in the conductivity of the composite membranes it is still lower than that of Nafion 117 due to the earlier mentioned reasons. This is also reflected in the water

permeability values, where composite membranes showed enhancement in the water permeability over re-cast Nafion, but again the values were still below those of Nafion 117 [75] and therefore lower conductivity. As temperature increases from 80 to 100 °C, the conductivity of Nafion 117 remained constant (under the same humidity content) while the composite membranes showed an increase (under the same humidity content).

Further enhancement in water retention can be achieved with better titania dispersion and correspondingly smaller agglomerate size. Chalkova et al [69] and Baglio et al [82] studied the effect of TiO_2 surface and physio-chemical properties on the performance, and found that the effect of filler surface area (for similar functional groups) become important determining the water retention properties at high temperatures.

2.8.2.2 SPEEK composite membrane

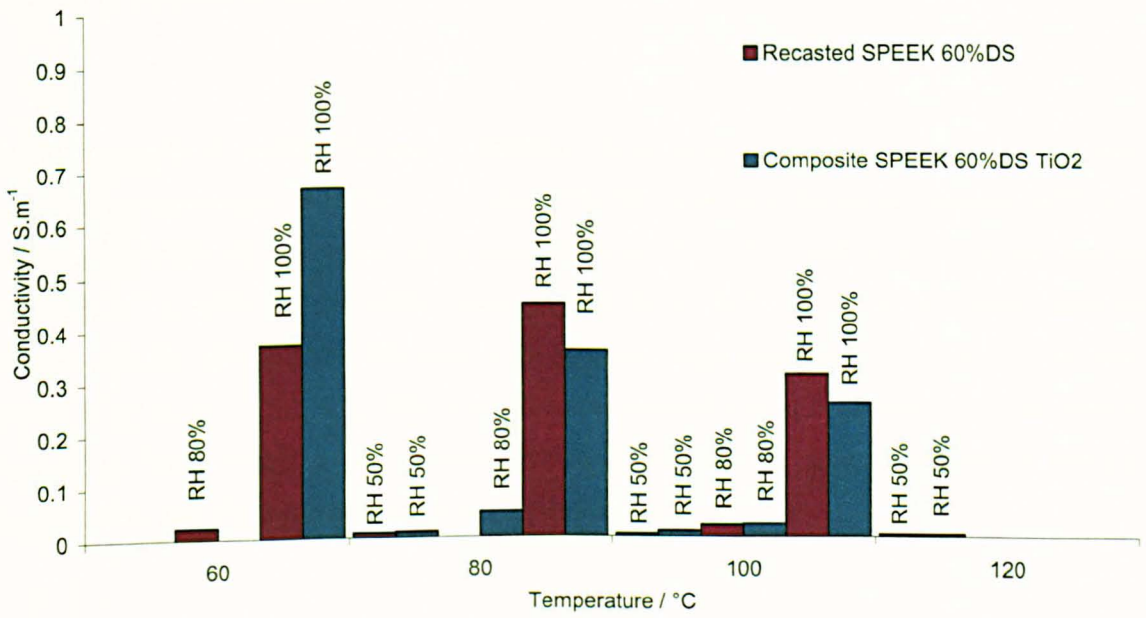

Figure 2-17. Proton conductivity of re-casted SPEEK & titania composite SPEEK with 60% DS.

Figure 2-17 shows the proton conductivity of SPEEK (with sulfonation degree of 60%) and that of its titania composite in the temperature range of 60 to 120 °C and relative humidity in the range of 50 to 100%. The maximum conductivity was achieved at 80 °C for SPEEK (DS 60%) over the entire humidity range with maximum value of 0.45 S m^{-1} at 100% RH. The results are in very good agreement with the work of Kobayashi et al [8] and Rikukawa et al [38], where they found, similarly, maximum conductivity for SPEEK (DS 65%) with 100% RH at 80 °C with conductivity values in the range of 0.1 S m^{-1}. Mikhailenko et al [83] found a similarly maximum conductivity for SPEEK (DS 50%) around 90 °C and they also reported a shift in the maximum conductivity towards 140 °C for SPEEK with sulfonation degree of 72% and above.

While for composite SPEEK the maximum conductivity depended on relative humidity, for high humidity content (RH 100%) a maximum value of 0.67 S m^{-1} was obtained at 60 °C, and for low humidity content (RH 50%) a maximum conductivity of 0.024 S.m^{-1} was obtained at 100 °C. At relative humidities up to 80%, the composite SPEEK showed advantages over standard SPEEK for temperatures up to 100 °C: above such temperature no improvements were observed. For relative humidity close to saturation (RH 100%), the composite showed enhancement only at low temperatures up to 60 °C, thereafter the conductivity of composite membranes was even lower than that of standard SPEEK (60% DS) at 100% RH.

SPEEK conductivity greatly depends on humidity, more so than that of Nafion 117 [84], as well as the sulfonation degree. For DS 65% conductivity values were in the range between 0.0079 and 0.81 S m^{-1} at 100% RH and temperature range of 25 to 100 °C [85], and for DS 50% between 0.4 and 0.2 S m^{-1} at 100% RH and temperature range of 25 to 100 °C [83]. The measured values for SPEEK with DS 60% at 100% RH were in the reported range between DS 50 – 65 % with value of 0.45 S m^{-1} at 80 °C [83, 85]. SPEEK membranes showed similar behaviour to re-cast Nafion, where they both exhibited poor conductivity and difficulty in water retention at elevated temperatures, partially caused by the low film thicknesses (~50 μm).

2.8.2.3 PBI composite membrane

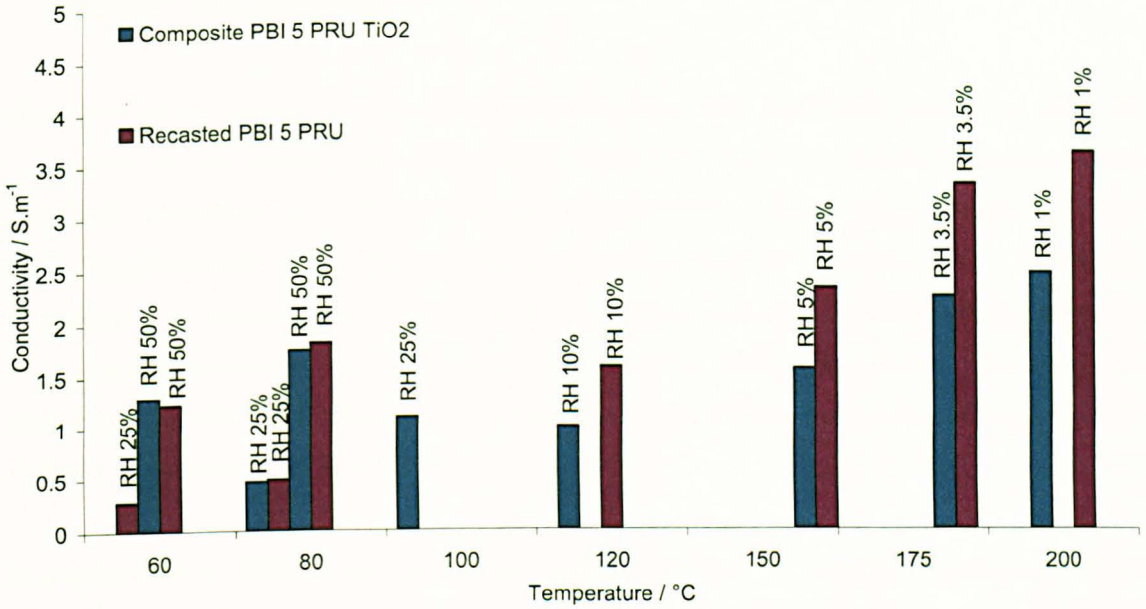

Figure 2-18. Proton conductivity of re-casted acid doped PBI & titania composite acid doped PBI (5 PRU).

Figure 2-18 shows the conductivity of phosphoric acid doped PBI and its titania composite with doping level of 5 moles acid per repeat unit of polymer. PBI (5 PRU) conductivity was in the range of 1 to 4 S m^{-1} at low humidity (RH ≥10%), close to the reported values for PBI (5.6) (Sec. 2.8.1). Good conductivities in the range of 1 to 2 S m^{-1} were obtained even at low operating temperatures 60-80 °C at intermediate humidity (RH 50%) which agree with those previously reported [86].

Titania nano particles did not offer any advantage for PBI based membranes; on the contrary it reduced its conductivity. PBI membranes showed good conductivity with doping level of 5 PRU even at low humidity and elevated temperatures. The main proton conduction mechanism occurs in the free excess phosphoric acid in the amorphous regions [73], and not in the polymer salt complex. The polymer forms crystalline salts with acid (one acid per imidazole group) which has only a small contribution to the conductivity [71], which means the interaction between the titania and the polymer matrix do not contribute to the overall conductivity. On the contrary, it

might have a negative influence by occupying space in the polymer matrix which is normally substituted with highly conducting mobile (free) phosphoric acid.

2.9 Summary and conclusions

Nafion membranes exhibit high proton conductivity under fully humidified conditions (RH~100 %), however Nafion conductivity falls sharply above 100 °C, due to reduced humidity under atmospheric conditions and fall in water uptake from water vapour, in comparison to liquid phase. Phosphoric acid doped PBI offers good proton conductivity extending over a wide range of operating temperature up to 200 °C, with no or very low humidity. PBI conductivity improves with increasing humidity; which is more significant at high temperatures. However, this dependency is much smaller than that of Nafion and makes PBI the best choice of membrane for anhydrous operation above 100 °C.

The conductivity of SPEEK showed an even higher dependency on humidity than that of Nafion; the conductivity values depended on the degree of sulfonation. For sulfonation degrees of 70 % and above, SPEEK become partially soluble in water and fully soluble in MEOH. A sulfonation degree of 60 % was considered to be a good compromise between conductivity and mechanical properties; at such sulfonation levels the conductivity was an order of magnitude lower than that of PBI, even at high humidity content (RH~100 %). A fall in conductivity was observed at temperatures above 100 °C for SPEEK, with sulfonation degree of 60 %. Even though there is published work in the literature [84, 87] showing good conductivity of SPEEK in the range of 1-4 S m^{-1} (similar to PBI) at temperatures up to 140 °C, the operating conditions of such systems are unrealistic requiring pressurised steam and very high sulfonation degree (brittleness and swelling / solubility issues).

In terms of methanol cross-over, PBI is an excellent barrier for methanol with a permeability one order of magnitude lower than SPEEK and two orders of magnitude lower than Nafion.

2.10 References

1. Li, Q., J.O. Jensen, R. He, G. Xiao, J.A. Gao, R.W. Berg, H.A. Hjuler, E. Hennesoe, and N.J. Bjerrum, *Recent Research Developments In Electrochemistry*, ed. S.G. Pandalai. Vol. 6. 2003: Transworld Research Network.
2. Kerres, J., A. Ullrich, T. Haring, M. Baldauf, U. Gebhardt, and W. Preidel, *Preparation, characterization and fuel cell application of new acid-base blend membranes.* Journal of New Materials for Electrochemical Systems, 2000. **3**(3): p. 229-239.
3. Bailly, C., D.J. Williams, F.E. Karasz, and W.J. Macknight, *THE SODIUM-SALTS OF SULFONATED POLY(ARYL-ETHER-ETHER-KETONE) (PEEK) - PREPARATION AND CHARACTERIZATION.* Polymer, 1987. **28**(6): p. 1009-1016.
4. Wang, F., T.L. Chen, and J.P. Xu, *Synthesis of poly(ether ether ketone) containing sodium sulfonate groups as gas dehumidification membrane material.* Macromolecular Rapid Communications, 1998. **19**(2): p. 135-137.
5. Daoust, D., J. Devaux, and P. Godard, *Mechanism and kinetics of poly(ether ether ketone) (PEEK) sulfonation in concentrated sulfuric acid at room temperature. Part 1. Qualitative comparison between polymer and monomer model compound sulfonation.* Polymer International, 2001. **50**(8): p. 917-924.
6. Huang, R.Y.M., P.H. Shao, C.M. Burns, and X. Feng, *Sulfonation of poly(ether ether ketone)(PEEK): Kinetic study and characterization.* Journal of Applied Polymer Science, 2001. **82**(11): p. 2651-2660.
7. Daoust, D., J. Devaux, P. Godard, A. Jonas, and R. Legras, *Poly(Ether Ether Ketone) Characterization.* Advanced Thermoplastic Composites: Characterization and Processing ed. C.H. Verlag. 1993, Germany. 3-56.
8. Kobayashi, T., M. Rikukawa, K. Sanui, and N. Ogata, *Proton-conducting polymers derived from poly(ether-etherketone) and poly(4-phenoxybenzoyl-1,4-phenylene).* Solid State Ionics, 1998. **106**(3-4): p. 219-225.
9. Shibuya, N. and R.S. Porter, *KINETICS OF PEEK SULFONATION IN CONCENTRATED SULFURIC-ACID.* Macromolecules, 1992. **25**(24): p. 6495-6499
10. Brinker, K.C. and I.M. Robinson, *aliphatic polybenzimidazole*, du-Point-de-Nemours, Editor. 1959: U.S.2895948.
11. Vogel, H.A. and C.S. Marvel, *Polybenzimidazoles, new thermally stable polymers.* Journal of Polymer Science, 1961. **50**: p. 511.
12. Iwakura, Y., K. Uno, and Y. Imai, *Polybenzimidazoles.* Journal of Polymer Science Part a-Polymer Chemistry, 1964. **2**: p. 2605.
13. Plummer, L. and C.S. Marvel, *Polybenzimidazoles (III).* Journal of Polymer Science Part a-Polymer Chemistry, 1964. **2**: p. 2559.
14. Vogel, H.A. and C.S. Marvel, *Polybenzimidazoles (II).* Journal of Polymer Science Part a-Polymer Chemistry, 1963. **1**: p. 1531.
15. Choe, E.W., A.B. Conciatori, and B.C. Ward, *Two stage high molecular weight polybenzimidazole production with Phosphorus containing catalyst.* 1985: U.S.4506068.
16. Ward, B.C., *Two stage polybenzimidazole process and product.* 1987: U.S.4672104.
17. Hedberg, F.L. and C.S. Marvel, *New Single-Step Process for Polybenzimidazole Synthesis.* Journal of Polymer Science Part a-Polymer Chemistry, 1974. **12**(8): p. 1823-1828.

18. Foster, R.T. and C.S. Marvel, *Polybenzimidazoles. IV. Polybenzimidazoles containing aryl ether linkages.* Journal of Polymer Science Part a-Polymer Chemistry, 1965. **3**: p. 417.
19. Kim, S.H., E.M. Pearce, and T.K. Kwei, *The Synthesis of a Precursor of Polybenzimidazole (Pbi) and Blends with Polyamic Acid (Paa).* Journal of Polymer Science Part a-Polymer Chemistry, 1993. **31**(13): p. 3167-3180.
20. Shin, G.I., J.I. Lee, and J.H. Kim, *A new synthetic route to poly(benzimidazole) and the related model reactions to imidazoline and benzimidazole.* Bulletin of the Korean Chemical Society, 1996. **17**(1): p. 29-33.
21. Trouw, N.S., *Method for the preparation of polybenzimidazole membranes* 1987: U.S.4693825.
22. Choe, E.W., A.B. Conciatori, and B.C. Ward, *Two stage high molecular weight polybenzimidazole production with Phosphorus containing catalyst.* 1984: U.S.4463167.
23. Choe, E.W. and A.B. Conciatori, *Synthesis of high molecular weight polybenzimidazole with Arylhalo Phosphorus compound catalyst.* 1985: U.S.4533725.
24. Li, Q., J.O. Jensen, R. He, G. Xiao, J.A. Gao, R.W. Berg, H.A. Hjuler, H. Hennesoe, and N.J. Bjerrum, *Acid-Doped Polybenzimidazole Membranes as Electrolyte for Fuel Cells Operating Above 100 °C.* Recent Research Developments in Electrochemistry, 2003. **6**: p. 1-26: p. 1.
25. Harrington, R.E. and P.G. Pecoraro, *Precise molecular weight distributions of high polymers by semiautomatic solvent extraction.* journal of Polymer Science Part a-Polymer Chemistry, 1966. **4**: p. 475.
26. Wainright, J.S., M.H. Litt, and R.F. Savinell, *High temperature membranes*. Handbook of Fuel cells. Vol. 3. 2003: Willey, New York.
27. Conciatori, A.B., E.W. Choe, and H.K. Hall, *High molecular weight polybenzimidazole preparation with Phosphorus containing polymerization catalyst.* 1983: U.S.4414383.
28. Conciatori, A.B., E.W. Choe, and H.K. Hall, *High molecular weight polybenzimidazole preparation with Phosphorus containing polymerization catalyst.* 1984: U.S.4452967.
29. Choe, E.W. and A.B. Conciatori, *Single stage production of improved high molecular weight polybenzimidazole with organosilicon Halide catalyst.* 1984: U.S.4431796.
30. Choe, E.W. and A.B. Conciatori, *Production of improved high molecular weight polybenzimidazole with Tin containing catalyst.* 1984: U.S.4452971.
31. Choe, E.W. and A.B. Conciatori, *Production of high molecular weight polybenzimidazole with Aryl Phosphonic acid or Aryl Phosphonic acid catalyst.* 1984: U.S.4452972.
32. Choe, E.W., *Catalyst for the preparation of Polybenzimidazoles.* Journal of Applied Polymer Science, 1994. **53**: p. 497.
33. Wrasidlo, W. and H.H. Levine, *Polybenzimidazoles (I) Reaction mechanism and kinetics.* Journal of Polymer Science Part a-Polymer Chemistry, 1964. **2**: p. 4795.
34. Colson, J.G., R.H. Michel, and R.M. Paufler, *Polybenzimidazoles.* Journal of Polymer Science Part a-Polymer Chemistry, 1966. **4**: p. 59.
35. Robertson, G.P., S.D. Mikhailenko, K.P. Wang, P.X. Xing, M.D. Guiver, and S. Kaliaguine, *Casting solvent interactions with sulfonated poly(ether ether ketone) during proton exchange membrane fabrication.* Journal of Membrane Science, 2003. **219**(1-2): p. 113-121.
36. Zaidi, S.M.J., S.D. Mikhailenko, G.P. Robertson, M.D. Guiver, and S. Kaliaguine, *Proton conducting composite membranes from polyether ether ketone and*

heteropolyacids for fuel cell applications. Journal of Membrane Science, 2000. **173**(1): p. 17-34.

37. Mikhailenko, S.U.D., K.P. Wang, S. Kaliaguine, P.X. Xing, G.P. Robertson, and M.D. Guiver, *Proton conducting membranes based on cross-linked sulfonated poly(ether ether ketone) (SPEEK).* Journal of Membrane Science, 2004. **233**(1-2): p. 93-99.
38. Rikukawa, M. and K. Sanui, *Proton-conducting polymer electrolyte membranes based on hydrocarbon polymers.* Progress in Polymer Science, 2000. **25**(10): p. 1463-1502.
39. Hogarth, M. and X. Glipa, *HIGH TEMPERATURE MEMBRANES FOR SOLID POLYMER FUEL CELLS*, D.o.T.a.I. (U.K), Editor. 2001, Johnson Matthey Technology Centre. p. 1-71.
40. Cioffi, M., *Rheo-kinetics* 2002, University of Groningen.
41. Gehatia, M. and D.R. Wiff, *Molecular-Weight Distribution of Polybenzimidazole - Regularizable Ill-Posed Problem.* Journal of Chemical Physics, 1972. **57**(3): p. 1070.
42. Guerra, G., S. Choe, D.J. Williams, F.E. Karasz, and W.J. Macknight, *Fourier-Transform Infrared-Spectroscopy of Some Miscible Polybenzimidazole Polyimide Blends.* Macromolecules, 1988. **21**(1): p. 231-234.
43. Musto, P., F.E. Karasz, and W.J. Macknight, *Fourier-Transform Infrared-Spectroscopy on the Thermooxidative Degradation of Polybenzimidazole and of a Polybenzimidazole Polyetherimide Blend.* Polymer, 1993. **34**(14): p. 2934-2945.
44. Musto, P., F.E. Karasz, and W.J. Macknight, *Hydrogen-Bonding in Polybenzimidazole Polyimide Systems - a Fourier-Transform Infrared Investigation Using Low-Molecular-Weight Monofunctional Probes.* Polymer, 1989. **30**(6): p. 1012-1021.
45. Samms, S.R., S. Wasmus, and R.F. Savinell, *Thermal stability of proton conducting acid doped polybenzimidazole in simulated fuel cell environments.* Journal of the Electrochemical Society, 1996. **143**(4): p. 1225-1232.
46. Brooks, N.W., R.A. Duckett, J. Rose, I.M. Ward, and J. Clements, *An Nmr-Study of Absorbed Water in Polybenzimidazole.* Polymer, 1993. **34**(19): p. 4038-4042.
47. Deimede, V., G.A. Voyiatzis, J.K. Kallitsis, L. Qingfeng, and N.J. Bjerrum, *Miscibility behavior of polybenzimidazole/sulfonated polysulfone blends for use in fuel cell applications.* Macromolecules, 2000. **33**(20): p. 7609-7617.
48. Bouchet, R. and E. Siebert, *Proton conduction in acid doped polybenzimidazole.* Solid State Ionics, 1999. **118**(3-4): p. 287-299.
49. Sandor, R.B. and T.S. Thornburg, *Polybenzimidazole solutions*. 1991: U.S.5066697.
50. Hoel, D. and E. Grunwald, *High Protonic Conduction of Polybenzimidazole Films.* Journal of Physical Chemistry, 1977. **81**(22): p. 2135-2136.
51. Li, Q.F., R.H. He, R.W. Berg, H.A. Hjuler, and N.J. Bjerrum, *Water uptake and acid doping of polybenzimidazoles as electrolyte membranes for fuel cells.* Solid State Ionics, 2004. **168**(1-2): p. 177-185.
52. Li, Q.F., R. He, J.O. Jensen, and N.J. Bjerrum, *PBI-based polymer membrane for high temperature fuel cells* fuel cells, 2004. **4**: p. 147.
53. Watanabe, M., H. Uchida, Y. Seki, and M. Emori, *Self-Humidifying Polymer Electrolyte Membranes for Fuel Cells.* J. Electrochem. Soc., 1996. **143**(12): p. 3847-3852.
54. Watanabe, M., H. Uchida, and M. Emori, *Polymer electrolyte membranes incorporated with nanometer-size particles of Pt and/or metal-oxides: Experimental analysis of the self-humidification and suppression of gas-crossover in fuel cells.* Journal of Physical Chemistry B, 1998. **102**(17): p. 3129-3137.

55. Watanabe, M., H. Uchida, and M. Emori, *Analyses of Self-Humidification and Suppression of Gas Crossover in Pt-Dispersed Polymer Electrolyte Membranes for Fuel Cells.* J. Electrochem. Soc., 1998. **145**(4): p. 1137-1141.
56. Baglio, V., A.S. Arico, A. Di Blasi, V. Antonucci, P.L. Antonucci, S. Licoccia, E. Traversa, and F.S. Fiory, *Nafion-TiO2 composite DMFC membranes: physico-chemical properties of the filler versus electrochemical performance.* Electrochimica Acta, 2005. **50**(5): p. 1241-1246.
57. Antonucci, P.L., A.S. Arico, P. Creti, E. Ramunni, and V. Antonucci, *Investigation of a direct methanol fuel cell based on a composite Nafion(R)-silica electrolyte for high temperature operation.* Solid State Ionics, 1999. **125**(1-4): p. 431-437.
58. Uchida, H., Y. Ueno, H. Hagihara, and M. Watanabe, *Self-humidifying electrolyte membranes for fuel cells - Preparation of highly dispersed TiO2 particles in Nafion 112.* Journal of the Electrochemical Society, 2003. **150**(1): p. A57-A62.
59. Kaliaguine, S., S.D. Mikhailenko, K.P. Wang, P. Xing, G. Robertson, and M. Guiver, *Properties of SPEEK based PEMs for fuel cell application.* Catalysis Today, 2003. **82**(1-4): p. 213-222.
60. Ameri, R., *Polybenzimidazole film containing phosphoric acid as proton exchange membrane (PEM).* 1997, Case Western Reserve University: Cleveland.
61. Li, X.F., Z. Wang, H. Lu, C.J. Zhao, H. Na, and C. Zhao, *Electrochemical properties of sulfonated PEEK used for ion exchange membranes.* Journal of Membrane Science, 2005. **254**(1-2): p. 147-155.
62. Pu, H.T., Q.Z. Liu, and G.H. Liu, *Methanol permeation and proton conductivity of acid-doped poly (N-ethylbenzimidazole) and poly(N-methylbenzimidazole).* Journal of Membrane Science, 2004. **241**(2): p. 169-175.
63. Pu, H.T. and Q.Z. Liu, *Methanol permeability and proton conductivity of polybenzimidazole and sulfonated polybenzimidazole.* Polymer International, 2004. **53**(10): p. 1512-1516.
64. Wainright, J.S., J.T. Wang, D. Weng, R.F. Savinell, and M. Litt, *Acid-Doped Polybenzimidazoles - a New Polymer Electrolyte.* Journal of the Electrochemical Society, 1995. **142**(7): p. L121-L123.
65. Gaowen, Z. and Z. Zhentao, *Organic/inorganic composite membranes for application in DMFC.* Journal of Membrane Science, 2005. **261**(1-2): p. 107-113
66. Moore, R.B. and C.R. Martin, *Procedure for preparing solution-cast perfluorosulfonate ionomer films and membranes.* Anal. Chem., 1986. **58**(12): p. 2569-2570.
67. Sacca, A., A. Carbone, E. Passalacqua, A. D'Epifanio, S. Licoccia, E. Traversa, E. Sala, F. Traini, and R. Ornelas, *Nafion-TiO2 hybrid membranes for medium temperature polymer electrolyte fuel cells (PEFCs).* Journal of Power Sources, 2005. **152**(1): p. 16-21.
68. Nunes, S.P., B. Ruffmann, E. Rikowski, S. Vetter, and K. Richau, *Inorganic modification of proton conductive polymer membranes for direct methanol fuel cells.* Journal of Membrane Science, 2002. **203**(1-2): p. 215-225.
69. Chalkova, E., M.V. Fedkin, D.J. Wesolowski, and S.N. Lvov, *Effect of TiO2 surface properties on performance of nafion-based composite membranes in high temperature and low relative humidity PEM fuel cells.* Journal of the Electrochemical Society, 2005. **152**(9): p. A1742-A1747.

70. Scott, K., S. Pilditch, and M. Mamlouk, *Modelling and experimental validation of a high temperature polymer electrolyte fuel cell.* Journal of Applied Electrochemistry, 2007. **37**: p. 1245-1259.
71. Ma, Y.L., *The Fundamental Studies of Polybenzimidazole/Phosphoric Acid Polymer Electrolyte For Fuel Cells.* 2004, CASE WESTERN RESERVE UNIVERSITY.
72. He, R.H., Q.F. Li, G. Xiao, and N.J. Bjerrum, *Proton conductivity of phosphoric acid doped polybenzimidazole and its composites with inorganic proton conductors.* Journal of Membrane Science, 2003. **226**(1-2): p. 169-184.
73. Ma, Y.L., J.S. Wainright, M.H. Litt, and R.F. Savinell, *Conductivity of PBI membranes for high-temperature polymer electrolyte fuel cells.* Journal of the Electrochemical Society, 2004. **151**(1): p. A8-A16.
74. Vallieres, C., D. Winkelmann, D. Roizard, E. Favre, P. Scharfer, and M. Kind, *On Schroeder's paradox.* J. Membr. Sci., 2006. **278** p. 357-364.
75. Zawodzinski, T.A., T.E. Springer, J. Davey, R. Jestel, C. Lopez, J. Valerio, and S. Gottesfeld, *A Comparative Study of Water Uptake By and Transport Through Ionomeric Fuel Cell Membranes.* J. Electrochem. Soc., 1993. **140**(7): p. 1981-1985 .
76. Elfring, G.J. and H. Struchtrup, *Thermodynamic considerations on the stability of water in Nafion.* Journal of Membrane Science, 2007. **297**(1-2): p. 190-198.
77. Hinatsu, J.T., M. Mizuhata, and H. Takenaka, *Water Uptake of Perfluorosulfonic Acid Membranes from Liquid Water and Water Vapor.* J. Electrochem. Soc., 1994 **141**(6): p. 1493-1498.
78. Springer, T.E., T.A. Zawodzinski, and S. Gottesfeld, *Polymer Electrolyte Fuel Cell Model.* J. Electrochem. Soc., 1991. **138**(8): p. 2334-2342.
79. Yang, C., S. Srinivasan, A.B. Bocarsly, S. Tulyani, and J.B. Benziger, *A comparison of physical properties and fuel cell performance of Nafion and zirconium phosphate/Nafion composite membranes.* Journal of Membrane Science, 2004. **237**: p. 145-161.
80. Casciola, M., G. Alberti, M. Sganappa, and R. Narducci, *On the decay of Nafion proton conductivity at high temperature and relative humidity.* Journal of Power Sources, 2006. **162**(1): p. 141-145.
81. Sone, Y., P. Ekdunge, and D. Simonsson, *Proton Conductivity of Nafion 117 as Measured by a Four-Electrode AC Impedance Method.* J. Electrochem. Soc., 1996. **143**(4): p. 1254-1259.
82. Baglio, V., A. Di Blasi, A.S. Arico, V. Antonucci, P.L. Antonucci, F.S. Fiory, S. Licoccia, and E. Traversa, *Influence of TiO2 nanometric filler on the behaviour of a composite membrane for applications in Direct Methanol Fuel Cells.* Journal of New Materials for Electrochemical Systems, 2004. **7**(4): p. 275-280.
83. Mikhailenko, S.D., S.M.J. Zaidi, and S. Kaliaguine, *Sulfonated polyether ether ketone based composite polymer electrolyte membranes.* Catalysis Today, 2001. **67**(1-3): p. 225-236.
84. Alberti, G., M. Casciola, L. Massinelli, and B. Bauer, *Polymeric proton conducting membranes for medium temperature fuel cells (110-160 degrees C).* Journal of Membrane Science, 2001. **185**(1): p. 73-81.
85. Mikhailenko, S.D., S.M.J. Zaidi, and S. Kaliaguine, *Electrical properties of sulfonated polyether ether ketone/polyetherimide blend membranes doped with inorganic acids.* Journal of Polymer Science Part B-Polymer Physics, 2000. **38**(10): p. 1386-1395.

86. Kawahara, M., J. Morita, M. Rikukawa, K. Sanui, and N. Ogata, *Synthesis and proton conductivity of thermally stable polymer electrolyte: poly(benzimidazole) complexes with strong acid molecules.* Electrochimica Acta, 2000. **45**(8-9): p. 1395-1398.
87. Gil, M., X.L. Ji, X.F. Li, H. Na, J.E. Hampsey, and Y.F. Lu, *Direct synthesis of sulfonated aromatic poly(ether ether ketone) proton exchange membranes for fuel cell applications.* Journal of Membrane Science, 2004. **234**(1-2): p. 75-81.

3 Oxygen Reduction in PBI/H_3PO_4 Interface

3.1 Introduction

In electrochemical systems, the exchange current density j_0, depends on both temperature and concentration. In PEMFC the effective exchange current density, for hydrogen oxidation is several orders of magnitude greater than that for oxygen reduction (cathode reaction), ca. 10^{-4} vs. 10^{-9} A cm^{-2} Pt at 25 °C and 1 atm [1]. The slow kinetics of oxygen reduction is a key factor that limits the performance of fuel cells. This means that, at a given current density, the voltage losses in the cathode are usually significantly higher than those of the anode. Therefore, enhancing the cathode activity has been a major focus for PEMFC electrode development.

In this chapter, the active specific areas of several commercial Pt/C catalysts were measured using the method based on the hydrogen under potential deposition charge. Half cell tests (three-electrode cell) were carried out in order to obtain kinetics information regarding oxygen reduction at a PBI/phosphoric acid interface. The three phase boundaries were discussed and the effect of ionomer properties (permeability, density & conductivity) and content in the catalyst layer were investigated. The active electrochemical surface area of the electrode was also measured and the corresponding platinum utilisation reported.

3.2 Cyclic Voltammetry and Electrochemical Surface Area (ESA)

The Electrochemical Surface Area (ESA) is one of the most important parameters for characterizing PEM fuel cell electrodes. A higher ESA implies a better electrode, as more catalyst sites are available for electrode reactions. The electro-catalysis mechanism is based on the electrode–electroactive species charge transfer through the electrode surface. Hence reaction rate, and consequently the current, is proportional to the real electrode surface area.

3.2.1 Cyclic Voltammetry and UPD

When comparing the activity of catalyst surfaces, knowledge of the catalyst electrochemical surface area (ESA) is essential. Table 3-1 summarises estimated ESAs, from XRD spectra, assuming spherical particles and its variation with the catalyst Pt:C ratio reported in [2].

The commonly used electrochemical technique for the determination of metal electrode active surface area is anodic stripping of hydrogen adsorbed in the under-potential deposition potential (UPD) region. This corresponds to the total charge passed during hydrogen adsorption/desorption after accounting for the double layer capacity [3].

Table 3-1. Platinum-carbon weight percentage relation with average particle size, data taken from Ref [2].

Catalyst	Pt Particle Size (Å)	Pt/ (m^2 g^{-1})
5%	15	185
10%	20	141
20%	22	128
30%	25	112
40%	28	100
50%	33	86
60%	37	76
80%	49	57

Hydrogen adsorption on the platinum electrode surface is achieved by applying sufficiently negative potentials to the electrode in contact with an aqueous solution. Three regions can be distinguished, (shown in Figure 3-1) in the cyclic voltammetric curve of a Pt electrode in contact with an acid solution [4].

The "oxygen region" is found at positive potentials. During the positive sweep prior to O_2 evolution, a hydrated Pt oxide monolayer is formed (anodic current). The reverse process will take place in the cathodic sweep.

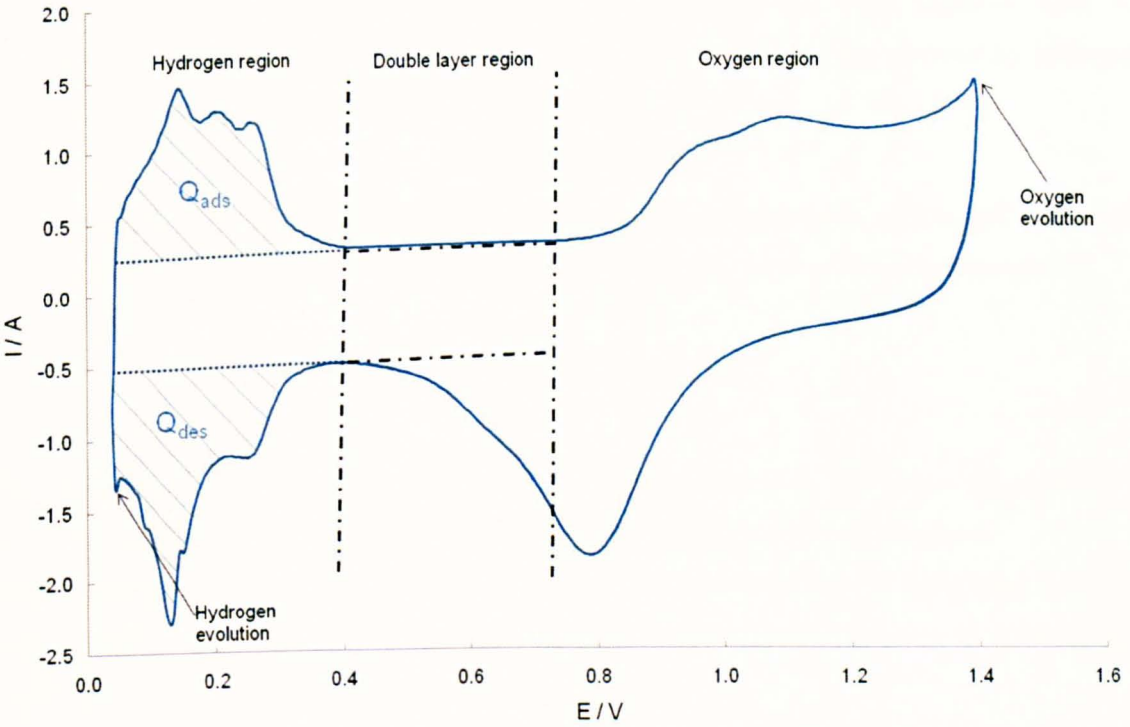

Figure 3-1. Typical observed platinum cyclic voltammogram in acidic media with regions of interest indicated, potentials are versus SHE at room temperature.

In the centre of the voltammetric curve is a region where only low currents (positive anodic for the positive sweep and negative for the negative sweep) can be found. This is the double-layer region where only capacitive processes take place. The value of the double layer charging current I_{dl} (non-faradic) is directly proportional to the capacity of the double layer and the scan rate:

$$I_{dl} = C_{dl} \cdot \upsilon \qquad [1]$$

Where C_{dl} is the capacity of the double layer and υ is the scan rate.

Finally, the "hydrogen region" is found at negative potentials. At more negative potentials the reduction of H^+ and the adsorption of H atoms become stronger:

$$H^+(aq) + e^- + site \rightarrow H(ad)$$

This process continues as electrode potentials become more and more negative, until the formation of a H(ad) monolayer is achieved. Once the Pt surface is fully covered by hydrogen atoms, the adsorption of H_2 molecules will take place:

$$2H(ad) \rightarrow H_2(ad)$$

These adsorbed molecules come together to form hydrogen molecules, which will eventually form bubbles that will leave the Pt electrode surface when they have grown large enough:

$$nH_2(ad) \rightarrow nH_2(g) + 2n\text{-sites}$$

The sharp rise in the cathodic current is due to hydrogen evolution [5]. When the potential is reversed, the opposite processes (anodic currents in the hydrogen region) take place.
The electrochemical surface area ($cm^2\ mg^{-1}$ Pt) of the electrode can be calculated from the charge transfer (Q_H, $mC\ mg^{-1}$ Pt) for the hydrogen adsorption and desorption in the hydrogen region (0.05–0.4 V vs SHE) of cyclic voltammograms [6].

An average value of 210 $\mu C\ cm^{-2}$ of the real electrode surface for a clean smooth platinum electrode can be considered for rough platinum polycrystalline surfaces- Pt(100,101&111) [7, 8].
The ESA obtained for a given catalyst layer is highly dependent on the method used to prepare the surface under investigation [3]. The use of binding agents (e.g. Nafion, PTFE) tends to change accessible ESA. A high loading will usually result in a thick electrode, limiting electrolyte access to the catalyst and a corresponding drop in the measured ESA.

The columbic charge for hydrogen desorption (Q_H) was used to calculate the active platinum surface of the electrodes. The value of Q_H was calculated as the mean value between the charge exchanged during the electro-adsorption (Q_{ads}) and desorption (Q_{des}) of H_2 on Pt sites. The contribution of charge from the double layer region was subtracted from both Q_{ads} and Q_{des} before calculating Q_H.

3.2.2 ESA measurement details

The experiment was performed in a glass cell with a silver/silver chloride reference electrode connected to a luggin capillary probe. The working electrode was glassy carbon electrode (GCE) with 3.0 mm dia. (BASi) with a geometric surface area of c.a. 0.07 cm^2. The counter electrode was a platinum wire. The electrolyte was 0.5 M H_2SO_4, The voltammetric experiment was carried out using EG&G Princeton applied research Model 273 digital Potentiostat/ Galvanostat.

Platinum supported on Vulcan XC-72R carbon from E-Tek Corporation (20%, 30%, 40%, 50%, 60% wt) was dispersed in dilute water-ethanol (1:1 v/v) ink, 0.014 mg_{Pt} (2 mg_{Pt} cm^{-2}) was applied to the surface of the glassy carbon by means of micro-pipette, then dried in an oven at 80 °C.

Three different scan rates were applied 20, 50 and 100 mV s^{-1}. The measurements were carried out three times each, the average values was reported with its corresponding standard error.

3.2.3 ESA results and conclusion

The ESA is calculated using:

$$ESA(cm^2) = \frac{Q_H\,(columb)}{0.21 * 10^{-3}\,(columb.cm^{-2})} \qquad [2]$$

Where Q_H is given by:

$$Q_H = \int_i^f I \cdot dt \qquad [3]$$

t_i is the time when the hydrogen adsorption (or desorption) starts and t_f is the moment when the monolayer is fully saturated (or cleared). The faradic current, I, is the measured current subtracted from the double layer current.

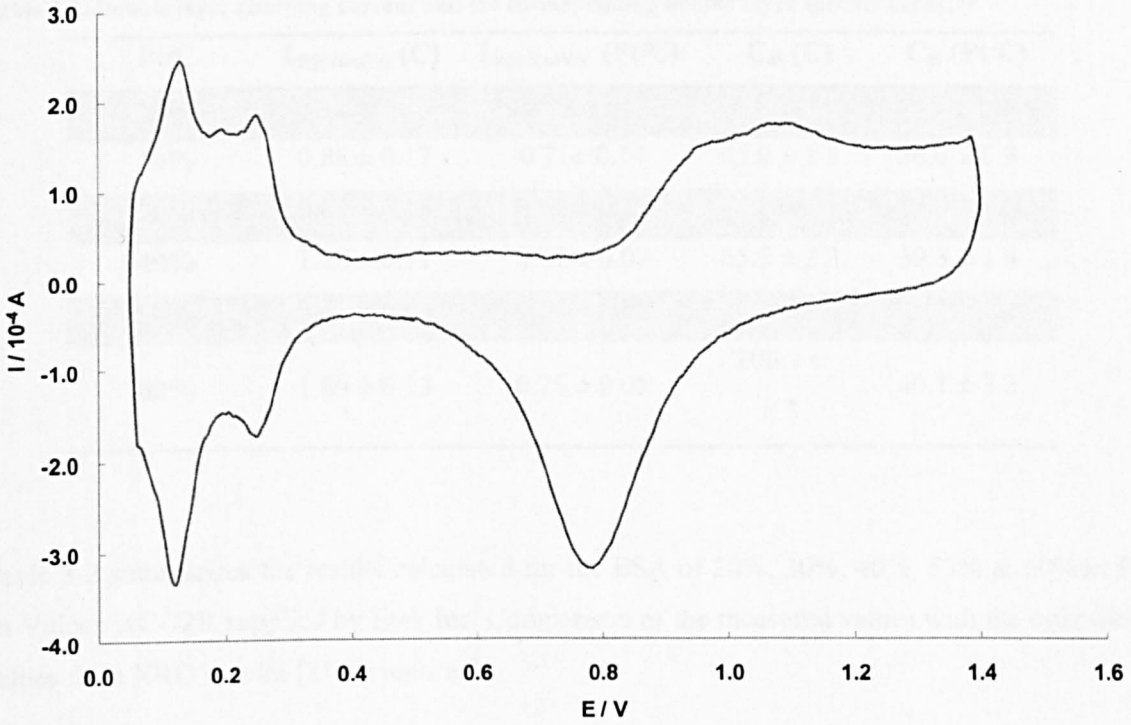

Figure 3-2. Cyclic voltammogram of 60% Pt on Vulcan XC-72R from Etek inc. using scan rate of 0.02 V s^{-1} in 0.5M H_2SO_4 potentials are versus SHE at room temperature.

Table 3-2. The electrochemical surface area measured from UPD and the estimated from x-ray diffraction

Pt/C	ESA_{UPD}	XRD*	ESA_{XRD}	Utilisation
%wt	$m^2 g_{Pt}^{-1}$	nm	$m^2 g_{Pt}^{-1}$	%
20%	51.1 ± 4.0	2.2	128	39.8 ± 3.1
30%	51.9 ± 3.6	2.5	112	46.4 ± 3.2
40%	47.3 ± 4.4	2.8	100	47.0 ± 4.4
50%	42.1 ± 5.4	3.3	86	48.8 ± 6.3
60%	36.2 ± 3.1	3.7	76	47.4 ± 4.0

*data taken from reference [2]

Table 3-3. Double layer charging current and the corresponding double layer specific capacity

Pt/C	$I_{dl@20mV/s}$ (C)	$I_{dl@20mV/s}$ (Pt/C)	C_{dl} (C)	C_{dl} (Pt/C)
%wt	$A.g^{-1}$	$A.g^{-1}$	$F.g^{-1}$	$F.g^{-1}$
20%	0.88 ± 0.17	0.71± 0.14	45.0 ± 1.2	36.0 ± 0.9
30%	0.89 ± 0.16	0.62 ± 0.11	45.6 ± 1.9	31.9 ± 1.3
40%	1.28 ± 0.11	0.77 ± 0.07	65.5 ± 2.3	39.3 ± 1.4
50%	1.11 ± 0.04	0.55 ± 0.02	56.7 ± 1.9	28.4 ± 1
60%	1.89 ± 0.13	0.75 ± 0.05	100.1 ± 8.3	40.1 ± 3.3

Table 3-2 summarises the results calculated for the ESA of 20%, 30%, 40%, 50% & 60%wt Pt on Vulcan XC-72R supplied by Etek Inc. Comparison of the measured values with the estimated values from XRD spectra [2] are reported.

It can be noticed that the measured ESAs are approximately half those of the estimated values. This is explained as follows:

- The estimate values exhibit large inherent error values arising from several assumptions: quoted metal to carbon percentage, homogenous spherical platinum distribution and accuracy of XRD average particle size.

- The measured values are affected by the binder [3] and the thickness of the measured layer, due to porosity issues and the hydrophobic properties of the carbon support- not all catalytic sites are accessible by the liquid electrolyte. This is clearly observed from the utilization of the catalyst, where all the studied catalyst exhibits values close to 50% except for 20% Pt/C, which had a value of ca. 40% due to its too thick layer.

The catalyst specific electrochemical surface area measured using cyclic voltammetery correspond to 50-30% of the given value by the manufacture (XRD) when placed in the electrode structure [1].

Table 3-3 summarises the results of the double layer charge: two values were reported, one denoted as (C) which consider the mass of carbon only, assuming that the charging current arises mainly from the carbon (specific area of 250 $m^2\ g^{-1}$) and neglecting the contribution from platinum (specific area of 30-50 $m^2\ g^{-1}$), and the other denoted as (Pt/C) where the total mass of the catalyst is considered.

The reported values of the charging current (scan rate of 20 mV s^{-1}) and the specific capacity are in close agreement with reported values in the literature: $I_{dl@20mV/s}$ of 0.6 A g^{-1} and C_{dl} of 22 F g^{-1} for untreated Vulcan [9] and $I_{dl@20mV/s}$ of 2 A g^{-1} with C_{dl} of 92-112 F g^{-1} for porous Vulcan electrode [10].

3.3 Electrodes and three phase boundaries

The electro-catalysts used in the PEMFC are usually based on platinum or its alloys for both anode and cathode. There have been numerous efforts to minimise the use of platinum in the catalyst layer by increasing catalyst activity. This has been achieved by supporting finely dispersed platinum nano particles, ca.~1.5 nm, with an area of 185 $m^2\ g^{-1}$ on suitable carbon blacks or graphite- the maximum theoretical area for platinum is 240 $m^2\ g^{-1}$ [1]-. In addition a high degree of optimisation of the electrode structure has taken place to enable low loadings of Pt catalyst, of the order of 0.1-0.2 mg cm^{-2} for anodes and 0.2-0.5 mg cm^{-2} for cathodes [11, 12].

There are three different participants in electrochemical reactions, electrons, protons and gaseous-liquid reactant/product. The reaction will only take place on the catalyst surface where all the three species have access (Figure 3-3). Electrons travel through electrically conductive solids, i.e. from the catalyst particles to carbon substrate (in case of supported platinum). Protons travel through the ionomer electrolyte, therefore an intimate contact between the catalyst and ionomer is required. Finally, gaseous reactant should be easily transported to reaction sites; similarly, product water should be easily removed to prevent flooding, i.e. restricted access of oxygen due to pore blocking. This problem can be solved by providing a porous structure next to the catalytic sites.

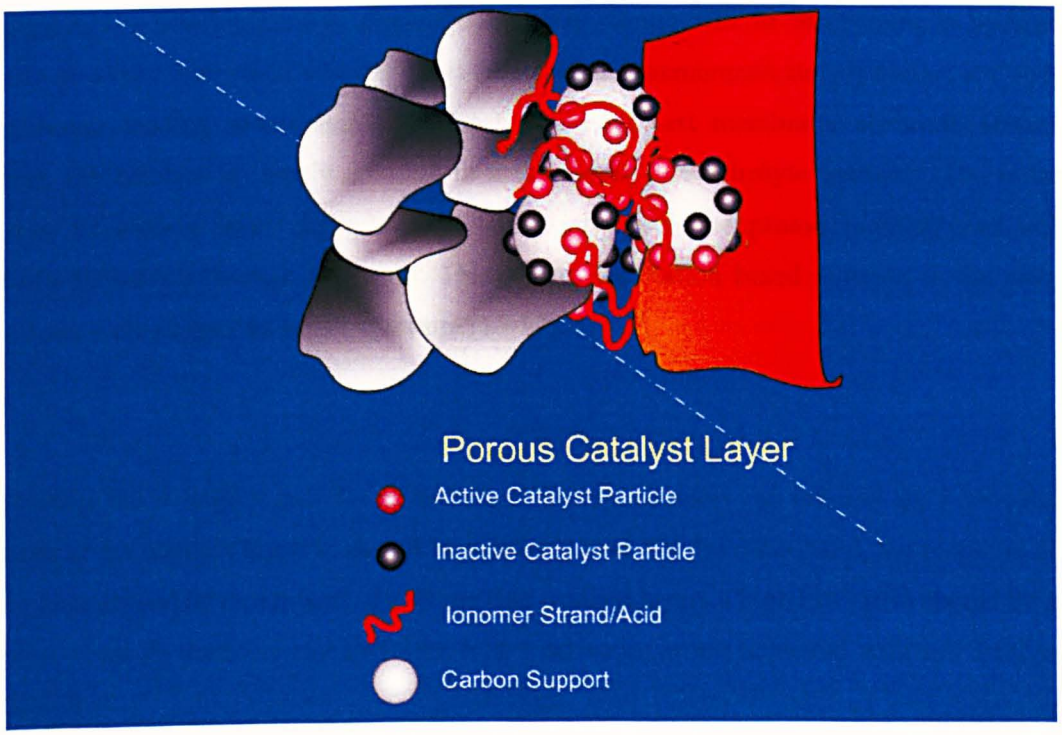

Figure 3-3. The three phase boundary for porous catalyst layer.

The electrochemical reaction will take place at the three phase boundary formed by the ionomer, solid and void phases. However, the reaction zone is not limited to a single three phase boundary line as gas permeates through the polymer electrolyte too.

Connecting the catalyst with a binder forms the electrode/catalyst layer in a PEMFC. The binder typically used was polytetrafluoroethylene (PTFE): a non-wetting component within the electrode. The bound catalyst structure is applied either to the membrane or first to the backing layer and then to the membrane. The binder performs very important functions. It "fixes" the catalyst particles within a layered structure and enables some degree of electronic conductivity between particles (contact between carbon particles). It also provides the overall architecture of the electrode, enabling access of gas into the structure (hydrophobic regions) while enabling movement of water (in hydrophilic regions).

One of the most important features required of any electrode structure is a high degree of intimacy of the catalyst particles and the membrane to ensure high proton mobility.

Consequently a development in electrode structure design was to incorporate a hydrophilic ionomer into the electrode as a binder. This enhanced the membrane/catalyst contact and reduced the platinum loading requirements. In most state-of-the-art membrane electrode assemblies (MEAs), the catalyst is largely covered in a thin layer of electrolyte ionomer. The optimum thickness of such a layer depends on a balance between the proton mobility and oxygen solubility/diffusivity through this layer. Thicknesses for Nafion based ionomer in the range of 0.5 to 3 nm were suggested in the literature [13-17].

To minimise the voltage losses due to the rate of proton transport and reactant gas permeation in the depth of the catalyst layer, it should be relatively thin. On the other hand, the platinum active surface area should be maximised. To obtain thin catalyst layers a high Pt:C ratio should be used; however, small Pt particles and therefore larger active areas are achieved with low Pt:C ratios (Table 3-1).
The influence of catalyst layer thickness and Nafion content on the electrode performance continues to be an area of study [11, 12, 14, 18-21]. Optimum Nafion contents range from 27 to 40 wt% depending on the nature of the electrodes: different Pt loading or Pt/carbon support, i.e. catalyst thickness and different ink preparations i.e. porosity.

Reshetenko et al [22] suggested that the Nafion content depended on porosity of the structure for high platinum loadings 3-4 mg cm^{-2} i.e. low overall porosity, the Nafion content should be in the range of 10 %wt, which increased to 20% when platinum loading fell to 1 mg cm^{-2}. The porosity, on the other hand, is inversely proportional to its ionomer content. The effect of Nafion on the catalyst layer pore size, pore size distribution, pore area, and pore volume were reported based on porosimetry measurements [23]. Sasikumar et al [20] similarly identified optimum nafion content of 20, 40 and 50% wt for lower platinum loadings of 0.5, 0.25 and 0.1 mg cm^{-2}, respectively.

Qi and Kaufman [11] recommended a Nafion content of 30% for electrodes with low platinum loading of 0.2-0.35 mg cm^{-2}. Similar Nafion contents were considered by Li and Pickup [24] and Lufrano [25]. A volcano plot relation was proposed [25] for the effect of nafion content on

conductivity and accessible electrochemical surface area (ESA), where increasing nafion content above 30% led to electrical isolation of the catalyst or carbon particles. Song et al [12] suggested that the sharp drop in performance observed when increasing nafion content above 35% (0.4 mg cm^{-2} using 20% Pt/C) was also attributed to slow oxygen transport through thick ionomer films, which became more significant at elevated temperatures. Other researchers suggested that the best Nafion content depended on the molecular weight of the ionomer or its ion exchange capacity (IEC) [26] or operating oxygen partial pressure and stoichiometry; 35% for oxygen operation compared to 22% for air operation [27].

Another approach to optimise the catalyst layer was to fabricate electrodes with different distribution or loading gradients for both ionomer and catalyst (Pt:C ratio).

Antoine et al. [28] studied the effect of catalyst loading gradients on performance. They reported a better performance for low porosity active layer when catalyst particles were located close to the gas diffusion layer, but for highly porous layers, the performance improved when they were located close to the proton exchange membrane. Wang et al. [29] numerically modelled the influence of gradients in Nafion contents on performance and concluded that an improvement in performance is obtained when the Nafion content increases toward the membrane. These results were also verified experimentally [30]. In the cathode catalyst layer, oxygen diffuses through two different components: gas pores and electrolyte. When the volume fraction of gas pores is sufficiently large, oxygen diffusion in the electrolyte is the dominant process and diffusion in gas pores may be neglected. When the volume fraction of gas pores is relatively small compared to the volume fractions of liquid or solid electrolyte, oxygen diffusion in gas pore is significant and cannot be neglected [31].

An increasing Nafion content distribution in the catalyst layer from GDL towards membrane results in a better performance overall, compared to that with a uniform nafion distribution. This is explained by improved oxygen transport near the GDL/CL interface by virtue of the increased porosity due to lower Nafion content, which leads to a lower electrochemical reaction rate near the GDL/CL interface than that with a uniform nafion distribution. Similarly, near the CL/PEM interface, proton migration is improved because of the higher ionomer content. However, oxygen

transport is compromised due to a decrease in porosity, leading to a lower electrochemical reaction rate in this region, compared with the uniform Nafion distribution case. In the middle region of the CL, the electrochemical reaction rate is larger than that of the uniform Nafion case and this is responsible for the increased performance [32].

Song et al [32] modelled the effect of platinum distribution with constant Nafion content (30 % wt). They used low Pt loading close to the GDL side (using low Pt:C ratios) and high Pt loading close to the membrane (using high Pt:C ratios). The reaction rate near the GDL/CL interface was slightly lower than in the case of the uniformly distributed Pt cathode, but the increase of Pt loading near the CL/PEM interface resulted in a higher reaction rate compared to the uniform Pt loading cathode. Because the overall increase of the electrochemical reaction rate near the CL/PEM interface was larger than the overall decrease near the GDL/CL interface, the catalyst layer with optimized distribution of Pt loading showed the higher performance than that for the uniform distributed case.

It can be concluded that the CL with a stepwise porosity distribution, with higher porosity near the GDL and lower near the membrane, performs better than that with uniform distribution, especially at high current density. This is attributed to better O_2 distribution in the CL, thus extending the reaction zone forward towards the membrane side [27].

3.4 Nafion, PBI and phosphoric acid

As mentioned above the optimum ionomer content in the catalyst is a balance between the ionomer conductivity and oxygen permeability. Tables 3-4, 3-5, 3-6, 3-7, 3-8 & 3-9 provide published values of conductivity, density, and oxygen, hydrogen and methanol permeability (diffusion and solubility) for pristine PBI, acid doped PBI, phosphoric acid, Nafion and PTFE.

Table 3-4. Proton conductivity of PBI, phosphoric acid and nafion at various temperature and relative humidity

Material	Temperature	RH	Conductivity	Ref
	°C	%	S cm^{-1}	
PBI 5.6 PRU	120[a]-200[b]	7[a]-1[b]%	0.02-0.056	This work
PBI 5 PRU	150[a]-190[b]	10[a]-1[b]%	0.01-0.04	[33]
H_3PO_4 99.8%wt	130	0.7%	0.4	[34]
H_3PO_4 90% wt	170	10%	0.643	[35]
Nafion 117	60-80	80-85	0.06-0.08	[36]
PBI 0 PRU	25	0-100%	$2\text{-}8\times10^{-4}$	[37]
PBI 5.6 PRU	80[a]-160[b]	80[a]-10[b]%	0.02-0.06	[33, 38]
Nafion 115	20-100	100%	0.01-0.03	[39]
Nafion 115	80	60-80%	0.04-0.067	[39]
Nafion 117	100	80%	0.09	[40]

Table 3-5. Density of PBI, phosphoric acid, Nafion and PTFE at various temperatures.

Material	Temperature	Density	Ref
	°C	g cm^{-3}	
PBI	25	1.34	[41]
H_3PO_4 101.6%wt	25[a],130[b],170[c]	1.8875[a],1.797[b],1.764[c]	[34]
H_3PO_4 88.28% wt	25[a],130[b],150[c]	1.726[a],1.632[b],1.614[c]	[34]
Nafion	25	2	[17, 42]
PTFE	25	2.15	[43]

The water content in Nafion greatly affects the degree of swelling and therefore gas permeation through the membrane, since water content has a significant influence on the diffusivity [44]. The permeation of gases through Nafion takes place in the intermediate region, which consists of the flexible amorphous part of the polytetrafluoroethylene backbone [45]. When fully hydrated,

Nafion's permeability is close to that of water and its conductivity is in the range of 0.1 $S.cm^{-1}$, on the other hand when dry, Nafion's permeability is close to that of PTFE and its conductivity is negligible.
Similarly, pristine PBI has negligible conductivity and oxygen permeability. On the other hand at extremely high doping levels, PBI's conductivity and oxygen permeability approach those of phosphoric acid under the same conditions.

When doped with 5 mol of phosphoric acid per mole repeat unit of the polymer, a level necessary to obtain high enough proton conductivity for fuel cells, the polymer membrane exhibits a volume swelling of 118 %, resulting in separation of the polymer backbones [46], and correspondingly increase in permeability. The permeation of both hydrogen and oxygen increases with increase in acid doping level [46, 47].

The ratio of the permeability coefficient for hydrogen and oxygen also varies with doping level, i.e. 40 for pristine PBI and 4 for the acid doped PBI [46]. Similarly, it falls from 3.5 to 2 for dry Nafion and 102 %wt wet nafion, respectively [44].

Wainright et al. [33] studied the vapour permeability of PBI at elevated temperatures. The permeation of methanol vapour at 80 °C was found to be 300 times lower than that for Nafion. The gas permeability of PBI membranes at 150 °C was comparable to that of Nafion, for hydrogen and lower in the case of oxygen at 80 °C [46].
Ayad et al. [48] studied the oxygen permeability through Nafion, sulfonated polyimide & PBI. Values differed by almost an order of magnitude: 9×10^{-12} mol cm cm^{-2} s^{-1} for Nafion and 0.5×10^{-12} & 10^{-12} mol cm cm^{-2} s^{-1} for PBI and S-PI, respectively at 25 °C. They suggested that the optimum amount of ionomer depended on its O_2 permeability 25% wt for nafion and 15% wt for SPEEK and P-IS.

Unlike Nafion based PEMFCs, there is limited data available in the literature on optimizing PBI / phosphoric acid based electrodes. Kim et al used platinum loading of 0.55 mg cm^{-2} (20 %Pt/C catalyst) and fixed the doping level in the catalyst layer to 6 moles acid per mole polymer (6

PRU) or 2:1 weight ratio, they achieved an optimum amount for acid-PBI of 20 %wt, corresponding to PBI and acid loading of 0.23 & 0.46 mg cm^{-2}, respectively.

Wang et al. [49] used platinum loading of 0.5 mg cm^{-2} (20% Pt/C catalyst) and PBI loading of 0, 0.3 & 0.9 mg cm^{-2} with no precise amounts of acid added (few micro litres). They found that the best performance was achieved with PBI loadings of 0.9, 0 & 0.3 mg cm^{-2}, respectively. They concluded the preparation method and ionomer-acid content had a severe impact on PBI based electrodes.

Pan et al. [50] used platinum loading of 0.5 mg cm^{-2} (20% Pt/C catalyst) and fixed the doping level in the catalyst layer to 12-15 moles acid per mole polymer or 4-5:1 weight ratio; they suggested PBI and acid loading of 0.7 & 2.8-3.5 mg cm^{-2}, respectively.

Seland et al. [51] studied different catalyst thickness using different Pt:C ratios. They concluded that the optimum performance was obtained with a thin catalyst layer using 50% Pt/C. They fixed the acid doping to 6 PRU (acid molecules per repeat PBI unit) and suggested optimum PBI loading of 0.4 and 0.6 mg cm^{-2} for anode and cathode, platinum loading of 0.36 and 0.6 mg cm^{-2}, respectively, accompanied by acid loading of 0.8-1.2 mg cm^{-2}.

Scott et al. [52] and Lobato et al. [53] studied the effect of catalyst ink solvent on the fuel cell performance, they reported enhancement using a colloidal ionomer in the ink (Acetone) compared with a standard ionomer solution method (DMAc), using platinum (20 % Pt/C) and PBI loadings of 0.5 & 0.7 mg cm^{-2}, respectively. This was attributed to different pore sizes and pore size distributions. Similar work was reported on Nafion systems [54].

Kongstein et al. [55] have recently shown that PBI based catalyst layer performance can be improved by using non homogenous platinum distribution, similar to the technique described earlier for Nafion. They used low Pt loading close to the GDL side, using 20% Pt:C ratio, and high platinum loading close to the membrane, with 50% Pt/C with total platinum loading of 0.6 mg cm^{-2}. This electrode showed advantages over standard 0.6 mg cm^{-2} 50% Pt/C. They also recommended PBI loading of 0.2-0.4 mg cm^{-2}.

Table 3-6. Vapour methanol permeability through PBI and nafion at various conditions.

Material	Temperature	RH	Species	Vapour activity	Permeability	Diffusion	solubility	Ref
	°C	%			10^{-12} mol cm cm^{-2} s^{-1} atm^{-1}	10^{-6} cm^2 s^{-1}	10^{-6} mol cm^{-3} atm^{-1}	
PBI5PRU	180	5-7.5	Methanol	0.25-0.5	280-298.5	-	-	[56]
PBI5PRU	180	0	Methanol	1	166.4	-	-	[56]
PBI5PRU	150	0	Methanol	0.01-0.1	6.7-67	0.01	2175-6526	[33]
PBI3PRU	80	n/a	Methanol	n/a	92.34	-	-	[57]
Nafion117	80	n/a	Methanol	n/a	27360	-	-	[47, 57]

Table 3-7. Liquid methanol permeability through PBI and nafion at 25°C and fully hydrated conditions.

Material	Temperature	Water content	Species	Concentration	Permeability	Ref
	°C			% wt	10^{-9} cm^2 s^{-1}	
Nafion 117	25	Fully hydrated	Methanol	3%	2300	[58]
PBI	25	Fully hydrated	Methanol	3%	8.3	[58]
PBI	25	Fully hydrated	Methanol	10-100%	18	[59]
Nafion115	25	Fully hydrated	Methanol	3%	850	[39]
Nafion117	25	Fully hydrated	Methanol	3%	2000	[60]
PBI	25	Fully hydrated	Methanol	100%	70	This work
Nafion 117	25	Fully hydrated	Methanol	100%	4000	This work

Table 3-8. Hydrogen and oxygen permeability through pristine and doped PBI, and phosphoric acid at various conditions.

Material	Temperature	RH%	Species	Permeability	Diffusion	solubility	Ref
	°C	%		10^{-12} mol cm cm^{-2} s^{-1} atm^{-1}	10^{-6} cm^2 s^{-1}	10^{-6} mol cm^{-3} atm^{-1}	
PBI 0 pru	120	0	O_2	0.06	-	-	[46]
PBI 0 pru	80	0	O_2	0.05	-	-	[46]
PBI 0 pru	180	0	O_2	0.1	-	-	[46]
PBI 0 pru	120	0	H_2	3	-	-	[46]
PBI 0 pru	80	0	H_2	1.6	-	-	[46]
PBI 0 pru	180	0	H_2	4.3	-	-	[46]
PBI 0 pru	25	100	O_2	0.5	-	-	[48]
PBI 3 pru	150	n/a	H_2	60	-	-	[61]
PBI 3 pru	150	n/a	O_2	3.3	-	-	[61]
PBI 5 pru	120	0	O_2	70	-	-	[46]
PBI 5 pru	80	0	O_2	30	-	-	[46]
PBI 5 pru	180	0	O_2	90	-	-	[46]
PBI 5 pru	120	0	H_2	250	-	-	[46]
PBI 5 pru	80	0	H_2	120	-	-	[46]
PBI 5 pru	180	0	H_2	380	-	-	[46]
PBI 6 pru	150	10	O_2	2.176	3.2	0.68	[62]
H_3PO_4 95%wt	150	10	O_2	7.31	17	0.43	[63]
H_3PO_4 98% wt	150	10	O_2	3.6	30	0.12	[64]

Table 3-9. Hydrogen and oxygen permeability through Nafion, PTFE and SPEEK at various conditions.

Material	Temperature	Water content	Species	Permeability	Diffusion	solubility	Ref
	°C			10^{-12} mol cm cm^{-2} s^{-1} atm^{-1}	10^{-6} cm^2 s^{-1}	10^{-6} mol cm^{-3} atm^{-1}	
Nafion117	25	0	O_2	2.8	-	-	[46]
Nafion117	25	0	H_2	4.1	-	-	[46]
Nafion117	80	0	H_2	15.7	-	-	[46]
Nafion117	80	0	O_2	4.1	-	-	[44]
Nafion117	80	0	H_2	14.4	-	-	[44]
Nafion117	80	0	O_2	3.1	-	-	[46]
Nafion117	80	102% wt	H_2	68.4	-	-	[44]
Nafion117	80	102% wt	O_2	34.2	-	-	[44]
Nafion125	80	0	O_2	7.5	-	-	[65]
Nafion125	80	0	H_2	48	-	-	[65]
Nafion125	80	0	N_2	3	-	-	[65]
Nafion125	30	0	O_2	0.49	0.088	5.7	[65]
Nafion125	30	0	H_2	4.79	2	2.4	[65]
Nafion125	30	0	N_2	0.223	0.092	2.4	[65]
Nafion	25	Fully hydrated	O_2	9.6	7	1.6	[47, 48]
SPEEK	25	Fully hydrated	O_2	2.5			[48]
PTFE	20	0	O_2	1.2	0.12	10.3	[66]
PTFE	80	0	O_2	6.1	0.88	6.9	[66]
PTFE	20	0	H_2	8.3	0.26	31.3	[67]
PTFE	20	0	O_2	3.8	0.14	26.8	[67]

3.5 Electrode preparation

The required PBI loadings were initially estimated using published data as shown below. Suggested PBI loading in the literature varied between 0.2 and 0.9 mg cm^{-2} for platinum loading of 0.5-0.6 mg cm^{-2}using 20%Pt/C. The acid loading varied in the range of 0.46 to 3.5 mg cm^{-2}. As shown earlier PBI conductivity and oxygen permeability depended on its acid content or doping level, whilst 25% wt was found to be the optimum amount for nafion, under the above mentioned conditions, leading to loading of 0.83 mg cm^{-2}. To maintain similar volume fractions (27%) and considering the density values, from table 3-5, Nafion loading of 0.83 mg cm^{-2} is equivalent to PBI loading of 0.556 mg cm^{-2}. From Table 3-4 it is seen that PBI (6PRU) exhibits half the conductivity of nafion under their nominal operating conditions (80˚C, 80-90% RH for Nafion and 150-175˚C, 1-10%RH for PBI), requiring twice the volume of PBI to maintain the same conductivity. On the other hand, from Tables 3-8 & 3-9 it can be seen that the hydrogen permeability for dry PBI (6 PRU) at 150 ˚C is similar to that of dry Nafion at 80 ˚C and the oxygen permeability of PBI (6 PRU) is 25-75 % of that of dry Nafion at 80 ˚C. However, Nafion's permeability increases almost an order of magnitude (8.5 times) by increasing its water content from dry to 102 % wt at 80 ˚C and RH 90-100 % , a typical operating conditions for Nafion. On the other hand, PBI's (6 PRU) permeability increases only by a factor of 2 when the relative humidity is increased from 1 to 10 % at 150 ˚C, the typical operative range for PBI. This means that the PBI film thickness over the catalyst layer should be 4 times less than that of Nafion to maintain similar oxygen transport. The above estimations are based on the PBI density only and ignore the contribution of the acid.

In this work a value of 0.72 mg cm^{-2} for PBI's loading was chosen for 20 %Pt/C with platinum loading of 0.5 mg cm^{-2}. Platinum loading was fixed and PBI loading was scaled to 0.27 and 0.12 for 40% Pt/C and 60% Pt/C, respectively, maintaining the ionomer film thickness over the catalyst or the volume fraction at 0.32. The acid loading was varied. Two different doping levels were investigated for each case; doping levels of 6 &16 PRU for 20% Pt/C, and 3 & 6 for both 40% and 60% Pt/C.

The PBI film thickness δ is calculated by

$$\delta_{PBI} = \frac{m_{PBI} / \rho_{PBI}}{S_C + S_{Pt}} \quad [4]$$

M_{PBI} is the mass of PBI per unit area (PBI loading), ρ is the density and S_c and S_{Pt} is the specific surface area of carbon and Platinum, respectively, per unit area.

The catalyst inks were prepared by mixing the required amount of PBI (6% wt in DMAc) with acetone under continuous sonication [52]. After achieving a stable colloid an appropriate amount of Pt/C catalyst (ETEK) was added, and the ink was airbrushed on top of a teflonised GDL/MPL(micro porous layer). After the desired weight was achieved the electrodes were dried at 160 °C to remove any traces of DMAc. The electrodes were later boiled in de-ionised water and dried at 100 °C. The necessary amount of high purity (99.999 %, Aldrich) 85% wt phosphoric acid was mixed with DI-water and airbrushed on top of the electrodes. The electrodes were later hot pressed on top of pre-doped PBI membranes (5.6 PRU) at 150 °C for 10 min applying a load of 40 kg cm^{-2} and left to cure for two weeks to obtain a uniform acid-PBI distribution.

3.6 Three electrode electrochemical cell

The electrodes were placed in specially designed mica-filled PTFE (Quadrant-EPP) body (Figure 3-4) equipped with gas inlet and outlet. The electrode was positioned so that the membrane faced downwards in contact with the liquid electrolyte and the GDL faced upwards in contact with a gold plated phenolic-resin impregnated graphite flow fields (parallel), to ensure good electrical contact. PTFE encapsulated Viton® O-ring was used to guarantee good sealing between the liquid electrolyte (hot phosphoric acid in the glass cell) and solid electrolyte (doped PBI membrane). The glass cell was heated by means of a circulating heating bath (Haake) with heating oil (Therminol). Platinum mesh was used as counter electrode as there was hot phosphoric acid electrolyte. A water cooled jacketed silver-silver chloride electrode was used as the reference and was connected to the cell by a luggin capillary.

Experiments were conduct at 100, 120 and 140 °C to ensure that only water vapour is produced. Above 140 °C 85% wt phosphoric acid produced large amounts of bubbles as the operating temperature approached the boiling point of 85% wt phosphoric acid (154-158 °C), and above such temperature poly-phosphoric acid started to be generated, dissolving the PBI membranes.

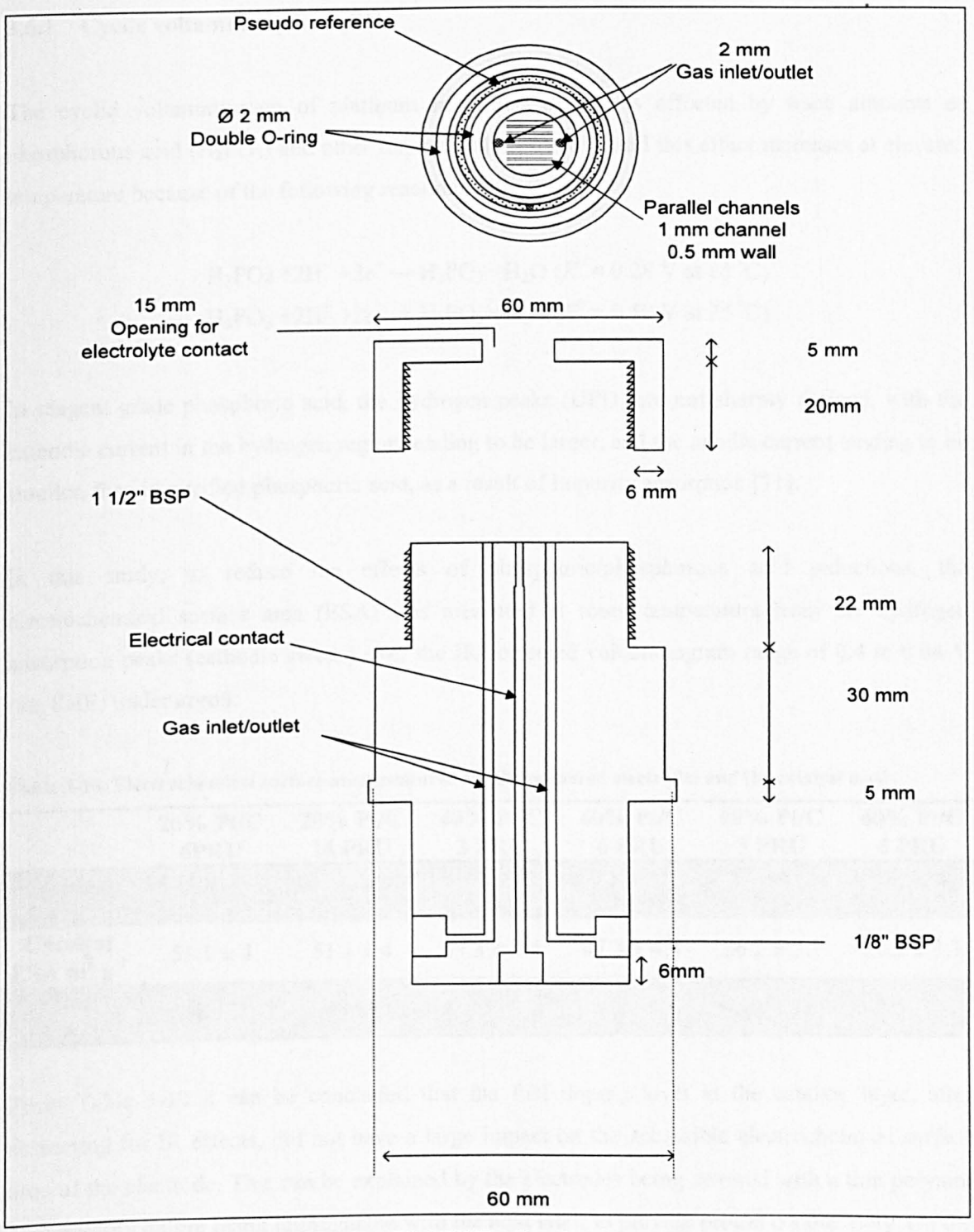

Figure 3-4. Schematic drawing of the mica-filled PTFE cell used to carry out the half cell tests.

3.6.1 Cyclic voltammetry in H_3PO_4

The cyclic voltammogram of platinum in H_3PO_4 system is affected by trace amounts of phosphorous acid (H_3PO_3) and other impurities [64, 68, 69], and this effect increases at elevated temperature because of the following reactions [70]:

$$H_3PO_4 + 2H^+ + 2e^- \rightarrow H_3PO_3 + H_2O \ (E^0 = 0.28 \text{ V at } 25\ ^\circ C)$$
$$H_3PO_3 + 2H^+ + 2e^- \rightarrow H_3PO_2 + H_2O \ (E^0 = 0.50 \text{ V at } 25\ ^\circ C)$$

In reagent grade phosphoric acid, the hydrogen peaks (UPD) are not sharply defined, with the cathodic current in the hydrogen region tending to be larger, and the anodic current tending to be smaller, than in purified phosphoric acid, as a result of impurity adsorption [71].

In this study, to reduce the effects of phosphoric/phosphorous acid reductions, the electrochemical surface area (ESA) was measured at room temperature from the hydrogen adsorption peaks (cathodic sweep) over the IR-corrected voltammogram range of 0.4 to 0.04 V (vs. SHE) under argon.

Table 3-10. Electrochemical surface area measured for the prepared electrodes and the catalyst used.

	20% Pt/C 6PRU	20% Pt/C 16 PRU	40% Pt/C 3 PRU	40% Pt/C 6 PRU	60% Pt/C 3 PRU	60% Pt/C 6 PRU
Electrode ESA $m^2\ g^{-1}$	34.81 ± 3.47	35.2 ± 3.62	16.55 ± 2.02	15.91 ± 1.88	14.46 ± 1.53	14.36 ± 1.41
Catalyst ESA $m^2\ g^{-1}$	51.1 ± 4	51.1 ± 4	47.3 ± 4.4	47.3 ± 4.4	36.2 ± 3.1	36.2 ± 3.1
Utilisation %	68.13	68.89	35	33.64	39.95	39.67

From Table 3-10 it can be concluded that the PBI doping level in the catalyst layer, after correcting for IR effects, did not have a large impact on the accessible electrochemical surface area of the electrode. This can be explained by the electrodes being covered with a thin polymer film initially before being impregnated with the acid later, to provide proton conductivity. On the other hand it can be noted that the measured electrochemical surface area using PBI (40 % volume) as electrolyte was lower than that of the catalyst measured ESA using 0.5 M sulphuric

acid. This is explained by easier access (porosity and wettability issues) to the catalytic sites for the liquid acid compared to the acid trapped in the solid polymer matrix, especially with thicker layers (1 mg_{Pt} of catalyst was studied in electrode case compared to 0.014 mg_{Pt} in the catalyst case).

3.6.2 Results and discussion

Linear sweep scans were carried out at a rate of 5 mV s^{-1} from 1.15 V to 0.1 V vs. SHE. After the electrode was held initially at 1.15V for 20 seconds prior to the sweep, differences in current densities at fixed potentials were used to measure differences in performance.

3.6.2.1 Effect of doping level on performance

With a constant volume fraction of PBI, increasing the doping level (acid content) will initially enhance the performance, as pristine PBI has a very low conductivity and oxygen permeability and ORR kinetics improves by increasing $[H^+]$. However, on the other hand the electrolyte film thickness surrounding the catalyst agglomerates will increase by increasing the doping level until it reaches a critical thickness beyond which mass transport will dominate. This can be derived from Fick's law for diffusion:

$$N_{O_2} = \frac{j}{4F} = \frac{D_{O_2}^{PBI-H_3PO_4}\left(C_{dissolve} - C_{Pt}\right)}{\delta} \qquad [5]$$

Where D_{O2}, $C_{dissolve}$ & δ are oxygen diffusion, solubility and film thickness ($\delta = \delta_{PBI} + \delta_{H3PO4}$), respectively.

Figure 3-5 shows the influence of doping level (in PRU) on linear sweep voltammograms for 20% Pt/C electrodes. Increasing the doping level from 6 to 16 PRU led to deterioration in the performance (lower current densities) especially under air operation which demonstrates mass

transport limitation. The difference in the performance between air and oxygen was much larger in the high doping case of 16 PRU than that of low doping case of 6 PRU.

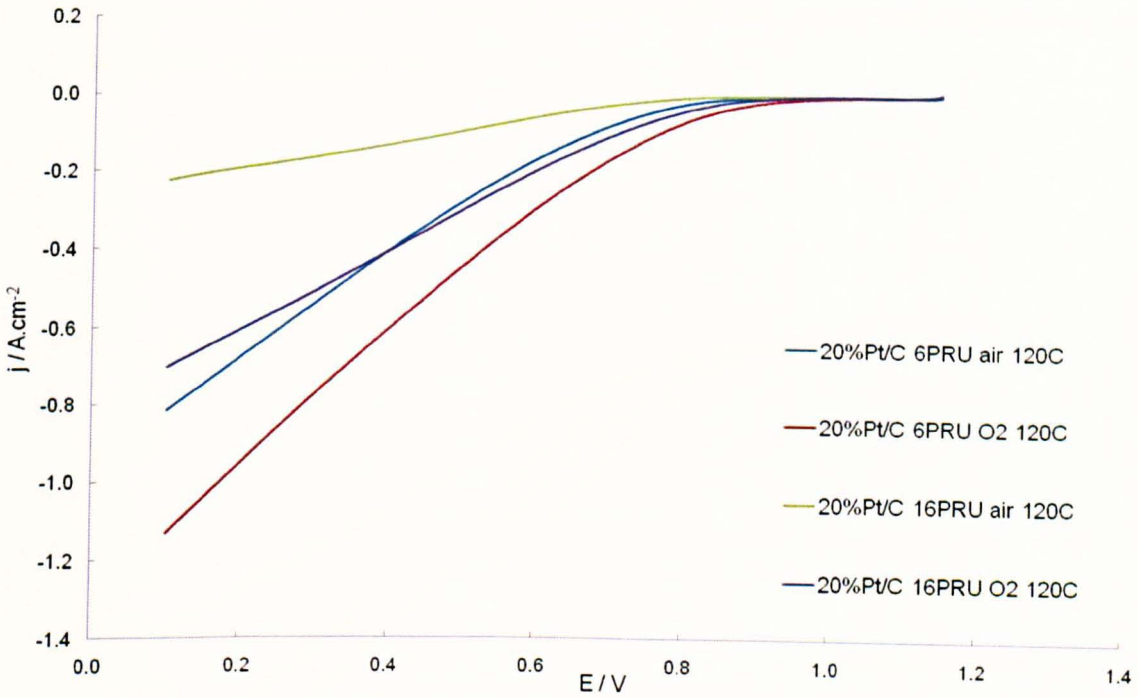

Figure 3-5. Linear sweep polarisation curves (vs. SHE) for oxygen reduction reaction using 20% Pt/C and doping levels of 6 & 16 PRU at 120 °C.

On the other hand, increasing doping level from 3 to 6 PRU for 40% Pt/C (Figure 3-6) led to a remarkable improvement in the performance when operating with oxygen (no mass transport limitation), but not with air. Kinetic enhancement, due to increased acid content, was observed with pure oxygen, but at a low oxygen concentration (air operation) mass transport effects dominated, leading to lower overall performance, which produced larger differences between air and oxygen performance at higher doping levels.

Similar behaviour was seen for the 60% Pt/C electrodes with doping levels of 3&6 PRU at 100 °C (Figure 3-7). However, after increasing the temperature (enhancement in kinetics and mass transport) to 120 °C (Figure 3-8), under air operation, higher doping level electrodes (6 PRU) showed better performance over lower doping level of 3 PRU. With pure oxygen operation, high

doping levels showed advantages over lower doping level of 3 PRU at low overpotentials (beginning of polarization curve). However at higher overpotentials (below 0.7 V vs. SHE) the performance of electrodes with a lower doping level (3 PRU) surpassed (overruns) that of 6 PRU. This is indicated by a lower value of transfer coefficient (α) for both high doping level electrodes, as will be discussed later.

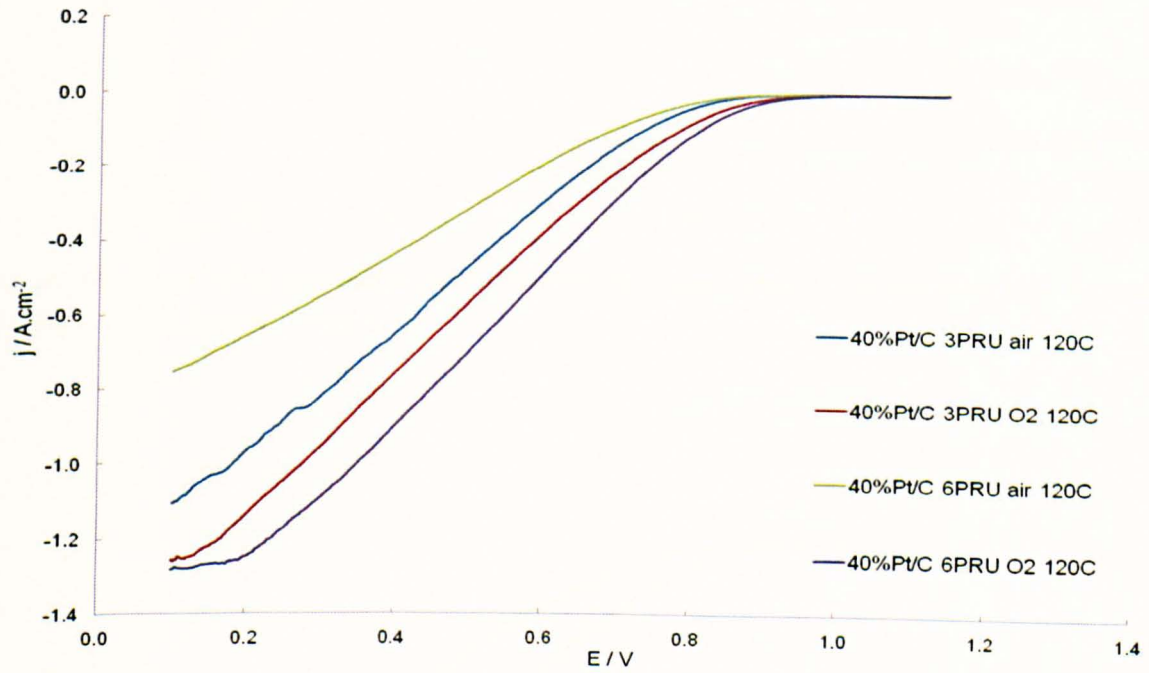

Figure 3-6. Linear sweep polarisation curves (vs. SHE) for oxygen reduction reaction using 40% Pt/C and doping levels of 3 & 6 PRU at 120 °C.

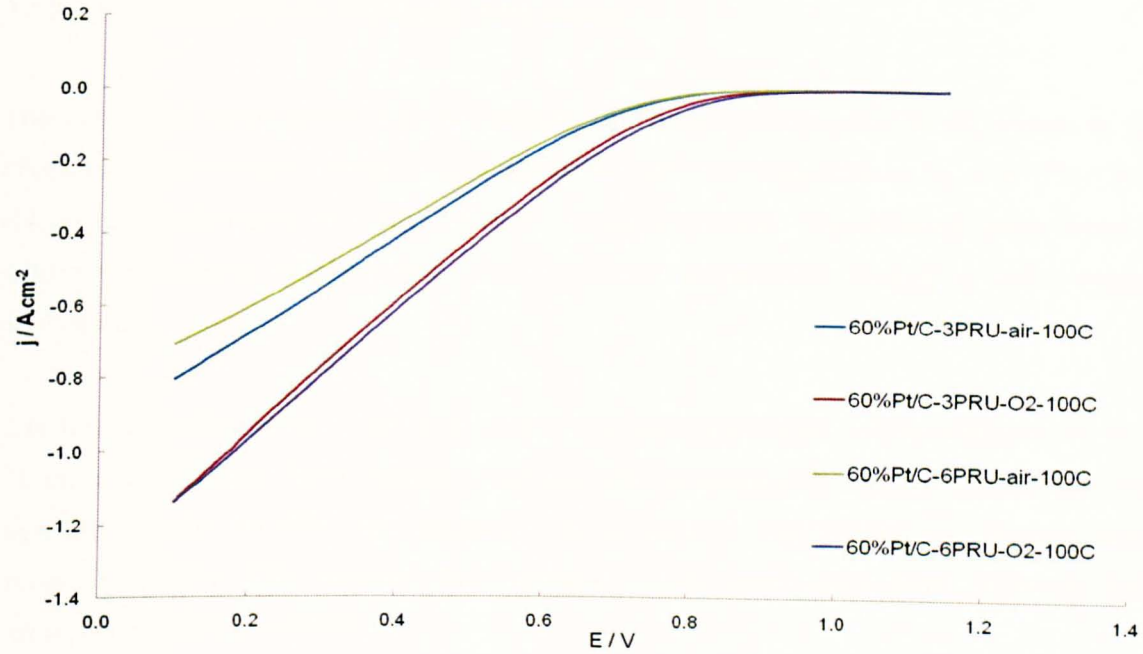

Figure 3-7. Linear sweep polarisation curves (vs. SHE) for oxygen reduction reaction using 60% Pt/C and doping levels of 3 & 6 PRU at 100 °C.

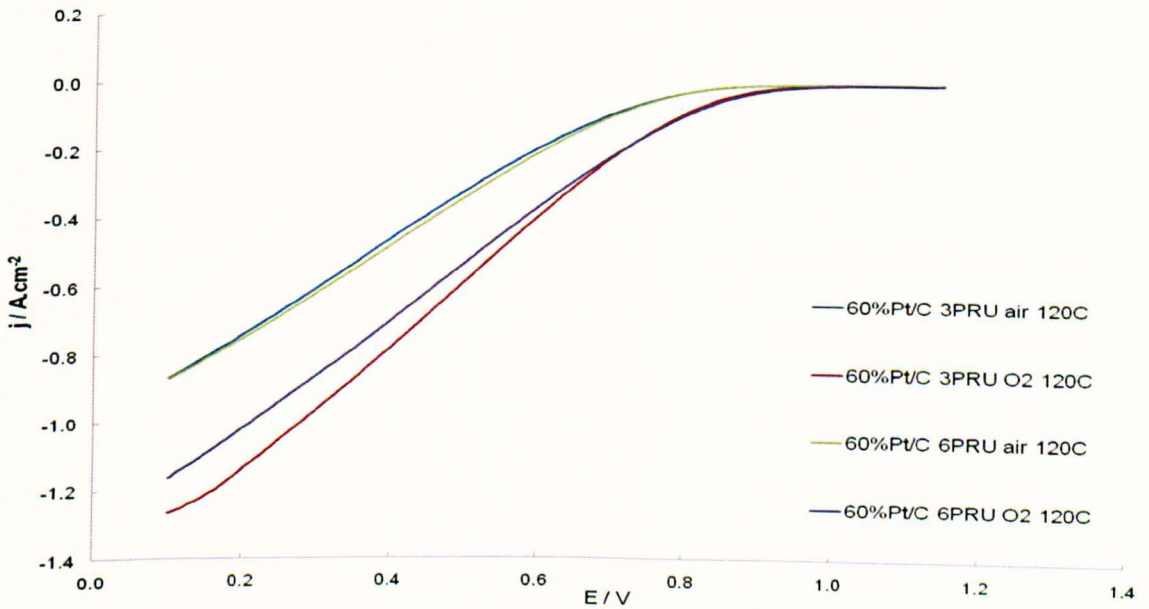

Figure 3-8. Linear sweep polarisation curves (vs. SHE) for oxygen reduction reaction using 60% Pt/C and doping levels of 3 & 6 PRU at 120 °C.

3.6.2.2 Effect of surfactant addition on performance

The addition of small amounts of perfluronated surfactant (as low as 0.1% wt), known as C6, (Trideca-fluroro hexane-1-sulfonic acid potassium salt) was suggested by Li et al [72, 73] to enhance the performance of oxygen reduction in phosphoric acid. The surfactant was believed to reduce the viscosity of phosphoric acid at elevated temperatures leading to better oxygen permeability.

Considerable enhancement in cell performance was observed (Figure 3-9) by adding 0.5% wt of C6 surfactant (Trideca-fluroro hexane-1-sulfonic acid potassium salt, Aldrich) to electrodes with high doping level (16 PRU) and operating with air, whilst a small impact was observed under oxygen operation. This suggests that surfactant enhancement arose from improved mass transport (oxygen permeability).

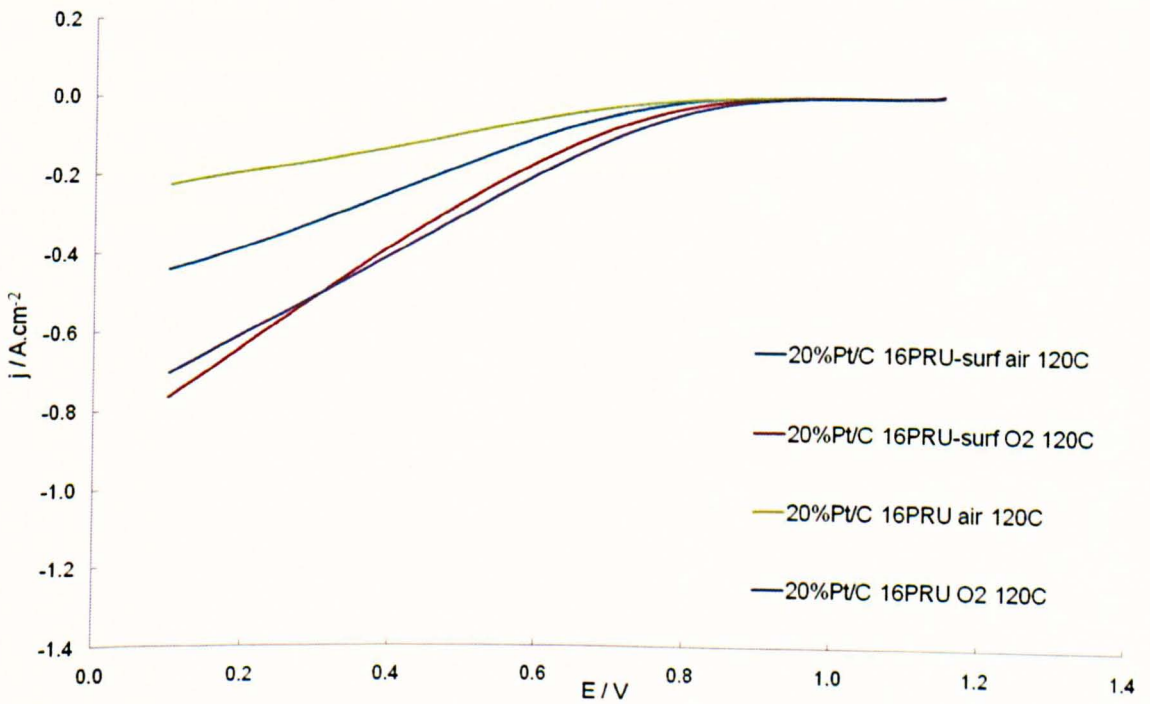

Figure 3-9. Effect of surfactant on linear sweep polarisation (vs. SHE) curves for oxygen reduction reaction using 20% Pt/C and doping level of 16 PRU at 120 °C.

3.6.2.3 Effect of catalyst layer thickness on performance

The effect of the catalyst layer on electrode performance at constant doping level of 6 PRU is shown in Figure 3-10 for pure oxygen operation. The 40% Pt/C electrode showed the best performance. However under air operation, 60% Pt/C (thinnest catalyst layer) showed the best performance, closely followed by 40% Pt/C as the performance was influenced by mass transport.

The data suggest that there was an optimum thickness for the catalyst layer, depending on the doping level in the membrane and the catalyst layer. It has already been shown in the literature [74] that there was an optimum thickness for a phosphoric acid fuel cell electrode of ~ 10 μm, where most of the catalytic reaction takes place. It can be seen from Figure 3-11 that, at low doping level of 3 PRU, a small difference in performance was obtained between air and oxygen operation for the 40% Pt/C electrode. However, 60% Pt/C electrode showed lower performance to that of 40% Pt/C under air and similar performance with oxygen. Mass transport limitations in the 60% Pt/C electrode performance, reflected by the large difference in performance with air or oxygen, can be explained by the thin layer 60% Pt/C electrode. This meant that most of the catalyst agglomerates were deposited or located near the membrane, and the actual doping level of the electrode was no longer 3 PRU, due to acid mobility (flooding) from the membrane (6 PRU) to the catalyst layer (initially 3 PRU).

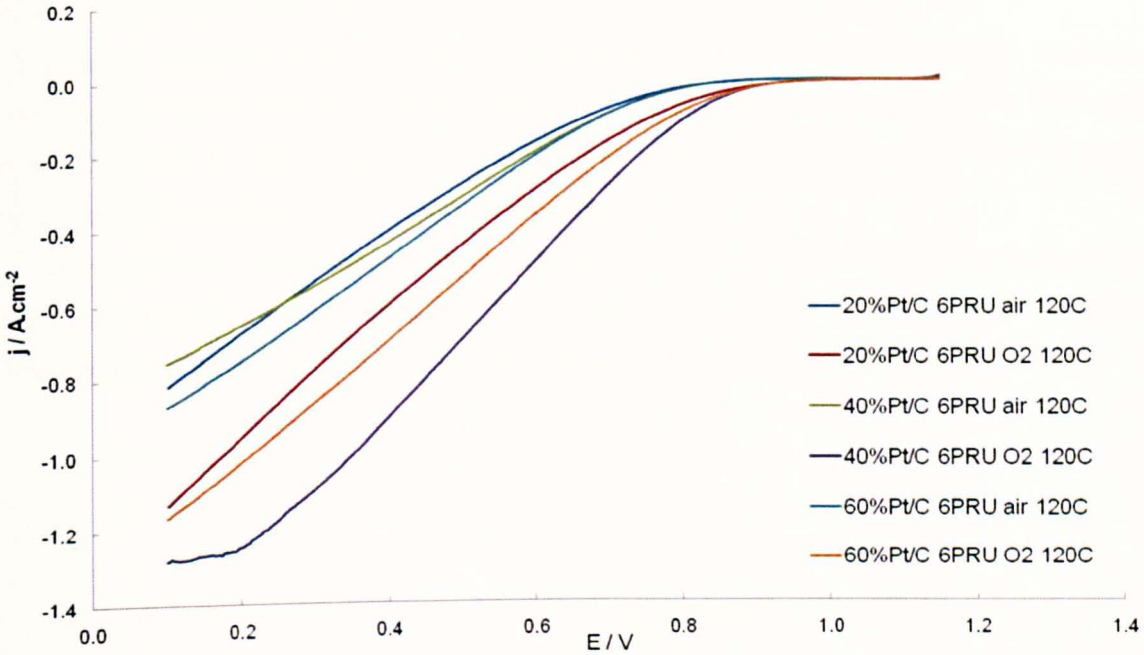

Figure 3-10. Effect of catalyst thickness using constant Pt loading of 0.5 mg_{Pt} cm^{-2} and various Pt:C ratio (20, 40 & 60% Pt wt) on linear sweep polarisation curves (vs. SHE) for oxygen reduction reaction at doping level of 6 PRU at 120 °C.

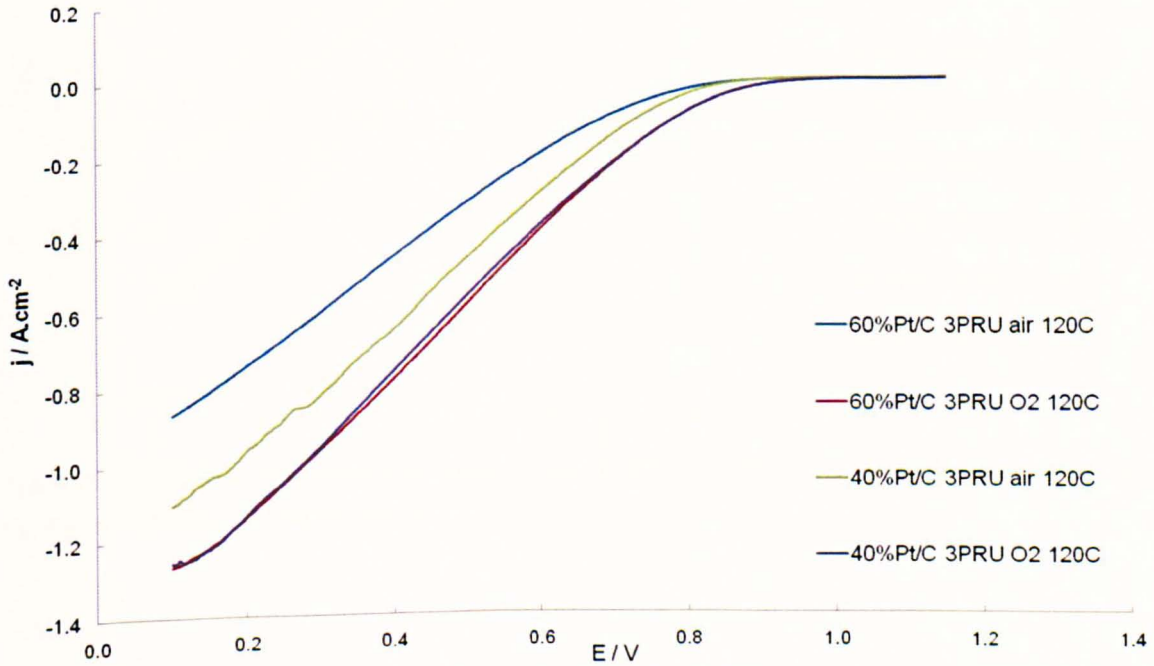

Figure 3-11. Effect of catalyst thickness using constant Pt loading of 0.5 mg_{Pt} cm^{-2} and various Pt:C ratio (40 & 60% Pt wt) on linear sweep polarisation curves (vs. SHE) for oxygen reduction reaction at doping level of 3 PRU at 120 °C.

3.6.2.4 Temperature effect on performance

The effect of temperature on the ORR electrode performance is shown in Figure 3-12. Increasing the operating temperature led to enhancement in the electrode performance, mainly in the kinetic region, with both air and oxygen operation. This was expected due to an increase in the exchange current density and therefore the kinetics of the reaction.

However the kinetic enhancement, due to increase in oxygen partial pressure (air to oxygen) was much more significant than that due to an increase in temperature of 40 °C. This is a typical characteristic of phosphoric acid fuel cell electrodes, owing to their low oxygen permeability.

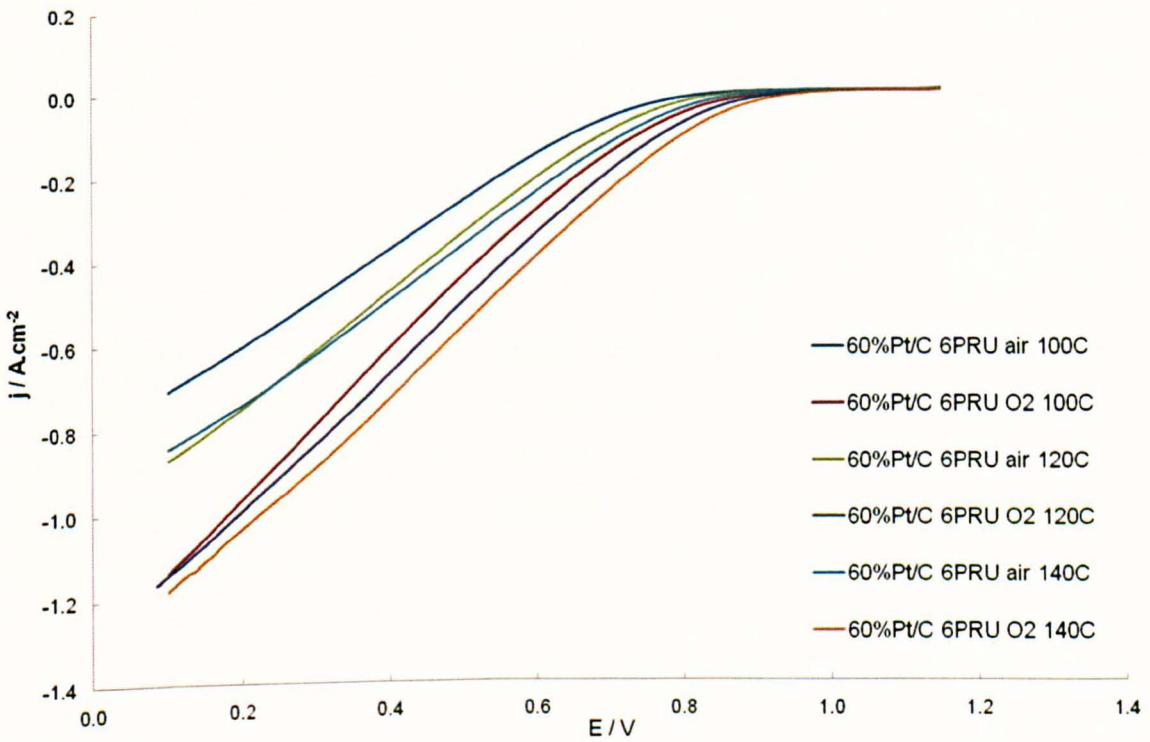

Figure 3-12. Effect of temperature on linear sweep polarisation curves (vs. SHE) for oxygen reduction reaction at 60% Pt/C and doping level of 6 PRU.

3.6.3 Chronoamperometry

Chronoamperometric current transients at the platinum micro electrodes have been recorded at a potential where the oxygen reduction is entirely diffusion controlled [75] (0.05 V vs SHE). The transient current equation obtained from Fick's first and second law of diffusion can be described by:

$$j(t) = \frac{nFC_{dissolve}\sqrt{D_{O_2}^{PBI/H_3PO_4}}}{\sqrt{\pi t}} + \frac{nFC_{dissolve}D_{O_2}^{PBI/H_3PO_4}}{\delta} \qquad [6]$$

It can be seen from equation 6 that plotting j(t)/nF vs. the inverse of square root of time will give a straight line slope of $CD^{1/2}$ and intercept (limiting current)of CD/δ. From these two values (for known δ) we can obtain $C_{dissolve}$ & D_{O2} separately. Due to experimental limitations the slope of the plot could not be obtained. The potentiostat used had maximum current of ~1.4 A which limited the transit current drop above such value; however the limiting currents were recorded at steady state since their values were below 1.4 A (Figure 3-13).

From Table 3-8 and reference [62] it can be seen that PBI and H_3PO_4 have similar oxygen solubilities ($C_{dissolve}$), and increasing the doping level enhanced oxygen diffusion and therefore overall oxygen permeability (D.C). It has been shown in [62] that oxygen diffusion varies logarithmically with doping level, and doping level is directly proportional to δ_{H3PO4} where $\delta = \delta_{PBI} + \delta_{H3PO4}$. This confirms the above observation (Sec. 3.6.2.1) regarding an optimum doping level for oxygen permeability.

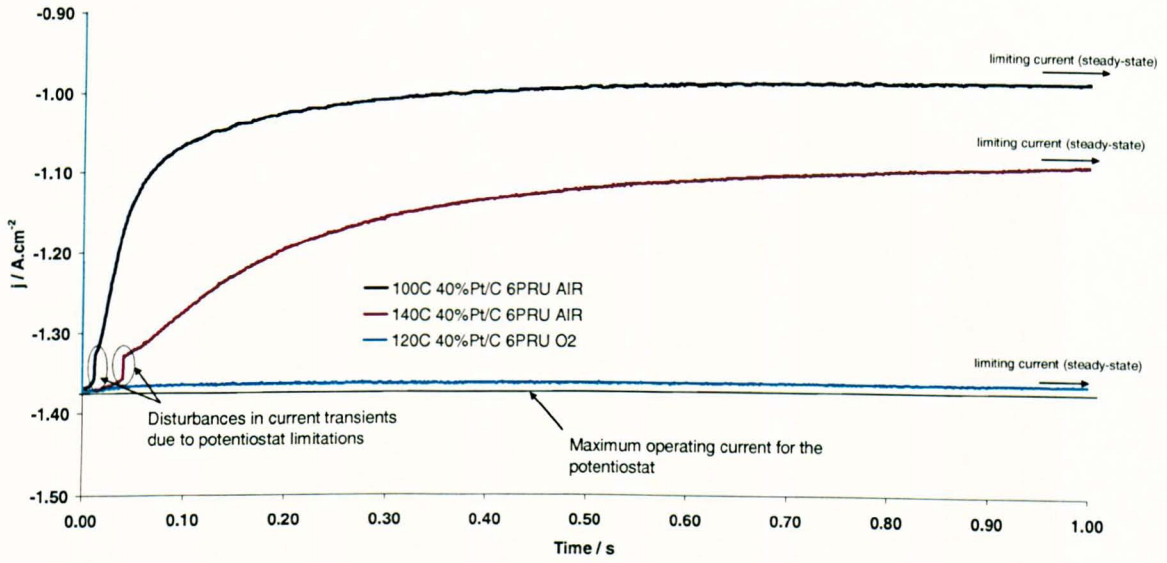

Figure 3-13. Limitations observed for current transients of 40% Pt/C at different conditions (0.5 mg_{Pt} cm^{-2}).

3.6.3.1 Effect of catalyst layer thickness on limiting current

Figure 3-14 shows the effect of catalyst layer thickness on the observed limiting current density. It can be seen that the 40% Pt/C electrode exhibited the highest limiting currents under air and oxygen operation, which suggests that 40% Pt/C had the maximum oxygen permeability among the studied electrodes, which is consistent with the data obtained from the polarization curves earlier.

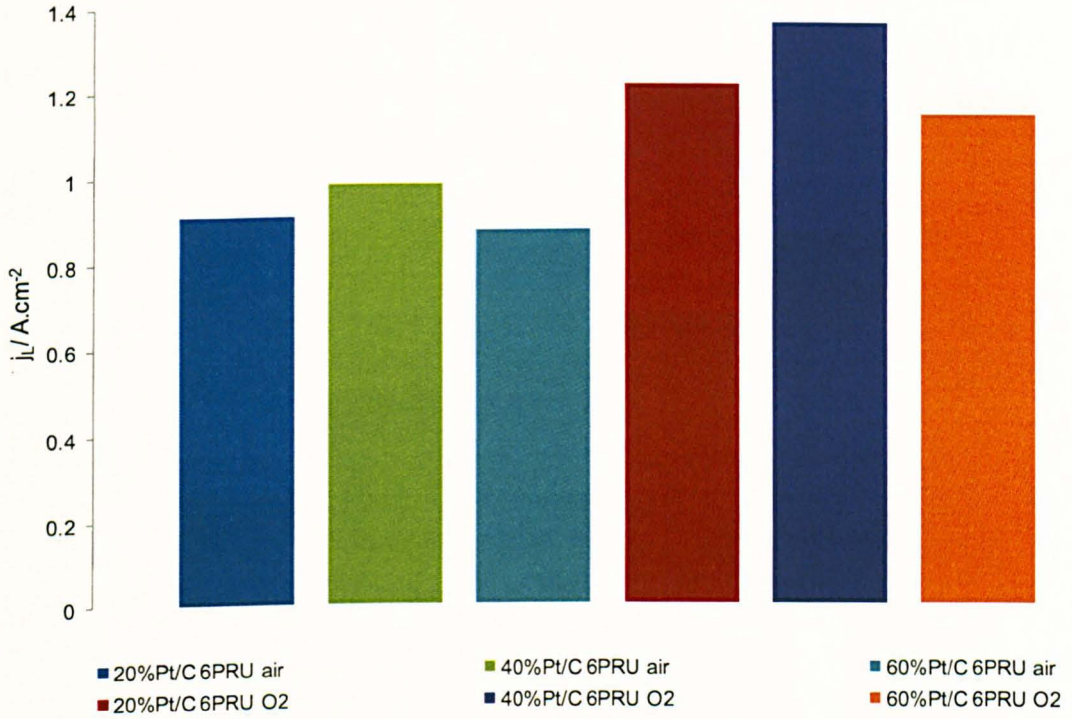

Figure 3-14. Effect of catalyst layer thickness on limiting current density for 20, 40 & 60% Pt/C electrodes with doping level of 6 PRU at 120 °C.

3.6.3.2 Surfactant addition effect on limiting current

Figure 3-15 shows the effect of surfactant addition on the observed limiting current density. Surfactant addition lead to higher limiting currents under air and oxygen operation, compared to that of the same electrode (16 PRU) without the surfactant, due to improvement in oxygen permeability for 20% Pt/C electrodes doped with 16 PRU. Increasing the doping level, from 6 to 16 PRU, lead to a large reduction in the limiting currents with both air and oxygen, indicating a decrease in the oxygen permeability, as discussed earlier.

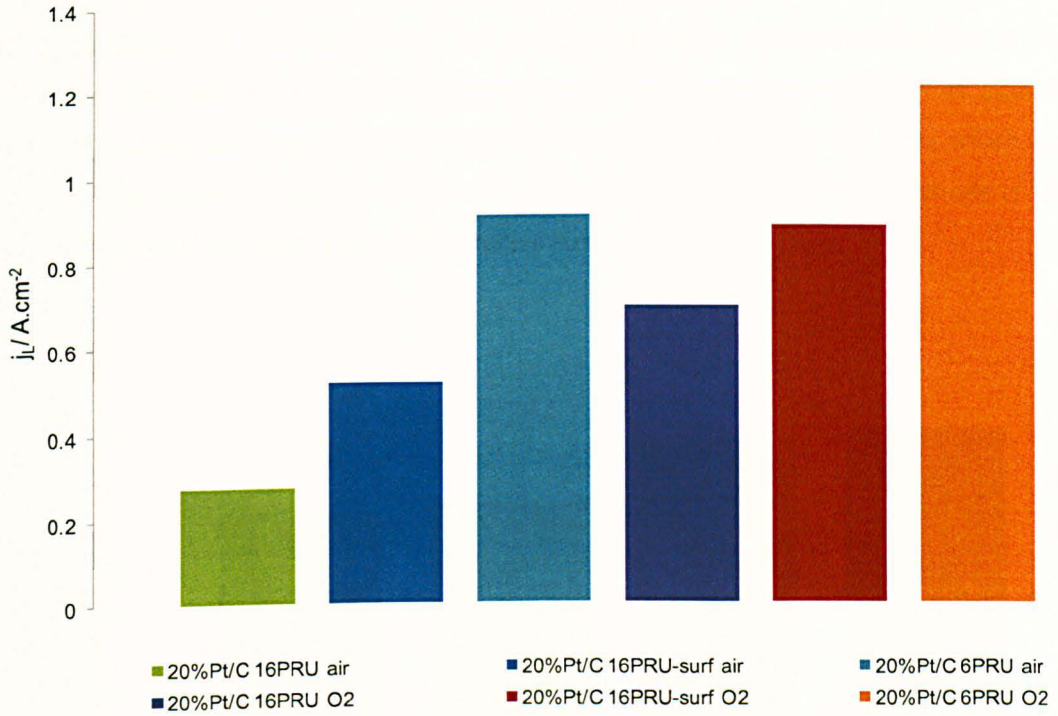

Figure 3-15. Limiting current density for 20% Pt/C electrodes with doping levels of 6 & 16 PRU at 120 °C with (16 PRU) & without surfactant (6&16 PRU).

3.6.3.3 Acid doping level effect on limiting current

As shown previously (Sec. 3.6.2.1) increasing the doping level above 6 PRU led to a reduction in oxygen permeability. Figure 3-16 shows the impact of doping level (from 3 to 6 PRU) on the limiting current of 40% Pt/C. An increase in oxygen permeability (limiting current) was obtained, with both air and oxygen operation, with increased doping level from 3 to 6 PRU. Similar results were obtained with a 60% Pt/C electrode (Figure 3-17) operating with oxygen. However it can be seen that the 60% Pt/C electrode with doping level 3 PRU gave higher limiting current than that for a 6 PRU doping level, under air operation. Additionally the 60% Pt/C electrode with doping level of 6 PRU had lower limiting current (oxygen permeability) than that of the 20% Pt/C electrode, with the same doping level. These results can be explained as follows:

Although the 60% Pt/C electrode was thinner than the 20% Pt/C, the catalyst layer was flooded by phosphoric acid resulted in very low porosity and mass transport limitations in the porous structure. Mass transport through the porous media was ignored in equation 6 ($C_{dissolve}$ is related to the P_{O2} inside the pores), in contrast to that through the electrolyte thin film, which is not valid in very thin layers flooded by acid. Additionally, the ESA of 60% Pt/C electrode is lower than that of 20% Pt/C electrode (larger Pt particles size).

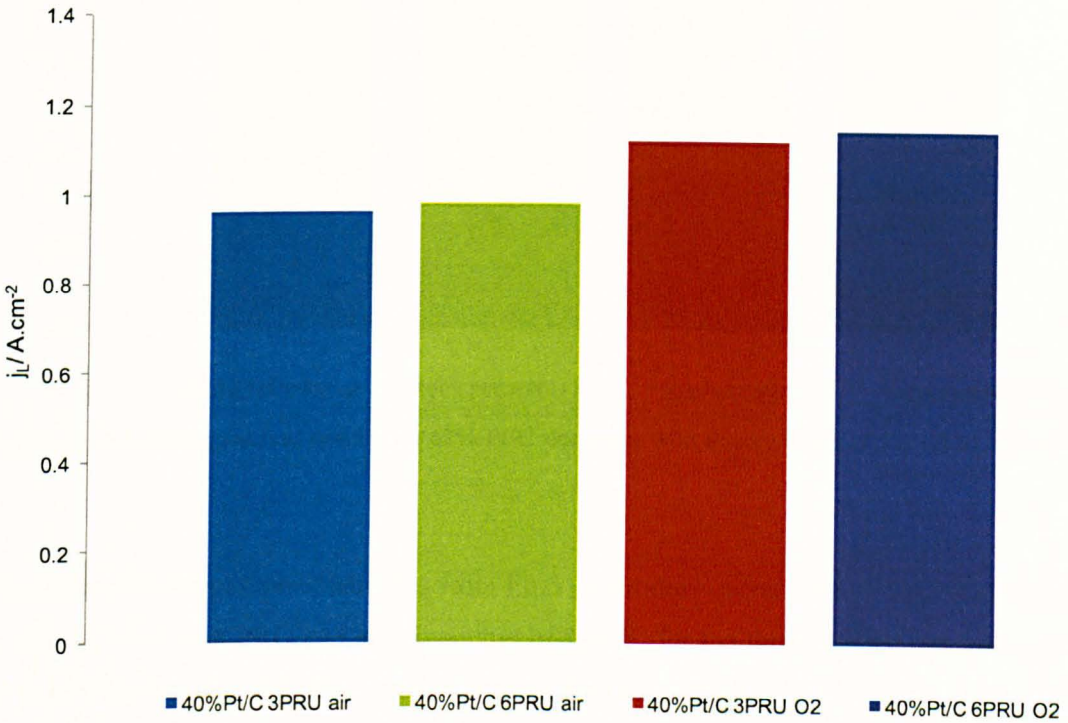

Figure 3-16. Limiting current density for 40% Pt/C electrodes with doping levels of 3 & 6 PRU at 100 °C.

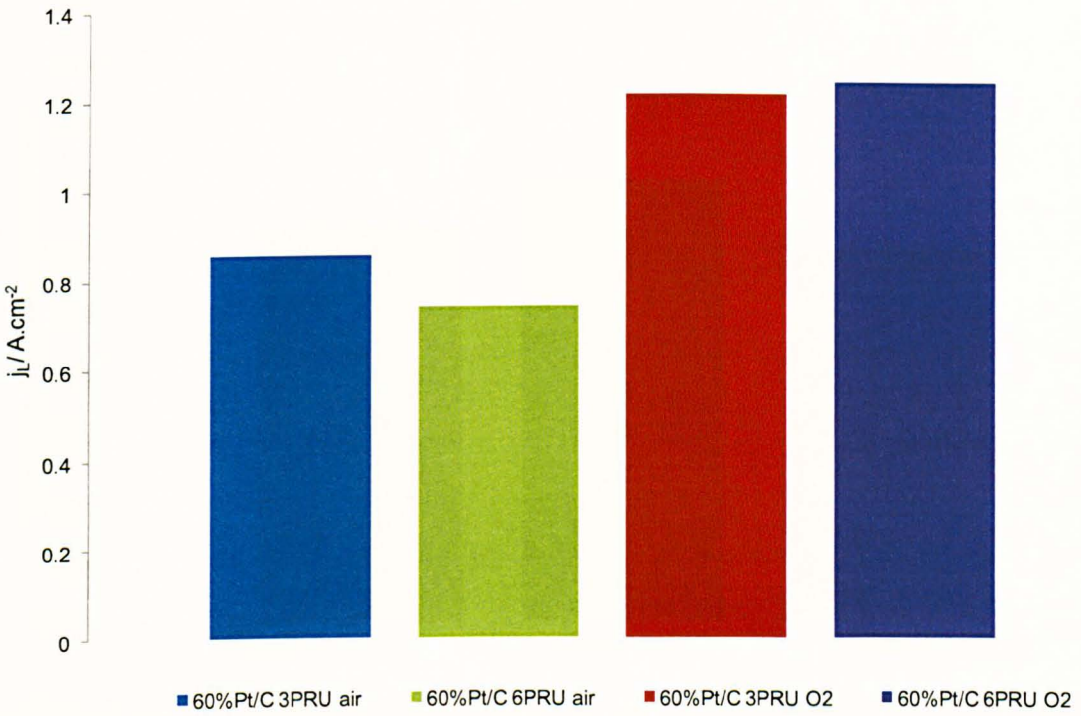

Figure 3-17. Limiting current density for 60% Pt/C electrodes with doping levels of 3 & 6 PRU at 100 °C.

The measured oxygen permeabilities from Eq.5 (at limiting current where $C_{Pt} = 0$) (Figure 3-18) at doping level of 6 PRU and a temperature of 120 °C for the three studied electrodes 20, 40 & 60% Pt/C under pure oxygen operation were in the range of $1.3\text{-}1.5\times10^{-12}$ mole cm cm^{-2} s^{-1} atm^{-1} which is in very good agreement with the data from [62] (2.2×10^{-12} mole cm cm^{-2} s^{-1} atm^{-1} at 150 °C Table 3-8).

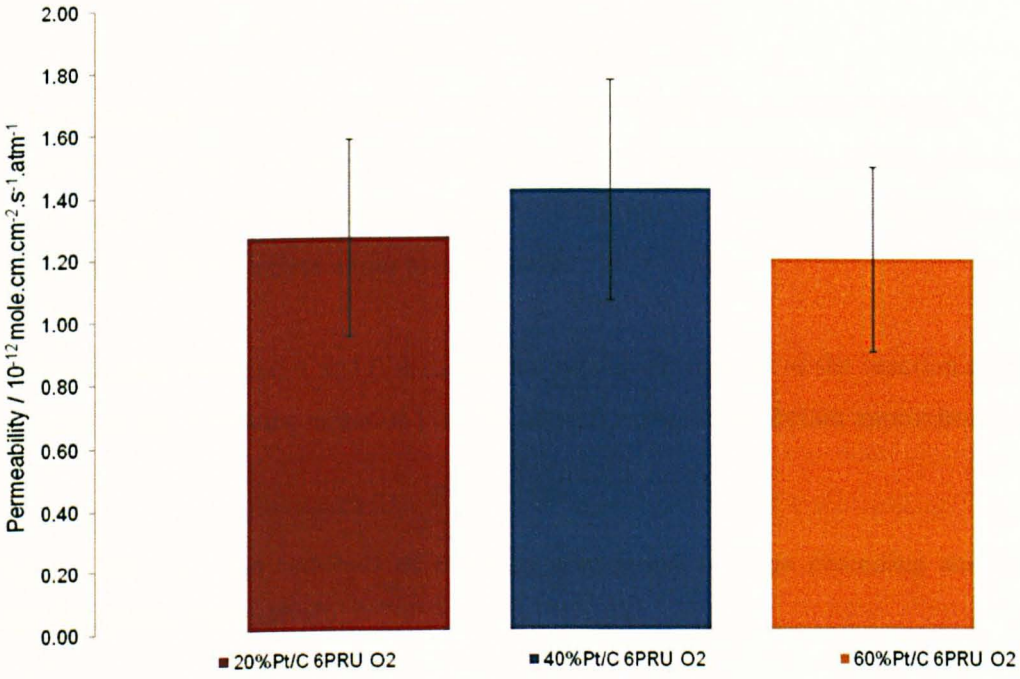

Figure 3-18. Average oxygen permeability through PBI thin film doped with 6 PRU at 120 °C for various electrodes.

3.7 Oxygen reduction kinetics in PBI-phosphoric acid interface

3.7.1 Transfer coefficient background literature

The symmetry factor β is the ratio between the effect of potential on the electrochemical free energy of activation and its effect on the electrochemical free energy of the reaction (formation of the activated complex). In other words, β is the fraction of an applied potential that influences the activation energy and hence the rate of electrochemical reaction. β is fundamental parameter, its value varies from 0 to 1 since it is only discussed with single step (one electron) reactions, i.e. $\beta_a + \beta_c = 1$. The β value is related to the shape of the free-energy barrier and the position of the activated complex along the reaction coordinates [76].

α, the transfer coefficient, is an experimental parameter obtained from current potential relationship. It is equal to the inverse of Tafel slope b expressed in units of 2.3 RT/F at high current densities.

The reaction rate relation to overpotential loss for a multi-step reaction can be written using the well known Butler-Volmer equation as:

$$i = i_0\left(\exp\left(\frac{\alpha_a F}{RT}\eta\right) - \exp\left(\frac{-\alpha_c F}{RT}\eta\right)\right) \quad [7]$$

η is the overpotential, i is the current (rate) and i_0 is the exchange current density. $\alpha_a + \alpha_c$ doesn't necessarily add to unity. Generally, $\alpha_a + \alpha_c = n/\upsilon$ [76, 77] where n is the electron transferred in the overall reaction. υ, the stoichiometric number, is the number of times the rate determining step must occur, for the overall reaction to occur once.

The relationship between α and β is dependant on the mechanism of the reaction [78]. α can be expressed by the following equation [76, 79] using the quais-equilibrium approximation:

$$\alpha = \frac{s}{\upsilon} + r\beta \quad [8]$$

Where s and r are the numbers of electrons transferred in steps preceding and in the rate-determining step, respectively.

Generally two Tafel slopes are observed for oxygen reduction on Pt in dilute acids. Damjanovic et al [80-82] attributed this phenomenon to a change in intermediate adsorption isotherm (adsorbed oxygen species) from Temkin conditions (60 mV dec^{-1}) which is applicable for narrow over-potential range (0.2-0.3 V) to Langmuir condition (120 $mV.dec^{-1}$) considering the first electron transfer as the rate determining step. Tarasevich [83] explained this behaviour by a change in the surface coverage of the chemisorbed oxygen-containing species.

Bagotzky and Tarasevich [84] studied the relationship between the surface coverage by oxygen θ_O and electrode potential in dilute sulphuric acid and found it to be, to a first approximation, linear and can be expressed by Temkin adsorption isotherm for medium coverage (1.45 to 0.95 V vs. SHE with coverage from 0.95 to 0.15, respectively):

$$\theta_O = A + \frac{1}{f}\ln P_{O_2} = A + \frac{1}{f}\frac{zF}{RT}\eta \quad [9]$$

Where f is the heterogeneity factor; 15-12 for platinum (assuming adsorbed species z = 2), and A is constant related to the standard free energy of adsorption at zero coverage θ_0. Similar results were concluded for concentrated phosphoric acid [85].

At potentials below 0.725 V (vs. SHE) oxygen coverage on a platinum surface approaches zero [84]. Similarly, Muller, Mansurov & Petrii [86] showed that alpha was independent of potential in the range of 1.6 to 0.8 V in dilute sulphuric acid, where the oxygen coverage depended linearly on potential in the studied range.

Conway et al [87-89] studied oxygen adsorption and oxide formation on platinum, and reported several stages of surface oxidation, where more stable oxide is produced at high potentials or at longer periods of time at fixed potential. The initial stage of surface oxidation at platinum [88] in the range of 0.7 to 0.9 V (vs SHE) in dilute acidic environment corresponds to faradaically electro-sorbed OH [89]. This is a reversible stage demonstrated by low Tafel slope (~27 mV dec^{-1}) of the reduction process and the lack of hysteresis between anodic and cathodic sweeps [87].

The first Tafel slope for ORR on Pt of 60 mV dec^{-1} suggests a value of $\alpha = 1$ (at room temperature). If the rate determining step (rds) was charge transfer with, typically, a β equal to 0.5 and considering one electron transfer, from Equation 8 this suggests that s/υ is equal to 0.5. Thus either a value for s equal to 1 and value to υ equal to 2 should be assumed, which is unlikely, as two identical charge transfers have to occur and reaction order of 0.5 with respect to oxygen should be observed, which is not the case (typically reaction order = 1) [80]. Alternatively, a value of s equal to 2 and value to υ equal to 4 can be disregarded as the total number of electrons involved in the reaction are 4.

If the rate determining step was chemical i.e. $r = 0$ and $s/\upsilon = 1$, several mechanisms can satisfy this condition have been proposed; such as the hydrogen peroxide path, metal peroxide path, electrochemical oxide path or Hoar's alkaline path. However, Riddiford [90], Appleby [85] and Damjanovic [80] showed that, although all the proposed mechanisms satisfied equation 8, they failed under Langmuir isotherm conditions to explain the reaction orders of 3/2 with respect to protons and 1 with respect to oxygen and Temkin isotherm should be considered to fulfil the observed reaction orders.

The obtained second Tafel slope for ORR on Pt of 120 mV dec^{-1} suggests a value of 0.5 for α (at room temperature). Several suggested mechanisms could explain the observed slope, with the first electron transfer as rate determining step (rds) [85] and β equal to 0.5.

$$S + O_2 \underset{k_{-1}}{\overset{k_1}{\rightleftarrows}} S\cdots O_2$$

$$S\cdots O_2 + H^+ + e^- \xrightarrow{k_2} SO_2H \quad (rds)$$

Or [83]:

$$S - O_2 + e^- \longrightarrow MO_2^- \quad (rds)$$

Where S is the available catalytic site.

Since intermediates of the reaction are adsorbed on the surface of the electrode substrate, Conway and Gileadi [91], Damjanovic et al [80, 82] and Appleby [85] gave the following rate equation (Eq. 10) for the rate controlling electrochemical step under Temkin conditions at potentials sufficiently far from equilibrium, assuming negligible free energy of adsorption for O_2 compared to that of O_2H radicals

$$i = k_2 F P_{O_2} [H^+] \exp\left(-\frac{\beta \Delta G_\theta}{RT}\right) \exp\left(-\frac{\beta \eta F}{RT}\right) \quad [10]$$

Where k_2 is constant, θ is the total coverage of all O_2H radicals, ΔG^0 is the Gibbs free energy for O_2H radicals adsorption at zero coverage (negative number), and q, enthalpy-coverage factor, is the rate of change (decrease) of free energy of adsorption with coverage (equal to zero for a Langmuir isotherm). Under Temkin isotherm ($\Delta G_\theta = \Delta G^0 + q\theta = \Delta H^0 + q\theta - T\Delta S^0$). The positive sign for $q\theta$ arise from the fact that

ΔG^0 is negative i.e. $|\Delta G_\theta| = |\Delta G^0| - q\theta$.

Assuming ΔS^0 does not vary with θ and since ΔH^0 is the heat of adsorption at zero coverage, we can write:

$$i \propto P_{O_2} [H^+] \exp\left(-\frac{\beta q \theta_T}{RT}\right) \exp\left(-\frac{\beta \eta F}{RT}\right) \quad [11]$$

For large values of q, i.e. Temkin isotherm and under quasi equilibrium conditions we can write [76]:

$$\left[\frac{\theta}{1-\theta}\right]\exp\left(\frac{q\theta}{RT}\right) = K_0 P_{O_2} \exp\left(\frac{VF}{RT}\right) \quad [12]$$

Where θ is the oxygen species coverage at potential V (vs. SHE), and K_0 is the equilibrium constant of adsorption at zero coverage.

Since q is large we can ignore the pre-exponential terms so we can write [85, 92] at constant pH

$$q\partial\theta = F\partial V \quad [13]$$

And therefore,

$$\left(\frac{\partial V}{\partial\theta}\right)_{pH} = q/F \quad [14]$$

Platinum surface coverage with oxygen species as function of potential and pH can be give by [80, 101, 102]:

$$\theta_{(V,pH)} = KV + K\frac{2.3RT}{F}pH - \theta_0 \quad [15]$$

However from equation (15) we can write:

$$\left(\frac{\partial V}{\partial\theta}\right)_{pH} = 1/K \quad [16]$$

Assuming β = 0.5 and θ_T =θ, comparing equations (14) and (16) and substituting equation (15) in (11) we obtain:

$$i \propto P_{O_2}[H^+]\exp\left(-\frac{0.5F\eta + 0.5RT\,pH}{RT}\right)\exp\left(-\frac{0.5\eta F}{RT}\right) \quad [17]$$

Or finally,

$$i \propto P_{O_2}[H^+]^{3/2}\exp\left(-\frac{\eta F}{RT}\right) \quad [18]$$

The obtained rate equation describes the observed oxygen partial pressure and pH dependence. It also has the observed first Tafel slope under Temkin conditions and the second observed Tafel slope under Langmuir conditions (q = 0).

Conway and Bockris [79] showed that, even under the Quasi-equilibrium approximation assumption, the rate constant of the rate determining step is 100 times (or more) smaller than that of other steps, there are limits to the overpotential range in which mechanistically significant Tafel slope can be derived. They simulated several curves and obtained two linear regions where the first slope was equal to the predicted value from the quasi-equilibrium treatment and the second slope was c.a ~120 mV dec^{-1}. They confirmed that it was the change of the effective concentration of the intermediate species involved in the rate determining step, with potential, that leads to a decrease in the usual one-electron Tafel slope of 118 mV dec^{-1}.

3.7.1.1 Transfer coefficient dependence on temperature

The transfer coefficient is affected by the double layer structure and adsorption of impurities [78, 93], and the latter generally increase the value of α. In the presence of impurities the assumption of $\theta_T = \theta$ is not valid, and since the heat of adsorption of impurities and phosphate ions is temperature dependant that will give rise to a transfer coefficient which depends on temperature. Conway et al [94] showed that the apparent temperature dependence of alpha can be caused by a change of $f(\theta)$ or free sites, $1-\theta_T$, with temperature (specifically adsorbed anions). This is explained by the following equation:

$$\frac{\partial \ln i}{\partial V} = \frac{\partial[\ln f(\theta)]}{\partial V} + \frac{\beta F}{RT} \qquad [19]$$

Where $f(\theta)$ involves potential and temperature dependent terms.

Parsons [95] suggested that the temperature dependence arose from the specific adsorption of anions. Anion adsorption will alter oxygen surface coverage because of competition with oxygen groups, columbic repulsion between the adsorbed anions and the adsorbed oxygen species (OH or O), and alteration in the interfacial field in the double layer [96]. It was shown that phosphoric acid adsorbs strongly on a platinum surface [114] with enthalpy of adsorption equal to -92 kJ

mole^{-1} and entropy of adsorption equal to -219 J mole^{-1} K^{-1}(at standard state of $\theta^0 = 0.5$ & $C^0 = 1$ mole L^{-1}), The adsorption is reported to be [114] potential dependant with an adsorption maximum at ~0.8V (SHE), where alpha is typically measured.

The dependence of alpha on temperature can also be explained by a change in the double layer thickness with temperature, due to variation in the adsorption of abnormal entities (impurities and phosphoric acid)[64]. Bockris and Gochev [115] suggested that, in the presence of adsorbed species, alpha will strongly depend on the double layer structure. If a non-aqueous solution contains a trace of water (e.g. concentrated phosphoric acid at elevated temperatures), the water occupancy of the double layer will depend on temperature.

Alternatively, Conway et al [94, 97] suggested that the entropy of the reaction may become more significant when the enthalpy of the reaction is small leading to an apparent temperature dependence of alpha. They explained the experimentally observed dependence of Tafel slope on temperature by the following equation:

$$b = \pm 2.3RT/(\beta_H + \beta_S T) \qquad [20]$$

β_H and β_S are the enthalpic and entropic components of the overall symmetry factor β.

They attributed the temperature dependence to a change in the entropy of activation, which could be caused by potential dependant solvent orientation.

On a Nafion interface, the variation of α with temperature was linear with slope of 0.0034 K^{-1} [98, 99]. Two activation energies were obtained, a high value of 73.2 kJ mole^{-1} at low current densities (oxide-covered platinum, with a Tafel slope of 60 mV dec^{-1}) and a lower value of 27.6 kJ mole^{-1} at high current densities (oxide-free platinum, with a Tafel slope of 120 mV dec^{-1}). Oxygen reduction in phosphoric acid exhibits higher activation energy than that for nafion, as result of the combined effect of heat of adsorption of anions and heat of solution of oxygen [100].

3.7.1.2 Transfer coefficient and activation energy in phosphoric acid systems

Damjanovic and Brusic [80] reported that oxygen coverage in 0.1 M $HClO_4$ changed linearly with potential in the range of 1 to 0.8 V (vs. SHE). The i/V curves also shifted by 100 mV for a unit change in pH in perchlorate acid solutions. In sulphuric acid solutions, at low current densities (Temkin conditions) the voltage dependence on pH was 90 mV per pH unit and changed to 110 mV per pH unit under Langmuir conditions [81].

The surface coverage of oxygen species on platinum, at low current densities, as a function of potential and pH can be given by [80, 101, 102]:

$$\theta_{(V,pH)} = KV + K\frac{2.3RT}{F}pH - \theta_0 \qquad [21]$$

Where K is constant (0.85 V^{-1}), θ_0 is constant, which depends on the reference potential, $\theta_0 = KV_0 = 0.85\times0.77 = 0.65$, when potentials are referred to SHE. V_0 is the potential, where θ extrapolates to zero, in zero pH solution. Equation 21 suggests that a positive shift in the potential range where the adsorption isotherm will change from Temkin conditions (which can prevail only in a narrow range of potential [82]) to Langmuir (at c.a. θ ~0.2) will occur as electrolyte pH decreases.

In hot concentrated phosphoric acid, 85% wt, c.a. 14.7 M (pK_{a1} = 2.148 or pH = 0.49 at 25 °C), the following equation for the 1st proton ionization were given [103]:

$$pK_{a1} = \frac{799.31}{T} - 4.5535 + 0.013486T \qquad [22]$$

At 150 °C pK_{a1} = 3.041, leading to pH = 0.94. Substituting this pH value in equation 21 with value of θ = 0.2, we obtain a value of V equal to 0.92 V (vs. SHE). This means that in hot phosphoric acid, high oxygen coverage will shift towards more positive potentials, and Langmuir (θ ~0.2) Tafel slope of 120 mV dec^{-1} is expected at potentials below 0.92 V. Sepa, Vojnovic and Damjanovic [102] showed that at pH = 1 for θ = 0.2 the potential was 0.9 V vs. SHE and increased to 0.96 V at pH = 0.

In hot phosphoric acid above 0.9 V (SHE), ORR using Pt supported on carbon is affected by mixed potentials (carbon and platinum oxidation) and therefore cannot be used to obtain Tafel slopes [104]. Using unsupported platinum it was possible to obtain the first Tafel slope at potentials above 0.9 V (SHE) on oxide-free Pt black in very pure 85% wt phosphoric acid at 120°C [105].

In very high purity phosphoric acid solutions α was temperature independent [64]. Petrii, Marvet and Malysheva [106] studied the effect of impurities in phosphoric acid, and attributed the observed hysteresis, between the anodic and cathodic sweeps for oxygen reduction, to inorganic (metallic cations) impurities. They also reported increase in oxygen adsorption overvoltage and reduction in its reversibility with increase in phosphoric acid concentration, which can be suppressed by using platinum oxide instead.

Appleby [85] studied the effect of impurities in phosphoric acid on the Tafel slope. He observed values of 60 mV dec^{-1} to 80 mV dec^{-1} in purified solutions in the temperature range of 25 to 136 °C, and values in the range of 80 to 90 mV dec^{-1} in analytical grade solutions. A Tafel slope in the range of 60 to 120 mV dec^{-1} is typically observed in impure phosphoric acid solutions, depending on the adsorption of the impurities and phosphoric ions [85]. This adsorption is concentration, temperature and potential dependant.

The effect of phosphorous acid impurities in phosphoric acid on oxygen reduction was investigated by Sugishima et al [68]. Tafel slopes varied from 125 mV dec^{-1} (alpha 0.473) to 215 mV dec^{-1} (alpha 0.275) when the impurity concentration (phosphorus acid) increased from 0 to 2.48×10^{-3} mol L^{-1}.
Clouser et al [107], studied the effect of temperature on α in phosphoric acid, and obtained Tafel slopes in the region of ~120 mV dec^{-1}, while alpha varied linearly with temperature with a slope of 0.0014 K^{-1}.

McBreen et al [108] also reported Tafel slope in the region of 120 mV dec^{-1}, but independent of temperature, which suggests a linear dependency of alpha with temperature. They also reported a

change in Tafel slope from 120 mV dec^{-1} to 60 mV dec^{-1} was observed, with increased oxygen partial pressure above 3 atmospheres.

Appleby [109] reported values of α from 0.49 at 25 °C to 0.562 at 95.9 °C in 85% wt phosphoric acid. Similarly, O'Grady et al [110] reported values from 0.53 at 25 °C to 0.68 at 70 °C in 85% wt phosphoric acid, and alpha varied linearly with temperature with a slope of 0.0034 K^{-1}. Huang et al [69] observed α value (85% wt H_3PO_4) of 0.47, 0.61 & 0.67 at temperatures of 25, 100 & 150 °C, respectively.

However, Liu et al [62] reported a value of α = 0.92 (Tafel slope 90 mV dec^{-1}) at 150 °C for phosphoric acid doped PBI (doping level is 6 and 1 RH %). The value is in good agreement with the work of Kunz and Gruver [104], who reported α = 0.94 (Tafel slope 90 mV dec^{-1}) at 160 °C (96% wt H_3PO_4) using Pt/C as catalyst.
In phosphoric acid doped PBI α values varied with doping level; Tafel slopes started from 90 mV dec^{-1} and increased with doping level approaching those of phosphoric acid of ~120 mV dec^{-1} at high doping levels. Liu et al [62] reported values of 92, 94, 101 & 104 mV dec^{-1} at doping levels of 4.5, 6, 8 & 10 PRU, respectively.

Various values has been reported for the activation energy of oxygen reduction, on platinum in phosphoric acid, 92 kJ $mole^{-1}$ with (α = 0.94) [104], 95.8 kJ $mole^{-1}$ with (α ~1) on oxide-free Platinum [85], 54.8 kJ $mole^{-1}$ (α = 0.5-0.56) [109] and 72.4 kJ $mole^{-1}$ with (α = 0.53-0.68) [64] on oxidized platinum. Similarly, activation energy on oxidised platinum at a nafion interface of 73.2 kJ $mole^{-1}$ (at α = 1) and oxide-free Pt on nafion of 27.6 kJ $mole^{-1}$(at α = 0.5) has been reported [98, 99].

3.7.2 Experimental results and discussion

In this work Tafel slopes measurements were made in the potential range of 0.9-0.8 V (vs. SHE) using the linear sweep curves , at potentials above 0.9 V, ORR in H_3PO_4 using carbon supported catalyst is affected by mixed potentials (carbon and platinum oxidation) and therefore cannot be used to obtain Tafel slopes [104]. Prior to calculations, the i-V curves were corrected for IR

losses (R obtained from AC impedance measurements) and mass transport losses using Nernst correction [62, 64, 68, 85, 104-110] $(i.i_L)/(i_L-i)$ where i_L is the limiting current observed for the given studied sweep (see Figures 9-1 & 9-2, Appendix: A).

Figure 3-19 shows the effect of temperature on the observed transfer coefficient at doping levels of 3, 6 & 16 PRU. An approximately linear dependence of alpha on temperature was observed experimentally with slope of 0.0043 K^{-1} obtained for high doping level of 16 PRU, 0.0052 K^{-1} for doping level of 6 PRU and 0.0053 K^{-1} for doping level of 3 PRU. The values are in good agreement with values obtained for phosphoric acid of 0.0034 K^{-1} [110].

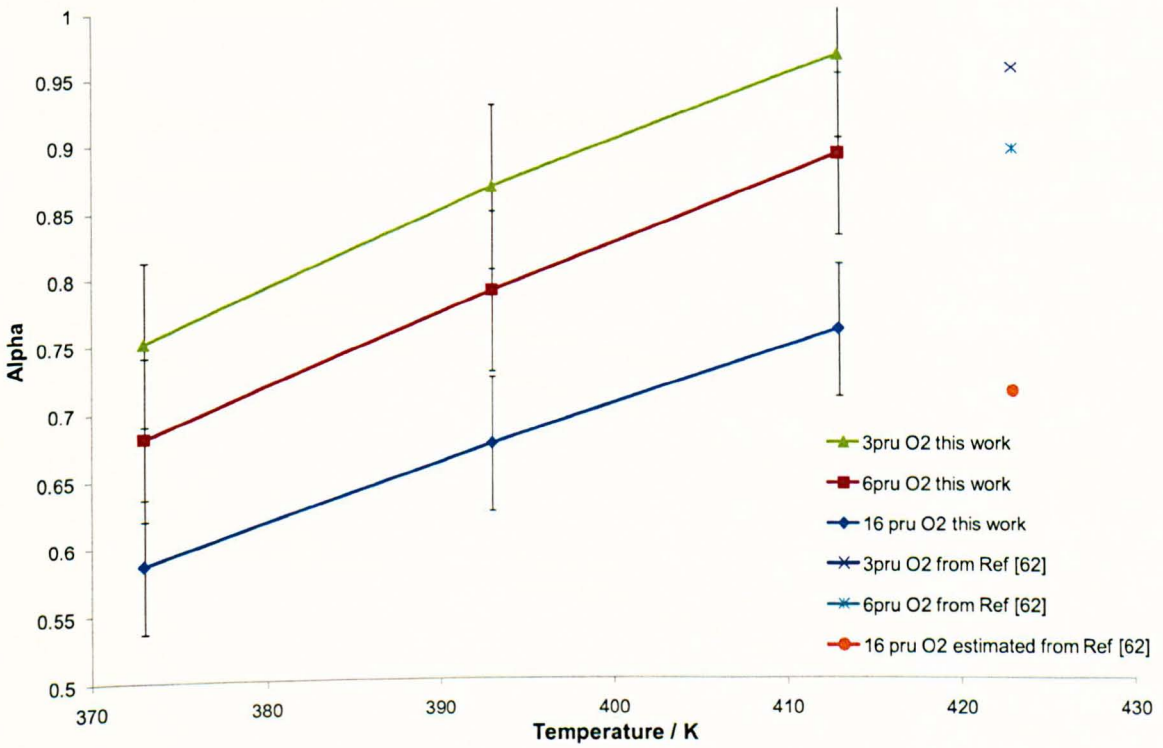

Figure 3-19. Transfer coefficient dependence on doping level and temperature.

Table 3-11 summarise the observed activation energy values and the pre-exponential factors (A) of ORR using doping levels of 3 & 6 PRU obtained from Arrhenius plots of the exchange current density at the temperatures of 100, 120 & 140 °C using air and oxygen.

It can be seen that the activation energy increased by lowering doping level. On the other hand, as shown in Figure 3-19, alpha decreased with increased doping level. This reflects the direct relation between alpha and activation energy where a value of ~60 kJ $mole^{-1}$ was obtained for alpha in the range 0.75-0.95 and ~40 kJ $mole^{-1}$ for alpha in the range 0.68-0.88. The values lie within the range given in the literature for oxidized (α ~0.5) and non-oxidized platinum (α ~1).

The observed high uncertainty in the calculated activation energy is caused by non-linear increase in $\ln(i_0)$ with temperature (Arrhenius plot, Figure 3-20). The increase in $\ln(i_0)$ from 100 to 120°C was larger in comparison to the increase from 120 to 140 °C. This non-linearity is caused by decreased oxygen concentration (solubility) at a given oxygen partial pressure with increased temperature (Henry's law).

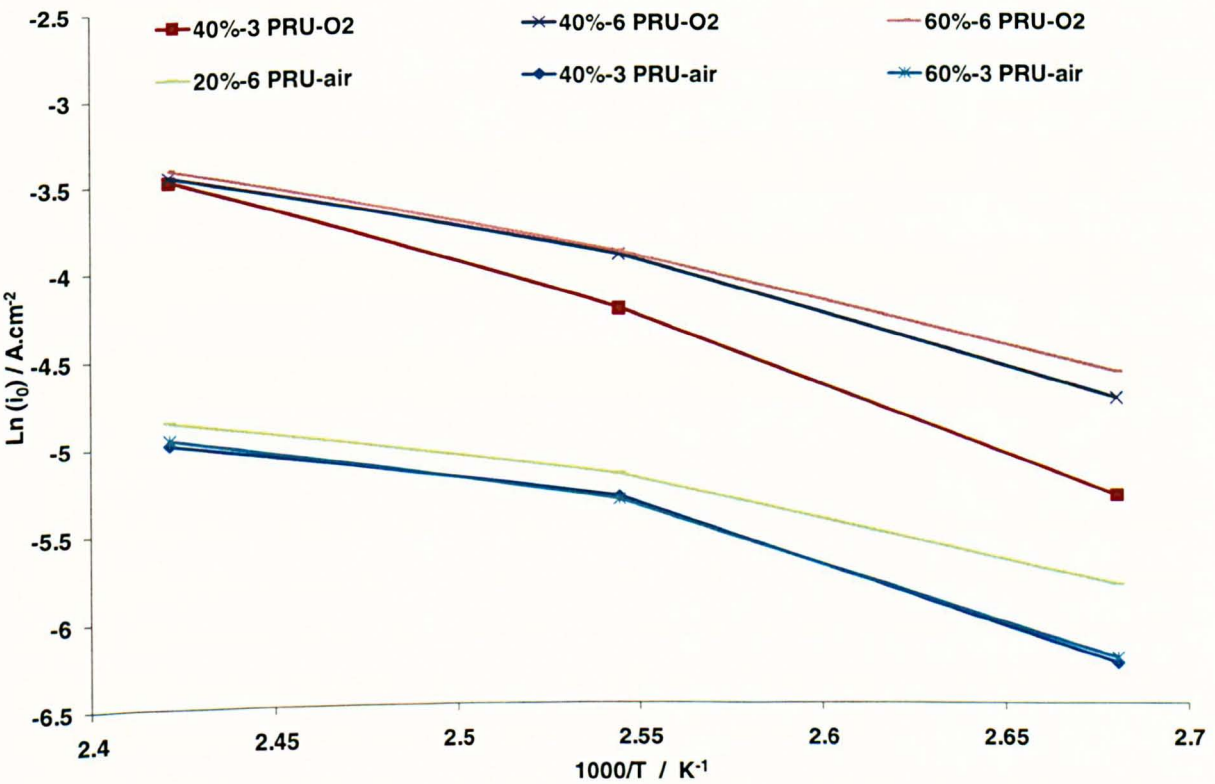

Figure 3-20. Arrhenius plot of ln (i_0) with temperature for various studied electrodes.

Increasing the doping level will increase the acid volume fraction and therefore $[H^+]$ and explains the increase of exchange current density, $j_{0\ Pt}$, with increasing doping level, from

reaction rate equation [4] (equation 18). The same conclusion can also be drawn from the dependence of alpha on doping level, where higher α values (at lower doping levels) lead to lower exchange current densities due to the dependency of current on potential (alpha). Exchange current densities on poly-crystalline 20% Pt/C of 2.1, 3.1 and 6.3×10^{-7} A cm^{-2}_{Pt} were obtained for doping level of 3, 6 & 16 PRU, respectively at 100°C. These results are in close agreement to $j_{0\,Pt}$ values in ortho-phosphoric acid at 100 °C [69, 85, 108].

Liu et al [62] reported a similar dependency of $j_{0\,Pt}$ on PBI doping level for ORR on a sputtered Pt micro band electrode. $j_{0\,Pt}$ varied from 0.18, 0.29 & 2.4×10^{-8} A cm^{-2}_{Pt} with doping levels of 4.5, 6 & 10 PRU, respectively at 150°C.

Table 3-21. Activation energy and pre-exponential factors for ORR at different doping levels.

Catalyst Pt/C	Doping Level	E_a Activation energy O_2	E_a Activation energy air	Ln(A) pre-exponential factor O_2	Ln(A) pre-exponential factor air
Wt%	PRU	kJ $mole^{-1}$	kJ $mole^{-1}$	-	-
20	6	38.8±0.7	30.3±12	7.99	4.18
40	3	58.5±10	40.2±25.7	8.771	1.87
40	6	41.2±12.8	23.5±0.9	13.47	7.18
60	3	59.8±30	40.3±21.8	7.78	2.92
60	6	38.1±5.9	26.8±6.2	14.57	7.15

It can be seen from Table 3-22 that the reaction order increased with increased temperature until reaching the typical value of ~1 (Equation 18) at 140 °C. This can be attributed to different reaction mechanisms, where the hydrogen peroxide route would be more favourable in the presence of adsorbed impurities [85, 112]. The influence of impurities, on the mechanism, will drop with increasing temperature due to their low heat of adsorption [85].

Another explanation for the observed reaction order temperature dependence is the non-linearity between θ and oxygen partial pressure P_{O2}, where under Langmuir isotherm is given by:

$$\frac{\theta}{1-\theta_T} \propto P_{O_2} \qquad [23]$$

The derived reaction rate equation 18, with reaction order of 1 with respect to P_{O2}, was obtained from the assumption that $\theta_T = \theta$ and θ is small enough so that

$$\frac{\theta}{1-\theta_T} \approx \theta \qquad [24]$$

However, in the presence of impurities $\theta_T \neq \theta$ but $\theta_T = \theta + \theta_{impurities}$, therefore for small values of θ equation 24 is no longer valid, and θ will not linearly depend on P_{O2} (smaller dependency leading to reaction order lower than 1). At elevated temperature, adsorption of impurities will decrease due to their low heats of adsorption, and therefore $\theta_T \approx \theta$ leading to a reaction order of 1 with respect to P_{O2}. Both explanations are consistent with the effect of temperature on α, from described in equation 19 where it depends on θ (impurities adsorption) and β (reaction mechanism).

Table 3-22. Reaction order with respect to P_{O2} at different temperatures and doping levels.

Catalyst Pt/C	Doping level	T	j at 0.9V_{SHE} P_{O2}=0.21	j at 0.9V_{SHE} P_{O2}=1	Reaction order P_{O2}
Wt%	PRU	°C	A	A	-
20	6	100	1.89E-03	4.91E-03	0.55
20	6	120	4.92E-03	1.44E-02	0.62
20	6	140	6.81E-03	3.09E-02	0.95
40	3	100	3.27E-03	8.62E-03	0.55
40	3	120	4.86E-03	1.97E-02	0.85
40	3	140	6.82E-03	3.16E-02	0.98
40	6	100	1.94E-03	5.06E-03	0.55
40	6	120	4.84E-03	1.92E-02	0.83
40	6	140	7.00E-03	3.40E-02	1.02
60	3	100	2.93E-03	1.00E-02	0.72
60	3	120	4.89E-03	2.00E-02	0.86
60	3	140	6.82E-03	3.31E-02	1.02
60	6	100	2.96E-03	1.08E-02	0.76
60	6	120	5.59E-03	2.05E-02	0.77
60	6	140	7.73E-03	3.62E-02	0.98

3.8 Conclusions

For oxygen reduction at platinum supported carbon in phosphoric acid doped PBI, the catalyst layer structure and composition play an important role in electrode performance.

The acid doping level in the catalyst layer affects the oxygen permeability, with a doping level of 6 PRU exhibiting the best oxygen permeability, of those studied. However an optimum doping level might lie in the range between 3 and 6 PRU which wasn't investigated. The optimum doping level depended on temperature and oxygen partial pressure, as both affects the permeability.

Similar to phosphoric acid systems, the transfer coefficient (α) depended on temperature. The dependency is explained by adsorption of impurities and thermodynamic effects.

The kinetics of oxygen reduction in PBI doped phosphoric acid is similar to that of phosphoric acid at high doping levels. Doping level affected the activation energy of the reaction, transfer coefficient and exchange current density. Increased doping level increased the exchange current density although decreased α values. The influence of doping level on electrode kinetics depended on temperature and oxygen partial pressure, where a compromise between exchange current density and transfer coefficient was realised. A high doping level was favourable at low temperatures, high oxygen concentrations or low operating overvoltages whilst low doping was favourable at high temperatures, low oxygen concentrations or high operating overvoltages.

An optimum catalyst layer thickness exists that provides a balance between good oxygen transport and fast kinetics. At loading of 0.5 mg_{Pt} cm^{-2}, 40% Pt/C (estimate catalyst thickness of ~12 μm assuming 40% porosity, see Sec. 6.2) gave better performance than 20% & 60% Pt/C (estimate catalyst thickness of ~7 μm assuming 40% porosity). However, the optimum thickness might lie in the range between 40 and 60% Pt/C (i.e. 50% Pt/C) due to the fact that, at low oxygen concentration and high doping level, 60% Pt/C showed advantage over 40% Pt/C. An optimum catalyst layer thickness of 10μm was reported in the literature for phosphoric acid fuel cells. This factor will be looked into more details in the next chapter.

3.9 References

1. Barbir, F., *PEM Fuel Cells: Theory and Practice (Sustainable World Series)*. 2005: Elsevier Academic Press.
2. E-TEK. *PRODUCT TECHNICAL INFORMATION* 2003 [cited; Available from: http://www.etek-inc.com/standard/product_NMC.php?prodid=59.
3. Pozio, A., M. De Francesco, A. Cemmi, F. Cardellini, and L. Giorgi, *Comparison of high surface Pt/C catalysts by cyclic voltammetry.* Journal of Power Sources, 2002. **105**(1): p. 13-19
4. Bard, A.J. and L.R. Faulkner, *Electrochemical Methods: Fundamentals and Applications*. 1980, New York: Wiley.
5. Rodríguez, J.M.D., J.A.H. Melián, and J.P. Peña, *Determination of the Real Surface Area of Pt Electrodes by Hydrogen Adsorption Using Cyclic Voltammetry.* Journal of Chemical Education, 2000. **77**(9): p. 1195.
6. Xing, Y., *Synthesis and Electrochemical Characterization of Uniformly-Dispersed High Loading Pt Nanoparticles on Sonochemically-Treated Carbon Nanotubes.* J. Phys. Chem. B, 2004. **108**(50): p. 19255 -19259.
7. Watanabe, M. and S. Motoo, *Chemisorbed CO on a polycrystalline platinum electrode: The effect of conditioning of the surface and of partial pressure of CO.* Journal of Electroanalytical Chemistry, 1986. **206**(1-2): p. 197-208.
8. Kordesch, K. and G. Simader, *Fuel Cells and Their Applications*. 1996, Cambridge.
9. Silva, S.A.M., et al., *Surface and electrochemical investigations of a fullerene soot.* Electrochimica Acta, 1999 **44**: p. 3565-3574.
10. Lufrano, F. and P. Staiti, *Conductivity and capacitance properties of a supercapacitor based on Nafion electrolyte in a nonaqueous system.* Electrochemical and Solid State Letters, 2004. **7**(11): p. A447-A450.
11. Qi, Z.G. and A. Kaufman, *Low Pt loading high performance cathodes for PEM fuel cells.* Journal of Power Sources, 2003. **113**(1): p. 37-43.
12. Song, J.M., S.Y. Cha, and W.M. Lee, *Optimal composition of polymer electrolyte fuel cell electrodes determined by the AC impedance method.* Journal of Power Sources, 2001. **94**(1): p. 78-84.
13. Tada, T., *Handbook of Fuel Cells: Fundamentals, Technology and Applications*. Part 3: Polymer Electrolyte Membrane Fuel Cells and Systems, High-dispersion Catalysts Including Novel Carbon Supports, ed. W. Vielstich, A. Lamm, and H.A. Gasteiger. Vol. 3. 2003, Chichester, UK: John Wiley & Sons.
14. Lee, S.J., S. Mukerjee, J. McBreen, Y.W. Rho, Y.T. Kho, and T.H. Lee, *Effects of Nafion impregnation on performances of PEMFC electrodes.* Electrochimica Acta, 1998. **43**(24): p. 3693-370115. Ralph, T.R. and M.P. Hogarth, *Catalysis for low temperature fuel cells.* Platinum Metals Rev, 2002. **46**(1): p. 3-14.
16. Makharia, R., M.F. Mathias, D.R. Baker, J. Iaculli, M.W. Murphy, *Electrolyte Resistance Measurement in the Catalyst Layer of Polymer Electrolyte Fuel Cells using Electrochemical Impedance Spectroscopy.* in *Proceedings of ECS Meeting.* October 2002. Salt Lake City, Utah, USA.
17. Gasteiger, H.A. and M.F. Mathias. *FUNDAMENTAL RESEARCH AND DEVELOPMENT CHALLENGES IN POLYMER ELECTROLYTE FUEL CELL*

TECHNOLOGY. in *Proceedings of ECS Meeting*. October, 2002. Salt Lake City, UTAH, USA

18. Antolini, E., L. Giorgi, A. Pozio, and E. Passalacqua, *Influence of Nafion loading in the catalyst layer of gas-diffusion electrodes for PEFC.* Journal of Power Sources, 1999. **77**(2): p. 136-142.
19. Passalacqua, E., F. Lufrano, G. Squadrito, A. Patti, and L. Giorgi, *Nafion content in the catalyst layer of polymer electrolyte fuel cells: effects on structure and performance.* Electrochimica Acta, 2001. **46**(6): p. 799-805.
20. Sasikumar, G., J.W. Ihm, and H. Ryu, *Dependence of optimum Nafion content in catalyst layer on platinum loading.* Journal of Power Sources, 2004. **132**(1-2): p. 11-17.
21. Uchida, M., et al., J. Electrochem. Soc., 1995. **142**: p. 4143.
22. Reshetenko, T.V., H.T. Kim, H. Lee, M. Jang, and H. Kweon, *Performance of a direct methanol fuel cell (DMFC) at low temperature: Cathode optimization.* Journal of Power Sources, 2006. **160**(2): p. 925-932.
23. Xie, J., K.L. More, T.A. Zawodzinski, and W.H. Smith, *Porosimetry of MEAs made by "Thin film decal" method and its effect on performance of PEFCs.* Journal of the Electrochemical Society, 2004. **151**(11): p. A1841-A1846.
24. Li, G.C. and P.G. Pickup, *Ionic conductivity of PEMFC electrodes - Effect of Nafion loading.* Journal of the Electrochemical Society, 2003. **150**(11): p. C745-C752.
25. Lufrano, F., P. Staiti, and M. Minutoli, *Influence of Nafion content in electrodes on performance of carbon supercapacitors.* Journal of the Electrochemical Society, 2004. **151**(1): p. A64-A68.
26. Xu, H., H.R. Kunz, L.J. Bonville, and J.M. Fenton, *Improving PEMFC performance using low equivalent weight PFSA ionomers and Pt-Co/C catalyst in the cathode.* Journal of the Electrochemical Society, 2007. **154**(2): p. B271-B278.
27. Liu, F. and C.-Y. Wang, *Optimization of cathode catalyst layer for direct methanol fuel cells, Part II: Computational modeling and design.* Electrochimica Acta, 2006. **52**: p. 1409-1416.
28. Antoine, O., Y. Bultel, P. Ozil, and R. Durand, *Catalyst gradient for cathode active layer of proton exchange membrane fuel cell.* Electrochimica Acta, 2000. **45**(27): p. 4493-4500
29. Wang, Q., M. Eikerling, D. Song, Z. Liu, T. Navessin, Z. Xie, and S. Holdcroft, *Functionally Graded Cathode Catalyst Layers for Polymer Electrolyte Fuel Cells, part I.* J. Electrochem. Soc., 2004. **151**: p. A950.
30. Xie, Z., T. Navessin, K. Shi, R. Chow, Q.P. Wang, D.T. Song, B. Andreaus, M. Eikerling, Z.S. Liu, and S. Holdcroft, *Functionally graded cathode catalyst layers for polymer electrolyte fuel cells - II. Experimental study of the effect of Nafion distribution.* Journal of the Electrochemical Society, 2005. **152**(6): p. A1171-A1179.
31. Pasaogullari, U. and C.Y. Wang, *Liquid Water Transport in Gas Diffusion Layer of Polymer Electrolyte Fuel Cells.* Journal of The Electrochemical Society, 2004. **151**(3): p. A399-A406.
32. Song, D.T., Q.P. Wang, Z.S. Liu, M. Eikerling, Z. Xie, T. Navessin, and S. Holdcroft, *A method for optimizing distributions of Nafion and Pt in cathode catalyst layers of PEM fuel cells.* Electrochimica Acta, 2005. **50**(16-17): p. 3347-3358.
33. Wainright, J.S., J.T. Wang, D. Weng, R.F. Savinell, and M. Litt, *Acid-Doped Polybenzimidazoles - a New Polymer Electrolyte.* Journal of the Electrochemical Society, 1995. **142**(7): p. L121-L12334. MacDonald, D.I. and J.R. Boyack, *Density,*

Electrical Conductivity, and Vapor Pressure of Concentrated Phosphoric acid. Journal of Chemical and Engineering Data, 1969. **14**(3): p. 380.

35. Zuruzi, A.S., B.C. Butler, N.C. MacDonald, and C.R. Safinya, *Nanostructured TiO2 thin films as porous cellular interfaces.* Nanotechnology, 2006. **17**(2): p. 531-535.
36. Li, Q.F., R.H. He, J.O. Jensen, and N.J. Bjerrum, *Approaches and recent development of polymer electrolyte membranes for fuel cells operating above 100 degrees C.* Chemistry of Materials, 2003. **15**(26): p. 4896-4915.
37. Hoel, D. and E. Grunwald, *High Protonic Conduction of Polybenzimidazole Films.* Journal of Physical Chemistry, 1977. **81**(22): p. 2135-2136.
38. He, R.H., Q.F. Li, G. Xiao, and N.J. Bjerrum, *Proton conductivity of phosphoric acid doped polybenzimidazole and its composites with inorganic proton conductors.* Journal of Membrane Science, 2003. **226**(1-2): p. 169-184.
39. Gaowen, Z. and Z. Zhentao, *Organic/inorganic composite membranes for application in DMFC.* Journal of Membrane Science, 2005. **261**(1-2): p. 107-113.
40. Sone, Y., P. Ekdunge, and D. Simonsson, *Proton Conductivity of Nafion 117 as Measured by a Four-Electrode AC Impedance Method.* J. Electrochem. Soc., 1996. **143**(4): p. 1254-1259.
41. Mecerreyes, D., H. Grande, O. Miguel, E. Ochoteco, R. Marcilla, and I. Cantero, *Porous polybenzimidazole membranes doped with phosphoric acid: Highly proton-conducting solid electrolytes.* Chemistry of Materials, 2004. **16**(4): p. 604-607.
42. Zook, L.A. and J. Leddy, *Density and Solubility of Nafion: Recast, Annealed, and Commercial Films.* Anal. Chem., 1996. **68**: p. 3793-3796.
43. DuPont. *Technical info: Fluoropolymer Comparison - Typical Properties.* Mechanical Properties 2007 [cited; Available from: http://www2.dupont.com/Teflon_Industrial/en_US/tech_info/techinfo_compare.html].
44. Sakai, T., H. Takenako, N. Wakabayashi, Y. Kawami, and E. Torikai, *Gas Permeation Properties of Solid Polymer Electrolyte (SPE) Membranes.* J. Electrochem. Soc., 1985. **132**(6): p. 1328.
45. Ogumi, Z., T. Kuroe, and Z.-i. Takehara, *Gas Permeation in SPE Method II. Oxygen and Hydrogen Permeation Through Nafion.* J. Electrochem. Soc., 1985 **132**(11): p. 2601.
46. He, R.H., et al., *Physicochemical properties of phosphoric acid doped polybenzimidazole membranes for fuel cells.* Journal of Membrane Science, 2006. **277**(1-2): p. 38-45.
47. Zecevic, S.K., J.S. Wainright, M.H. Litt, S.L. Gojkovic, and R.F. Savinell, *Kinetics of O-2 reduction on a Pt electrode covered with a thin film of solid polymer electrolyte.* Journal of the Electrochemical Society, 1997. **144**(9): p. 2973-2982.
48. Ayad, A., J. Bouet, and J.F. Fauvarque, *Comparative study of protonic conducting polymers incorporated in the oxygen electrode of the PEMFC.* Journal of Power Sources, 2005. **149**: p. 66-71.
49. Wang, J.T., R.F. Savinell, J. Wainright, M. Litt, and H. Yu, *A H-2/O-2 fuel cell using acid doped polybenzimidazole as polymer electrolyte.* Electrochimica Acta, 1996. **41**(2): p. 193-197.
50. Pan, C., Q. Li, J.O. Jensen, R. He, L.N. Cleemann, M.S. Nilsson, N.J. Bjerrum, and Q. Zeng, *Preparation and operation of gas diffusion electrodes for high-temperature proton exchange membrane fuel cells.* Journal of Power Sources, 2007. **172**: p. 278-286.

51. Seland, F., T. Berning, B. Borresen, and R. Tunold, *Improving the performance of high-temperature PEM fuel cells based on PBI electrolyte.* Journal of Power Sources, 2006. **160**(1): p. 27-36.
52. Scott, K. and M. Mamlouk, *High temperature polymer electrolyte membrane fuel cell.* Battery Bimonthly, 2006. **36**(5): p. 11.
53. Lobato, J., M.A. Rodrigo, J.J. Linares, and K. Scott, *Effect of the catalytic ink preparation method on the performance of high temperature polymer electrolyte membrane fuel cells.* Journal of Power Sources, 2006. **157**(1): p. 284-292.
54. Kim, J.-H., H.Y. Ha, I.-H. Oh, S.-A. Hong, and H.-I. Lee, *Influence of the solvent in anode catalyst ink on the performance of a direct methanol fuel cell.* Journal of Power Sources, 2004. **135**(1-2): p. 29-35.
55. Kongstein, O.E., T. Berning, B. Borresen, F. Seland, and R. Tunold, *Polymer electrolyte fuel cells based on phosphoric acid doped polybenzimidazole (PBI) membranes.* Energy, 2007. **32**(4): p. 418-422.
56. Wang, J.T., S. Wasmus, and R.F. Savinell, *Real-time mass spectrometric study of the methanal crossover in a direct methanol fuel cell.* Journal of the Electrochemical Society, 1996. **143**(4): p. 1233-1239.
57. Jones, D.J. and J. Roziere, *Recent advances in the functionalisation of polybenzimidazole and polyetherketone for fuel cell applications.* Journal of Membrane Science, 2001. **185**(1): p. 41-58.
58. Pivovar, B.S., Y.X. Wang, and E.L. Cussler, *Pervaporation membranes in direct methanol fuel cells.* Journal of Membrane Science, 1999. **154**(2): p. 155-162.
59. Pu, H.T., Q.Z. Liu, and G.H. Liu, *Methanol permeation and proton conductivity of acid-doped poly (N-ethylbenzimidazole) and poly(N-methylbenzimidazole).* Journal of Membrane Science, 2004. **241**(2): p. 169-175.
60. Gil, M., X. Ji, X. Li, H. Na, J. Eric Hampsey, and Y. Lu, *Direct synthesis of sulfonated aromatic poly(ether ether ketone) proton exchange membranes for fuel cell applications.* Journal of Membrane Science, 2004. **234**(1-2): p. 75-81.
61. Wainright, J.S., J.T. Wang, D. Weng, R.F. Savinell, and M. Litt, *Acid-Doped Polybenzimidazoles - a New Polymer Electrolyte.* Journal of the Electrochemical Society, 1995. **142**(7): p. L121-L123.
62. Liu, Z.Y., J.S. Wainright, M.H. Litt, and R.F. Savinell, *Study of the oxygen reduction reaction (ORR) at Pt interfaced with phosphoric acid doped polybenzimidazole at elevated temperature and low relative humidity.* Electrochimica Acta, 2006. **51**(19): p. 3914-3923.
63. Klinedinst, K., J.A.S. Bett, J. MacDonald, and P. Stonehart, *Oxygen solubility and diffusivity in hot concentrated H_3PO_4.* J. Electroanalytical Chemistry and Interfacial Electrochemistry, 1974. **57**: p. 281-289.
64. Scharifker, B.R., P. Zelenay, and J.O.M. Bockris, *The Kinetics of Oxygen Reduction in Molten Phosphoric Acid at High Temperatures.* J. Electrochem. Soc., 1987. **134**.
65. Sakai, T., H. Takenaka, and E. Torikai, *Gas Diffusion in the Dried and Hydrated Nafions.* J. Electrochem. Soc., 1986. **133**(1): p. 88.
66. Pasternak, R.A., M.V. Christensen, and J. Heller, *Diffusion and Permeation of Oxygen, Nitrogen, Carbon Dioxide, and Nitrogen Dioxide through Polytetrafluoroethylene.* Macromolecules, 1970. 3(3): p. 366.

67. Gibbs, T.K. and D. Pletcher, *THE ELECTROCHEMISTRY OF GASES AT METALLIZED MEMBRANE ELECTRODES.* Electrochim. Acta, 1980. **25**: p. 1105.
68. Sugishima, N., J.T. Hinatsu, and F.R. Foulkes, *Phosphorous Acid Impurities in Phosphoric Acid Fuel Cell Electrolytes II. Effects on the Oxygen Reduction Reaction at Platinum Electrodes.* J. Electrochem. Soc., 1994. **141**(12): p. 3332-3335.
69. Huang, J.C., R.K. Sen, and E. Yeager, *Oxygen Reduction on Platinum in 85% Orthophosphoric Acid.* J. Electrochem. Soc., 1979. **126**(5): p. 786-792.
70. Liu, Z.Y., J.S. Wainright, and R.F. Savinell, *High-temperature polymer electrolytes for PEM fuel cells: study of the oxygen reduction reaction (ORR) at a Pt-polymer electrolyte interface.* Chemical Engineering Science, 2004. **59**(22-23): p. 4833-4838.
71. Sugishima, N., J.T. Hinatsu, and F.R. Foulkes, *Phosphorous Acid Impurities in Phosphoric Acid Fuel Cell Electrolytes I. Voltammetric Study of Impurity Formation.* J. Electrochem. Soc., 1994. **141**(12): p. 3325-3331.
72. Li, Q.F., H.A. Hjuler, and N.J. Bjerrum, *Oxygen reduction on carbon supported platinum catalysts in high temperature polymer electrolytes.* Electrochimica Acta, 2000. **45**(25-26): p. 4219-4226.
74. Bevers, D., M. Wohr, K. Yasuda, and K. Oguro, *Simulation of a polymer electrolyte fuel cell electrode.* Journal of Applied Electrochemistry, 1997. **27**(11): p. 1254-1264.
75. Whiteley, L.D. and C.R. Martin, *Fresh look at transport in perfluorosulfonate ionomers: ultramicroelectrode investigations of Nafion and the Dow ionomers.* J. Phys. Chem., 1989. **93**: p. 4650 - 4658.
76. Gileadi, E., *Electrode Kinetics for Chemists, Chemical Engineers and Materials Scientists.* 1993: John Wiley & Sons.
77. Bockris, J.O.M., et al., *Modern aspects of electrochemistry*, ed. J.O.M. Bockris and B.E. Conway. Vol. 5. 1954-, London: Butterworths Scientific Publications.
78. Bockris, J.O.M., *Fuel cells: their electrochemistry.* 1969, New York: McGraw-Hill
79. Bockris, J.O.M., et al., *Modern aspects of electrochemistry*, ed. J.O.M. Bockris and B.E. Conway. Vol. 32. 1954-, London: Butterworths Scientific Publications.
80. Damjanovic, A. and V. Brusic, *Electrode kinetics of oxygen reduction on oxide-free platinum electrodes.* Electrochimica Acta, 1967. **12**(6): p. 615-628.
81. Damjanovic, A., D.B. Sepa, and M.V. Vojnovic, *New evidence supports the proposed mechanism for O2 reduction at oxide free platinum electrodes.* Electrochimica Acta, 1979. **24**(8): p. 887-889.
82. Damjanovic, A. and M.A. Genshaw, *Dependence of the kinetics of O2 dissolution at Pt on the conditions for adsorption of reaction intermediates.* Electrochimica Acta, 1970. **15**(7): p. 1281-1283.
83. Tarasevich, M.R., *Parallel-consecutive stages of oxygen and hydrogen peroxide reactions. IX. Mechanism of oxygen electroreduction on platinum metals.* Russian journal of electrochemistry (Elektrokhimiya), 1973. **9**(5): p. 599-605.
84. Bagotzky, V.S. and M.R. Tarasevich, *Oxygen Adsorption on Platinum and Platinum Metals. Part I: Investigation of the adsorption mechanism by the potentiodynamic method.* J. Electroanal. Chem. Interfacial Electrochem., 1979. **101**(1): p. 1-17.
85. Appleby, A.J., *Oxygen Reduction on Oxide-Free Platinum in 85% Orthophosphoric Acid: Temperature and Impurity Dependence.* J. Electrochem. Soc., 1970. **117**(3): p. 328-335.

86. Muller, L., G.N. Mansurov, and O.A. Petrii, *The measurment of strong adsorption on platinum film electrodes by surface conductance.* J. Electroanal. Chem., 1979. **96**: p. 159-164.
87. Angerstein-Kozlowska, H., B.E. Conway, and W.B.A. Sharp, *The real condition of electrochemically oxidized platinum surfaces: Part I. Resolution of component processes.* Journal of Electroanalytical Chemistry, 1973. **43**(1): p. 9-36.
88. Conway, B.E. and S. Gottesfeld, *Real Condition of Oxidized Platinum Electrodes. Part2. Resolution of reversible and irreversible process by optical and impedance studies.* J. Chem. Soc. Faraday Trans. I, 1973. **69**: p. 1090-1107.
89. Tilak, B.V., B.E. Conway, and H. Angerstein-Kozlowska, *The real condition of oxidized pt electrodes: Part III. Kinetic theory of formation and reduction of surface oxides.* Journal of Electroanalytical Chemistry, 1973. **48**(1): p. 1-23.
90. Riddiford, A.C., *Mechanisms for the evolution and ionization of oxygen at platinum electrodes.* Electrochimica acta, 1961. **4**: p. 170-178.
91. Conway, B.E. and E. Gileadi, *Kinetic theory of pseudocapacitance and electrode reactions at appreciable surface coverage.* J. Chem. Soc., Faraday Trans.,, 1962. **68**: p. 2493-2509.
92. Wroblowa, H., M.L.B. Rao, A. Damjanovic, and J.O.M. Bockris, *Adsorption and kinetics at platinum electrodes in the presence of oxygen at zero net current.* Journal of Electroanalytical Chemistry, 1967. **15**: p. 139-150.
93. Bockris, J.O.M. and S. Srinivasan, Electrochim Acta, 1964. **9**: p. 31.
94. Bockris, J.O.M., B.E. Conway, R.E. White, C.G. Vayenas, and M. Gamboa-Aldeco, *Modern aspects of electrochemistry* ed. J.O.M. Bockris and B.E. Conway. Vol. 16. 1954-, London: Butterworths Scientific Publications.
95. PARSONS, R., *THE EFFECT OF SPECIFIC ADSORPTION ON THE RATE OF AN ELECTRODE PROCESS.* J. Electroanal. Chem. Interfacial Electrochem., 1969. **21**: p. 35-43.
96. Angerstein-Kozlowska, H., et al., *The role of ion adsorption in surface oxide formation and reduction at noble metals: General features of the surface process.* Journal of Electroanalytical Chemistry, 1979. **100**(1-2): p. 417-446.
97. Conway, B.E., D.F. Tessier, and D.P. Wilkinson, *Experimental evidence for the potential-dependence of entropy of activation in electrochemical reactions in relations to the temperature-dependence of tafel slopes.* Journal of Electroanalytical Chemistry, 1986. **199**(2): p. 249-269.
98. Sun, W., B.A. Peppley, and K. Karan, *An improved two-dimensional agglomerate cathode model to study the influence of catalyst layer structural parameters.* Electrochimica Acta, 2005. **50**(16-17): p. 3359-3374.
99. Parthasarathy, A., S. Srinivasan, and A.J. Appleby, *Temperature Dependence of the Electrode Kinetics of Oxygen Reduction at the Platinum/Nafion® Interface-A Microelectrode Investigation.* J. Electrochem. Soc., 1992. **139**(9): p. 2530-2537.
100. Appleby, A.J. and B.S. Baker, *Oxygen reduction on platinum in trifluoromethane sulfonic acid.* J. Electrochem. Soc., 1978. **125**(3): p. 404-406.
101. Sepa, D.B., M.V. Vojnovic, and A. Damjanovic, *Kinetics and mechanism of O2 reduction at Pt IN alkaline solutions.* Electrochimica Acta, 1980. **25**(11): p. 1491-1496.

102. Sepa, D.B., M.V. Vojnovic, and A. Damjanovic, *Reaction intermediates as a controlling factor in the kinetics and mechanism of oxygen reduction at platinum electrodes.* Electrochimica Acta, 1981. **26**(6): p. 781-793.
103. *Corrosion*, ed. L.L. Shreir, G.T. Burstein, and R.A. Jarman. 1994, Oxford, Boston: Butterworth Heinemann. 21:34.
104. Kunz, H.R. and G.A. Gruver, *The Catalytic Activity of Platinum Supported on Carbon for Electrochemical Oxygen Reduction in Phosphoric Acid.* J. Electrochem. Soc., 1975. **122**(10): p. 1279-1287.
105. Vogel, W.M. and J.T. Lundquist, *Reduction of Oxygen on Teflon-Bonded Platinum Electrodes.* J. Electrochem. Soc., 1970. **117**(12): p. 1512-1516.
106. Petrii, O.A., R.V. Marvet, and Z.N. Malysheva, *Charging curves of a platinum electrode in phosphoric acid solutions at various temperatures.* Russian journal of electrochemistry (Electrokhimiya), 1967. **3**(8): p. 962-965.
107. Clouser, S.J., J.C. Huang, and E. Yeager, *Temperature dependance of the Tafel slope for oxygen reduction on platinum in concentrated phosphoric acid.* Journal of Applied Electrochemistry, 1993. **23**: p. 597-605.
108. McBreen, J., W.E. O'Grady, and R. Richter, *A Rotating Disk Electrode Apparatus for the Study of Fuel Cell Reactions at Elevated Temperatures and Pressures.* J. Electrochem. Soc., 1984. **131**(5): p. 1215-1216.
109. Appleby, A.J., *Evolution and reduction of oxygen on oxidized platinum in 85% orthophosphoric acid.* J. Electroanal. Chem. Interfacial Electrochem., 1970. **24**: p. 97.
110. O'Grady, W.E., E.J. Taylor, and S. Srinivasan, *Electro-reduction of oxygen on reduced platinum in 85% phoshporic acid.* J. Electroanal. Chem. Interfacial Electrochem., 1982. **132**: p. 137.
111. Damjanovic, A., *Modern aspects of electrochemistry* ed. J.O.M. Bockris and B.E. Conway. Vol. 5 1954-, London: Butterworths Scientific Publications. 369.
112. Damjanovic, A., M.A. Genshaw, and J.O.M. Bockris, *The Role of Hydrogen Peroxide in Oxygen Reduction at Platinum in H2SO4 Solution.* J. Electrochem. Soc., 1967. **114**(5): p. 446-472.
113. Klinedinst, K., J.A.S. Bett, J. MacDonald, and P. Stonehart, *Oxygen solubility and diffusivity in hot concentrated H_3PO_4.* J. Electroanalytical Chemistry and Interfacial Electrochemistry, 1974. **57**: p. 281-289.
114. Zelenay, O.P., B.R. Scharifker, J.O.M. Bockris, and D. Gervasio, *A Comparison of the Properties of CF_3SO_3H and H_3PO_4 in Relation to Fuel Cells.* J. Electrochem. Soc., 1986. **133**(11): p. 2262-2267.
115. Bockris, J.O.M. and A. Gochev, *Temperature dependence of the symmetry factor in electrode kinetics.* Journal of Electroanalytical Chemistry, 1986. **214**(1-2): p. 655-674.

4 Optimisation of PBI Membrane Electrode Assembly

4.1 Introduction

As discussed in the previous chapter, the catalyst structure plays a major part in determining an electrode's performance; whilst on the other hand increasing the ESA of the catalyst layer by utilizing catalyst with lower Pt to carbon ratio (smaller particles size) did not necessarily enhance the performance of the PBI-phosphoric acid fuel cell. At a loading of 0.5 mg_{Pt} cm^{-2} the best performance achieved in this work was with catalysts with Pt content in the range of 40-60% Pt/C. This can be explained by:

i) an optimum particle size for mass activity; reported to be ~3.5 nm for phosphoric acid fuel cells [1]; which was in good agreement with the findings of this work 2.8-3.7 nm, and

ii) an optimum thickness for the catalyst layer, reported to be ~10 μm [2] for phosphoric acid fuel cells and found to be in the range of 5.6-12.7 μm in this work (assuming 40 % porosity in the catalyst layer 40-60% Pt/C).

In this chapter data from several fuel cells is presented and discussed. The effects of catalyst thickness (Pt:C ratio), PBI loading, acid loading, catalyst loading and binder/electrolyte materials; for both anode and cathode are described to enable more detailed study of the catalyst layer.

4.2 PBI based MEA'S

4.2.1 Experimental

4.2.1.1 Cell design

In the corrosive environment of hot phosphoric acid, the choice of materials available to stand the operating harsh conditions is limited. Graphite and Titanium are good candidates due to their relatively low cost and high stability. For the experimental single cell, titanium was selected due to better mechanical properties and low hydrogen permeability over graphite. However it was necessary to gold plate the surface in contact with the MEA, as oxide formation in this increase its contact resistance.

The fuel cell is shown schematically in Figure 4-1. The titanium cell body used had a 3 cm x 3 cm gold plated parallel flow fields. Mica filled PTFE inserts were used to surround the flow

fields and provide location for the O-ring seal and dynamic hydrogen electrode (DHE). The solid state DHE consisted of two platinum wires on each side of the membrane located outside the O-ring: a distance of 10 mm away from the MEA edge to avoid side current effects (the membrane used ~50μm). A small current of 1.0 mA cm^{-2} (~10 μA) was applied (to perform hydrogen evolution reaction) by means of 9 V battery connected in series with appropriate resistance.

The temperature of the cell was controlled by thermostatically controlled cartridge heaters inserted into the cell body The gases were passed into a home-made humidifier at 16 °C prior to entering the cell at ambient temperature, this provided small humidification of 0.36% RH at 150 °C (unless otherwise mentioned). The flow rates were controlled manually by means of appropriate flow meter designated for each gas (Platon (RM&C), U.K). The cell was tested under ambient pressure unless otherwise specified.

4.2.1.2 Instruments

A Powerstat 20 A potentiostat (Sycopel, U.K) combined with high impedance multi channel data acquisition card (national instrument, NI6010) was used to carry out the electrochemical measurements, which enabled continuous monitoring of anode, cathode (vs DHE) and cell performances separately. Polarisation curves were recorded using a cathodic sweep at a scan rate of 5 mV s^{-1}. Previous tests confirmed that this was slow enough to approximate to steady state operation.

The conductivity of each MEA was measured using Gill AC frequency response analyzer (ACM instruments, U.K) in the range of 30 kHz to 30 mHz (15 mA amplitude) and the relative humidity was obtained from an intrinsically safe humidity sensor (Vaisala HUMICAP®, Finland).

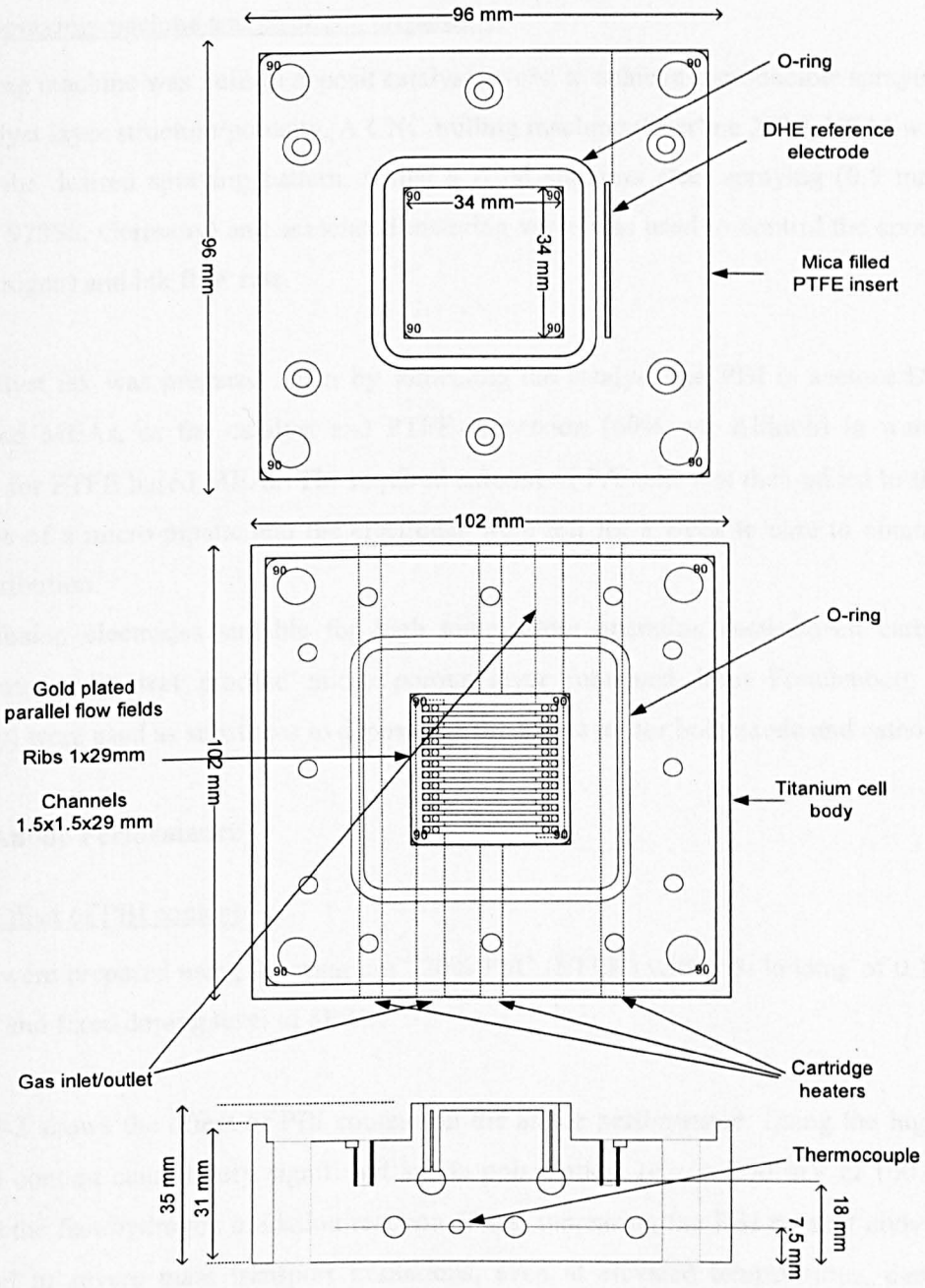

Figure 4-1. Schematic diagram of the titanium testing fuel cell.

4.2.1.3 Spraying machine and electrode preparation

A spraying machine was built to deposit catalyst layers; to achieve reproducible spraying pattern and catalyst layer structure/porosity. A CNC milling machine (Sherline 2010, USA) was used to provide the desired spraying pattern, whilst a fixed stainless steel spraying (0.5 mm) nozzle (Schlick 970S8, Germany) and associated metering valve was used to control the spray mixture (with nitrogen) and ink flow rate.

The catalyst ink was prepared either by sonicating the catalyst and PBI in acetone/DMAc, for PBI based MEAs, or the catalyst and PTFE dispersion (60% wt, Aldrich) in water-ethanol mixture, for PTFE based MEAs. The required amount of PA acid was then added to the surface by means of a micro-pipette and the electrodes were left for a week to cure to obtain uniform acid distribution.

Gas diffusion electrodes suitable for high temperature operation (non-woven carbon cloth) incorporated with wet proofed micro porous layer (obtained from Freudenberg (FFCCT, Germany) were used as substrates to deposit the catalyst layer for both anode and cathode.

4.2.2 Anode Performance

4.2.2.1 Effect of PBI content

Anodes were prepared using 0.2 mg_{Pt} cm^{-2} 20% Pt/C (ETEK) with PBI loading of 0.28 and 0.7 mg cm^{-2} and fixed doping level of 8PRU.

Figure 4-2 shows the effect of PBI content on the anode performance. Using the higher of the two PBI content caused very significant anode polarisation, (e.g. > 200 mV at 100 mA cm^{-2}) even for the fast hydrogen oxidation reaction. Thus, increasing the PBI content above 0.28 mg cm^{-2} lead to severe mass transport limitations, even at elevated temperatures, due to lower porosity and hydrogen permeability through a thicker PBI ionomer film. This counteracted any potential advantages of increased ionic conductivity provided by PBI in the catalyst layer. Notably with the lower PBI content the anode polarisation was low, cf. 20 mV at 500 mA cm^{-2}.

As oxygen permeability through PBI is even lower than that of hydrogen, especially under air operation, this suggested that a minimum PBI content would be required for cathodes.

4.2.2.2 Effect of acid doping

Figure 4-3 shows the effect of doping level on the anode performance with a PBI loading of 0.7 mg cm^{-2}. Increasing the doping level dramatically enhanced the anode performance even at very high doping level of 20 PRU. Increasing the acid content lead to enhancement in conductivity across the catalyst layer, more accessible ESA and better hydrogen permeability over pristine PBI. For anodes using 0.5 mg_{Pt} cm^{-2} 20%Pt/C with doping level of 20 PRU a superior performance was obtained, for example with an overpotential value of only ~10 mV at a current density of 600 mA cm^{-2} and temperature of 150 °C. Increasing the doping level up to 20 PRU did not appear to impose mass transport limitation on the anode when operating with pure hydrogen.

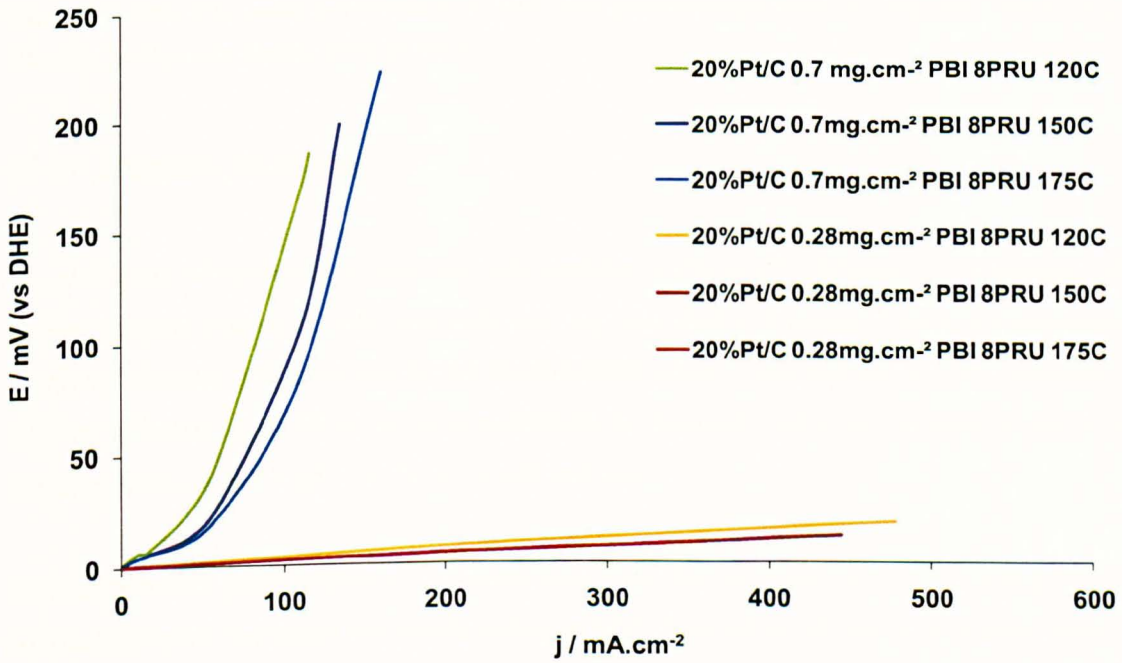

Figure 4-2. Effect of temperature and PBI content on anode polarisation performance, potentials measured vs. DHE, Anode 20 %Pt/C, platinum loading 0.2 mg_{Pt} cm^{-2}.

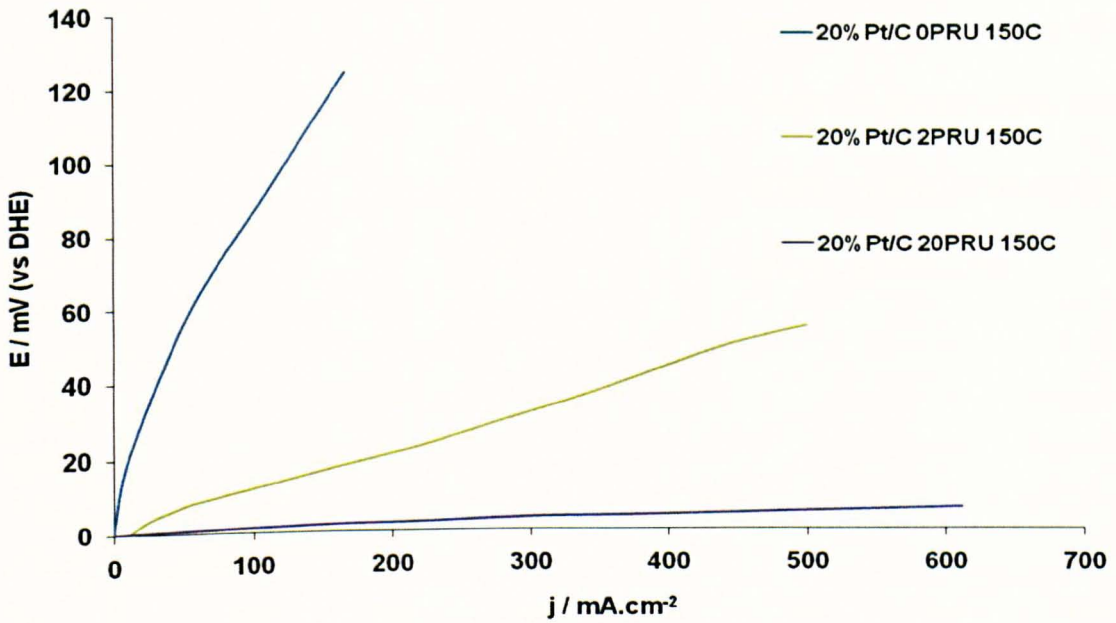

Figure 4-3. 20% Pt/C anode performance vs. DHE with pure hydrogen using 0.5 mg_{Pt} cm^{-2} and 0.7 mg cm^{-2} PBI with various acid doping levels at 150 °C.

4.2.2.3 Reformate gas tolerance

An advantage of operating at elevated temperatures is improved platinum CO tolerance, which enables simpler operation with reformate gas, e.g. less shift reforming. Figure 4-4 demonstrates the effect of using reformate gas on the anode performance in comparison to pure hydrogen. The dilution effect of using 50 % vol carbon dioxide, for example, led to an increase in anode over-potential from 24 to 37 mV (vs. DHE) at 600 mA cm^{-2}.

The cell showed good tolerance to carbon monoxide, for example, at 175 °C, using 10 % vol carbon monoxide increased the anode over-potential from 24 to 62 mV at a current density of 600 mA cm^{-2} and low platinum loading of 0.2 mg cm^{-2}. Above 10% vol CO a dramatic fall in anode activity was observed due to poisoning. For example with 30% vol CO, (Fig. 4-4) the anode performance was limited and current densities up to 600 mA cm^{-2} were not achievable.

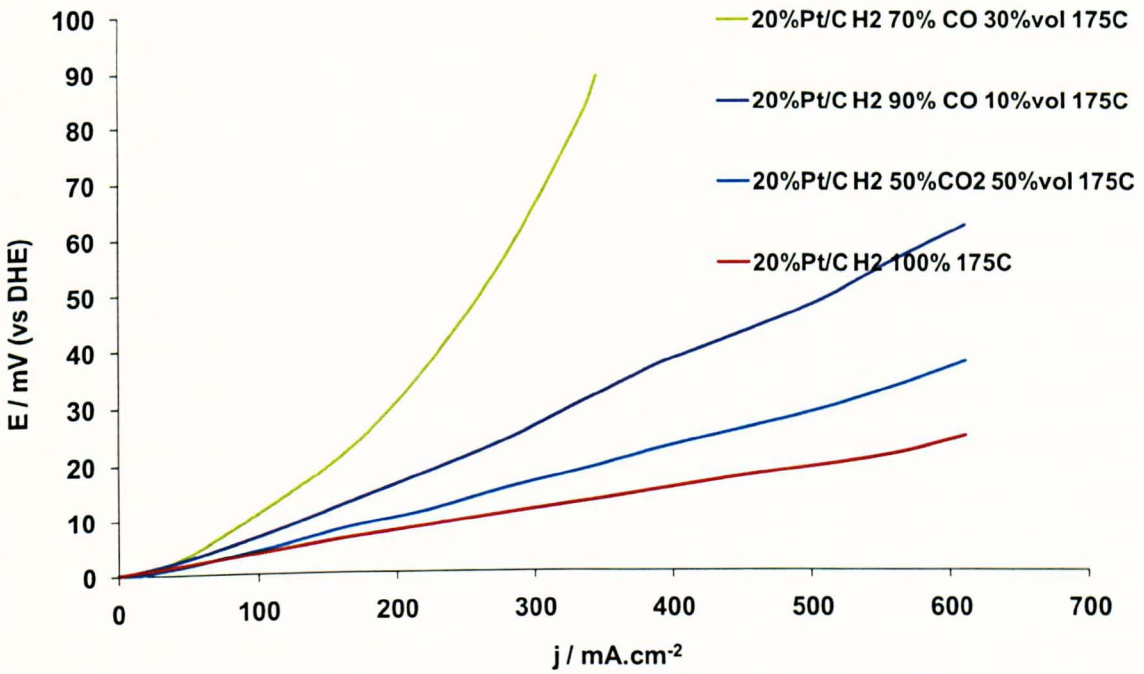

Figure 4-4. Effect of CO & CO2 on anode performance vs. DHE using 0.2 mg_{Pt} cm^{-2} 20% Pt/C and 0.28 mg cm^{-2} PBI with doping level of 8 PRU, H2 flow rate of 0.2 lpm and temperature of 175 °C.

4.2.3 Cathode Performance

The effect of acid loading, surfactant addition and ionomer on cathode performance were studied and described in this section. Cathodes were prepared using 0.5 mg_{Pt} cm^{-2} of 30% Pt/C (ETEK) with a PBI content of 0.55 mg cm^{-2} in order to maintain ionomer volume fraction of ~ 32% in the catalyst layer (see Chapter 3).

4.2.3.1 Effect of acid doping

As seen in Chapter 3 there was an "optimum" acid loading for a given PBI content and catalyst layer thickness. Figure 4-5 shows the effect of doping level on cathode performance. Using oxygen, increasing the doping level from 0 to 2.5 PRU shifted the polarisation curve to lower over-potentials without an apparent change in the slope of the curve; suggesting no considerable change in the transfer coefficient, mass transport or resistance. Increasing the doping level further to 11 PRU led to a greater reduction in cathode performance, compared to that with 2.5

PRU. The slope of the polarisation curve also increased compared to that with 2.5 and 0 PRU. The addition of acid should enhance electrolyte conductivity and potentially reduce the potential drop through the catalysts layer which may be seen in smaller slope of the polarisation curve. However greater quantities of PA may cause kinetic limitations through co-adsorption of phosphate, and also mass transport limitations. With pure oxygen and for small over-potentials it is not expected that severe mass transport limitation would occur. This is confirmed from operation with 1 bar (gauge) oxygen (Figure 4-5) where increasing the oxygen partial pressure did not affect dramatically the slope of the polarisation curve, even though the kinetics enhancement shifted the polarisation curves to lower over-potentials. Overall, from the data, the further addition of the acid decreased the transfer coefficient (α), which was confirmed in Chapter 3 (see effect of acid doping on α).The calculated values of α were 0.92, 0.905 & 0.79 for doping levels of 0, 3 & 11 PRU at 150 °C, respectively.

Comparing the electrode performance with air (Figure 4-6) and oxygen (Figure 4-5), it can be seen that electrodes with doping level of 2.5 PRU did not suffer major mass transport limitations within the current densities used; the slopes of the polarisation curves slope were also similar. Similar conclusions can be drawn for the 11 PRU doping level, where even though the slopes under oxygen at 0 and 1bar (gauge) were different from that of low doping level, the slopes were similar under air operation which confirmed the influence of acid on the transfer coefficient.

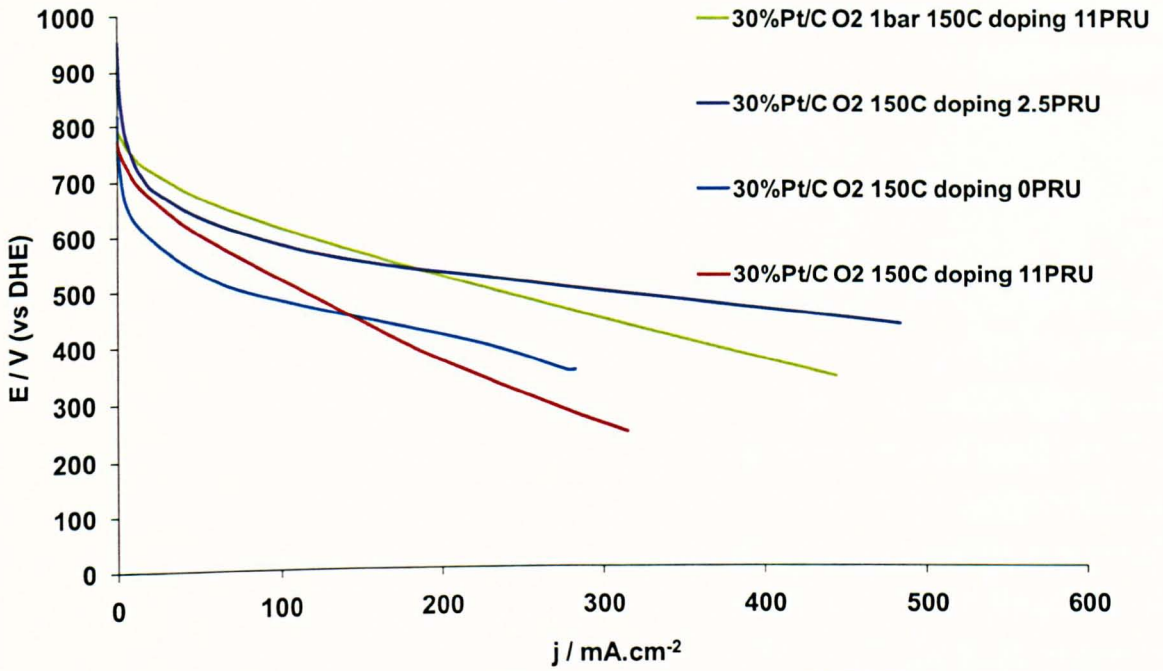

Figure 4-5. Effect of doping level on cathode performance under oxygen vs. DHE (IR included) using 0.5 mg_{Pt} cm^{-2} 30% Pt/C and 0.55 mg cm^{-2} PBI with various doping levels.

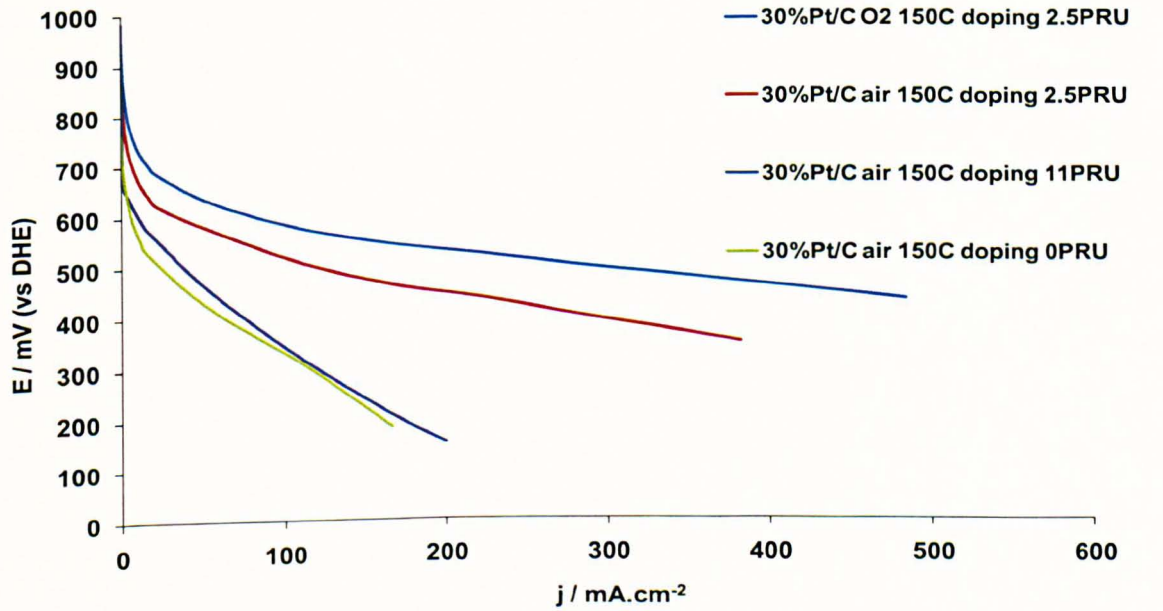

Figure 4-6. Effect of doping level on cathode performance under air & oxygen vs. DHE (IR included) using 0.5 mg_{Pt} cm^{-2} 30% Pt/C and 0.55 mg cm^{-2} PBI.

Non-doped electrodes (0 PRU) using oxygen produced similar polarisation curve slopes to that with 2.5 PRU. However with air the slope decreased compared to that with oxygen operation, suggesting mass transport limitations, which is expected due to the very low permeability of oxygen through pristine PBI.

4.2.3.2 Effect of surfactant addition

As seen from Chapter 3, the addition of perfluorinated surfactant (0.5% wt known as C6) lead to enhancement in oxygen permeability through the PBI/H_3PO_4 interface. Figure 4-7 shows the effect of surfactant addition on cathode performance for 40%Pt/C electrodes prepared with 0.5 mg_{Pt} cm^{-2} 40% Pt/C, 0.45 mg cm^{-2} PBI and doping level of 6 PRU. An enhancement in activity is clearly seen with both air and oxygen operation. For example, using air, at current density of 100 mA cm^{-2} a potential increase from 100 to 500 mV was observed with the surfactant addition. In addition, an apparent limiting current density of ~180 mA cm^{-2} was observed with oxygen, without surfactant addition, whilst no limiting current was observed with 0.5% wt surfactant within the current density range studied. The measured transfer coefficient was ~0.85 and did not vary with C6 addition.

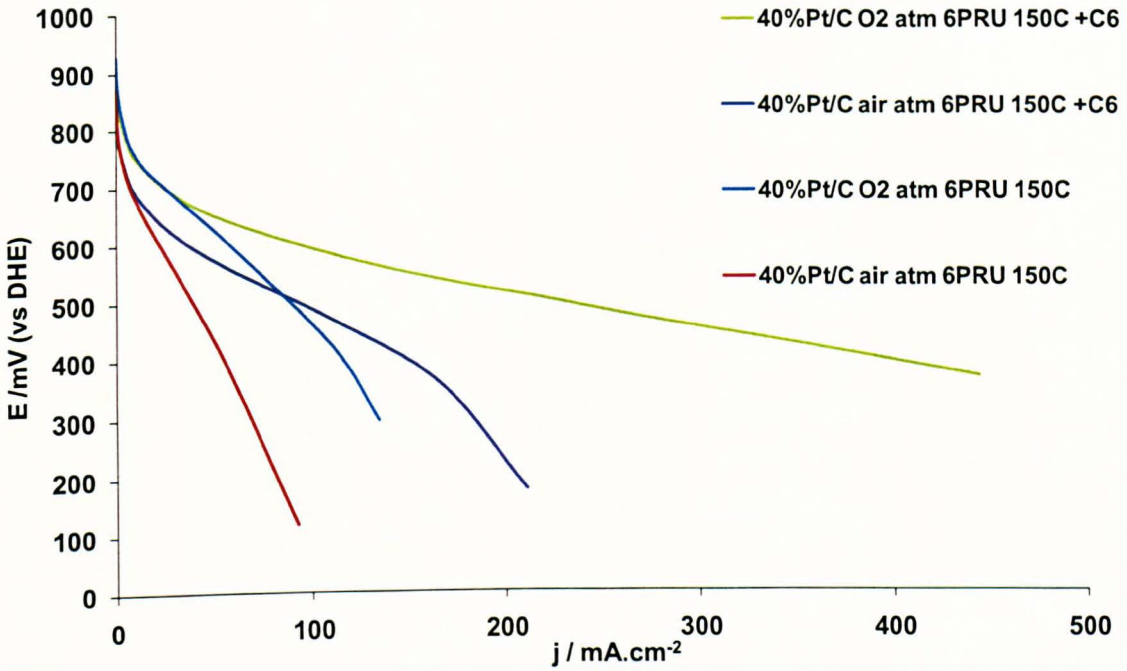

Figure 4-7. Effect of 0.5% wt surfactant addition on cathode performance vs. DHE (IR included) using 0.5 mg_{Pt} cm^{-2} 40% Pt/C and 0.45 mg cm^{-2} PBI with doping level of 6 PRU.

4.2.3.3 Doping level influence on conductivity

Figure 4-8 shows the effect of electrode doping level on the through plane conductivity of MEA's. Increasing the doping level above 2.5 PRU led to a slight increase in the overall conductivity. Electrodes without doping had very low conductivity, 0.005 S cm^{-1}, compared to ~0.025 S cm^{-1} with the doped electrodes, at 150 °C and RH 2 %.

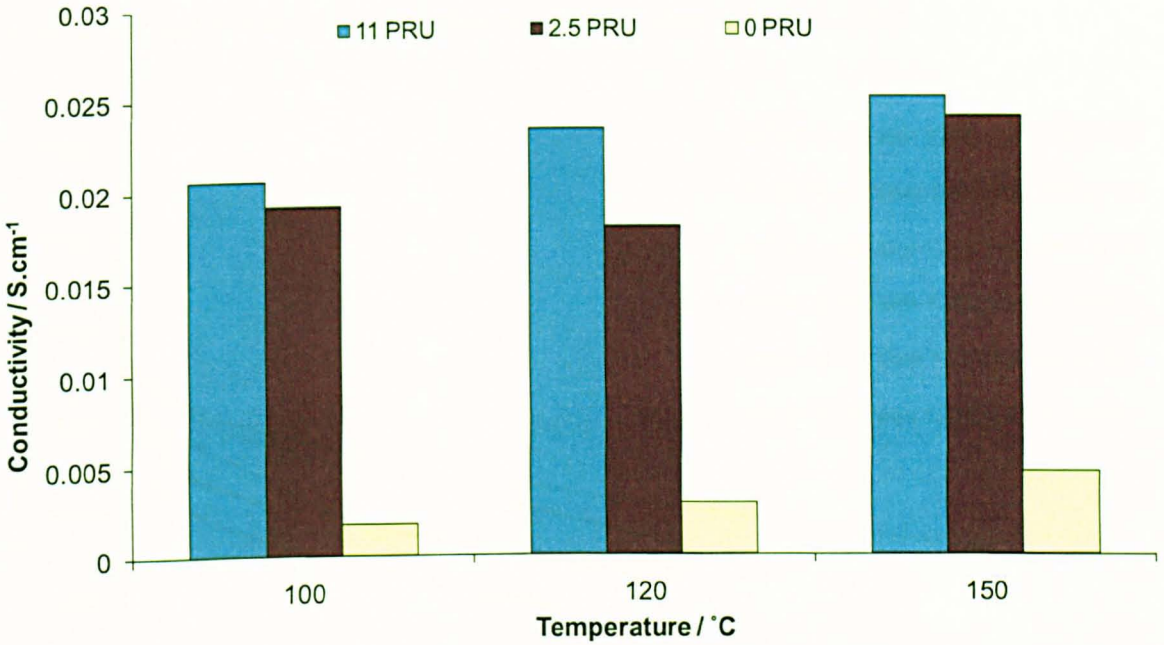

Figure 4-8. Doping level effect on MEA's through plane conductivity using 0.5 mg_{Pt} cm^{-2} 20% Pt/C at the anode and 0.5 mg_{Pt} cm^{-2} 30% Pt/C at the cathode, with PBI loading of 0.7 & 0.55 mg cm^{-2}, respectively, and RH 10% at 100 & 120 °C and 2% at 150 °C.

4.2.3.4 Effect of ionomer materials, Nafion or PBI/H_3PO_4

From tables 3-8 and 3-9 in Chapter 3, it was noted that hydrated Nafion has a much higher conductivity and oxygen permeability (at 80 °C, 34.2×10^{-12} mol cm cm^{-2} s^{-1} atm^{-1}) [3] than that of pristine PBI (at 80 °C, 0.05×10^{-12} mol cm cm^{-2} s^{-1} atm^{-1}) [4]. However Nafion water uptake falls dramatically at elevated temperatures (above 80 °C) and with low humidity. For dry Nafion the oxygen permeability (at 80 °C, $3.1\text{-}4.1\times10^{-12}$ mol cm cm^{-2} s^{-1} atm^{-1}) [3, 4] is similar to that of PTFE (at 80°C, 6.1×10^{-12} mol cm cm^{-2} s^{-1} atm^{-1}) [5] and PBI with doping level of 6 PRU (at 150°C, 2.18×10^{-12} mol cm cm^{-2} s^{-1} atm^{-1}) [6].

The Nafion conductivity in the temperature range of 100-140 °C, at low relative humidity (<2 %) is in the range of $10^{-6}\text{-}10^{-7}$ S cm^{-1} [7]. In accordance to theoretical models, the apparent Tafel slope should be ~240 mV dec^{-1} double the true value of 120 mV dec^{-1} in the situation of very large electrolyte resistivity inside the catalyst layer [8, 9]. This was also demonstrated

experimentally for Nafion in dry conditions and was explained by the logarithmic dependence of IR losses on current density and consequently product water generation [10].

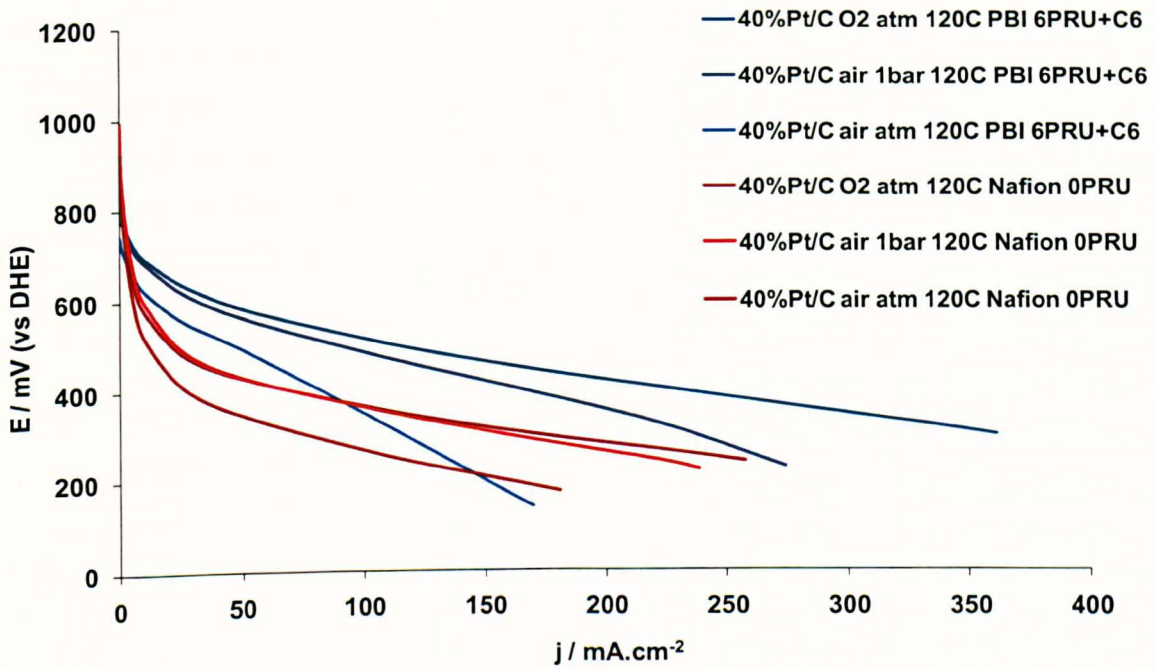

Figure 4-9. Effect of binder/electrolyte on cathode performance vs. DHE (IR included) with nafion 30% wt and PBI 0.45 mg cm^{-2} PBI (6 PRU with 0.5 %wt C6) at 120 °C.

In this study, cathodes with 40% Pt/C 0.5 mg_{Pt} cm^{-2} were prepared with 30% wt nafion as ionomer or 0.45 mg cm^{-2} PBI with 6 PRU. Both electrodes used the standard 20% Pt/C 0.2 mg_{Pt} cm^{-2} anode and were hot pressed on the standard 5.6 PRU PBI 50 μm thick membrane.

Figure 4-9 shows the effect of ionomer type (nafion or PBI/H_3PO_4) on cathode performance. It can be seen that PBI/6 PRU (with perfluronated surfactant C6) gave better performance than Nafion; with greater transfer coefficient; the polarisation curve exhibited lower overpotentials. However, Nafion has, even under dry conditions, a better oxygen permeability than PBI 6 PRU, which was reflected in the similar slopes of the polarisations curves with air, air 1 bar and oxygen at the studied high current densities. With PBI 6 PRU the slopes of the polarisation curves fell, beyond current density of 50 mA cm^{-2}, with lower oxygen partial pressure, even with surfactant addition, also indicating mass transport losses. The enhanced mass transport of nafion

was also seen in its higher limiting current. PBI based electrode had lower limiting current than that of nafion based electrode under air operation (Fig. 4-7 & 4-9).

The measured apparent Tafel slopes were 261 mV dec^{-1} for nafion in comparison to 96 mV dec^{-1} for PBI (6 PRU) at 120 °C. This corresponds to transfer coefficient values of 0.3 & 0.81, respectively. The observed high value of Tafel slope for dry Nafion was in close agreement to the estimated value of 240 mV dec^{-1} given in [8, 9].

On the other hand, the obtained exchange current densities (by extrapolating Tafel slope to 1.1 V) for nafion was three orders of magnitude higher than that of PBI. This can be explained by higher oxygen solubility and lower ions adsorption. Value of 1.28×10^{-6} A cm_{Pt}^{-2} was obtained for nafion with oxygen, which is in good agreement with the reported value of 1.41×10^{-6} A cm_{Pt}^{-2} (O_2, 80 °C) [11]. A value of 3.19×10^{-9} A cm_{Pt}^{-2} was obtained for PBI (6 PRU), which is in good agreement with the reported value of 2.9×10^{-9} A cm_{Pt}^{-2} for PBI (6PRU) at 150 °C with oxygen [6]. Catalyst specific area of 16 m^2 g^{-1} was considered in the calculations for the used 40% Pt/C (roughness factor of 80), this value was obtained from hydrogen under potential deposition (UPD) for 40% Pt/C electrode utilising PBI (6 PRU) (Chapter 3).

4.3 New PEMFC MEA development

While PBI is considered a good candidate for membrane materials due to its low permeability, addition of PBI to the catalyst layer as ionomer for proton conduction through the catalyst layer and binder, imposes mass transport limitation on anode and cathode performances depending on the thickness of the film formed on the catalyst sites. Furthermore, addition of phosphoric acid is necessarily to facilitate oxygen permeability and proton conduction, as the conductivity of non-doped PBI is very low (in the range of 10^{-4} S cm^{-1}[12]).

In this study, it was decided to eliminate PBI from the catalyst structure and rely on the conductivity of phosphoric acid as electrolyte, to give the following advantages:

- Conductivity of Phosphoric acid 0.568 S cm^{-1} at 150 °C is an order of magnitude higher than that of doped PBI 6 PRU ~0.047 S cm^{-1} at 150 °C and 5% RH [6].
- Oxygen diffusion in Phosphoric acid (98% wt) 30×10^{-6} cm^2 s^{-1} is an order of magnitude higher than that of doped PBI 6 PRU 3.2×10^{-6} cm^2 s^{-1} at 150 °C [6].

- Dissolved oxygen concentrations (solubility), 0.68×10^{-6} mole cm^{-3} for doped PBI 6 PRU compared to 0.5×10^{-6} mole cm^{-3} for 95%wt phosphoric acid at 150 °C and atmospheric pressure [6].

PTFE was introduced in the catalyst layer to provide the following functions:

1. Binder.
2. Amorphous phase to hold the phosphoric acid.
3. Enhance porosity.
4. Facilitate transport of oxygen to the catalyst layer by repelling the phosphoric acid from the catalyst structure (hydrophobic properties) and provide higher oxygen permeability (two order of magnitude), e.g. at 80 °C PTFE exhibits an oxygen permeability of 6.1 mol cm cm^{-2} s^{-1} atm^{-1} [5] compared to 0.05 mol cm cm^{-2} s^{-1} atm^{-1} for pristine PBI [4].

In phosphoric acid fuel cells, typically 30-50% wt of PTFE is used [13]. In this work the effect on MEA performance of the following factors were investigated: Catalyst loading, Pt:C ratio/thickness, acid content, PTFE content, membrane doping level, dehydration (175 °C), air flow rate, oxygen partial pressure, reformate operation, PFM addition, heat treatment, catalyst carbon support, Pt-alloys effect and flow field pattern.

4.3.1 Catalyst loading effect

The effect of catalyst loading (0.4, 0.52 & 0.61 mg_{Pt} cm^{-2}) on cell performance, at 120 °C using oxygen and air as oxidants, is shown in Figures 4-10 and 4-11 respectively. The anodes used 20% Pt/C with loading of 0.2 mg_{Pt} cm^{-2} and 2 mg cm^{-2} acid as electrolyte. The cathodes had no added-acid and conductivity purely relied on mobile acid from the membrane (doped at 5.6 PRU); 40%wt PTFE was added as binder for 0.4 & 0.52 and 20% wt for 0.61 mg_{Pt} cm^{-2} electrode. The data shows that increasing the catalyst loading, increased the cell potential as a result of higher electrochemical surface area (i.e. enhanced kinetic region). However, an increase in the catalyst loading would increase the catalyst layer thickness, resulting in potential losses due to mass transport and resistance. Moreover, there is an optimum catalyst thickness that provides maximum accessible surface area in terms of proton conductivity from mobile acid

from the membrane and oxygen diffusing from the gas channel. This optimum depends on oxygen concentration: at high oxygen concentration higher loading/thickness is favourable whilst the opposite case applies at lower oxygen concentration (air operation).

With oxygen (minimum mass transport limitations), increasing the loading increased the performance. However IR losses countered the kinetics enhancement at higher current densities when increasing the loading from 0.4 to 0.52 & 0.61 mg cm^{-2}. Whilst with air operation (apparent mass transport limitations) increasing the catalyst loading above 0.52 mg cm^{-2} (whilst maintaining Pt:C ratio) did not significantly improve overall performance as mass transport seems to dominate at low oxygen concentration.

Another effect of changing the cathode layer loading/thickness was on the OCP. With the cell running on oxygen, increasing the loading increased the OCP due to smaller influence of hydrogen cross-over on the mixed potential. Increasing the cathode thickness means more surface area is available for oxygen reduction when hydrogen is oxidized at catalyst sites closer to the membrane.

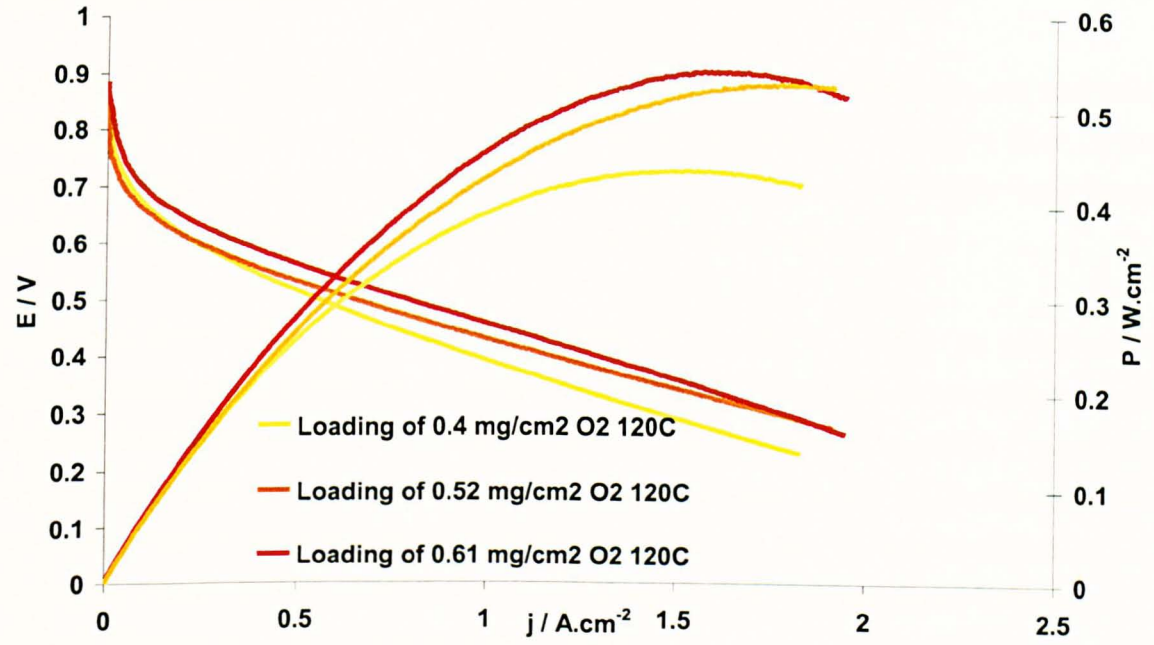

Figure 4-10. MEA performance using oxygen at 120 °C with 0.4, 0.52 & 0.61 mg_{Pt} cm^{-2} (50% wt) on the cathode and 0.2 mg_{Pt} cm^{-2} (20% wt) on the anode.

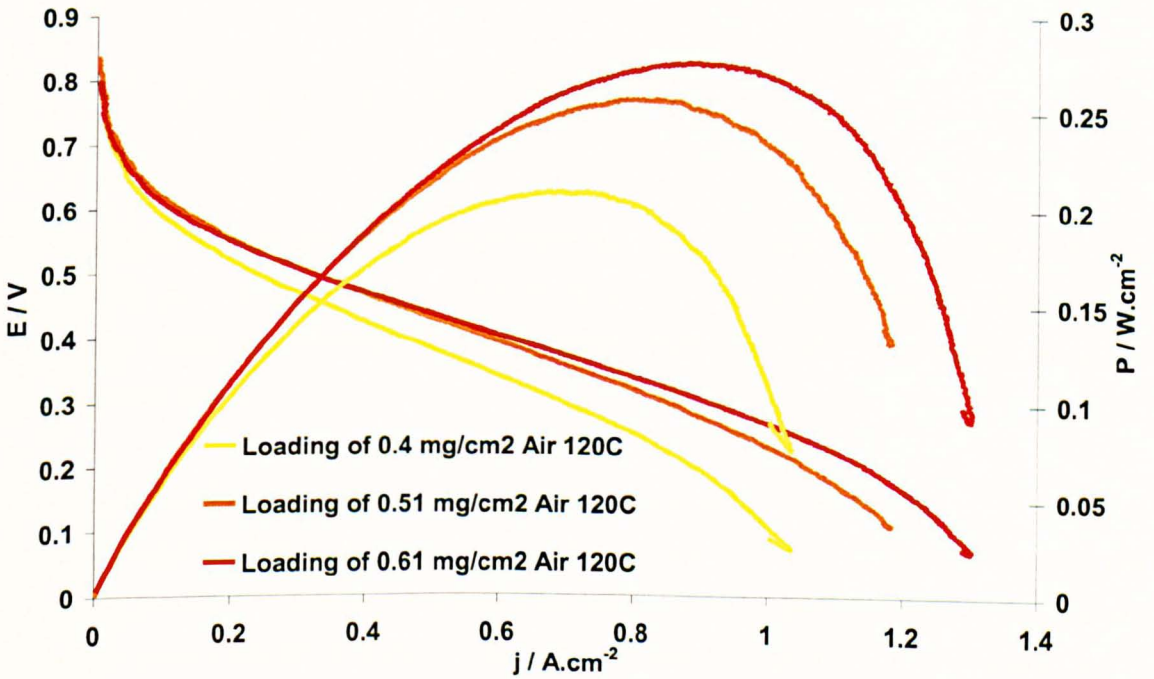

Figure 4-11. MEA performance using air at 120 °C with 0.4, 0.52 & 0.61 mg_{Pt} cm^{-2} (50% wt) on the cathode and 0.2 mg_{Pt} cm^{-2} (20% wt) on the anode.

4.3.2 PTFE loading effect

Typically, 30-50% wt PTFE is added to the cathode catalyst layer in phosphoric acid fuel cells. PTFE offers several advantages; particularly enhancing mass transport through a more porous structure. However, excess PTFE will lead to further IR drop, due to a thicker layer (more porous) and less ionic & electronic conductivity (PTFE is non-conductive).

Figure 4-12 shows cell performance at 120 °C using 20 and 40% wt PTFE in the cathode. The observed enhancement at high current densities using 40% PTFE resulted from superior oxygen transport through the catalyst layer. To investigate the mass transport effect further a mixture of oxygen/helium (20% vol oxygen) was passed through the cathode and the performance was compared to that of air. While air and hele-ox have similar oxygen concentrations (~20% vol) the oxygen binary diffusion with helium is much higher (order of magnitude) than that with nitrogen. This can be readily established from Slattery-Bird correlation for binary diffusion [14], D_{ij}. The effects of porosity and tortuosity can be accounted for using Bruggeman correlation leading to the effective binary diffusion $D_{ij}^{eff} = D_{ij} \times \varepsilon^{\tau}$:

$$D_{ij}^{eff} = \frac{a}{P}\left(\frac{T}{\sqrt{T_{c,i}T_{c,j}}}\right)^{b}\left(P_{c,i}P_{c,j}\right)^{1/3}\left(T_{c,i}T_{c,j}\right)^{5/12}\left(\frac{1}{M_i}+\frac{1}{M_j}\right)^{1/2}\varepsilon^{\tau} \qquad [1]$$

Where T_c and P_c are the gas critical temperature and pressure, respectively. M is the molecular weight of the gas, ε is the porosity and τ is the tortuosity. a and b are constants, a is 0.0002745 for di-atomic gases and 0.000364 for water vapour, while b is 1.832 for di-atomic gases and 2.334 for water vapour.

For example, the binary diffusion for oxygen-nitrogen (air) at 175 °C is 4.4×10^{-5} m^2 s^{-1} compared to that of oxygen-helium under the same conditions; 1.8×10^{-4} m^2 s^{-1}. The performance was enhanced noticeably by replacing nitrogen with helium, which highlights the fact that the cell suffers from mass transport limitation in the gaseous phase (through the porous structure) and is not only dominated by permeability through the thin film (acid/polymer); which obeys Henry's law (depends on oxygen partial pressure).

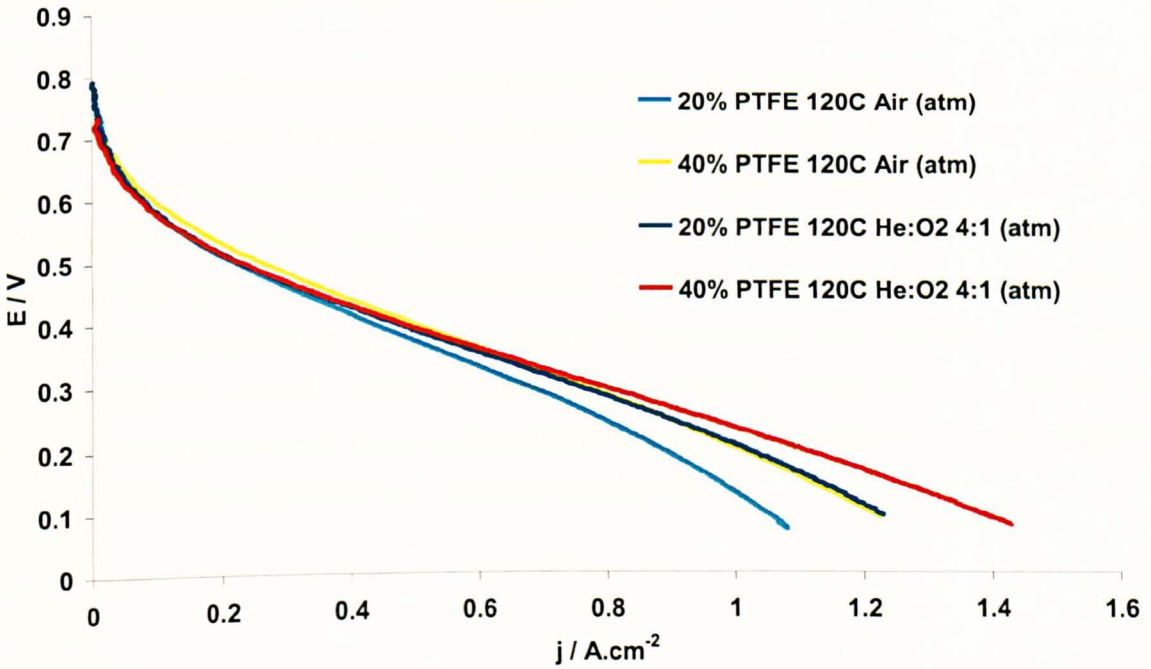

Figure 4-12. MEA performance using air/heleox at 120 °C with 0.4 mg_{Pt} cm^{-2} (50% wt) on the cathode and 0.2 mg_{Pt} cm^{-2} (20% wt) on the anode.

4.3.3 Acid loading effect and surfactant addition

The acid doping level or acid film thickness over the catalyst site plays an important role on overall performance. Increasing film thickness, δ, will lead to better protonic conductivity as the volume fraction of the acid in the catalyst layer will increase. On the other hand, increasing δ will lead to a smaller oxygen flux across the thin film, which will impose further mass transport limitations, as defined from Fick's law:

$$N_{O_2} = \frac{-D_{O_2}^{H_3PO_4}\varepsilon^{\tau}\left(C_{Pt} - C_{dissolve}\right)}{\delta} \qquad [2]$$

Where N_{O2} is the molar flux of oxygen, C_{Pt} is the oxygen concentration on the catalyst surface, and $C_{dissolve}$ is the oxygen concentration in the acid film at the studied temperature.

In this work two separate studies of acid content in the anode and cathode have been carried out.

4.3.3.1 Acid and surfactant effects on cathode performance

Figure 4-13 shows the acid doping level effect on the cathode performance at 120 °C, with air and oxygen operation. Increasing the doping level from 0 to 1 mg cm^{-2} lead to a shift in the polarisation curve towards lower over potentials due to improved kinetics. Note that with no added acid to the cathode it was still present due to acid mobility from the membrane. When operating with pure oxygen an enhancement in voltage was observed over the entire studied current density range. However with air operation the enhancement was observed at low current densities (kinetic control) whilst at high current densities (mass transport control) no improvement was observed, due to mass transport limitations countering the effect of enhanced kinetics arising from the thicker acid film over the catalyst sites.

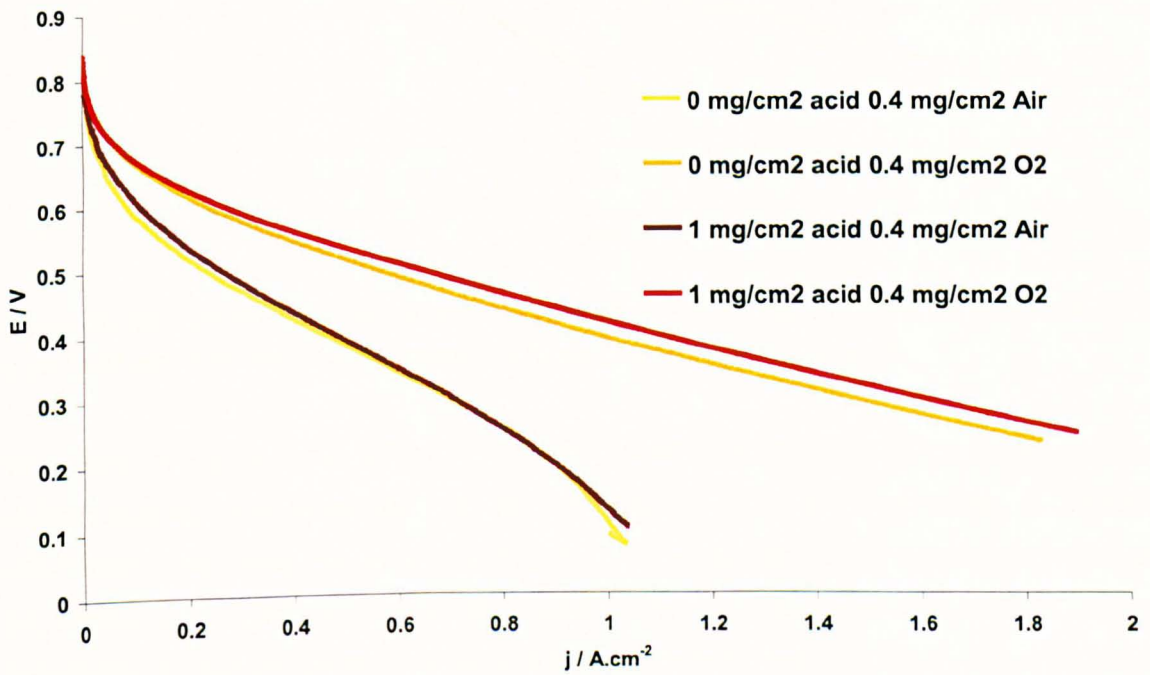

Figure 4-13. MEA performance using air and oxygen at 120 °C with 0.4 mg_{Pt} cm^{-2} (50% wt) doped with 0&1 mg cm^{-2} acid on the cathode and 0.2 mg_{Pt} cm^{-2} (20% wt) on the anode.

Figure 4-14 shows the effect of acid doping level and surfactant on cathode performance at 120 °C with air & oxygen operation. Increasing the doping level above 1 mg cm^{-2} to 2 mg cm^{-2} in the

cathode imposed mass transport limitation on the cathode performance with both air and oxygen operation. This was seen in lower performance at high current densities (mass transport control) where the acid film thickness increased beyond a crucial optimum point balancing between conductivity and mass transport.

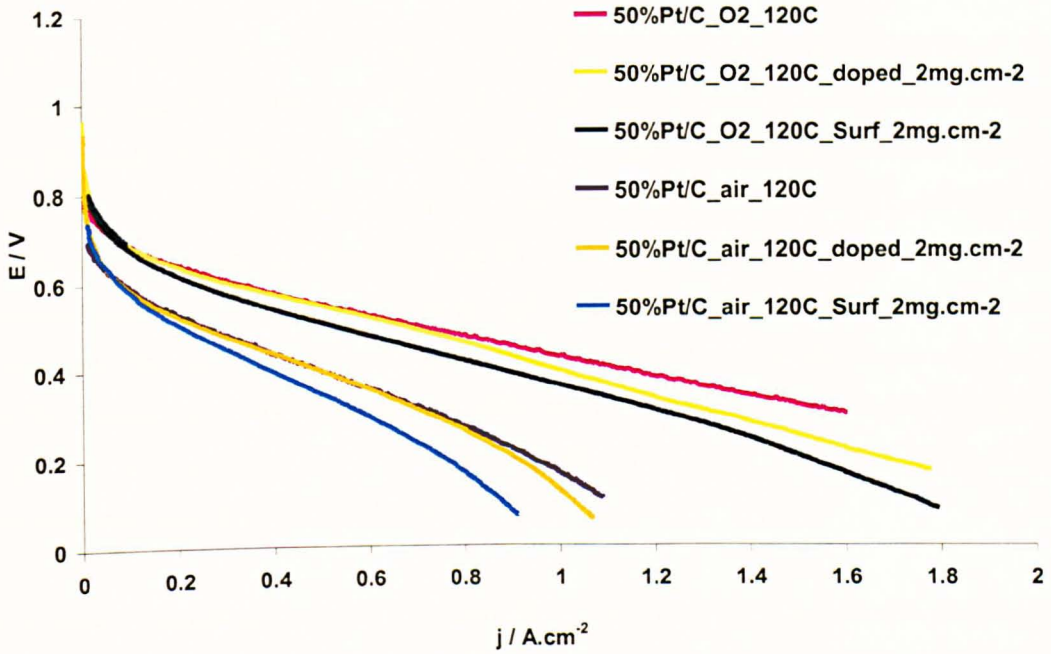

Figure 4-14. MEA performance using air and oxygen at 120 °C with 0.4 mg_{Pt} cm^{-2} (50% wt) doped with 0 & 2 mg cm^{-2} acid with 0.5% wt C6 on the cathode and 0.2 mg_{Pt} cm^{-2} (20% wt) on the anode.

Also shown in Fig. 4-14 the influence of Surfactant addition (0.5% wt of C6 Trideca-fluroro hexane-1-sulfonic acid potassium salt) gave as shown earlier, an improvement in cathode performance when using PBI as binder (Fig. 4-7), by enhancing oxygen permeability through PBI. Similarly, surfactant addition at low concentrations has been reported to enhance oxygen permeability through phosphoric acid by reducing its viscosity, enabling faster oxygen diffusion [15, 16]. Figure 4-14 on the contrary shows that for PBI-free electrode surfactant addition reduced cell performance due to mass transport limitations (lower performance at high current densities and lower limiting current) in comparison to that with a cathode contain 2 mg cm^{-2} acid without surfactant. The different results obtained with PBI and PTFE as binder are explained by the hydrophobic properties of PTFE and hydrophilic properties of PBI. The surfactant led to

reduction in the surface tension between the added acid and PTFE, increasing cathode flooding with acid [17] and reducing the overall cathode porosity and thereby imposing oxygen mass transfer limitation.

4.3.3.2 Acid effect on anode performance

Figure 4-15 shows the effect of acid and PBI content on the anode potential (vs. DHE) at 120 °C. It can be seen that the addition of PBI to the anode catalyst layer (0.2 mg_{Pt} cm^{-2} 20% Pt/C) reduced the anode performance (increased potentials) even at the same acid content. This can be attributed to slower hydrogen diffusion through and lower conductivity of PBI and the fact that free acid (liquid) has greater access to catalytic sites (electrochemical surface area) than the polymer/polymer acid mix due to reduced porosity. Increasing the acid content from 0.2 to 2 mg cm^{-2} increased the anode performance substantially; this can be attributed to a smaller IR drop across the catalyst layer and more catalyst sites becoming accessible. However, increasing the acid loading, beyond 2 mg cm^{-2}, led to a small enhancement in anode performance at high current densities (resistance improvement).

With a system operating on pure hydrogen the mass transport effect in the anode can be neglected, thus increasing doping level in the anode up to 4 mg cm^{-2} led to the enhancement in the performance without apparent mass transport limitation.

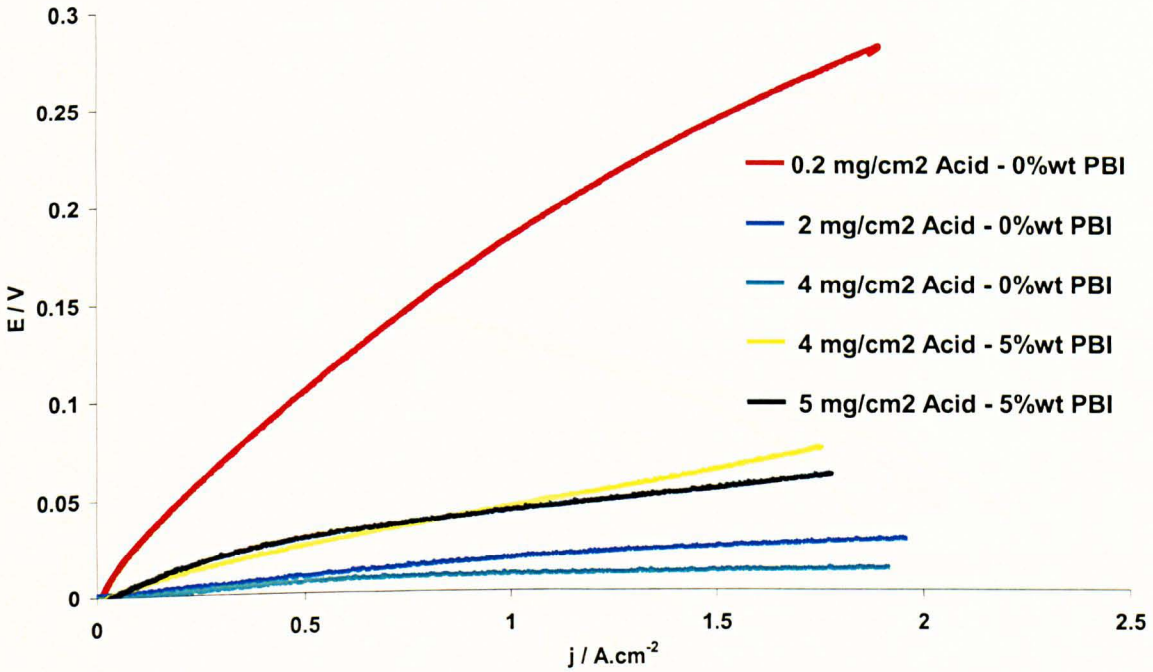

Figure 4-15. Anode performance vs. DHE using hydrogen at 120 °C with 0.2 mg_{Pt} cm^{-2} (20% wt) on the anode with different acid/PBI content.

4.3.4 Oxidant flow rate/concentration effect

Figure 4-16 shows the cell performance with different air flow rates at atmospheric pressure and 120 °C. An increase in performance, at higher current densities, was observed when flow rate was increased, resulting from enhanced mass transport and therefore limiting current density. A maximum increase was obtained at 0.45 lpm (STP) (air stoichiometry of $\lambda = 2$) and increasing λ any further did not lead to any noticeable improvement.

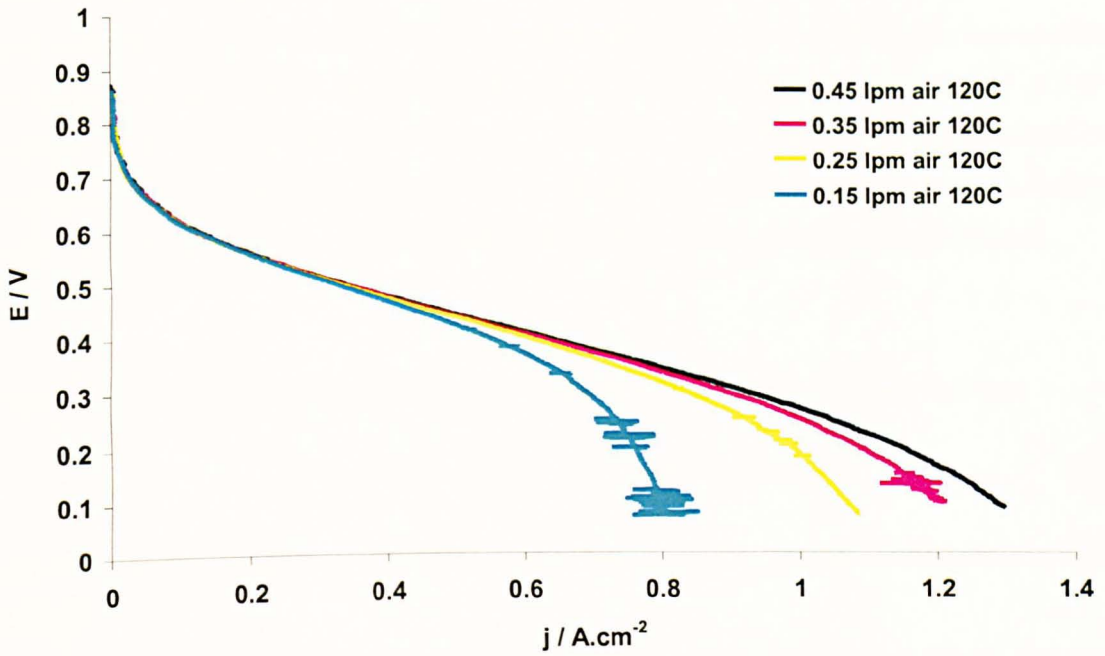

Figure 4-16. Cell performance using air at 120 °C with 0.2 mg_{Pt} cm^{-2} (20% wt) on the anode and 0.61 mg_{Pt} cm^{-2} (50% wt) with 40% wt PTFE on the cathode at different air flow rates.

It is well established that an increase in operating pressure enhances the performance of PAFCs due to the low oxygen permeability through phosphoric acid [18, 19]. The effect of oxygen partial pressure was examined using; atmospheric air, air 1.0 bar, atmospheric oxygen and oxygen at 1 bar. Figure 4-17 shows that increasing the oxygen partial pressures, at 150 °C, enhanced the cell performance in both the kinetic region (low current densities) and mass transport region (high current densities).

Improvements in kinetics arise from an increase in the exchange current density due to an increase in oxygen partial pressure (lower diffusion polarisation) and therefore surface concentration:

$$j_0 = i_0^{ref} a_c L_c \left(\frac{C_{Pt}}{C_{Pt}^{ref}} \right)^{\gamma} \exp\left[-\frac{E_C}{RT} \left(1 - \frac{T}{T_{ref}} \right) \right] \qquad [3]$$

Where j_0 (A $cm^{-2}_{geometric}$) is the reference current density, i_0^{ref} (A cm^{-2}_{Pt}) is the exchange current density at reference temperature T_{ref} and concentration C^{ref}, C_{Pt} is the oxygen concentration on the catalyst surface which directly proportional to oxygen partial pressure. a_c (m^2 g^{-1}) is the catalyst specific (electrochemical surface area) L_c is the catalyst loading, which correspond to the weight of platinum per unit area (g cm^{-2}). γ is the pressure coefficient or the reaction order with respect to oxygen, E_c is the activation energy of oxygen reduction in hot phosphoric acid.

This reduces the kinetic overpotential losses as defined by the Butler-Volmer equation:

$$j_c = j_{0,c}\left(\exp\left(\frac{-\alpha_{Rd,c}F}{RT}(\eta_c)\right) - \exp\left(\frac{\alpha_{Ox,c}F}{RT}(\eta_c)\right)\right) \qquad [4]$$

Where η_c is the cathode overpotential losses and α_c is the transfer coefficient for cathode reaction.

The kinetic improvement is also accompanied by a thermodynamic improvement (increase in cell reversible potential), using Nernst equation:

$$O.C.P_{T,P} = -\left(\frac{\Delta H_T^0}{nF} - \frac{T\,\Delta S_T^0}{nF}\right) + \frac{RT}{nF}\ln\left[\frac{\left(C_{H_2}/C_{H_2}^0\right)\left(C_{O_2}/C_{O_2}^0\right)^{0.5}}{\left(a_{H_2O}/a_{H_2O}^0\right)}\right] \qquad [5]$$

Where ΔH^0 and ΔS^0 are the enthalpy and entropy of the reaction, respectively. C^0_{H2}, C^0_{O2}& a^0_{H2O} are the reference hydrogen, oxygen concentration and water activity, respectively.C_{O2} is the dissolved oxygen concentration on the catalyst surface (referred to earlier as C_{Pt}).

In the data of Fig. 4-17 improvements in mass transport can be clearly distinguished at higher current densities, whilst operation with oxygen did not show apparent mass transport limitation. Increasing the air pressure from 0 to 1 bar, increased the limiting current from 1.4 to 1.8 A cm^{-2} at 150 °C. In addition, a pressure increase can also enhance the overall cell ionic conductivity, where it shifts the equilibrium between phosphoric acid and water vapour, leading to a lower acid concentration and therefore higher conductivity. It has been reported that at 169 °C an increase in pressure from 1 to 4.4 atmosphere led to shift in phosphoric acid concentration from 100% wt to 97% wt [13].

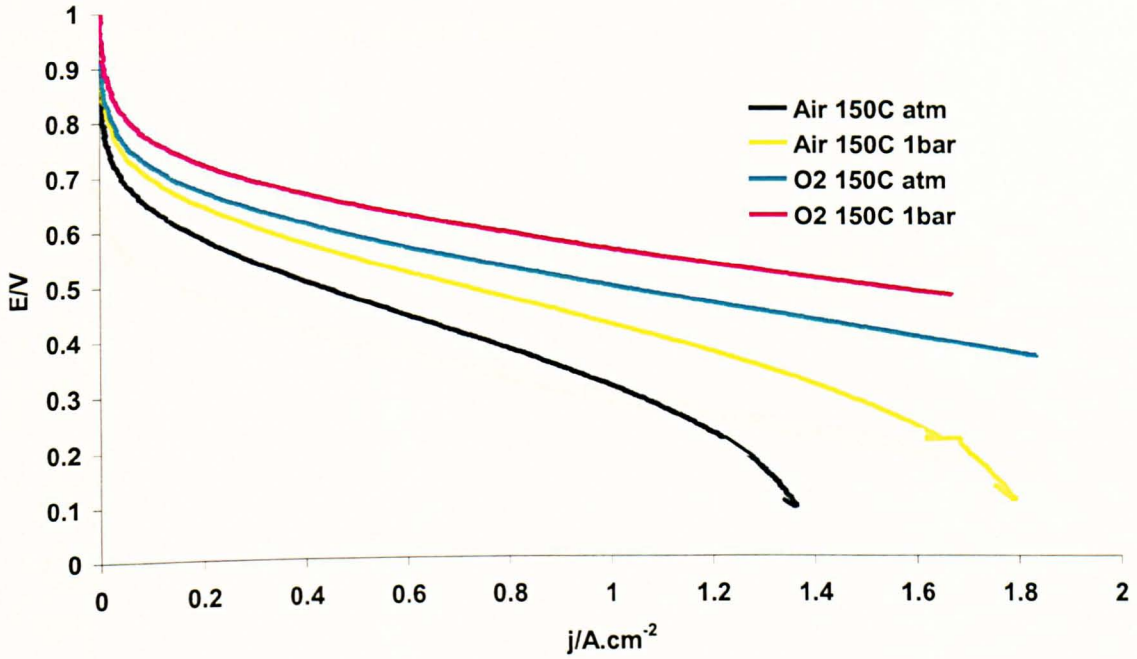

Figure 4-17. Cell performance using different oxygen partial pressure at 150 °C with 0.2 mg_{Pt} cm^{-2} (20% wt) on the anode and 0.61 mg_{Pt} cm^{-2} (50% wt) with 40% wt PTFE on the cathode.

4.3.5 Performance under reformate feed and CO influence

Carbon monoxide and carbon dioxide was introduced in the anode gas stream to study the performance with a simulated reformate feed. Carbon dioxide would impose some mass transport limitation at high concentration and current densities (ignoring any effect of reduction of carbon dioxide to carbon monoxide by hydrogen at the studied temperature [20]). Carbon monoxide would slow the kinetics of hydrogen oxidation because of its adsorption (poisoning) on platinum active catalytic sites. As the temperature rises Pt tolerance to CO poisoning increases.

Figure 4-18 shows the cell performance with 20% & 33% vol CO_2 and 2.5% vol CO at 150 °C. The anode exhibited a high tolerance to impurities in the gas feed even at temperature as low as 150 °C. The voltage losses at a current density of 1.5 A cm^{-2} were only 8, 12 & 22 mV when switching from pure hydrogen to 20%, 33% vol CO_2 and 2.5% vol CO, respectively. This

demonstrated a major advantage for HT-PEMFC where cells can operate with high CO tolerance offering simpler and lower cost reformer design.

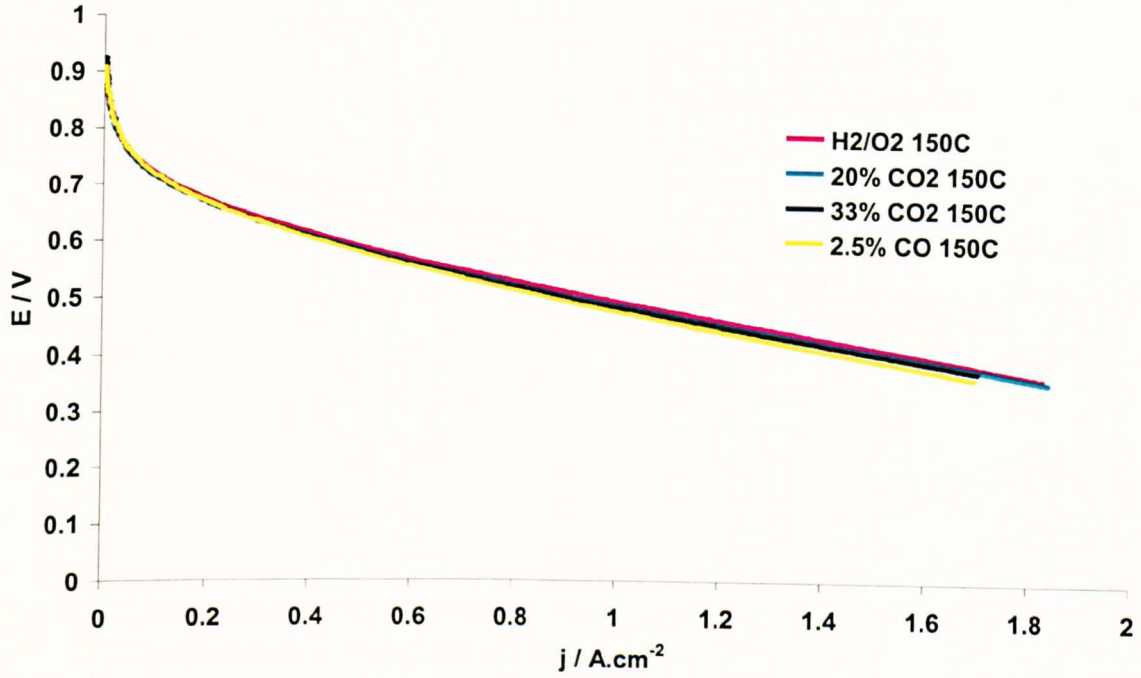

Figure 4-18. Cell performance under reformate using oxygen at 150 °C with 0.2 mg_{Pt} cm^{-2} (20% wt) on the anode and 0.61 mg_{Pt} cm^{-2} (50% wt) on the cathode.

4.3.6 Dehydration and relative humidity effects

Figure 4-19 shows the effect of dehydration on the I-V curves for HT-PEMFC at temperature of 175°C and various RH and time intervals.

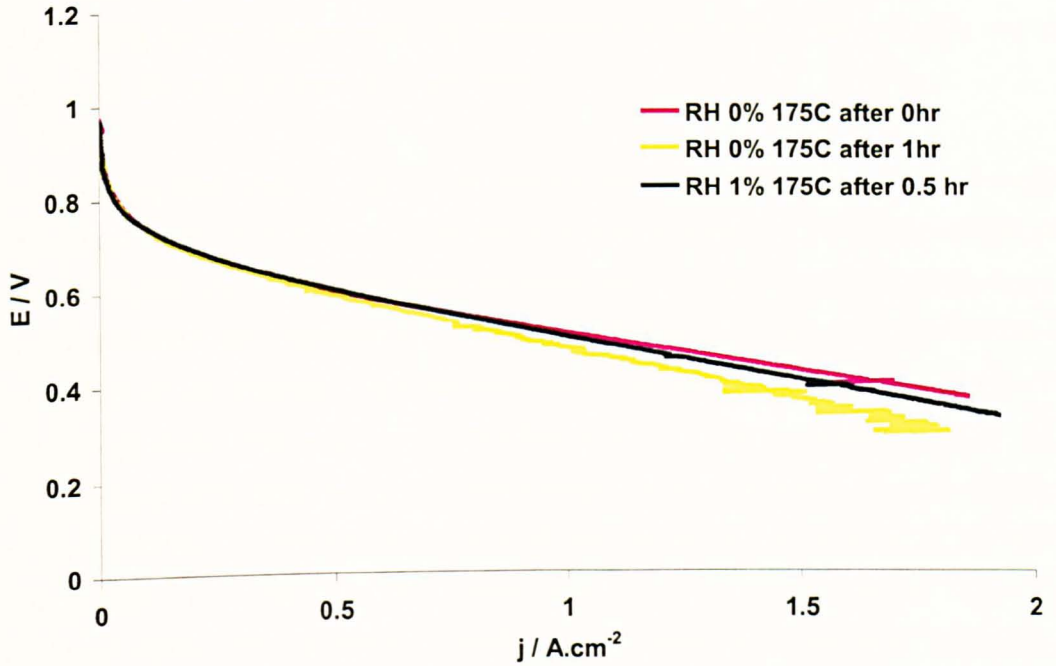

Figure 4-19. Cell performance using oxygen at 175 °C with 0.2 mg_{Pt} cm^{-2} (20% wt) on the anode and 0.61 mg_{Pt} cm^{-2} (50% wt) on the cathode at different RH and time intervals.

A noticeable decrease in the slope of the I -V curve (mainly attributed to membrane resistance) for a cell operating at 175 °C (or above) was observed with no external humidification. The polarization curves were obtained immediately after the system has reached 175 °C. Later, the data was collected at intervals with a further reduction in performance observed, until a steady sate condition was reached after 1 hour. This effect was likely to be a result of the water loss produced by acid dimerisation. At elevated temperatures, phosphoric acid starts to dehydrate, which can occur in many stages, the first two of which are illustrated below:

First stage: $2H_3PO_4 \leftrightarrow H_4P_2O_7 + H_2O \uparrow$

Second stage: $H_4P_2O_7 + H_3PO_4 \leftrightarrow H_5P_3O_{10} + H_2O \uparrow$

The equilibrium concentrations of these reversible reactions are temperature and relative humidity dependent. The dimerised products are less proton conductive than phosphoric acid [21] which explains the above observation. To illustrate the above suggestion, 1% RH

humidification was introduced into the hydrogen stream and the system was held for 30 mins before taking the first measurement. An enhancement in the slope of the I- V plots was observed, presumably due to an increase in conductivity.

Frequency response analysis was used to measure the cell conductivity at elevated temperatures. A frequency range of 30 KHz - 30 mHz was used with amplitude of 15 mA around the OCP. The resistance value can be obtained when the phase shift is equal to zero (the impedance is pure resistance without any capacitance or conductance behaviour). Figure 4-20 shows the effect of temperature on the frequency response and thus the overall system resistance at RH <1 %. The total through plane resistance was 0.075, 0.068 & 0.0787 ohm for temperatures of 125, 150 & 175 °C, respectively. This results in overall average conductivities of 1.07, 1.18 & 1.02 × 10^{-2} S cm^{-1}, considering a membrane thickness of 60 μm (anode catalyst layer of 20 μm and cathode catalyst layer of 13 μm). The resistivities were two to three times higher than that of the membrane alone. This difference is attributed to protonic and electronic resistance through catalyst layers, to contact resistance and electrical resistance in gas diffusion layer and micro porous layers.

The above observations confirm that the loss of conductivity, when the temperature was increased to 175 °C without humidification, can be explained by dehydration of the phosphoric acid (boiling point of H_3PO_4 85% wt is ca.154 °C).

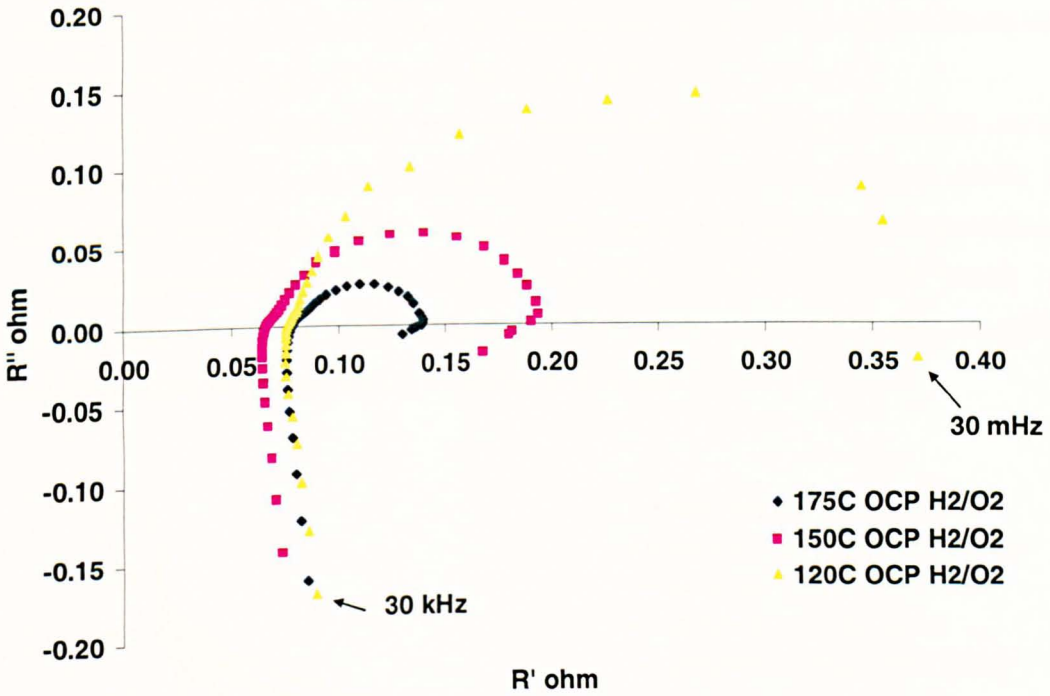

Figure 4-20. Frequency response analysis Nyquist plots at range of 30 KHz - 30 mHz for MEA operating at temperatures of 120, 150 & 175 °C and RH <1 % around OCP.

4.3.7 Membrane doping level effect on cell performance

Pristine PBI has a negligible conductivity and requires doping with phosphoric acid to facilitate proton conduction. The higher the doping level, the higher the conductivity. However, the mechanical properties and tensile stress of PBI deteriorate dramatically on increasing the doping level. A balance between conductivity and mechanical properties is achieved at doping level of c.a. 5.6 PRU [22]. Apart from its effect on the overall conductivity, the membrane doping level will affect the cathode performance. As seen earlier, whilst the cathode did not contain added acid, it relied on acid mobility from the membrane to provide proton conduction and access to catalytic sites. The anode utilized 0.2 mg_{Pt} cm^{-2} of 20% Pt/C with an added acid content of 2 mg cm^{-2}.

Each PBI unit can hold 2 acid molecules by hydrogen bonding to the two imidazole rings. After the maximum degree of protonation of the nitrogen atoms is reached (at 2 PRU), any further acid

will be free mobile acid, held in the membrane matrix. Infra Red spectra has shown the presence of free H_3PO_4 at doping level above 2 PRU (2.1 PRU) [23].

Figure 4-21 shows a comparison between standard doping membrane (5.6 PRU) and low doping membrane (4 PRU) on cell performance at 150 °C. Reducing the membrane doping level, from 5.6 to 4 PRU, had severe impact on polarisation curves; significantly reducing cell potentials due to lower membrane and catalyst layer conductivities. Additionally, the kinetic region was severely affected (at low current densities); which can be explained by less accessible catalytic sites (ESA) due to less electrolyte available in the cathode catalyst layer.

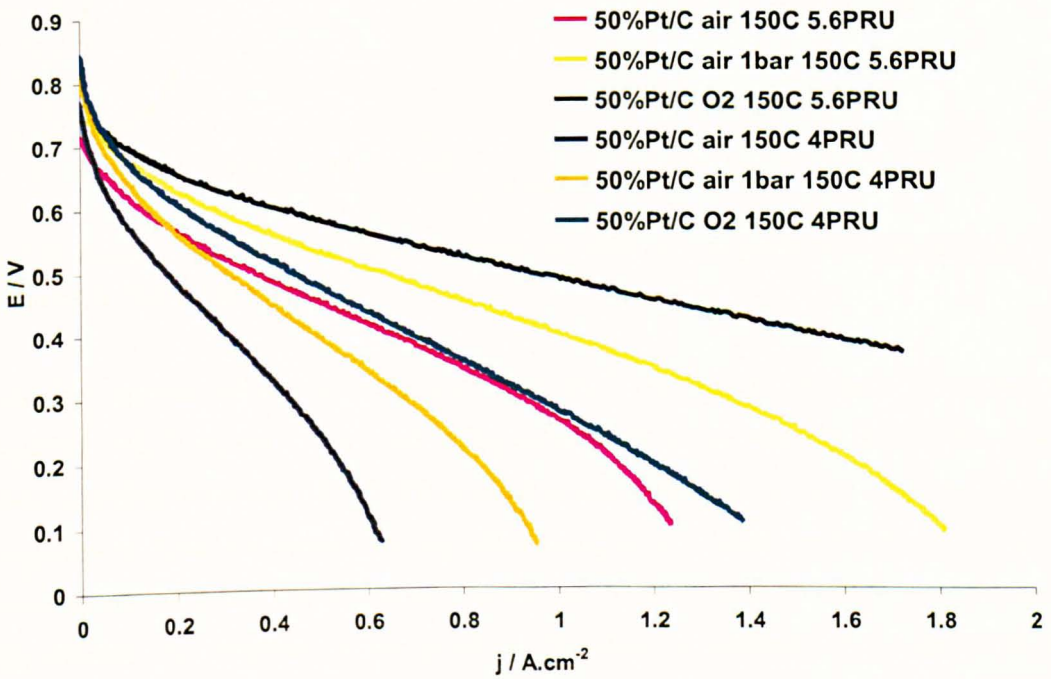

Figure 4-21. Comparison between standard doping membrane (5.6 PRU) and low doping membrane (4 PRU) influence on cell performance at 150 °C using 50% Pt/C at the cathode with loading of 0.4 mg_{Pt} cm^{-2}.

High doping level membranes (20 PRU) were also investigated. The high acid content in the membrane means that there was a large quantity (18 PRU) of free acid available to flood the catalyst layer. To accommodate this free acid a change in the anode and cathode structures would be needed. Figure 4-22, shows the impact of catalyst layer structure (anode and cathode) on cell performance using a highly doped membrane (20 PRU) at 120 °C.

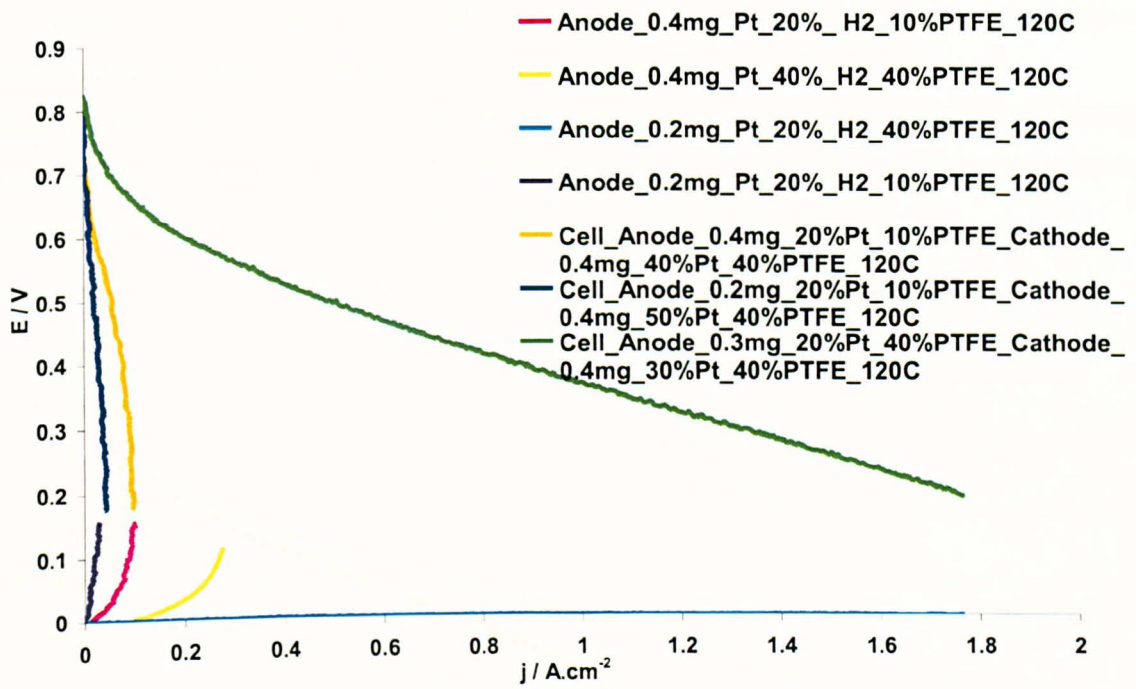

Figure 4-22. Catalyst layer structure impact on anode (vs. DHE) & cell performances using highly doped membrane of 20 PRU at 120°C.

The standard anodes utilised 0.2 mg_{Pt} cm^{-2} 20% Pt/C, and did not contain PTFE and were impregnated with 2 mg cm^{-2} acid when using membranes doped with 5.6 PRU. This structure had to be modified to include 10 %PTFE in order to accommodate the large quantities of mobile acid expected to flood the anode structure when using highly doped membrane. However, this measure was not sufficient, where the cell performance was limited by anode mass transport: a limiting current was observed in the anode performance at extremely low current densities (Figure 4-22). Increasing the anode catalyst layer thickness by increasing the Pt loading from 0.2 to 0.4 mg_{Pt} cm^{-2} 20% Pt/C and maintaining the PTFE content of 10 % led to an increase in the observed limiting current value at the anode, although the overall cell performance was still dictated by poor mass transport through the flooded anode. Increasing the anode catalyst layer hydrophobicity (using 40% wt PTFE) and reducing the catalyst thickness by maintaining the Pt loading of 0.4 mg_{Pt} cm^{-2} and changing Pt:C ratio to 40% Pt/C led to a remarkable increase in anode limiting current density to 300 mA cm^{-2}. Finally, using anode platinum loading of 0.3 mg_{Pt}

cm^{-2} (20% Pt/C) with high PTFE content (40% wt) resulted in no apparent mass transport limitations in the anode performance, at the studied current densities up to 1.8 A cm^{-2}.
Similarly, the PTFE content in the cathode was kept fixed (40% wt), and the platinum loading was fixed at 0.4 mg_{Pt} cm^{-2}, however, the cathode catalyst layer thickness was increased by utilising a lower platinum to carbon ratio (30% Pt/C instead of 50% Pt/C).

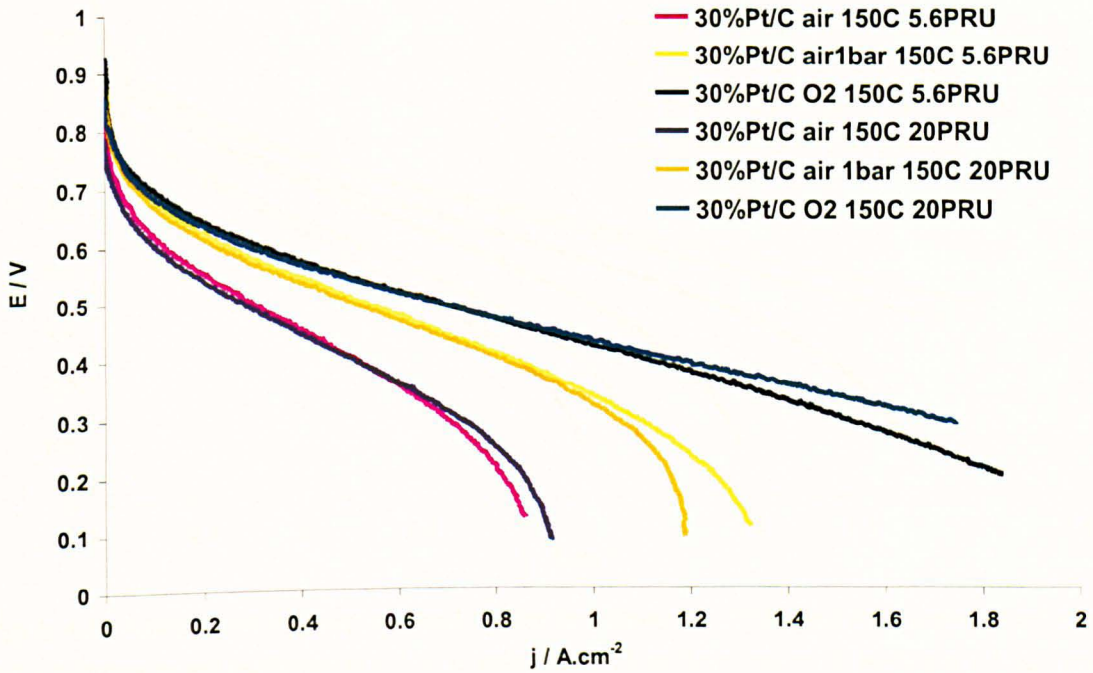

Figure 4-23. Comparison between standard doping membrane (5.6 PRU) and high doping membrane (20 PRU) influence on cell performance at 150 °C using 30 % Pt/C at the cathode with loading of 0.4 mg_{Pt} cm^{-2}.

Figures 4-23 and 4-24 compare the cell performance with MEAs utilising the standard doped membrane of 5.6 PRU and higher doped membrane of 20 PRU, at temperatures of 150 & 175 °C, respectively. Utilising a highly doped membrane gave no major advantage over the standard doped membrane at 150 °C, and a small improvement in the polarisation curves (resistance effects) at 175 °C. However, considerable enhancement in the limiting current was observed with air and air at 1 bar which is attributed to a superior "three phase zone structure" arising from more available electrolyte for the thicker electrode layer. Whilst a large difference in the doping level was expected to have a major impact on the membrane resistance, the use of thick catalyst layers for both anode and cathode, to restrict access of free acid from the membrane flooding the

active layer, resulted in large IR losses through the catalyst layer countering the enhancement in membrane resistance.

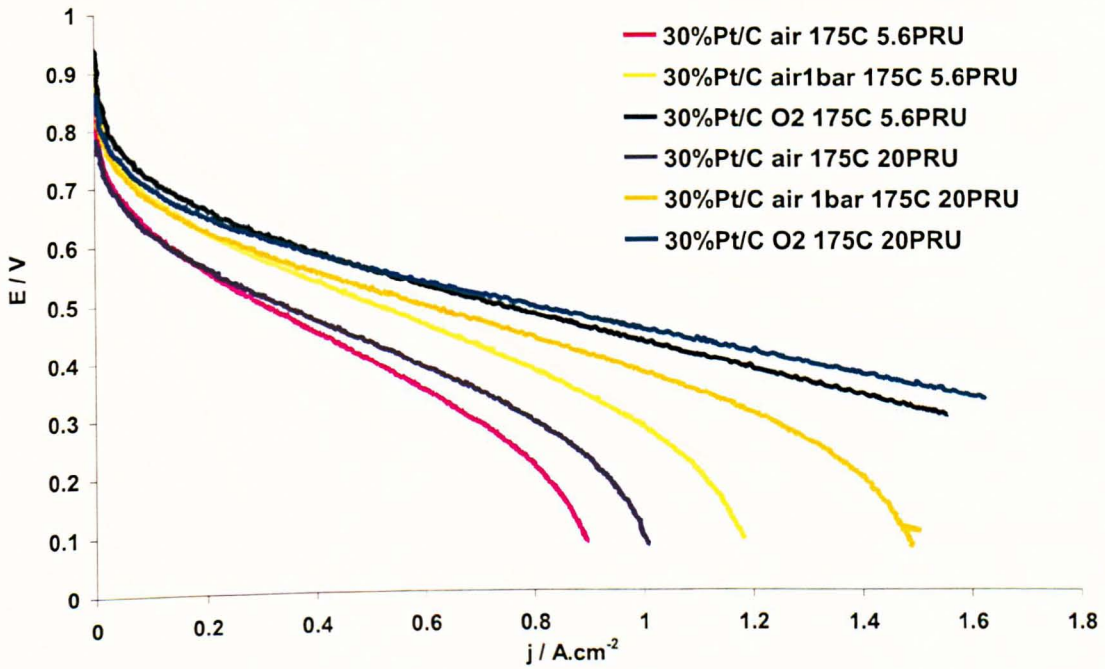

Figure 4-24. Comparison between standard doping membrane (5.6 PRU) and high doping membrane (20 PRU) influence on cell performance at 175 °C using 30% Pt/C at the cathode with loading of 0.4 mg_{Pt} cm^{-2}.

4.3.8 Heat treatment effect on electrode performance

As shown earlier, hydrophobicity of the catalyst layer (PTFE content), membrane acid content and cathode catalyst content play major roles in determining cell performance. All the mentioned factors dictate acid (electrolyte) volume fraction in the catalyst layer and therefore the three phase boundaries.

Heat treatment of PTFE, at temperature of 350 °C for 30 mins under an inert atmosphere (sintering) leads to a more hydrophobic structure (for the same PTFE content) where Teflon fibres, usually less than 10 nm thick, are formed spreading over all carbon particles or clusters [24]. This process is normally applied to phosphoric acid fuel cell electrodes [25], where a high degree of hydrophobicity is required to stop the electrode flooding from highly mobile acid (no

hydrogen bonds between the matrix and the phosphoric acid within) from the fully saturated silicon carbide matrix (used as solid electrolyte).

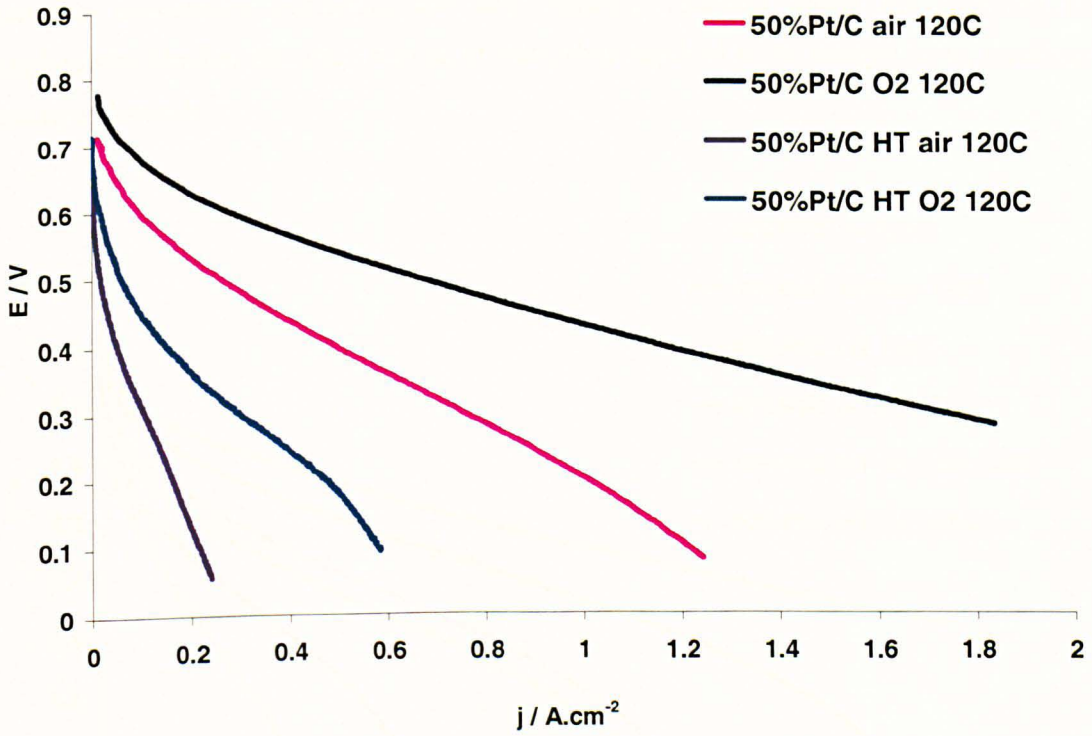

Figure 4-25. Compares cell performance at 120 °C of MEAs using standard cathode electrode and heat treated cathode electrode utilising 0.4 mg_{Pt} cm^{-2} 50% Pt/C with 40% wt PTFE.

Figures 4-25 & 4-26 show a comparison in cell performance, at 120 °C, between the standard cathode and heat treated cathode utilising 0.4 mg_{Pt} cm^{-2} with 40% wt PTFE fabricated using 50% Pt/C and 40% Pt/C, respectively. Heat treatment produced a dramatic reduction in cathode performance, where the heat treated cathode exhibited a very high degree of hydrophobicity repelling any mobile acid coming from the membrane. Therefore, the cathode had a very low acid (electrolyte) content, resulting in a very small active three phase zone close to membrane boundary, whilst the remainder of the cathode layer remained relatively inactive. This is clearly seen in the large fall in potential at low current densities, due to kinetic losses and low active electrochemical surface area.

Whilst PTFE heat treatment (sintering) has proved useful in the presence of high quantities of mobile acid i.e. phosphoric acid fuel cells and perhaps highly doped PBI, it had a negative impact for membranes exhibiting low acid mobility (doping) where the inherited high hydrophobicity blocked the small amount of electrolyte required in the catalyst layer; resulting in an inactive electrode.

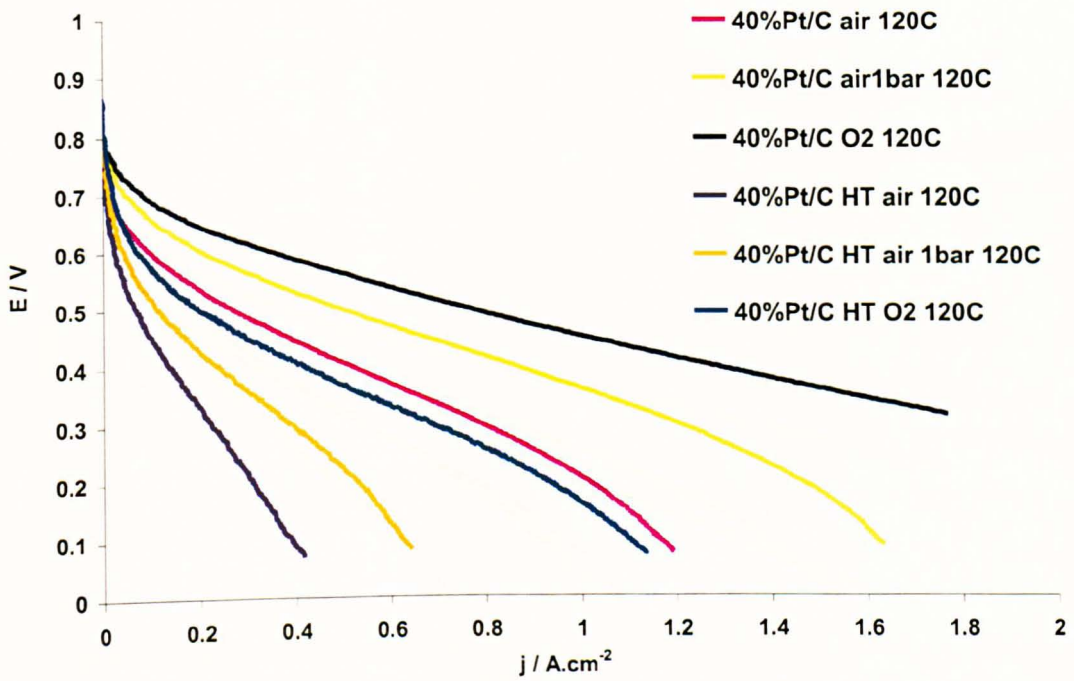

Figure 4-26. Compares cell performance at 120 °C of MEAs using standard cathode electrode and heat treated cathode electrode utilising 0.4 mg_{Pt} cm^{-2} 40% Pt/C with 40% wt PTFE.

4.3.9 Effect of catalyst's carbon support on cell's performance

The effect of catalyst carbon support on cell performance, using two materials; Vulcan XC-72R (ETEK, U.S.A) and AC01 advanced carbon (Johnson Matthey, U.K) was examined. The Platinum to carbon ratio was constant to 40% Pt/C, whilst both catalysts exhibited similar electrochemical surface area and average particles sizes (as determined from X-ray Diffraction); 2.8 nm (ETEK) and 2.3 nm (JM).

The two carbons supports had different morphologies and hydrophobic properties, and therefore would produce different catalyst layer structures, in terms of three phase boundaries and their interaction with the acid electrolyte (wettability). The density of the carbon support determines the thickness of the catalyst layer and thus electrode performance accordingly. Whilst Vulcan XC-72R has a density of 1.7 - 1.9 g cm^{-3} at 20 °C [26], no information was available on the density of the advanced carbon support AC01 from JM.

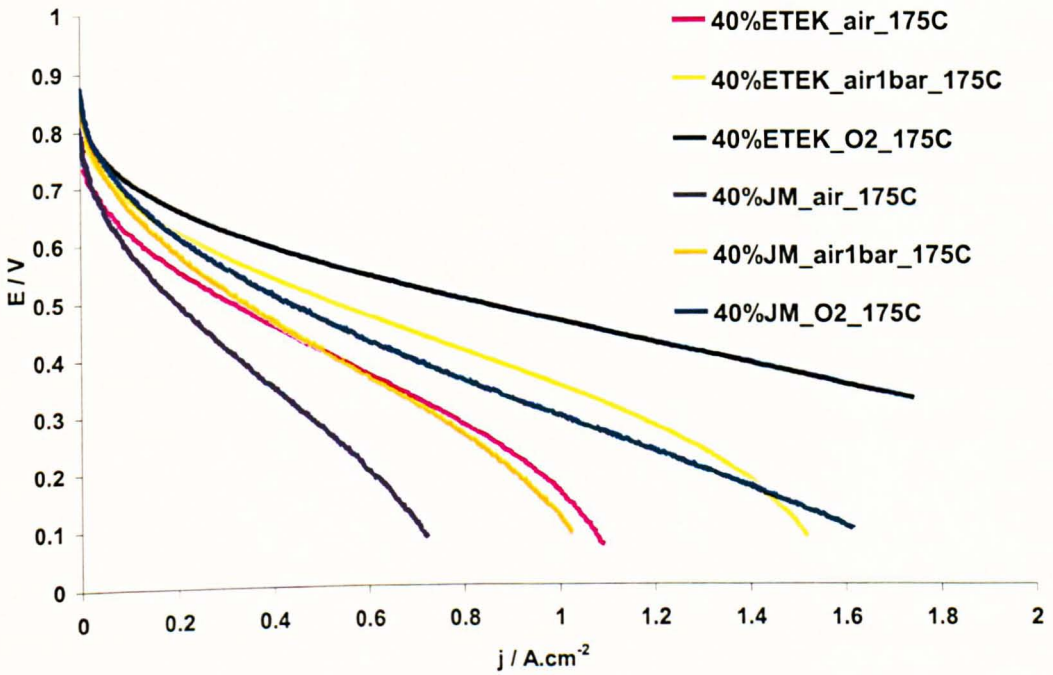

Figure 4-27. Shows the effect of catalyst carbon support on cell performance at 175 °C, electrodes utilised 0.4 mg_{Pt} cm^{-2} 40% Pt/C with 40% wt PTFE with Vulcan XC-72R (ETEK) & AC01 Advanced carbon support (Johnson Matthey).

Figure 4-27 shows the effect of catalyst carbon support on cell performance at 175 °C, with cathodes utilising 0.4 mg_{Pt} cm^{-2} 40% Pt/C with 40% wt PTFE. At low current densities, Vulcan gave superior performance to the AC01 support, suggesting better oxygen reduction kinetics due to higher available electrochemical surface area. Similarly, the slope of the I-V curves of the cathodes utilising Vulcan as catalyst support exhibited less IR losses, compared to that of AC01. This data suggests that AC01 has a lower interaction with the acid electrolyte (more hydrophobic

than Vulcan) leading to a lower acid content in the catalyst layer and therefore lower conductivity and accessible electrochemical surface area. Another explanation is that AC01 had a lower density than that of Vulcan leading to thicker catalyst layer thickness (higher IR losses) and, since the acid electrolyte can diffuse from the membrane to a limited catalyst layer thickness, a large portion of the catalyst surface would become inaccessible, resulting in slower kinetics. It is also reasonable to consider the combination of both factors.

4.3.10 Pt:C weight ratio & catalyst layer thickness

With a fixed acid content in the membrane, there is an optimum thickness for the cathode catalyst layer (with no added acid) that provides the best balance between mobile acid electrolyte, from the membrane, and supply by diffusion of gaseous oxygen from the flow channel, in other words to maximize the available three phase boundaries.
Figure 4-28 shows the cell performance using 40, 50 & 60% Pt/C (at fixed Pt loading of 0.4 mg_{Pt} cm^{-2}) with oxygen at 120 °C. At low temperatures and pure oxygen operation (minimum mass transport limitations) 40% Pt/C gave the best performance, followed by 50% Pt/C and 60% Pt/C. This directly corresponded with the order of electrochemical surface area (smallest average particles size).

Figures 4-29 & 4-30 show cell performance using 40, 50 & 60% Pt/C with air at 150 °C & 175 °C, respectively. With air operation and high operating temperatures leading to lower oxygen solubility and higher phosphoric acid viscosity (dehydration), 50% Pt/C showed advantages over 40% Pt/C, suggesting the optimum thickness shifted towards lower values as the oxygen concentration fell. As temperature increased from 150 to 175 °C, the viscosity of phosphoric acid increased due to dehydration [21] and furthermore, oxygen solubility fell (Henry's law) leading to a greater impact of mass transport on cell performance, reflected by a slightly lower limiting current at 175 °C compared to 150 °C. This makes selection of the optimum thickness of the catalyst layer more critical and therefore broadens the difference between the best performance obtained by 50%Pt/C and those of 40 & 60% Pt/C.

Whilst 60% Pt/C showed the smallest limiting current value (under air), explained by the flooded cathode structure, from acid electrolyte in the membrane, when utilising very thin catalyst layer. The slope of the polarisation curves was affected by a combination of mass transport effects (for example the difference in the slope between air and oxygen operation) and the typical effect of resistance. It can be seen that 60% Pt/C gave the worst polarisation performance and the smallest limiting current, while it exhibited the smallest IR loss through its thin catalyst layer. This confirms that the poorer polarisation obtained with the 60% Pt/C layer was attributed to mass transport effects (flooded structure).

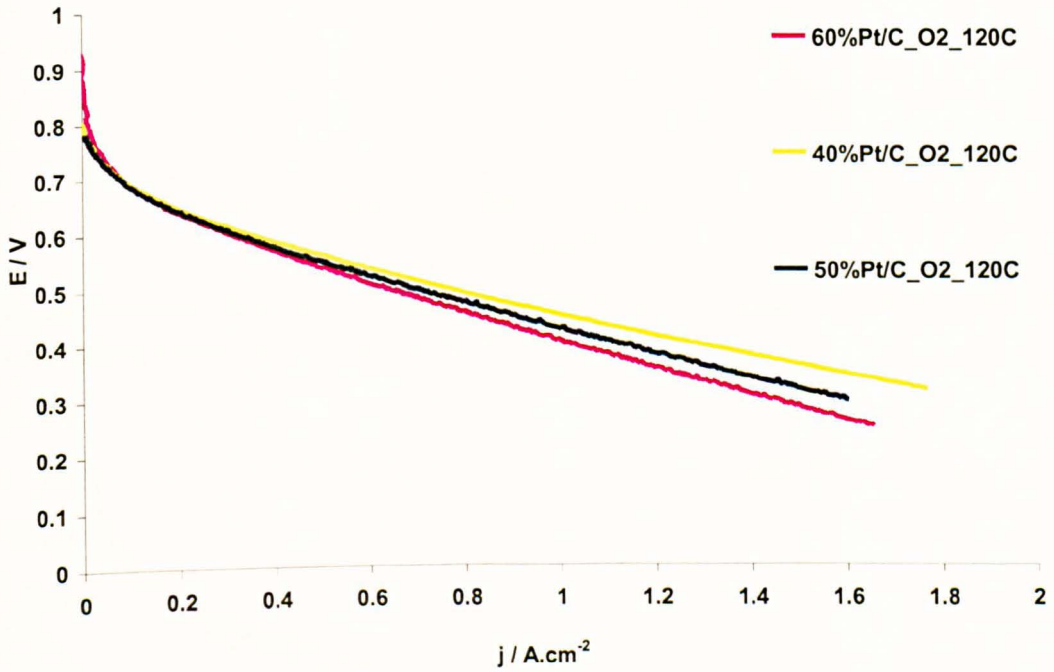

Figure 4-28. Compares cell performance under pure oxygen at 120 °C of MEAs using 40, 50 & 60% Pt/C cathode electrodes utilising 0.4 mg_{Pt} cm^{-2} with 40% wt PTFE.

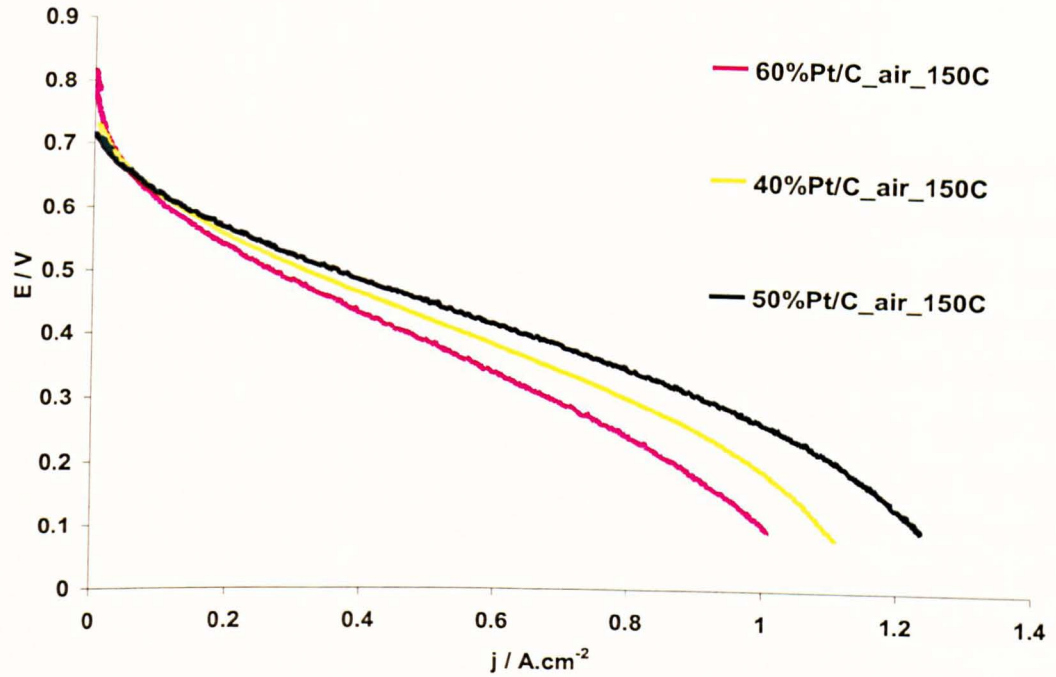

Figure 4-29. Compares cell performance under air at 150 °C of MEAs using 40, 50 & 60% Pt/C cathode electrodes utilising 0.4 mg_{Pt} cm^{-2} with 40% wt PTFE.

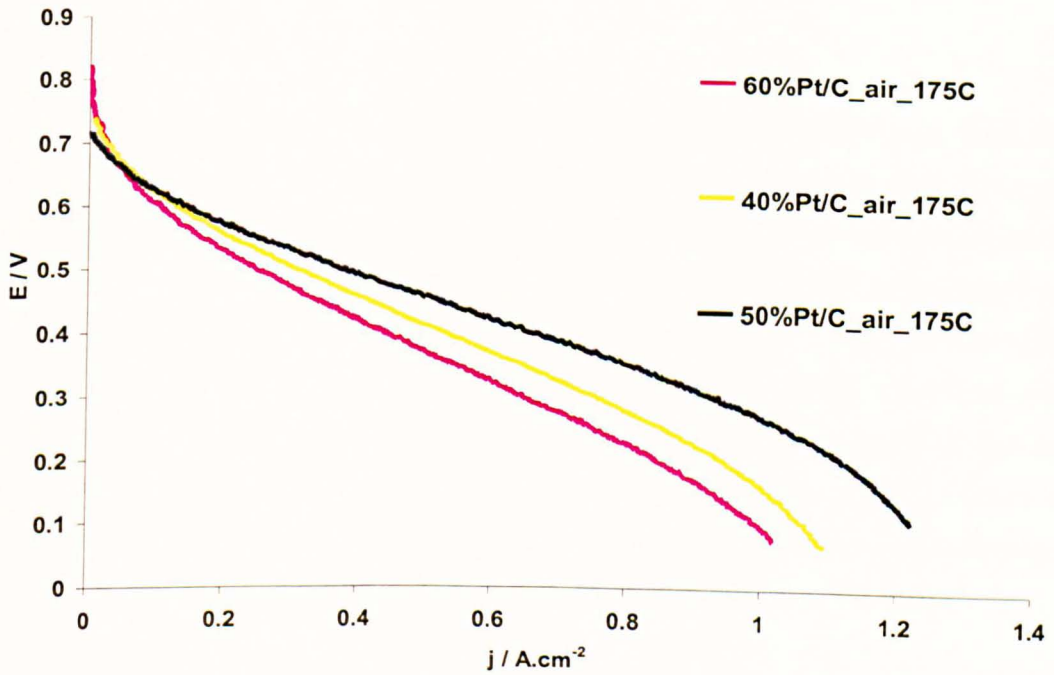

Figure 4-30. Compares cell performance under air at 175 °C of MEAs using 40, 50 & 60% Pt/C cathode electrodes utilising 0.4 mg_{Pt} cm^{-2} with 40% wt PTFE.

4.3.11 Pt-alloys effect on cathode performance

4.3.11.1 Introduction

A correlation between the nearest-neighbour distance (d_{n-n}) and the oxygen reduction activity of various platinum alloys has been reported for phosphoric acid electrolytes [27, 28]. The oxygen reduction activity in hot phosphoric acid (200 °C) on platinum and platinum alloys increases linearly as the nearest-neighbour distance in the electro-catalyst decreases. A composite analysis shows that data for supported platinum alloys [28] are consistent with bulk metal data [27] with respect to specific activity, activation energy, pre-exponential factor and percent d-band character. The kinetic parameters of the oxygen reduction reaction, in hot concentrated phosphoric acid, on highly dispersed platinum have been rationalized in terms of the rate determining step being the rupture of the O-O bond via various dual site mechanisms [29]. The spacing between the sites at which the O-O bond rupture occurs would play a critical role in the overall reaction rate and an optimum spacing should exist if the rate-determining step was assumed to be oxygen reduction involving dual sites mechanism with lateral adsorption of oxygen molecules on the electro-catalyst surface (bridge model) followed by rupture of the O-O bond [13].

The optimum nearest-neighbour distance (d_{n-n}) will facilitate rapid adsorption and bond rupture, while larger d_{n-n}, will lead to restricted adsorption and therefore dissociation might occur prior to adsorption. On the other hand smaller d_{n-n} will lead to limited adsorption due to repulsive forces [28]. The enhanced activity of platinum alloys over platinum can also be explained by the number of unpaired electrons in the d band and therefore, the oxygen coverage on the surface, as each oxygen requires two electrons from the metal d-orbit to form a bond. There is an optimum value for the d-band vacancy (per atom) [13] which controls the strength of the oxygen adsorption bond, or the %d character, the extent of the participation of the d orbitals in the metallic bond, influencing the heat of adsorption, where a balance between oxygen coverage and the strength of the M-O bond of the adsorbed oxygenated groups ($-O_2H$) is reached.

In phosphoric acid the (Pt-M/C) alloyed, disordered structure interact more strongly with impurities than the ordered structures (Pt/C). Chromium addition caused a decrease in Tafel

slope due to oxide reduction effects [30]. It was found that the Tafel slope measured at room temperature and atmospheric pressure on platinum increased from -110 mV dec^{-1} in low H_3PO_4 concentrations (10% wt) to -134 mV dec^{-1} in 85% wt H_3PO_4. This agrees with the findings of this work where the Tafel slope increased by increasing the doping level (Chapter 3). While the Tafel slopes for Pt-Co (90:10 a/o) and Pt-Cr (65:35 a/o) changed from 111 and 101, at low concentration, to 126 and 118 mV dec^{-1} with 85% wt H_3PO_4, respectively [31]. Anodic adsorption isotherms indicated that the high H_3PO_4 concentrations also obstructed adsorption of oxygen from solution. These effects were attributed to blockage of electro-active sites by the adsorption of H_3PO_4 molecules [31].

Appleby [32-34] studied oxygen reduction on various metals and alloys in phosphoric acid. For Pt-Ru alloys it was concluded that i_0 for ORR decreased and Tafel slope increased by increasing the ruthenium content in the alloy. Similarly, the activation energy for ORR in H_3PO_4 fell when moving from pure platinum (22.9 kcal $mole^{-1}$) to pure ruthenium (11.7 kcal $mole^{-1}$). This means that at elevated temperatures the platinum exchange current density will overtake that of pure ruthenium at (~80°C) and Pt-Ru (1:1) at (~100°C).

Wakabayashi & Watanabe et al studied oxygen reduction on Pt-Fe (54:46), Pt-Co (68:32), and Pt-Ni (63:37) a/o electrodes in 0.1 M $HClO_4$. The apparent rate constants for ORR at these electrodes were found to be 2.4-4.0 times larger than that at a pure Pt electrode, whereas their apparent activation energies were comparable to that at the Pt electrode. However, the apparent rate constants for ORR at the alloy electrodes decreased with higher temperatures, above 60°C, and were almost the same values as for the Pt electrode [35].

Pt-Fe (75:25 a/o) catalysts were also studied for oxygen reduction in PAFC. The mass activity (mA g^{-1} Pt) of the alloyed catalyst is about the same as that of the pure Pt catalyst due to the particle sintering in the alloyed catalyst. However, the specific activity (mA m^{-2} Pt, based on UPD) of the alloyed catalyst is estimated at twice that of pure Pt catalyst [36].

On the contrary, different Pt-Co activity testing under phosphoric acid fuel cell conditions demonstrated that the most highly alloyed catalysts were not significantly more active than pure

Pt catalyst of comparable crystallite size [37]. Loss of cobalt in the phosphoric acid environment was the lowest in catalysts which were the most alloyed, and where the Pt-Co (3:1) ordered phase was present [37]. It was found that the clean annealed surface of the alloy is pure Pt and the subsurface is enriched in Co [38]. Furthermore, this Pt surface does not behave like pure Pt for the chemisorption of carbon monoxide or oxygen [39]. The alloyed Pt-surface binds CO less strongly and oxygen more strongly. However, when heated in oxygen at fuel cell temperatures, even at very low pressures, the surface region is de-alloyed by oxidation to form a cobalt oxide over-layer [39]. The oxide over-layer dissolves in hot concentrated phosphoric acid, leaving a de-alloyed pure Pt surface region on top of the bulk alloy.

Alloying platinum (Pt-Co/C and Pt-Fe/C) affects the initiation and extent of surface oxide formation. Correlation of water activation and surface properties was reported [40]. Shift and lowering of water activation on supported Pt alloy electrocatalysts relative to Pt at high water activity or high relative humidity (low acid concentrations, trifluoromethane sulfonic acid (TFMSA 1 M)) was observed. At low acid concentration the alloys shift the formation and extent of water activation on the Pt alloy surfaces, namely the formation of oxygenated species above 0.75 V (typical potential for initiation of surface oxides on Pt) [40]. The lowering of oxide formation agrees well with the extent of enhancement of ORR activity. Activation energies at low acid concentration (1 M) were similar for Pt and Pt alloys, indicating that the rate limiting step remains unchanged [35]. Comparison between the inherent activity for ORR on supported Pt and Pt alloy nano-particles without the effect of oxide formation via activation of water was achieved by using high acid concentrations (6 M). At lower water activity (6 M) with negligible water activation (and hence surface oxides), the Pt surface was found to possess a higher activity for ORR as compared to the alloys [40].

The reduction in oxide formation, a surface poison for molecular oxygen adsorption on Pt alloys in the fully hydrated state (1 M TFMSA) is correlated to an increase in ORR activity. However, lowering of water activity, resulting from a shift in concentration to 6 M, shows that while there is an increase in ORR activity for Pt/C, due to lowering of surface oxide formation, a corresponding effect with Pt alloys does not occur [40]. This further supports the assumption of ORR activity being dependent on surface coverage by oxides [41]. The relatively similar values

of activation energy for Pt and Pt alloys seem to indicate that the differences in ORR activity arises primarily from contributions to the pre-exponential term in the Arrhenius expression, of which the prime contributor is the surface coverage of oxides [40].

4.3.11.2 Effect of Pt alloy cathode catalysts

Four different Pt alloys were studied, 40% Pt-Fe/C, 60%Pt-Ru/C, 20%Pt-Ni/C & 20%Pt-Co/C (Etek, U.S.A). All the studied alloys exhibited the atomic ratio of (1:1 a/o) while the average particles size (from XRD) were in the range of 3-4 nm except for Pt-Ru alloys which was in the range of 2-3 nm. Their performance was compared to that of pure Pt/C with similar platinum weight percentages, i.e. 20, 30 & 40% Pt/C, with average particles size (XRD) of 2.2, 2.5 & 2.8 nm, respectively. The platinum loading was 0.4 mg_{Pt} cm^{-2} for Pt-Fe and Pt-Ru, whilst a loading of 0.2 mg_{Pt} cm^{-2} was used for Pt-Ni and Pt-Co, due to the low metal to carbon ratio, to try and maintain a desired catalyst layer thickness to minimize mass transport effects on the cell polarisation.

Figure 4-31 compares cell performance under various oxygen concentrations at 150 °C of MEAs using 40% Pt-Fe/C (~30% Pt) & 30% Pt/C cathode electrodes utilising 0.4 mg_{Pt} cm^{-2} with 40 % wt PTFE. Pt-Fe alloy showed clear advantages in the kinetic region (low current densities) over standard platinum at all the studied oxygen concentrations. The observed kinetic enhancement was not due to catalyst layer structure, as both electrodes had similar Pt:C ratios (30% wt) and loading of 0.4 mg_{Pt} cm^{-2} and therefore similar catalyst layer thickness with close limiting currents values (for each oxygen concentration). The data confirms the reported advantage of Pt alloying (with iron) for ORR kinetics [35].

Figure 4-32 compares cell performance under various oxygen concentrations at 150 °C of MEAs using 60% Pt-Ru/C (~40% Pt) & 40% Pt/C cathode electrodes utilising 0.4 mg_{Pt} cm^{-2} with 40 % wt PTFE. From the data it can be concluded that Pt-Ru is not a suitable catalyst for oxygen reduction as large overvoltage losses were encountered in the kinetic region. This was seen in the large potential losses in the polarisation curves, without an apparent linear region or limiting currents; suggesting that the electrode was mainly under pure activation control due to the slow kinetics of oxygen reduction in Pt-Ru alloy electro-catalyst surface [32].

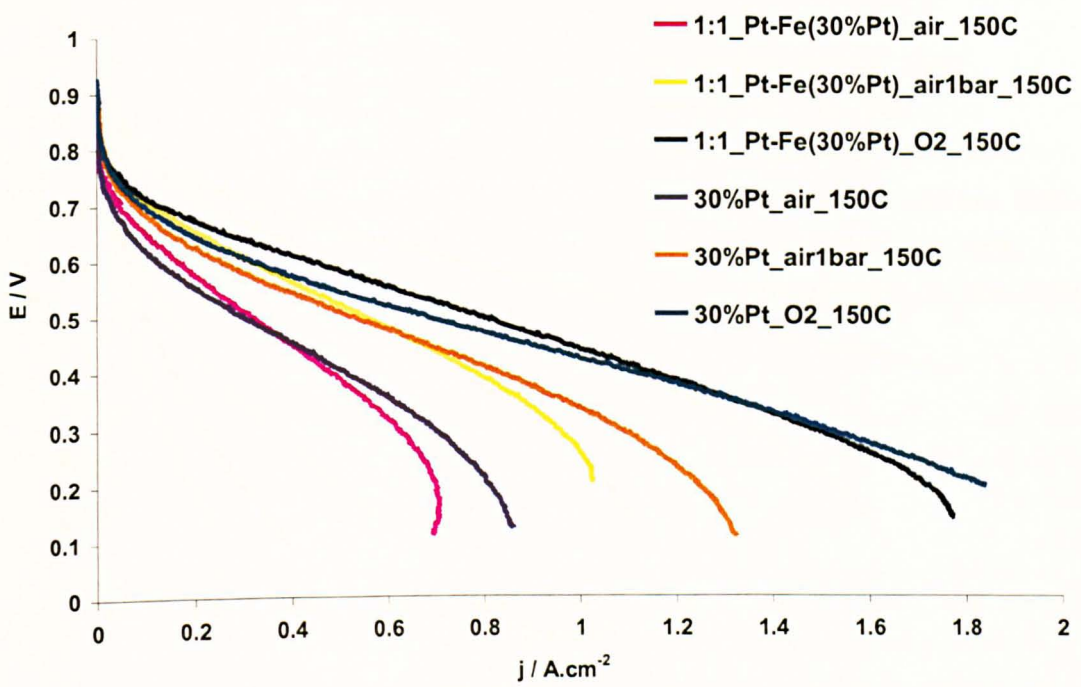

Figure 4-31. Compares cell performance under various oxygen concentrations at 150 °C of MEAs using 40% Pt-Fe/C (~30% Pt) & 30% Pt/C cathode electrodes utilising 0.4 mg_{Pt} cm^{-2} with 40% wt PTFE.

Figure 4-33 compares cell performance under various oxygen concentrations at 120 °C of MEAs using 20% Pt-Ni/C (~17% Pt) & 20% Pt/C cathode electrodes utilising 0.2 mg_{Pt} cm^{-2} with 40% wt PTFE. Figures 4-34 & 4-35 compare the alloy performance (0.2 mg_{Pt} cm^{-2}) with 0.4 mg_{Pt} cm^{-2} for 30% Pt/C at temperatures of 120 & 175 °C, respectively. All data show the expected improvement in cell performance on increasing the oxygen partial pressure.

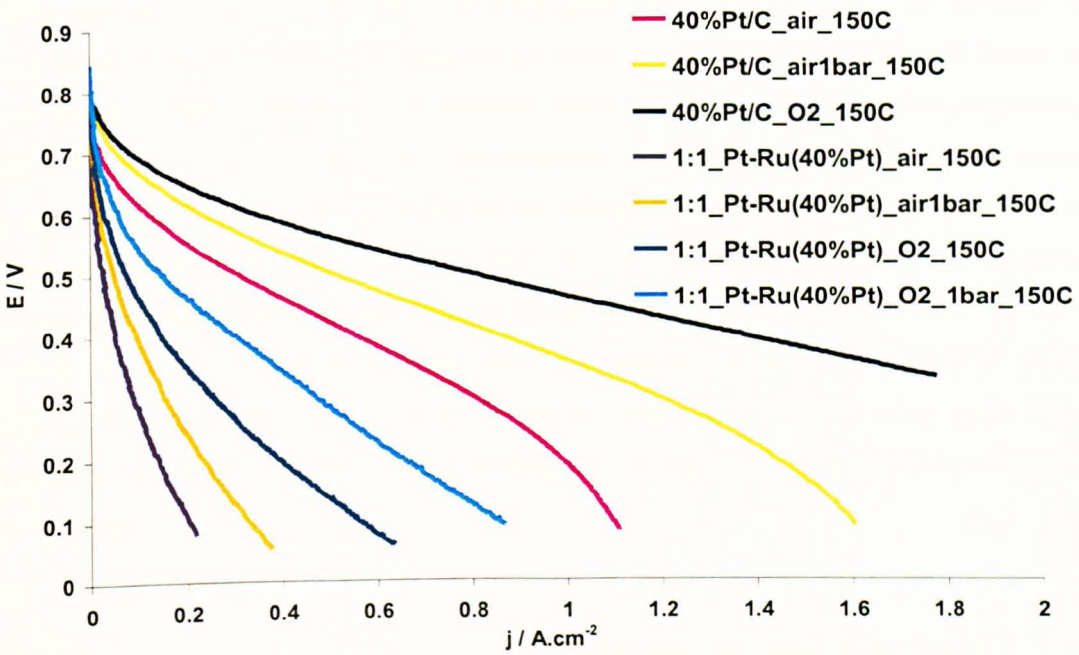

Figure 4-32. Compares cell performance under various oxygen concentrations at 150 °C of MEAs using 60% Pt-Ru/C (~40%Pt) & 40% Pt/C cathode electrodes utilising 0.4 mg_{Pt} cm^{-2} with 40% wt PTFE.

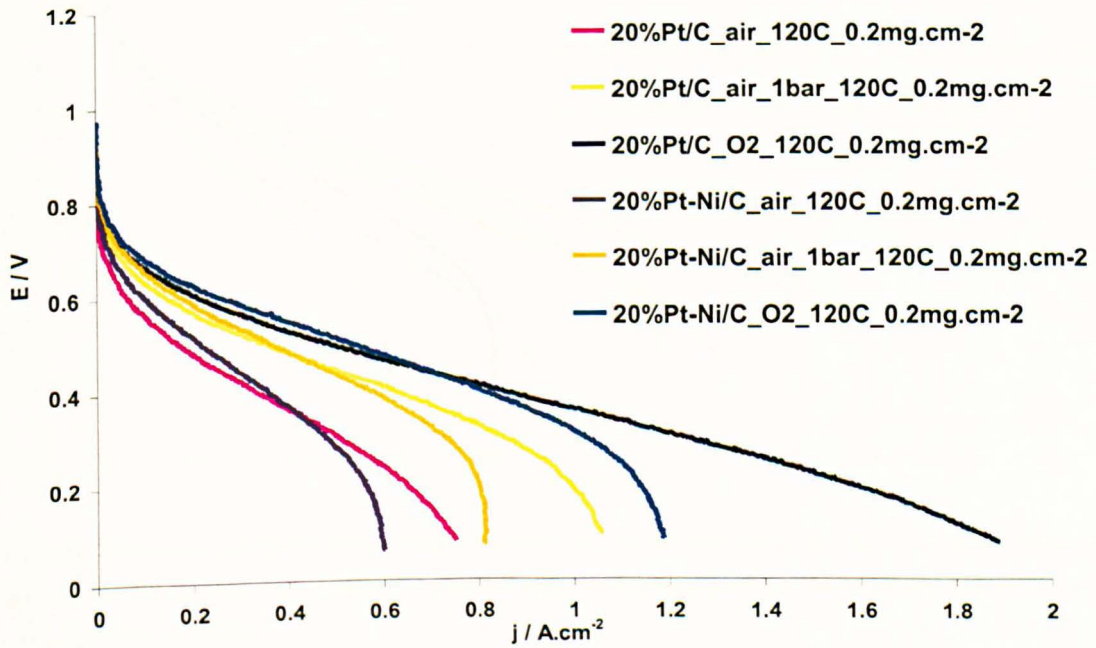

Figure 4-33. Compares cell performance under various oxygen concentrations at 120 °C of MEAs using 20% Pt-Ni/C (~17% Pt) & 20% Pt/C cathode electrodes utilising 0.2 mg_{Pt} cm^{-2} with 40% wt PTFE.

It can be seen from Fig. 4-33 that the Pt-Ni alloy produced enhanced kinetics for the ORR (low current densities) when compared to standard platinum (20%Pt/C, same loading) at 120°C, even though the alloy had a smaller electrochemical surface area, as a result of alloying (average particles size of 3-4 nm) in comparison to the standard platinum (2.2 nm). Additionally, the Pt-Ni alloy at loading of 0.2 mg_{Pt} cm^{-2} gave similar cell voltage characteristics in the kinetic region (up to a typical operating voltage of 0.6 V) to that of 30% Pt/C with a loading of 0.4 mg_{Pt} cm^{-2}. However, any enhancement in performance disappeared at elevated temperatures. At 150 °C (Fig. 9-3, Appendix A) the Pt-Ni alloy showed a similar performance to that of platinum (20%Pt/C, 0.2 mg_{Pt} cm^{-2}) and at 175 °C the 0.2 mg_{Pt} cm^{-2} Pt-Ni/C alloy gave inferior performance to that of 30% Pt/C with a loading of 0.4 mg_{Pt} cm^{-2} (Fig. 4-34) over the entire potential range.

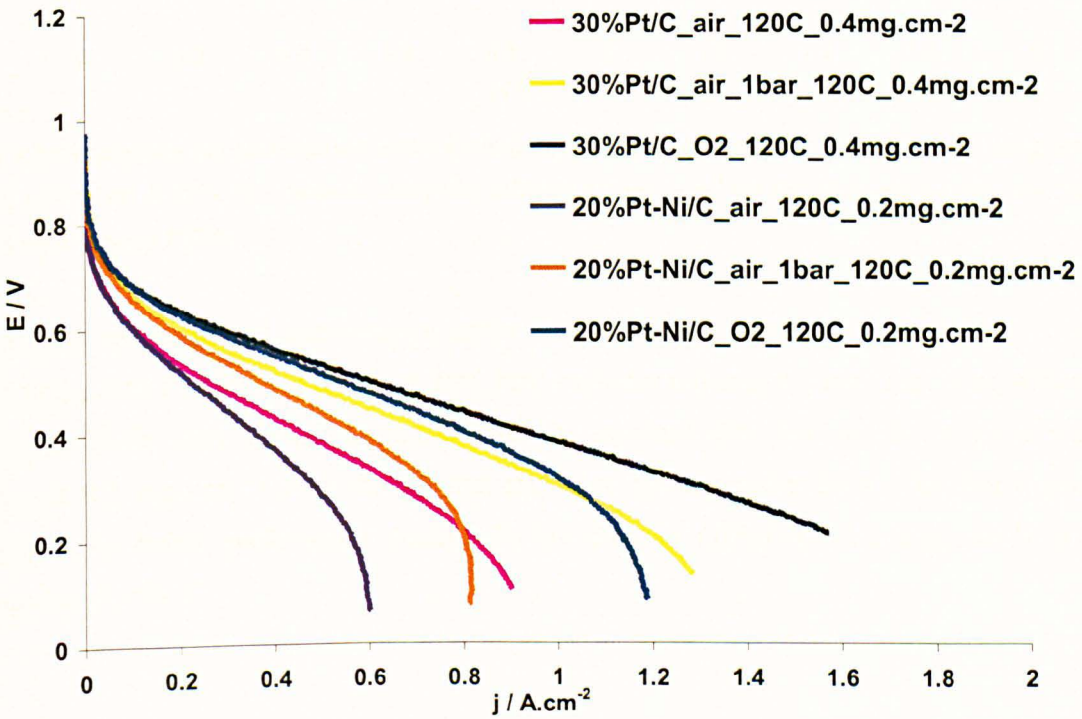

Figure 4-34. Compares cell performance under various oxygen concentrations at 120 °C of MEAs using 20% Pt-Ni/C (~17% Pt) & 30% Pt/C cathode electrodes utilising 0.2 mg_{Pt} cm^{-2} for the alloy and 0.4 mg_{Pt} cm^{-2} for pure Pt with 40% wt PTFE.

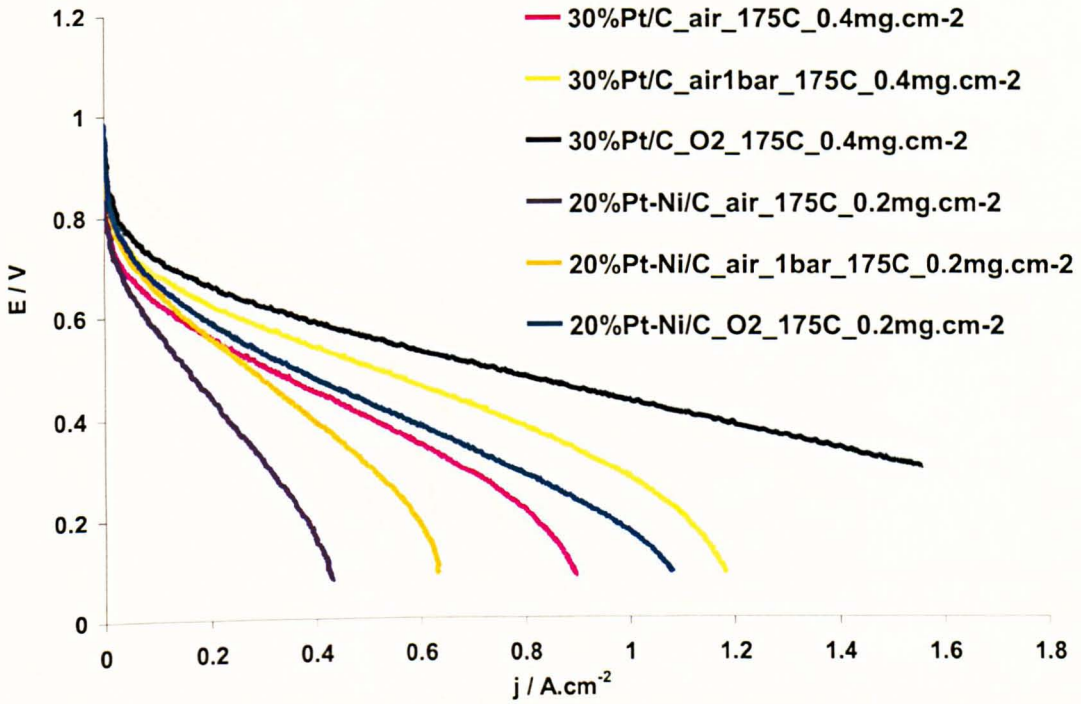

Figure 4-35. Compares cell performance under various oxygen concentrations at 175 °C of MEAs using 20% Pt-Ni/C (~17% Pt) & 30% Pt/C cathode electrodes utilising 0.2 mg_{Pt} cm^{-2} for the alloy and 0.4 mg_{Pt} cm^{-2} for pure Pt with 40% wt PTFE.

Figure 4-36 compares cell performance under various oxygen concentrations at 150 °C for MEAs using 20% Pt-Co/C (~17% Pt) & 20% Pt/C cathodes utilising 0.2 mg_{Pt} cm^{-2} with 40% wt PTFE. The Pt-Co alloy showed advantage over the standard 20% Pt/C at 120 °C (both with loading of 0.2 mg_{Pt} cm^{-2}) even though that the alloy had a smaller ESA. The Pt-Co alloy maintained its better performance (unlike Pt-Ni) than Pt (20%Pt/C, 0.2 mg_{Pt} cm^{-2}) at a temperature of 150 °C.

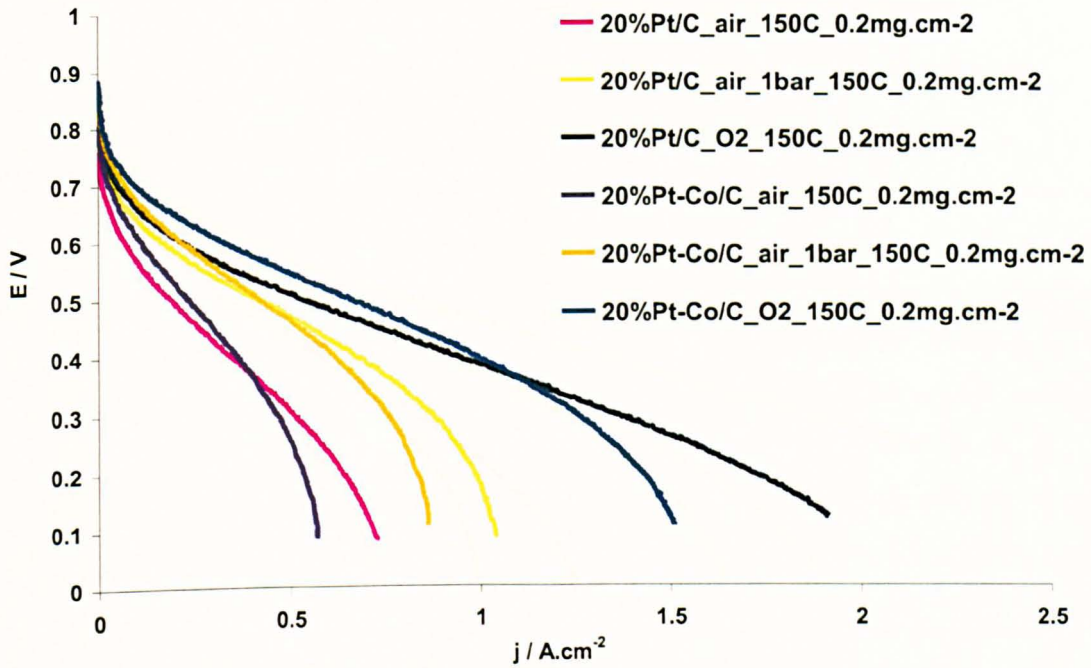

Figure 4-36. Compares cell performance under various oxygen concentrations at 150 °C of MEAs using 20% Pt-Co/C (~17% Pt) & 20% Pt/C cathode electrodes utilising 0.2 mg_{Pt} cm^{-2} with 40% wt PTFE.

Figure 4-37 shows cell performance under various oxygen concentrations at 175 °C of MEAs using 20% Pt-Co/C (~17% Pt) & 30% Pt/C cathode electrodes utilising 0.2 mg_{Pt} cm^{-2} for the alloy and 0.4 mg_{Pt} cm^{-2} for pure Pt with 40% wt PTFE. It is clear that at 175 °C the 0.2 mg_{Pt} cm^{-2} Pt-Co alloy had an inferior performance compared to 0.4 mg_{Pt} cm^{-2} 30% Pt/C, whilst at 150 °C both electrodes shows comparable performance in the kinetic region of the polarisation curves. This behaviour suggests that the alloy performance does not depend on temperature as much as the standard platinum. However, it has been shown in the literature that Pt-Ni and Pt-Co alloys exhibit similar activation energies for oxygen reduction to that of platinum [35, 37].

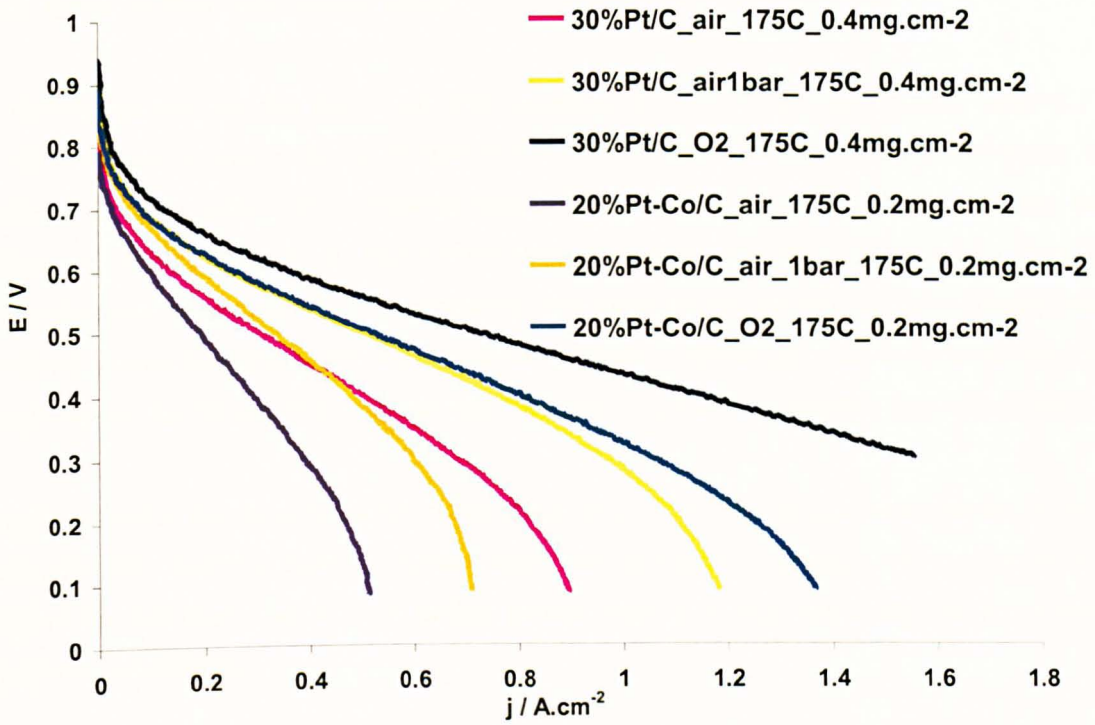

Figure 4-37. Compares cell performance under various oxygen concentrations at 175 °C of MEAs using 20% Pt-Co/C (~17% Pt) & 30% Pt/C cathode electrodes utilising 0.2 mg_{Pt} cm^{-2} for the alloy and 0.4 mg_{Pt} cm^{-2} for pure Pt with 40% wt PTFE.

It is reported that cobalt dissolution was a common problem for Pt-Co alloy in PAFCs [37]. The degradation and the dissolution process is expected to occur over hundreds hours of operation and not over the short period of experiments (three days) used in this study. In this study it was observed that recovery in the performance (or in other words the alloys enhanced performance) over standard platinum returned when the temperature was lowered back to 120 °C in case of Pt-Ni and 150 °C in case of Pt-Co. This suggests that the observed effect of temperature was not due to dissolution, but due to a drop in water activity at elevated temperatures, where phosphoric acid started to dehydrate [21]. The fall in water activity at elevated temperatures results in an increase in ORR activity for Pt/C due to lowering of surface oxide formation, a corresponding effect with Pt alloys does not occur [40].

4.3.12 Effect of Flow field design effect

The flow-fields used for this study were with geometry of 29 x 29 mm and channel depth of 1.5 mm with channel to land ratio maintained at 1.5 (1.5 mm wide channel & 1 mm wide for the contact rib). Three cells were fabricated with different patterns (graphite blocks inserted into titanium cell body) utilising the same flow-fields geometry. The first pattern was a standard parallel channel, the second utilised serpentine flow channels and the third utilised interdigitated flow-fields (same as parallel but with dead-end channels, where gas had to flow through the channel across the rib and exit from the opposite side of the next neighbour channel) (Figure 4-40).

It should be noted that as seen earlier in the effect of air flow rate on cell performance, or more specifically the observed limiting current under air operation, a lambda value close to 2 is sufficient for cell operation with no further enhancement was observed in the limiting current beyond this stoichiometry.

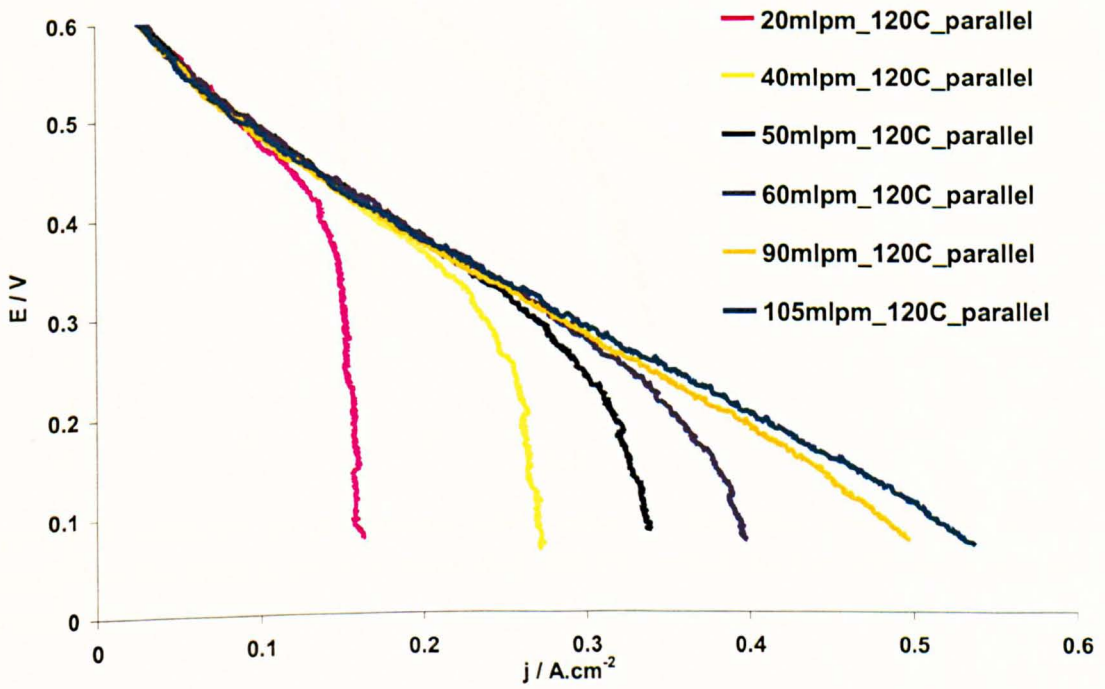

Figure 4-38. Compares cell performance under various air flow rates using standard parallel flow fields at 120 °C of MEAs using 40% Pt/C cathode electrode utilising 0.2 mg_{Pt} cm^{-2} with 40% wt PTFE.

Figure 4-38 shows cell performance at various air flow rates using the standard parallel flow fields at 120 °C with MEAs using 40% Pt/C cathode electrode utilising 0.2 mg_{Pt} cm^{-2} with 40% wt PTFE. When the air flow rate (atmospheric) was increased from 20 to 105 cm^3 min^{-1} (STP) (mLpm) the observed limiting current increased accordingly. Above 105 cm^3 min^{-1} (or λ of 1.2) no clear enhancement was observed as there was no clear limiting current. The observed effect of the low value of stoichiometry of 1.2 in comparison to the earlier reported value of 2 is due to the lower platinum loading in the catalyst layer (0.2 mg_{Pt} cm^{-2}) in comparison with 0.6 mg_{Pt} cm^{-2} used earlier. The low platinum loading led to large overpotential losses, due to kinetic activation, and the cell potential reached zero volts at a current density of 0.55 A cm^{-2} in comparison to 1.38 A cm^{-2} obtained earlier.

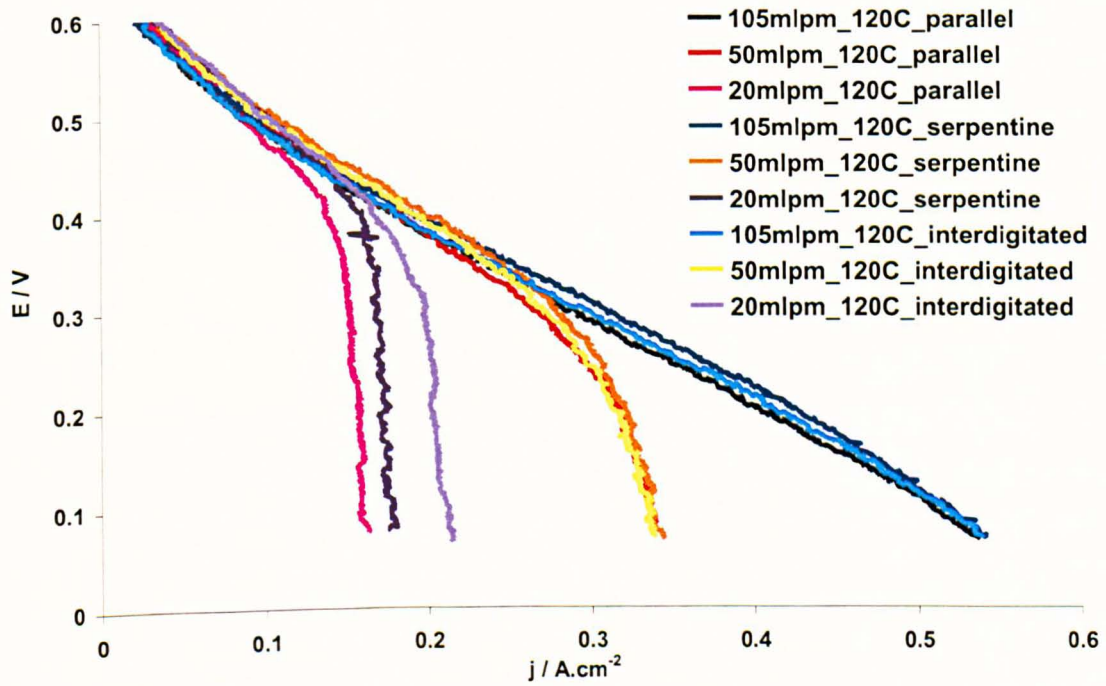

Figure 4-39. Compares cell performance under various air flow rates using parallel, serpentine & interdigitated flow fields at 120 °C of MEAs using 40% Pt/C cathode electrode utilising 0.2 mg_{Pt} cm^{-2} with 40% wt PTFE.

Figure 4-39 compares the performance of the three flow fields with different air flow rates at 120 °C using MEAs with 40% Pt/C cathode electrode utilising 0.2 mg_{Pt} cm^{-2} with 40% wt PTFE. It

can be seen that at 105 cm^3 min^{-1} and 50 cm^3 min^{-1} there was no apparent difference in the observed limiting current between the three flow-fields, with air operation. This is likely to be a result of the use of the small 9 cm^2 geometry as differences are more likely to occur with electrodes of large geometry, especially at high operating temperature. However, reducing the air flow rate to 20 cm^3 min^{-1}(STP), where the system was under complete mass transport control some small difference in the limiting current was observed with the three patterns. The interdigitated flow field offered the highest limiting current, or in other words the best oxygen distribution (current) over the electrode surface, followed by serpentine and finally the parallel flow field.

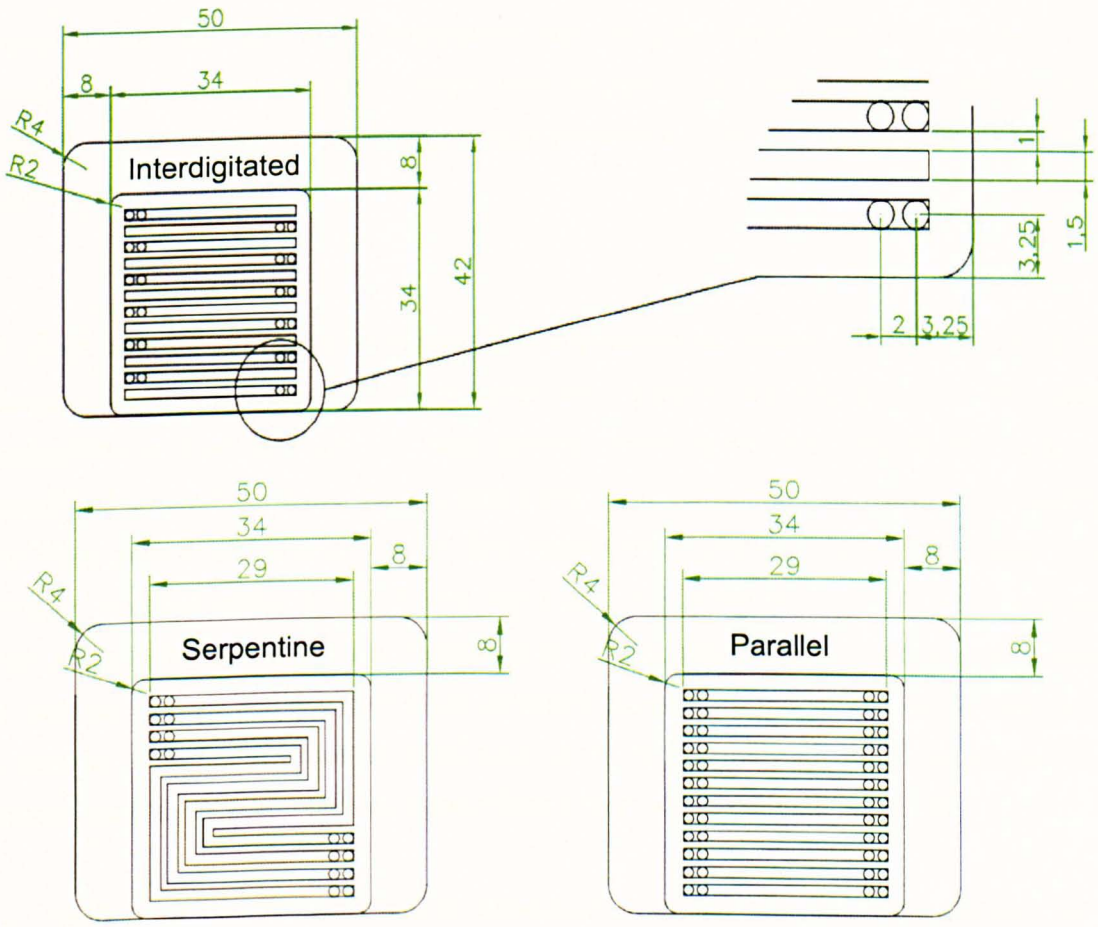

Figure 4-40. Schematic drawing of the graphite inserts with the three studied flow fields patterns.

4.4 Conclusions

For higher temperature proton exchange membrane fuel cells, phosphoric acid doped PBI appears to be good candidate for the membrane material. It exhibits good conductivity at elevated temperatures and low hydrogen & oxygen permeability. This however makes PBI/H_3PO_4 less attractive as a candidate for the ionomer material in the catalyst layer. Alternative structure based on PTFE and H_3PO_4 shows advantages over PBI based electrodes due to higher oxygen permeability.

There was an optimum thickness [2] for the catalyst layer that provided a balance between acid content in the catalyst layer (added or mobile from the membrane) and oxygen permeability from the flow channel. This optimum thickness was achieved using 40% to 50% Pt/C catalyst and it depended on the operating temperature and oxygen partial pressure. Lower oxygen concentrations required a thinner catalyst layer or higher Pt:C ratio. Electrodes fabricated from 60% Pt/C (thin catalyst layer) showed limited performance due to flooding from mobile H_3PO_4 acid from the membrane.

Pt alloys showed advantages over non-alloyed platinum as cathode catalysts, allowing lower platinum loading at 0.2 mg_{Pt} cm^{-2}. However, such enhancement was subject to the operating temperature or more precisely the water activity, where at elevated temperatures (under non-humidified conditions) above 150 °C, phosphoric acid dehydration started to occur leading to low water activity and conductivity. At low water activity, platinum showed advantage over Pt-Ni alloy at temperatures of 150 °C and above or Pt-Co at temperatures of 175 °C and above. With a high water content, Pt alloys suppress the initiation and extent of surface oxide formation on platinum surface and therefore offers enhanced oxygen adsorption. The fall in water activity at elevated temperatures resulted in an increase in ORR activity for Pt/C, due to lowering of surface oxide formation, a corresponding effect with Pt alloys does not occur [40].

The stability of the Pt alloys in hot phosphoric acid and high operating voltages is also questionable. The degradation of the alloyed catalyst in short term testing was not apparent,

however, it is evident from the literature that the de-alloying process and formation of cobalt oxide and cobalt dissolution in hot phosphoric acid does occur [37].

Finally, the impact of flow fields' pattern is minimal at the studied cell geometry (9 cm^2). Interdigitated flow-fields offered the best oxygen distribution over the electrode geometry followed by serpentine pattern and lastly parallel pattern. The system required an air stoichiometry (λ) of 2 at the maximum operating current density under atmospheric air operation (1.2-1.4 A cm^{-2}).

4.5 References

1. Sattler, M.L. and P.N. Ross, *The surface structure of Pt crystallites supported on carbon black.* Ultramicroscopy, 1986. **20**(1-2): p. 21-28.
2. Bevers, D., M. WOHR, K. YASUDA, and K. OGURO, *Simulation of a polymer electrolyte fuel cell electrode.* JOURNAL OF APPLIED ELECTROCHEMISTRY, 1997. **27**: p. 1254-1264.
3. Sakai, T., H. Takenako, N. Wakabayashi, Y. Kawami, and E. Torikai, *Gas Permeation Properties of Solid Polymer Electrolyte (SPE) Membranes.* J. Electrochem. Soc., 1985. **132**(6): p. 1328.
4. He, R.H., Q.F. Li, A. Bach, J.O. Jensen, and N.J. Bjerrum, *Physicochemical properties of phosphoric acid doped polybenzimidazole membranes for fuel cells.* Journal of Membrane Science, 2006. **277**(1-2): p. 38-45.
5. Pasternak, R.A., M.V. Christensen, and J. Heller, *Diffusion and Permeation of Oxygen, Nitrogen, Carbon Dioxide, and Nitrogen Dioxide through Polytetrafluoroethylene.* Macromolecules, 1970. **3**(3): p. 366.
6. Liu, Z.Y., J.S. Wainright, M.H. Litt, and R.F. Savinell, *Study of the oxygen reduction reaction (ORR) at Pt interfaced with phosphoric acid doped polybenzimidazole at elevated temperature and low relative humidity.* Electrochimica Acta, 2006. **51**(19): p. 3914-3923.
7. Yang, C., S. Srinivasan, A.B. Bocarsly, S. Tulyani, and J.B. Benziger, *A comparison of physical properties and fuel cell performance of Nafion and zirconium phosphate/Nafion composite membranes.* Journal of Membrane Science, 2004. **237**: p. 145-161.
8. Springer, T.E. and I.D. Raistrick, *Electrical Impedance of a Pore Wall for the Flooded-Agglomerate Model of Porous Gas-Diffusion Electrodes.* J. Electrochem. Soc. , 1989. **136**(6): p. 1594-1603.
9. Giner, J. and C. Hunter, *The Mechanism of Operation of the Teflon-Bonded Gas Diffusion Electrode: A Mathematical Model.* J. Electrochem. Soc., 1969. **116**(8): p. 1124-1130.
10. Passos, R.R. and E.A. Ticianelli, *Effects of the Operational Conditions on the Membrane and Electrode Properties of a Polymer Electrolyte Fuel Cell.* J. Braz. Chem. Soc., 2002. **13**(4): p. 483-489.
11. Parthasarathy, A., S. Srinivasan, and A.J. Appleby, *Temperature Dependence of the Electrode Kinetics of Oxygen Reduction at the Platinum/Nafion® Interface-A Microelectrode Investigation.* J. Electrochem. Soc., 1992. **139**(9): p. 2530-2537
12. Hoel, D. and E. Grunwald, *High Protonic Conduction of Polybenzimidazole Films.* Journal of Physical Chemistry, 1977. **81**(22): p. 2135-2136.
13. Kinoshita, K., *Electrochemical oxygen technology* 1992, New York: Wiley.
14. Scott, K., S. Pilditch, and M. Mamlouk, *Modelling and experimental validation of a high temperature polymer electrolyte fuel cell.* Journal of Applied Electrochemistry, 2007. **37**: p. 1245-1259.
15. Li, Q.F., H.A. Hjuler, and N.J. Bjerrum, *Oxygen reduction on carbon supported platinum catalysts in high temperature polymer electrolytes.* Electrochimica Acta, 2000. **45**(25-26): p. 4219-4226.

16. Li, Q., G. Xiao, H.A. Hjuler, R.W. Berg, and N.J. Bjerrum, *Oxygen Reduction on Gas-Diffusion Electrodes for Phosphoric Acid Fuel Cells by a Potential Decay Method.* J. Electrochem. Soc., 1995. **142**(10): p. 3250-3256.
17. Razaq, M., A. Razaq, E. Yeager, D.D. DesMarteau, and S. Singh, *Perfluorosulfonimide as an Additive in Phosphoric Acid Fuel Cell.* J. Electrochem. Soc., 1989. **136**(2): p. 385-390.
18. McBreen, J., W.E. O'Grady, and R. Richter, *A Rotating Disk Electrode Apparatus for the Study of Fuel Cell Reactions at Elevated Temperatures and Pressures.* J. Electrochem. Soc., 1984. **131**(5): p. 1215-1216.
19. Appleby, A.J., *The energy crisis: An electrochemical viewpoint.* Journal of Electroanalytical Chemistry, 1981. **118**: p. 31-50.
20. Li, Q.F., R.H. He, J.A. Gao, J.O. Jensen, and N.J. Bjerrum, *The CO poisoning effect in PEMFCs operational at temperatures up to 200 degrees C.* Journal of the Electrochemical Society, 2003. **150**(12): p. A1599-A1605.
21. Ma, Y.L., *The Fundamental Studies of Polybenzimidazole/Phosphoric Acid Polymer Electrolyte For Fuel Cells.* 2004, CASE WESTERN RESERVE UNIVERSITY.
22. Li, Q.F., R. He, J.O. Jensen, and N.J. Bjerrum, *PBI-based polymer membrane for high temperature fuel cells* fuel cells, 2004. **4**: p. 147.
23. Bouchet, R. and E. Siebert, *Proton conduction in acid doped polybenzimidazole.* Solid State Ionics, 1999. **118**(3-4): p. 287-299.
24. Pebler, A., *Transmission Electron Microscopic Examination of Phosphoric Acid Fuel Cell Components.* J. Electrochem. Soc., 1986. **133**(1): p. 9-17.
25. Kunz, H.R. and G.A. Gruver, *The Catalytic Activity of Platinum Supported on Carbon for Electrochemical Oxygen Reduction in Phosphoric Acid.* J. Electrochem. Soc., 1975. **122**(10): p. 1279-1287.
26. SDS@cabot-corp.com, *SAFETY DATA SHEET of Vulcan XC-72 R.* 2007, Cabot Corporation, France.
27. Appleby, A.J., *ELECTROCATALYSIS AND FUEL CELLS.* Catalysis Reviews, 1970. **4**(1): p. 221 - 244.
28. Jalan, V. and E.J. Taylor, *Importance of Interatomic Spacing in Catalytic Reduction of Oxygen in Phosphoric Acid.* J. Electrochem. Soc., 1983. **130**(11): p. 2299-2302
29. Vogel, W.M. and J.M. Baris, *The reduction of oxygen on platium black in acid electrolytes.* Electrochimica Acta, 1977. **22**(11): p. 1259-1263.
30. Glass, J.T., G.L. Cahen, G.E. Stoner, and E.J. Taylor, *The Effect of Metallurgical Variables on the Electrocatalytic Properties of PtCr Alloys.* J. Electrochem. Soc., 1987. **134**(1): p. 58-65.
31. Glass, J.T., G.I. Cahen, and G.E. Stoner, *The Effect of Phosphoric Acid Concentration on Electrocatalysis.* J. Electrochem. Soc., 1989. **136**(3): p. 656-660.
32. Appleby, A.J., *Oxygen reduction on platinum-ruthenium alloy electrodes in 85% orthophosphoric acid.* Journal of Electroanalytical Chemistry, 1970. **27**(3): p. 347-354.
33. Appleby, A.J., *Oxygen reduction studies at smooth pre-reduced ruthenium and rhodium electrodes in 85% orthophosphoric acid.* Journal of Electroanalytical Chemistry, 1970. **27**(3): p. 335-345.
34. Appleby, A.J., *Oxygen reduction at smooth pre-reduced gold and iridium electrodes in 85% orthophosphoric acid.* Journal of Electroanalytical Chemistry, 1970. **27**(3): p. 325-334.

35. Wakabayashi, N., M. Takeichi, H. Uchida, and M. Watanabe, *Temperature Dependence of Oxygen Reduction Activity at Pt-Fe, Pt-Co, and Pt-Ni Alloy Electrodes.* J. Phys. Chem. B, 2005. **109**: p. 5836-5841.
36. Kim, K.T., J.T. Hwang, Y.G. Kim, and J.S. Chung, *Surface and Catalytic Properties of Iron-Platinum/Carbon Electrocatalysts for Cathodic Oxygen Reduction in PAFC.* J. Electrochem. Soc., 1993. **140**(1): p. 31-36.
37. Beard, B.C. and P.N. Ross, *The Structure and Activity of Pt-Co Alloys as Oxygen Reduction Electrocatalysts.* J. Electrochem. Soc., 1990. **137**(11): p. 3368-3374.
38. Bardi, U., A. Atrei, P.N. Ross, E. Zanazzi, and G. Rovida, *Study of the (001) surface of the Pt-20at%Co alloy by LEED, LEISS and XPS.* Surface Science, 1989. **211-212**: p. 441-447.
39. Bardi, U., B. Beard, and P. Ross, *Surface oxidation of a Pt-20% CO alloy.* J. Vac. Sci.Technol. A, 1988. **6**(3): p. 665-670.
40. Murthi, V.S., R.C. Urian, and S. Mukerjee, *Oxygen Reduction Kinetics in Low and Medium Temperature Acid Environment: Correlation of Water Activation and Surface Properties in Supported Pt and Pt Alloy Electrocatalysts.* J. Phys. Chem. B, 2004. **108**: p. 11011-11023.
41. Damjanovic, A. and V. Brusic, *Electrode kinetics of oxygen reduction on oxide-free platinum electrodes.* Electrochimica Acta, 1967. **12**(6): p. 615-628.

5 High Temperature Direct Methanol Fuel Cell

5.1 Introduction

Pristine PBI has a very low methanol permeability compared to Nafion® 117, which makes PBI a potential membrane for Direct Methanol Fuel Cells (DMFCs). For example at 25 °C permeabilities of PBI and Nafion are 0.0083×10^{-12} and 2.3×10^{-12} mol cm cm^{-2} s^{-1} atm^{-1} respectively [1]. However, the data are for non-doped PBI films; as the experiment involved liquid water which would have leached the doped acid out of the membrane. The methanol cross-over is expected to increase dramatically at elevated temperature as methanol diffusion in the gaseous phase is much higher than that in liquid phase and doped PBI is more permeable than non-doped PBI; considering the fact that PBI swells and expand when acid doped, resulting in a more porous structure. Moreover typical PBI membranes used are c.a. 50 μm thick compared to c.a. 180 μm for Nafion 117 (200 μm under humidified conditions). This chapter examines the use of PBI membranes in the direct methanol fuel cell.

5.2 Background and review

Jones and Roziere [6] showed that, at 80 °C, methanol's vapour permeability through doped PBI (3PRU) and Nafion 117 were 92.34×10^{-12} & 27360×10^{-12} mol cm cm^{-2} s^{-1} atm^{-1}, respectively. Similarly, Wang et al [2] reported methanol vapour permeability, through doped PBI (5PRU) at 180 °C, of 166.4×10^{-12} mol cm cm^{-2} s^{-1} atm^{-1} at 0 RH% and increased to 298.5×10^{-12} mol cm cm^{-2} s^{-1} atm^{-1} at RH 7.5 %.

Methanol crossover rates through doped PBI membranes have been determined by direct measurement of the methanol permeability [3], by a methanol sorption technique [4] and by real-time analysis of the cathode exhaust stream of an operating cell using mass spectrometry [2]. Each of these measurements yielded crossover rates equivalent to 10 mA cm^{-2} for (~76 μm) thick films, at least ten times less than that observed with Nafion [5]. Methanol permeability data are summarised in Tables 5-1 and 5-2 for vapour and liquid phases.

At a doping level of 5 PRU PBI membrane have been reported to have near zero osmotic drag coefficients in the range of (0.01-0.09) with vapour water: methanol molar ratio feed in the range of (1:0-1:1) [3].

Table 5-1. Vapour methanol permeability through PBI and nafion at various conditions.

Material	Temperature	RH	Species	Vapour activity	Permeability	Diffusion	solubility	Ref
	°C	%			10^{-12} mol cm cm^{-2} s^{-1} atm^{-1}	10^{-6} cm^2 s^{-1}	10^{-6} mol cm^{-3} atm^{-1}	
PBI5PRU	180	5-7.5	Methanol	0.25-0.5	280-298.5	-	-	[2]
PBI5PRU	180	0	Methanol	1	166.4	-	-	[2]
PBI5PRU	150	0	Methanol	0.01-0.1	6.7-67	0.01	2175-6526	[4]
PBI3PRU	80	n/a	Methanol	n/a	92.34	-	-	[6]
Nafion117	80	n/a	Methanol	n/a	27360	-	-	[6, 7]

Increasing cell temperature above 60 °C in Nafion based DMFCs causes a significant increase in cell performance and at 90 °C and above, high power densities of 200 mW cm^{-2} were achieved [8]. However, this required operation with pressurised oxygen (2-5 bar) to maintain the required water content in the nafion membrane and minimise mass transport losses at the cathode.

Early work [9] on the performance of DMFC used relatively high loading of Pt-Ru catalyst in the range of 4-8 mg_{Pt} cm^{-2} to achieve high power densities (>200 mW cm^{-2}) with pressurised oxygen and temperature of 130 °C. More recently, an equivalent performance has been reported with half the catalyst loading at 110 °C [8].

The feed concentration of methanol is an important consideration in Nafion based DMFCs. Half cell studies (0.5 M H_2SO_4) showed enhancement in methanol oxidation with increased concentration up to 8 M [10]. However, in practice the enhancement in methanol oxidation

above 1-2 M does not translate into higher cell performance due the problem of methanol cross-over [8].

Table 5-2. Liquid methanol permeability through PBI and nafion at 25 °C and fully hydrated conditions.

Material	Temperature	Water content	Species	Concentration	Permeability	Ref
	°C			% wt	10^{-9} cm^2 s^{-1}	
Nafion 117	25	Fully hydrated	Methanol	3%	2300	[1]
PBI	25	Fully hydrated	Methanol	3%	8.3	[1]
PBI	25	Fully hydrated	Methanol	10-100%	18	[11]
Nafion115	25	Fully hydrated	Methanol	3%	850	[12]
Nafion117	25	Fully hydrated	Methanol	3%	2000	[13]
PBI	25	Fully hydrated	Methanol	100%	70	This work
Nafion 117	25	Fully hydrated	Methanol	100%	4000	This work

Lim et al [14] reported cell performance of 0.39 V at current density of 100 mA cm^{-2} at 90 °C with 2.0 M methanol. The catalyst loadings were 2 mg_{Pt} cm^{-2} unsupported Pt-Ru (1:1) at the anode and 4.5 mg_{Pt} cm^{-2} 60% Pt/C at the cathode. Allen et al [15] reported cell voltage of 0.4V at current density of 100 mA cm^{-2} and 90 °C, with 1.0 M methanol, utilising 1 mg_{Pt} cm^{-2} of 60% Pt-Ru/C (1:1) at the anode and 1 mg_{Pt} cm^{-2} of 60% Pt/C at the cathode. Shen and Scott [16] obtained 0.39 V at 100 mA cm^{-2} with 2 M methanol feed at 80 °C; with 1 mg_{Pt} cm^{-2} 60% Pt-Ru (1:1) at the anode and 1 mg_{Pt} cm^{-2} 60% Pt/C cathode. Shukla et al [17] obtained higher performance of 0.5 V at 100 mA cm^{-2} and 90 °C with 1.0 M methanol by increasing the cathode loading to 4.6 mg_{Pt} cm^{-2} 60% Pt/C and maintaining the anode loading at 1 mg_{Pt} cm^{-2} 60% Pt-Ru (1:1).

Scott et al [18] also showed improved performance of 0.52 V at 100 mA cm^{-2} and 75 °C by increasing the anode loading to 2 mg_{Pt} cm^{-2} (50% Pt-Ru/C, 1:1) and maintaining the cathode loading at 1 mg_{Pt} cm^{-2} (Pt black). Typical OCPs with Nafion based DMFCs were in the range of 0.6-0.7 V depending on methanol concentration (0.125-2 M), oxygen pressure and temperature (25-90 °C). All the reported data were with atmospheric pure oxygen.

There is limited data available in the literature on PBI based DMFC. Wainright et al [4, 5, 19] &Wang et al [20, 21] reported PBI/H_3PO_4 (5 PRU) based MEAs for high temperature direct methanol fuel cells. They used high catalyst loadings of 4 mg_{Pt} cm^{-2} on both anode (Pt:Ru 1:1 a/o) and cathode (Pt-black). Wang et al [21] obtained a current density of 100 mA cm^{-2} at 0.42 V with (water : methanol) molar ratio of 2:1 and pure oxygen at 150 °C. The open circuit voltage was 0.8 V with a cross-over current of 10 mA cm^{-2} for 110 μm membrane (5 PRU). Wainright et al [4, 19] obtained a current density of 100 mA cm^{-2} at 0.52 V with methanol: water molar ratio of1: 4 and pure oxygen at 200 °C using the same catalyst loading and membrane thickness.

More recently, Wainright et al [5] studied the effect of temperature and methanol feed on cell performance. They used the same membrane doping level of 5 PRU and reduced its thickness to 75 μm whilst maintaining high catalyst loading of 4 mg_{Pt} cm^{-2} on both anode (Pt:Ru 1:1 a/o) and cathode (Pt-black). At a fixed anode feed of 2:1 (water : methanol) and temperatures of 150, 170, 190 & 200 °C they observed cell potentials of 0.42, 0.44, 0.47 & 0.51V, respectively at a current density 100 mA cm^{-2} with pure oxygen. They also observed increase in cell potential (performance) from 0.45 to 0.5 to 0.55 V at current density of 100 mA cm^{-2} when the methanol mole ratio in the anode feed was decreased from 1:1 to1: 2 to1: 4, (methanol: water) respectively at 200 °C with pure oxygen.

This suggests that PBI based DMFCs has inferior performance to that of Nafion at similar catalyst loading, even though PBI based DMFCs operates at higher temperatures than those based on Nafion.

5.3 Experimental

MEA's (9 cm^2 geometry) were fabricated using 1 mgPt cm-2 60% wt Pt-Ru alloy 1:1 a/o supported on Vulcan XC-72R (ETEK) as anode electro-catalyst and 0.5 mgPt cm-2 30% and 50 % wt Pt/C as cathode electro-catalyst (ETEK). A 1.0 or 2.0 M methanol solutions (in DI-water) was pumped, using a valve-less piston head pump head (Masterflex, U.S.A) through home-made vaporizer heated to the desired temperature. The vapour was then fed to the anode of the cell held at the studied temperature. Methanol solutions of 1 and 2 M corresponded to a volumetric concentration in the vapour of 1.88 and 3.92% vol, respectively. Polarisation curves were recorded manually by holding the specific current density for two minutes until a stable voltage was obtained. The other cell detailes are given in Chapter 4 (same testing cell).

5.4 Results and discussion

5.4.1 Temperature effect on performance

Higher open circuit potentials around 800 mV have been observed with PBI fuel cells compared to those of 650 mV with Nafion 117 with pure oxygen and similar methanol concentration feed [18]. This indicates that lower cross-over rate occurred through the PBI membrane leading to higher cathode potentials.

Polarization curves were recorded at different operating temperatures (120, 150 & 175 °C) and with oxygen and air at the cathode (30% Pt/C). Figure 5-1 shows polarization curves using ~2 %vol MeOH in the vapour phase (1.0 M solution). The PBI loadings were 0.35 (6 PRU) and 0.55 mg cm^{-2} (6 PRU), in the anode and cathode, respectively. The difference in voltages with air and oxygen was similar at all temperatures, ca.72 mV starting from OCP, which suggests that there were no mass transport limitations at the cathode in the operating current density range. This was expected as the same cathodes operated at very high current densities using hydrogen as fuel (limiting current of 1.5 A cm^{-2} with air at 150 °C). Similarly, no major mass transport limitations were expected at the anode due to the high operating temperature, and low operating current densities (the electrode is under kinetic control).

In contrast to the theoretical behaviour the open circuit voltage decreased as the methanol concentration increased or temperature decreased due to the fact that the PEM is permeable to protons, water and methanol. Consequently, there was a crossover flux of methanol from the anode to the cathode; which is a major reason why the observed (rest) cell voltages were lower than the theoretical estimated potential. Higher methanol concentrations will increase the rate of methanol diffusion across the membrane and thus, under steady state conditions, higher concentrations of methanol are present at the cathode. Higher methanol concentrations at the cathode will increase the cathode polarisation due to the mixed potential caused by methanol oxidation.

Increasing the operating temperature was expected to enhance both anode and cathode kinetics, due to increased exchange current density. This was reflected by a shift in the polarisation curves towards lower over-potentials, without apparent changes in the slopes of the polarisation curves. Increasing temperature should lead to better CO (adsorbed) tolerance and therefore better methanol tolerance at the cathode. Increasing oxygen concentration in the cathode (from air to oxygen) will enhance the oxygen reduction reaction activity and help CO removal (oxidize it) and therefore the mixed potential in the cathode and consequently the observed open circuit will increase. These factors are also accompanied by thermodynamic effect of oxygen concentration (Nernst equation). This is clearly reflected in the open circuit voltage values at different oxidant concentrations and temperatures shown in Table 5-3.

Table 5-3. Open circuit voltage of ~2%vol (1.0 M) MeOH and air or oxygen as oxidant.

	120 °C	**150 °C**	**175 °C**
Air PBI (5PRU)	692 mV	704 mV	712 mV
Oxygen PBI (5PRU)	768 mV	778 mV	785 mV
E_{rev} Air (Nernst)	1.07 mV	1.06 mV	1.05 mV
E_{rev} Oxygen (Nernst)	1.10 mV	1.09 mV	1.08 mV
	50 °C	**75 °C**	**90 °C**
Air Nafion 117 [18]	532 mV	555 mV	616 mV
Oxygen Nafion 117[18]	620 mV	642 mV	675 mV
E_{rev} Air (Nernst)	1.13 mV	1.11 mV	1.08 mV
E_{rev} Oxygen (Nernst)	1.15 mV	1.13 mV	1.11 mV

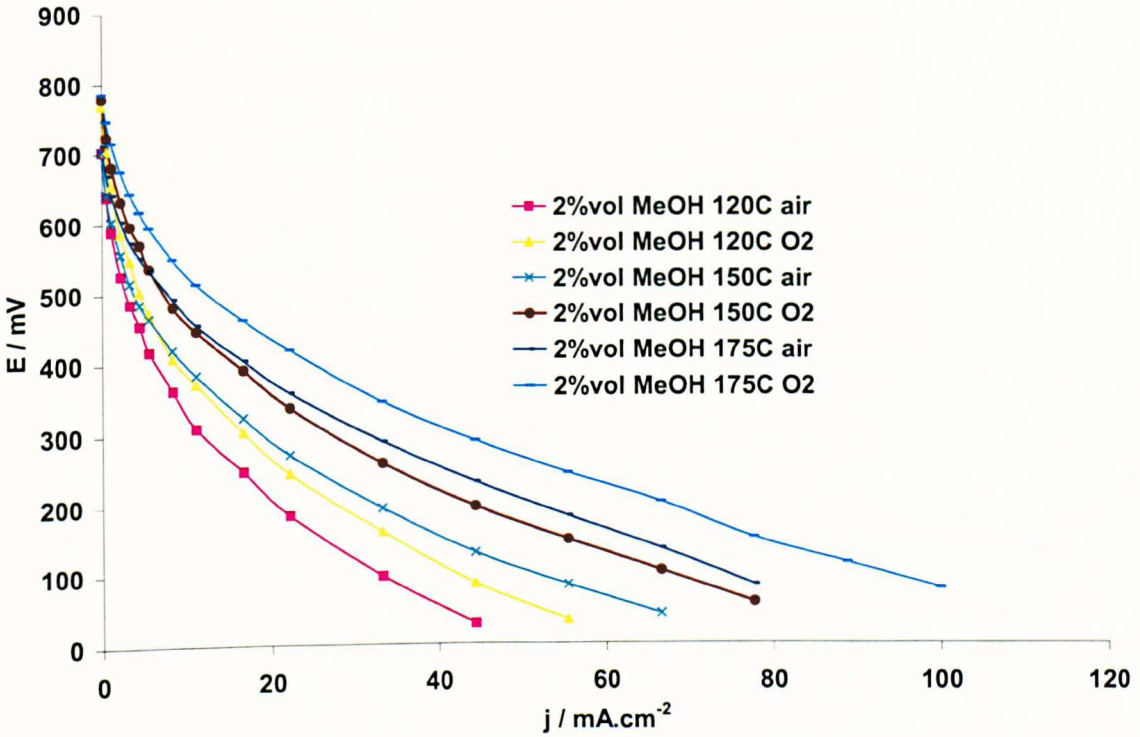

Figure 5-1. HT-DMFC operating at temperatures of 120, 150 & 175 °C with oxygen and air with loadings of 1/0.5 mg cm^{-2} Pt-Ru/Pt for anode/cathode, respectively.

5.4.2 Methanol feed concentration

Figure 5-2 shows the DMFC performance using ~4% vol methanol feed. The performance generally is lower than that achieved with a 2% methanol vapour. The difference in performance with air and oxygen increased as temperature increased. The difference was also larger in the case of ~4% methanol feed in comparison to 2% feed; at a given temperature. Overall, the data indicate that increasing the methanol concentration intensified the effect of methanol crossover on the cathode, especially when a low cathode loading was used (0.5 mg cm^{-2}).

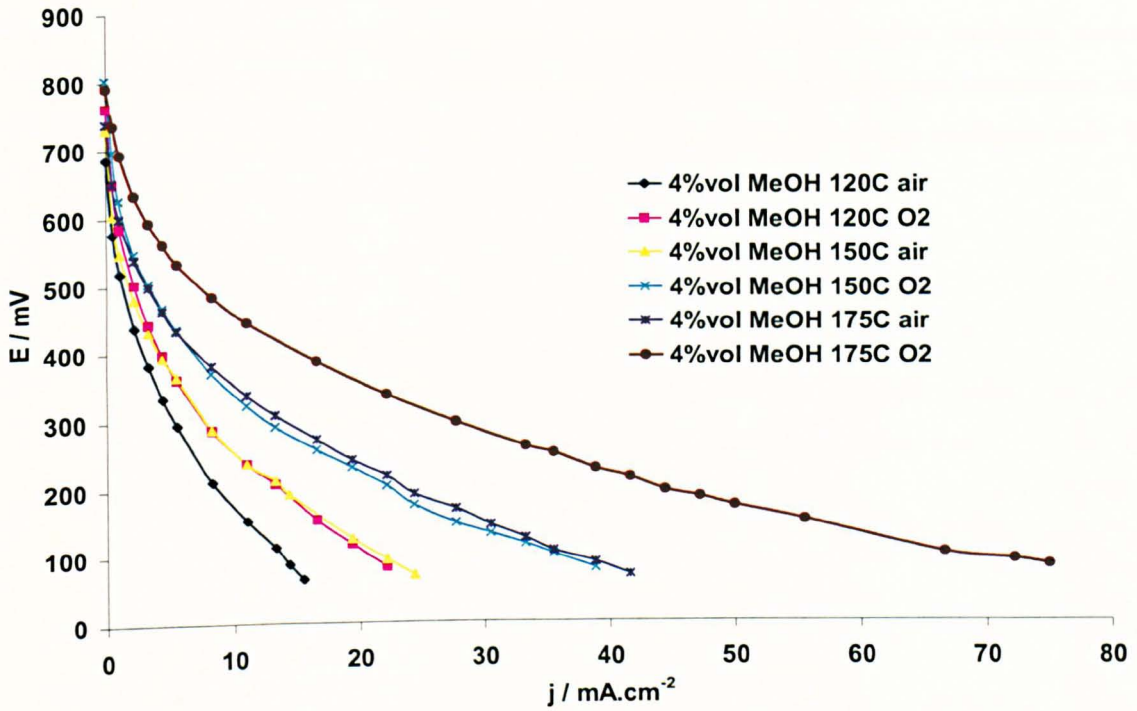

Figure 5-2. HT-DMFC operating at temperatures of 120, 150 & 175 °C with oxygen and air with loadings of 1/0.5 mg cm^{-2} Pt-Ru/Pt for anode/cathode, respectively.

5.4.3 Methanol oxidation in phosphoric acid

Figure 5-3 shows anode polarisation curves measured in the DMFC (vs. DHE) at various temperatures, with a 2% vol methanol feed. The high over-potentials, e.g > 400 mV at 100 mA cm^{-2}, at relatively low current densities, reflect the slow kinetics and low exchange current density of methanol oxidation in hot phosphoric acid (see Fig. 5-6 below).

The activity of methanol oxidation in hot PBI/H_3PO_4 electrolyte was not as high as might be expected, at the elevated operating cell temperature, compared with results obtained at low temperatures with Nafion or H_2SO_4. This slow enhancement of activity with temperature can be caused by strong adsorption of anions from the high concentration of H_3PO_4 and low water activity, which blocks adsorption of water or oxygen species necessary to react with the adsorbed organic species [22]. It has been previously shown that apart from the effect of un-dissociated acid molecules adsorption, the gains in activity arising from the Arrhenius factor (activation

energy) may not exceed losses in activity due to lower water activity in the concentrated acid [23]. While the activation energy of methanol oxidation in phosphoric acid is similar to Nafion and sulphuric acid c.a. 20.9 kJ mole^{-1}, the exchange current density of methanol oxidation in 100 % H_3PO_4 at 190 °C is 1.7×10^{-7} A cm^{-2} [24] this is very low compared to that of Nafion at 90 °C 5×10^{-5} A cm^{-2} [17].

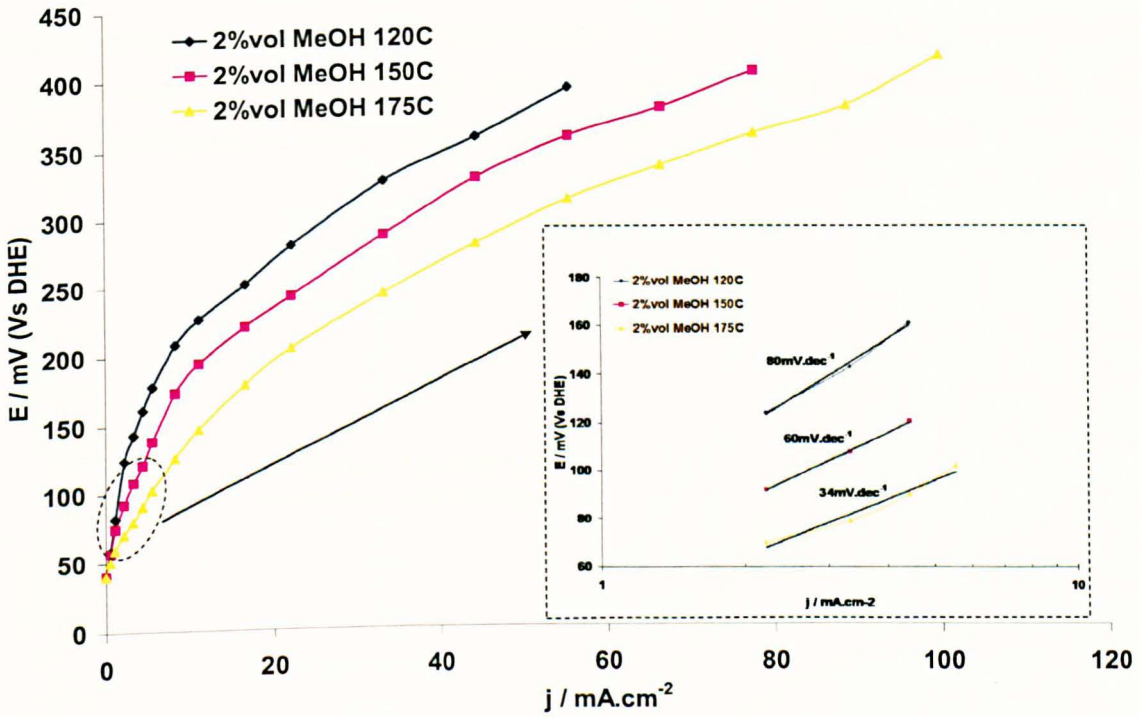

Figure 5-3. Anode performance for methanol oxidation operating at temperatures of 120, 150 & 175 °C using 2% vol MeOH and a loading of 1 mg cm^{-2} Pt-Ru for anode.

5.4.4 Electrolyte effect on methanol oxidation

Because of the observed derogatory influence of phosphoric acid on methanol oxidation the effect of the electrolyte on methanol oxidation was studied. A catalyst loading of 0.02 mg Pt-Ru/C (60%wt Pt:Ru 1:1 a/o) was placed on a glassy carbon tip, a 20 % wt Nafion was used as binder. The potential was swept from -180 mV vs. Ag/AgCl with scan rate of 2 mV s^{-1}. The electrolyte was either 0.5 M sulphuric acid or 0.5 M phosphoric acid.

Figure 5-4 shows the effect of electrolyte on methanol oxidation reaction using Pt-Ru/C 1:1 a/o. The performance decreased dramatically when replacing sulphuric acid with phosphoric acid as electrolyte, even when Nafion was used as the binder. Although at low overpotentials (the beginning of the kinetic region) the performance was similar, at higher current densities there was a large reduction in current with phosphoric acid, which can be related to strong adsorption of phosphate anions [22, 23].

Another observation was that the limiting current value with phosphoric acid was half that for sulphuric acid. This suggests a lower methanol's surface concentration (adsorbed), or lower diffusion coefficient, (or a combination of both) in H_3PO_4 (with respect to H_2SO_4).

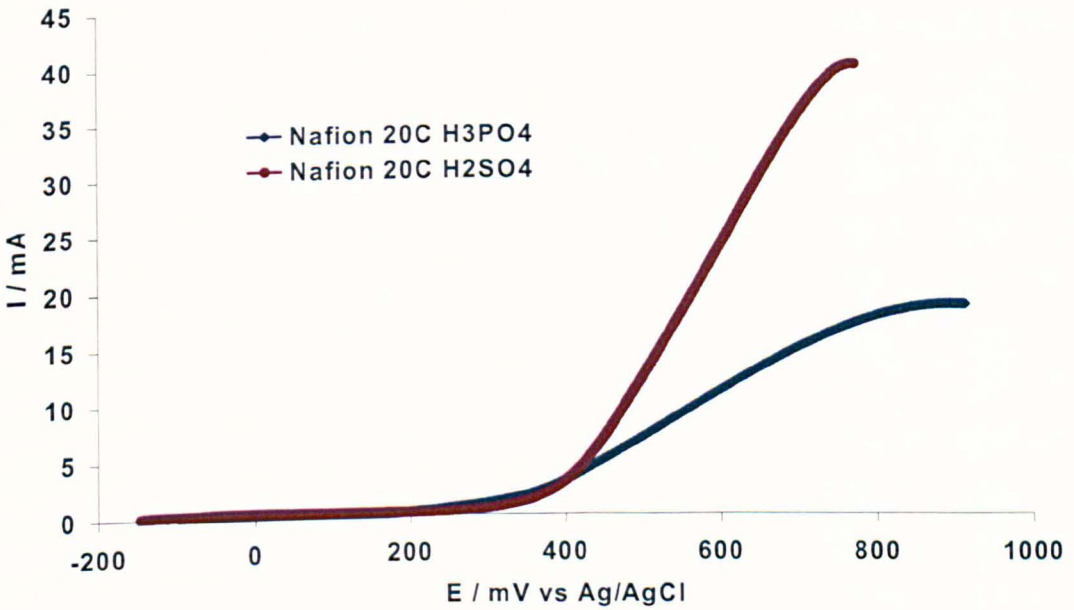

Figure 5-4. Methanol oxidation (1.0 M) at a temperature of 20 °C using 0.5 M sulphuric and 0.5 M phosphoric acids, the catalyst loading was 0.02 mg cm^{-2} Pt-Ru.

Figure 5-5 shows the effects of temperature on methanol oxidation in 0.5 M phosphoric acid, with PBI as a binder. Increasing the temperature lead to enhancement in kinetics due to an increase in the exchange current density i_0. Figure 5-6 shows the Arrhenius plots for methanol

oxidation in PA. The activation energy was calculated from the slope of the plot of Ln (i_0) with respect to 1/T (K^{-1}).

$$\ln i_0 = \frac{-E_a}{RT} + \ln A \qquad [1]$$

where E_a is the activation energy, A is the pre-exponential factor; the slope of the line is give by $-E_a/R$.

The activation energy of methanol oxidation on Pt-Ru (1:1) was 17.7 kJ $mole^{-1}$, which is in close agreement to the value reported in the literature for hot phosphoric acid of 20.9 kJ $mole^{-1}$ [25].

The obtained transfer coefficient for methanol oxidation in phosphoric acid was 0.825 ± 0.01 in the temperature range of 20-80 °C using 1.0 M methanol. This value is in very good agreement with the reported value of 0.832 ± 0.075 in phosphoric acid [24].

Scott et al [18] reported transfer coefficient value of 1.425 ± 0.015 for methanol oxidation at a Nafion interface in the temperature range of 70-95 °C and methanol concentration range of 0.125-1 M. The observed lower value in phosphoric acid was caused by the adsorption of phosphate anions and other impurities from phosphoric acid [22].
Similarly, transfer coefficient values of 0.974, 1.4 & 2.61 were obtained for methanol oxidation on PBI/H_3PO_4 interface (6 PRU) at temperatures of 120, 150 & 175°C, respectively using 2% vol methanol vapour feed. The higher values of α in PBI/H_3PO_4; in comparison to pristine phosphoric acid, were also observed for oxygen reduction, where α decreased with doping level and approached the value in phosphoric acid at high doping levels (>16 PRU). Similarly, an increase in transfer coefficient with temperature was also observed for oxygen reduction, the increase was caused by reduction in phosphate /impurities adsorption with temperature (low heat of adsorption) and other thermodynamic effects (Chapter 3).

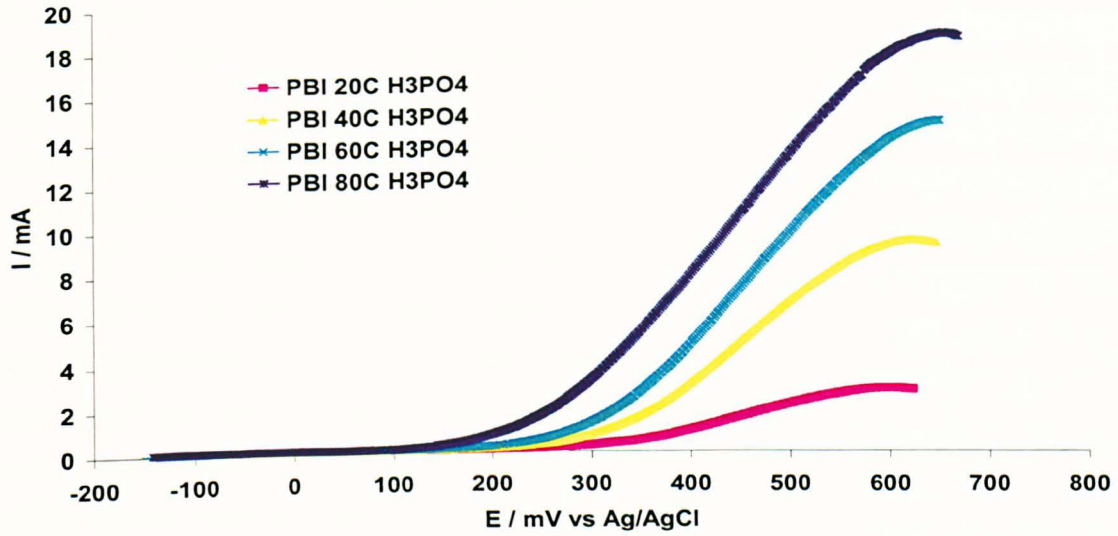

Figure 5-5. Methanol oxidation (1.0 M) at different temperatures using 0.5 M phosphoric acids, the catalyst loading was 0.02 mg cm^{-2} Pt-Ru and 20% wt PBI.

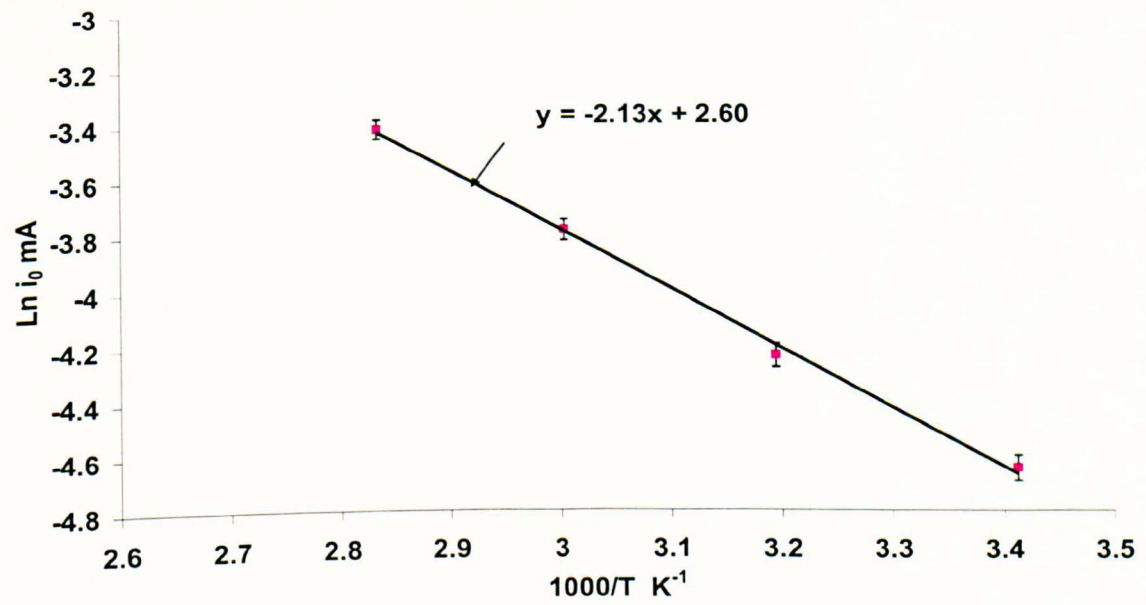

Figure 5-6. Arrhenius plot for 1 M methanol oxidation at different temperatures using 0.5 M phosphoric acids, the catalyst loading was 0.02 mg cm^{-2} Pt-Ru and 20% wt PBI.

5.4.5 Binder effect on methanol oxidation

A study was carried out to investigate the effects of binder in the catalyst layer. The amount of binder was constant at 20 %wt, the electrolyte was 0.5 M H_3PO_4, and the catalyst loading was 0.02 mg cm^{-2} Pt-Ru; similar to that used the previous experiments. Figure 5-7 shows the performance comparison between PBI and Nafion as binder. It is clear that Nafion brought both kinetics and mass transport advantages. The data using Nafion at 20 °C were similar to that for PBI at 50 °C, and the mass transport limiting current using Nafion at 20 °C was similar to that for PBI's at 80 °C. This can be explained by the lower methanol permeability through the PBI thin film in comparison to Nafion. Previous measurements showed methanol permeability of 0.0867×10^{-12} mol cm cm^{-2} s^{-1} atm^{-1} for pristine PBI compared to $2.5\text{-}4.65\times10^{-12}$ mol cm cm^{-2} s^{-1} atm^{-1} for Nafion at room temperature, i.e. a difference of approximately two orders of magnitude. Similar results have been reported for oxygen permeability [26]. However PBI permeability improves dramatically by increasing the doping level [2].

Overall despite the advantages of using Nafion as binder the problem with the material is its limitations as an ionic conductor at temperatures above 80 °C which severely limits its use in HT-PEMFC. What is required is a material that will enhance its water retention at higher temperatures.

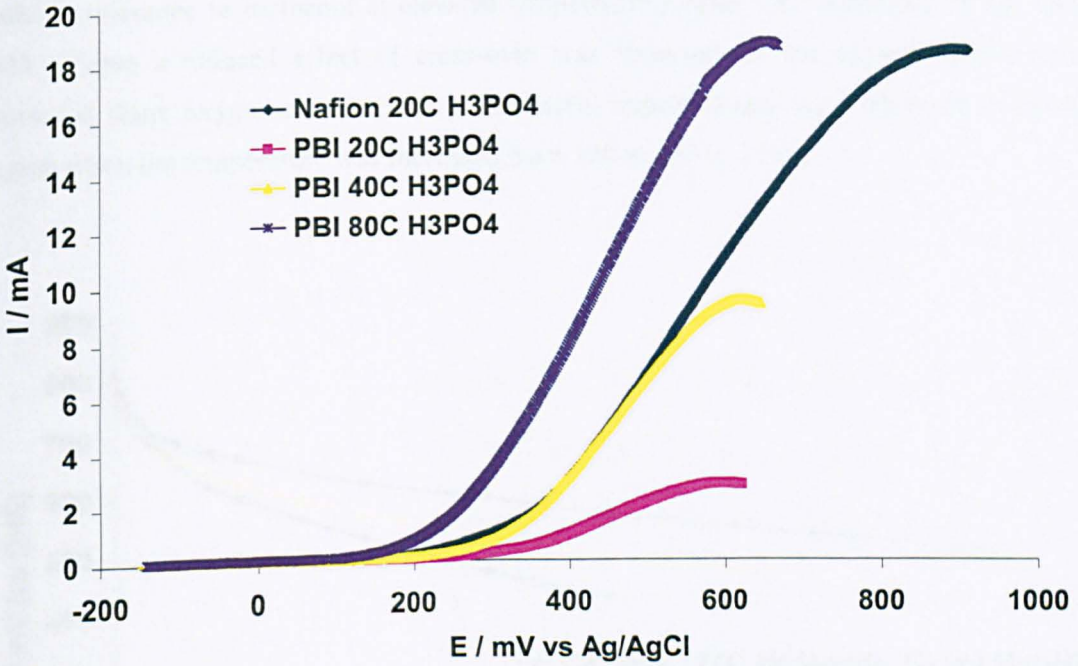

Figure 5-7. Methanol oxidation (1.0 M) comparison between PBI and Nafion as binder at different temperatures using 0.5 M phosphoric acids, catalyst loading was 0.02 mg.cm^{-2} Pt-Ru.

5.4.6 HT-DMFC Cathode performance

In this work a low loading of 0.5 mg cm^{-2} Pt/C was used for the catalyst layer. Figures 5-8 and 5-9 show DMFC cathode performance (vs. DHE) using air and oxygen, respectively, at various temperatures. The voltage loss due to cross over was reflected in the open circuit voltages (vs. DHE) of ca. 880 mV with oxygen and 810 mV with air. These values reflect a low cross over effect due to a low methanol feed concentration, low methanol permeability through PBI and thick cathode layer (30% Pt/C was used).

It can also be highlighted that, when operating with air, cross-over effects were more apparent due to the low oxygen concentration. Only a small gain was observed in the kinetic region when the temperature was increased from 120 to 150 °C; this can be attributed to cross-over effects

countering the effect of temperature on oxygen reduction kinetics. However, increasing the temperature further to 175 °C led to noticeable improvement in kinetics, caused by higher cathode tolerance to methanol at elevated temperature (higher CO tolerance). When operating with oxygen a reduced effect of cross-over was observed, as the oxygen surface coverage increased (high oxygen concentration). Consistent improvements were observed in the kinetic region when the temperature was increased from 120 to 150 to 175 °C.

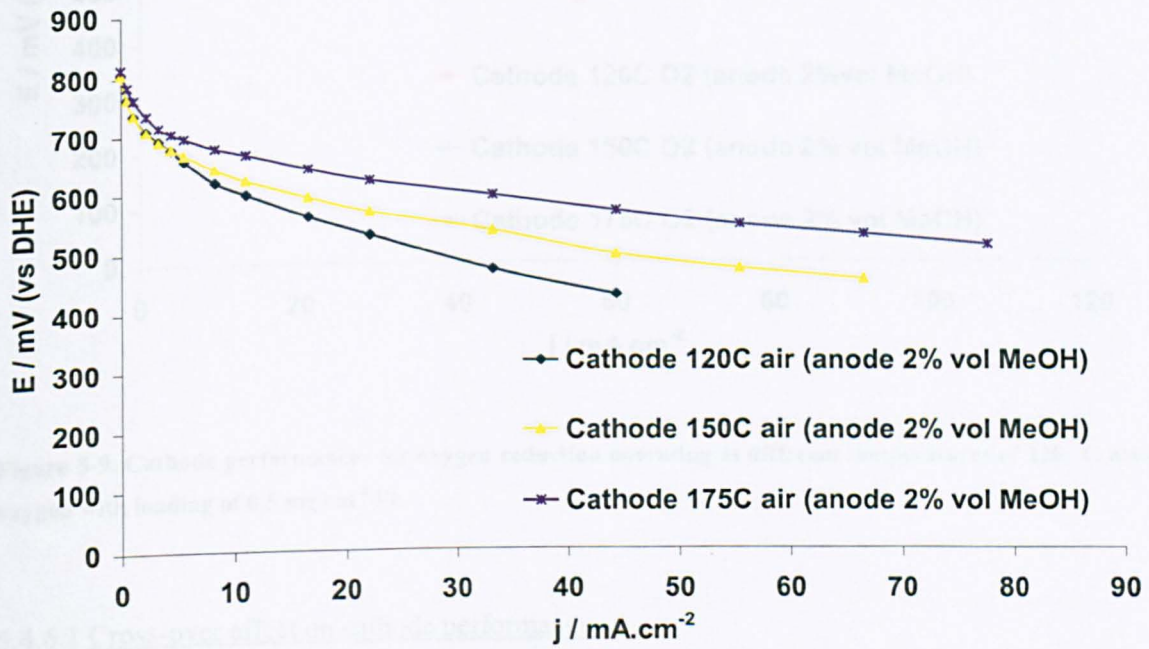

Figure 5-8. Cathode performances for oxygen reduction operating at different temperatures of 120 °C using air with loading of 0.5 mg cm^{-2} Pt.

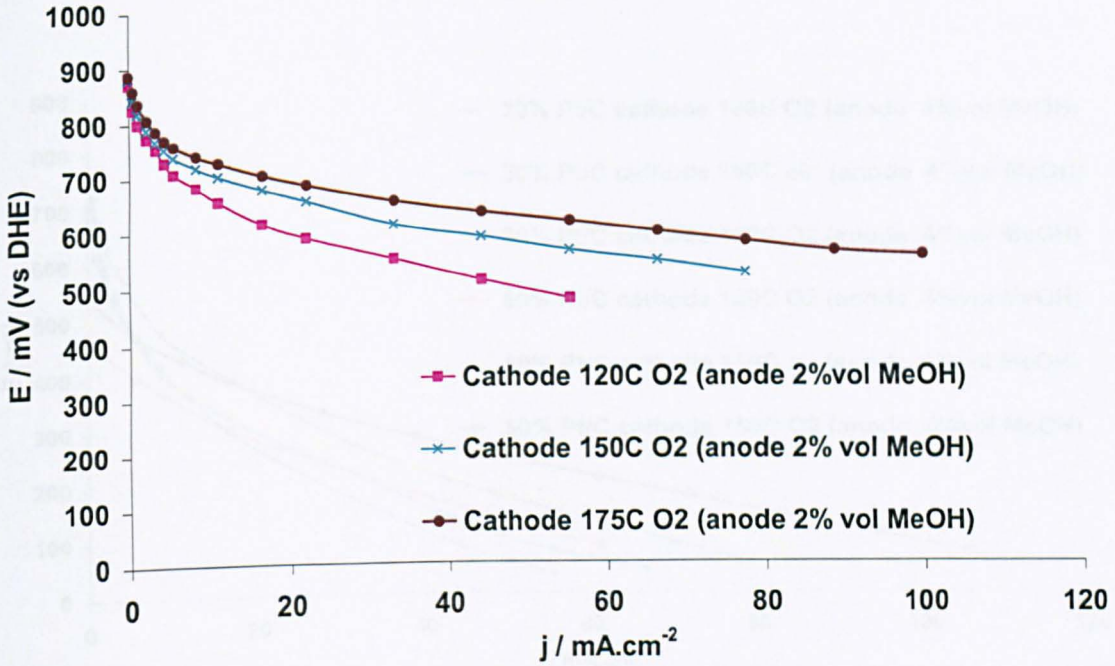

Figure 5-9. Cathode performances for oxygen reduction operating at different temperatures of 120 °C using oxygen with loading of 0.5 mg cm^{-2} Pt.

5.4.6.1 Cross-over effect on cathode performance

The effect of using a 50% Pt/C as catalyst rather than 30% Pt/C was investigates whist keeping the loading at 0.5 mg_{Pt} cm^{-2}, which meant that cathode thickness was more than halved. This ideally should have imposed lower IR drop, lower mass transport, and greater cross-over effects. Figure 5-10 shows the effect using 30% & 50% Pt/C on cell performance with 4 % vol MeOH at various temperatures. Relatively low open circuit potentials were observed with the 50% Pt/C catalyst (540 mV 50% Pt/C compared to 780 mV 30% Pt/C at 150 °C with oxygen) indicating a greater influence from methanol cross-over. Due to the high rate of methanol crossover, the kinetic region was not observed very clearly. At higher current densities, an improvement in the

performance over the 30% Pt/C was observed, due to the higher conductivity through the thinner catalyst layer.

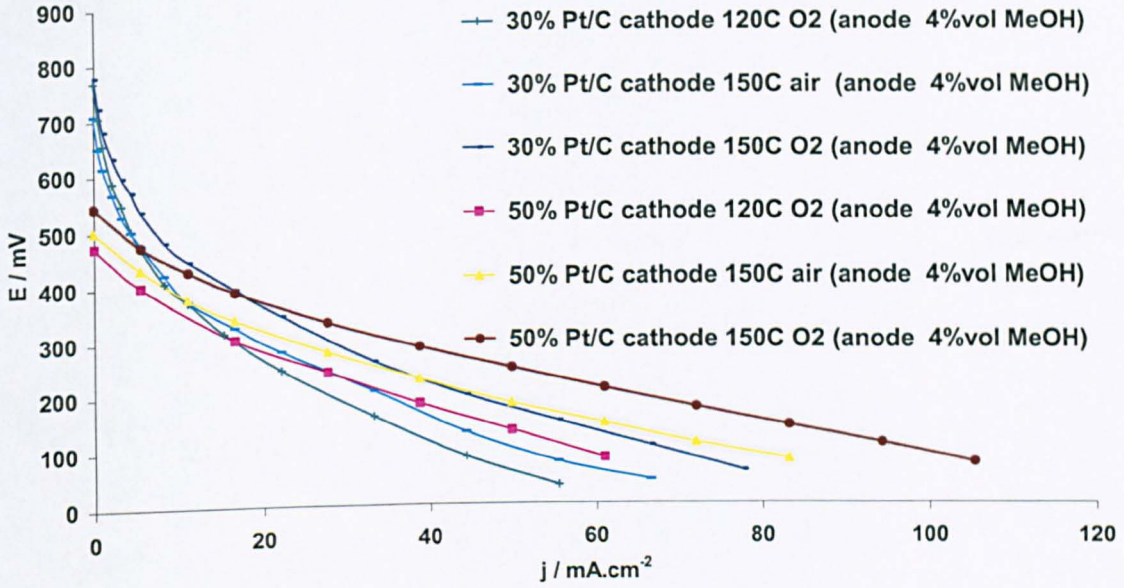

Figure 5-10. HT-DMFC operating with oxygen and air using 30% and 50% Pt/C on the cathode, the catalyst loadings was 1/0.5 mg cm^{-2} Pt-Ru/Pt for anode/cathode.

The cross-over rate was measured by supplying inert gas to the cathode, and oxidizing the crossed over methanol at 1.1 V vs. DHE (Figure 5-11). The limiting current density j_{lim} approached a value of c.a. 17 mA cm^{-2} with the operating conditions of 150 °C and 4% vol methanol. The methanol permeability characteristics can be determined from the limiting current density using the following equation

$$Flux_{methanolcross-over} = \frac{D.C}{\delta} = \frac{j_{\lim}}{nF} \qquad [2]$$

Where the product DC is the methanol permeability through a membrane of thickness δ and F is Faraday constant (96485 C mole^{-1}).

The calculated permeability was 1.47×10^{-12} mol cm cm^{-2} s^{-1} atm^{-1}, and was in close agreement with the reported value in the literature for similar conditions [4]. Similarly, the limiting current density for methanol cross-over of c.a. 17 mA cm^{-2} using a membrane with thickness of 50 μm was comparable to the reported value in the literature of c.a. 10 mA cm^{-2} for a membrane of thickness of 110 μm [4].

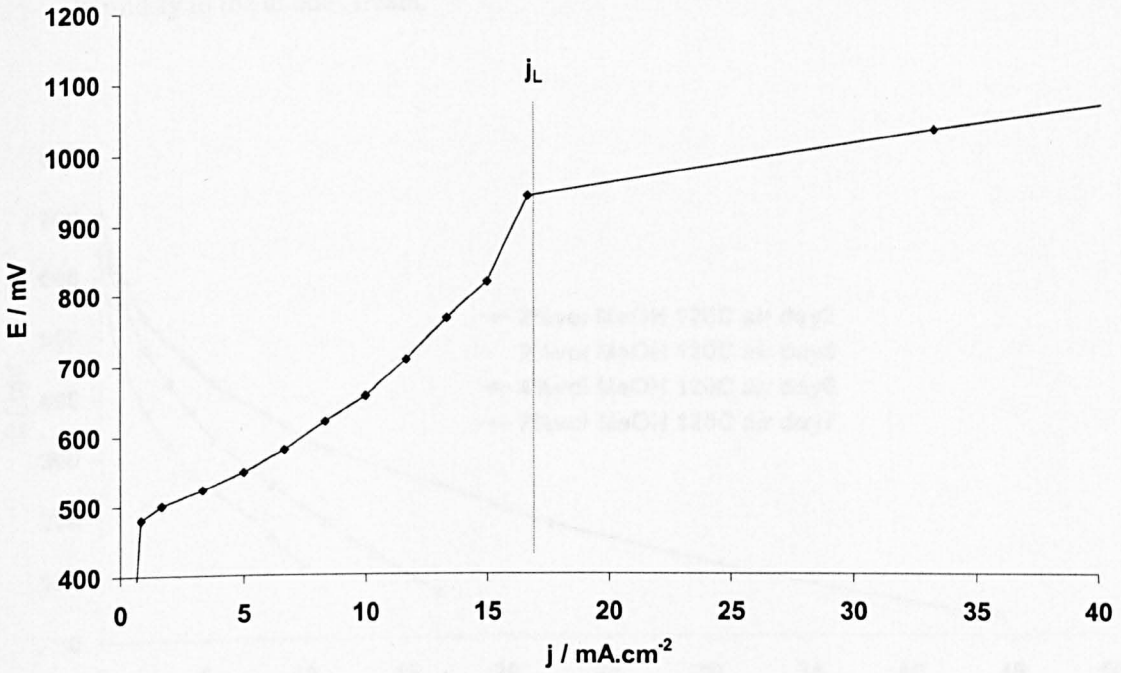

Figure 5-11. Methanol cross-over rate determined by steady-state electro-oxidation of crossed-over methanol and determining the limiting current on the cathode at 150 °C using 4% vol MeOH in the anode.

5.4.7 Performance degradation

A potential limitation for HT-DMFC using phosphoric acid doped polybenzimidazole is the degradation of the performance over time. Similar degradation was observed in phosphoric acid fuel cells [24], and it has been suggested that ruthenium metal dissolves at high temperatures and potentials.

Figure 5-12 shows the typical performance of the HT-DMFC over a week of operation. The system was purged with nitrogen for 10 mins before shutting down everyday (7 hours of

operation each day).The performance fell continuously on a day by day basis and, for example, the current density fell from 37 to 27 to 15 to 10 mA cm^{-2} at 100 mV, on day 2, 4, 6 & 7, respectively, operating at 120 °C using air. The degradation in the performance can be attributed to two main factors:

- Losses of ruthenium and activity of Pt-Ru in phosphoric acid [24].
- Acid losses in the membrane and catalyst layer leads to high IR drop due to very high humidity in the anode stream.

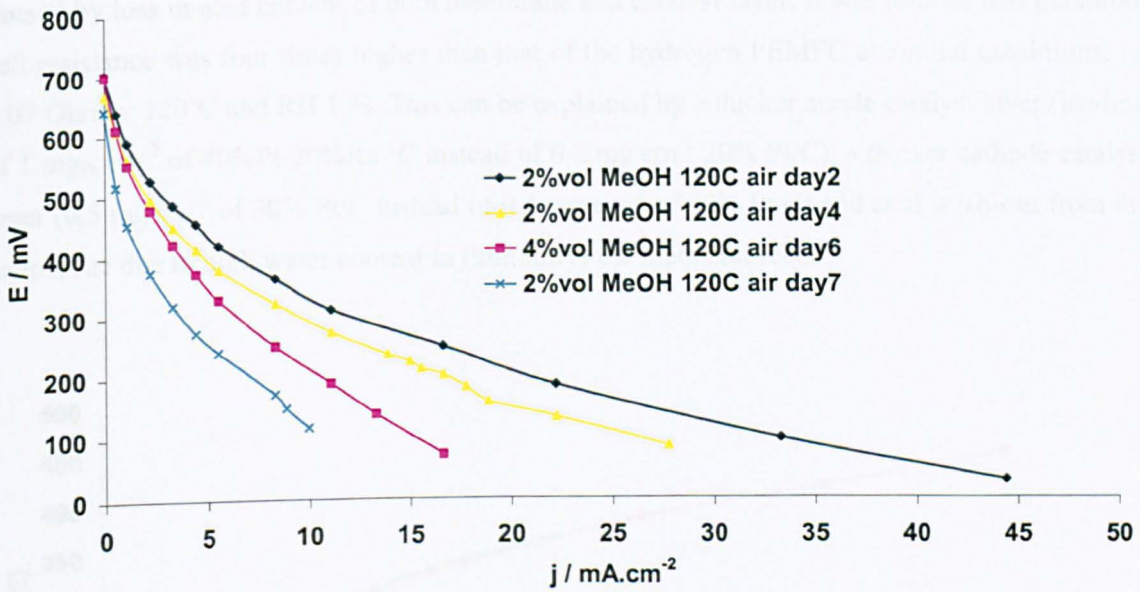

Figure 5-12. Cell performance for methanol oxidation operating at temperature of 120 °C using 2 & 4% vol MeOH and a loading of 1 mg cm^{-2} Pt-Ru for anode over a week of operation.

To identify the cause of the degradation behaviour, the anode performance was recorded (vs. DHE) for a period of one week (data is IR free) and is shown in Figure 5-13. Noticeably anode performance did not change significantly; tending to rule out the assumption of a major loss of performance due to ruthenium dissolution within the one week period. However if a slight Ru loss and consequently migration to the cathode occurred, this may still have a negative impact on oxygen reduction kinetics due to the materials lower ORR activity.

Frequency response analysis was used to measure the cell conductivity at 120 °C and 2 % vol methanol feed over the studied week and the results are summarised in Table 5-4.

Table 5-4. MEA through plane resistance variation over different operating days.

Day	2	4	6
Resistance Ω	0.33	0.63	1.5

A dramatic decrease in the cell conductivity was observed over the week, which was probably caused by loss in acid content of both membrane and catalyst layer. It was noticed that the initial cell resistance was four times higher than that of the hydrogen PEMFC at similar conditions, i.e 0.07 Ohm at 120°C and RH 1 %. This can be explained by a thicker anode catalyst layer (loading of 1 mg_{Pt} cm^{-2} of 40%Pt-20%Ru /C instead of 0.2 mg cm^{-2} 20% Pt/C), a thicker cathode catalyst layer (0.5 mg cm^{-2} of 30% Pt/C instead of 0.4 mg cm^{-2} of 50% Pt/C) and acid wash-out from the membrane due to high water content in (humidity) the methanol feed.

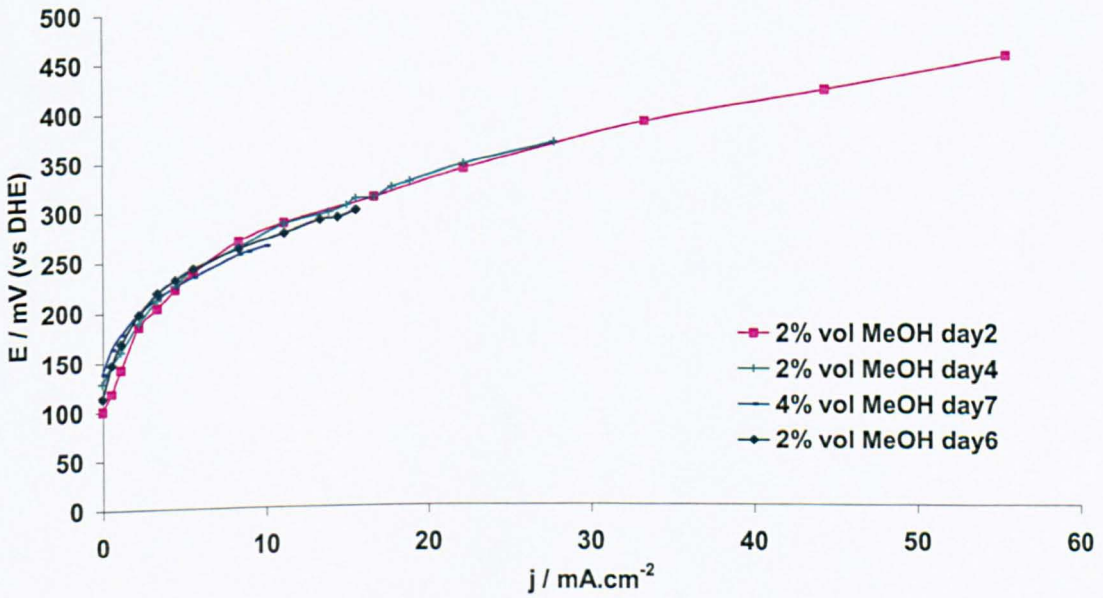

Figure 5-13. Anode performances for methanol oxidation operating at temperature of 120 °C using 2 & 4% vol MeOH and a loading of 1 mg cm^{-2} Pt-Ru for anode over a week of operation.

In addition, the complete shut down of the system might also have caused formation (condensation) of liquid water which enhanced wash out of the acid. Slower performance degradation was observed when the system was kept at a temperature of 120 °C during the shut down of the system (stopping the fuel vapour feed) for a period of three days. However, due to the high water content in the anode feed (2-4% vol methanol feed); loss in phosphoric acid and therefore loss in conductivity and performance still occurred. This was confirmed by the presence of phosphoric acid in the water-methanol condensate from the anode exhaust.

5.5 Conclusions

A vapour feed HT- DMFC was demonstrated with reasonable performance and high open circuit potential arising from low cross-over (permeability) of methanol through the membrane and high CO tolerance at the cathode at elevated temperatures. The cell suffered from high anode polarisation which resulted in significantly lower performance even at higher temperatures than that achievable with low temperature cells using Nafion as the membrane. A major factor is the very poor methanol oxidation kinetics in a phosphoric acid environment.

An improvement in performance may be possible by using a higher methanol concentration to enhance methanol oxidation, which may offset the detrimental effect of increased methanol crossover, The latter effect is further compounded by the fact that only relatively low current densities have been achieved with PBI membranes, although can be partially overcome by using higher catalyst loadings [4, 5, 19-21]. Higher methanol concentrations [5] may also result in higher methanol sorption (kinetics) and lower electro-osmotic drag of water /methanol with protons.

In addition, acid wash out and therefore conductivity loss was a major limitation for HT-DMFC based on phosphoric acid doped PBI.

5.6 References

1. Pivovar, B.S., Y.X. Wang, and E.L. Cussler, *Pervaporation membranes in direct methanol fuel cells.* Journal of Membrane Science, 1999. **154**(2): p. 155-162.
2. Wang, J.T., S. Wasmus, and R.F. Savinell, *Real-time mass spectrometric study of the methanal crossover in a direct methanol fuel cell.* Journal of the Electrochemical Society, 1996. **143**(4): p. 1233-1239.
3. Weng, D., J.S. Wainright, U. Landau, and R.F. Savinell, *Electro-osmotic drag coefficient of water and methanol in polymer electrolytes at elevated temperatures.* Journal of the Electrochemical Society, 1996. **143**(4): p. 1260-1263.
4. Wainright, J.S., J.T. Wang, D. Weng, R.F. Savinell, and M. Litt, *Acid-Doped Polybenzimidazoles - a New Polymer Electrolyte.* Journal of the Electrochemical Society, 1995. **142**(7): p. L121-L123.
5. Wainright, J.S., J.T. Wang, and R.F. Savinell, *Direct methanol fuel cells using acid doped polybenzimidazole as apolymer electrolyte*, in *Energy Conversion Engineering Conference (IECEC) Proceedings of the 31st Intersociety.* 1996, IEEE: Washington, DC, USA. p. 1107-1111.
6. Jones, D.J. and J. Roziere, *Recent advances in the functionalisation of polybenzimidazole and polyetherketone for fuel cell applications.* Journal of Membrane Science, 2001. **185**(1): p. 41-58.
7. Zecevic, S.K., J.S. Wainright, M.H. Litt, S.L. Gojkovic, and R.F. Savinell, *Kinetics of O-2 reduction on a Pt electrode covered with a thin film of solid polymer electrolyte.* Journal of the Electrochemical Society, 1997. **144**(9): p. 2973-2982.
8. Pu, H.T., Q.Z. Liu, and G.H. Liu, *Methanol permeation and proton conductivity of acid-doped poly (N-ethylbenzimidazole) and poly(N-methylbenzimidazole).* Journal of Membrane Science, 2004. **241**(2): p. 169-175.
9. Gaowen, Z. and Z. Zhentao, *Organic/inorganic composite membranes for application in DMFC.* Journal of Membrane Science, 2005. **261**(1-2): p. 107-113.
10. Gil, M., X.L. Ji, X.F. Li, H. Na, J.E. Hampsey, and Y.F. Lu, *Direct synthesis of sulfonated aromatic poly(ether ether ketone) proton exchange membranes for fuel cell applications.* Journal of Membrane Science, 2004. **234**(1-2): p. 75-81.
11. Scott, K. and A.K. Shukla, *Direct Methanol Fuel Cells: Fundamentals, Problems and Perspectives.*, in *Modern aspects of electrochemistry V.40*, R.E. White, Editor. 2007, Springer: New York.
12. Grune, H., G. Kruftand, and M. Waidaus. in *Fuel Cell Seminar pp474-478.* 28 Nov-01 Dec 1994. San Diego, CA, USA.
13. Surampudi, S., S.R. Narayanan, E. Vamos, H. Frank, G. Halpert, A. LaConti, J. Kosek, G.K.S. Prakash, and G.A. Olah, *Advances in direct oxidation methanol fuel cells.* Journal of Power Sources, 1994. **47**(3): p. 377-385.
14. Lim, C., R.G. Allen, and K. Scott, *Effect of dispersion methods of an unsupported Pt-Ru black anode catalyst on the power performance of a direct methanol fuel cell.* Journal of Power Sources, 2006. **161**(1): p. 11-18.
15. Allen, R.G., C. Lim, L.X. Yang, K. Scott, and S. Roy, *Novel anode structure for the direct methanol fuel cell.* Journal of Power Sources, 2005. **143**(1-2): p. 142-149.

16. Shen, M. and K. Scott, *Power loss and its effect on fuel cell performance.* Journal of Power Sources, 2005. **148**: p. 24-31.
17. Shukla, A.K., C.L. Jackson, K. Scott, and R.K. Raman, *An improved-performance liquid-feed solid-polymer-electrolyte direct methanol fuel cell operating at near-ambient conditions.* Electrochimica Acta, 2002. **47**(21): p. 3401-3407.
18. Scott, K., W.M. Taama, P. Argyropoulos, and K. Sundmacher, *The impact of mass transport and methanol crossover on the direct methanol fuel cell.* Journal of Power Sources, 1999. **83**(1-2): p. 204-216.
19. Wainright, J.S., J.T. Wang, R.F. Savinell, M. Litt, H. Moaddel, and C. Rogers. *Acid doped polybenzimidazoles, a new polymer electrolyte.* in *Proc. Electrochem. Soc.* 1994.
20. Wang, J.T., J.S. Wainright, R.F. Savinell, and M. Litt, *A direct methanol fuel cell using acid-doped polybenzimidazole as polymer electrolyte.* Journal of Applied Electrochemistry, 1996. **26**(7): p. 751-756.
21. Wang, J.T., W.F. Lin, M. Weber, S. Wasmus, and R.F. Savinell, *Trimethoxymethane as an alternative fuel for a direct oxidation PBI polymer electrolyte fuel cell.* Electrochimica Acta, 1998. **43**(24): p. 3821-3828.
22. Andrew, M.R., B.D. McNicol, R.T. Short, and J.S. Drury, *Electrolytes for methanol-air fuel cells. I. The performance of methanol electro-oxidation catalysts in sulphuric acid and phosphoric acid electrolytes* Journal of Applied Electrochemistry, 1977. 7(2): p. 153-160.
23. McNICOL, B.D., *ELECTROCATALYTIC PROBLEMS ASSOCIATED WITH THE DEVELOPMENT OF DIRECT METHANOL-AIR FUEL CELLS.* J. Electroanal. Chem., 1981. **118**: p. 71-87.
24. He, C., H.R. Kunz, and J.M. Fenton, *Evaluation of Platinum-Based Catalysts for Methanol Electro-oxidation in Phosphoric Acid Electrolyte.* J. Electrochem. Soc., 1997. **144**(3): p. 970-979.
25. Watanabe, M., Y. Genjima, and K. Turumib, *Direct Methanol Oxidation on Platinum Electrodes with Ruthenium Adatoms in Hot Phosphoric Acid.* J. Electrochem. Soc., 1997. **144**(2): p. 423-428.
26. Ayad, A., J. Bouet, and J.F. Fauvarque, *Comparative study of protonic conducting polymers incorporated in the oxygen electrode of the PEMFC.* Journal of Power Sources, 2005. **149**: p. 66-71.

6 Chronoamperometry and Frequency Response Analysis for HT-PEMFC

6.1 Introduction

It was found earlier that with varying amounts of PBI/ H_3PO_4 /PTFE there was an optimum catalyst thickness that provides a balance between oxygen permeability and proton transfer or on other words, mass transport and accessible ESA (kinetics). This layer was found to be in the range of 40-50% Pt/C with loading of 0.4-0.6 mg_{Pt} cm^{-2}, this is in good agreement with the results reported for PBI/H_3PO_4 system [1].

This chapter contains SEM (scanning electron microscopy) images used to determine the catalyst layer thickness and the results were compared with chronoamperometry data to establish the contribution of mass transport on system performance.

EIS (electrochemical impedance spectroscopy) was also used to provide further information about electrodes structure and effect on the overall cell performance. A simplified circuit model was built and an attempt was made to relate the circuit components to the physical phenomenon taking place at the electrode's surface in terms of kinetics, mass transport and IR losses.

6.2 Catalyst layer thickness

To calculate the average catalyst layer thickness for both anode and cathode electrodes a cross section of the studied MEAs was made by fracturing them, after the tests, in liquid nitrogen and then using the obtained SEM images (Figure 6-1). Analysis was performed using the UTHSCSA Image Tool Kit Tool 3.0 program (University of Texas Health Science Centre at San Antonio, San Antonio, TX) calibrated prior to measurement in micrometers. Sixty measurements were taken from different sections of the fracturedMEAs for each electrode. An average thickness value was obtained accordingly with the standard deviation.

Table (6-1 & 6-2) summarises the results of cathode and anode electrodes, respectively. The estimated thickness was calculated based on the following densities measured at 25 °C:

- PBI 1.34 g cm^{-3} [2].
- PTFE 2.15 g cm^{-3} [3].
- Carbon Vulcan XC-72R 1.8 g cm^{-3} [4] (similar value was considered for advanced carbon support AC01 form Johnson Matthey 40% Pt/C (JM) electrode as no information is available on the density of this carbon).

- Platinum 21.45 g cm^{-3} [5].
- Cobalt 8.92 g cm^{-3} [6].
- Phosphoric acid (88.28-101.6) wt% 1.726-1.8875 g cm^{-3} [7].

The estimated porosity was calculated from the measured and estimated thickness. Phosphoric acid was not considered in the thickness calculations as the acid was added after the fabrication of the catalyst layer. This means that the actual porosity was lower than the value reported due to acid filling some of the available void space. The acid added to the anode layer was 2-4 mg cm^{-2} corresponding to 1.06 to 2.32 μm thickness (similar amounts for cathode layer will be considered in the analysis for mobile acid from the membrane).

The following observations on the electrodes can be made:

- The best performance anode and cathodes had a thickness c.a. 10 μm, in agreement with the reported 10 μm optimum thickness for PAFCs [8].
- In-situ measured membrane thickness was in the range of (39.34 ± 6.16 μm), while the pristine membrane was 40 μm thick and the doped membrane thickness was in the range of 55-60 μm. During hot pressing the membrane was compressed to an average measured thickness of (~ 40 μm): this confirms that some of the acid in polymer matrix had to move away to the catalyst layer due to compression. The non-uniformity in the catalyst layer thickness leads to non-uniformity in the membrane thickness after compression reflecting high value of standard deviation (STDEV) in the membrane thickness measurement (± 6.16 μm).
- The non-uniformity (STDEV) in the catalyst layer increased with increase in catalyst layer thickness and carbon to metal ratio. This can be explained by the fact that the stability of the aqueous based catalyst ink dispersions was deteriorating by increasing carbon content in the ink. Carbon dispersion depends on the carbon surface pre-treatment (oxygenated group on the surface), however generally it was easy to disperse carbon in ethanol or water : ethanol (1:1 v/v) inks. On the other hand initial, PTFE dispersions used to prepare the catalyst inks were aqueous based due to hydrophobic properties of PTFE. Therefore ethanol addition will lead to agglomeration in the PTFE dispersion (ethanol wets PTFE surface). For PBI based anode electrodes (no PTFE) non aqueous inks were used (DMAc/acetone) reflecting small STDEV value and low porosity.

- The porosity increased with increasing PTFE content at fixed Pt:C ratio. PBI based electrodes had much lower porosities than those of PTFE electrodes. For similar PTFE and PBI content, PBI electrodes were expected to be thicker (PTFE have bigger density than PBI) and have lower porosity, therefore poorer mass transport behaviour.
- Anodes with 10% PTFE had an average porosity of ~ 55% compared to ~ 35% for anodes with 5% PBI. The porosity fell to 43.6% for PTFE electrode and ~10% for PBI electrodes when loading of 4 mg cm^{-2} of phosphoric acid were considered.
- Considering the same quantity of acid for the cathode meant that, for 60, 50, 40 & 30% Pt/C (0.4 mg_{Pt} cm^{-2}) electrodes, the acid volume fractions (with no porosity) were 62, 47, 35 & 24% v/v, respectively. On the other hand, taking an average porosity of 50 % for the mentioned electrodes or corresponding thickness of 7.48, 9.78, 13.24 & 19.02 μm, acid addition will lead to drop in porosity to 19, 26.3, 32.5 & 37.8% for 60, 50, 40 & 30 % Pt/C electrodes, respectively. Considering Fick's law for diffusion with a Bruggeman correlation for a porous structure:

$$N_{O_2} = \frac{-D_{O_2}\varepsilon^{\tau}(C_{Pt} - C_{Channel})}{\delta} \qquad [1]$$

Where ε is the porosity, τ is the tortuosity and δ is the diffusion layer thickness.

The average oxygen concentration in the catalyst layer C_{Pt} at a given current density (or oxygen flux N_{O2}) is inversely proportional to the ratio ($\varepsilon^{\tau}/\delta$). The values of ($\varepsilon^{\tau}/\delta$), taking τ as 1.5 [9] and using the values quoted above for porosity and thickness, were 110.6, 137.7, 139.8 & 122.2 cm^{-1} for 60, 50, 40 & 30% Pt/C electrodes with 4 mg cm^{-2} acid, respectively.

It can be concluded that electrodes fabricated with 40-50% Pt/C exhibited the highest oxygen concentration in the catalyst layer at a given current density and therefore were expected to exhibit the best performance (IR effects are minimal due to high conductivity of pristine H_3PO_4). Similarly, the 50-40% Pt/C electrode porosity was ~30% (after acid impregnation) with acid volume fraction to Pt+C (without porosity) in the range of 47-35% (50-40% Pt/C). This means that the 50% Pt/C electrode had one third of its structure as voids (oxygen transport or vapour

water removal), one third for catalytic sites and electrical connection (Pt+C) and the last third for proton conduction (acid electrolyte).

As found above the volume fraction of acid electrolyte in the standard anodes (0.2 mg_{Pt} cm^{-2}, 20% Pt/C) & cathode (0.4 mg_{Pt} cm^{-2}, 50% Pt/C), exhibiting similar porosity and thickness (Table 6-1&6-2), was around one third of the catalyst layer, which also agrees with the measured electrode ESA (from UPD) utilisation of 31.55 ± 5.75% & 35.45 ± 5.05% for cathode & anode, respectively. The reported utilisation was with respect to the standard catalyst ESA measured in half cell using liquid electrolyte reported in Chapter 3 (42.1 & 68.1 m^2 g^{-1} for 50% & 20% Pt/C, respectively).

The 60% Pt/C electrodes exhibited the highest acid volume fraction (to Pt+C) of 62% v/v and the lowest oxygen concentration in the catalyst layer ($\varepsilon^{\tau}/\delta$), therefore its lower performance was due to acid flooding in comparison to 50% Pt/C electrodes. Finally, PBI based electrodes experienced the lowest porosity and smallest thickness (low density), which makes the layer even more critical after acid addition in comparison to PTFE based structures. All the above remarks agree with the observation of the experimental electrode performance (see Chapter 4).

Table 6-1. Cross-section measurements of cathode electrodes fractured in liquid nitrogen.

mg_{Pt} cm^{-2}	M/C (wt %)	Pt:C (wt)	PTFE (wt%)	Theoretical thickness (µm)	Estimated porosity (%)	Average-measured thickness (µm)	Thickness STDEV
0.4	60% Pt	3:2	40%	3.74	57.56	8.8	±2.21
0.4	60%Pt-Ru	1:1	40%	4.98	33.21	7.46	±2.41
0.61	50% Pt	1:1	20%	5.09	40.1	8.5	±1.28
0.4	50% Pt	1:1	40%	4.89	53.12	10.44	±2.05
0.44	50% Pt	1:1	40%	5.38	58.44	12.94	±3.15
0.4(Etek)	40% Pt	2:3	40%	6.62	42.03	11.42	±3.8
0.4(JM)	40% Pt	2:3	40%	6.62	51.89	13.76	±3.24
0.4	30% Pt	3:7	40%	9.51	52.71	20.97	±4.27
0.2	20% Pt	1:4	40%	7.81	37.75	12.27	±2.39
0.19	20%Pt-Co	1:5	40%	7.64	37.61	12.51	±2.57

Table 6-2. Cross-section measurements of anode electrodes fracturedin liquid nitrogen.

20% Pt/C (mg_{Pt} cm^{-2})	PBI (wt %)	Theoretical thickness (µm)	Estimated porosity (%)	Average-measured thickness (µm)	Thickness STDEV
0.22	5%	5.93	34.22	9.02	±2.01
0.22	5%	5.93	36.54	9.35	±2
20% Pt/C (mg_{Pt} cm^{-2})	**PTFE (wt %)**	**Theoretical thickness (µm)**	**Estimated porosity (%)**	**Average-measured thickness (µm)**	**Thickness STDEV**
0.183	10%	4.63	50.51	10.16	±4.54
0.183	10%	4.63	62.57	7.8	±3.5
0.183	10%	4.63	54.63	12.34	±5.48
0.24	10%	6.07	60.77	15.46	±4.35
0.24	10%	6.07	58.63	19.92	±6.06
0.265	10%	6.7	62.52	14.76	±3.78
0.265	10%	6.7	40.71	17.89	±4.74
0.27	20%	7.7	54.48	15.55	±3.39
0.29	20%	8.27	50.51	10.16	±4.54
0.29	20%	8.27	62.57	7.8	±3.5
0.29	20%	8.27	54.63	12.34	±5.48
0.2	40%	7.64	69.55	14.66	±5.13

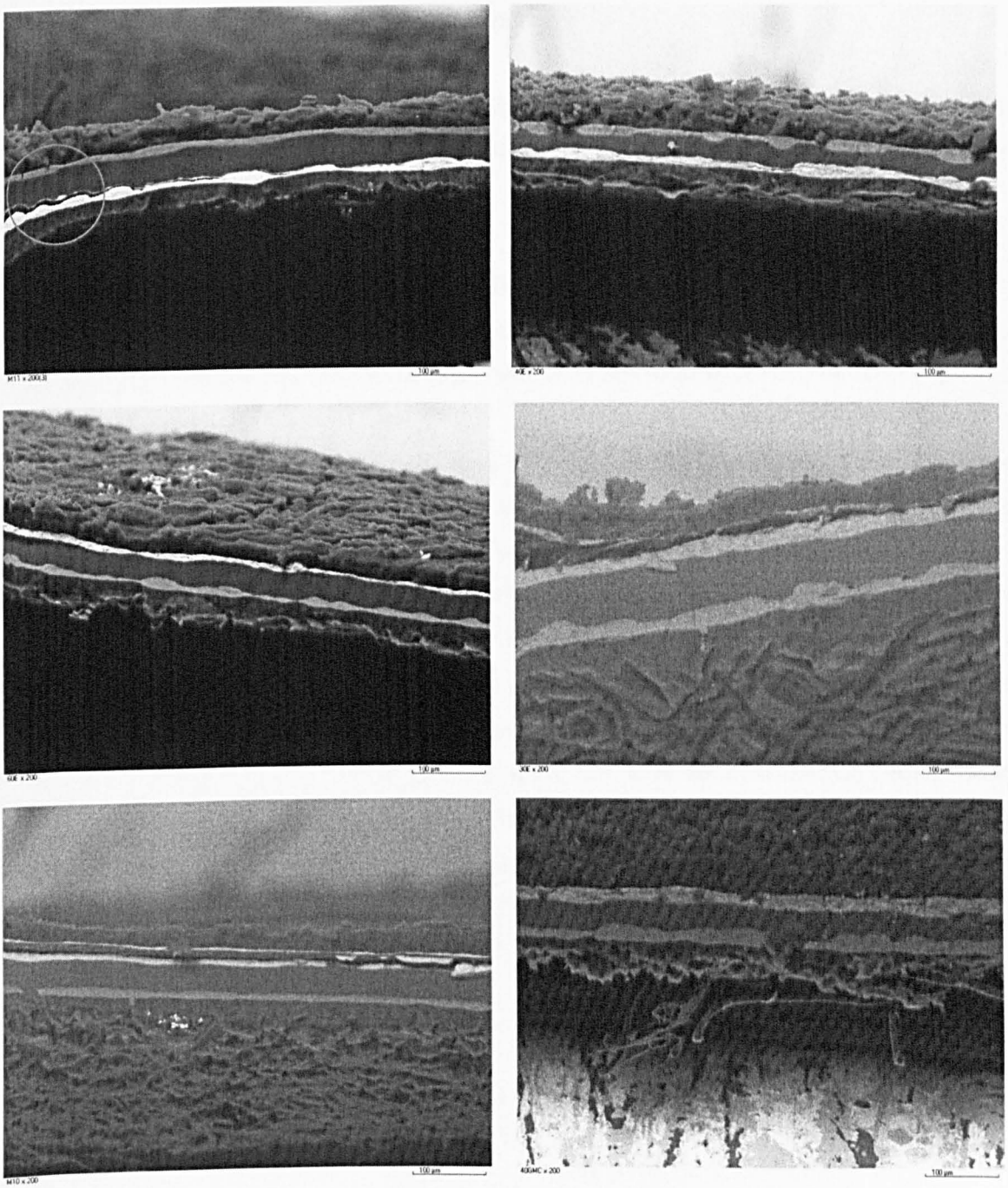

Figure 6-1. Shows SEM cross-sectional images of the liquid nitrogen fractioned MEAs.

6.3 Chronoamperometry and mass transport

Chronoamperometry is an electrochemical technique in which the potential of the working electrode is stepped, and the resulting current from Faradic processes occurring at the electrode is monitored as a function of time.

The double layer capacitance, measured from cyclic voltammetery, were 0.88 & 0.82 Farads for 11.56 cm^2 cathode (0.4 mg_{Pt} cm^{-2} 50% Pt/C) and anode (0.2 mg_{Pt} cm^{-2} 20% Pt/C) respectively, corresponding to an average specific capacity (with reference to catalyst Pt:C) of 71-94 F g^{-1}.

The measured current is the sum of both faradic current and charging current. The current-time transient was recorded at 0.01 sec intervals. To separate Faradic and non-Faradic effects the measurements were considered at time $t \geq 0.8$ s of the step potential. This is justified as follow: The limiting current, a steady state faradic current at t = 60 s and E = 0.02 V, for the studied electrodes varied in the range of 0.4-1.7 A cm^{-2} under various oxygen partial pressures (air, air at 1 bar & air at 2 bar). With geometric area of 9 cm^2 the total current was in the range of 3.6 and 15.3 A. The measured current at 0.8 s for all the studied electrodes -with limiting current range between 1.7 and 1.4 A cm^{-2}- was equal to or below 115 % of the final limiting current value. This lead to maximum faradic current for the studied electrodes of 17.6 A. The potentiostat used was capable of a maximum current of 20 A which leaves us with a minimum of 2.4 A available for the charging double layer current. Considering a potential step of 0.85 V (from OCP to diffusion control potential) and maximum double layer capacitance of 1.78 F (measured for the anode), using the equation below [10]:

$$T_C = \frac{C_{load} \times V_{charge}}{I_{charge}} \qquad [2]$$

Where C_{load} is the capacity of the capacitance to be charged, V_{charge} is the voltage step and I_{charge} is the maximum amount of current available for the charging (or discharging) process. The time to charge the double layer, T_C, will be 0.76 s which is below the minimum chosen value of 0.8 s.

6.3.1 Diffusion in finite and semi-infinite length:

In this section two diffusion cases were considered to explain oxygen diffusion in the electrode:

I. Diffusion in semi-infinite length

II. Diffusion in finite length.

6.3.1.1 Diffusion in semi-infinite length

At a potential where the oxygen reduction is entirely diffusion controlled, we can write for a planer electrode [11]:

$$i(t) = \frac{nFAC_{O_2}\sqrt{D_{O_2}}}{\sqrt{\pi t}} + \frac{nFAD_{O_2}C_{O_2}}{\delta} \qquad [3]$$

Where the first term of the equation is the well know Cottrell equation (from Fick's second law of diffusion) and the second term is the case of Fick's first law of diffusion (equation 1) when the system is running at the steady-state (limiting current) i.e. oxygen surface's concentration C_{Pt} = 0. Chronoamperometry has been commonly used to obtain oxygen mass transport parameters in phosphoric acid and nafion [12-15] from the plots of current vs. inverse of the square root of time. From the slope and intersect (or $CD^{0.5}$ & CD values), respectively, the diffusion coefficient and concentration (solubility) can be obtained.

However, in this work plotting the current from 0.8 to 60 s with the inverse of square root of time did not lead to a straight line. This was not totally un-expected as the Cottrell equation was derived for planar, non-porous structures. Pajkossy et al [16-18] have shown that for porous electrode (rough and partially active) the decay of the diffusion controlled current from an initially homogeneous medium to a completely absorbing fractal boundary, exhibit $t^{-\alpha}$ time-dependence instead of the conventional $t^{-1/2}$ (Cottrell equation) with the exponent α being determined by the fractal dimension, D_F, of the interface as $\alpha = (D_F - 1)/2$ [19]. Where $1 < D_F < 2$ for partially blocked surface or active islands on inactive support. Pajkossy and Nyikos suggested [18] the general form of Cottrell equation:

$$i(t) = \frac{nFAC\sqrt{D}}{\sqrt{\pi}\, t^{\alpha}}\left[\gamma\lambda^2/D\right]^{\alpha-0.5} \qquad [4]$$

Where γ & λ are geometrical factors and the rest symbols have their usual meanings.

It can be seen that Cottrell equation is a special case when $\alpha = 0.5$ for non-porous planar structures.

By plotting log $[i_{(t)}]$ vs log [t] a straight line should be obtained with slope of $-\alpha$ and (at t = 1s) an intercept of log $[\sigma_F]$ (Fig. 9-4, Appendix A), where σ_F is fractal Cottrell coefficient given by [17]:

$$\sigma_F = \frac{nFAC\sqrt{D}}{\sqrt{\pi}}\left[\gamma\lambda^2/D\right]^{\alpha-0.5} \qquad [5]$$

Table 6-3 shows fractal Cottrell coefficient and fractal dimension for 40% Pt/C electrodes; the fractal dimension was around 1.1 and was unaffected by heat treatment. On the other hand the fractal Cottrell coefficient increased slightly with increasing temperature and significantly by increasing oxygen partial pressure or oxygen binary diffusion (changing the inert gas from nitrogen (air) to heleox (80% He- 20% O_2)) while maintaining oxygen partial pressure. This was expected as the fractal Cottrell coefficient is directly proportional to the oxygen concentration and diffusion. This shows that oxygen mass transport to the electrode was not only limited by diffusion through electrolyte thin film, but also through diffusion in the gaseous phase; which cannot be ignored. Additionally, it can be seen (Table 6-3) that the difference in fractal Cottrell coefficient (or observed current) is established at very small time intervals 1 s (or less) between air (Log $[\sigma_F]$ =1.041) and heleox (Log $[\sigma_F]$ = 1.151) even though the initial oxygen partial pressure was the same, suggesting an equilibrium is established quickly in the gaseous phase even at short time intervals due to the fast oxygen diffusion in the porous structure (4.53×10^{-6} & 1.85×10^{-5} m^2 s^{-1} for air and heleox at 175 °C, respectively) in comparison to diffusion through the electrolyte film 10^{-9} m^2 s^{-1} at 175 °C (steady-state current is reached after ~60 s).

Considering steady-state operation at limiting current i_L and using Fick's first law of diffusion we can write equation 6 &7 for oxygen permeability through the thin film electrolyte and the porous gaseous phase, respectively:

$$N_{O_2} = \frac{i_L}{nFA} = \frac{-D_{O_2}(C_{Pt} - C_{Cat})}{\delta} \qquad [6]$$

$$N_{O_2} = \frac{i_L}{nFA} = \frac{-D'_{O_2}\left(P_{Cat} - P_{Channel}\right)}{\delta'} \qquad [7]$$

Where D_{O2}, $D`_{O2}$ are oxygen diffusion coefficient through the thin electrolyte film and porous media, respectively. δ & δ` are diffusion length (thickness) of electrolyte film and porous media, respectively. C_{Pt} is oxygen concentration at the platinum surface (zero for limiting current condition), C_{Cat} is the oxygen concentration or solubility in the polymer electrolyte equilibrated with an oxygen partial pressure in the catalyst layer boundary P_{Cat} where $HC_{Cat} = P_{Cat}$ (H is Henry's constant for oxygen solubility in the electrolyte) and $P_{channel}$ is oxygen partial pressure in the channel (assumed constant under high stoichiometry excess of 2.2).

Considering a planer Pt electrode (roughness factor of 1) i.e. A in equation 6&7 is the same, and by solving equation 7 for P_{cat} and substituting in equation 6, with re-arranging:

$$N_{O_2} = \frac{i_L}{nFA} = \frac{-D'_{O_2} D_{O_2}\left(C_{Pt} - H^{-1} P_{Channel}\right)}{H^{-1} D_{O_2}\delta' + D'_{O_2}\delta} \qquad [8]$$

The obtained equation suggests that the system overall behaviour will still follow Fick's law with an overall diffusion coefficient equal to D_{O2} $D`_{O2}$ and equivalent diffusion length equal to $D_{O2}$ δ + $D`_{O2}$ δ` $H^{-1}$. For $D_{O2} << D`_{O2}$ equation 8 reduces to Eq. 6.

Table 6-3. Fractal Cottrell coefficient and fractal dimension for 40% Pt/C electrodes.

Electrode	T (°C)	P_{O2} (atm)	D_F	Log [σ_F]
40% Pt/C heat treated air	120	0.21-N_2	1.1	0.658
40% Pt/C no heat treatment air	120	0.21-N_2	1.12	1.077
40% Pt/C no heat treatment heleox	120	0.21-He	1.13	1.151
40% Pt/C no heat treatment air 2atm	120	0.42-N_2	1.1	1.226
40% Pt/C no heat treatment air	150	0.21-N_2	1.1	1.072

Although, equation 4 showed a good fit for most of the data, it lacked, in some cases, agreement over the entire time range (0.8-60 s) whilst good agreement was obtained for all the electrodes in the range of 0.8-10 s. This arises from the fact that the Cottrell equation assumes that concentration changes due to potential step (known as Nernst diffusion layer) do not reach the end of the electrolyte layer during the time of the experiment (i.e. $t \rightarrow \infty$, $i \rightarrow 0$) and therefore valid

for very short period of time. The finite length diffusion is not appropriate for the presentation of the studied electrode case where during the experiment the diffusion layer will reach the end of the thin film and equilibrium will be established between gas-electrolyte-electrode (i.e. $t \rightarrow \infty$, $i \rightarrow i_L$).

6.3.1.2 Diffusion in finite length

The Cottrell equation is derived from the solution of Fick's second law of diffusion for one dimensional transport [20]:

$$\frac{\partial C_O(x,t)}{\partial t} = D_O \frac{\partial^2 C_O(x,t)}{\partial x^2} \qquad [9]$$

With boundary conditions for semi-infinite system.

$$C_O(x,0) = C_O^* \qquad [10]$$

$$\lim_{x \to \infty} C_O(x,t) = C_O^* \qquad [11]$$

$$C_O(0,t) = 0 \qquad (\text{for } t > 0) \qquad [12]$$

The first condition (Eq 10) expresses the homogeneity of the solution before applying the potential step. The second condition (Eq 11) states the semi-infinite diffusion condition, i.e. the regions distant from the electrode are unaffected by potential step and therefore have constant concentration equal to the initial concentration. The third condition (Eq 12) expresses the condition at the electrode surface after the potential step (and equal to zero because the system under pure diffusion control).

However, for finite length systems (also known as bonded diffusion) or for diffusion of species through thin films (un-stirred electrolyte) of thickness (L) the Cottrell equation is no longer valid as the boundary conditions change to:

$$C_O(x,0) = C_O^* \qquad 0 \leq x \leq L \qquad [13]$$

$$\frac{\partial C_O(x,t)}{\partial x} = 0 \quad (\text{for } x = L \ \& \ t > 0) \qquad [14]$$

$$C_O(0,t) = 0 \qquad (\text{for } t > 0) \qquad [15]$$

The first condition remains unchanged, restricted to the electrolyte thickness (L), while the second condition expresses no flow of the diffusing substrate beyond the thickness (L) or in other words the phase boundary at x = L is impermeable (reflective boundaries). The third condition remains unchanged. The solution for (Eq. 9) using the above boundary conditions is either a series of error function (or related integrals) which is suitable for small times or a trigonometrical series which converges more satisfactorily at large time values [21, 22] . It has been shown [23] that, by neglecting the higher order terms in error function series and trigonometrical series, the solutions for (Eq. 9) are equations (16&17) respectively:

For short time periods $t << L^2/D$ $$i(t) = \frac{nFAC_{O_2}\sqrt{D_{O_2}}}{\sqrt{\pi t}} + i_L \quad [16]$$

For long time periods $t >> L^2/D$ $$i(t) = \frac{2nFACD_{O_2}}{L}\exp\left(-\frac{\pi^2 D_{O_2} t}{4L^2}\right) + i_L \quad [17]$$

Where i_L is the limiting current obtained as t approach infinity.

Equation 16 is the Cottrell equation which is valid for short periods of time (less than L^2/D) i.e. when the concentration effects of the potential step do not reach the finite length L (infinite diffusion). While Equation 17 is valid for longer periods of time (more than L^2/D) for the finite length diffusion.

Considering diffusion through the electrolyte thin film with D_{O2} for oxygen in (85-98 %wt) phosphoric acid in the range of 10^{-5} cm^2 s^{-1} for temperature range 100-150 °C [12, 14], while L the electrolyte film thickness normally range 0.5-3 nm for nafion [24, 25]. The film thickness L is calculated by:

$$L = \frac{m_{H_3PO_4}}{\rho_{H_3PO_4}(S_C + S_{Pt})} \quad [18]$$

M_{H3PO4} is the mass of acid per unit area, ρ is the acid density and S_c and S_{Pt} is the specific surface area of carbon and Platinum, respectively, per unit area. For acid loading of 2 mg cm^{-2}, the corresponding film thickness for cathode (0.4 mg_{Pt} cm^{-2} 50% Pt/C) and anode (0.2 mg_{Pt} cm^{-2}

20% Pt/C) is 5.4 and 9.1 nm, respectively (assuming uniform distribution and 100% ESA utilization).

This means that $L^2/D = 2.9\times10^{-8}$& 8.3×10^{-8} s for cathode and anode, respectively and suggests that only equation 17 can be used for the studied current transient as L^2/D has an extremely small value.

For diffusion with finite length L with a transmissive boundary i.e. $\partial C_{(L)}/\partial x \neq 0$, the solution of the diffusion equation becomes [26]:

$$i(t) = \frac{nFAC_{O_2}\sqrt{D_{O_2}}}{\tanh\left(\sqrt{\frac{L^2}{D_{O_2}t}}\right)\sqrt{t}} = \frac{nFAC_{O_2}\sqrt{D_{O_2}}}{\sqrt{t}} \frac{\exp\left(\sqrt{\frac{4L^2}{D_{O_2}t}}\right)+1}{\exp\left(\sqrt{\frac{4L^2}{D_{O_2}t}}\right)-1} \qquad [19]$$

For short time periods $t << L^2/D$ $\quad i(t) = \frac{nFAC_{O_2}\sqrt{D_{O_2}}}{\sqrt{t}}$ [20]

For large time periods $t >> L^2/D$ $\quad i(t) = \frac{nFAC_{O_2}D_{O_2}}{L}$ [21]

While equation 20 is the same as the Cottrell equation, equation 21 is the limiting current expression obtained from Fick's first law of diffusion (equation 3 & 6). The solution given by equation 19 should satisfy the observed response, however, it is difficult to extract directly terms that can express the observed exponential dependency on time. The applied large amplitude transients lead to nonlinear, often exponential, responses [27].

Crank [21] has shown that the total amount of diffusing species through unit area of the face x = L of the membrane in time t, Q_t, for a plane electrode covered by membrane with finite length film L is given by a series expression. Taking only the leading terms of this series we can write:

$$Q_t = \frac{D(C_1 - C_2)t}{L} - \frac{2L(C_1 + C_2)}{\pi^2}\left(1 - \exp\left(-\frac{\pi^2 Dt}{L^2}\right)\right) + \frac{4LC_0}{\pi^2}\left(1 - \exp\left(-\frac{\pi^2 Dt}{L^2}\right)\right) \quad [22]$$

Where:

$$\frac{i(t)}{nFA} = \frac{\partial Q_t}{\partial t} \quad [23]$$

Where C_1 & C_2 are the constant (O_2) species concentration at the membrane boundary and electrode boundary, respectively. C_0 is the initial uniform concentration within the membrane. In our case C_0=C_1 & C_2= 0 (diffusion control) & D is the diffusion coefficient of the diffusing species (O_2) through the membrane.

Therefore we can write:

$$\frac{i(t)}{nFA} = \frac{DC_1}{L} - \frac{2D(C_1 - 2C_0)}{L}\exp\left(-\frac{\pi^2 Dt}{L^2}\right) \quad [24]$$

In this special case where $C_0 = C_1$ equation 24 becomes similar to the suggested Eq. 17 [23].

For $t \to \infty$, $i(\infty) \to i_L$ limiting current, we can write:

$$\frac{i(t)}{nFA}_{t\to\infty} = \frac{DC_1}{L} \quad [25]$$

For $t \to 0$ & i(0) we can write:

$$\frac{i(t)}{nFA}_{t\to 0} = \frac{DC_1}{L} + \frac{2DC_1}{L} \quad [26]$$

Equation 24 can be rewritten considering j = i/A:

$$j(t) = j_L + (j_0 - j_L)\exp\left(-\frac{\pi^2 Dt}{L^2}\right) \quad [27]$$

Or

$$j(t) = j_L + K\exp\left(-\frac{t}{\tau}\right) \quad [28]$$

Where K, known as the system gain, is equal to j_0-j_L= 2 $nS_{Pt}FLDC_1$ and τ is the response time constant equal L^2/π^2D. S_{Pt} is the platinum surface area (covered by thin film acid) per electrode unit geometrical area, also known as roughness factor. C_1 is the dissolved oxygen in the electrolyte film, using Henry's law for solubility at temperature T (Kelvin) we can write $P_{O2} = H_TC_0$, for example for 96% wt H_3PO_4, $H_{423} = 2$ m^3 atm $mole^{-1}$ [11] . P_{O2} ((atm), denoted earlier as P_{Cat}) is the oxygen partial pressure at the membrane face boundary at x =L. We can thus write K as:

$$K = 2nFS_{Pt}LDC_1 = 2nS_{Pt}LFDP_{O2}H^{-1} \qquad [29]$$

6.3.2 Transient response time constant

The current transient decayed exponentially with time (Fig. 6-2). The time constant, τ, is obtained from equation 28 where $t = \tau$ for $j(t) = j_L + 0.368K$ and $K = j_0$-j_L (data was extrapolated based on best fit to obtain j_0).

Tables 6-4 & 6-5 summarise the values for K & τ, for various electrodes at 120, 150 & 175 °C and with air, air at 2 atm and heleox (21%O_2-79% He).

Table 6-4. Values of cathode electrodes chronoamperometry response gain K in A cm^{-2}.

	Air (1 atm)			Air (2 atm)			Heleox (1 atm)		
mg_{Pt}-Pt%-mg^*_{H3PO4}	**120C**	**150C**	**175C**	**120C**	**150C**	**175C**	**120C**	**150C**	**175C**
0.4-60%-0	0.22	0.17	0.09	0.29	0.25	0.16	0.30	0.25	0.11
0.6-50%-0†	0.26	0.24	0.15	n/a	n/a	n/a	0.35	0.34	0.17
0.4-50%-0†	0.15	0.14	n/a	n/a	n/a	n/a	0.21	0.18	0.04
0.4-50%-0	0.21	0.20	0.12	0.39	n/a	0.16	0.30	0.25	0.17
0.4-50%-2	0.18	0.07	0.04	n/a	n/a	n/a	0.25	0.13	0.05
0.4-50%-2-F*	n/a	0.12	0.07	n/a	0.18	0.13	n/a	0.19	0.11
0.4-50%0LD*	0.13	0.19	0.077	0.22	0.28	0.158	0.23	0.27	0.096
0.4-40%-0	0.20	0.19	0.09	0.30	0.29	0.16	0.30	0.30	0.15
0.4-40%-0HT*	0.08	0.12	0.06	0.14	0.16	0.12	0.13	0.13	0.08
0.4-40%0JM *	0.06	0.06	0.015	0.09	0.12	0.03	0.12	0.07	0.015

0.4-30%-0HD*	0.21	0.16	0.11	0.45	0.31	0.19	0.24	0.17	0.11
0.4-30%-0	0.31	0.27	0.14	0.41	0.43	0.22	0.42	0.39	0.19
0.2-20%-0	0.16	0.16	n/a	0.29	n/a	n/a	0.24	0.26	n/a
0.2-18%-0-Co*	0.20	0.29	0.13	0.39	0.40	0.26	0.38	0.39	0.15
0.2-16%-0-Ni*	0.25	0.25	0.16	0.43	0.39	0.30	0.39	0.26	0.16

It can be observed (Table 6-5) that the response time constant τ for a given electrode was independent of oxygen partial pressure (dissolved oxygen concentration) and independent of diffusion coefficient in the porous media (same for air and heleox). τ values varied in the range of 2-17 s and decreased with increase in temperature. This confirms that, for a given electrode (or L), τ depended on oxygen diffusion through the thin film only (Eq. 27), where the latter decreases with temperature. For calculated values of L (using equation 18) in the range of 10^{-8} m and time constant values 2-17 s this (τ is equal $L^2/\pi^2 D$) leads to diffusion coefficient (D) values in the range of 0.6-5 $\times$ 10^{-14} cm^2 s^{-1}. By considering diffusion coefficient in thin film electrolyte (phosphoric acid) D ~10^{-5} cm^2 s^{-1} for temperature range 100-150 °C [12, 14] and the previous values for the time constant, we obtain L in the range of 1.4 - 4.1 $\times$ 10^{-4} m. The value is unrealistic as it is an order of magnitude larger than the thickness of the overall catalyst layer and four orders of magnitude larger than the estimated thin film thickness.

Table 6-5. Various cathode electrodes chronoamperometry response time constant τ values in s.

	Air (1 atm)			**Air (2 atm)**			**Heleox (1 atm)**		
mg_{Pt}-Pt%-mg^*_{H3PO4}	**120C**	**150C**	**175C**	**120C**	**150C**	**175C**	**120C**	**150C**	**175C**
0.4-60%-0	6.25	3.58	2.815	5.19	3.08	2.8	6.08	3.39	2.6
0.6-50%-0†	6.31	4.52	4.2	n/a	n/a	n/a	7.48	3.89	4
0.4-50%-0†	7.03	5.73	n/a	n/a	n/a	n/a	9.08	5.77	4.14
0.4-50%-0	4.39	3.88	3.59	4.2	n/a	3.13	4	2.84	2.65
0.4-50%-2	3.19	5.51	4.27	n/a	n/a	n/a	2.45	6.02	3.95
0.4-50%-2-F*	n/a	5.69	4.8	n/a	4.69	4.25	n/a	5.92	4.4
0.4-50%-0LD*	11.5	4.7	3.28	9.65	3.74	2.73	8.14	4.36	2.85

0.4-40%-0	4.44	2.72	2.36	3.68	2.13	2.03	4.4	2.38	2.17
0.4-40%-0HT*	9.01	5.6	3.35	11.5	4.72	2.85	10.3	6.27	3.03
0.4-40%0JM *	10.46	3.76	0.81	13.26	4.72	1.84	9.9	3.4	0.84
0.4-30%-0HD*	10.58	11.73	14.71	6.68	5.84	8.55	10.73	13.03	16.67
0.4-30%-0	9.68	6.02	5.54	8.7	4.61	4.52	10.07	5.7	5.26
0.2-20%-0	7.25	3.37	n/a	8.05	n/a	n/a	7.91	3.16	n/a
0.2-18%-0-Co*	8.66	4.72	5.2	10.7	4.38	3.78	8.41	4.37	4.76
0.2-16%-0-Ni*	12.16	6.67	n/a	13.8	6	7.45	9.73	5.21	n/a

mg_{H3PO4}: amount of added acid loading, †: with 20% PTFE content while rest of the electrode contained 40% wt, F: with added perfluronated surfactant (0.5% wt), LD: low doping membrane (4 PRU), HT: heat treated cathode, JM: Johnson Matthey with advanced carbon support catalyst AC01, HD: high doping membrane (20 PRU), Ni: 20%Pt-Ni/C catalyst & Co: 20%Pt-Co/C catalyst.

As shown in Table 6-4, K decreased with increased temperature and was greater with a greater diffusion coefficient in the porous media and oxygen partial pressure. K should be (Eq. 29) directly proportional to C_1 and D (diffusion in the thin film). However, it is usually less dependant on oxygen diffusion through the porous media, D_{porous}, which will influence slightly P_{O2} and therefore C_1. The observed decrease of K with temperature can be explained by a decrease in solubility C_1 and decrease in diffusion due to increase in phosphoric acid concentration (viscosity) with temperature. However, the product C_1D increased with temperature (at least from 120 to 150 °C) which can be observed from the steady-state limiting current values. It is also expected from equation (25 & 26) that K is equal to twice the limiting current value or j(0) is equal to 3 j(∞) which was not observed experimentally.

The above disagreements between observed and predicted K arise from the fact that equations 24 (or 17), used to derive K, are suitable for long periods of time only and therefore are not suitable to estimate j(0) (at t = 0). Similarly using equation 16, suitable for short periods of time, will lead to unrealistic $j(0) \rightarrow \infty$. Additionally, there are limitations in the solution due to the assumption of constant C_1 during the experiment, whilst in reality C_1 depended on P_{O2} which in turn depended upon j(t) through diffusion in the porous media and diffusion of vapour water product.

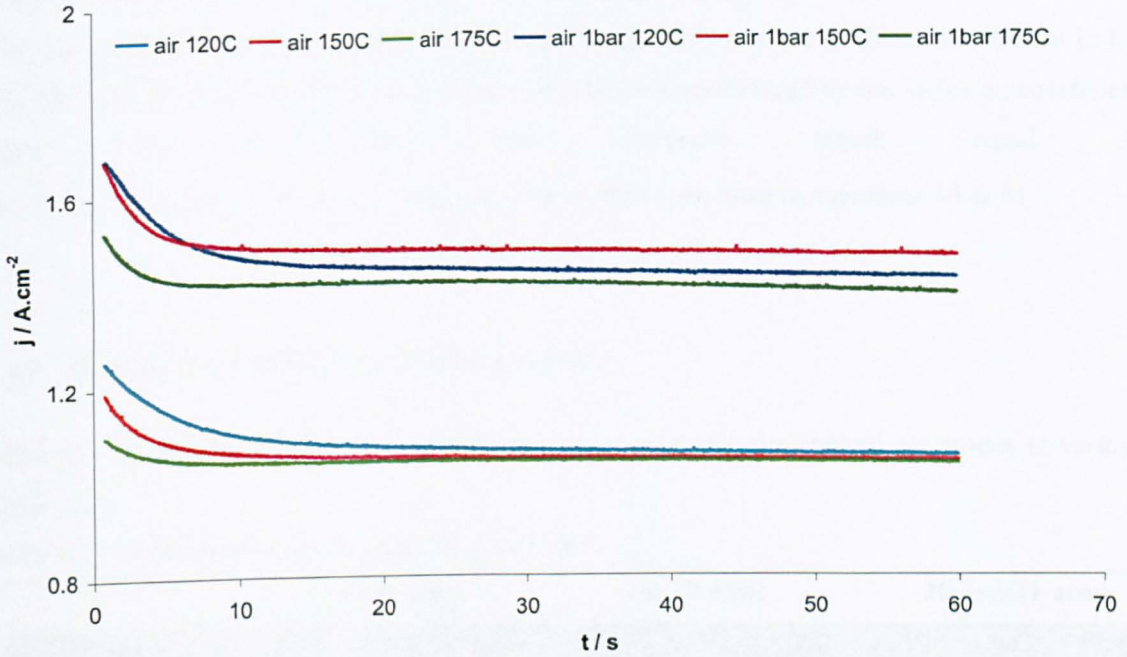

Figure 6-2. Shows typical current-time transient response for MEA utilising 60% Pt/C cathode.

The large deviation between the observed and estimated time constants and consequently between the observed diffusion coefficient values obtained from the transient time constant of $0.6\text{-}5 \times 10^{-14}$ cm^2 s^{-1} and the values obtained from steady-state conditions (limiting current) or the reported values in the literature D $\sim 10^{-5}$ cm^2 s^{-1} can be explained by slow solubility equilibrium between P_{O2} and C_1. As the film was very thin, the diffusion length would have reached the end of the film in a very short period of time and the observed diffusion in the thin film would be limited by how fast oxygen could dissolve in the thin film. This effect can be considered as a diffusion process with coefficient $D_{solubility}$ and how fast dissolved oxygen can diffuse through the thin film. So we can write $D_{observed} = D \times D_{solubility}$ suggesting $D_{solubility} \sim 10^{-9}$ cm^2 s^{-1}. In this analysis it was assumed that S_{Pt} is independent of oxygen concentration and therefore independent of time; however in reality a drop in S_{Pt} is expected with increasing j or decreasing C_1 due to oxygen starvation and therefore S_{Pt} is expected to be function of time and therefore contribute to τ. Additionally, the diffusion of product water out of the thin film was ignored, which was another contribution to τ.

Another explanation for the small observed values of D could be that D and L, used to determine the time constant τ (given in equation 24) are not the explicit oxygen diffusion coefficient in the thin film and the thin film thickness, respectively, but are represented by the diffusion coefficient equal to $D`_{O2}D`_{H2O}D_{O2}$ and diffusion length equal to $D_{O_2}D'_{H_2O}\delta' + D'_{H_2O}D'_{O_2}\varepsilon^{\tau}LH/S_{Pt} + 2D'_{O_2}D_{O_2}\delta'$ as will be seen later in equations 30 & 31.

6.3.3 Oxygen permeability and limiting current

Table 6-6 summarize the observed limiting current values for the studied electrodes at various conditions.

Table 6-6. Cathode limiting current densities, j_L in A cm^{-2}.

	Air (1 atm)			Air (2 atm)			Heleox (1 atm)		
mg_{Pt}-Pt%-mg*$_{H3PO4}$	**120C**	**150C**	**175C**	**120C**	**150C**	**175C**	**120C**	**150C**	**175C**
0.4-60%-0	1.06	1.05	1.04	1.44	1.48	1.40	1.20	1.18	1.17
0.6-50%-0†	1.22	1.32	1.33	n/a	n/a	n/a	1.30	1.51	1.55
0.4-50%-0†	1.03	1.20	n/a	n/a	n/a	n/a	1.20	1.39	1.49
0.4-50%-0	1.19	1.28	1.25	1.54	1.82	1.67	1.43	1.46	1.50
0.4-50%-2	1.13	1.36	1.48	n/a	n/a	n/a	1.34	1.54	1.71
0.4-50%-2-F*	n/a	1.00	1.03	n/a	1.22	1.27	n/a	1.10	1.13
0.4-50%-0LD*	0.57	0.63	0.65	0.87	0.95	0.88	0.60	0.68	0.74
0.4-40%-0	1.13	1.12	1.09	1.65	1.62	1.50	1.31	1.27	1.21
0.4-40%-0HT*	0.42	0.52	0.56	0.69	0.76	0.84	0.46	0.55	0.61
0.4-40%0JM *	0.67	0.70	0.75	0.98	0.98	1.05	0.73	0.78	0.83
0.4-30%-0HD*	0.55	0.87	1.11	0.95	1.36	1.58	0.64	1.02	1.29
0.4-30%-0	0.90	0.87	0.90	1.31	1.35	1.17	0.98	0.97	1.01
0.2-20%-0	0.78	0.75	0.70	1.10	n/a	n/a	0.85	0.83	n/a
0.2-18%-0-Co*	0.63	0.55	0.49	0.94	0.86	0.68	0.62	0.57	0.53
0.2-16%-0-Ni*	0.56	0.42	0.40	0.79	0.68	0.56	0.56	0.45	0.43

Figures 6-3, 6-4 & 6-5 show the limiting current density for non-doped 60, 50, 40, 20, 17 & 15% Pt/C cathodes at different temperatures and oxygen partial pressures. It can be easily concluded that 50% Pt/C electrodes gave the highest limiting current densities at most of the studied conditions apart from a high oxygen concentration (air at 2 atm) and low temperature (120 °C). This directly agrees with the polarisation curves results obtained earlier (Chapter 4) where 50% Pt/C showed the best performance under air operation, while 40% Pt/C showed advantages with pure oxygen at 120 & 150°C.

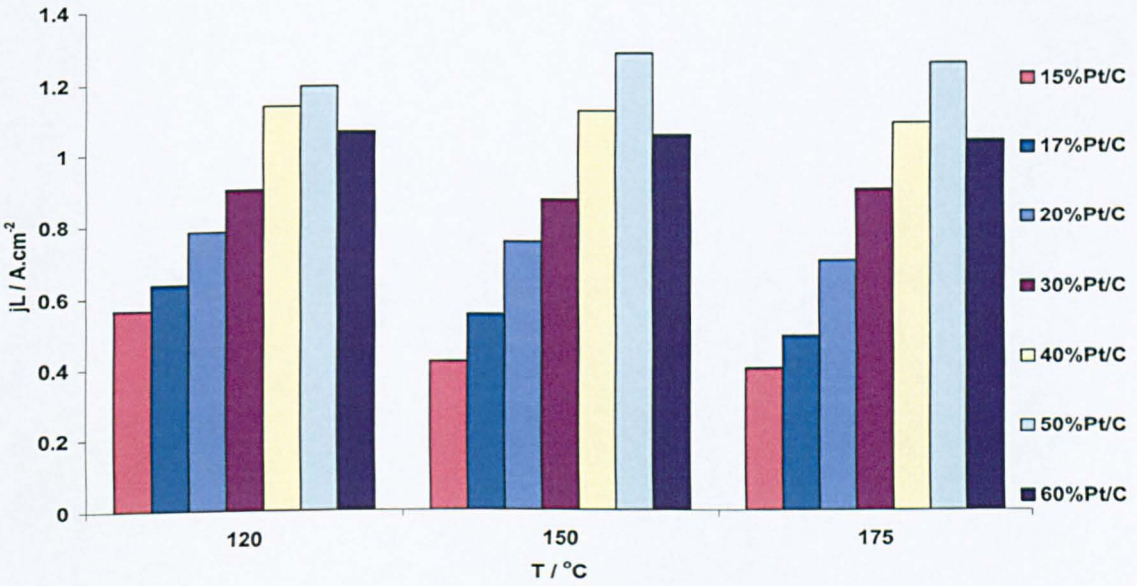

Figure 6-3. Shows the effect of Pt:C ratio or catalyst thickness on the observed limiting current density when operating with air at temperatures of 120, 150 & 175°C.

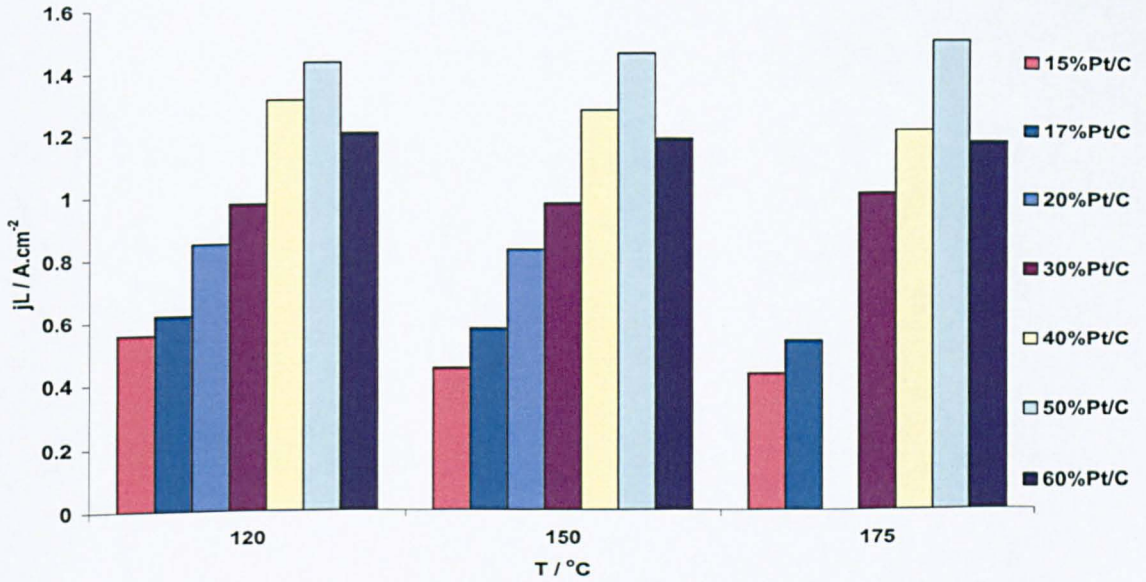

Figure 6-4. Shows the effect of Pt:C ratio or catalyst thickness on the observed limiting current density when operating with heleox at temperatures of 120, 150 & 175°C.

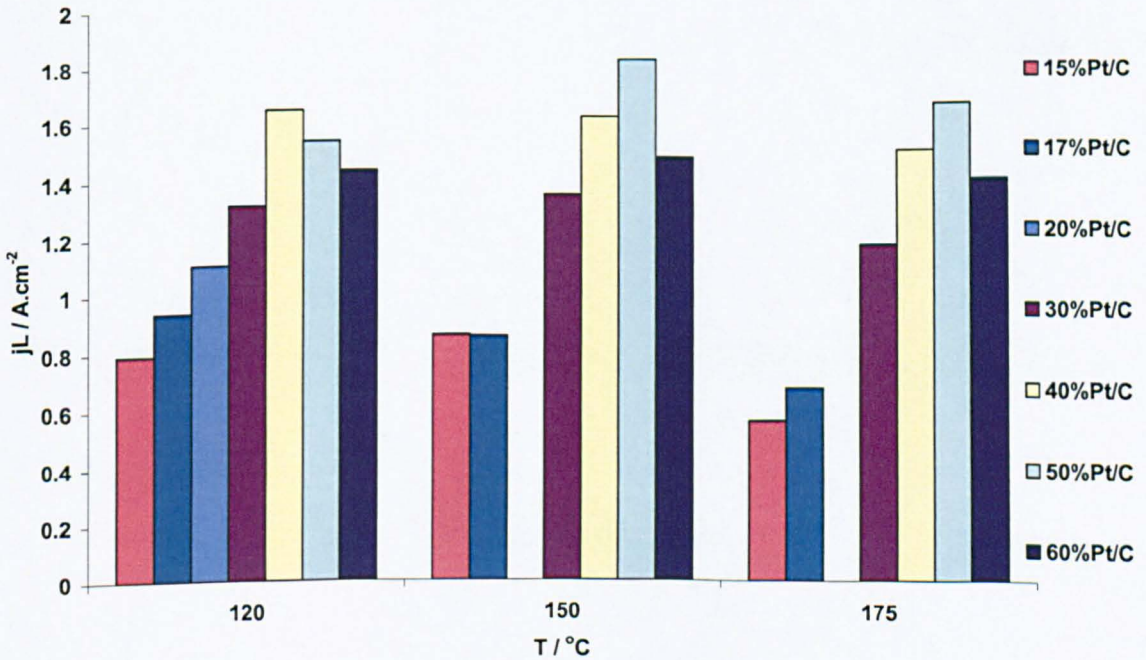

Figure 6-5. Shows the effect of Pt:C ratio or catalyst thickness on the observed limiting current density when operating with air 2 atm at temperatures of 120, 150 & 175 °C.

Figure 6-6 shows the effect of acid content on 30% Pt/C electrodes. The electrode with high acid content was denoted as HD where high doping level membrane of 20 PRU was used in comparison to a standard doping level of 5.6 PRU. Although electrodes contained no added acid the electrode associated with a high doping level membrane should exhibit much higher acid content in the catalyst layer in comparison to the other electrodes. It can be seen that a greater acid content lead to lower limiting current values at 120 °C; however the limiting current increased rapidly with temperature, where it became similar to that with a low acid content at 150 °C and much higher at 175 °C. On the other hand the limiting current of electrodes with low acid content did not vary significantly with temperature or dropped slightly at 175 °C. This can be explained by increases in S_{Pt} and L with increase in acid content: therefore the system became more dependant on D_{O2} and consequently on T.

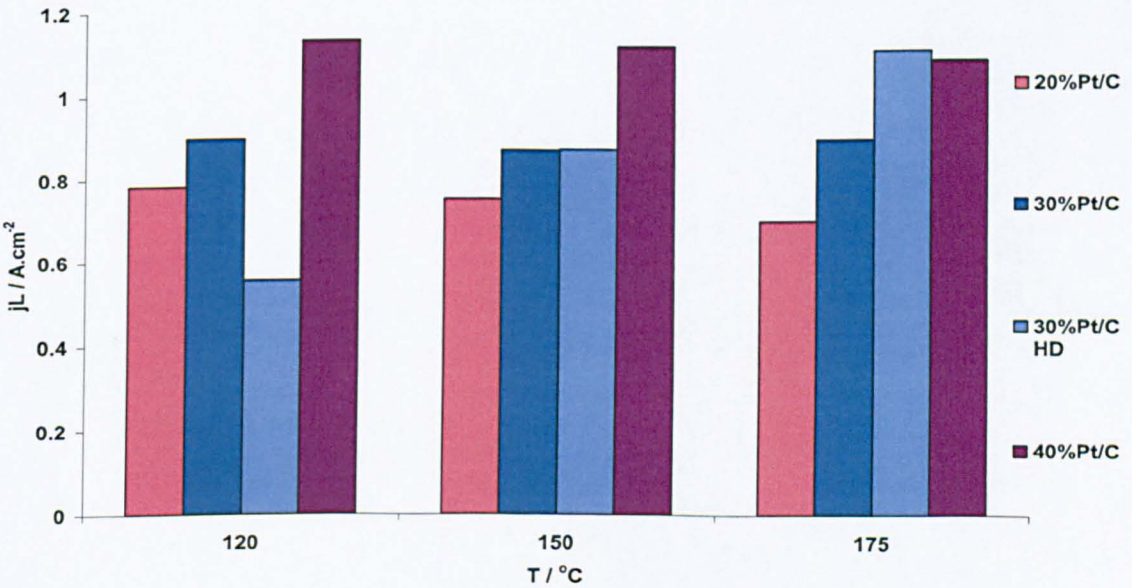

Figure 6-6. Shows the effect of 30% Pt/C electrode's acid content on the observed limiting current density when operating with air at temperatures of 120, 150 & 175 °C.

Figure 6-7 shows the effect of acid content on 50% Pt/C electrodes. The electrode containing low acid content was denoted as LD where a low doping level membrane of 4 PRU was used in comparison to a standard doping level of 5.6 PRU. Although two electrodes contained no added acid and the third one contained added acid (2 mg cm^{-2} with standard doping level membrane),

the electrode associated with low doping level membrane should exhibit much lower acid content in the catalyst layer in comparison to the other electrodes. It can be seen that more acid (2 mg cm^{-2}) lead to lower limiting current values at 120 °C; however the limiting current increased rapidly with temperature where it became higher than that with the standard acid content (0 mg cm^{-2}) at 150 °C and much higher at 175 °C. On the other hand the limiting current of electrodes with low acid content (0 mg cm^{-2} & LD) did not vary significantly with temperature or dropped slightly at 175 °C.

Electrodes with very low acid content (LD) gave very low limiting currents over the entire temperature range, due to very low S_{Pt} as there was a very small amount of mobile acid in the membrane matrix available to move to the catalyst layer and therefore low accessible platinum surface area. This was also reflected in the cell performance where low doping electrodes showed the worst performance. Similarly, standard doping electrode showed advantages over high doping level at high current densities at 120 °C while the case reversed at 150 and 175 °C.

From equation (8) we can write for electrode with platinum surface area S_{Pt}:

$$j_L = \frac{nFS_{Pt}D_{O_2}^{'}D_{O_2}P_{Channel}\varepsilon^{\tau}}{S_{Pt}D_{O_2}\delta^{'} + D_{O_2}^{'}\varepsilon^{\tau}L\,H} \qquad [30]$$

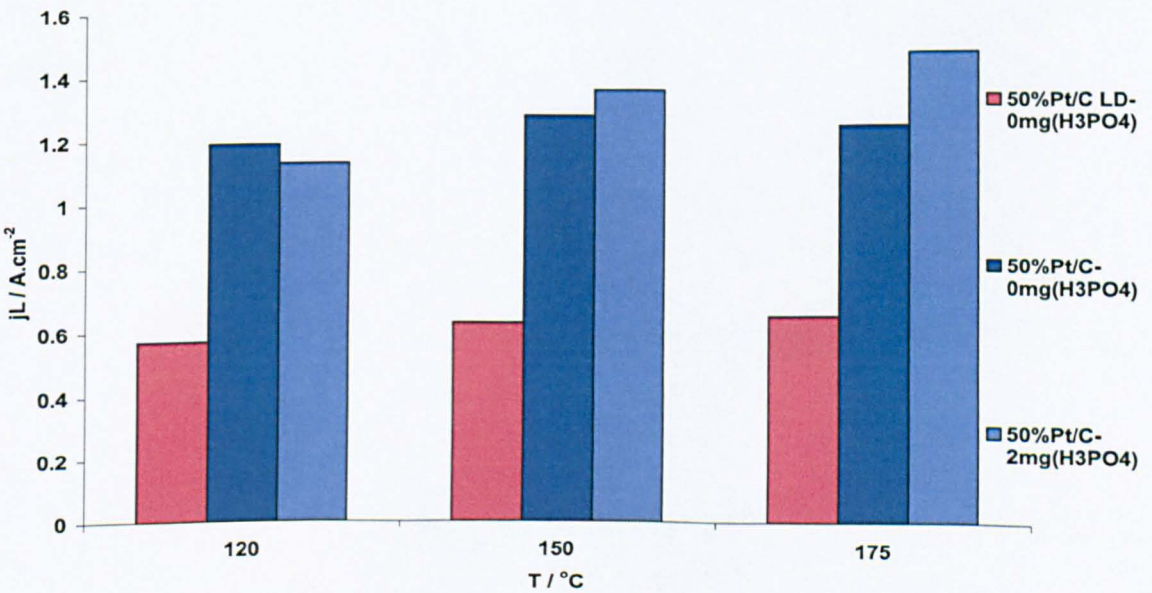

Figure 6-7. The effect of 50% Pt/C electrode's acid content on the observed limiting current density when operating with air at temperatures of 120, 150 & 175 °C. LD denotes membrane with low doping level of 4 PRU.

Figure 6-8 & 6-9 show the effects of electrode hydrophobic properties on the observed limiting current for 40 & 50% Pt/C electrodes, respectively. Increasing the hydrophobicity of the electrode by heat treatment, or by utilising different carbon support (40% Pt/C case), will lead to lower acid content and therefore lower S_{Pt} and accordingly lower limiting current. The lower S_{Pt} will also lead to slower kinetics as seen earlier from the polarisation curves (Chapter 4). Similar conclusions can be drawn for increasing the hydrophobicity of the electrode by increasing PTFE content (50% Pt/C case) where a high PTFE content, (lower acid content) led to higher porosity and therefore higher limiting current at 120 °C. However, the limiting current for electrodes with high PTFE content or low acid content did not vary significantly with temperature. On the contrary the limiting current with low PTFE content electrodes (high acid) showed greater dependency on temperature (increase) and therefore the limiting current value for both electrodes became very close at 175 °C.

These results are in good agreement with the results obtained from the polarisation curves (Chapter 4) where higher acid doping was favourable at high operating temperatures.

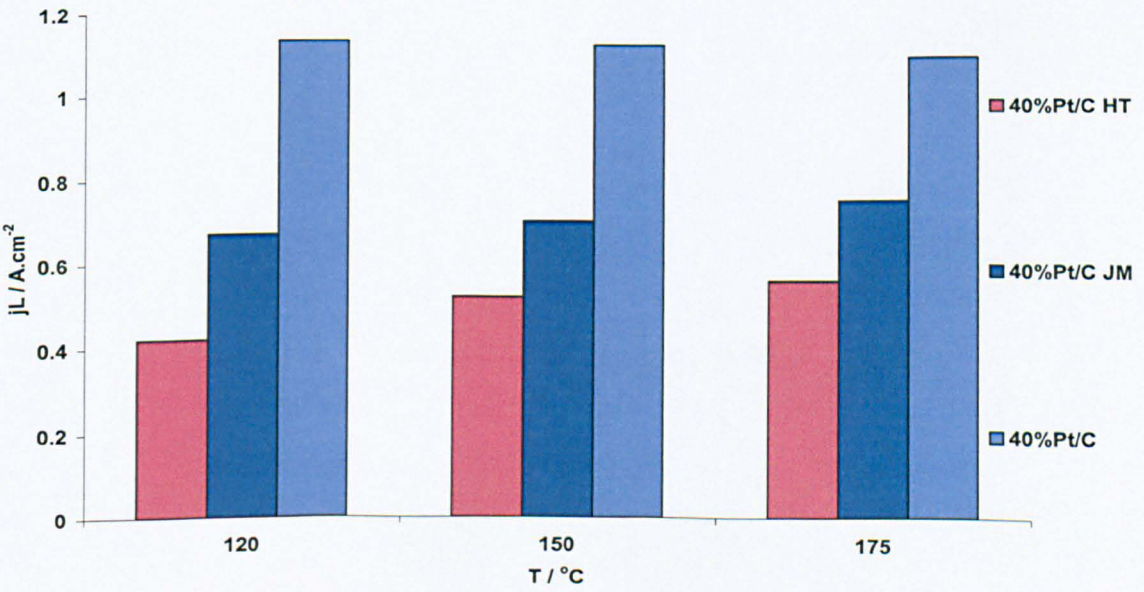

Figure 6-8. The effect of 40% Pt/C electrode's hydrophobic properties on the observed limiting current density when operating with air at temperatures of 120, 150 & 175 °C. HT denotes heat treatment & JM denotes Johnson Matthey advanced carbon support AC01.

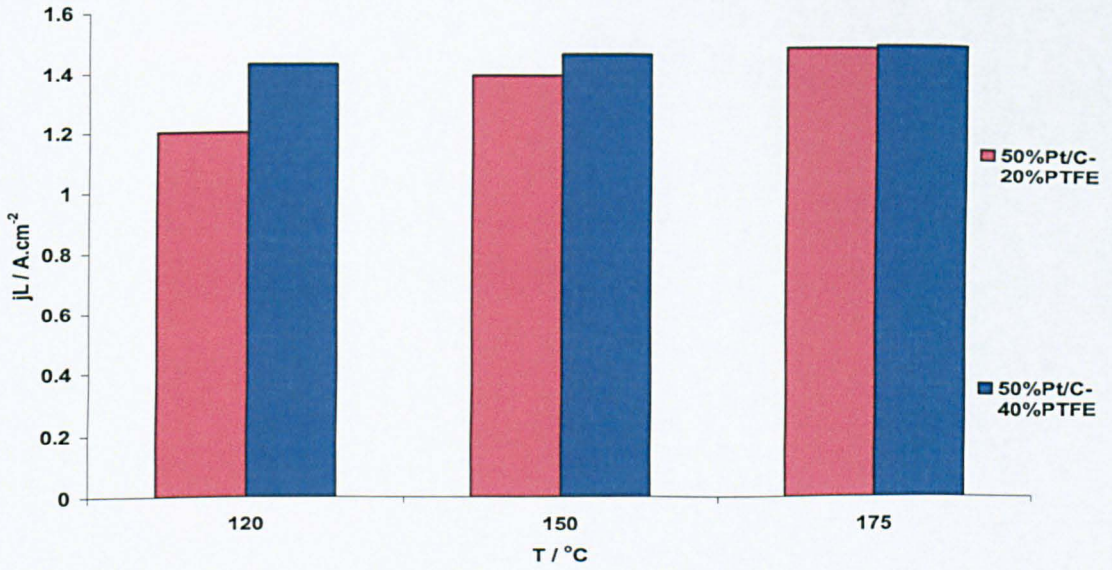

Figure 6-9. The effect of PTFE content of 50% Pt/C electrodes on the observed limiting current density when operating with heleox at temperatures of 120, 150 & 175 °C.

Table 6-7 summarises the limiting current ratio $j_{L(150)}/ j_{L(120)}$ and $j_{L(175)}/ j_{L(150}$ for temperature ratios of 150/120 °C and 175/150 °C for all electrodes at various oxygen partial pressure. It can be seen by comparison of the limiting current ratio that the second ratio was always lower than the first, suggesting that the permeability through the thin film DC_1 increased from 120 to 150 °C and fell thereafter at 175 °C. Both the oxygen diffusion coefficient in porous media D` and the diffusion coefficient through thin phosphoric acid film, D increased with temperature while C_1 or (H^{-1}) oxygen solubility decreased with temperature. The rest of the parameters in equation 30 are temperature independent. It has been shown [14] that the activation energy of oxygen diffusion is around three times larger than the heat of oxygen solution in 85-96% wt H_3PO_4 for the temperature range of 100-150 °C, therefore the overall product DC_1 increased with temperature up to 150 °C [14], above which 85% wt phosphoric acid started to dehydrate and became more dependant on humidity content and operating temperature which will led to a sharp increase in the viscosity and therefore sharp decrease in diffusion coefficient. On the other hand although solubility decreases with temperature, it increases with the phosphoric acid concentration for a given temperature [28]. At 175 °C the overall product DC_1 is expected to decrease in comparison to the value at150 °C under relatively low humidity conditions (RH <10 %).

Table 6-7. Limiting current ratios for various electrodes at different temperatures

	Air (1 atm)		Air (2 atm)		Heleox (1 atm)	
mg_{Pt}-Pt%-mg*$_{H3PO4}$	**150/120C**	**175/150C**	**150/120C**	**175/150C**	**150/120C**	**175/150C**
0.4-60%-0	0.99	0.99	1.03	0.95	0.98	0.99
0.6-50%-0†	1.08	1.01	n/a	n/a	1.16	1.03
0.4-50%-0†	1.17	n/a	n/a	n/a	1.16	1.07
0.4-50%-0	1.08	0.98	1.18	0.92	1.02	1.03
0.4-50%-2	1.20	1.09	n/a	n/a	1.15	1.11
0.4-50%-2-F*	n/a	1.03	n/a	1.04	n/a	1.03
0.4-50%-0LD*	1.11	1.03	1.09	0.93	1.13	1.09
0.4-40%-0	0.99	0.97	0.98	0.93	0.97	0.95
0.4-40%-0HT*	1.24	1.08	1.10	1.11	1.20	1.11
0.4-40%0JM *	1.04	1.07	1.00	1.07	1.07	1.06
0.4-30%-0HD*	1.58	1.28	1.43	1.16	1.59	1.26
0.4-30%-0	0.97	1.03	1.03	0.87	0.99	1.04
0.2-20%-0	0.96	0.93	n/a	n/a	0.98	n/a
0.2-18%-0-Co*	0.87	0.89	0.91	0.79	0.92	0.93
0.2-16%-0-Ni*	0.75	0.95	0.86	0.82	0.80	0.96

Table 6-8 summarises the limiting current ratios $j_{L\ heleox}$ / $j_{L\ air}$ and $j_{L\ air\ 2atm}$ / $j_{L\ air}$ at 120, 150 & 175 °C. The first ratio reflects losses of mass transport through the porous media by increasing D` by a factor of four (air and heleox) and the second ratio reflects losses of mass transport through the thin film where P_{O2} was doubled (air at 1 atm and 2 atm). From equation 30 it was expected that the limiting current ratio of $j_{L(air\ 2atm)}$/ $j_{L(air)}$ should be equal to 2. However, all the observed values were below 2. While equation 30 expresses the oxygen partial pressure in the catalyst layer, P_{O2} falls with increase in the flux (current density) due to mass transport through the porous structure. Equation 30 also lacks terms representing water flux of vapour product out of the thin film through the porous media which would lead to a further fall in P_{O2}. Including such a term with the simplifying assumption that $P_{Channel\ (H2O)} = 0$, we can write:

$$j_L = \frac{nFS_{Pt}D'_{O_2}D'_{H_2O}D_{O_2}P_{Channel}\varepsilon^{\tau}}{S_{Pt}D_{O_2}D'_{H_2O}\delta' + D'_{H_2O}D'_{O_2}\varepsilon^{\tau}L\,H + 2D'_{O_2}D_{O_2}\delta'S_{Pt}} \quad [31]$$

Where $D`_{H2O}$ is the vapour water diffusion coefficient through the porous structure.

Table 6-8. Limiting current ratios using different oxygen partial pressure and diffusion coefficient (porous media).

	$j_{L\ heleox}$ / $j_{L\ air}$			$j_{L\ air\ 2atm}$ / $j_{L\ air}$			b/a %		
mg_{Pt}-Pt%-mg*$_{H3PO4}$	**120C**	**150C**	**175C**	**120C**	**150C**	**175C**	**120C**	**150C**	**175C**
0.4-60%-0	1.13	1.12	1.13	1.36	1.41	1.35	15.8	14.7	14.9
0.6-50%-0†	1.07	1.14	1.17	n/a	n/a	n/a	7.7	17.2	19.8
0.4-50%-0†	1.17	1.16	n/a	n/a	n/a	n/a	19.8	19.0	n/a
0.4-50%-0	1.20	1.14	1.20	1.29	1.42	1.34	24.3	16.8	24.1
0.4-50%-2	1.19	1.13	1.16	n/a	n/a	n/a	22.4	15.8	18.6
0.4-50%-2-F*	n/a	1.10	1.10	n/a	1.22	1.23	n/a	11.9	11.5
0.4-50%0LD*	1.05	1.08	1.14	1.53	1.51	1.35	6.2	9.4	16.5
0.4-40%-0	1.16	1.13	1.11	1.46	1.45	1.38	19.1	16.0	13.1
0.4-40%-0HT*	1.10	1.06	1.09	1.64	1.46	1.50	11.3	6.8	10.6
0.4-40%0JM *	1.09	1.11	1.11	1.46	1.40	1.40	10.6	13.6	12.7
0.4-30%-0HD*	1.16	1.17	1.16	1.73	1.56	1.42	19.6	20.7	19.4
0.4-30%-0	1.09	1.11	1.12	1.46	1.55	1.30	10.5	13.7	14.6
0.2-20%-0	1.09	1.11	n/a	1.41	n/a	n/a	10.6	12.7	n/a
0.2-18%-0-Co*	0.98	1.04	1.08	1.49	1.56	1.39	-1.8	4.3	9.7
0.2-16%-0-Ni*	1.00	1.07	1.08	1.41	1.62	1.40	0.0	8.4	8.9

The proposed solution (Eq. 31) still predicts $j_{L(air\ 2atm)}/\ j_{L(air)}$ to be equal to 2 while all the observed values were < 2 (Table 6-8). This suggests that Fick's first law of diffusion is not suitable to represent diffusion in the porous media as it cannot account for interactions between gas

molecules;. Additionally the assumption of $P_{Channel(H2O)} = 0$ predicts a linear relation between $P_{Cat(H2O)}$ and j, while in reality an increase in j will lead to an increase in $P_{Channel(H2O)}$ and therefore an exponential dependence. The Stefan-Maxwell equation is more suitable in this case and will be discussed in more details in the Chapter 7. Additionally, the humidity or P_{H2O} effects on H and D_{O2} should be accounted for, especially at elevated temperatures, as they are affected by phosphoric acid concentrations which in turn are functions of water content and temperature. We can re-write equation 31 as:

$$j_L = \frac{nFP_{Channel}}{\frac{LH}{S_{Pt}D_{O_2}} + \frac{\delta'}{(D'_{O_2} + 2D'_{H_2O})\varepsilon^{\tau}}} \qquad [32]$$

The first term in the denominator represents mass transport losses through the thin film while the second represents losses through the porous media. It shows that the limiting current will increase when we have a structure with a high S_{Pt} and low L. For a given acid content, a more uniform distribution of acid, will lead to an increase in S_{Pt} and decrease in L. However increasing acid content will also have a counter effect from its effect on the porosity ε and consequently on j_L.

The higher $j_{L(heleox)} / j_{L(air)}$ value indicate greater mass transport losses through the porous media. Calculations using the Slattery-Bird correlation [29] show that oxygen-helium mixture exhibits binary diffusion coefficient four times higher than that of oxygen-nitrogen and water-helium mixture exhibits binary diffusion coefficient eight times higher than that of water-nitrogen over the studied temperature range. If we considered the first term in the denominator of Eq. 32 to be (a) and the second to be (b), then b/a is the ratio of the mass transport contribution between the porous phase and the thin film phase. By using the diffusion coefficient ratios obtained from the Slattery-Bird correlation we can write:

$$\frac{j_{L(heleox)}}{j_{L(air)}} = \frac{\frac{1}{a + b/7}}{\frac{1}{a+b}}, \text{ re-arranging: } \Rightarrow \frac{b}{a} = \frac{1 - \frac{j_{L(heleox)}}{j_{L(air)}}}{\frac{j_{L(heleox)}}{7j_{L(air)}} - 1} \qquad [33]$$

Table 6-8 shows the corresponding b/a% for the studied electrodes. The average values for non-doped electrodes with 40% PTFE utilising 0.4 mg_{Pt} cm^{-2} of 60, 50, 40 & 30% Pt/C are 15.1, 21.8, 16.1 & 12.9 %, respectively. While diffusion in the pores of the catalyst layer is controlled by its length and porosity $\varepsilon^{\tau}/\delta`$, the diffusion through the electrolyte film is controlled by $S_{Pt}/L$. The 60% Pt/C electrode had the smallest catalyst layer thickness, $\delta`$ and for a given acid content had the smallest porosity. On the other hand it had a relatively high L as it had the highest acid volume fraction and a medium value for S_{Pt} where most of the catalytic sites are accessible. However 60% Pt/C exhibited the largest average Pt particle size. Moving towards 50 %Pt/C the catalyst layer thickness increased ($\delta`$) and correspondingly the porosity (lower acid volume fraction) also increased, while L fell and S_{Pt} increased therefore the ratio of b/a increased; reaching its maximum. As the thickness of the cathode catalyst layer increased further (40 & 30% Pt/C), the porosity remained the same (as acid volume fraction became low) and for similar L values to 50% Pt/C, S_{Pt} fell, therefore b/a values decreased accordingly.

Values of b/a increased from 12.9 to 19.9 for 30 %Pt/C by increasing acid content (from standard 5.6 PRU membrane to 20 PRU HD). Also b/a values decreased from 21.8 to 10.7 for 50% Pt/C, by reducing the acid content from the standard 5.6 PRU membrane to 4 PRU LD. This is explained by the increased acid content increasing S_{Pt} and reducing ε^{τ}, leading to increased b/a values and vice versa.

6.4 Study of HT-PEMFCs using frequency response analysis

6.4.1 Introduction

The PBI based HT-PEMFCs were studied earlier using polarisation curves (linear sweep), cyclic voltammogram and chronoamperometry, where the electrodes were driven to a condition far from equilibrium through large perturbations on the system. Another approach is to perturb the system with very small magnitude signal and monitor the system's response around the steady-state, allowing the system to be studied over wide range of frequencies (time). Electrode systems with non-linear polarisation show linearity when subjected to small perturbations in current or potential. For an activation controlled process we can write:

$$i = i_0 \exp(\frac{\alpha \eta_{ac} F}{RT}) \quad [34]$$

For small perturbation of Δi and resulting potential response Δη, we obtain:

$$i + \Delta i = i_0 \exp\left((\eta_{ac} + \Delta \eta_{ac}) \frac{\alpha F}{RT} \right) \quad [35]$$

Subtracting equation 35 from 34 and dividing the result by equation 34, we obtain:

$$\frac{\Delta i}{i} = \exp\left(\frac{\alpha F \Delta \eta_{ac}}{RT} \right) - 1 \quad [36]$$

For small values of αFΔη/RT << 1 or for Δη ≤10 mV at 150 °C, we can write (with accuracy above 99 %):

$$\exp\left(\frac{\alpha F \Delta \eta}{RT} \right) = 1 + \frac{\alpha F \Delta \eta}{RT} \quad [37]$$

Combining equations (36) & (37), we finally obtain:

$$\frac{\Delta i}{i} = \frac{\alpha F \Delta \eta_{ac}}{RT} \Rightarrow R_{ac}^{\Delta} = \frac{\Delta \eta_{ac}}{\Delta i} = \frac{RT}{\alpha F} \frac{1}{i} \quad [38]$$

The overpotential loss due to kinetic activation at current i can be expressed simply by a resistor R_{ac}^{Δ}. The physical meaning of this equation is that even when the j vs. η relationship is exponential, a small interval of this curve near any steady state value can be linearised [27]. Figure 6-10 shows the linearisation of the j/E curve around steady-state using small perturbation in the current.

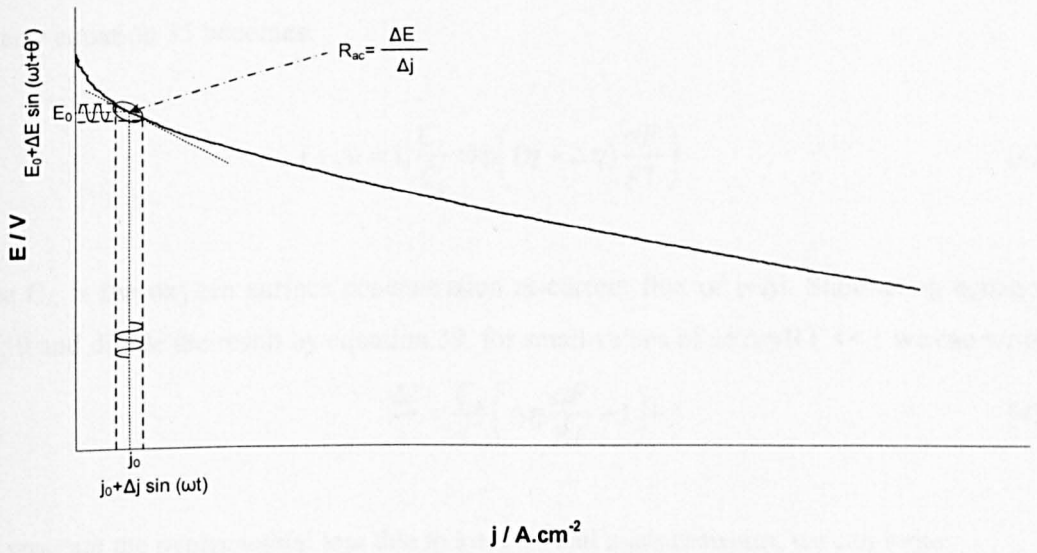

Figure 6-10. Linearisation of the j/E curve around the steady-state using small perturbation in the current.

For small current or voltage perturbations, the changes in concentration of reactants/products near the electrode surface are small therefore the associated equations can be linearised too. Considering that the system is affected by mass transport of reactants, at steady- state equation 34 becomes:

$$i = i_0(\frac{C}{C_0})^{\gamma} \exp(\frac{\alpha\eta F}{RT}) \qquad [39]$$

Where γ is the reaction order (equal to 1 for oxygen), C_0 is the reactant reference surface concentration where i_0 is measured (O.C.P) and C is the surface concentration at current i ($i > i_0$ & $C < C_0$).

If we separate the overpotential losses due to kinetics and mass transport, $\eta = \eta_{ac} + \eta_{mass}$ we can write:

$$i = i_0 \exp(\frac{\alpha\eta_{ac}F}{RT}) \Rightarrow \eta_{ac} = \frac{RT}{\alpha F}\ln(\frac{i}{i_0}) \Rightarrow R_{ac} = \frac{RT}{\alpha F i}\ln(\frac{i}{i_0}) \qquad [40]$$

$$C_0 = C\exp(\frac{\alpha\eta_{mass}F}{RT}) \Rightarrow \eta_{mass} = \frac{RT}{\alpha F}\ln(\frac{C_0}{C}) \Rightarrow R_{mass} = \frac{RT}{\alpha Fi}\ln(\frac{C_0}{C}) \quad [41]$$

Similarly equation 35 becomes:

$$i + \Delta i = i_0 \frac{C_\Delta}{C_0}\exp\left((\eta + \Delta\eta)\frac{\alpha F}{RT}\right) \quad [42]$$

Where C_Δ is the oxygen surface concentration at current flux of i+Δi. Subtracting equation 42 from 39 and divide the result by equation 39, for small values of $\alpha F\Delta\eta/RT << 1$ we can write:

$$\frac{\Delta i}{i} = \frac{C_\Delta}{C}\left(\Delta\eta\frac{\alpha F}{RT} + 1\right) - 1 \quad [43]$$

If we separate the overpotential loss due to kinetics and mass transport, we can write:

$$R_{ac}^{\Delta} + R_{mass}^{\Delta} = \frac{\Delta\eta}{\Delta i} = \frac{\Delta\eta_{ac}}{\Delta i} + \frac{\Delta\eta_{mass}}{\Delta i} \quad [44]$$

$$\frac{1}{i} = \frac{C_\Delta}{C}\frac{\alpha F}{RT}R_{mass}^{\Delta} + \frac{C_\Delta}{C}\frac{\alpha F}{RT}R_{ac}^{\Delta} + \frac{1}{\Delta i}(\frac{C_\Delta}{C} - 1) \quad [45]$$

Substituting R_{ac}^{Δ} from 38, and re-arranging:

$$R_{mass}^{\Delta} = \frac{RT}{\alpha F}\left(\frac{1}{i} + \frac{1}{\Delta i}\right)\left(\frac{C}{C_\Delta} - 1\right) = \frac{RT}{\alpha F}\left(\frac{1}{i} + \frac{1}{\Delta i}\right)\left(\frac{C - C_\Delta}{C_\Delta}\right) \quad [46]$$

Therefore:

$$R_{total}^{\Delta} = R_{ac}^{\Delta} + R_{mass}^{\Delta} = \frac{RT}{\alpha F}\left(\frac{C}{C_\Delta}\left(\frac{1}{i} + \frac{1}{\Delta i}\right) - \frac{1}{\Delta i}\right) \quad [47]$$

It can be seen that with a small current perturbation Δi, the mass transport losses can be separated from kinetics losses and be represented by a resistor at low frequencies. As $C_\Delta(\omega) = C_\Delta$ is a function of frequency (time), at low frequencies (close to steady-state condition) $\omega \rightarrow 0$ $C_\Delta(0) \rightarrow C_\Delta < C$, while at high frequencies as $\omega \rightarrow \infty$ $C_\Delta(\infty) \rightarrow C$ and $R^{\Delta}_{mass} \rightarrow 0$. This means in very

short periods of time, the system will be under pure kinetic control before mass transport effects takes place.

It should be stressed here that R^{Δ}_{ac} refers to the activation loss around the steady-state operation of current $i+\Delta i$ and overpotential $\eta+\Delta\eta$ and is completely different from R_{ac} given by equation 40. While R^{Δ}_{ac}, the charge transfer resistant, does not contain mass transport contribution from the ac perturbation signal, i.e. $C_{\Delta} \rightarrow C$, however it contains inherited mass transport effect from the steady state operation as can be seen from equation 38. The current density at the steady-state potential η, is measured at a steady-state surface concentration C and not the initial surface concentration at rest potential C_0.

Similarly, R^{Δ}_{mass} is completely independent from R_{mass} (equation 41), while R^{Δ}_{mass} expresses mass transport losses due to perturbation in current Δi and therefore perturbation in concentration $C\text{-}C_{\Delta}$ with respect to the steady-state current i and therefore the steady-state concentration C. While R_{mass} expresses the mass transport losses at concentration C, due to current flux I, with respect to the initial rest potential conditions i_0 and C_0.

A focus of this work was to utilise the AC impedance technique to obtain more information about the performance of the cathode electrodes, in other words to gain more knowledge about conductivity, kinetic and mass transport phenomena in the electrode.

6.4.2 Model selection

While EIS is a very sensitive technique used to clarify electrode process and derive its characteristic parameters, it does not provide a direct measure of physical phenomena. Interpretation of impedance data requires the use of an appropriate model, which can be a mathematical model based on probable physical theory (such as kinetics & diffusion processes) that predicts theoretical impedance [30, 31], or relatively empirical model [32-35] in which the parameters obtained do not necessarily have a clear physicochemical significance, or a hybrid of both.

The principal disadvantage of the physical method is the level of mathematics required to properly analyse impedance data [31]. For example a system with one adsorbed species is expected to produce two semi circles in the impedance plan (two time constants), while the experimental data often shows only one, this will lead to too many free parameters. Instead a simple model using one time constant should be used [26].

Another limitation of impedance data modelling is that the same data can be represented by different equivalent circuits [36]. For example system displaying two capacitive loops (two time constants) can be adequately presented by three types of circuits as shown below (a, b & c):

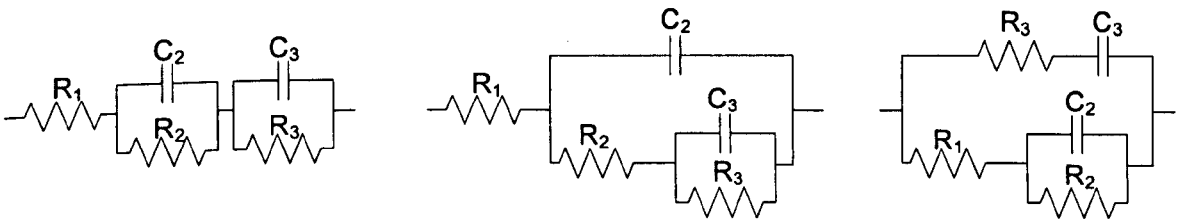

For a proper choice of parameters the behaviour of the three circuits is indistinguishable, as they will display the same impedance spectrum over the entire frequency range [26, 37].

In this section analysis of the obtained PBI impedance spectra was carried out, and four equivalent circuits were suggested to fit the observed spectra. An attempt was also made to relate the components of the circuits to physical phenomenon occurring on the electrode.

The impedance spectra were obtained by employing Autolab PGSTAT 30 (Eco Chemie, The Netherlands) controlled by FRA 4.9. The frequencies were swept from 30 KHz to 10 mHz recording six points per decade with an AC signal aptitude of 15 mA. The obtained data was fitted to the chosen circuit using ZSimpWin V3.21 software (Princeton Applied Research, U.S.A) utilizing Complex Non-linear Least Square errors technique (CNLS).

The impedance spectra are commonly plotted in Nyquist diagrams. The X and Y axis of the diagram represents the real and the imaginary impedances, respectively with no direct information regarding the applied frequency.

For a monochromatic input signal, $v(t) = V_m \sin(\omega t)$, at a given frequency f ($f \equiv \omega/2\pi$) the resulting steady-state current is $i(t) = I_m \sin(\omega t+\theta)$. Where θ is the phase angel between voltage and current and is 0° for pure resistance, +90° for pure capacitance and -90° for pure inductance, ω is the angular frequency, and the impedance magnitude is given by $|Z| = V_m / i_m$.

The impedance is given by:

$$|Z(\omega)| = Z'(\omega) + Z''(j\omega) \qquad [48]$$

Where Z' is known by the real part of the impedance and Z'' is known by the imaginary part of the impedance due to its association with j (the imaginary number).

$$Z' = |Z|\cos(\omega) \;\&\; Z'' = |Z|\sin(\omega) \qquad [49]$$

The phase shift and the modulus are equal to:

$$\theta = \tan^{-1}(Z''/Z') \;\&\; |Z| = \sqrt{(Z')^2 + (Z'')^2} \qquad [50]$$

Figure 6-11 shows a typical obtained Nyquist plot of the impedance spectra for a PBI based PEMFC. The spectra were very similar to that reported in the literature [38]. At very high frequencies (above 10 kHz) the observed inductive behaviour was due to mutual inductance (i.e., cable) effects [37] while the intercept on the real axis in the high-frequency range of the spectrum (1-10 kHz) corresponded to the ohmic resistance, R_s (electronic + protonic). The overall resistance (anode + cathode), R^{Δ}_{total}, the sum of mass transport and charge transfer resistance, is obtained from the difference between the high-frequency real Z-axis intercept and the low frequency real Z-axis intercept. Similarly, in Nafion based PEMFCs, a single semicircle is observed in the complex plane, reflecting a combination of the charge transfer resistance, the mass transport resistance, and ohmic resistances in the cathode [39].

The lower frequency part of the spectrum, typically when frequency is less than 1 Hz, represents the sum of a capacitive loop in the anode spectrum and an inductive loop in the cathode spectrum, which appear in a similar frequency range where it is not possible to extract quantitative data from the lower frequency part of the local two-electrode spectra [38]. The low frequency inductance is also explained by several factors: instrumental artifacts [40], adsorbed intermediates or solution soluble intermediates (thin film) [41], oxygen starvation in the pores of PAFCs cathode [42], reaction consisting of two successive electron transfer step proceeded by an adsorbed intermediate species [43, 44], an indirect four-electron reaction or a two-electron reduction oxygen reduction followed by a disproportionation reaction [45].

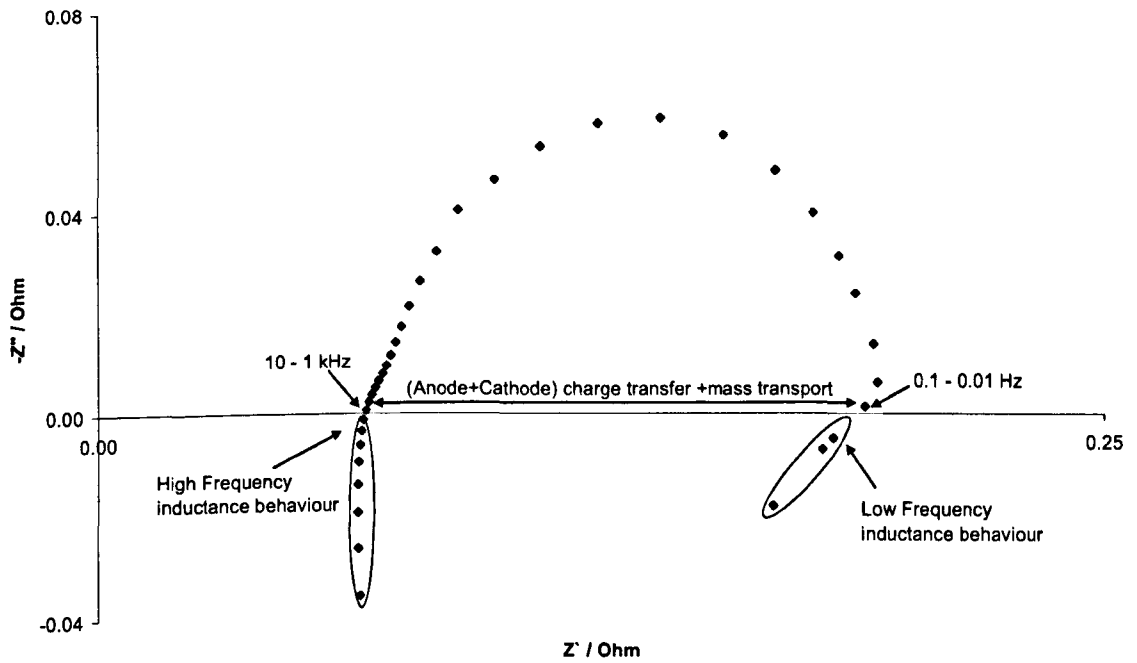

Figure 6-11. Typical Nyquist plot of the impedance spectra for PBI based PEMFC.

By taking closer look at the spectra we can see that there are two semi circles merged together rather than one large one, small one at high frequencies and larger one at lower frequencies.

Bode diagram can give clearer image about the time constants of the system as it shows plot of the phase angle and impedance magnitude relation with frequency, separately.

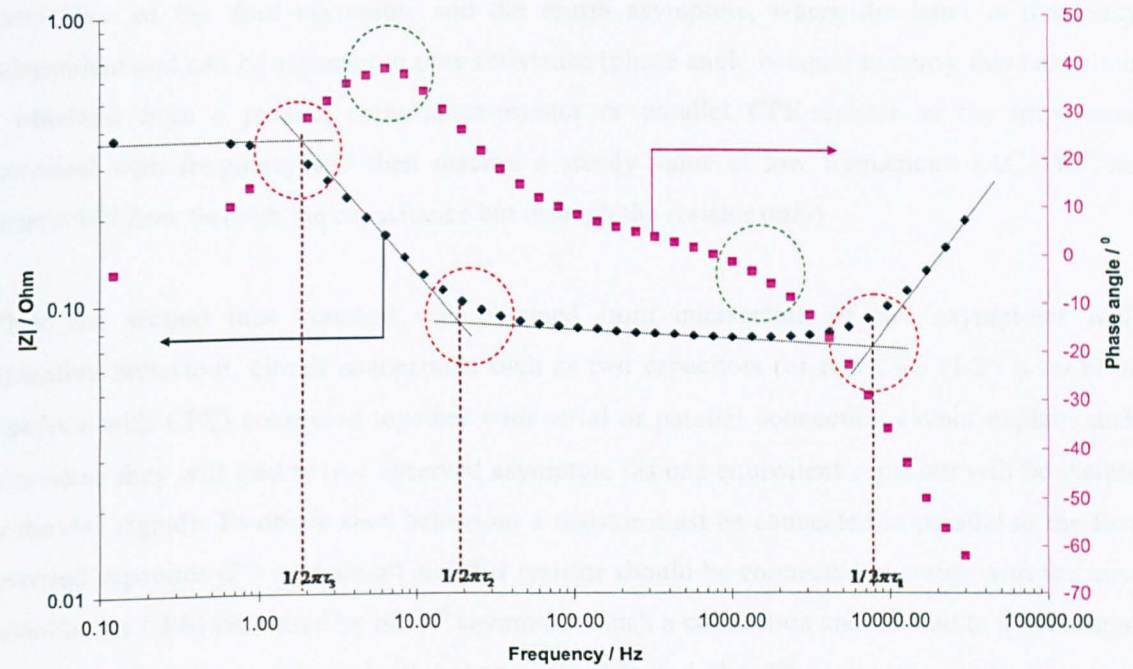

Figure 6-12. Typical Bode diagram for PBI based MEA running at OCP.

Figure 6-12 shows typical obtained PBI based MEA Bode diagram. It can be observed from the logarithm of impedance magnitude plot Log |Z| (also known as amplitude ratio AR) that there are four asymptotes corresponding to three break point or corner frequencies. This corresponds to three time constants ($\tau = 1/\omega = 1/2\pi f$) [46]. Starting from high frequency towards the low frequency we observed the first break point frequency ($1/2\pi\tau_1$) from the intersection of the first two asymptotes. The first asymptote is directly proportional to frequency (positive slope) which is typical inductance (L) behaviour ($Z_L=-\omega L/j$), this can also be concluded from the negative values of the phase shift. The second asymptote is inversely proportional to frequency (negative slope) which is typical capacitance behaviour; this can also be concluded from the positive values of the phase shift. The capacitive behaviour can be represented by either a capacitance (C) or constant phase element (CPE) ($Z_C = 1/ j\omega C$ & $Z_{CPE} = Z_0/(j\omega)^n$). The first time constant is not due to the studied system characteristic but due to a series inductance-capacitor circuit, where the inductance is the machine wires self-inductance. The second time constant is obtained from the intersection of the second and third asymptotes; where the latter also exhibits capacitive

behaviour with a higher dependency on frequency. The third time constant is obtained from the intersection of the third asymptote and the fourth asymptote, where the latter is frequency independent and can be assigned to pure resistance (phase angle is equal to zero): this behaviour is obtained from a parallel capacitance-resistor or parallel CPE-resistor as the impedance decreased with frequency and then reaches a steady value at low frequencies (AC→DC no current will flow through the capacitance but through the resistor only).

While the second time constant was obtained from intersection of two asymptotes with capacitive behaviour, circuit connections such as two capacitors (or two CPE (1.2> n >0.8) or capacitor with CPE) connected together with serial or parallel connection cannot explain such behaviour; they will lead to one observed asymptote (as one equivalent capacitor will be visible by the AC signal). To obtain such behaviour a resistor must be connected in parallel to the first observed capacitor (2nd asymptote) and this resistor should be connected in series with the next capacitor (or CPE) presented by the 3rd asymptote. Such a connection should lead to a horizontal asymptote (frequency independent) between the 2nd and the 3rd asymptotes with two time constants ($\tau`_2$ & $\tau``_2$) arising from its intersection with the 2rd and the 3th asymptotes. However if the frequency, where the charging of the second capacitance becomes important, is higher than ($1/2\pi\ \tau`_2$), no such horizontal asymptote will be observed and two asymptotes with different negative slopes will be seen. This means that the impedance of the second capacitance will start to become important at a given frequency higher than the frequency where the impedance of the first capacitance becomes negligible. This can also be seen from the Nyquist diagram where the second semi-circle starts before the first one is complete. Similarly, there is a possibility of a horizontal asymptote between the first and the second asymptote, suggesting a series connection between the inductor and resistor, which in turn is connected in series to the first capacitor.

Simply each semi-circle (time constant) is presented by a resistor connected in series with capacitor which in turn is connected in parallel to a resistor (known as Randles circuit). Or in some cases the first resistor can be equal to zero and the semi circle is presented by capacitance in parallel with resistor. Two circuit configurations (Voigt and ladder) explaining the above observations are given below (d, e, f & g) with the two possibilities for the series connection between the resistor and capacitor (asymptotes 2 and 3).

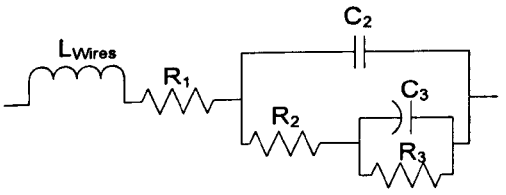

Ladder

(d)

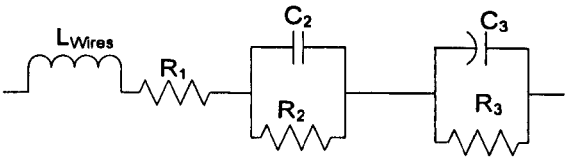

Voigt

(e)

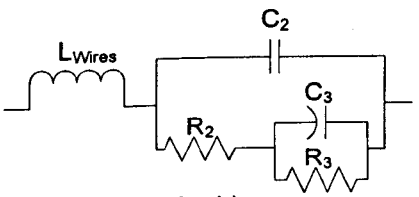

Ladder

(f)

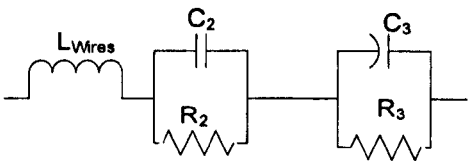

Voigt

(g)

While the suggested four simple circuits can describe the observed impedance spectra, more complex circuits involving more elements can also lead to the same impedance spectra, however, they will lead to too many free parameters as discussed earlier.

Inevitably, all the electrolytic cells are disturbed in space, thus their impedance often cannot be well approximated by the impedance of an equivalent circuit involving only a finite number of ideal circuit elements (C, R & L). The use of disturbed impedance elements (such as CPE) will greatly aid in the process of fitting the observed impedance data for a cell with disturbed properties [37].

Impedance studies on the double layer capacitance at solid electrodes usually show deviation from ideal behaviour manifested by frequency dependence [37]. The deviation from ideal capacitance behaviour corresponds to a frequency–dependent phase angle which is presented by CPE. The capacitance dispersion depends strongly on the state of the electrode's surface (roughness) and ion adsorption [26].

As shown earlier the impedance of CPE is given by $Z_{CPE} = Z_0/(j\omega)^n = 1/Y_0(j\omega)^n$ where Y_0 is the admittance in F s^{n-1}, when n = 1, 0.5, 0 & -1, CPE presents pure capacitor, infinite Warburg impedance, pure resistance, and pure inductance, respectively.
Two semi circles were observed in the impedance spectra for the oxygen reduction reaction, the high frequency semi circle was assigned to kinetic losses whilst the low frequency semi circle was assigned to mass transport losses [47].

The mass transport losses in this study can not be represented by introducing the conventional Warburg element. The Warburg element (W) is limited to semi-infinite linear diffusion and does not take into account the finite size of electrochemical cells, which means that the diffusion layer thickness cannot be greater than the cell dimensions or in our case the thin film thickness. This difficulty arises at low frequencies [48]. This is clear from the impedance spectra where when dealing with the Warburg element a straight line with 45° angle is expected in the Nyquist plot at low frequencies ($Z_W = \sigma\omega^{-0.5} - j\sigma\omega^{-0.5}$, see equation (53) for σ), which is not the case. The capacitive arc, seen in the low frequency range, was attributed to a finite diffusion process [37]; as discussed earlier we are dealing with finite length diffusion with a transmissive boundary. Therefore a new element, known as O element (or finite length Warburg) with parameters Y_o & B, given by equation 52, is required.

Holze et al studied [49-51] the kinetics of oxygen reduction at porous teflon-bonded fuel cell electrodes and showed that the process was limited by diffusion and adsorption of oxygen species. They represented the diffusion impedance Z_d by a resistor R_d (or here R^{Δ}_{mass}) connected in parallel with capacitor. The solution of Fick's diffusion equation for finite length layer L, using Nernstian diffusion impedance theory was given by Lasia et al [26], Armstrong [52], Diard et al [53] and others [54]:

$$C_{\Delta} = \frac{i_{\Delta}}{nF\sqrt{j\omega D}} \tanh\left(L\sqrt{\frac{j\omega}{D}}\right) \qquad [51]$$

Therefore, the diffusion impedance becomes:

$$Z_d = \frac{\sigma(1-j)}{\sqrt{\omega}} \tanh\left(L\sqrt{\frac{j\omega}{D}}\right) = \frac{\sigma\sqrt{2}}{\sqrt{j\omega}} \tanh\left(L\sqrt{\frac{j\omega}{D}}\right) = \frac{1}{Y_o\sqrt{j\omega}} \tanh\left(B\sqrt{j\omega}\right) \qquad [52]$$

Where σ is the mass-transfer coefficient given by:

$$\sigma = \sigma_O + \sigma_R = \frac{RT}{n^2F^2\sqrt{2}}\left[\frac{1}{C_O\sqrt{D_O}} + \frac{1}{C_R\sqrt{D_R}}\right] = \frac{RT}{n^2F^2C_\Delta\sqrt{2}\sqrt{D}} \quad [53]$$

For simplification the assumption that the diffusion coefficients for O and R species were similar was made ($D = D_O = D_R$). Separation of the imaginary and non-imaginary part is now possible:

$$Z_d = R_d \frac{\left[\sinh(2L\sqrt{\frac{\omega}{2D}}) + \sin(2L\sqrt{\frac{\omega}{2D}})\right] - j\left[\sinh(2L\sqrt{\frac{\omega}{2D}}) - \sin(2L\sqrt{\frac{\omega}{2D}})\right]}{2L\sqrt{\frac{\omega}{2D}}\left[\cosh(2L\sqrt{\frac{\omega}{2D}}) + \cos(2L\sqrt{\frac{\omega}{2D}})\right]} \quad [54]$$

Where the resistive part (non-imaginary), represented by a resistor R_d, of the equation is given by:

$$R_d = \frac{RTL}{n^2F^2DC_\Delta} = \frac{\sqrt{2}\sigma L}{\sqrt{D}} \quad [55]$$

Similarly, adsorption can be separated into a capacitive and resistive part connected in parallel[50]:

$$R_{ads} = \frac{RT}{n^2F^2Ck} \quad [56]$$

$$C_{ads} = \frac{n^2F^2C}{RT} \quad [57]$$

Where k is the adsorption rate constant, equal to ($1/R_{ads}.C_{ads}$), and C is the adsorbed species surface concentration.

From the diffusion impedance given in equation 52, it can be seen that when $L\rightarrow\infty$ or $\omega\rightarrow\infty$ ($\omega > 4\pi D/L^2$) we end up with a traditional Warburg element for semi-infinite diffusion as expected and a straight line with slope of 45° degree should be observed in the high frequency range followed by semi circle. However, such observations are not always found due to the coalescence (masking) problem of the double layer semi-circle and the 45° straight line [54]. The

same conclusion was drawn, from the chronoamperometry measurements earlier, where the time required for the diffusion layer to reach the end of the thin film L (infinite to finite length) is smaller than the time required to charge the double layer.

At low frequencies ($\omega \rightarrow 0$) the diffusion impedance becomes pure resistance (C_{mass} or CPE works as insulator when AC→ DC) equal to R_d (or R^{Δ}_{mass}) given in equation (55), with a diffusion time constant equal to:

$$\tau_d = 1/\omega_{max} = R_d.C_d = L^2/\sqrt{2\pi}\, D \qquad [58]$$

This is similar to the time constant expression given earlier during the chronoamperometry measurements.

If we represent mass transfer diffusion in terms of resistor R_d and capacitance C_d, from equation 55 & 58 we can write:

$$C_d = \frac{n^2F^2}{RT}\frac{LC_{\Delta}}{\sqrt{2\pi}} \qquad [59]$$

This is very similar to the adsorption capacitance C_{ads} given in equation 57.

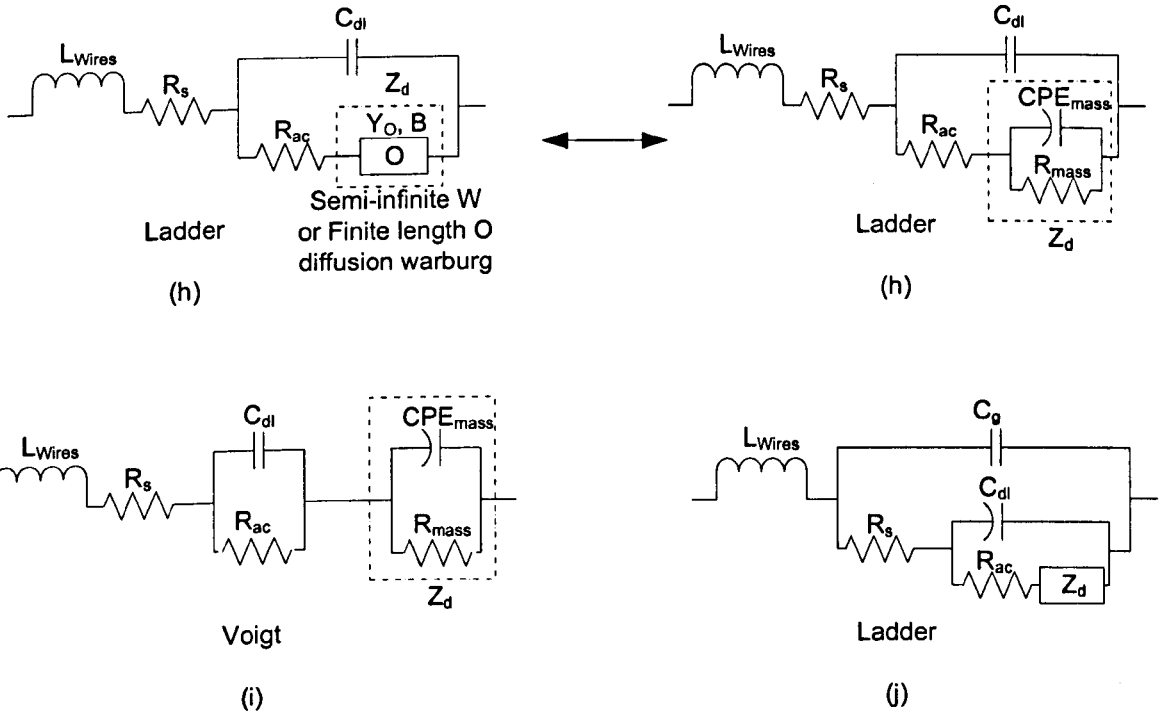

Equivalent circuit (h) has been suggested for simple one step reaction with diffusion limitation by Randles [55], Armstrong et al [56] and Franceschetti [57], on the other hand equivalent circuit (i) was suggested by Wagner [58] and Wang et al [59, 60] for the oxygen reduction reaction with diffusion limitation.

PBI based PEMFCs have also been represented, with no mass transport effects, as a resistor in parallel with CPE (circuit h or i) [61] or by equivalent circuit h with mass transport effects Z_d expressed as a finite length Warburg element [62] (element O, or CPE_d connected with in parallel resistor R_d). Here R_s was the total ionic and electronic resistance of the studied system, C_{dl} was the double layer capacitance, R_{ac} was the charge transfer resistance and Z_d was the mass transfer impedance expressed in different forms.

For a single fuel cell consisting from two electrodes circuit (j) was suggested [37], assuming the anode and cathode were identical, C_{dl} in this case was $C_{dl}/2$, similarly, R_{ac} was 2 R_{ac} (R_{ac} anode+ R_{ac} cathode) and Z_d was $2Z_d$. An additional capacitance C_g, known as geometric impedance was introduced. This capacitance explained the cell capacitive behaviour at high frequencies; in

particularly when using a solid electrolyte, due to high surface electrodes with an insulator in between, and can be given by:

$$C_g = \frac{\varepsilon \varepsilon_0 S_A}{l} \quad [60]$$

Where ε & ε_0 are the dielectric constant of the electrolyte and vacuum, respectively, S_A is the surface area and, l, is thickness of the membrane electrolyte (electrodes separation).

With S_A equal to 0.1344 m^2 (catalyst loading of 0.4 mg_{Pt} cm^{-2} 50% Pt/C, with Pt and carbon specific areas of 86 and 250 m^2 g^{-1}), $\varepsilon_0 = 8.85\times10^{-12}$ F m^{-1} and l = 4×10^{-5} m, C_g is equal to 9.5×10^{-4} F considering a dielectric constant for PBI equal to 3.2 [63], or C_g is equal to 9×10^{-3} F considering dielectric constant for phosphoric acid doped PBI (5.6 PRU) equal to 29.21. The latter was obtained from the assumption that the dielectric constant for phosphoric acid doped PBI is given by:

$$\varepsilon = \varepsilon_{PBI}\varphi_{PBI} + \varepsilon_{H_3PO_4}\varphi_{H_3PO_4} \quad [61]$$

Where φ is the volume fraction and $\varepsilon_{H3PO4} = 61$ [64].

This data show that C_g (10^{-3}-10^{-4} F) should be between one to two orders of magnitude smaller than C_{dl} (in the range of 0.1-1 F, measured values from cyclic voltammogram were 0.88 & 0.82 F for 11.56 cm^2 cathode (0.4 mg_{Pt} cm^{-2} 50% Pt/C) and anode (0.2 mg_{Pt} cm^{-2} 20% Pt/C)) and therefore it should appear (charge) at much higher frequencies before C_{dl}.

Armstrong [52] has shown that for electrochemical reactions involving simultaneous adsorption and finite length diffusion, the latter cannot be taken into account by simply adding the Warburg element, as the mass transfer coefficient, involved in the low frequency limit, will no longer be expressed by equation 53 but it will involve much more complex terms; that are beyond the purpose of this study.

The use of the Warburg finite element is unjustified in the case of slow electrode reactions [65] or in the case of slow diffusion of species through electrode/electrolyte interface, where even a

small surface imperfections would be sufficient to dominate motion of atoms within the electrode [66].

Gileadi [27] has shown that that the charge transfer time constant (relaxation time) under a small-amplitude transient is given by:

$$\tau_{ct} = C_{dl} R_{ct} = \frac{\upsilon RT}{nF} \frac{1}{i} C_{dl} \qquad [62]$$

And the diffusional time constant is given by:

$$\sqrt{\tau_d} = \frac{RT}{n^2 F^2} C_{dl} \left(\frac{\upsilon_O}{C_O \sqrt{D_O}} + \frac{\upsilon_R}{C_R \sqrt{D_R}} \right) = \sqrt{2} \sigma C_{dl} \qquad [63]$$

Where υ is the stoichiometric coefficient for oxidized (O) and reduced form (R) of the diffusing species.

Assuming υ=1 and D_O=D_R for simplification, we can write:

$$\tau_{ct} / \tau_d = \frac{n^3 F^3}{4RT} \frac{C^2 D}{i C_{dl}} \qquad [64]$$

If the ratio τ_{ct}/τ_d is larger than 10^3 the reaction can be said to be kinetic controlled. Below such a value the system will be under mixed control and separation of kinetic and diffusion processes is possible, however when $\tau_{ct} \leq \tau_d$ the system is under diffusion control and the separation of kinetic from diffusion parameters is not possible [27]. In other words the diffusion limitation will become important (at high frequencies) even before the double layer capacitance is charged. Considering that the current density (i) is a linear function of concentration (C), τ_{ct}/τ_d becomes also (Eq. 64) a linear function of concentration (C), and therefore drops by increasing i or polarising the electrode.

To estimate τ_{ct}/τ_d the following data is used: The oxygen solubility in 85% wt Phosphoric acid at 150 °C of 0.25 mol L^{-1} atm^{-1} [14] and the oxygen diffusion coefficient of ~10^{-5} cm^2 s^{-1} [12, 14], with the earlier measured double layer capacitance (cyclic voltammogram) of 0.88 F (or 0.098 F cm^{-2}) and minimum current density of 0.015 A (or 0.00167 A cm^{-2}) around OCP, which is the

amplitude of the impedance signal or 0.115 A (or 0.013 A cm^{-2}) which is the amplitude of the AC impedance signal in addition to the minimum stationary (DC) current of 0.1 A used to polarise the electrode (9 cm^2). This will lead to τ_{ct}/τ_d values of 0.2 & 0.0265, under air operation and 5 & 0.658, under oxygen operation, respectively. The obtained τ_{ct}/τ_d values suggest that the separation of Z_{tot} into Z_{mass} and Z_{ac} is not possible. Therefore it is expected that R_{ac},C_{dl} & R_d,C_d are expressed using a single resistor $R_{tot} = R_{ac} + R_d$ and capacitance $C_{tot} = C_{dl} + C_d$.

The discussed circuits h, i and j match the suggested equivalent circuits from the PBI impedance spectra observation of d, e & f, respectively. Further analysis is required to find the most suitable circuit and if possible assign each of the circuit elements to its physical meaning.

At high frequency, fast processes become visible and as we move towards lower frequencies slower processes become visible instead. The following processes are expected to occur from high towards lower frequencies:

- Electron/proton conduction, i.e. R_s.
- Charging/discharging the smallest capacitance in the system, in this case C_g.
- Second capacitance (in size) charging/discharging, i.e. double layer (C_{dl}).
- Kinetic losses (R_{ac})
- Finite length diffusion (thin film) accompanied with semi-infinite diffusion (porous structure) (capacitance/CPE C_d in parallel with resistor R_d).

There can also be adsorption of oxygen intermediates species on the catalyst surface (capacitance C_{ads} in parallel with resistor R_{ads}). However, some of the above processes will occur at similar time periods (frequency), making it difficult to clearly separate all the mentioned processes individually, for example as seen earlier that diffusion effects will start even before the whole double layer is charged.

The interpretation of EIS data remains a complex problem, however, a simplified model of the porous electrode response can help to understand and optimise fuel cell performance [67]. Further analysis will be required by studying different operating conditions in order to help in understanding the observed spectra and separate the parameters' effects.

6.4.3 Cell around OCP impedance

6.4.3.1 Temperature effect on cell impedance spectra

Figure 6-13 shows the effect of temperature on impedance spectra. The overall system through plane resistance values R_s, which correspond to the first high-frequency real Z-axis intercept, at RH <1 % were 0.075, 0.068 & 0.0787 ohm for temperatures of 125, 150 & 175 °C, respectively. These results suggest overall average conductivities of 0.0107, 0.0118 & 0.0102 S cm^{-1}, considering a membrane thickness of 60 μm (anode catalyst layer of 20 μm and cathode catalyst layer of 13 μm). The resistivities were two to three times higher than that of the membrane alone. This difference is attributed to protonic and electronic resistance through catalyst layers, contact resistance, and electrical resistance in gas diffusion layer and micro porous layers.
The above observations confirm that the loss of conductivity, when the temperature was increased to 175 °C without humidification, was due to dehydration of phosphoric acid (boiling point of H_3PO_4 85 %wt is ca ~154 °C).

The difference between the high-frequency real Z-axis intercept and the low frequency real Z-axis intercept correspond to $R_{tot} = R_{ac} + R_{mass}$. The system is idling around the OCP, therefore diffusion effects are excepted to be minimum and the reduced arc diameter Z_{tot} with increase in temperature indicates enhancement in the kinetics (drop in Z_{ac}) due to increase in the exchange current density (activation energy). The observed R_{tot} at temperature of 120, 150, 175 °C were 0.3, 0.126 & 0.06 ohm, respectively. The ratio of R_{tot} at 120°C /150 °C and 150°C /175°C were 2.38 & 2, respectively. It can be seen that the higher the temperature, the lower is the decrease in the ratio of resistance [61]. In other words the relationship is not the expected exponential relation; this is either due to mass transfer countering the kinetic enhancement (concentration) or reduction in the kinetics itself due to a fall in water activity [68] especially above 150°C.

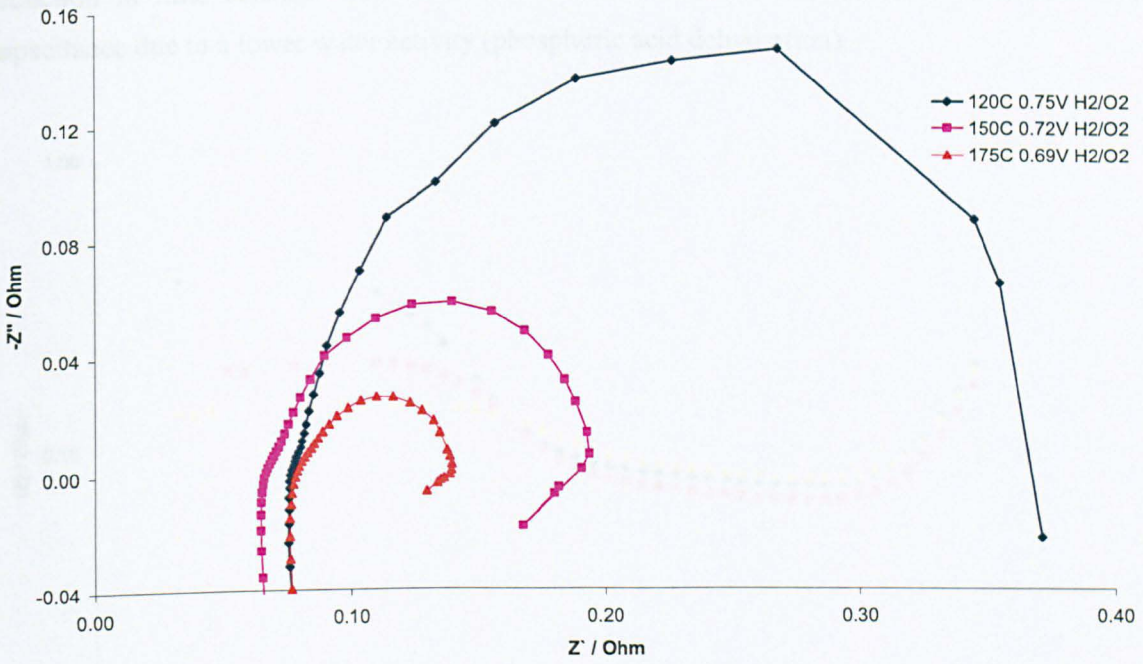

Figure 6-13. Impedance spectra at different temperature around OCP for MEA utilizing 4 mg_{H3PO4} cm^{-2} in the anode and 0.52 mg_{Pt} cm^{-2} (50% Pt/C) in the cathode with 40% PTFE.

Figure 6-13 shows the Bode diagram of the impedance amplitude for the data given in Fig. 6-12. While the capacitive behaviour of the first high frequency arc did not seem to vary with temperature, a decrease in the second capacitive behaviour was observed with increase in temperature. The time constants for the low frequency arc at temperature of 120, 150, 175 °C were 0.0583, 0.0245 & 0.0084 s, respectively (frequencies of 2.73, 6.5 & 19 Hz, respectively corresponding to max -Z''). The time constant is equal to $R_{tot}C_{lf}$ where C_{lf} is the capacity of the large low frequency arc. The ratio of $\tau_{120}/\ \tau_{150}$ and $\tau_{150}/\ \tau_{175}$ were, 2.38 & 2.92 respectively. By comparing the time constant ratios we can conclude that the decrease in the time constant from 120 to 150°C was solely attributed to the decrease in total resistance Z_{tot} (i.e. C_{lf} is unaffected). However, the lower time constant (ratio) from 150 to 175 °C is much larger than the fall in the R_{tot} ratio, suggesting a lowering in C_{lf} from 0.194 F at 120 & 150 °C to 0.14 F at 175 °C.

The low frequency arc can be assigned mainly to contributions from the double layer, as mass transport effects should be minimal around OCP. This suggests that the additional observed

reduction in time constant from 150 to 175 °C was related to a decrease in double layer capacitance due to a lower water activity (phosphoric acid dehydration).

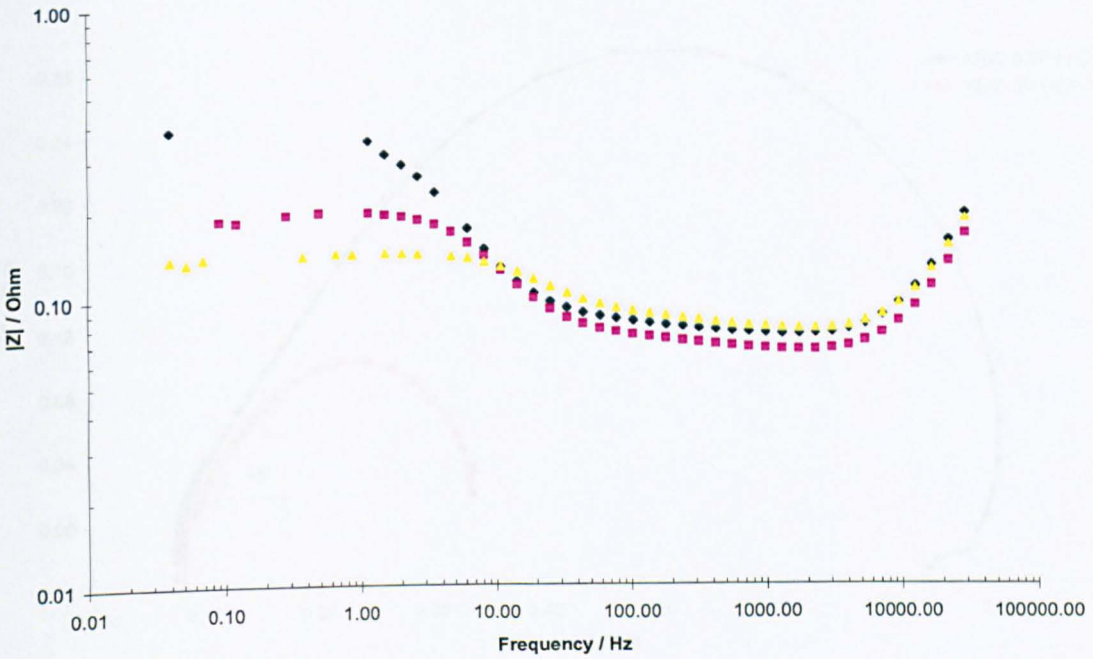

Figure 6-14. Bode diagram at different temperature around OCP for MEA utilizing 4 mg_{H3PO4} cm^{-2} in the anode and 0.52 mg_{Pt} cm^{-2} (50% Pt/C) in the cathode with 40% PTFE.

6.4.3.2 Anode/Cathode effects on cell impedance spectra

Figure 6-15 shows impedance spectra around OCP obtained with hydrogen at the anode and oxygen or hydrogen at the cathode. The total resistance largely fell when switching cathode gas feed from oxygen to hydrogen due to a change in the reaction occurring at the cathode; from oxygen reduction to hydrogen evolution (proton reduction to hydrogen). The total resistance fell by factor of 2.9 from 0.726 to 0.251 ohm, because the hydrogen evolution reaction is much faster than oxygen reduction.

A straight line with slope of 45° was observed in both spectra at high frequencies. This slope is related to finite length mass transport limitations (as discussed earlier). The fact that such a line was not observed in the rest of the studied MEAs and was observed in both spectra (hydrogen & oxygen feed) suggests that the mass transport limitation was anode related, due to a large PBI

content in the anode of 0.28 mg_{PBI} cm^{-2} (20% Pt/C 0.2 mg_{Pt} cm^{-2}). This was also confirmed from the low limiting current value observed in the anode polarisation (Chapter 4).

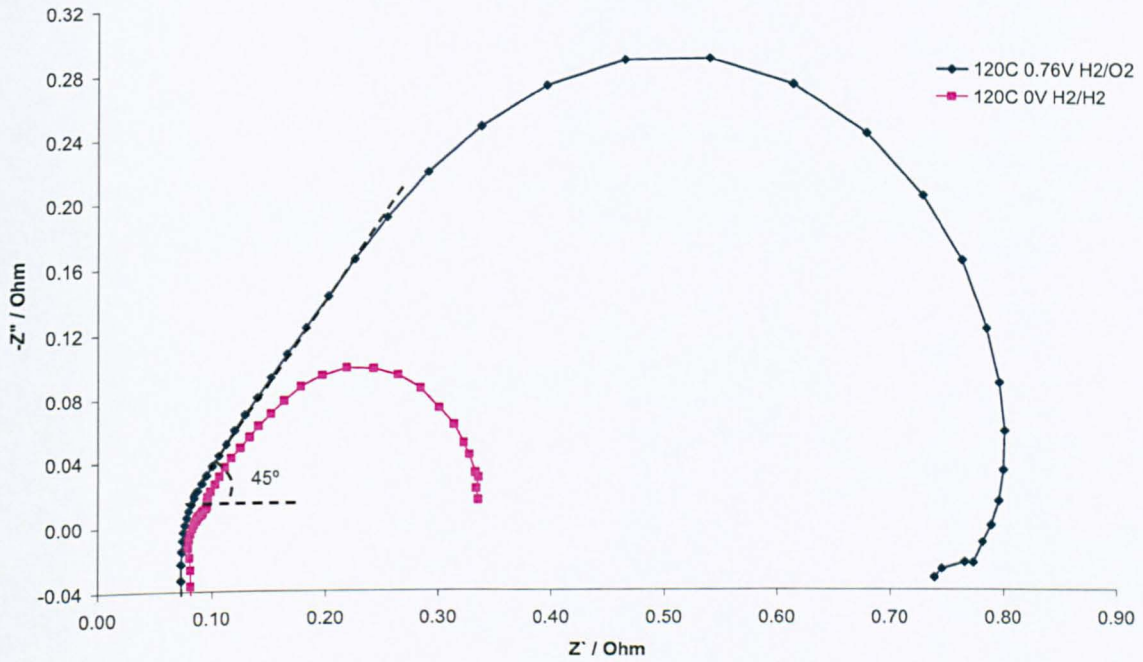

Figure 6-15. Impedance spectra with hydrogen at the anode and oxygen or hydrogen in the cathode around OCP at 120 °C for MEA utilizing 2.5 mg_{H3PO4} cm^{-2} with 0.28 mg_{PBI} cm^{-2} in the anode and 0.4 mg_{Pt} cm^{-2} (50% Pt/C) in the cathode with 40% PTFE.

On the contrary to R_{tot} the time constant of the low frequency arc increased by factor of 4.2 (2.73 & 0.64 Hz) when switching from oxygen to hydrogen. This suggests that C_{lf} for the cathode under hydrogen was larger than that under oxygen. This can be explained by a larger double layer with hydrogen than oxygen, due to under potential deposition of hydrogen (UPD).

6.4.3.3 Oxygen partial pressure effects on cell impedance spectra

Figure 6-16 shows impedance spectra for different oxygen partial pressure in the cathode, using air and oxygen, and are compared to that of heleox (0.21 O_2 / 0.79 He). It can be seen that losses in the porous structure did not contribute to the total impedance, where Z_{tot} for air was the same

as that with heleox, around OCP, even though the oxygen binary diffusion with helium was almost four times faster than that with nitrogen. Increasing oxygen partial pressure from air to oxygen led to drop in total impedance R_{tot} from 1.336 to 1.216 ohm (corresponding to ratio of 0.91). Similar observations were reported in the literature [69].

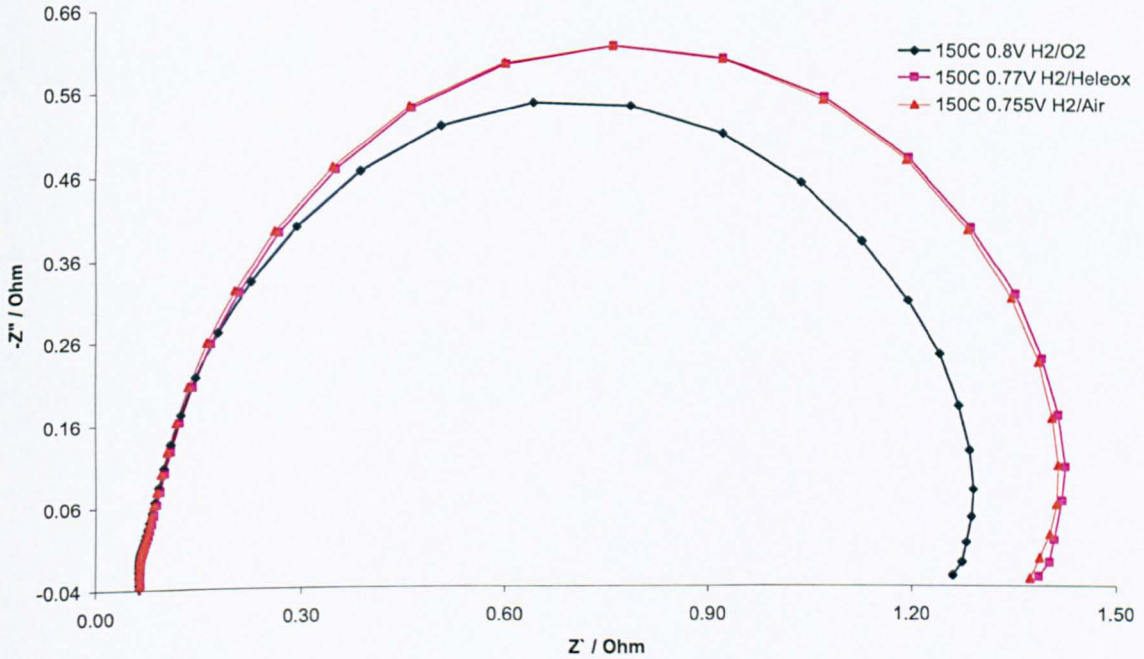

Figure 6-16. Impedance spectra for different cathode oxidants around OCP at 150 °C for MEA utilizing 4 mg_{H3PO4} cm^{-2} with 0.05 mg_{PBI} cm^{-2} in the anode and 0.4 mg_{Pt} cm^{-2} (50% Pt/C) in the cathode with 40% PTFE.

It can be seen that the high frequency arcs were identical, while the time constant of the low frequency arc (the large arc) slightly decreased when switching from air to oxygen with time constant ratio of 0.86 corresponding to a fall in R_{tot}. This suggests that C_{lf} around OCP was not affected by oxygen partial pressure (or concentration) in the film around OCP.

It can be concluded that the high frequency arc was related to the electrode structure and independent of the reaction or reactant concentration and therefore can be assigned to C_g, whilst the low frequency arc, around OCP, can be attributed mainly to double layer as it was independent of oxygen concentration, it was also affected by water activity. For a polarised

electrode this will change as the double layer will vary with potential and there will be mass transport contributions.

While the intercept at low frequency represent $R_{tot} = R_d + R_{ac}$ and considering negligible R_d around OCP, R_{ac} fell with temperature and oxygen concentration increase. However, R_{ac} is equal to $RT/\alpha F i_0$ (equation 38) around OCP and therefore it is expected that $R_{ac\text{-}o2}/R_{ac\text{-}air} = 0.21$ while the observed value was only 0.91. R_{ac} values varied using the same cathode materials at OCP at similar operating conditions (temperature of 150 °C & pure oxygen) where it increased from 0.126 to 1.22 ohm, when the rest potential varied from 0.72 to 0.8 V (different MEAs). The estimated value for standard potential of oxygen reduction is 1.14 -1.1 V for temperature range of 125-180 °C [12], while the observed OCP is a lower mixed potential, depending on the cross-over rate i_{cross} and other phenomena (carbon corrosion, platinum oxidation, etc..). Therefore $I \neq i_0$ at OCP, and the overvoltage $| E_0 - E |$ is no longer equal to zero. Therefore we can re-write equation (38) at OCP as:

$$R_{ac}^{\Delta} = \frac{\Delta\eta_{ac}}{\Delta i} = \frac{RT}{\alpha F} \frac{1}{i_0 + i_{cross}} \qquad [65]$$

The higher the cross-over rate i_{cross} the higher the overvoltage loss η (or the lower the observed OCP) and consequently the lower the observed Z_{tot} (R_{ac}^{Δ}). When switching from oxygen to air the OCP fell from 0.8 to 0.755 V due to a fall in oxygen concentration- thermodynamically (Nernst) it is expected to fall by ~29 mV- therefore the kinetic concentration effect was suppressed by the thermodynamic effect and the overvoltage in the case of air was higher than that with oxygen, reducing the estimated resistance ratio of 0.21 (at equal overvoltage) to the observed ratio of 0.91.

6.4.4 Impedance of polarisable cathode electrode

To eliminate the anode contribution in the spectra, a Dynamic Hydrogen Electrode (DHE) was used as reference electrode [70, 71] and the cathode impedance was studied for various MEAs. As seen earlier the impedance was greatly affected by the steady-state potential, however, in this case an external potentiostat Powerstat 20 A (Sycopel Scientific Ltd, U.K) was used to polarise

the electrode, as the potentiostat used for FRA measurements was limited to 1 A Autolab PGSTAT 30 (Eco Chemie, The Netherlands). The external potentiostat had to operate in the galvanostat mode (fixed current) rather than potentiostat mode (fixed potential) due to conflict between the two systems in the potentiostatic mode, where the external potentiostat would try to hold the potential at the fixed set value and the other would try to perturb the potential (or current) with the specified AC amplitude.

6.4.4.1 Effect of steady-state current

It should be noted in the case of a polarisable electrode, the measured impedance does not correspond to the cell impedance alone but incorporates the impedance of the resistor used to polarise the cell R_{polar} (external galvanostat) to achieve the desired steady-state current, as shown in circuit (k) below:

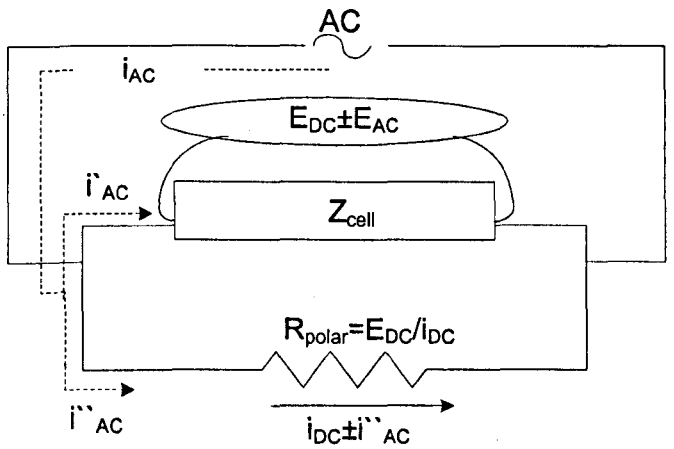

Equivalent circuit
k

We can therefore write:

$$\frac{1}{Z_{observed}} = \frac{1}{Z_{cell}} + \frac{1}{Z_{Polar}} \Rightarrow Z_{observed} = \frac{1}{\frac{1}{Z_{cell}} + \frac{i}{E_{cell}}} \qquad [66]$$

Similarly,

$$R^{\Delta}_{ac\_observed} = \frac{1}{\frac{1}{R^{\Delta}_{ac}} + \frac{i}{E_{cell}}} = \frac{RTE_{cell}}{\alpha F E_{cell} + RT}\left(\frac{1}{i}\right) = \frac{R^{\Delta}_{ac}}{1 + \frac{RT}{\alpha F E_{cell}}} \quad [67]$$

And,

$$R^{\Delta}_{total\_observed} = R^{\Delta}_{ac\_observed} + R^{\Delta}_{mass\_observed} = \frac{R_{tot}}{1 + \frac{i}{E_{cell}} R_{tot}} = \frac{\frac{RT}{\alpha F}\left(\frac{C}{C_{\Delta}}\left(\frac{1}{i} + \frac{1}{\Delta i}\right) - \frac{1}{\Delta i}\right)}{1 + \frac{i}{E_{cell}}\frac{RT}{\alpha F}\left(\frac{C}{C_{\Delta}}\left(\frac{1}{i} + \frac{1}{\Delta i}\right) - \frac{1}{\Delta i}\right)} \quad [68]$$

We can then conclude that the measured (observed) charge transfer impedance of the polarisable cell is lower than the actual charge transfer impedance (cathode in this case) by a factor of $(1+RT/\alpha FE_{cell})$, except for the case where $E_{cell} = E_{OCP}$ as there is no net DC current flowing in this case and $Z_{polar} \rightarrow \infty$.

This means that $Z_{observed}$ will decline quickly with an increase in, I, due to two effects; the first fall in R^{Δ}_{ac} (directly proportional to the inverse of i) and the second a fall in E_{cell} (exponentially dependant on the inverse of current under kinetic control). $Z_{observed}$ will continue to fall when i is increased until mass transport effects become dominant (C/C_{Δ}) and $Z_{observed}$ will increase. However, when mass transport effects become very severe, the value of (i/E_{cell}) will become very large and $Z_{observed}$ will decrease again. Therefore it is expected that Z_{mass} will decrease with increasing i, reaching a minimum and then increase again. This behaviour has been reported experimentally when studying the polarization-dependent mass transport parameters for ORR in perfluorosulfonic acid ionomer membranes (Nafion) [70].

Equation 68 also shows that the difference between $Z_{observed}$ of active and inactive electrodes, concentration effects or temperature is minimized (except OCP case) especially at low E_{cell} values. Under a given steady-state current i, the more active electrode will exhibits smaller values of R_{ac} or smaller R_{mass}, however, it will exhibit higher values of E_{cell} and therefore the overall effect will be minimized.

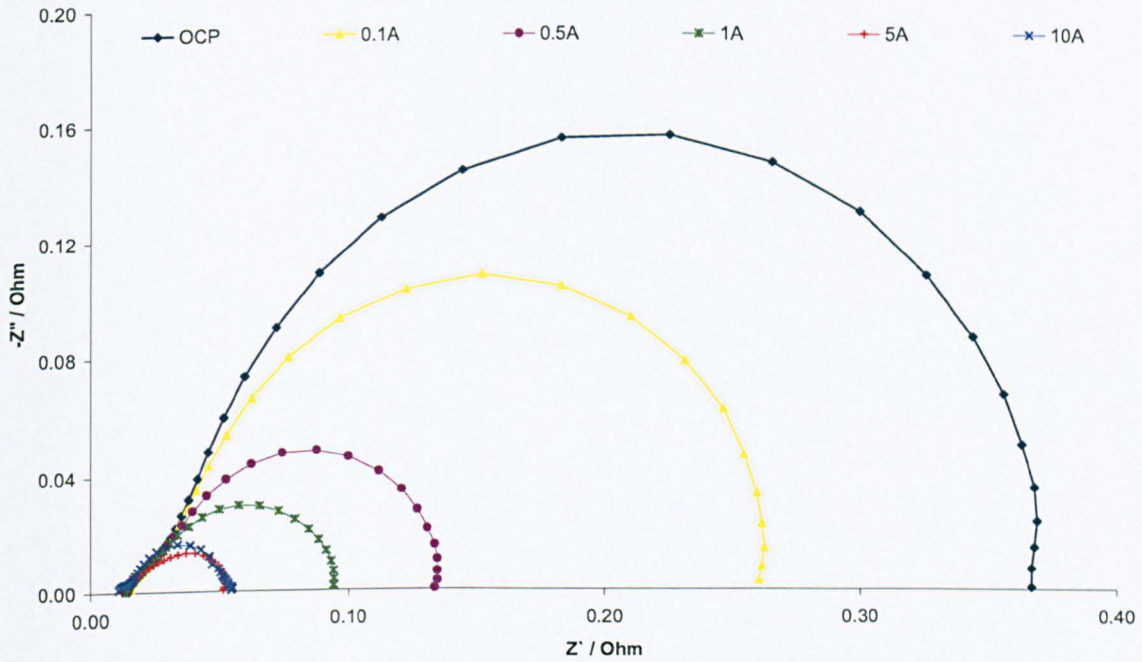

Figure 6-17. Nyquist plot for 40% Pt/C cathode using 40% PTFE and 0.4 mg_{Pt} cm^{-2} vs. DHE at 120 °C under air operation and various current loads.

Figure 6-17 shows impedance spectra for a 40 %Pt/C cathode under various steady-state currents. As expected from equation 68 when the current i increased, the potential E_{cell} fell and the total impedance decreased rapidly. As the impedance decreased, the large low frequency semi circle decreased until it merged with the high frequency semi circle at 5.0 Amps. With a further increase in the current, beyond 5.0 A, an increase in cell impedance was observed and an additional small semi circle was observed at very low frequencies and a new phase-shift was observed at ~3 Hz. This was attributed to mass transport processes leading to additional overvoltage losses [37] as the impedance related to diffusion are usually found in the low frequency region.

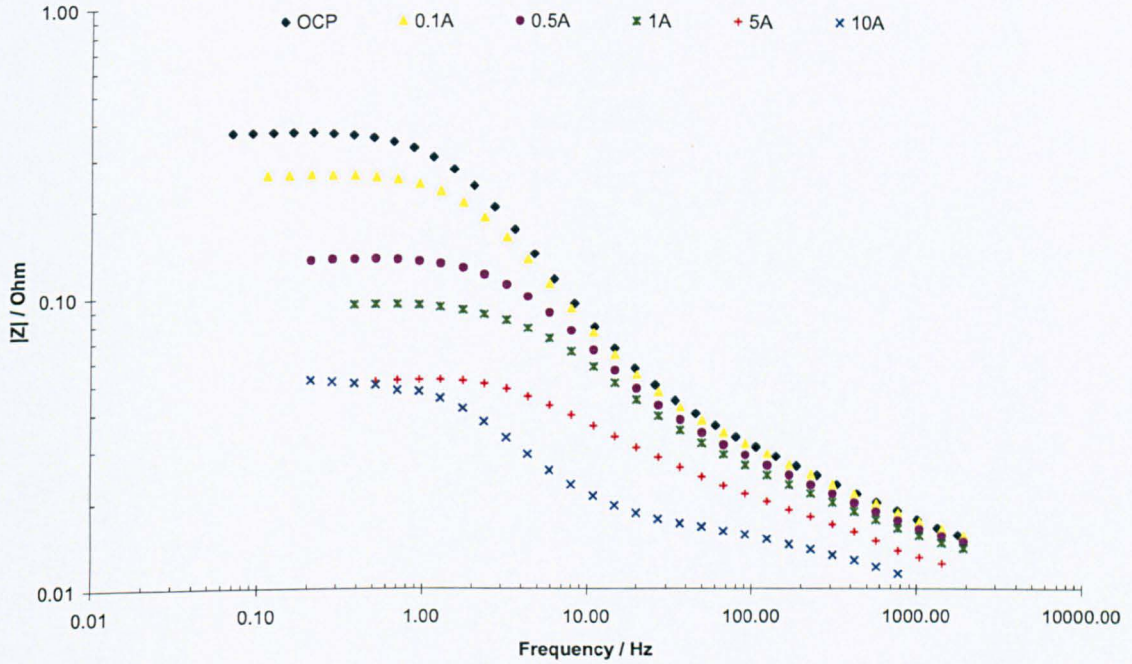

Figure 6-18. Amplitude ratio Bode plots for 40% Pt/C cathode using 40% PTFE and 0.4 $mg_{Pt}\,cm^{-2}$ vs. DHE at 120 °C under air operation and various current loads.

Figures 6-18 & 6-19 show the corresponding Bode diagram of the impedance spectra in Fig. 6-17. It can be seen that the slope of the high frequency asymptote and therefore the time constant (corresponding to the small high frequency semi-circle) did not change with current i. On the other hand the slope of low frequency asymptote decreased rapidly with i due to a decrease in $R_{tot\_observed}$ and therefore reduced the time constant. At 5.0 A the slope of the low frequency asymptote became similar to that at high frequency (time constant); while at 10.0 A, a new asymptote (slope) was found at low frequencies; attributed to a mass transfer time constant.

Similarly, the phase shift peak shifted towards higher frequencies as the current increased. While a new phase shift appeared at 10 A at low frequencies, caused by mass transport effects [37]. Similarly the PTFE content and correspondingly mass transfer effects was found to affect the low frequency intercept [72].

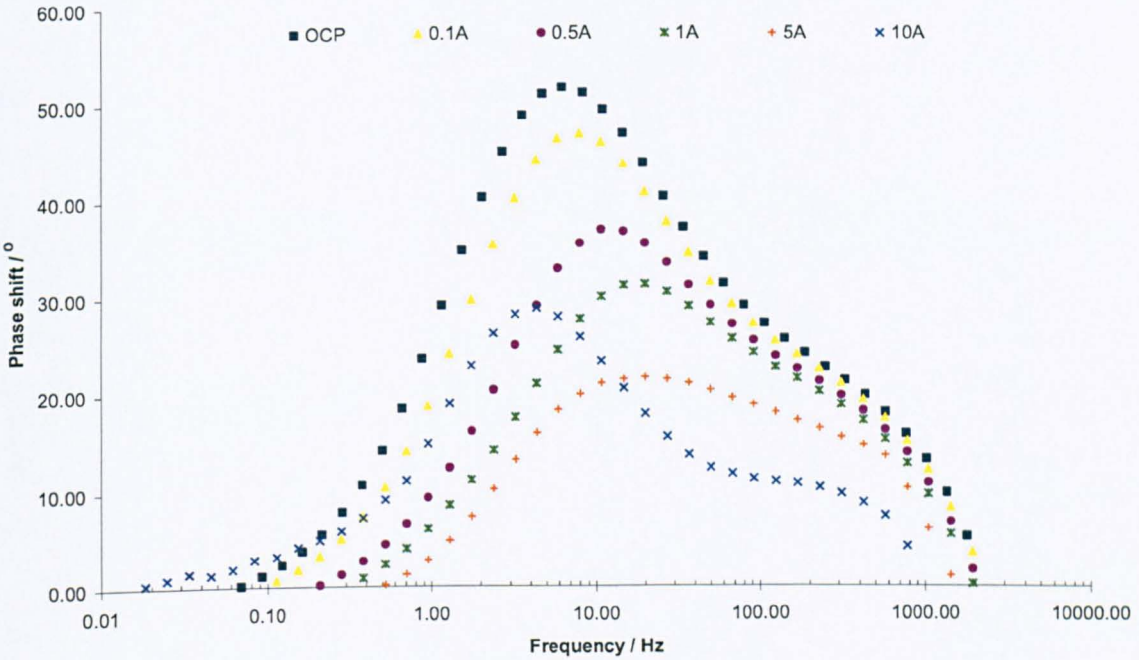

Figure 6-19. Phase shift Bode plot for 40% Pt/C cathode using 40% PTFE and 0.4 mg_{Pt} cm^{-2} vs. DHE at 120 °C under air operation and various current loads.

6.4.4.2 Effect of oxygen partial pressure

Figure 6-20 shows Nyquist plots for a 40% Pt/C cathode electrode at 150 °C under air and oxygen operation. At 0.1 A, a large difference between $Z_{tot\_observed}$ was seen for oxygen and air, the reduction in Z_{tot} when switching to oxygen was mainly attributed to enhancement in i_0 and therefore reduction in R_{ac} , as mass transport effects were minimal under these conditions. When the current increased to 10 A, a large contribution from mass transport is expected and therefore a large difference in Z_{tot} is expected. However, there was a very small difference between $Z_{tot\_observed\ (air)}$ and $Z_{tot\_observed\ (O2)}$ because of the counter effect of the very low value of E_{cell} under air operation in comparison to E_{cell} under oxygen operation at 10 A.

Even though similar low frequency impedance intercepts were observed under air and oxygen at 10 A, the shape of the semi circles varied. In the case of oxygen, the high frequency semi circle

was larger than the low frequency arc. On the contrary, with air operation the high frequency semi circle was smaller than that of the low frequency semi circle.

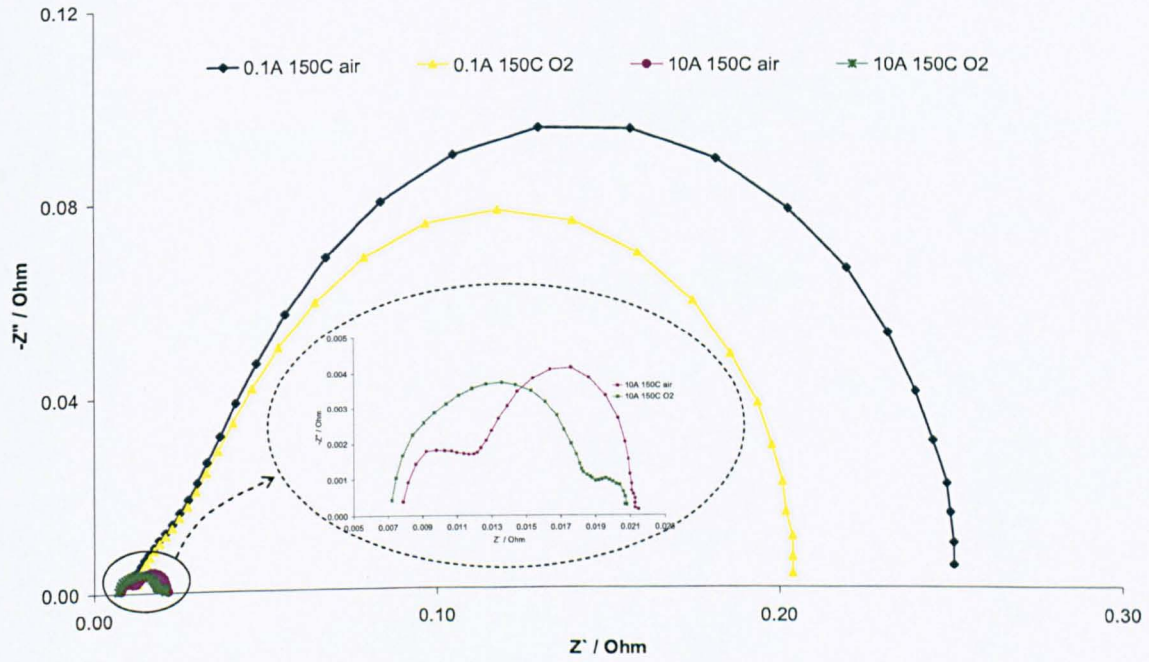

Figure 6-20. Nyquist plot for 40% Pt/C cathode using 40% PTFE and 0.4 mg_{Pt} cm^{-2} vs. DHE at 150 °C under air and oxygen operation and current load of 0.1 & 10 A.

This can be explained further by observing the corresponding Bode diagrams in Figure 6-21 & 6-22. For a 10 A, steady-state current, and under oxygen operation, no new asymptote (slope) was observed, whilst a new asymptote was observed under air operation, corresponding to the large arc observed at low frequencies arising from mass transport losses. This effect can also be confirmed from phase shift diagram where no new phase shift peak was observed under oxygen operation, whilst a new low frequency phase shift was observed at ~5 Hz under air operation.

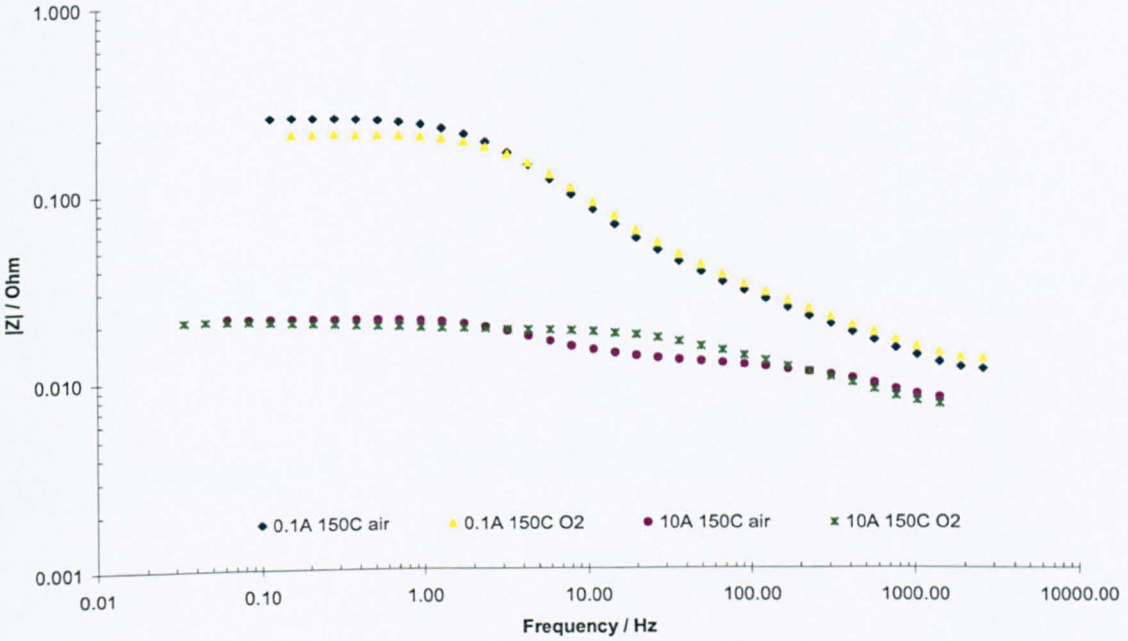

Figure 6-21. Amplitude ratio Bode plot for 40% Pt/C cathode using 40% PTFE and 0.4 mg_{Pt} cm^{-2} vs. DHE at 150 °C under air and oxygen operation and current load of 0.1 & 10 A.

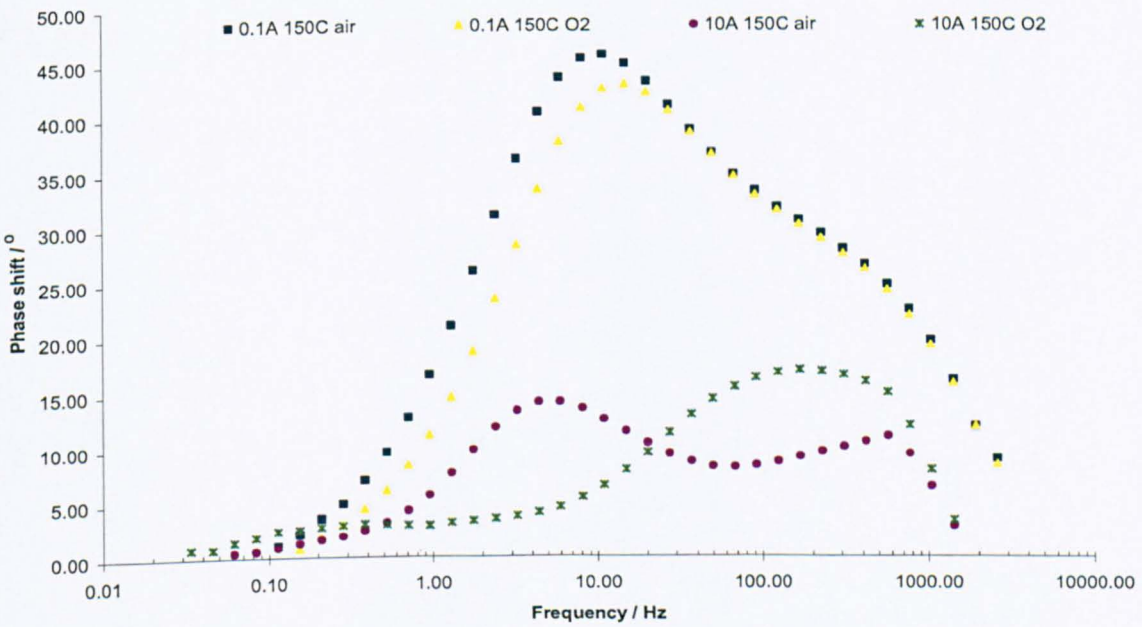

Figure 6-22. Phase shift Bode plot for 40% Pt/C cathode using 40% PTFE and 0.4 mg_{Pt} cm^{-2} vs. DHE at 150 °C under air and oxygen operation and current load of 0.1 & 10 A.

6.4.4.3 Effect of temperature

Figure 6-23 shows Nyquist plots for a 40 %Pt/C cathode at temperature of 120, 150 & 175 °C under air operation. Similar conclusions (to whole cell impedance) can be drawn about electrode/membrane interface resistivity, as the high frequency intercept exhibited a minimum at 150 °C without humidification, due to dehydration of 85% wt phosphoric acid beyond 154 °C. At 0.1 A, $Z_{tot\_observed}$ (low frequency intercept subtracted from high frequency intercept) decreased as the temperature increased, due to an increase in i_0 and reduction in R_{ct}.

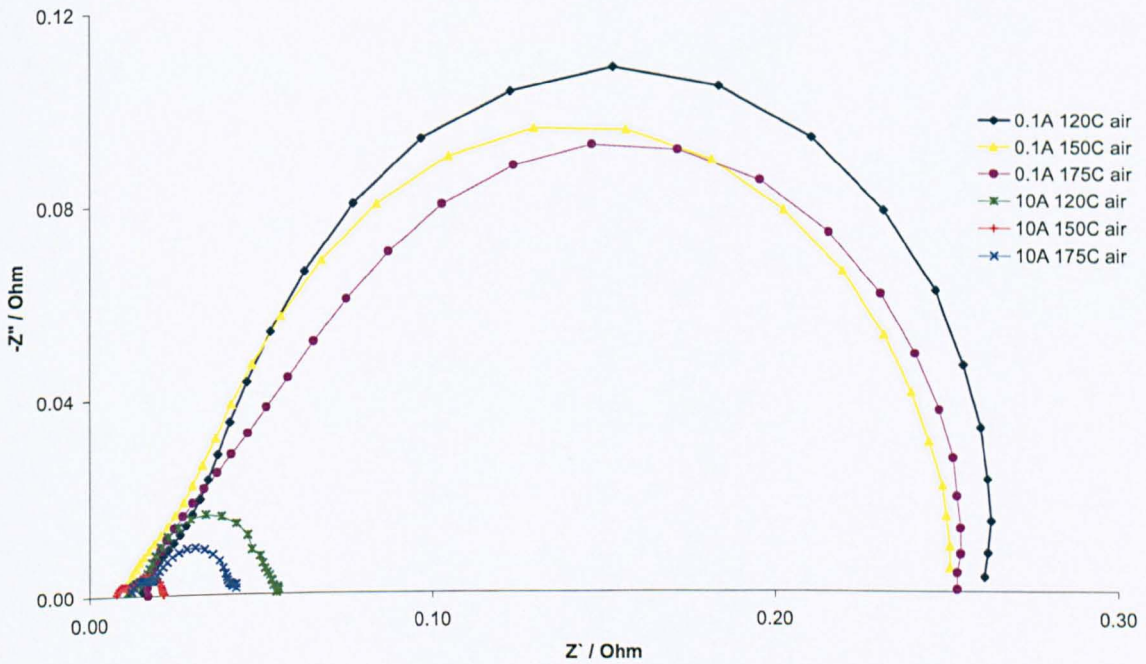

Figure 6-23. Nyquist plot for 40% Pt/C cathode using 40% PTFE and 0.4 mg_{Pt} cm^{-2} vs. DHE at 120, 150& 175 °C under air operation and current load of 0.1 & 10 A.

At 10 A, a temperature of 150 °C gave the smallest $Z_{tot\_observed}$ followed by 175 and 120°C. This suggests that 150 °C provided the minimum Z_{mass} or the best oxygen permeability. This can be linked with the best conductivity observed at 150 °C, where a temperature increase would reduce solubility (Henry's law) and enhance diffusivity. However, dehydration above 154 °C would lead

to an increase in phosphoric acid viscosity and consequently a decrease in diffusivity. This can also be observed from the limiting current value which fell from 150 to 175 °C.

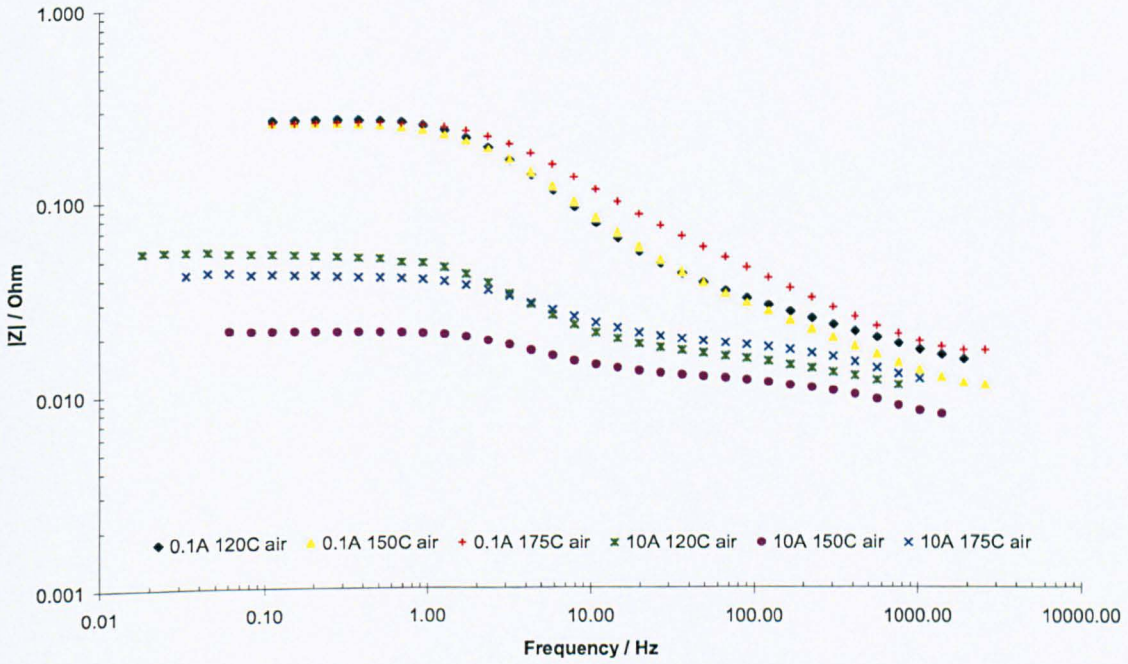

Figure 6-24. Amplitude ratio Bode plot for 40% Pt/C cathode using 40% PTFE and 0.4 mg_{Pt} cm^{-2} vs. DHE at 120, 150 & 175 °C under air operation and current load of 0.1 & 10 A.

The mass transfer effects are clearly apparent in Bode diagrams shown in Figure 6-23 & 6-24, where a new asymptote (slope) appeared in the low frequency region at 10 A for all the studied temperatures. Similarly, a new phase shift peak appeared ~5 Hz under 10 A operation, for all the studied temperatures. 150 °C exhibited the smallest amplitude ratio and phase angle shift in comparison to the other electrodes at 10 A. The total impedance at low frequencies $R_{tot\_observed}$ did not vary at 150 °C using either air or oxygen (0.0135 ohm), whilst at 175 °C it increased from 0.0151 to 0.029 ohms when switching from oxygen to air.

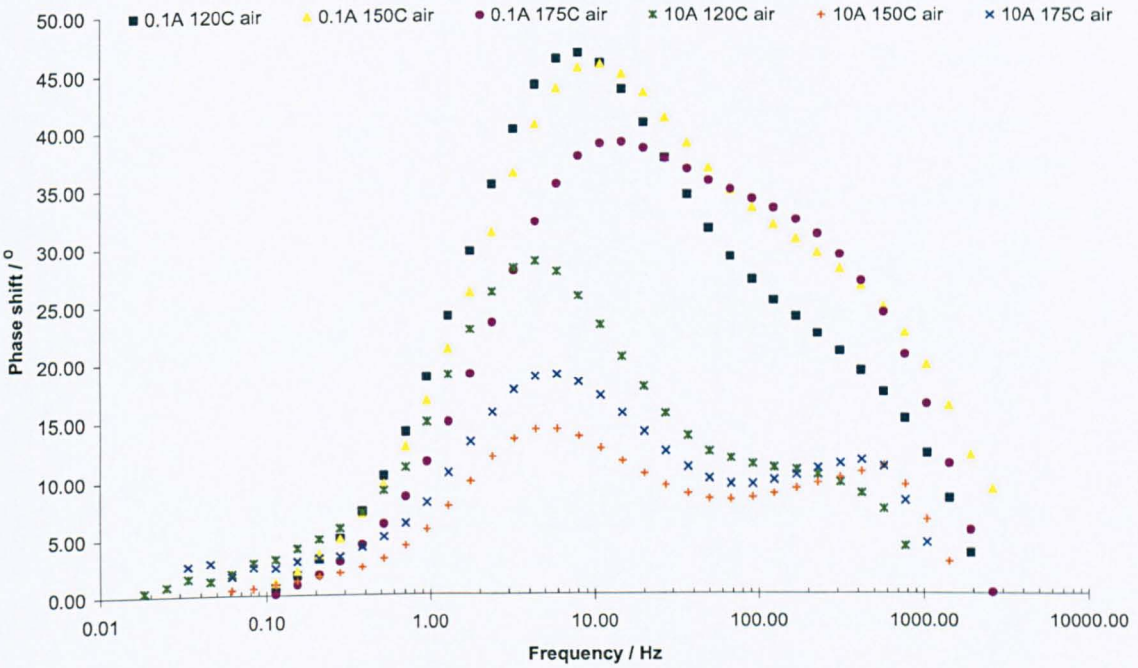

Figure 6-25. Phase shift Bode plot for 40% Pt/C cathode using 40% PTFE and 0.4 mg_{Pt} cm^{-2} vs. DHE at 120, 150 & 175 °C under air operation and current load of 0.1& 10A.

6.4.5 Data modelling using equivalent circuits

The experimental data were fitted to the three suggested circuits (h, i & j) using ZSimpWin V3.21 software (Princeton Applied Research, U.S.A) utilising Complex Non-linear Least Square errors technique (CNLS). The data for circuit i (two forms for mass transport element O and CPE/R), j & h are presented in Tables 6-9, 6-10, 6-11 & 6-12, respectively.

As stated earlier the inductance in this case was due to mutual inductance, i.e., cable effects in the range of 10^{-7}-10^{-8} Henri. The first resistor related to the high frequency intercept represented the ohmic resistance (ionic + electric) in the range of 10^{-2} ohm, the value of the resistance decreased slowly with increase in I, due to a fall in Z_{polar} and increase in proton conductivity with increase in water production (relative humidity). It has been shown previously that membrane resistance decreased with increase in current density for PBI based MEAs [73].

Table 6-9 shows the result of circuit, e, with mass transport in finite length L represented by element O with parameters Y_0 equal to $1/(2^{0.5}\sigma)$ (σ is the mass transfer coefficient equal to $\frac{RT}{n^2F^2C_\Delta\sqrt{2}\sqrt{D}}$) and B^2 is equal to L^2/D corresponding to diffusion time constant. Values of B were in the range of 0.2-0.3 $s^{0.5}$ and did not change with current (I) or when switching from air to oxygen. These values were smaller than the value, obtained from chronoamperometry measurements around the limiting current of 1.64 $s^{0.5}$, however, they were still three orders of magnitude higher than the estimated value from the reported diffusion coefficient and estimated film thickness (Sec. 6.3.2).

On the other hand the admittance of element O is expected to be inversely proportional to mass transfer coefficient σ and consequently directly proportional to oxygen concentration (dissolved) in the thin film (Eq. 52). On the contrary, the observed Y_0 increased with an increase in I and increased more rapidly at higher I values. Y_0 also increased when switching from oxygen to air; this increase became larger at higher operating currents. This suggests that the observed Y_0 is inversely proportional to C_Δ rather than directly proportional (Eq. 52 & 53). Additionally, with increased current, R_{ac} should decrease (Eq. 38), R_{mass} should increase (Eq. 46) and, since R_{mass} is equal to B/Y_0 and B is independent of I (B^2 is equal to L^2/D), Y_0 should also decrease. The reason behind the unexpected behaviour of the apparent Y_0 was that $R_{tot\_observed}$ decreased continuously with an increase in current (I), especially at high currents, due to a large decrease in Z_{polar} masking the effect of the increase in R_{mass} which wasn't considered in circuit e.
It thus can be concluded that circuit e, is not appropriate to describe the studied system.

While Z_{polar} is pure resistance and will only affect the values of R in the equivalent circuit (R_{mass}, R_{ac} & R_s), it will have no effect on the capacitance. Z_{polar} can be included in the equivalent circuit, but it will lead to more difficult fitting due to free parameters. On the other hand the value of Z_{polar} should be known from the steady-state value of current I and E_{cell} and therefore the subtraction of its effect is possible.

Circuits e and h are similar and their parameters are presented in Tables 6-10 & 6-12, respectively. Where the high frequency arc is represented with a resistor-capacitance and the low

frequency arc is represented by a resistor-CPE. The resistors in both cases are in series, as the total resistor is the sum of both resistors (R_{tot} = R_{mass}+R_{ac}). In the equivalent circuit e, the capacitors are connected in series $1/C_{eq}=1/C_1+1/C_2$ and therefore their values are larger than that of circuit h, where the capacitances are connected in parallel $C_{eq}= C_1+C_2$.

Table 6-9. Equivalent circuit (e or i) with O element parameters using CNLS technique for 40% Pt/C cathode electrode at 150 °C under air and oxygen operation.

LR(CR)O (O_2 150 °C)	0.1A	0.5A	1A	5A	10A
L (Henri)	8.59E-08	7.77E-08	7.14E-08	1.04E-07	8.52E-08
R (Ohm)	0.009026	0.009292	0.008817	0.006776	0.006893
C (Faraday)	4.348	0.2127	0.1474	0.1024	0.1368
R (Ohm)	0.02402	0.004363	0.00576	0.00529	0.005011
O-Y_o(Ohm^{-1} $sec^{0.5}$)	1.66	2.207	2.766	6.652	17.22
O-B ($sec^{0.5}$)	0.2852	0.1967	0.1563	0.09433	0.1291
LR(CR)O (air 150 °C)					
L (Henri)	8.08E-08	1.12E-07	9.05E-08	6.74E-08	1.02E-07
R (Ohm)	0.008046	0.008751	0.008727	0.007898	0.007376
C (Faraday)	2.182	0.7106	0.2973	0.09579	0.09762
R (Ohm)	0.05745	0.001562	0.004375	0.009227	0.003541
O-Y_o(Ohm^{-1} $sec^{0.5}$)	1.814	2.47	3.194	7.303	30.91
O-B ($sec^{0.5}$)	0.3352	0.2668	0.225	0.2192	0.3183

For circuit e (Table 6-10) the capacitance responsible for the high frequency arc remained constant at ~ 0.3 F until a current of 1.0 A, and then slightly increased at 5.0 A and reached unrealistic value of 426 F at 10 A under oxygen operation. While the CPE, responsible for the low frequency arc, decreased and then increased with an increase in (I), in the range of 0.2 -1.0 F and had similar values under air and oxygen operation (Table 6-10).

Circuit e can be discarded as it led to unrealistic values for the high frequency capacitance and the low frequency capacitance (CPE) was not affected by mass transport as would be excepted-(air and oxygen operation led to similar capacitances).

Table 6-10. Equivalent circuit (e or i) with CPE/R elements parameters using CNLS technique for 40% Pt/C cathode electrode at 150 °C under air and oxygen operation.

LR(CR)(QR) (O_2 150 °C)	0.1A	0.5A	1A	5A	10A
L (Henri)	9.87E-08	8.55E-08	8.35E-08	1.09E-07	1.37E-07
R (Ohm)	0.008943	0.009607	0.009051	0.007039	0.005838
C (Farad)	0.2789	0.2828	0.2926	0.4219	426.2
R (Ohm)	0.1369	0.06004	0.03703	0.009316	0.001564
Q-Y_o (F^{-1} s^{1-n})	1.169	0.6518	0.501	0.2179	1.114
Q-n	0.5331	0.6249	0.6696	0.8288	0.6497
R (Ohm)	0.06174	0.03507	0.0261	0.01003	0.01346
LR(CR)(QR) (air 150 °C)					
L (Henri)	1.11E-07	1.01E-07	5.48E-08	1.41E-07	1.11E-07
R (Ohm)	0.007123	0.009461	0.0101	0.006498	0.007123
C (Farad)	0.3411	0.3995	0.07816	1.524	0.3411
R (Ohm)	0.1686	0.07635	0.006116	0.01671	0.1686
Q-Y_o (F^{-1} s^{1-n})	1.737	0.983	0.561	0.6958	1.737
Q-n	0.4865	0.6119	0.781	0.6469	0.4865
R (Ohm)	0.08137	0.03449	0.07485	0.02487	0.08137

Circuit j and h (Table 6-11 & 12) are very similar. The only difference is that circuit h contains two sets of capacitor (or CPE) resistors in a ladder form representing two different time constants (high and low frequency arcs), while circuit j contains three sets of capacitor-resistor in a ladder form representing three different time constants, in an attempt to separate the kinetics effect from mass transport effects or in other words in order to split the low frequency arc into two different time constants. To fit circuit j to experimental data was not successful where it can be seen (Table 6-11) that the first time constant was extremely small with small values for the first capacitance, in the range 10^{-3}-10^{-4} F obtained. Additionally the values of the second and the third capacitances-resistor (time constant) were very similar to the first and second capacitances-resistor of circuit h (Table 6-12), respectively. This confirmed the previous conclusion that the

separation of the charge transfer time constant from the diffusion time constant was not possible for the studied system.

Table 6-11. Equivalent circuit (j or f) parameters using CNLS technique for 40% Pt/C cathode electrode at 150 °C under air and oxygen operation.

L(C(R(C(R(QR))))) (O_2 150 °C)	0.1A	0.5A	1A	5A	10A
L (Henri)	2.21E-07	1.74E-07	1.61E-07	1.25E-07	1.77E-07
C (Farad)	0.001397	0.001095	0.001104	0.000631	8.09E-4
R (Ohm)	0.01461	0.01311	0.01177	0.007806	0.004862
C (Farad)	0.03428	0.0346	0.03615	0.05182	9.53E-23
R (Ohm)	0.02109	0.01697	0.01444	0.008644	4.87E-13
Q-Y_o (F^{-1} s^{1-n})	0.2814	0.2973	0.3116	0.4911	1.708
Q-n	0.8536	0.857	0.8612	0.8961	0.5633
R (Ohm)	0.1744	0.0759	0.0466	0.01004	0.01537
L(C(R(C(R(QR))))) (air 150°C)					
L (Henri)	2.38E-07	1.75E-07	1.46E-07	2.67E-07	7.24E-07
C (Farad)	0.001824	0.001051	0.000864	0.002801	0.005288
R (Ohm)	0.01358	0.01218	0.01108	0.009997	0.01276
C (Farad)	0.03821	0.04912	0.04882	0.05744	0.2231
R (Ohm)	0.02043	0.01571	0.01278	0.01113	0.004501
Q-Y_o (F^{-1} s^{1-n})	0.3373	0.4112	0.5196	1.416	2.406
Q-n	0.8423	0.8546	0.8254	0.7744	0.8797
R (Ohm)	0.224	0.09487	0.06295	0.02758	0.03637

Equivalent circuit h (Table 6-12) seemed to provide the best fit for the studied system as discussed below.

Values of the first capacitance-resistor pair, responsible for the high frequency arc, did not vary when switching from air to oxygen. The first capacitance increased slowly with I, in the range of 10^{-2} F; the values were very close to the estimated value for the geometric capacitance C_g and

very low for the double layer capacitance C_{dl}. The first resistance (in parallel with the first capacitor) had low values in the range of 10^{-2} ohms and slowly fell with an increase in current I; values were similar for air and oxygen. The first resistor does not have a physical meaning but corresponds to the end of the first semi circle and the beginning of the second semicircle, in other words the end of the effects of the geometric capacitance and the beginning of the double layer capacitance effects.

The second capacitor (CPE) increased with I, where it started from the same value for air and oxygen at OCP of 0.291 F (not shown in the table) or close values of 0.291 F and 0.32 F for oxygen and air, respectively at 0.1 A. As I increased the capacitance increased slowly under oxygen and rapidly under air. This result means that the observed capacitance was the sum of the double layer capacitance and mass transport capacitance.

The double layer capacitance can be obtained at OCP, where the mass transport contribution is negligible and is in the region of 10^{-1} F, which is in good agreement with the results obtained from cyclic voltammetry. The mass transport capacitance can be obtained from the subtraction of the double layer capacitance (the second capacitance at OCP) from the second capacitance (low frequency) at given current I. The increase of C_{mass} with I is expected, from equation (63) it can be seen that the diffusion time constant τ_d was directly proportional to the square of the mass transfer coefficient, σ, and consequently inversely proportional to the square of oxygen concentration at the Pt surface C_Δ. τ_d is equal to $R_d.C_d$ (or $R_{mass}.C_{mass}$), and from equation (46) R_{mass} is inversely proportional to i and directly proportional to $((C/C_\Delta)-1)$ and therefore the time constant value will decrease with I and increase only when C_Δ becomes very small or $((C/C_\Delta)-1)$ very large. Therefore, C_{mass} should increase rapidly with a decrease in C_Δ or an increase in I.

The second resistance (incorporated with the second capacitor) had large values (order of 10^{-1} ohm) and fell rapidly with I. This is typical behaviour of R_{tot}, where at OCP, ignoring cross-over current, R_{tot} is equal to R_{ac} (R_{mass} is minimal and Z_{polar} is infinity) and the second capacitance associated with it, is equal to C_{dl} ($C_{mass} \approx 0$). As I increases Z_{polar} decreases $R_{tot\_observed} = ((R_{ac}+R_{mass})/(1+(R_{ac}+R_{mass})/Z_{polar}))$ and the associated capacitance becomes equal to $C_{dl}+C_{mass}$. R_{tot} in this case is equal to the low frequency intercept subtracted from the high frequency intercept or the sum of the first and the second resistors (in series).

Table 6-12. Equivalent circuit (h or d) parameters using CNLS technique for 40% Pt/C cathode electrode at 150 °C under air and oxygen operation.

LR(C(R(QR))) (O_2 150 °C)	0.1A	0.5A	1A	5A	10A
L (Henri)	6.20E-08	1.02E-07	2.04E-07	2.08E-07	1.20E-07
R (Ohm)	0.01272	0.01205	0.011	0.008107	0.006731
C (Farad)	0.03031	0.03331	0.03647	0.06578	0.06496
R (Ohm)	0.02056	0.01742	0.01539	0.0101	0.004
Q-Y_o (F^{-1} s^{1-n})	0.2907	0.2986	0.308	0.4969	1.738
Q-n	0.8463	0.8565	0.8674	0.9533	0.7371
R (Ohm)	0.1776	0.07653	0.04631	0.008134	0.007462
LR(C(R(QR))) **(air 150 °C)**					
L (Henri)	1.05E-07	7.64E-09	4.55E-08	8.37E-08	2.04E-07
R (Ohm)	0.01246	0.0116	0.01082	0.008805	0.008141
C (Farad)	0.0437	0.04983	0.05249	0.05612	0.1237
R (Ohm)	0.02046	0.01648	0.01396	0.01225	0.00407
Q-Y_o (F^{-1} s^{1-n})	0.3226	0.4085	0.5098	1.396	5.883
Q-n	0.8767	0.8585	0.8356	0.7807	0.877
R (Ohm)	0.1966	0.09449	0.06174	0.02758	0.009286

In summary, even though the interpretation of impedance spectra is complicated, vital information about electrode performance can be obtained. The double layer capacitance can be obtained from the low frequency arc capacitance around OCP. $R_{tot\_observed}$ corresponds to the low frequency intercept (subtracted from the high frequency intercept) and is equal to R_{ac} and $\frac{RT}{\alpha F}\frac{1}{i_0 + i_{cross}}$ at OCP. The mass transport capacitance C_{mass} gives direct information about the mass transport coefficient and can be used to compare electrode performances. It can be obtained from the double layer capacitance subtracted from the low frequency capacitance. Similarly, $R_{tot\_observed}$ can be used to compare various electrodes performance; where low $R_{tot\_observed}$ at lower currents suggests better kinetics, while at higher currents suggest better mass transport performance.

6.4.5.1 Double layer capacitance

Figure 6-26 shows the double layer capacitance of electrodes with various Pt:C ratio at temperatures of 120, 150 & 175 °C with no added acid in the catalyst layer. It can be seen that increasing the carbon content in the catalyst layer (thickness), with fixed Pt content, lead to an increase in the double layer capacitance due to the larger surface area (interface). However, increasing the catalyst thickness beyond 40% Pt/C i.e. towards 30% Pt/C, did not lead to a further increase in C_{dl} as the catalyst was too thick and only a fraction of it was accessible to the mobile acid electrolyte from the membrane.

A decrease in the double layer capacitance was also observed with a temperature increase from 150 to 175 °C, due to a fall in water activity (dehydration of phosphoric acid); the change in the double layer with temperature was one of the reasons given for the observed dependency of the transfer coefficient on temperature in phosphoric acid systems (see Chapter 3).

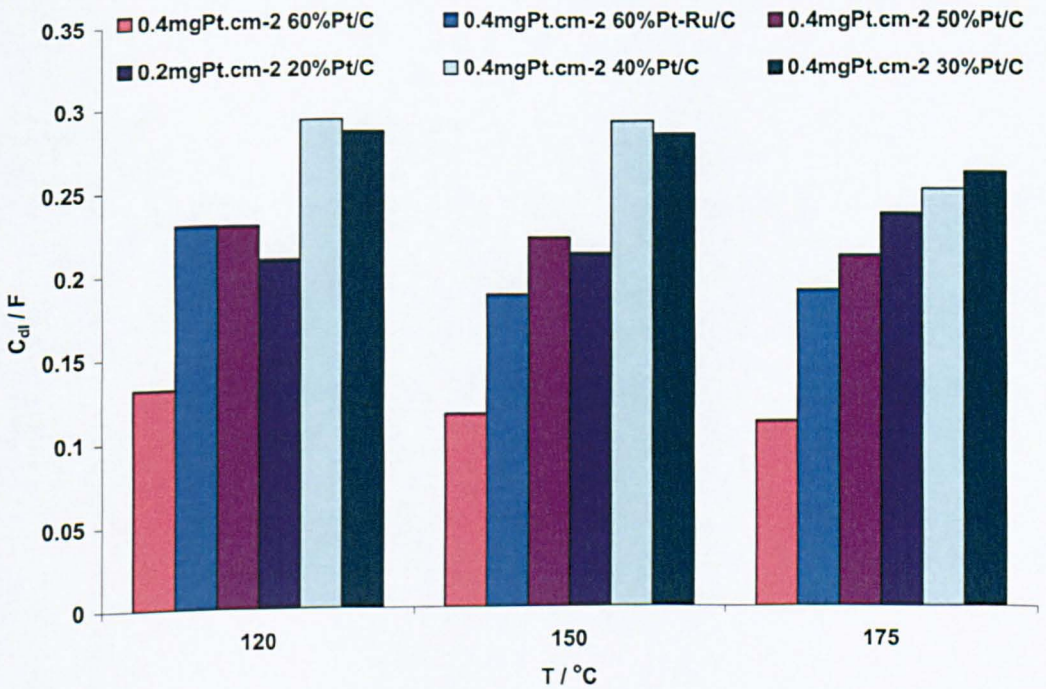

Figure 6-26. Double layer capacitance of various electrodes with different thickness (or Pt:C ratio) at different temperatures.

The effect of acid content on the double layer capacitance is shown in Figure 6-27. Decreasing acid content in the catalyst layer, by using a membrane with lower acid doping, LD, (4 instead of 5.6 PRU) or by increasing the electrode hydrophobic properties with heat-treatment, HT, meant a smaller acid/Pt-carbon interface and therefore smaller C_{dl}. It is also shown that the catalyst carbon support affects the double layer, as carbon was responsible for large portion of the electrolyte-catalyst interface surface area. Changing the catalyst support form Vulcan XC-72R (40% Pt/C, ETEK) to advanced carbon support AC01 from Johnson Matthey. JM, (40 %Pt/C, JM) led to sharp increase in the double layer capacitance from 0.3 to 0.47 F at 120 °C (using loading of 0.4 mg_{Pt} cm^{-2} with electrode area of 9 cm^2).

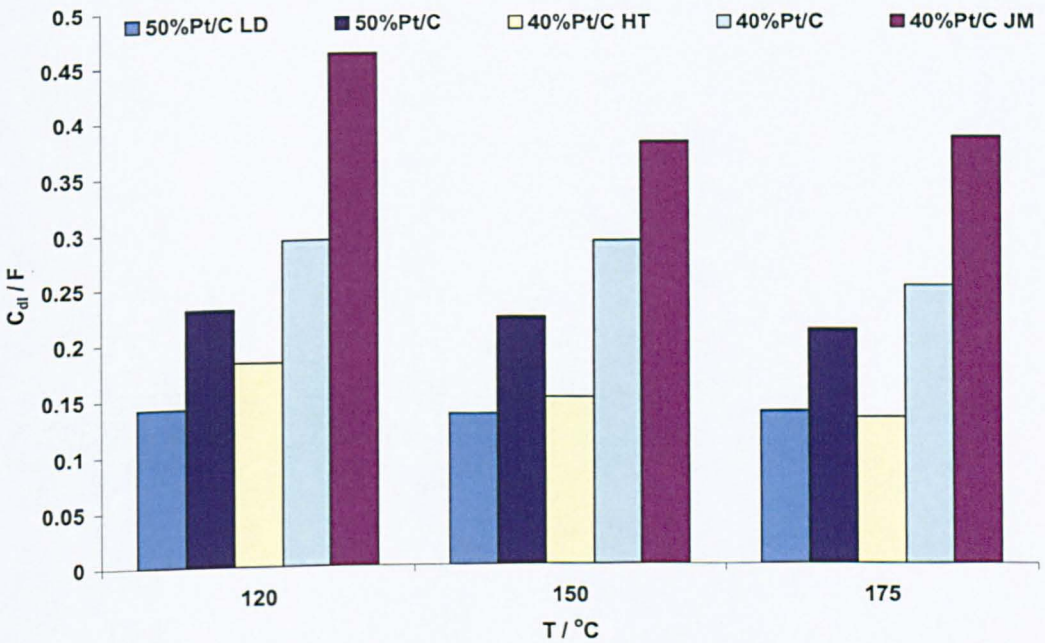

Figure 6-27. Double layer capacitance of various electrodes with different acid content at different temperatures.

6.4.5.2 Charge transfer resistance Rac

Figure 6-28 shows the charge transfer resistance, at OCP, for various electrodes at temperatures of 120, 150 & 175 °C using oxygen. It can be clearly see that there was an optimum thickness for

the catalyst layer for a given mobile acid content in the membrane. The smallest charge transfer resistance and therefore the fastest kinetics was observed with 50% Pt/C followed by 40% Pt/C electrodes; which agrees with the results obtained from the polarisation curves. The 60% Pt/C electrode exhibited the largest average Pt particle size, the smallest surface area and therefore the largest charge transfer resistance amongst the Pt based catalyst.

The 60% Pt-Ru/C (40% Pt -20% Ru) electrode showed very high charge transfer resistance in comparison to Pt/C catalyst; the value was 17 times higher than that of 40% Pt/C (similar Pt ratio and average particles size) at 120 °C, reflecting very slow kinetics (i_0 17 times smaller) for oxygen reduction and therefore a large activation energy. This was also observed in the polarisation curves where the electrode was completely under activation control. The large activation energy explains the high dependency of R_{ac} on temperature where it fell sharply from 120 to 150 °C.

It should be noticed that there was no considerable change in R_{ac} for Pt/C and Pt-Ru/C catalysts from 150 to 175 °C. PBI-based PEMFCs have shown less prominent decrease in R_{ac} from 150 to 175 °C in comparison to that from 120 to 150 °C [61]. It was also shown that R_{ac} did not vary considerably in the range of 150 to 180 °C [38, 73], while an increase in R_{ac} was reported above 175 °C [73]. This phenomenon can be explained by a fall in the oxygen solubility and therefore concentration countering any kinetic enhancement due to a temperature increase (activation energy).

Whilst the low frequency intercept R_{tot} at OCP and low currents were governed solely by R_{ac} and R_{mass} was negligible, there were inherent concentration effects in R_{ac}, because it represented the charge transfer resistance, at a given steady state condition (OCP or with current I), with a steady state concentration. Therefore increasing the steady-state current or increasing the temperature will lead to a fall in the steady-state concentration and therefore increase in R_{ac}. The concentration effects were different from R_{mass}, which represented the concentration effects (losses) due to signal perturbation and were only visible when C_Δ (surface concentration with perturbation) was sufficiently smaller than C (steady-state concentration) as expected from equation (46).

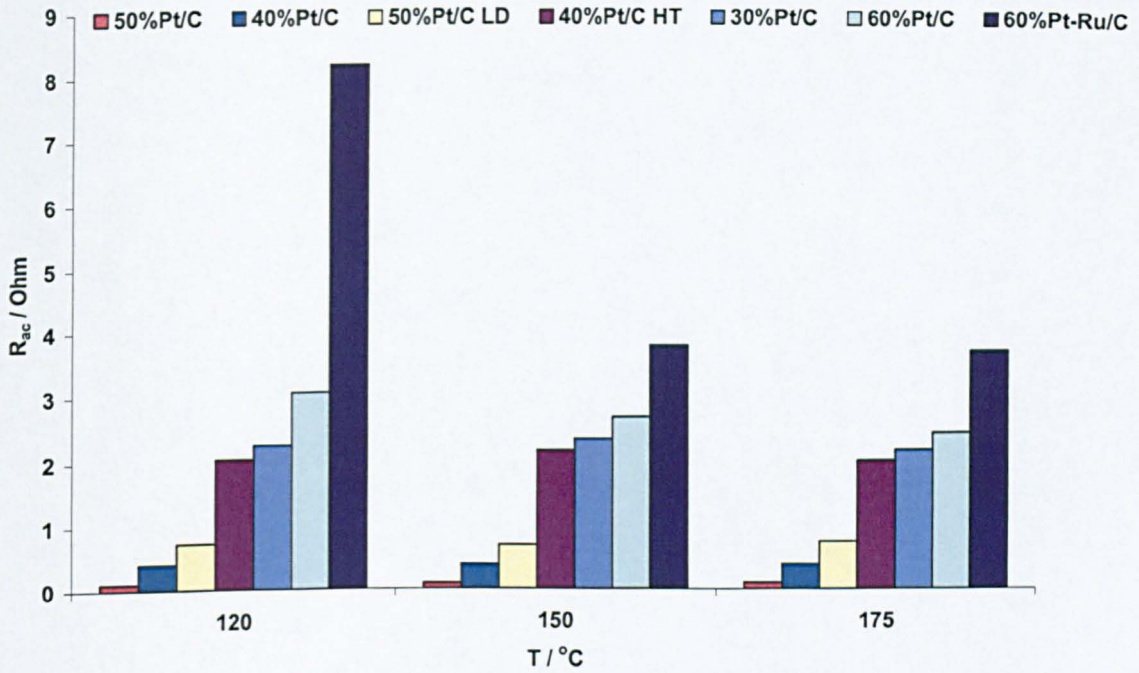

Figure 6-28. Charge transfer resistance at OCP for various electrodes at temperatures of 120, 150 & 175 °C using oxygen.

6.4.5.3 Mass transport capacitance and low frequency intercept

As discussed earlier mass transport capacitance is related to C_{Δ}, because as I increases C & C_{Δ} decrease, and (C/C_{Δ}) increases. When (C/C_{Δ}) becomes large enough, mass transport effects (due to perturbation) become apparent, leading to the appearance of a new arc at low frequencies, corresponding to R_{mass} , and a sharp increase in the capacitive).

R_{mass} is more difficult to detect due to the masking effect of Z_{polar} (both resistors are connected in parallel) as it only appears at high values of I, where cell voltage becomes low and therefore Z_{polar} becomes very small and the increase in R_{tot}, due to R_{mass}, becomes invisible, apart from the severe mass transport cases, where R_{mass} appears at low current values. On the other hand Q_{mass} capacitive behaviour is not affected by Z_{polar} because Z_{polar} is a pure polarisation resistor and has no capacitive behaviour.

Figure 6-29 shows the mass transfer capacitance Q_{mass} for various electrodes at temperature of 120 °C using air. The sharp increase in Q_{mass} indicates the development of new arc due to mass transport effects arising from the large value of (C/C_{Δ}) and the low value of C (steady-state surface concentration). It is clear from the Q_{mass} values that the mass transport coefficient of the electrodes decreased in the following order 40% Pt/C, 60% Pt/C, 30% Pt/C, 20% Pt/C & 40% Pt/C (HT), which agrees with the observed limiting current at the same conditions; 10.17, 8.1, 9.54, 5.67& 3.78 A, respectively.

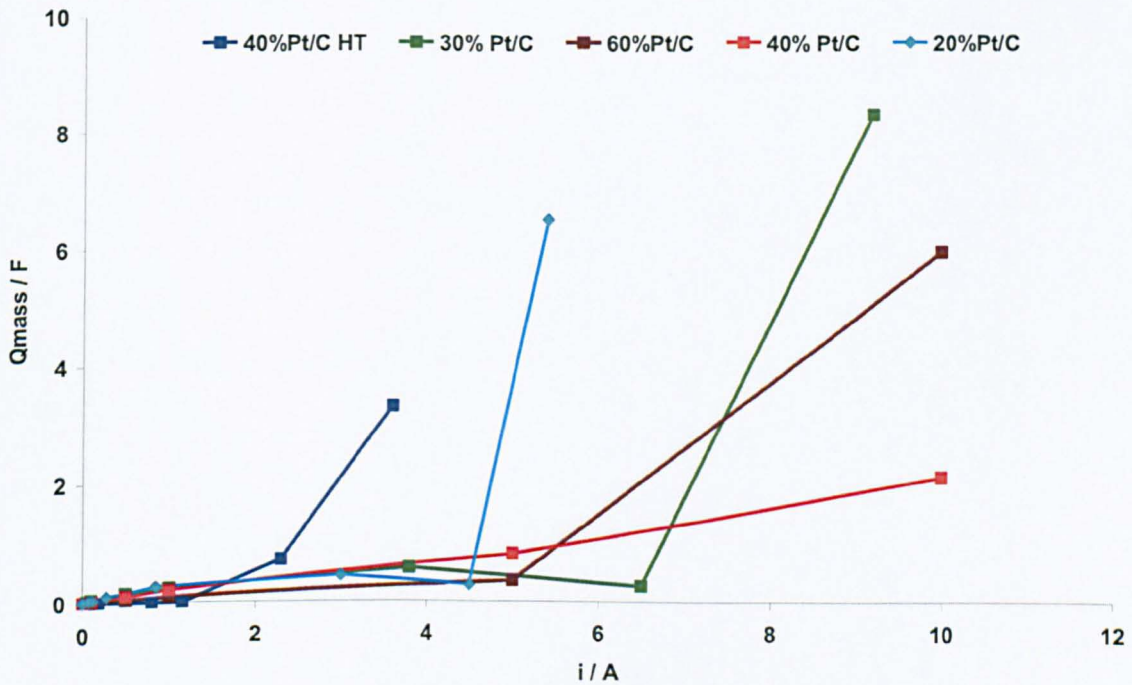

Figure 6-29. Mass transfer capacitance Q_{mass} for various electrodes at temperature of 120 °C using air.

Figure 6-30 shows the mass transfer capacitance Q_{mass} for 60% Pt/C electrode at temperatures of 120, 150 & 175 °C using air and oxygen. It can be seen that mass transport effects became less apparent when switching from air to oxygen and more apparent with a temperature increase reflected by a shift in the sharp increase of Q_{mass} towards lower operating current. This is because Q_{mass} is affected by the square of the transfer coefficient σ $(1/CD^{0.5})$, and therefore it depends more on oxygen concentration (C) than on oxygen diffusion (D).

On the other hand, values of the limiting current (C.D) for the 60% Pt/C electrode, using air fell from 9.54 to 9.45 to 9.36 A when the temperature increased from 120 to 150 to 175 °C, respectively.

As the concentration decreased rapidly with temperature (enthalpy of solution) and diffusion on the other hand increased with temperature (activation energy of diffusion), the overall product (limiting current) did not vary considerably with temperature, on the contrary the product $1/(C^2.D)$ and as result Q_{mass} greatly depends on temperature.

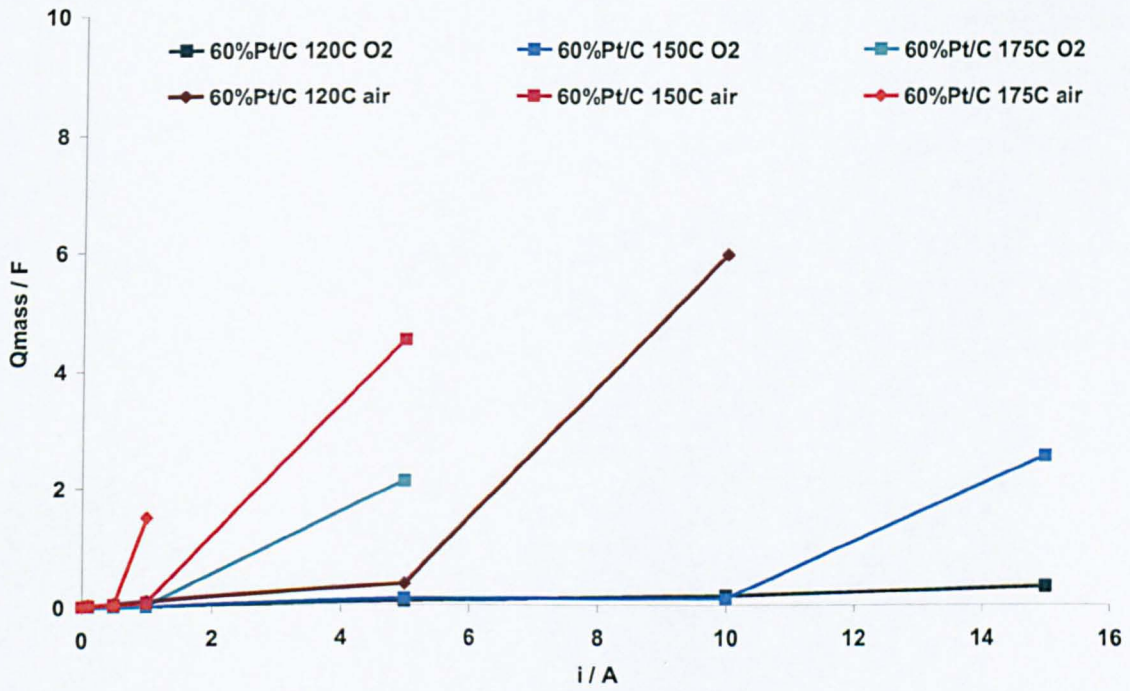

Figure 6-30. Mass transfer capacitance Q_{mass} for 60% Pt/C electrode at various temperatures using air and oxygen.

The low frequency intercept, $R_{tot\_observed}$, can be used to compare electrode performance, in terms of kinetics and mass transport, where it is equal to $1/((1/(R_{ac}+R_{mass}))+(1/R_{polar}))$. At small values of current I, R_{ac} dominates ($R_{mass}\rightarrow 0$ & $R_{polar}\rightarrow\infty$) while at high values of current R_{polar} dominates as cell potential $E_{cell}\rightarrow 0$ ($R_{mass}\rightarrow 0$& $R_{ac}\rightarrow 0$).

Figure 6-31 shows the low frequency intercept R_{tot} for 60% Pt/C, 40% Pt/C and 40% Pt/C HT electrodes at temperature of 150 °C using oxygen. It can be seen that 40% Pt/C exhibited the

sharpest fall in $R_{tot\_observed}$ with a small current increase; from OCP to 1.0 A (0.11 A cm^{-2}), followed by 60% Pt/C and finally 40% Pt/C HT. This corresponds to larger cell voltage at the measured operating current and correspondingly faster kinetic, which was also confirmed from the observed improved kinetic region in the polarisation curves.

In the middle current range, an increase in $R_{tot\_observed}$ was observed with 40 %Pt/C HT, indicating severe mass transport limitations. This results agrees with the limiting current values obtained under the same conditions (150 °C, O_2) where no limiting current was observed for 40% Pt/C and 60% Pt/C; a limiting current of ~ 11 A was observed in the case of 40% Pt/C HT (1.22 A cm^{-2}). At high currents, $R_{tot\_observed}$ became very small and no further useful information could be obtained.

The observed reduction in both mass transport and kinetics of 40% Pt/C HT, suggests that the heat treatment led to a reduction in the accessible electrochemical surface area by the mobile acid electrolyte, because of increased hydrophobicity and possible sintering (agglomeration) of platinum particles.

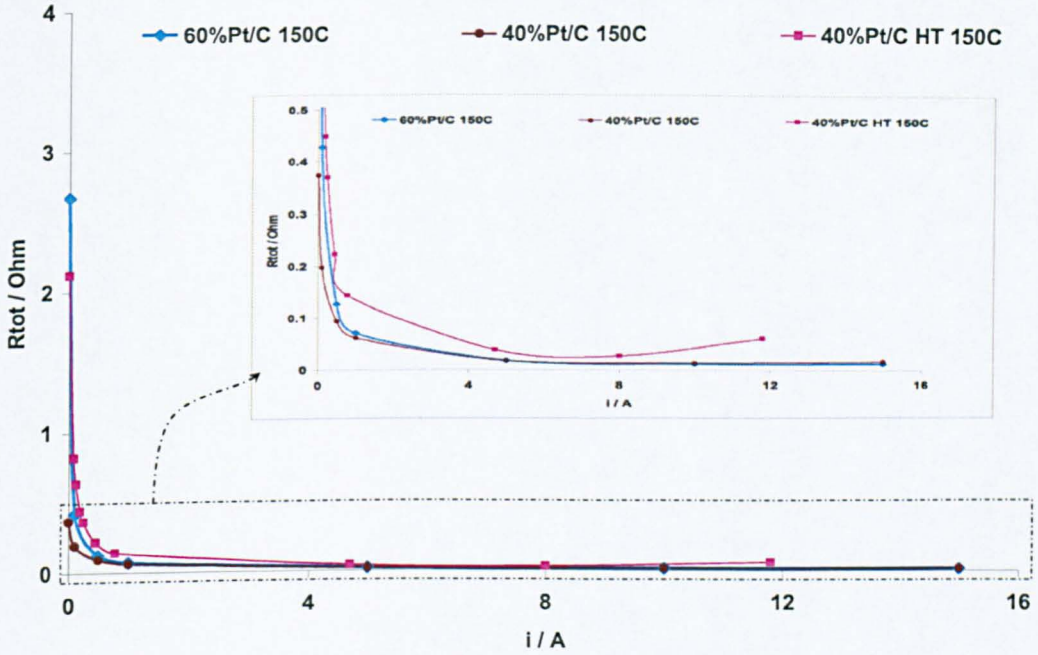

Figure 6-31. Low frequency intercept R_{tot} for various electrodes at temperature of 150 °C using oxygen.

Figure 6-32 shows the low frequency intercept $R_{tot\_observed}$ for various electrodes at temperature of 120 °C using air. The 40% Pt/C showed the sharpest drop in $R_{tot\_observed}$ as current increased and thereby the best kinetic behaviour and on the contrary 40% Pt/C HT showed the slowest change in $R_{tot\_observed}$ with current and therefore the worst kinetic behaviour. Once again this data agrees with the data obtained from polarisation curves. In the middle current range, an increase in $R_{tot\_observed}$ was observed in the 40% Pt/C HT electrode response, followed by another increase observed for 30% Pt/C at higher current, due to R_{mass}, while $R_{tot\_observed}$ values for 60% Pt/C and 40% Pt/C continued to decrease, with 40% Pt/C exhibiting the lowest value. As the current became too large, the $R_{tot\_observed}$ of the 60% Pt/C electrode continued to fall whilst the value for the 30% Pt/C electrode fell again, after the previous increase, below that for the 40% Pt/C which showed a slight increase.

The observed limiting current values under the studied conditions had the following order 40% Pt/C > 60% Pt/C > 30% Pt/C > 40% Pt/C HT. While the first increase in R_{tot} by 40% Pt/C HT followed by 30% Pt/C -caused by mass transport effects- confirmed the limiting current

observation, the low values for 60% Pt/C followed by 30% Pt/C and finally 40% Pt/C, at very high current (10 A under air), might be misleading. Where at high currents, $R_{tot\_observed} \rightarrow R_{polar}$ and the electrode with the lowest R_{polar} will show the lowest $R_{tot\_observed}$. However, the lowest R_{polar} corresponded to the electrode with the lowest E_{cell} and correspondingly the worst performance (mass transport). The same conclusion can be drawn by observing the behaviour of $R_{tot\_observed}$ for the 30% Pt/C electrode, which decreased below the value for 40% Pt/C at high currents (9 A) after the observed increase at 6.5 A. Similar behaviour could have occurred in the case of 60% Pt/C in the range of 5 to 10 A, (increase followed by decrease) where no data is available.

Therefore in the middle current range (5 A) where R_{mass} effects were apparent and $R_{tot\_observed}$ was not dominated by R_{polar}, the same sequence of limiting current was obtained for $R_{tot\_observed}$.

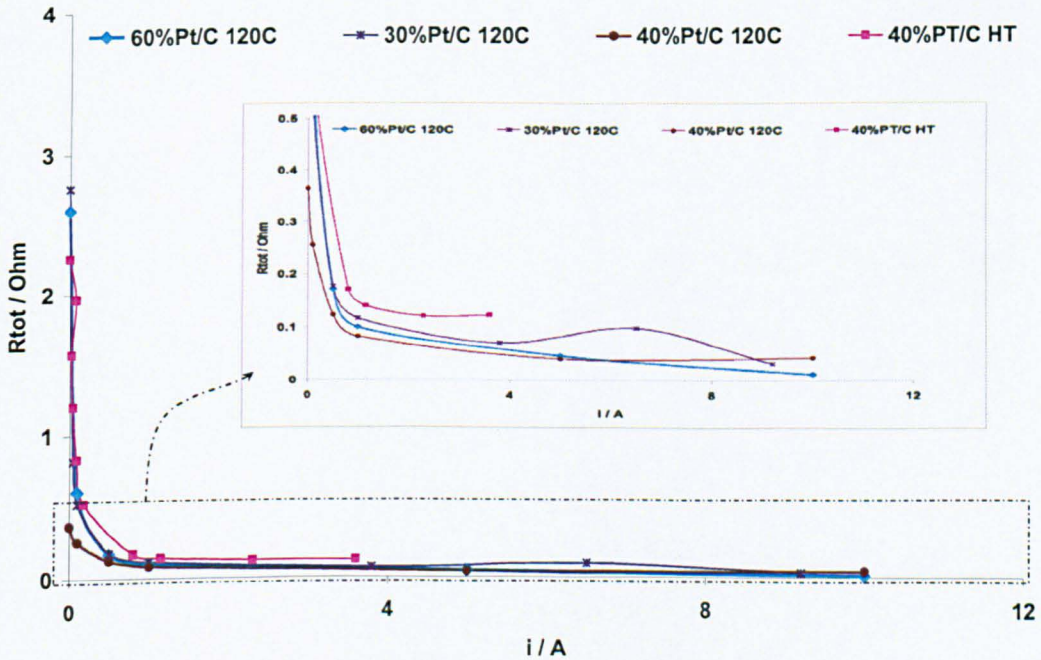

Figure 6-32. Low frequency intercept R_{tot} for various electrodes at temperature of 120 °C using air.

Figure 6-33 shows the low frequency intercept $R_{tot\_observed}$ for the highly doped 50% Pt/C (HD) and standard 40% Pt/C electrodes at temperatures of 120 & 150 °C using air & oxygen. It can be seen that the highly doped 50% Pt/C (2 mg cm^{-2} acid added) had faster kinetics (fall in

$R_{tot\_observed}$) than that of the standard 40% Pt/C, due to a larger acid (electrolyte) volume fraction in the catalyst layer and correspondingly higher ESA. However, for a given initial porosity, higher acid content leads to lower final overall porosity and as a result poorer mass transport. This can be observed from the large difference in $R_{tot\_observed}$ between air and oxygen operation for the 50% Pt/C HD electrode, in comparison to that for the 40% Pt/C electrode or from the early increase of $R_{tot\_observed}$ at relatively low currents under air operation and the lower $R_{tot\_observed}$ values (under air & oxygen) at medium currents (5 A) of 40% Pt/C in comparison to 50% Pt/C HD.

The temperature increase led to a sharper decrease in $R_{tot\_observed}$ with increased current (for small currents) due to the expected enhancement in the kinetics. Whilst at medium and high currents, $R_{tot\_observed}$ increased slowly with increased current (or remained steady) and the rate of increase became faster with increased temperature. This suggests a decrease in mass transport with increased temperature caused by fall in oxygen solubility.

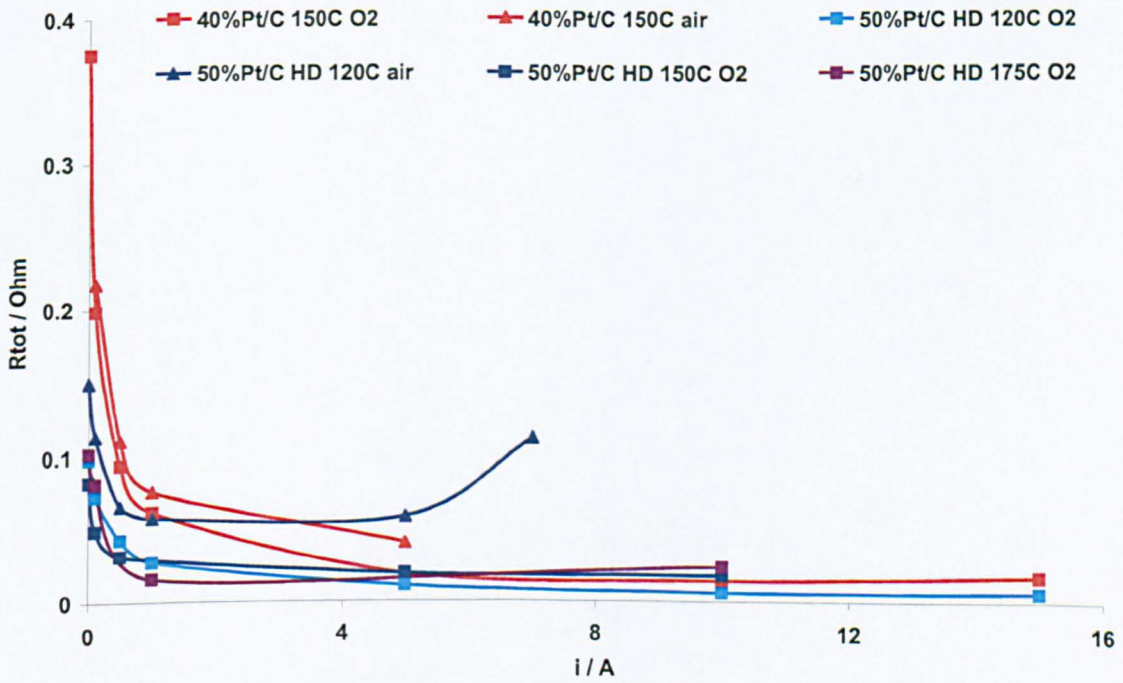

Figure 6-33. Low frequency intercept R_{tot} for highly doped 50% Pt/C (HD) and standard 40% Pt/C electrodes at temperatures of 120 & 150 °C using air & oxygen.

6.5 Conclusions

Electrodes fabricated with 40-50% Pt/C exhibited the highest oxygen concentration in the catalyst layer at a given current density and therefore exhibited the best performance. Similarly, 50-40% Pt/C electrode's porosity was ~30% (after acid impregnation) with acid volume fraction to Pt+C (without porosity) ratios in the range of 47-35 % (50-40% Pt/C). This means that 50% Pt/C electrodes have one third of its structure as free space (void) for oxygen transport or vapour water removal, one third for catalytic sites and electrical connection (Pt+C) and one third for proton conduction (acid electrolyte).

Chronoamperometry measurements were performed in attempt to obtain mass transport information for the studied electrodes. The current transient varied exponentially with time, having a time constant which depended on L^2/D for finite length (L) diffusion, as the conventional Cottrell equation for semi-infinite diffusion is not valid for expressing the system response.

The obtained values for oxygen diffusion in the thin film, D, using the response time constant where much smaller than the reported values measured using semi-infinite diffusion in phosphoric acid electrolyte (Cottrell equation) or the calculated values obtained from the steady-state limiting current (D.C/L) of the same system using the reported oxygen solubility values. The slow system response or the slow observed diffusion under transient conditions arose from the slow equilibrium between oxygen partial pressure and oxygen concentration in the thin film, in other words, in very short times the diffusion layer reached the end of the thin film (L) and the oxygen diffusion (flux) was limited by the rate of oxygen dissolving into the thin film, which can be represented by a diffusion process ($D_{solubility}$).

The response time constant did not vary with oxygen partial pressure, and decreased with increased temperature as expected. However, there was a larger decrease in the time constant from temperatures of 120 to 150 °C in comparison to that from 150 to 175 °C. This was caused by phosphoric acid dehydration and consequently increased viscosity slowing down both the solubility process $D_{solubility}$ and oxygen diffusion through the electrolyte film D_{O2}.

Three different relationships for the steady-state oxygen permeability (D.C) or limiting current values with increase in temperature (from 120 to 150 to 175 °C), were observed depending on electrode thickness, acid content and oxygen partial pressure. While a temperature increase will lead to a decrease in oxygen solubility, it will also lead to an increase in diffusion. However the rate of increase in diffusion will fall as temperature increases due to dehydration and increase in viscosity. The solubility and diffusion at a given temperature also depends on water activity or in other words phosphoric acid concentration. Therefore, the product (D.C) can experience the three observed possibilities, either increase, decrease or exhibit a maximum value with an increase in temperature.

The decrease in solubility with temperature has counteracting effect on the increase in kinetics with temperature; where both processes vary exponentially with temperature (heat of solution and activation energy). This was reflected by the slow increase of kinetics above 150 °C for PBI-free electrodes- half cell tests also showed non-linearity in the variation of $Ln[i_0]$ with temperature at a given oxygen partial pressure for PBI-based electrodes (Chapter 3). This was also reflected in the kinetic region of the polarisation curves, where no remarkable enhancement was observed for PTFE-H_3PO_4 electrodes above 150 °C, and a slow enhancement was still observed in the PBI based electrodes (Chapter 4). Therefore, as temperature increased the performance of PBI based electrodes approached that of PBI-free electrode, whilst at lower temperatures, PBI-free electrodes had superior performance over that of PBI-based electrodes. In other words, at 150 °C fast oxygen diffusion in phosphoric acid (liquid) in comparison to PBI/H_3PO_4 (gel) gave rise to enhanced performance (solubility values are similar), whilst at 175 °C this enhancement was suppressed by a lower solubility and slower increase in diffusion due to increased viscosity of phosphoric acid caused by dehydration; effecting mainly PBI free electrodes.

Frequency response analysis was used to compare electrode performance in terms of kinetics, ohmic and mass transport losses. Simple equivalent circuit was used to fit the observed spectra. For polarisable electrodes under small to medium steady-state current operation, the model was capable of identifying electrodes with the best kinetic or mass transport behaviour and classifying behaviour in terms of relative performance.

However, care must be taken in interoperating the results at OCP or high steady-state currents. At OCP the charge transfer resistance is equal to $\frac{RT}{\alpha F}\frac{1}{i_0 + i_{cross}}$, where the OCP is no longer equal to the reversible potential given by Nernst equation, and electrodes with higher cross-over rate (combined with corrosion rate, etc..) will have smaller OCP and therefore exhibit smaller apparent charge transfer resistance. Similarly the thermodynamic oxygen concentration effects at OCP (Nernst equation) will counter the kinetic effect and correspondingly a small difference, if any, will be observed in the charge transfer resistance when changing oxygen concentration, where lower oxygen concentration will lead to a lower cell voltage and therefore reduce the observed charge transfer resistance.

At high current densities the effect of the equivalent resistance used to polarise the electrode to steady-state current i (R_{polar}= E_{cell}/i) dominates the observed circuit impedance and electrodes with the worst performance, at a given current i, will exhibits the smallest cell voltage E_{cell} and the smallest R_{polar} and consequently will show the smallest overall circuit impedance.

6.6 References

1. Seland, F., T. Berning, B. Borresen, and R. Tunold, *Improving the performance of high-temperature PEM fuel cells based on PBI electrolyte.* Journal of Power Sources, 2006. **160**(1): p. 27-36.
2. Mecerreyes, D., H. Grande, O. Miguel, E. Ochoteco, R. Marcilla, and I. Cantero, *Porous polybenzimidazole membranes doped with phosphoric acid: Highly proton-conducting solid electrolytes.* Chemistry of Materials, 2004. **16**(4): p. 604-607.
3. DuPont. *Technical info: Fluoropolymer Comparison - Typical Properties*. Mechanical Properties 2007 [cited; Available from: http://www2.dupont.com/Teflon_Industrial/en_US/tech_info/techinfo_compare.html.
4. SDS@cabot-corp.com, *SAFETY DATA SHEET of Vulcan XC-72 R.* 2007, Cabot Corporation, France.
5. *Marks' Standard Handbook for Mechanical Engineers III (10th Edition).* Thermophysical Properties of Selected Solid Elements. , ed. E.A. Avallone and T. Baumeister. 1996: McGraw-Hill.
6. Knovel, *Knovel Critical Tables.* 2003, http://www.knovel.com/knovel2/Toc.jsp?BookID=761&VerticalID=0.
7. MacDonald, D.I. and J.R. Boyack, *Density, Electrical Conductivity, and Vapor Pressure of Concentrated Phosphoric acid.* Journal of Chemical and Engineering Data, 1969. **14**(3): p. 380.
8. Bevers, D., M. WOHR, K. YASUDA, and K. OGURO, *Simulation of a polymer electrolyte fuel cell electrode.* JOURNAL OF APPLIED ELECTROCHEMISTRY, 1997. **27**: p. 1254-1264.
9. Scott, K., S. Pilditch, and M. Mamlouk, *Modelling and experimental validation of a high temperature polymer electrolyte fuel cell.* Journal of Applied Electrochemistry, 2007. **37**: p. 1245-1259.
10. Lambda-Americas-Inc. *App Note 500 - Calculating Capacitor Charge Time.* 2008 [cited; Available from: http://www.lambda-hp.com/pdfs/application%20notes/93008500rC.pdf.
11. Liu, Z.Y., J.S. Wainright, M.H. Litt, and R.F. Savinell, *Study of the oxygen reduction reaction (ORR) at Pt interfaced with phosphoric acid doped polybenzimidazole at elevated temperature and low relative humidity.* Electrochimica Acta, 2006. **51**(19): p. 3914-3923.
12. Scharifker, B.R., P. Zelenay, and J.O.M. Bockris, *The Kinetics of Oxygen Reduction in Molten Phosphoric Acid at High Temperatures.* J. Electrochem. Soc., 1987. **134**: p. 2714-2725.
13. Parthasarathy, A., S. Srinivasan, and A.J. Appleby, *Temperature Dependence of the Electrode Kinetics of Oxygen Reduction at the Platinum/Nafion® Interface-A Microelectrode Investigation.* J. Electrochem. Soc., 1992. **139**(9): p. 2530-2537.
14. Klinedinst, K., J.A.S. Bett, J. MacDonald, and P. Stonehart, *Oxygen solubility and diffusivity in hot concentrated H_3PO_4.* J. Electroanalytical Chemistry and Interfacial Electrochemistry, 1974. **57**: p. 281-289.

15. Zelenay, O.P., B.R. Scharifker, J.O.M. Bockris, and D. Gervasio, *A Comparison of the Properties of CF_3SO_3H and H_3PO_4 in Relation to Fuel Cells.* J. Electrochem. Soc., 1986. **133**(11): p. 2262-2267.
16. Pajkossy, T. and L. Nyikos, *Comments on J. C. Wang's paper on the impedance of a fractal electrolyte--electrode interface.* Electrochimica Acta, 1988. **33**(5): p. 713-715
17. Pajkossy, T. and L. Nyikos, *Diffusion to fractal surfaces--II. Verification of theory.* Electrochimica Acta, 1989. **34**(2): p. 171-179.
18. Pajkossy, T. and L. Nyikos, *Diffusion to fractal surfaces--III. Linear sweep and cyclic voltammograms.* Electrochimica Acta, 1989. **34**(2): p. 181-186.
19. Pajkossy, T., *Electrochemistry at fractal surfaces.* Journal of Electroanalytical Chemistry, 1991. **300**(1-2): p. 1-11.
20. Bard, A.J. and L.R. Faulkner, *Electrochemical Methods: Fundamentals and Applications*. 1980, New York: Wiley.
21. Crank, J., *The mathematics of diffusion, 2nd edition* 1979, Oxford: Clarendon Press.
22. Macdonald, D.D., *Transient techniques in electrochemistry* 1977, New York Plenum Press.
23. Wen, C.J., B.A. Boukamp, R.A. Huggins, and W. Weppner, *Thermodynamic and Mass Transport Properties of "LiAl".* J. Electrochem. Soc., 1979. **126**(12): p. 2258-2266.
24. Tada, T., *Handbook of Fuel Cells: Fundamentals, Technology and Applications*. Part 3: Polymer Electrolyte Membrane Fuel Cells and Systems, High-dispersion Catalysts Including Novel Carbon Supports, ed. W. Vielstich, A. Lamm, and H.A. Gasteiger. Vol. 3. 2003, Chichester, UK: John Wiley & Sons.
25. Gasteiger, H.A. and M.F. Mathias. *FUNDAMENTAL RESEARCH AND DEVELOPMENT CHALLENGES IN POLYMER ELECTROLYTE FUEL CELL TECHNOLOGY.* in *Proceedings of ECS Meeting.* October, 2002. Salt Lake City, UTAH, USA.
26. Bockris, J.O.M., B.E. Conway, R.E. White, C.G. Vayenas, and M. Gamboa-Aldeco, *Modern aspects of electrochemistry*, ed. J.O.M. Bockris and B.E. Conway. Vol. 32. 1954-, London: Butterworths Scientific Publications.
27. Gileadi, E., *Electrode Kinetics for Chemists, Chemical Engineers and Materials Scientists*. 1993: John Wiley & Sons.
28. Kinoshita, K., *Electrochemical oxygen technology* 1992, New York: Wiley.
29. Slattery, J.C. and R.B. Bird, *Calculation of the Diffusion Coefficient of Dilute Gases and of the Self-diffusion Coefficient of Dense Gases.* J. A.I.Ch.E, 1958. **4**(2): p. 137-142.
30. Wu, X., H. Ma, S. Chen, Z. Xu, and A. Sui, *General Equivalent Circuits for Faradaic Electrode Processes under Electrochemical Reaction Control.* Journal of The Electrochemical Society, 1999. **146**(5): p. 1847-1853.
31. MACDONALD, D.D., *REVIEW OF MECHANISTIC ANALYSIS BY ELECTROCHEMICAL IMPEDANCE SPECTROSCOPY.* Electrochimica Acta, 1990. **35**(10): p. 1509-1525.
32. Ahn, S. and B.J. Tatarchuk, *Air Electrode: Identification of Intraelectrode Rate Phenomena via AC Impedance.* J. Electrochem. Soc., 1995. **142**(12): p. 4169-4175.
33. Ren, X. and P.G. Pickup, *Simulation and analysis of the impedance behaviour of electroactive layers with non-uniform conductivity and capacitance profiles.* Electrochimica Acta, 2001. **46**: p. 4177-4183.

34. NISHIKATA, A., Y. ICHIHARA, and T. TSURU, *ELECTROCHEMICAL IMPEDANCE SPECTROSCOPY OF METALS COVERED WITH A THIN ELECTROLYTE LAYER.* J. Electrochimica Acta, 1996. **41**: p. 1057-1062.
35. JAMNIK, J., J. MAIER, and S. PEJOVNIK, *A NEW PENETRATION IMPEDANCE TECHNIQUE.* J. Electrochimica acta, 1996. **41**: p. 1011-1015.
36. Zoltowski, P., *A new approach to measurement modelling in electrochemical impedance spectroscopy.* Journal of Electroanalytical Chemistry, 1994. **375**(1-2): p. 45-57.
37. Macdonald, J.R., N. Wagner, W.B. Johnson, I.D. Raistrick, and D.R. Franceschetti, *Impedance Spectroscopy: Theory, Experiment, and Applications 2nd edition.*, ed. E. Barsoukov and J.R. Macdonald. 2005, New Jersey: Wiley-Interscience.
38. Jalani, N.H., M. Ramani, K. Ohlsson, S. Buelte, G. Pacifico, R. Pollard, R. Staudt, and R. Datta, *Performance analysis and impedance spectral signatures of high temperature PBI-phosphoric acid gel membrane fuel cells.* Journal of Power Sources, 2006. **160**(2): p. 1096-1103.
39. Li, G. and P.G. Pickup, *Ionic Conductivity of PEMFC Electrodes Effect of Nafion Loading.* Journal of The Electrochemical Society, 2003. **150**(11): p. C745-C752.
40. Fleig, J., J. Jamnik, J. Maier, and J. Ludvig, *Inductive Loops in Impedance Spectroscopy Caused by Electrical Shielding.* J. Electrochem. Soc., 1996. **143**: p. 3636.
41. ARMSTRONG, R.D. and R.E. FIRMAN, *IMPEDANCE PLANE DISPLAY OF A REACTION WITH A SOLUTION SOLUBLE INTERMEDIATE.* Journal of Electroanalytical Chemistry and Interfacial Electrochemistry, 1973. **45**: p. 3-10.
42. Pyun, S.-I. and Y.-G. Ryu, *A study of oxygen reduction on platinum-dispersed porous carbon electrodes at room and elevated temperatures by using a.c. impedance spectroscopy.* Journal of Power Sources, 1996. **62**: p. 1-7.
43. Epelboin, I. and M. Keddam, *Faradaic Impedances: Diffusion Impedance and Reaction Impedance.* J. Electrochem. Soc., 1970. **117**(8): p. 1052-1056.
44. Diard, J.P., B. Le Gorrec, and C. Montella, *Calculation, simulation and interpretation of electrochemical impedances : Part 3. Conditions for observation of low frequency inductive diagrams for a two-step electron transfer reaction with an adsorbed intermediate species.* Journal of Electroanalytical Chemistry, 1992. **326**(1-2): p. 13-36.
45. Itagaki, M., H. Hasegawa, K. Watanabe, and T. Hachiya, *Electroreduction mechanism of oxygen investigated by electrochemical impedance spectroscopy.* Journal of Electroanalytical Chemistry 2003. **557**: p. 59-73.
46. Tham, M.T., *Why Frequency Response?*, in *Robust Control study notes (Control 3).* 1999, Newcastle University: Newcastle upon Tyne.
47. Springer, T.E., T.A. Zawodzinski, M.S. Wilson, and S. Gottesfeld, *Characterization of Polymer Electrolyte Fuel Cells Using Ac Impedance Spectroscopy.* Journal of The Electrochemical Society, 1996. **143**(2): p. 587-599.
48. ARMSTRONG, R.D., *Equivalent circuits for electrochemical cells.* Journal of Electroanalytical Chemistry and Interfacial Electrochemistry, 1972. **40**: p. 473-476.
49. Holze, R. and W. Vielstich, *Double-layer capacity measurements as a method to characterize porous fuel cell electrodes.* Electrochimica Acta, 1984. **29**(5): p. 607-610.
50. Holze, R., I. Vogel, and W. Vielstich, *New oxygen cathodes for fuel cells with organic fuels.* Journal of Electroanalytical Chemistry, 1986. **210**(2): p. 277-286.
51. Holze, R. and W. Vielstich, *The Kinetics of Oxygen Reduction at Porous Teflon-Bonded Fuel Cell Electrodes.* J. Electrochem. Soc., 1984. **131**(10): p. 2298-2303.

52. Armstrong, R.D., *Impedance Plane Display for an Electrode with Diffusion Restricted to a Thin Layer.* J. Electroanal. Chem., 1986. **198**: p. 177-180.
53. Diard, J.-P., N. Glandut, C. Montella, and J.-Y. Sanchez, *One layer, two layers, etc. An introduction to the EIS study of multilayer electrodes. Part 1: Theory.* Journal of Electroanalytical Chemistry, 2005. **578**(2): p. 247-257.
54. Gabrielli, C., *IDENTIFICATION OF ELECTROCHEMICAL PROCESSES BY FREQUENCY RESPONSE ANALYSIS,* in *Solatron analytical:TECHNICAL REPORT NUMBER 004/83.* 1998.
55. Randles, J.E.B., *Kinetics of Rapid Electrode Reactions.* Faraday Soc., 1947. **1**: p. 11-19
56. Armstrong, R.D., M.F. Bell, and A.A. Metcalfe, *The AC Impedance of Complex Electrochemical Reactions*, in *Electrochemistry.* 1978, Chemical Society Specialist Periodical Reports. p. 98-127.
57. Franceschetti, D.R., *Small Signal AC response Theory for Electrochromic Thin Films.* J. Electrochem. Soc., 1982. **129**: p. 1754-1756.
58. WAGNER, N., *Characterization of membrane electrode assemblies in polymer electrolyte fuel cells using a.c. impedance spectroscopy.* Journal of Applied Electrochemistry, 2002. **32**: p. 859-863.
59. Wang, D.Y. and A.S. Nowick, *Diffusion-Controlled Polarization of Pt, Ag, and Au Electrodes with Doped Ceria Electrolyte.* J. Electrochem. Soc., 1981. **128**(1): p. 55-63.
60. Wang, D.Y. and A.S. Nowick, *Cathodic and Anodic Polarization Phenomena at Platinum Electrodes with Doped CeO_2 as Electrolyte II. Transient Overpotential and A-C Impedance.* J. Electrochem. Soc., 1979. **126**(7): p. 1166-1172.
61. Lobato, J., P. Canizares, M.A. Rodrigo, and J.J. Linares, *PBI-based polymer electrolyte membranes fuel cells - Temperature effects on cell performance and catalyst stability.* Electrochimica Acta, 2007. **52**(12): p. 3910-3920.
62. Lobato, J., M.A. Rodrigo, J.J. Linares, and K. Scott, *Effect of the catalytic ink preparation method on the performance of high temperature polymer electrolyte membrane fuel cells.* Journal of Power Sources, 2006. **157**(1): p. 284-292.
63. GoodFellow, *Polybenzimidazole (PBI) Material Information.* 2008, http://www.goodfellow.com/scripts/web.wl?MGWLPN=MNT&PROG=SEARTOW&LAN=A&HEAD=BI30&SPAGE=BI30.
64. Munson, R.A., *Dielectric Constant of Phosphporic acid.* J. Chem. Phys. , 1963. **39**: p. 435-439.
65. Franceschetti, D.R., J.R. Macdonald, and R.P. Buck, *Interpretation of Finite-Length-Warburg-Type Impedances in Supported and Unsupported Electrochemical Cells with Kinetically Reversible Electrodes.* J. Electrochem. Soc., 1991. **138**(5): p. 1368-1371.
66. Franceschetti, D.R. and J.R. Macdonald, *Diffusion of neutral and charged species under small-signal a.c. conditions.* Journal of Electroanalytical Chemistry, 1979. **101**(3): p. 307-316.
67. SELMAN, J.R. and Y.P. LIN, *APPLICATION OF AC IMPEDANCE IN FUEL CELL RESEARCH AND DEVELOPMENT.* Electrochimica Acta, 1993. **38**(14): p. 2063-2073.
68. Murthi, V.S., R.C. Urian, and S. Mukerjee, *Oxygen Reduction Kinetics in Low and Medium Temperature Acid Environment: Correlation of Water Activation and Surface Properties in Supported Pt and Pt Alloy Electrocatalysts.* J. Phys. Chem. B, 2004. **108**: p. 11011-11023.

69. Mirzazadeh, J., E. Saievar-Iranizad, and L. Nahavandi, *An analytical approach on effect of diffusion layer on ORR for PEMFCs.* Journal of Power Sources 2004. **131**: p. 194-199.
70. Xie, Z. and S. Holdcroft, *Polarization-dependent mass transport parameters for orr in perfluorosulfonic acid ionomer membranes: an EIS study using microelectrodes.* Journal of Electroanalytical Chemistry, 2004. **568**: p. 247-260.
71. Li, G. and P.G. Pickup, *Measurement of single electrode potentials and impedances in hydrogen and direct methanol PEM fuel cells.* Electrochimica Acta 2004. **49**: p. 4119-4126.
72. Song, J.M., S.Y. Cha, and W.M. Lee, *Optimal composition of polymer electrolyte fuel cell electrodes determined by the AC impedance method.* Journal of Power Sources, 2001. **94**: p. 78-84.
73. Tang, Y., J. Zhang, C. Song, and J. Zhang, *Single PEMFC Design and Validation for High-Temperature MEA Testing and Diagnosis up to 300°C.* Electrochemical and Solid-State Letters, 2007. **10**(9): p. B142-B146.

7 Modelling of HT-PEMFCs

7.1 Introduction

A model of a high temperature fuel cell using PBI membranes has been developed using thermodynamics, transport and kinetic equations. The model considers mass transport through a thin film electrolyte as well as through the porous media. The model uses available experimental physical and chemical property data for the related phosphoric acid fuel cell, when appropriate. This Chapter reviews the area of PEMFc modelling and introduces a pseudo one dimensional model for the cell made up of a membrane (PBI phosphoric acid doped) sandwiched between two catalyst layers bounded by gas diffusion layers. The catalyst interface was presented using macro-homogeneous model. The model is used to simulate the influence of operating condition, cell parameters and different fuel gas compositions on the cell voltage current density characteristics.

7.2 Literature Review

There are numerous mathematical models of Nafion® type PEMFCs that have been reported in the literature. The models vary from empirical (curve fitting) and zero dimensional; essentially coupled thermodynamic; kinetic and resistance approaches; to one/two dimensional phenomenological approaches. One of the early phenomenological models of a PEMFC with Nafion® membrane was developed by Bernardi and Verbrugge [1]; since then, significant developments have been made. Models were used to study concentration and current distributions in PEMFCs [2], to map liquid saturation and temperature distributions [3] for comparison with experimental data, to solve equations describing multi-component flow in diffusion layers and flow channels [4] or to modle mass transport in porous electrodes[5].

The mass transport in PEMFC electrodes was considered to be either a single phase [6] where no water liquid is formed or a two phase [7] involving an electrolyte/water film. It was found [8, 9]

that under the assumption of no liquid water formation, the model consistently over predicted measured polarization behaviour.
On the other hand, results showed that the inclusion of liquid water transport greatly enhanced the predictive capability of the model and was necessary to match experimental data at high current density [10]. This could be achieved in the form of one dimensional [11], two dimensional [12] and three dimensional models [13, 14].

In comparison, there has been little modelling of PEMFCs based on PBI membranes. The first proposed model was a parametric model; a very low value of 9.2 % was used for cathode porosity with a high value for the transfer coefficient (α) equal to 2. However such a model could not explain the limiting current observed under air operation [15].

A second one dimensional model; assumed the Tafel approximation to describe the electrode kinetics, with a transfer coefficient equal to 0.5 while the exchange current density was fitted to the polarisation curves using least square error method leading to reaction order for oxygen equal to 0.7 [16]. The simulated polarisation curve showed a better fit for air than for oxygen; where the model underestimated the performance at the higher current densities. The influence of humidity and consequently product water generation on membrane conductivity was given as a reason for the observed behaviour (the model assumed constant membrane conductivity).

A third model considered a three dimensional structure, with transfer coefficient (α) equal to 2 and reaction order (γ) equal to 1. However, once again the model failed to explain the observed difference between air and oxygen operation: oxygen simulation underestimated the experimental data, whilst with air operation the simulated data over predicted the experimental data at high current densities; where contrary to experimental results, no limiting current was observed [17].

Scott et al, has also proposed a one dimensional model for PBI based fuel cells. They described electrode kinetics by the Butler-Volmer equation and mass transport by the multi-component Stefan Maxwell equations coupled with Darcy's law. The model had a good fit with the experimental data but failed to show limiting current under air operation [18].

Similarly, one and two dimension degradation models were constructed to simulate the steady state polarisation curves recorded at different times during aging test. The models again failed to show any apparent mass transport limitations under air operation (limiting current) and used α equal to 1 and γ equal to 1[19, 20].

The failure of the reported models to predict the mass transport limitations under air operation and therefore over estimating cell performance particularly at high current densities was caused by the assumption that mass transport solely occurred through the porous media. This is similar to the single phase mass transport observation discussed earlier in Nafion based PEMFC models. In reality an electrolyte (PBI/Acid) thin film surrounding the catalyst sites (particles) is present and mass transport though this phase should be considered. In this film reactants have to dissolve in the electrolyte media and diffuse through it to reach the catalytic sites, in a similar way to two phase mass transport approach where diffusion through liquid water is considered. Diffusion through the acid electrolyte is much slower in comparison to that through porous media and can explain the observed PBI-PEMFC mass transport behaviour. The effect of the electrolyte thin film has been realised and modelled in phosphoric acid fuel cells [21, 22].

This absence of a thin film model approach also explains the relatively thick catalyst layers and very low porosity used in previous reported models [15, 16] in attempts to compensate for the thin film effects and to try matching the experimental data.
Similarly, while most the models used value for reaction orders equal to one, alpha values varied from 0.5 to 2. This corresponds to; at 150 °C unrealistic Tafel slopes of 168, 84 & 42 mV dec^{-1}, respectively. No such values have been reported for oxygen reduction in PBI or phosphoric acid environment at the studied conditions. As shown erliear (Chapter 3) alpha values change with doping level, for example at 150 °C; the lowest Tafel slope observed at the minimum doping level of 4.5 PRU was 92 mV dec^{-1} (α = 0.91) increasing to 104 mV dec^{-1} (α = 0.81) at doping level of 10 PRU [23, 24] and 90-135 mV dec^{-1} (α = 0.93-0.62) for phosphoric acid fuel cells [25-31].

Additionally, empirical models have been developed to study temperature effects in PBI based PEMFCs. A change in the transfer coefficient (increase) with temperature was obtained using non linear square errors fitting method [32]. This result agrees with the finding of this work (Chapter 3) and similar documented behaviour in PAFC [25, 27, 28, 33].

Modelling of PBI PEMFCs will increase understanding of their behaviour, enable prediction of their performance and assist with their operational control. Thus, a one dimensional (1D) model of the high temperature PBI based PEMFC was developed and is described below that includes the potential and current distribution in the catalyst layers and considers multi-component mass transport through porous media and a thin electrolyte film.

7.3 Mathematical Model of the Fuel Cell

The mathematical model of the fuel cell is one dimensional where the gas flow channels are not considered. The fuel cell consists of two diffusion layers, anode and cathode catalyst layers and the membrane. The assumptions adopted in the model are:

- Steady state and isothermal operation.
- Mass transport is solely due to diffusion where convection effects are negligible.
- Ideal gas behaviour.
- Membrane was impermeable to hydrogen and oxygen.
- Negligible contact resistances between components.
- No membrane swelling.
- Only gas phases present (no water condensation T>120°C).
- Catalyst layer treated as interface rather than a region (0D).
- Isotropic macro-homogeneous porous regions.

Isothermal operation was a reasonable assumption as the test cell temperature was controlled using electrical heating. Ideal gas behaviour was appropriate, as the cell was not operated at high pressure. As the cell was operated at relatively high temperatures, above the normal boiling point of water, it was reasonable to assume there was no liquid saturation and single phase behaviour

applied. The flow channel was not included in the model; the boundary conditions between the flow channel and the diffusion layer are taken as the feed gas compositions, this can be justified by the high gas flow stoichiometry used (> 2.2).

The macro-homogeneous model for the catalyst layer [34] assumes that the porous electrode is an 'average' of the solid electrode and the electrolyte. Thus, the effective conductance of the porous electrode is the weighted volume average of the respective conductance. Diffusion coefficients and other properties are similarly averaged.

The objective of the model is to determine the effect of a range of operating variables and parameters on the cell voltage of the PBI based fuel cell. The overall cell voltage is given from a combination of the thermodynamic cell potential and voltage losses associated with Ohmic resistances in the electrodes and membrane, and kinetic losses at the anode and cathode which are influenced by mass transport restriction by:

$$U_{cell} = E_{rev} - |\eta_c| - |\eta_a| - iR \qquad [i]$$

Where E_{rev} is the reversible cell potential, η refers to electrode polarisation losses and iR is the Ohmic resistance losses.

7.4 Thermodynamic equilibrium potential

The overall electrochemical reaction in a PEM fuel cell running on H_2 as fuel and O_2 as oxidant at temperature above 100 °C can be written as

$$H_{2(g)} + 1/2\,O_{2(g)} \xrightarrow{Pt} H_2O_{(g)}$$

The thermodynamic equilibrium potential can be calculated using the Nernst equation:

$$E_{T,P}^{rev} = -\left(\frac{\Delta H_T^0}{nF} - \frac{T\,\Delta S_T^0}{nF}\right) + \frac{RT}{nF}\ln\left[\frac{P_{H_2}\left(P_{O_2}\right)^{0.5}}{\alpha_{H_2O}}\frac{\alpha_{H_2O}^0}{P_{H_2}^0\left(P_{O_2}^0\right)^{0.5}}\right] \qquad [1]$$

Where P_x is the partial pressure of the species x, ΔH^0 and ΔS^0 are respectively the standard enthalpy and entropy of the given reaction at temperature T and unit activity, and α_{H2O} is the water activity at the studied temperature. P^0_{O2}, P^0_{H2} & α^0_{H2O} are the reference oxygen, hydrogen partial pressure and water activity, respectively. Their values are equal to unity.

The following equation is proposed [31] to calculate the change in the standard Gibbs free energy ΔG^0 for the above reaction with temperature T (K):

$$\Delta G_T^0\ kJ.mol^{-1} = -0.0000487792T^2 + 0.1934130924T - 290.039925263 \quad [2]$$

The enthalpy of water formation in the gaseous phase can be written accordingly

$$\Delta H^f_{g,T} = \Delta H^f_l - \Delta H^{Vap}_T \quad [3]$$

Where ΔH_l^f is the enthalpy of water formation in liquid phase and ΔH_T^{Vap} is the heat of vaporisation (water) at temperature T (K).

The change of entropy of water formation in the gaseous phase with temperature was calculated from the thermodynamic tables [35]. Least square errors technique (Fig. 7-1) was used to build a function representing these changes:

$$\Delta S_T = -9967.35\ln(T) + 12414.83 \quad [4]$$

Where ΔS_T is in $J\ K^{-1}$ and T in K.

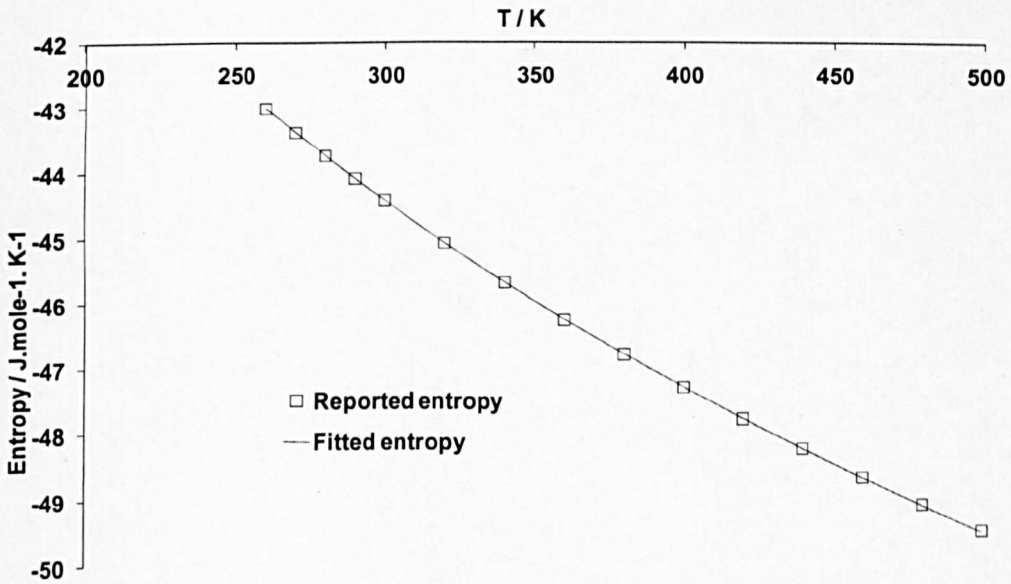

Figure 7-1. Calculated entropy of water vapour [35] and the estimated values from the built logarithmic function (Eq. 4).

The change of heat of vaporisation of water with temperature was obtained from [36], and fitted using a third order polynomial (Fig. 7-2):

$$\Delta H_T^{Vap} = -3.6985255 \times 10^{-4} T^3 + 0.4833076 T^2 - 152.42584114 T + 68260.578987 \quad [5]$$

Where $\Delta H_T{}^{Vap}$ is in Joule and T is in K.

The enthalpy of vapour water formation (Fig. 7-3) can be easily calculated from equation 3 as [37]:

$$\Delta H^f = -238.41 - 0.012256 T + 2.7656 \times 10^{-6} T^2 \quad [6]$$

Where ΔH^f is in kJ and T is in K.

Figure 7-4 shows the calculated standard cell reversal potential in the temperature range of 273-500 K using the standard Gibbs free energy from equation 2 or 4 & 6. While equation 2 counts

for the change of Gibbs free energy for water formation reaction with temperature including phase change (liquid at low temperatures and vapour at higher temperatures), standard Gibbs free energy calculated from equation 4 & 6 is for vapour water formation (even at low temperatures).

While water formation is an exothermic reaction (ΔH is negative), and water vaporisation is endothermic (ΔH is positive); the sum is exothermic because the magnitude of the exotherm is greater than the magnitude of the endotherm and $|\Delta H^f|$ increases with temperature. Since the entropy of water formation is negative and it is lower for gaseous water than for liquid water, the overall standard free energy $|\Delta G_T|$ decreases with temperature, the entropy temperature effects counters the enthalpy of formation temperature effects and the standard cell reversal potential falls with temperature.

Equation 2 includes the gradual phase change in water with temperature, therefore it is expected that the change in ΔG_T and consequently E_{rev} with temperature is not linear (in the studied temperature range of 275-475 K) due to the gradual change in water phase from liquid to vapour, however, on the contrary linear dependency was observed for the calculated E_{rev} (from Eq. 2) with temperature. On the other hand, ΔG_T obtained from equations 4&6 assumes water vapour generation over the entire studied temperature range and was considered in this study. The excepted linear dependency of E_{rev} on temperature was observed (no phase change) and the two simulated lines of Eq.2 and Eq. 4&6 intersects at temperature of 373 K at atmospheric conditions.

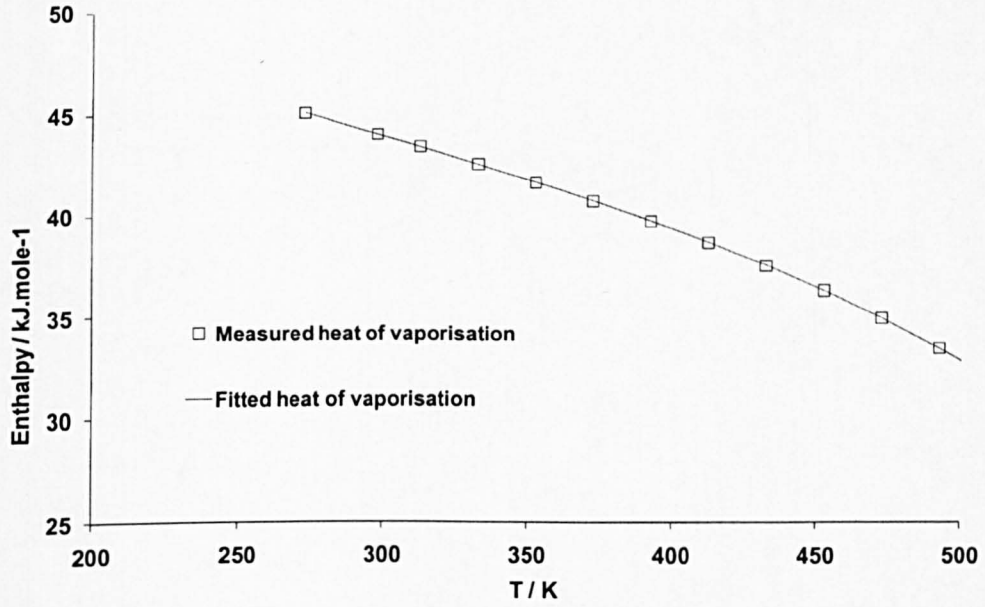

Figure 7-2. Comparison of the measured heat of water vaporization values from ref [36] with the estimated values from the polynomial equation.

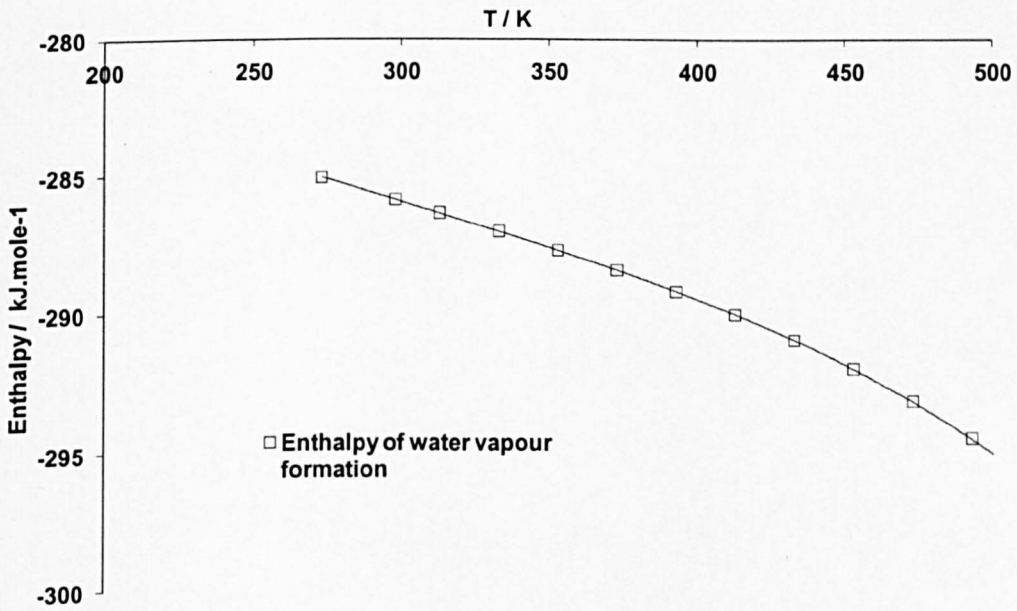

Figure 7-3. Correlated values for water vapour formation enthalpy in the temperature range of 273-500 K.

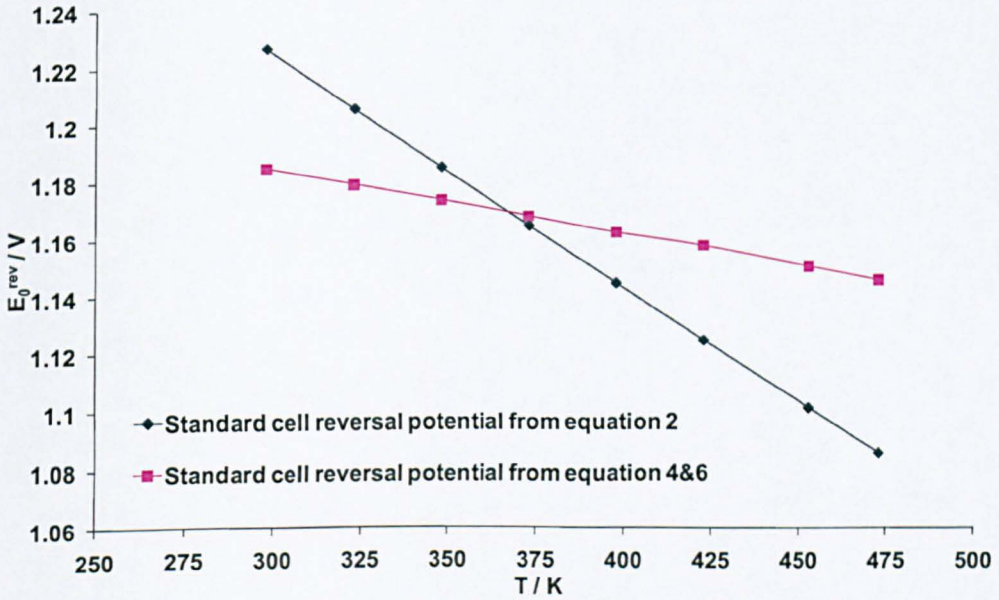

Figure 7-4. Standard cell reversal potential in the temperature range of 273-500 K using Gibbs free energy from equation 2 or 4&6.

The cell reversal potential will deviate from the standard reversal potential depending on the water activity and oxygen/hydrogen partial pressure (Nernst equation).

The water activity is given by [38]:

$$a_{H_2O} = P_{H_2O} / P^*_{H_2O} = \frac{RH\%}{100} \qquad [7]$$

Where P_{H2O} is the water vapour pressure in equilibrium with the acid electrolyte, P^*_{H2O} is the saturation vapour pressure of pure water at the same temperature.

Typically PBI based fuel cells can operate under dry conditions (negligible humidification), in this study the gas reactants where passed through a humidifier at room temperature (16 °C) prior to entering the cell (RH = 0.36% at 150 °C), the initial water vapour pressure (O.C.P conditions) was considered to be equal to water saturation pressure at 16 °C (289 K) i.e. $P_{H2O}=P^*_{291}=0.017$ atm.

Saturated water vapour pressures were obtained from steam tables [39]. The following polynomial function (Fig. 7-5) was build to present this data in the temperature range of 273-500 K.

$$P_{H_2O}^{sat^*} = \begin{pmatrix} 142.07682T^4 - 171026.12676T^3 + 78013638.11584T^2 \\ -15953375633.8471T + 1231888491801.45 \end{pmatrix} \times 10^{-10} \qquad [8]$$

Where P is in atm and T is in Kelvin.

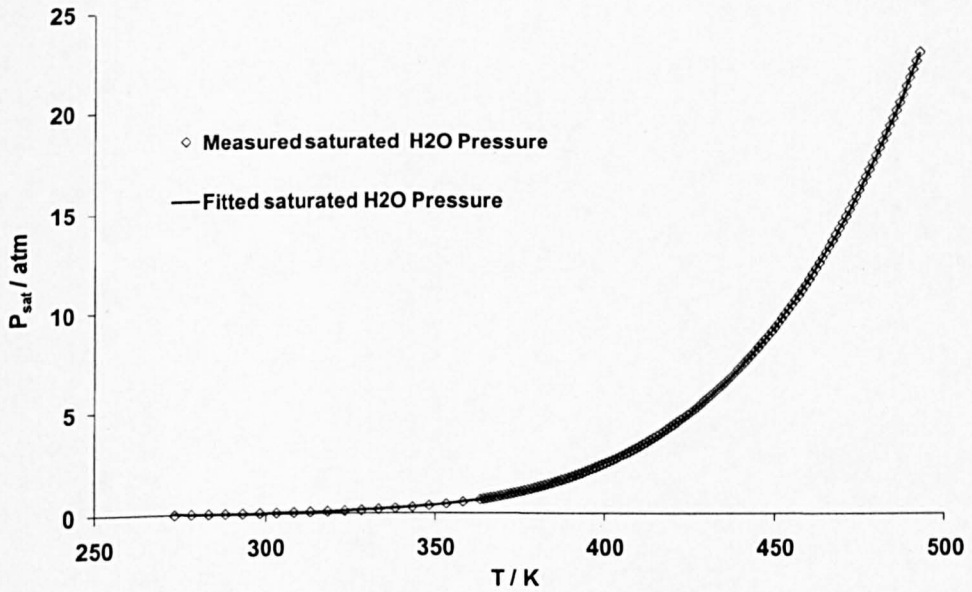

Figure 7-5. Comparison of measured saturated water vapour pressure from ref [39] with the estimated values from the polynomial equation in the range of 273-200 K.

Considering that thin electrolyte film covering the catalyst surface, the partial pressure of the reactants/products should be replaced with their activity in the electrolyte. The activity of hydrogen and oxygen can be replaced by their concentration in the thin film considering their activity coefficient is close to 1 (the concentrations are very low).

We can then write:

$$E_{rev} = E^0_{rev} + \frac{RT}{nF}\ln\left[\frac{(RT)^{1.5} C_{H_2}\left(C_{O_2}\right)^{0.5}}{a_{H_2O}} \frac{a^0_{H_2O}}{P^0_{H_2}\left(P^0_{O_2}\right)^{0.5}}\right] \quad [9]$$

Where oxygen and hydrogen concentration (solubility) is obtained using Henry's law:

$$C_{H_2} = \frac{P_{H_2}}{H^{H_2}_{T,C_{H_3PO_4}}} \qquad C_{O_2} = \frac{P_{O_2}}{H^{O_2}_{T,C_{H_3PO_4}}} \quad [10]$$

Where P_x (atm) is the equilibrium partial pressure of species x above the electrolyte film and H^x (atm cm^3 $mole^{-1}$) is Henry's constant for the given species-electrolyte (H_3PO_4) pair at a given temperature T.

The term RT inside the logarithm expression in equation (9) was introduced to convert the concentration C_x (mole cm^{-3}) into pressure units (atm) to calculate the standard cell reversal potential.

In reality the observed cell O.C.P is lower than the estimated value from the thermodynamics E_{rev} due to the effect of cross-over and other phenomena (carbon corrosion, etc..) where $i \neq i_0$ leading to an overvoltage $\eta_{cross\text{-}over}$ equal to (as will be shown later in the kinetic Sec. 7.7, equation 58):

$$\eta_{cross-over} = \frac{-RT}{\alpha F}\ln\left[\frac{i_{cross-over}}{2i_{0,c}} + \sqrt{1+\left(\frac{i_{cross-over}}{2i_{0,c}}\right)^2}\right] \quad [11]$$

Where α is the transfer coefficient and i_o is the exchange current density.

The observed open circuit will be equal to $E_{rev} + \eta_{cross\text{-}over}$; typically for PBI membrane with thickness 80-40 μm the observed OCP with oxygen at 150 °C was in the range of 0.88-1 V. OCP values of 0.95 V [32] and 0.9 V [15, 17] have been previously used for PBI PEMFCs models.

It should be stressed here that the observed OCP cannot replace E_{rev} as i_o is solely measured at E_{rev}. The effects of cross-over on polarisation curves can be ignored, as it is only important at very small currents and become negligible when polarising the electrode, where the total current $i + i_{cross\text{-}over}$ becomes equal to i ($i >> i_{cross\text{-}over}$) as can be seen in equation 12, in other words the overvoltage losses due to mass transport becomes negligible:

$$\eta_{cross-over} = \frac{-RT}{\alpha F} \ln \left[\frac{\frac{i + i_{cross-over}}{2i_{0,c}} + \sqrt{1 + \left(\frac{i + i_{cross-over}}{2i_{0,c}} \right)^2}}{\frac{i}{2i_{0,c}} + \sqrt{1 + \left(\frac{i}{2i_{0,c}} \right)^2}} \right] \quad [12]$$

7.5 Gas transport in porous media

7.5.1 Diffusion in the porous cathode

There are three species in the cathode gas stream; oxygen, nitrogen and water.

For the purpose of this model only one-dimensional diffusion, normal to the face of the electrode is considered. Diffusion of multi-component gas streams through the porous carbon electrode can be described using the Stefan-Maxwell equation:

$$\frac{\partial X_i}{\partial z} = \frac{RT}{P} \sum_j \frac{X_i N_j - X_j N_i}{D_{ij}^{eff}} \quad [13]$$

X_i is the molar fraction of species i, N_i is the molar flux of species i and D_{ij}^{eff} is the effective binary diffusion coefficient for the pair i-j in the porous medium.

D_{ij}^{eff} can be calculated using the Slattery-Bird correlation [40] and corrected to account for the porosity/tortuosity effects using the Bruggeman correlation [18]:

$$D_{ij}^{eff} = \frac{a}{P} \left(\frac{T}{\sqrt{T_{c,i} T_{c,j}}} \right)^b \left(P_{c,i} P_{c,j} \right)^{1/3} \left(T_{c,i} T_{c,j} \right)^{5/12} \left(\frac{1}{M_i} + \frac{1}{M_j} \right)^{1/2} \varepsilon^r \quad [14]$$

Where T_c and P_c are the gas critical temperature and pressure, respectively. M is the gas molecular weight, ε is the porosity and τ is the tortuosity. a and b are constants, a is 0.0002745 for di-atomic gases and 0.000364 for water vapour and b is 1.832 for di-atomic gases and 2.334 for water vapour.

The species' flux can be given as follows:

Since nitrogen is inert species we can write:

$$N_{N_2,g} = 0 \qquad [15]$$

And from mass balance we can write:

$$N_{O_2,g} = \frac{j}{4F} \qquad [16]$$

$$N_{H_2O,g} = \frac{-j}{2F} \qquad [17]$$

The sign of the flux determine the direction of flux; negative N_{H2O} means the species is produced, while positive N_{O2} means the species is consumed. j is the current density per geometric electrode area and F is Faraday's constant.

Substituting the species flux in equation 14, we obtain:

$$\frac{dX_{N_2}}{dz} = \frac{RT}{p} X_{N_2} \left(\frac{N_{O_2,g}}{D^{eff}_{N_2,O_2}} + \frac{N_{H_2O,g}}{D^{eff}_{N_2,H_2O}} \right) \qquad [18]$$

$$\frac{dX_{H_2O}}{dz} = \frac{RT}{p} \left[X_{H_2O} \left(\frac{N_{O_2,g}}{D^{eff}_{O_2,H_2O}} \right) - N_{H_2O} \left(\frac{X_{O_2}}{D^{eff}_{O_2,H_2O}} + \frac{X_{N_2}}{D^{eff}_{N_2,H_2O}} \right) \right] \qquad [19]$$

Re-arranging equation 18:

$$\frac{dX_{N_2}}{X_{N_2}} = \frac{RT}{p} \left(\frac{N_{O_2,g}}{D^{eff}_{N_2,O_2}} + \frac{N_{H_2O,g}}{D^{eff}_{N_2,H_2O}} \right) dz \qquad [20]$$

Integrating equation (20) with boundary conditions at the electrode channel interface z = 0, $X_{N2}=X^0_{N2}$ (for air 0.79)) and z = Z, $X_{N2}=X_{N2}$ at the catalyst layer where Z is thickness of the gas diffusion electrode:

$$X_{N_2} = X^0_{N_2} e^{\left[\frac{RT}{p}\left(\frac{N_{O_2,g}}{D^{eff}_{N_2,O_2}}+\frac{N_{H_2O,g}}{D^{eff}_{N_2,H_2O}}\right)Z\right]} \quad [21]$$

The oxygen molar fraction is given by:

$$X_{O_2} = 1 - X_{N_2} - X_{H_2O} \quad [22]$$

Combining Eq. (22) and (19) and rearranging for X_{H2O}

$$\frac{dX_{H_2O}}{dz} = \frac{RT}{p} X_{H_2O}\left(\frac{N_{O_2,g}+N_{H_2O}}{D^{eff}_{O_2,H_2O}}\right) + \frac{RT}{p} X_{N_2}\left(\frac{N_{H_2O}}{D^{eff}_{O_2,H_2O}} - \frac{N_{H_2O}}{D^{eff}_{N_2,H_2O}}\right) - \frac{RT}{p}\frac{N_{H_2O}}{D^{eff}_{O_2,H_2O}} \quad [23]$$

Substituting X_{N2} from 21

$$\frac{dX_{H_2O}}{dz} = \frac{RT}{p} X_{H_2O}\left(\frac{N_{O_2,g}+N_{H_2O}}{D^{eff}_{O_2,H_2O}}\right) + \frac{RT}{p} X^0_{N_2} e^{\left[\frac{RT}{p}\left(\frac{N_{O_2,g}}{D^{eff}_{N_2,O_2}}+\frac{N_{H_2O,g}}{D^{eff}_{N_2,H_2O}}\right)Z\right]}\left(\frac{N_{H_2O}}{D^{eff}_{O_2,H_2O}} - \frac{N_{H_2O}}{D^{eff}_{N_2,H_2O}}\right) - \frac{RT}{p}\frac{N_{H_2O}}{D^{eff}_{O_2,H_2O}} \quad [24]$$

For simplification, define constants a, b, h and c:

$$a = \frac{RT}{p}\left(\frac{N_{O_2,g}+N_{H_2O}}{D^{eff}_{O_2,H_2O}}\right), \; b = \frac{RT}{p}\left(\frac{N_{H_2O}}{D^{eff}_{O_2,H_2O}}\right), \; h = \frac{RT}{p}\left(\frac{N_{O_2,g}}{D^{eff}_{N_2,O_2}} + \frac{N_{H_2O}}{D^{eff}_{N_2,H_2O}}\right)$$

$$\& \; c = \frac{RT}{p} X^0_{N_2}\left(\frac{N_{H_2O}}{D^{eff}_{O_2,H_2O}} - \frac{N_{H_2O}}{D^{eff}_{N_2,H_2O}}\right) \quad [25]$$

Equation 24 becomes:

$$\frac{dX_{H_2O}}{dz} = aX_{H_2O} + ce^{hz} - b \quad [26]$$

Integrating 26 with boundary conditions (z = 0, $X_{H2O} = X^0_{H2O}$) at the channel interface, and (z = Z, $X_{H2O} = X_{H2O}$) at the catalyst layer:

$$X_{H_2O} = e^{az}\left(X^0_{H_2O} - \frac{b}{a} - \frac{c}{h-a}\right) + \frac{c}{h-a}e^{hz} + \frac{b}{a} \quad [27]$$

Substituting 16 &17 in 25 leads to

$$\frac{b}{a} = 2,\ h = \frac{RTj}{4FP}\frac{D^{eff}_{N_2,H_2O} - 2D^{eff}_{N_2,O_2}}{D^{eff}_{N_2,H_2O}D^{eff}_{N_2,O_2}},\ a = \frac{-RTj}{4FP\,D^{eff}_{O_2,H_2O}} \quad [28]$$

$$\frac{c}{h-a} = X^0_{N_2}\frac{2D^{eff}_{N_2,O_2}\left(D^{eff}_{O_2,H_2O} - D^{eff}_{N_2,H_2O}\right)}{D^{eff}_{N_2,H_2O}\left(D^{eff}_{N_2,H_2O}D^{eff}_{O_2,H_2O} - 2D^{eff}_{N_2,O_2}D^{eff}_{O_2,H_2O} + D^{eff}_{N_2,H_2O}D^{eff}_{N_2,O_2}\right)} \quad [29]$$

And finally,

$$X_{H_2O} = \left[\begin{array}{l} e^{\frac{-jRT}{4FPD^{eff}_{O_2,H_2O}}z}\left(X^0_{H_2O} - X^0_{N_2}\frac{2D^{eff}_{N_2,O_2}\left(D^{eff}_{O_2,H_2O} - D^{eff}_{N_2,H_2O}\right)}{D^{eff}_{N_2,H_2O}\left(D^{eff}_{N_2,H_2O}D^{eff}_{O_2,H_2O} - 2D^{eff}_{N_2,O_2}D^{eff}_{O_2,H_2O} + D^{eff}_{N_2,H_2O}D^{eff}_{N_2,O_2}\right)} - 2\right) \\ + X^0_{N_2}\frac{2D^{eff}_{N_2,O_2}\left(D^{eff}_{O_2,H_2O} - D^{eff}_{N_2,H_2O}\right)}{D^{eff}_{N_2,H_2O}\left(D^{eff}_{N_2,H_2O}D^{eff}_{O_2,H_2O} - 2D^{eff}_{N_2,O_2}D^{eff}_{O_2,H_2O} + D^{eff}_{N_2,H_2O}D^{eff}_{N_2,O_2}\right)}e^{\frac{RTj}{4FP}\frac{D^{eff}_{N_2,H_2O} - 2D^{eff}_{N_2,O_2}}{D^{eff}_{N_2,H_2O}D^{eff}_{N_2,O_2}}z} + 2 \end{array}\right] \quad [30]$$

X_{O2} can therefore be obtained from equation 21, 22 and 30.

7.5.2 Diffusion in the porous anode

The anode gas feed consists of a mixture of CH_4, CO_2, CO, H_2O & H_2 when running on reformate, for five multi-component gas anode species, we can write balances:

$$\frac{dX_{CO_2}}{dz} = \frac{RT}{p}X_{CO_2}\left(\frac{N_{H_2,g}}{D^{eff}_{H_2,CO_2}}\right) \quad [31]$$

$$\frac{dX_{H_2O}}{dz} = \frac{RT}{p}X_{H_2O}\left(\frac{N_{H_2,g}}{D^{eff}_{H_2,H_2O}}\right) \quad [32]$$

$$\frac{dX_{CO}}{dz} = \frac{RT}{p}X_{CO}\left(\frac{N_{H_2,g}}{D^{eff}_{H_2,CO}}\right) \quad [33]$$

$$\frac{dX_{CH_4}}{dz} = \frac{RT}{p} X_{CH_4} \left(\frac{N_{H_2,g}}{D^{eff}_{H_2,CH_4}} \right) \quad [34]$$

Where:

$$N_{CH_4,g} = 0,\ N_{CO_2,g} = 0,\ N_{CO,g} = 0\ \&\ N_{H_2O,g} = 0 \quad [35]$$

$$N_{H_2,g} = \frac{j}{2F} \quad [36]$$

This leads to,

$$X_{CO_2} = X^0_{CO_2} e^{\left[\frac{RT}{p} \left(\frac{N_{H_2,g}}{D^{eff}_{H_2,CO_2}} \right) Z \right]} \quad [37]$$

$$X_{H_2O} = X^0_{H_2O} e^{\left[\frac{RT}{p} \left(\frac{N_{H_2,g}}{D^{eff}_{H_2,H_2O}} \right) Z \right]} \quad [38]$$

$$X_{CO} = X^0_{CO} e^{\left[\frac{RT}{p} \left(\frac{N_{H_2,g}}{D^{eff}_{H_2,CO}} \right) Z \right]} \quad [39]$$

$$X_{H_2} = 1 - X_{CO_2} - X_{H_2O} - X_{CO} - X_{CH_4} \quad [40]$$

For pure (low) humidified hydrogen feed $X_{CO2} = X_{CO} = X_{CH4} = 0$.

7.6 Transport through thin film electrolyte

The macro-homogeneous model (Fig. 7-6) for the catalyst layer assumes that the catalyst layer is an 'average' of the solid electrode and the electrolyte. Thus, the effective conductance of the catalyst layer is the weighted volume average of the respective conductance; diffusion coefficients & film thickness are similarly averaged, and so on.

Oxygen transport from the porous media to the catalyst active surface area occurs through a thin polymer/acid film covering the catalyst agglomerates. The film provides proton conductive paths from the catalyst active sites to the membrane. The average film thickness δ can be estimated using the following equation:

$$\delta = \frac{m_{H_3PO_4} / \rho_{H_3PO_4} + m_{PBI} / \rho_{PBI}}{S_C + S_{Pt}} \qquad [41]$$

m is the total mass of PBI/H_3PO_4 per unit area(loading), ρ is the density and S_c/S_{Pt} is the surface area of carbon/platinum per unit area covered by the electrolyte.

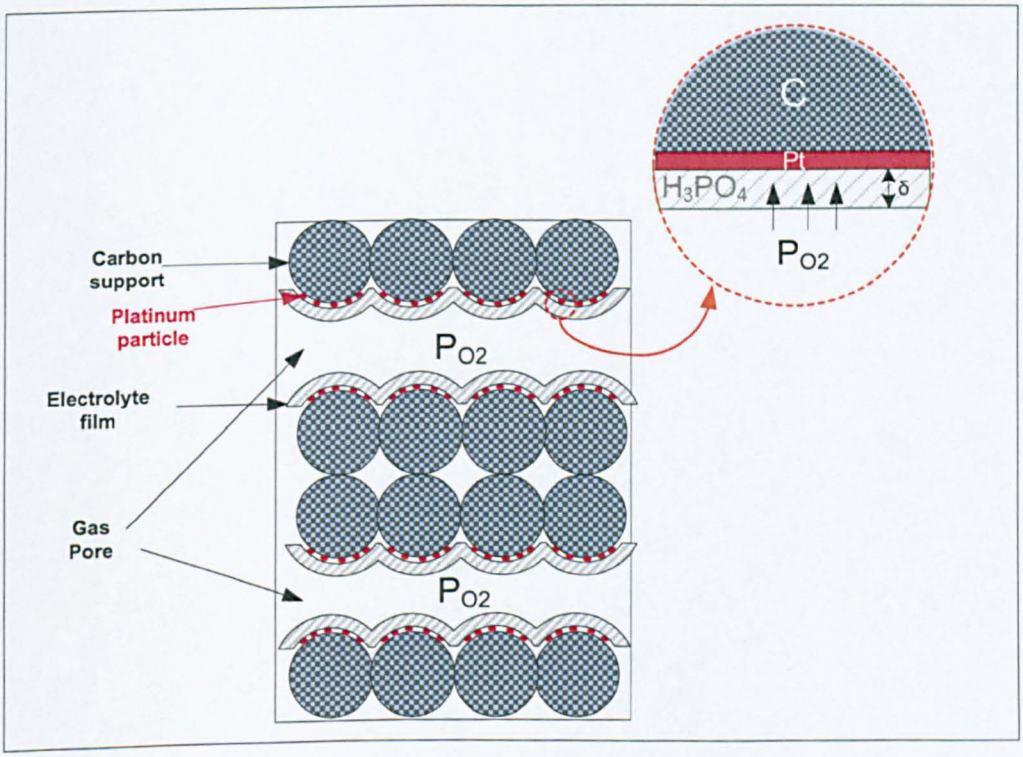

Figure 7-6. Shows diagram of catalyst layer using the thin film assumption.

Values of oxygen diffusion in phosphoric acid (98% wt) were reported to be 30 $\times 10^{-6}$ cm^2 s^{-1}, an order of magnitude higher than that of doped PBI (doping level of 6 PRU) 3.2 $\times$ 10^{-6} cm^2 s^{-1} at 150 °C. Similar values of dissolved oxygen concentration was obtained for doped PBI (doping level of 6 PRU) 0.68×10^{-6} mole cm^{-3} and for 95% wt phosphoric acid 0.5 mole cm^{-3} at 150 °C and atmospheric pressure [23].

Savinell et al, studied oxygen reduction at the platinum/phosphoric acid doped PBI interface, and found that oxygen diffusion was increased by increasing the volume fraction of amorphous (free)

H_3PO_4 (i.e. doping level) . They also suggested that the crystalline PBI regions are not involved in proton or oxygen transport [23, 24].

To determine the oxygen/hydrogen concentration at the catalyst surface, we can derive from Fick's law for diffusion:

$$\frac{N_{O_2}}{S_{Pt-cathode}} = \frac{-D_{O_2}^{H_3PO_4}\left(C_{O_2-Pt} - C_{O_2(dissolve)}\right)}{\delta_{Cathode}} \quad [42]$$

$$\frac{N_{H_2}}{S_{Pt-anode}} = \frac{-D_{H_2}^{H_3PO_4}\left(C_{H_2-Pt} - C_{H_2(dissolve)}\right)}{\delta_{Anode}} \quad [43]$$

N is the molar flux (geometric area) obtained from equations 16 and 36, C_{Pt} is the reactant concentration on the catalyst surface, $C_{dissolve}$ is the equilibrium reactant concentration in the acid film at the studied temperature. S_{Pt} as mentioned erliear is the real platinum surface area (ESA) per unit area that is covered with an electrolyte film (also known as the roughness factor RF).

Due to insufficient data on hydrogen solubility in phosphoric acid at high temperature, it was considered that hydrogen solubility is similar to that of oxygen [41] at the same conditions (pressure, temperature & phosphoric acid concentration).We can write using Henry's law for solubility:

$$C_{H_2(dissolve)} = \frac{P_{H_2}}{H_{T,C_{H_3PO_4}}^{H_2}} \quad [44]$$

$$C_{O_2(dissolve)} = \frac{P_{O_2}}{H_{T,C_{H_3PO_4}}^{O_2}} \quad [45]$$

Where C_{H2}, C_{O2} are the dissolved hydrogen and oxygen concentration in phosphoric acid, respectively. H is Henry's constant at a given temperature and phosphoric acid concentration.

Similarly, for the hydrogen diffusion coefficient in phosphoric acid electrolyte we can write [42]:

$$D_{H_2}^{H_3PO_4} = D_{O_2}^{H_3PO_4}\sqrt{\frac{M_{O_2}}{M_{H_2}}} = 4D_{O_2}^{H_3PO_4} \qquad [46]$$

Figure 7-7 shows the limiting current (steady-state value) for 60%Pt/C at various oxygen partial pressures and temperatures. At the limiting current, C_{Pt} becomes zero, and j_L is directly proportional with $DC_{dissolve}$ (Eq. 42). It can be seen that under air (atm) operation the product $DC_{dissolve}$ decreased slowly with temperature, while for the same electrode under air (1 bar relative) the product $DC_{dissolve}$ exhibits a maximum at 150 °C. This effect is caused by variations in diffusion coefficient D and Henry's constant H at a given temperature with phosphoric acid concentration and consequently water partial pressure above the electrolyte film, in other words the concentration and viscosity of phosphoric acid at a given temperature depends on the humidity content.

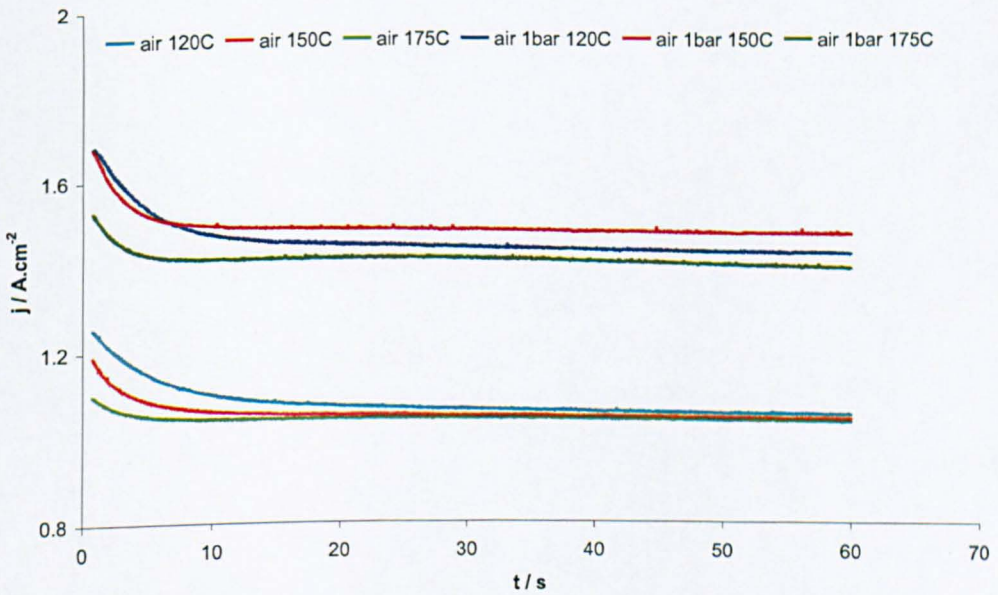

Figure 7-7. The current-time transient response to a potential step where the electrode is entirely under diffusion control.

Klinedinst et al studied oxygen solubility and diffusivity in hot phosphoric acid [43]. They suggested that both gas diffusivities and solubilities exhibit exponential reciprocal temperature dependencies, therefore:

$$D_{O_2}^{H_3PO_4} = A\exp(-E_a / RT) \quad [47]$$

$$C_{O_2}^{dissolved} = B\exp(-\Delta H_{O_2}^{solu} / RT) \quad [48]$$

A and B are pre-exponential factors, E_a is the diffusion activation energy and ΔH is the enthalpy of solution. Both E_a and ΔH change with the concentration of phosphoric acid.

7.6.1 Diffusion, temperature and phosphoric acid concentration

A second order polynomial was fitted using least squared error technique to fit the data obtained by Klinedinst et al [43], for the activation energy of oxygen in phosphoric acid at different acid weight concentrations (W). The correlation of the data with equation (49) is shown in Figure 7-8.

$$E_a\,(\text{kcal mole}^{-1}) = -0.011607142857\,W^2 + 1.9642142857W - 75.376 \quad [49]$$

The high values of the diffusion activation energy were assigned to the extensive hydrogen bond network and high viscosity of concentrated H_3PO_4 [44]. This also explains the decrease in diffusion coefficient with increasing phosphoric acid concentration.

The calculated diffusion values were in the range of (10^{-5}-10^{-6} cm s^{-1}) depending on the temperature and phosphoric acid concentration; values were in good agreement with values obtained in the literature [31, 43, 45, 46].

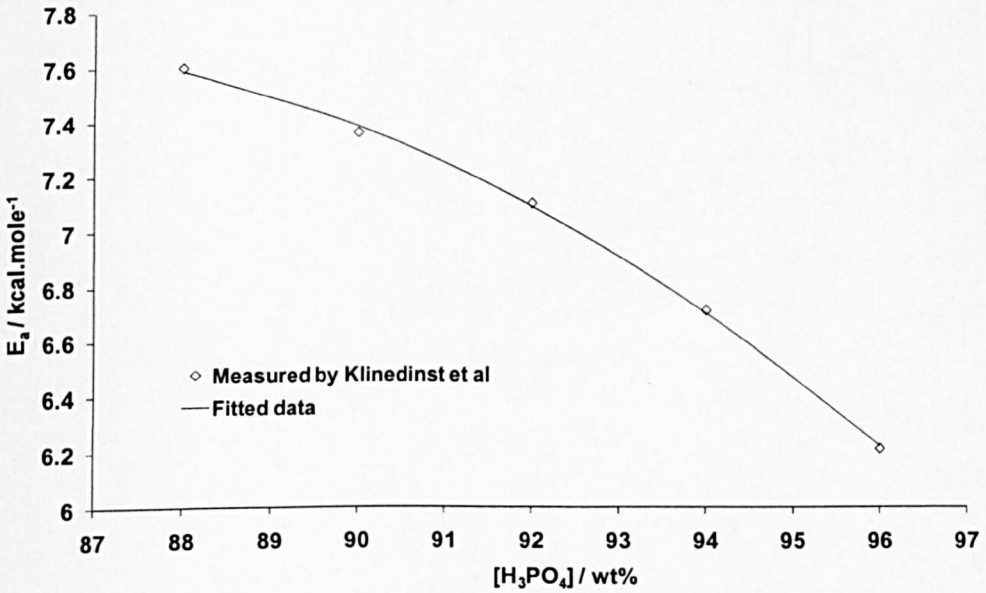

Figure 7-8. Comparison of the measured activation energy of oxygen diffusion in hot phosphoric acid at different concentration from ref [43] with the estimated values from the fitted polynomial equation.

7.6.2 Solubility, temperature and phosphoric acid concentration

A third order polynomial was built to fit oxygen enthalpy of solution data obtained from ref [43]:

$$\Delta H \text{ (kcal)} = (-0.003125W^3 + 0.8371429W^2 - 74.95179W + 2244.786) \qquad [50]$$

Figure 7-9 shows the variation of enthalpy of solution for oxygen in phosphoric acid with acid concentration. The enthalpy of solution ($-\Delta H$, as $\Delta H < 0$ for $W < 96\%$ wt) decreases with increase in phosphoric acid concentration until it reaches negative values at 96% wt; this means that a smaller decrease in the solubility of oxygen in phosphoric acid with temperature will occur as the acid concentrations increases from 85 %wt to 95 %wt; beyond this concentration a slow increase in solubility with temperature will occur.

When calculating the oxygen enthalpy of solution from (ln (C_{O2}) vs. 1/T plots), oxygen concentrations were corrected to one atmosphere pressure assuming Henry's law. This is because

of the corresponding water vapour pressure above the electrolyte (H_3PO_4) at studied temperature and electrolyte concentration [31].

Figure 7-10 shows the variation in oxygen solubility in hot phosphoric acid at different acid concentration and temperatures from ref [43] with the estimated values from the fitted polynomial equation.

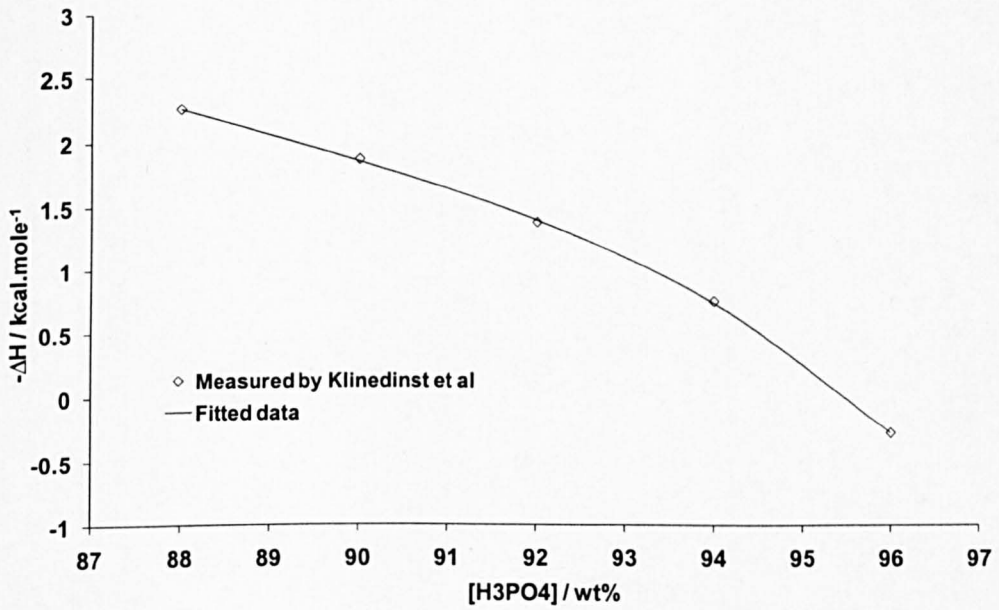

Figure 7-9. Comparison of measured enthalpy of solution for oxygen in hot phosphoric acid at different concentration from ref [43] with the estimated values from the fitted polynomial equation.

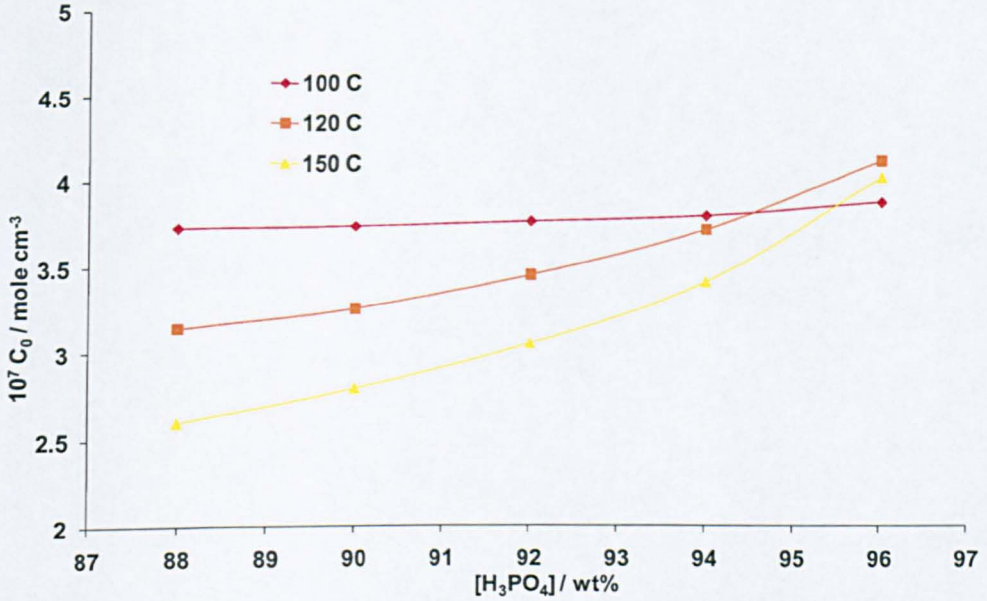

Figure 7-10. Variation in oxygen solubility in hot phosphoric acid at different acid concentration and temperatures from ref [43] with the estimated values from the fitted polynomial equation.

C_{O2} and D_{O2} can be obtained from equations 47 and 48 for a given acid weight concentration. By substituting their values into equations 42 and 43 will finally lead to C_{Pt}, the oxygen concentration on the catalyst surface required in the Butler-Volmer kinetic equation.

7.6.3 Phosphoric acid concentration, temperature and water vapour pressure

MacDonald and Boyak [47] studied the density, conductivity and equilibrium water vapour pressure of concentrated phosphoric acid from room temperature to 170 °C. Data from their work was used to determine phosphoric acid concentrations (wt %) at a given temperature and water vapour pressure.

To obtain a good fit without using polynomials of very high order, they suggested expressing concentrations as mole per cent X, instead of W (wt %) using the formula:

$$X = \frac{0.01W}{0.01W + 0.0544(100 - W)} \qquad [51]$$

At any given concentration, a linear relation was obtained between log (P_{H2O} /mmHg) the equilibrium water vapour pressure and 1/T ($^oC^{-1}$):

$$\log\left(P_{H_2O}\right) = -aT^{-1} + b \qquad [52]$$

Values of a and b are listed in table 7-1 below at different mole %

Table 7-1. Values of constants a & b used in equation 52, at various acid concentration (expressed as mole %)

X (mole%)	W (wt%)	a	b
35	74.55	246.92	4.7781
50	84.5	278.24	4.7086
65	91	303.24	4.5563
80	95.6	321.6	4.3028
90	98	344.05	4.1491
100	100	416.36	4.2476

Two functions were built to correlate a and b with X

$$a = a_1X^4 - a_2X^3 + a_3X^2 - a_4X + a_0 \qquad [53]$$

$$b = b_1X^4 - b_2X^3 + b_3X^2 - b_4X + b_0 \qquad [54]$$

Values for theses constants are given in the appendix.

During simulation of the model in this work, X and W were continuously updated based on water vapour pressure (or relative humidity) and temperature. W was obtained from X using:

$$W = \frac{98X}{0.98X + (18.016 - 0.18016X)} \quad [55]$$

Figure 7-11 compares the measured equilibrium water vapour pressure above phosphoric acid solutions at different temperatures and concentrations from ref [47] with the estimated values from the built polynomial in equation 52. It can be seen that P_{H2O} (or humidity) is highly dependant on phosphoric acid concentration at the typical low humidity conditions for PBI based PEMFCs gas feed. This means that phosphoric acid concentrations will vary greatly with the water produced by the fuel cell (logarithmic relation).

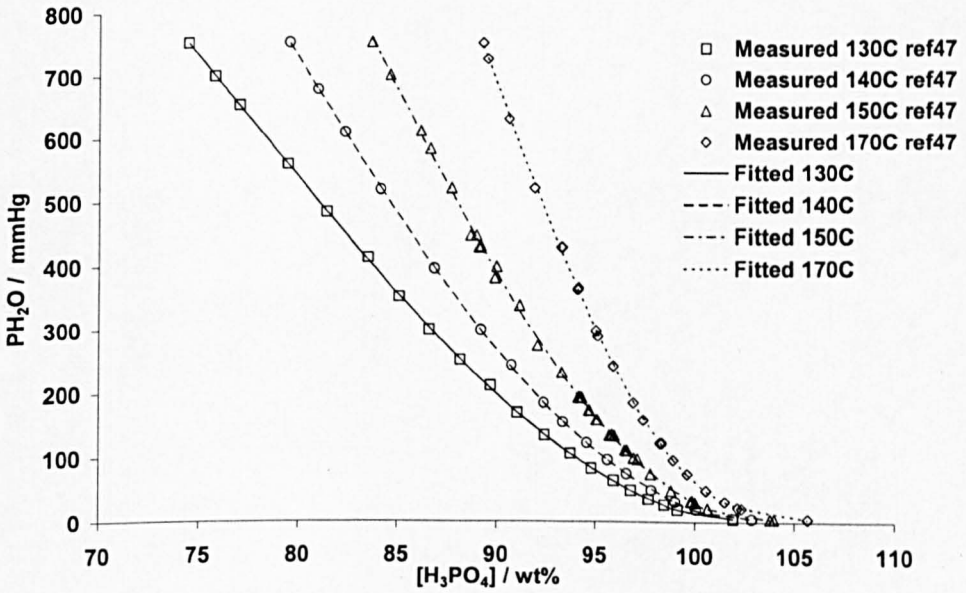

Figure 7-11. Comparison of measured equilibrium water vapour pressure above phosphoric acid solutions at different temperatures and concentrations from ref [47] with the estimated values from the built polynomial in equation (52).

7.7 Kinetics

The Butler-Volmer equation was used to describe the kinetics at the anode and cathode:

$$j_a = i_{0,a}\left(\exp\left(\frac{-\alpha_{Rd,a}F}{RT}(\eta_a)\right) - \exp\left(\frac{\alpha_{Ox,a}F}{RT}(\eta_a)\right)\right) \quad [56]$$

$$j_c = i_{0,c}\left(\exp\left(\frac{-\alpha_{Rd,c}F}{RT}(\eta_c)\right) - \exp\left(\frac{\alpha_{Ox,c}F}{RT}(\eta_c)\right)\right) \quad [57]$$

Where the subscripts a & c are for anode and cathode, respectively. α is the transfer coefficient, i_0 is the exchange current density at the studied conditions per Pt unit area given by equation 60 below.

Assuming $\alpha_{Rd,c} = \alpha_{Ox,c}$, it is convenient to substitute the hyperbolic sine function in 57 to give:

$$\eta_c = \frac{-RT}{\alpha_c F}\sinh^{-1}\left(\frac{i_c}{2i_{0,c}}\right) = \frac{-RT}{\alpha_c F}\ln\left[\frac{i_c}{2i_{0,c}} + \sqrt{1+\left(\frac{i_c}{2i_{0,c}}\right)^2}\right] \quad [58]$$

Values of α can be obtained from Tafel slope b = 2.3 RT/ α F: as shown earlier (Chapter 3) alpha values change with doping level, for example at 150 °C the lowest Tafel slope observed at the minimum doping level of 4.5 PRU was 92 mV dec^{-1}(α = 0.91) increasing to 104 mV dec^{-1} (α = 0.81) at a doping level of 10 PRU [23, 24].

Oxygen reduction in PBI-free electrodes environment (or for PBI electrodes with very high doping level) is the same as that in phosphoric acid, while for PBI based electrodes, appropriate transfer coefficient should be chosen; depending on the doping level.

Various Tafel slopes have been reported for phosphoric acid fuel cells in the range of 90 and 135 mV dec^{-1} (α = 0.93-0.62) at 150 °C [25-31]. A value of alpha equal to 0.75 (112 mV dec^{-1}) in the middle of the reported range was considered. In this work, the closest available experimental data for a PBI-free environment at 150 °C is from half cells results (Chapter 3) with a high

doping (16 PRU) PBI electrode at temperature of 140°C, the obtained alpha value was 0.75, this value agrees with the chosen reported alpha value for phosphoric acid.

While the discussed value for alpha are for temperature of 150 °C, alpha values vary with operating cell temperature. Appleby [48] reported variations in of α with temperature from 0.56 at 25 °C to 0.66 at 136 °C in 85% wt phosphoric acid. Similarly, O'Grady et al [16] reported values from 0.53 at 25 °C to 0.68 at 70 °C in 85% wt phosphoric acid. Huang et al [17] observed α value (85 %wt H_3PO_4) of 0.47, 0.61 & 0.67 at temperatures of 25, 100 & 150 °C, respectively. Kunz and Gruver [18] reported α = 0.94 at 160 °C (96%wt H_3PO_4) using Pt/C as catalyst.

The variation of dependency with temperature can be expressed as [49]:

$$\alpha = a + cT \qquad [59]$$

Where a & c are constants. Values for c, the rate change of alpha with temperature, were 0.0014 [27], 0.0015 [48], 0.0034 [33] & 0.0043 (this work PBI 16 PRU).

The value of alpha and its variation with temperature (Table 7-2) depend on the catalyst treatment and the impurity content in the acid [28, 48].

Table 7-2. Summarise alpha variation in temperature values from this work (chapter three) and Ref. [27, 33]

T C°	This work 16PRU	Extrapolated from Ref [33]H_3PO_4	Obtained from Ref [27]H_3PO_4	Extrapolated from Ref [48]H_3PO_4
100	0.5864	0.7624	0.6022	0.6098
120	0.6724	0.8304	0.6302	0.6398
150	0.8014	0.9324	0.6722	0.6848
175	0.9089	1.0174	0.7072	0.7223

The exchange current density was obtained using:

$$i_0 = i_0^{ref} a_c L_c \left(\frac{C_{Pt}}{C_{Pt}^{ref}}\right)^{\gamma} \exp\left[-\frac{E_C}{RT}\left(1-\frac{T}{T_{ref}}\right)\right] \qquad [60]$$

i_0^{ref} ($A.cm_{Pt}^{-2}$ ESA) is the exchange current density measured at a reference temperature T_{ref} and reference dissolved oxygen concentration (solubility) C_{ref}. C_{Pt} is the reactant concentration on the catalyst surface calculated from equation 42 (or 43 for hydrogen). a_c ($m_{Pt}^2\ g^{-1}$) is the catalyst specific accessible electrochemical surface area (covered by electrolyte) in the electrode measured using cyclic voltammetry (31.55 & 35.45 $m^2\ g^{-1}$ for cathode and anode electrodes utilizing 50% Pt/C & 20% Pt/C, respectively); which correspond to 50-30 % of the given value by the manufacture (128 $m^2\ g^{-1}$ for 20% Pt/C & 86 $m^2\ g^{-1}$ for 50% Pt/C [50]) when placed in the electrode structure [51]. a_c can also be estimated by multiplying the ionomer's volume fraction in the catalyst layer by the catalyst ESA.

L_c is the catalyst loading, which corresponds to the weight of platinum per unit geometric area (mg cm^{-2}). The product $a_c.L_c$ is the roughness factor (dimensionless), which is the Pt electrochemical surface area divided by the electrode geometric area, referred to earlier as S_{Pt}. The units of the product $i_0^{ref}\ S_{Pt}$ or i_0 will be A cm^{-2} (current density per electrode geometric area).

γ is the pressure coefficient or the reaction order with respect to oxygen in phosphoric acid/PBI, a value of 1 (first order) was reported in references [23, 31].

E_c the activation energy of oxygen reduction in hot phosphoric acid was found to be independent of phosphoric acid concentration 92 kJ $mole^{-1}$ [21], 54.8 kJ $mole^{-1}$ [15], 62.34 kJ $mole^{-1}$ [48] and 72.4 kJ $mole^{-1}$ [9]. The latter value was used as it lies in the middle of the range.

Values for i_0^{ref} vary in the literature, depending on the temperature, phosphoric acid concentration and the dissolved oxygen concentration. Most values (Table 7-3) were in the range of 10^{-8} A cm_{Pt}^{-2} and i_0 value from ref [30, 48] was used.

Table 7-3. Summarise the reported exchange current densities for oxygen reduction in phosphoric acid.

i_0 /A.cm$_{Pt}^{-2}$	H_3PO_4 /wt%	T /°C	C_{O2} /mole.L^{-1}	Ref
$6x10^{-8}$	96	160	4.13×10^{-4} √	[52]
$2.8x10^{-7}$	85	136	2.61×10^{-4} √	[48]
$4x10^{-8}$	85	96	3.94×10^{-4} √	[30, 48]
$2.4x10^{-8}$	85	136	2.61×10^{-4} √	[25]
$3.8x10^{-9}$	98	100	0.996×10^{-4}	[30]
$3.9x10^{-8}$	98	125	0.971×10^{-4}	[30]
$2.63x10^{-8}$	98	150	1.07×10^{-4}	[30]
$8x10^{-8}$	85	60	6.23×10^{-4} √	[26]
$1.7x10^{-6}$	85	160	2.11×10^{-4} √	[26]
$1x10^{-8}$	85	120	3.05×10^{-4} √	[25]
$1.6\ x10^{-8}$	85	136.1	2.61×10^{-4} √	[28]

√ Calculated concentrations from equations 48&50.

Similarly, a value of $i_0^{ref} = 0.144$ A cm^{-2} at 160 °C (C_{H2}^{ref} 2.11×10^{-4} mole L^{-1}), E_a= 16.9 kJ mole^{-1}, $\alpha = 0.5$ and $\gamma = 1$ for hydrogen oxidation in phosphoric acid was obtained from [41].

7.8 Conductivity and IR losses

To express the proton conductivity of acid doped PBI at different temperatures a modified Arrhenius equation has been suggested initially [53] for polymer/acid (salt) complexes, and later used by other researchers [54-57].

$$\sigma.T = A\exp\left(\frac{-B}{R(T-T_0)}\right) \qquad [61]$$

Values of A, the pre-exponential factor, and B, the activation energy, are humidity and doping level dependant and are given in [54].

Polynomial functions (equations 62 & 63) were fitted for A & B based on the relative humidity at a given doping level (membrane doping level of 5.6 PRU in this case), which is given by:

$$A = \exp\left[\left(k_1^a RH^3\right) + \left(k_2^a RH^2\right) + \left(k_3^a RH\right) + k_0^a\right] \quad [62]$$

$$B = \left(k_1^b RH^3\right) + \left(k_2^b RH^2\right) + \left(k_3^b RH\right) + k_1^b \quad [63]$$

The values of constants k^a & k^b are given in the Appendix.

The conductivity obtained from equation 61 along with the membrane thickness of (40 μm) were used to determine the IR losses through the membrane. On the other hand the IR losses (protonic) through the catalyst layer where obtained from the catalyst layer thickness (15 μm) and the effective phosphoric acid conductivity (product of phosphoric acid conductivity at the studied condition and its volume fraction in the electrode). The conductivity of phosphoric acid varies with temperature T and relative humidity (RH) (or phosphoric acid concentration W (wt %)).

The following functions for conductivity were given [47] for $84 \leq W \leq 94\%$:

$$K(S\,cm) = 1.01365 - 1.21548 \times 10^{-2} W - (1.5447 \times 10^{-7} - 6.42463 \times 10^{-5} W)T \quad [64]$$

for $95 \leq W \leq 99\%$:

$$K(S\,cm) = -3.45285 + 7.77294 \times 10^{-2} W - 4.50762 \times 10^{-4} W^2 - (6.24637 \times 10^{-2} - 1.387186 \times 10^{-3} W + 7.18336 \times 10^{-6} W^2)T \quad [65]$$

The overall cell voltage is given by:

$$U_{cell} = E_{rev} - |\eta_c| - |\eta_a| - iR$$

The iR drop is calculated from (61, 64 & 65) using Ohm's law, anode/cathode activation & mass transport over-potential from equation 58, and thermodynamic cell reversible potential from equation 9.

7.9 Results and discussion

Matlab® V.7.3 and Simulink® V.6.5 equipped with Ordinary Differential Equation solver (ODE 45) was used to solve the model governing equations. The model results were compared to that of experimental data for a 50 %Pt/C (0.4 mg cm^{-2}) cathode and 20 %Pt/C (0.2 mg cm^{-2}) anode. The cathodic sweep (from OCP to 0 V) was considered under pseudo steady-state conditions (5 mV s^{-1}); the conditions at which the quoted alpha values were measured. High resolution experimental data were sampled every 1.0 mV step in order to allow for good comparison with the model results.

7.9.1 Mass transport losses through the gas diffusion layer

The influence of the diffusion layer porosity, temperature and current density on the effective oxygen concentration at the cathode is simulated to judge the impact of this component on cell behaviour.

Figure 7-12 shows the effect of porosity on the cathode species' mole fraction at the interface of the diffusion layer and catalyst. The oxygen mole fraction as well as nitrogen mole fraction show exponential dependency on porosity while the water mole fraction shows a logarithmic dependency on porosity. This can also be concluded from equations 21, 22 & 30. We can also see that at a current density of 5 A cm^{-2} using air as cathode feed, the oxygen molar fraction is only significantly affected at porosities less than 50 % and reaches zero at porosity of ~22 %; where a limiting current will be observed.

Figure 7-13 shows the effect of temperature on the cathode mixture mole fraction at a current density of 5 A cm^{-2}. As temperature increases diffusion becomes faster and mass transport limitations reduce, i.e. the mole fraction of species i (X_i) becomes closer to its initial value X_i^0, therefore oxygen and nitrogen mole fractions at the catalyst layer boundary increases with an increase in temperature, while the water mole fraction decreases.

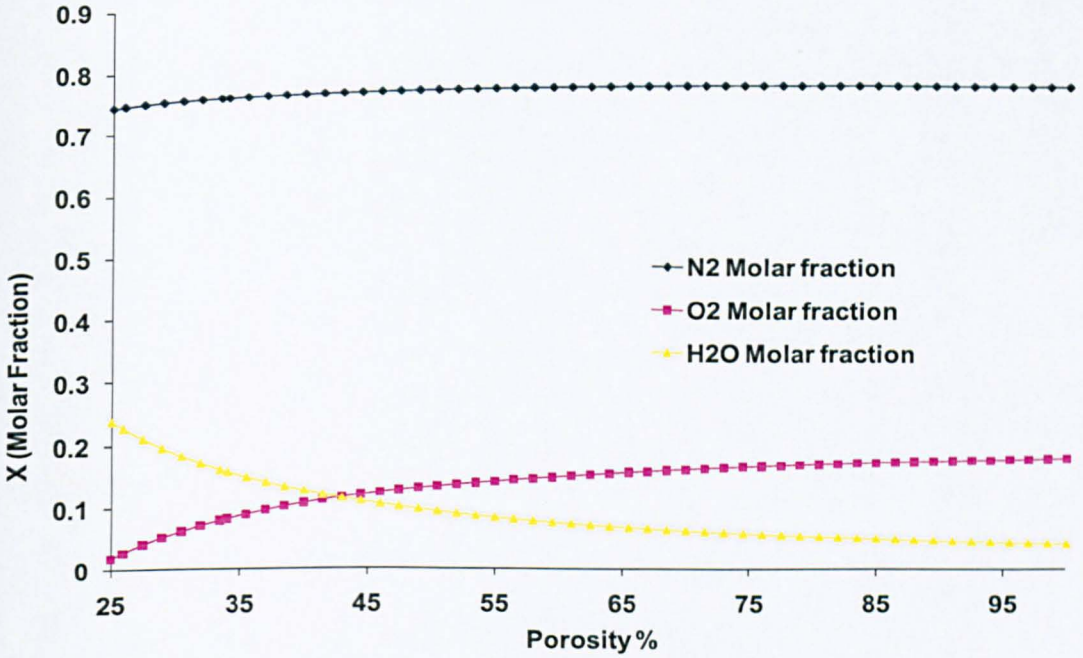

Figure 7-12. The effect of porosity on the cathode gas mixture (air) at 150°C, under operating current density of 5 A cm-2, Z= 200 μm and τ = 1.5.

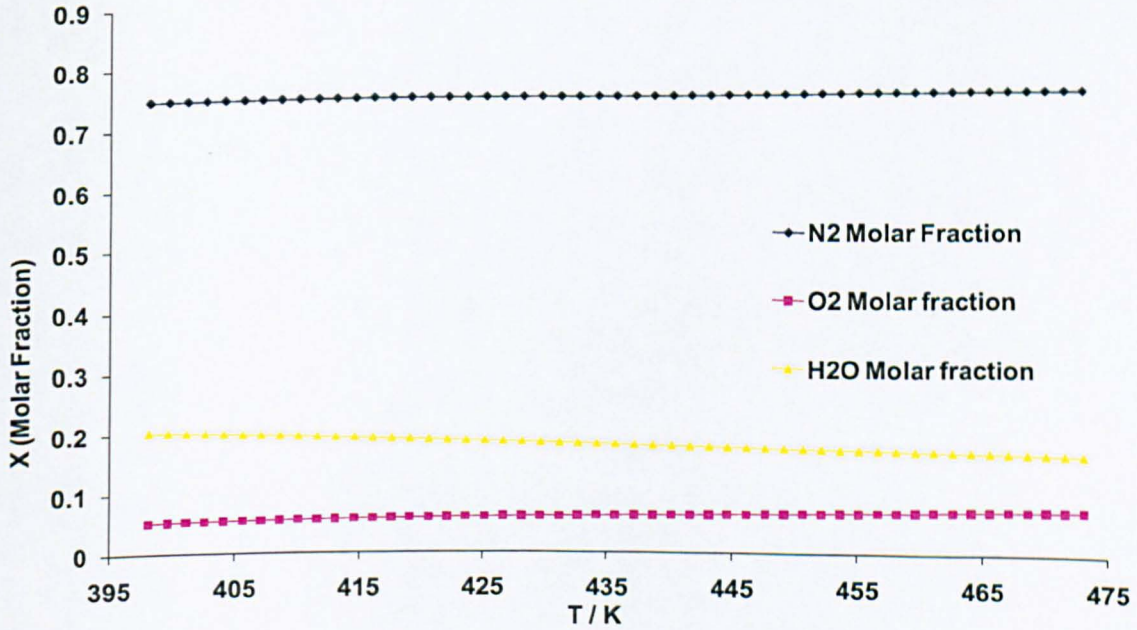

Figure 7-13. The effect of temperature on the cathode gas mixture (air) under operating current density of 5 A cm-2, Z = 200 μm, porosity of 30% and τ = 1.5.

Figure 7-14 shows the effect of current density on water and oxygen mole fractions at the cathode boundaries for a 30% porosity and diffusion length of 200 μm. No limiting current is visible ($X_{O2} > 0$) even at high current density of 5 A cm^{-2} using air. This confirms the above conclusion (Sec.7.2) regarding the failure of single phase models, with no electrolyte thin film consideration, to explain the observed low limiting current 1 -1.5 A cm^{-2} of PBI based fuel cells under air operation.

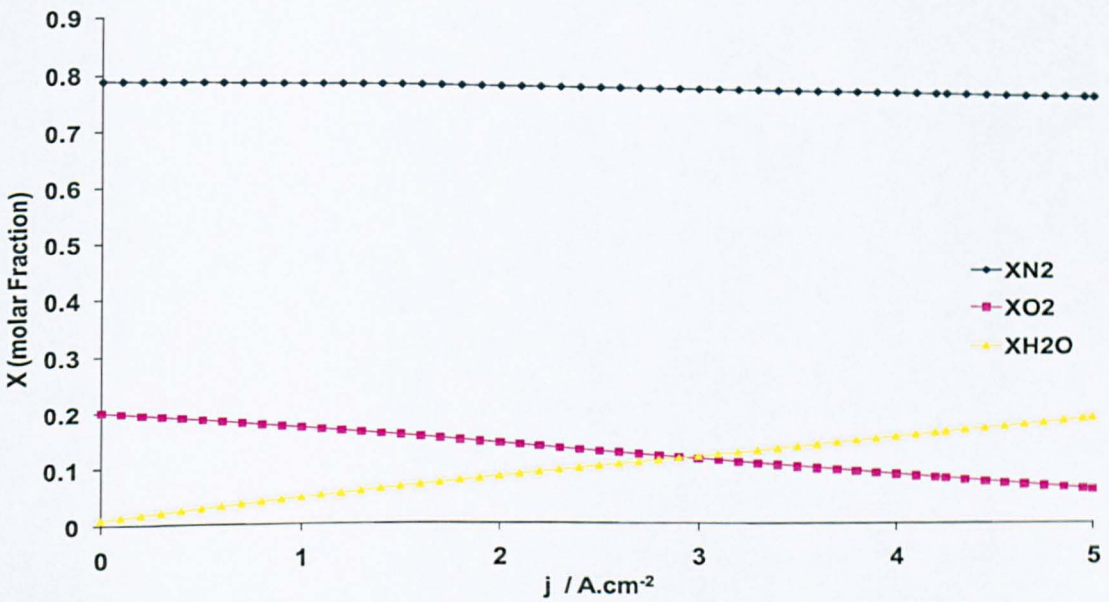

Figure 7-14. The effect of operating current density on the cathode gas mixture (air) at temperature of 150 °C, Z = 200 μm, porosity of 30 % and τ = 1.5.

7.9.2 Oxygen partial pressure effects

Figure 7-15 compares simulated and experimental data for PBI based HT-PEMFC at different oxygen partial pressures; from air (atm) to air (1 bar) and pure oxygen. Large increases in voltage were seen in both modelled and experimental data due to enhancement in kinetics and mass transport when increasing oxygen concentration (partial pressure). This effect is due to the low oxygen permeability in hot concentrated phosphoric acid. The experimental observed limiting current increased from (~1.4 to 2.1 A cm^{-2}) when doubling oxygen partial pressure (1 atm to 1.99 atm). The model data and the experimental data were in good agreement. However,

small differences were observed in the slope of the polarisation curves, at high current densities, where the model over-estimated the cell performance with air and air (1 bar pressure) whilst not under oxygen operation.

The slope of the polarisation curves is affected by a combination of kinetic, mass transport and IR effects. The observed difference of the slope at high current densities in this case was probably caused by unknown kinetic or mass transport effects, and not IR effects, as a good match in the slope was observed at high current densities under oxygen operation.

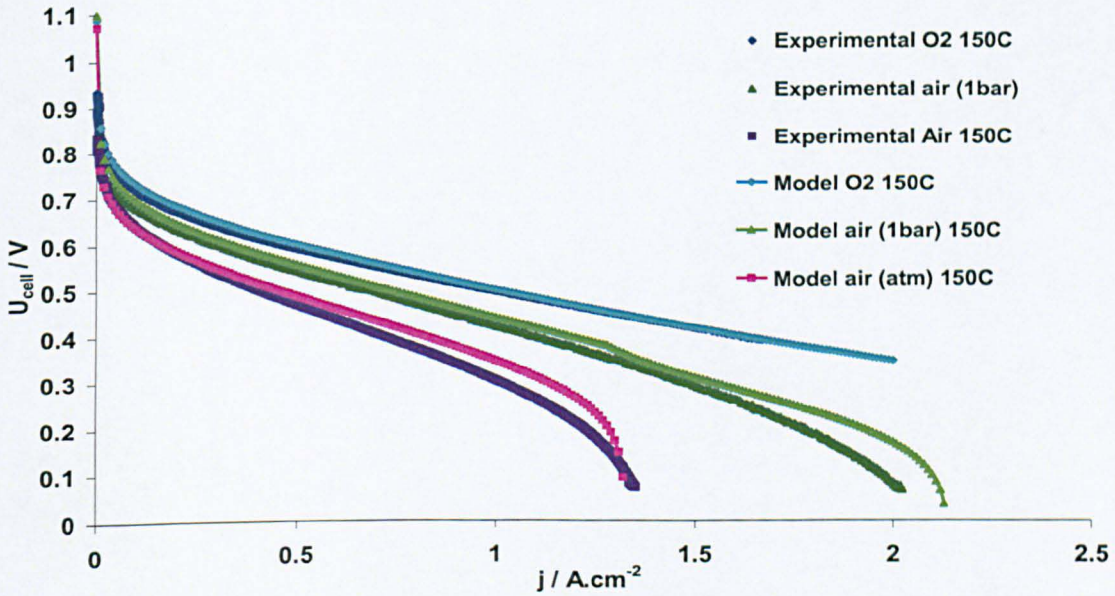

Figure 7-15. Comparison between modelled and experimental results for HT-PEMFC utilising 50% Pt/C at the cathode and 20% Pt/C on the anode at temperature of 150 °C and various pressures- alpha value of 0.75 was used for the cathode.

In order to improve the fit between the experimental data and the model prediction, it would seem that a correction at high current densities should be made to the kinetic effect (lower α) or mass transport (higher γ).

Figure 7-16 shows the same experimental data set (as Fig. 7-15) with a lower alpha value for the modelled data of 0.72 (~117 mV dec^{-1}) opposed to the standard value used in the model of 0.75 (~112 mV dec^{-1}). As excepted an improved fit was observed between both modelled and

experimental data at high current densities and low oxygen concentrations (partial pressure), however, on the other hand the model underestimates cell performance at high current densities under oxygen operation. This effect was observed in previous PBI models [16, 17]. While the authors related such behaviour to a change in membrane conductivity with water produced, this suggestion can not be substantiated in this case as such variation was considered in this model (Sec. 7.8). The behaviour can be caused by either a variation (increase) in the transfer coefficient with current produced due to an increase in humidity [23], or a decrease in cathode's potential leading to a decrease in impurities [49] and phosphoric ions adsorption [58] on the catalyst surface (has a maximum adsorption peak at 0.85 V [45]). However, if such effects were taking place then alpha should also improve under air & air (1 bar) operation and the model should underestimate cell performances; which weren't observed. This suggests that the observed deviation in the slope is caused by mass transport effects rather than kinetic effects.

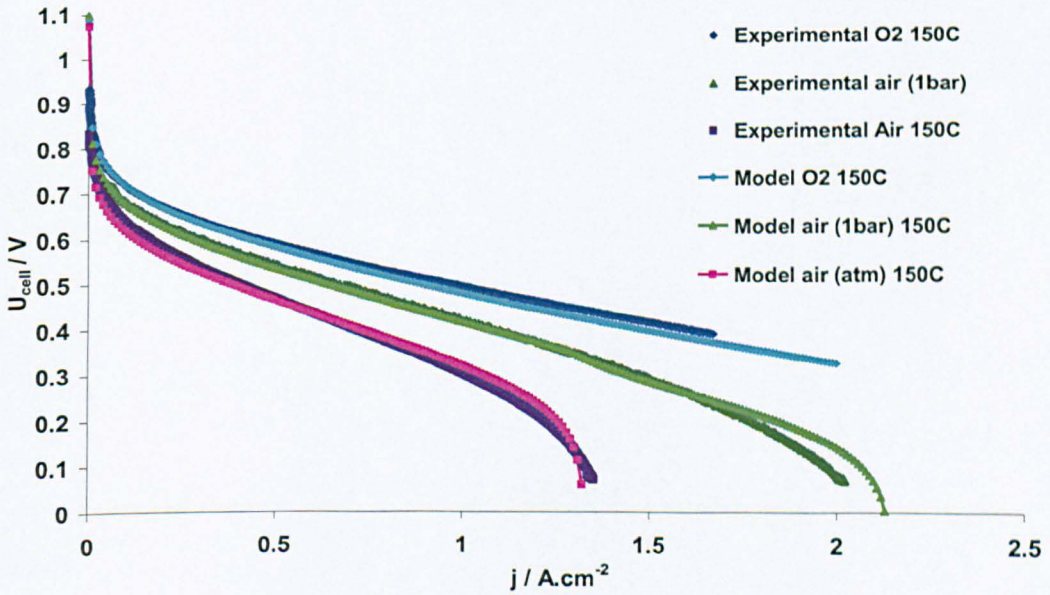

Figure 7-16. Comparison between modelled and experimental results for HT-PEMFC utilising 50% Pt/C at the cathode and 20% Pt/C on the anode at temperature of 150°C and various pressures- alpha value of 0.72 was used for the cathode.

To introduce increased mass transport losses, the reaction order (γ) with respect to oxygen in phosphoric acid was increased from the commonly reported value of 1 [31] to 1.375, values above 1 have also been reported for PBI/H_3PO_4 interface [23]. The reported values of reaction order was measured at constant over-voltage η (and not constant voltage E) i.e. they where measured from the exchange current density ratios ($\eta = 0$) where i_0 was measured at equilibrium potential E_{rev} which in turn is affected by a concentration change (Nernst equation) as will be discussed shortly.

Figure 7-17 shows the effect of the higher reaction order (1.375) on the cell voltage polarisation curve and maintaining the standard value of alpha (0.75). An improvement in the model fit with the experimental data at various oxygen pressures is seen where the model predictions followed the experimental data very closely even at high current densities and different oxygen concentration

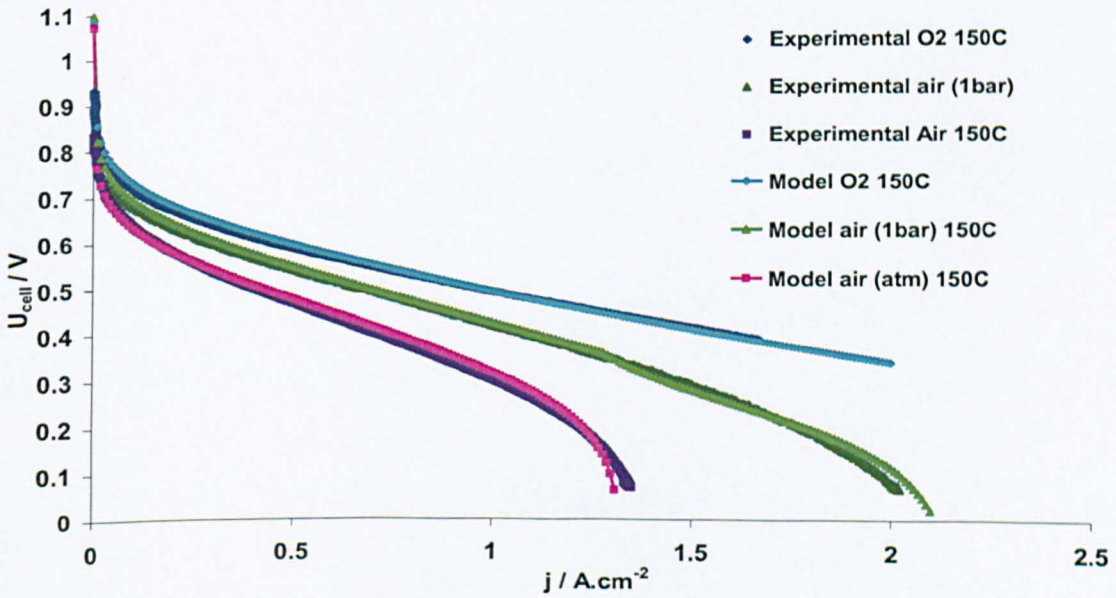

Figure 7-17. Comparison between modelled and experimental results for HT-PEMFC utilising 50% Pt/C at the cathode and 20%Pt/C on the anode at temperature of 150 °C and various pressures- alpha value of 0.75 & $\gamma = 1.375$ was used for the cathode.

A higher value of gamma than 1.0 can be caused by one or a combination of the following two factors:

i- Thermodynamic effect of oxygen concentration losses:

While the oxygen concentration influence was accounted for in the Butler-Volmer equation (60), the cell reversible potential was considered constant over the cell polarisation where the equilibrium concentrations at rest potential (zero current) was considered. An additional change in the reversible potential will occur due to lower oxygen concentrations (see equation 9). This shift is equal to (RT/2F) ln (C_{O2}/C^{0}_{O2}) as given by the Nernst equation.

Thus, rather than writing equation 58 for high current densities as:

$$\eta_c = \frac{RT}{\alpha F}\ln(\frac{j}{i_0}) + \frac{\gamma RT}{\alpha F}\ln(\frac{C_{O_2}}{C^0_{O_2}}) \qquad [66]$$

The overpotential is given by:

$$\eta_c = \frac{RT}{\alpha F}\ln(\frac{j}{i_0}) + \frac{\gamma RT}{\alpha F}\ln(\frac{C_{O_2}}{C^0_{O_2}}) + \frac{RT}{2F}\ln(\frac{C_{O_2}}{C^0_{O_2}}) \qquad [67]$$

This can be re-written as:

$$\eta_c = \frac{RT}{\alpha F}\ln(\frac{j}{i_0}) + \frac{\gamma' RT}{\alpha F}\ln(\frac{C_{O_2}}{C^0_{O_2}}) \qquad [68]$$

Where γ' is equal to $\gamma + \alpha/2$ or in this case 1+0.75/2=1.375, the value used for gamma in the latest simulation.

ii- Losses of surface area (ESA) due to oxygen starvation:

Losses in the accessible electrochemical surface area might occur due to oxygen starvation, where at very low concentrations, oxygen will not be able to reach parts of the catalyst surface even though they are available for reaction (covered with electrolyte).This effect would lead to a further decline in performance at high current densities and low oxygen concentrations (in comparison to gamma =1). Unfortunately, such an effect is not accounted for in this model and is one of the limitations of the macro-homogeneous model, where it is assumed that the average accessible catalyst layer is constant. However if such effects are present then the ESA can be

written as function of ln (C_{O2}/C^{0}_{O2}) which would effectively cause an increase in the apparent reaction order.

7.9.3 Porous media effects

The effect of mass transport losses due to diffusion through porous media can be seen by comparing cell performances using air (O_2-N_2) and heleox mixture (O_2-He) as oxidant at the cathode. While both mixtures contain the same oxygen concentration ($X_{O2} = 0.21$), the inert gas used in the mixture is different. The binary diffusion coefficients of oxygen-helium and water-helium are four and eight times higher than that of oxygen-nitrogen and water-nitrogen, respectively.

Figure 7-18 shows the enhancement in cell performance observed when switching from air to heleox caused by mass transport enhancement through the porous structure.

Generally, a larger difference between the limiting currents using air or heleox is due to a greater contribution of the porous media mass transport losses or the smaller the value of (ε^{τ}). Similarly, to the earlier observation (Sec. 7.9.2) using $\alpha = 0.75$ & $\gamma = 1$, the model provided good predictions of cell performance, however it over estimated the performance at high current densities. On the other hand the model successfully estimated the limiting current values with air and heleox. This suggests that the chosen value for porosity ε of 22 % ($\tau = 1.5$ [18]) is appropriate for the studied electrode.

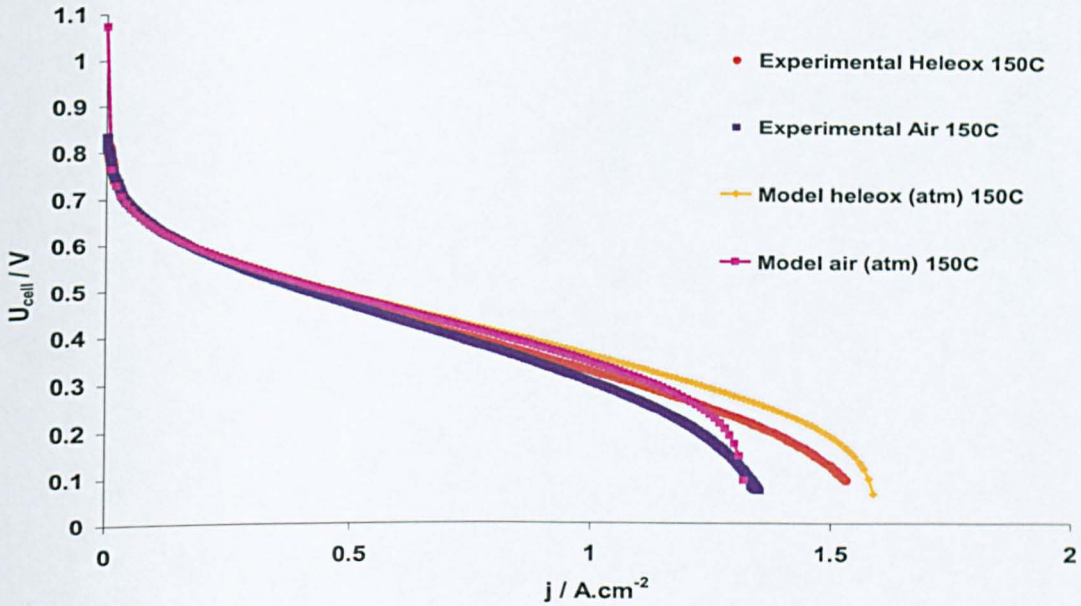

Figure 7-18. Comparison between modelled and experimental results for HT-PEMFC utilising 50% Pt/C at the cathode and 20% Pt/C on the anode at temperature of 150 °C using air and heleox mixture- alpha value of 0.75 was used for the cathode.

Figure 7-19 shows that when increasing the gamma value to 1.375, whilst maintaining the standard value of alpha (0.75), an improvement in the model fit with the experimental data is achieved. The model predictions followed the experimental data very closely even at high current densities and with different oxidant of air and heleox.

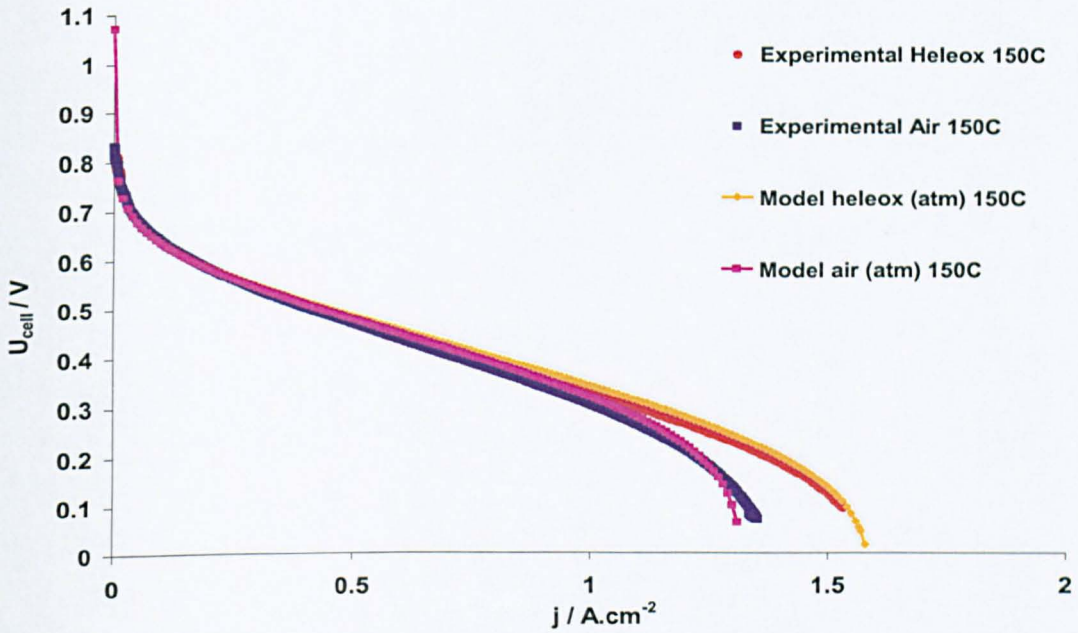

Figure 7-19. Comparison between modelled and experimental results for HT-PEMFC utilising 50% Pt/C at the cathode and 20% Pt/C on the anode at temperature of 150 °C using air and heleox mixture- alpha value of 0.75 & $\gamma = 1.375$ was used for the cathode.

7.9.4 Thin film and electrolyte distribution

As discussed earlier incorporation of the thin film in the model is essential to enhance the model ability to predict cell performance at high current densities and low oxygen concentrations. The thin film is responsible for the major contribution of the observed mass transport losses and without it no limiting current will be observed below 5 A cm^{-2} (Sec. 7.9.1).

The electrolyte content is a crucial parameter for optimising the three phase boundaries and therefore the electrode performance. Increasing the electrolyte content in the electrode will increase the accessible ESA and increase the film thickness whilst reducing the porosity. The electrolyte film thickness can be estimated using equation 41. Values of 50 &160 nm were obtained for the studied cathode & anode, respectively.

Figure 7-20 shows the effect of cathode film thickness on cell performance under air operation. Increasing the film thickness by factor of 2 and 4 led to a severe impact on cell performance even

at relatively small current densities, as a consequence the limiting current fell from 1.32 to 0.78 & 0.43 A cm^{-2}, respectively. This shows the crucial impact of electrolyte content on cathode and cell overall performance. Similarly, decreasing the film thickness enhanced the overall performance due to enhancement in mass transport and correspondingly an increase in the observed limiting current. These behaviours agreed with experimental observations (Chapter 4 and 6), where electrodes with the highest observed limiting current showed the best overall performance over the entire potential range.

While the above analysis assumed fixed ESA, conductivity and porosity, in practice there is a minimum film thickness below which the ESA will fall rapidly (conductivity also will fall, while porosity will increase).

Considering a case where the film thickness is maintained constant and the ESA is halved this corresponds to decrease in the acid content (volume fraction) in the cathode layer by half. Such a change led to dramatic fall in cell performance in both the kinetic (activation) and the mass transport regions of the polarisation curve; where the limiting current decreased from ~1.4 to 0.78 A cm^{-2}. On the other hand if the electrolyte content is increased (let say doubled) above the optimum content, where no further significant increase in ESA is achieved, then the overall performance will decrease due to mass transport effects caused by a doubling in the film thickness.

This behaviour agrees with the experimental finding of the importance of acid loading (content) in the cathode layer: excess acid (high doping case) led to severe mass transport limitations and heat treatment (low doping case) led to dramatic impact on both the kinetic and mass transport losses.

The effect of electrolyte material was also examined by changing the electrolyte in the cathode from phosphoric acid to PBI doped phosphoric acid (6 PRU) and would effectively correspond to change in the diffusion coefficient. The oxygen diffusion coefficient in phosphoric acid (98 %wt) 30 $\times 10^{-6}$ cm^2 s^{-1} is almost an order of magnitude higher than that of doped PBI (6 PRU) of 3.2×10^{-6} cm^2 s^{-1} at 150 °C, while oxygen solubilities are similar in both cases [23, 24]. Considering a case where the diffusion coefficient in the thin film was reduced by a factor of five, by changing the electrolyte to PBI/ H_3PO_4, while the film thickness, ESA and oxygen

solubility are maintained constant, the performance correspondingly dropped severely due to the large impact of mass transport on the limiting current; which fell from ~1.32 to 0.35 A cm^{-2}. This behaviour is in accord with experimental observations (Chapter 4) that PBI is not a suitable ionomer material for the catalyst layer, due to its low oxygen permeability, in comparison to H_3PO_4.

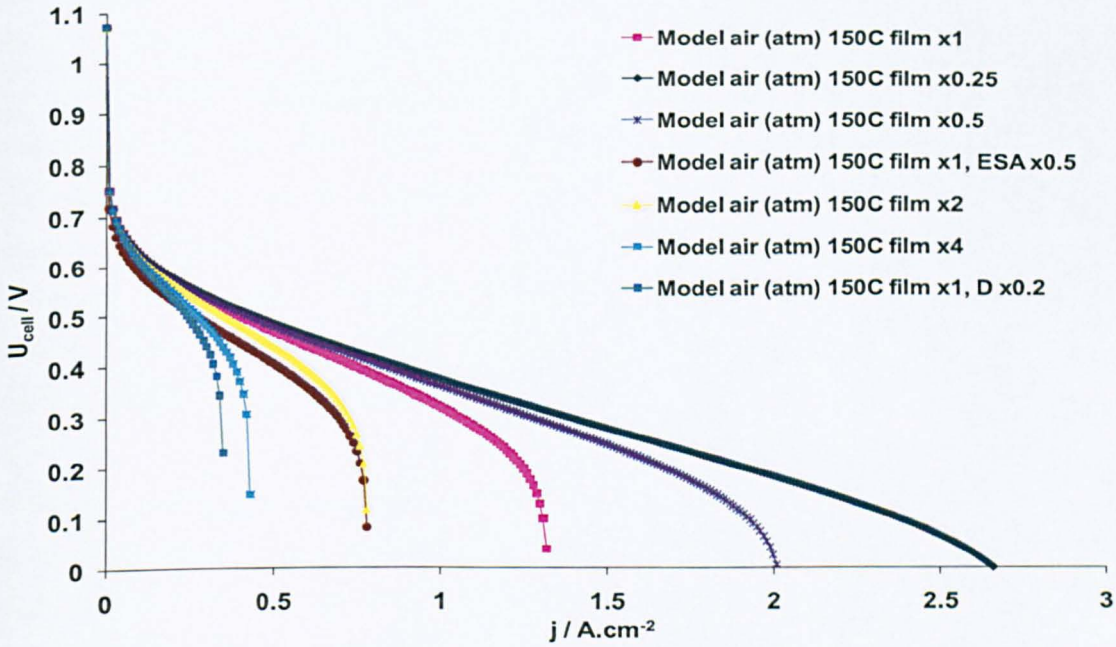

Figure 7-20. The effect of cathode film thickness and electrolyte type/content on cell performance utilising 50% Pt/C at the cathode and 20% Pt/C on the anode at temperature of 150 °C using air - alpha value of 0.75 & γ = 1.375 was used for the cathode.

The effect of anode ionomer content and film thickness on cell performance is shown in figure 7-21. A variation in anode film thickness had a less crucial effect on performance than that of the cathode film, even though the anode initial film thickness was ~3 times higher than that of the cathode: no limiting current was observed with oxygen operation (no mass transport limitation from the cathode) up to 2 A cm^{-2} (no experimental data is available beyond 2 A cm^{-2} due to instrument limitations). This was caused by the high hydrogen concentration in the anode feed (pure hydrogen) in comparison to air operation in the cathode. Even when the film thickness was increased by factor of 2, no difference in performance was observed (up to 2.1 A cm^{-2}) in the first instance and on increasing the thickness by 4 a limiting current of 2.1 A cm^{-2} was observed.

Similarly a small impact on cell performance was observed by reducing the electrolyte content by a factor of four, i.e. maintaining the film thickness and decreasing ESA by a factor of four. A small decrease in the performance was observed at very high current densities (>1.5 A cm^{-2}) and a limiting current of 2.1 A cm^{-2} was also visible.

By changing the electrolyte type in the anode electrode from phosphoric acid to PBI doped phosphoric acid (6 PRU) and thereby decreasing the diffusion coefficient in the thin film by a factor of five and maintaining the initial film thickness, ESA & hydrogen solubility, a considerable reduction in cell performance was observed at high current densities due to mass transport effects; where a limiting current was observed at ~1.6 A cm^{-2}: such limitation will not be visible when the system is operated with air (typical limiting current with air due to the cathode is 1.32 A cm^{-2}).

However, if the electrode film thickness was increased by 4, a major fall is observed in cell performance and a limiting current is observed at low current densities of ~ 0.4 A cm^{-2} with PBI based electrode, cf. PBI-free electrode which exhibited a limiting current of 2.1 A cm^{-2}.

Overall the model predictions agree closely with the experimental findings (Chapter 4): during anode catalyst layer optimisation, acid content was far less crucial than that of the cathode, the anode catalyst layer was able to handle more acid before considerable mass transport limitations became visible. Also a low PBI content in the anode catalyst layer (5% wt) did not show mass transport limitation up to the studied current density of 2 A cm^{-2}. However, a larger PBI content did lead to severe mass transport limitations and an observed limiting current (due to anode) at low current densities.

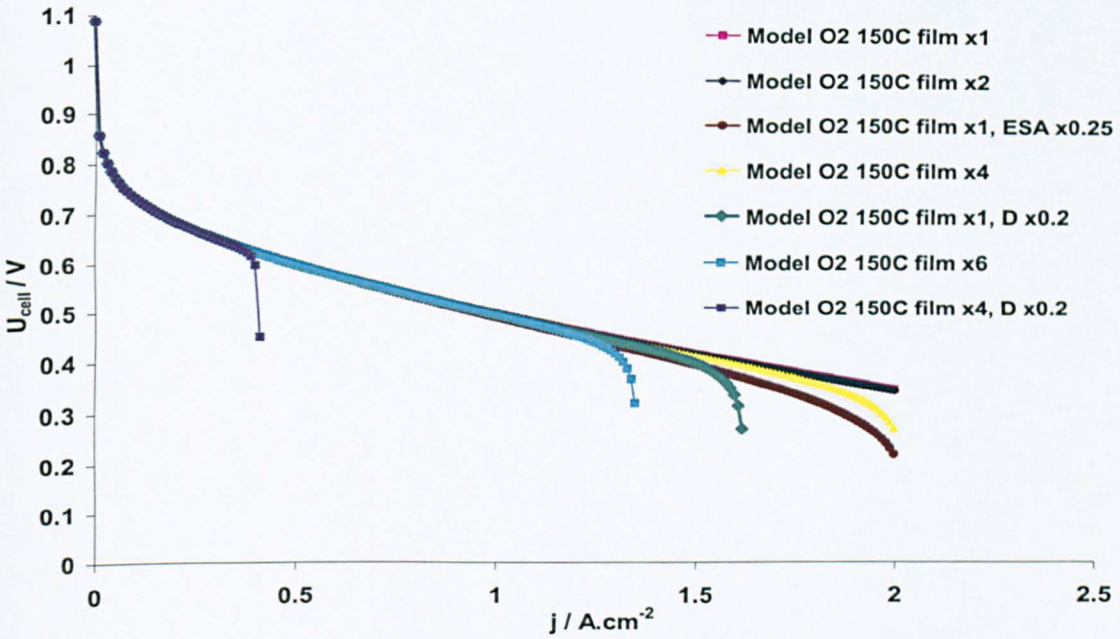

Figure 7-21. The effect of anode film thickness and electrolyte type/content on cell performance utilising 50% Pt/C at the cathode and 20% Pt/C on the anode at temperature of 150 °C using oxygen - alpha value of 0.75 & $\gamma = 1.375$ was used for the cathode.

7.10 Reformate operation

One of the major advantages of high temperature operation is the high CO tolerance and therefore the systems ability to operate with reformate gas feed without considerable losses in performance. Reformate gas composition varies depending on the hydrocarbon used in the reformation process. A typical diesel reformate composition, obtained from [59], contains 3% CH_4, 19% CO_2& 2.2% CO. Experiments earlier (Chapter four) have shown the high system tolerance to CO and CO_2 impurities in the hydrogen stream.

The model was expanded to account for the poisoning effect of CO and possibly methane on the catalyst surface. Model results were compared to experimental data on CO and CO_2 and was later used to estimate the cell performance with a diesel reformate feed.

CO poisoning effects on Pt in phosphoric acids system has been studied by several groups [41, 42, 60, 61]. There are two main effects of CO on anode performance; the first is a dilution effect already accounted for in the Butler-Volmer equation and the other is a kinetic effect arising from a reduction in active surface area because of CO adsorption on the Pt surface.

The rate determining step for hydrogen oxidation is the dissociation reaction (known as Volmer) giving rise to the second order dependency of hydrogen oxidation rate on surface coverage and Vogel et al [41] suggested the following equation:

$$i_0^{CO} = i_0\left(1-\theta_{CO}\right)^2 \qquad [69]$$

i_0^{CO} is the exchange current density for hydrogen oxidation after CO poisoning, i_0 is the exchange current density for hydrogen oxidation without CO presence, and θ_{CO} is the surface coverage by CO given by:

$$\theta_{CO} = 1 - \frac{Volume\ Hydrogen\ adsorbed\ after\ CO}{Volume\ Hydrogen\ adsorbed\ before\ CO} \qquad [71]$$

θ_{CO} is reported to vary linearly with $\ln(CO/H_2)$ [41, 42, 60], although various values for the constants of their relation dependency have been reported. Kohlmayr and Stonehart [61] suggested that CO coverage is independent of temperature, in the range from 100 to 150 °C in phosphoric acid media. Considering the heat of CO adsorption, it is expected that CO coverage should exhibit an exponential dependency on temperature. Dhar et al [60] suggested the following equation for the variation of CO coverage variation with temperature in H_3PO_4:

$$\theta_{CO} = 19.9\exp\left[-7.69\times10^{-3}T\right] - 0.085\ln\frac{[CO]}{[H_2]} \qquad [72]$$

In this work equation 72 was used to express CO coverage on a platinum surface and its variation with CO content, temperature and hydrogen content.

Figure 7-22 shows the variation in CO coverage on platinum surface at various temperatures and CO content in phosphoric acid taken from references [41, 42, 60, 61]. The data quoted from reference [60] are the values used in equation 72 and adopted in this work.

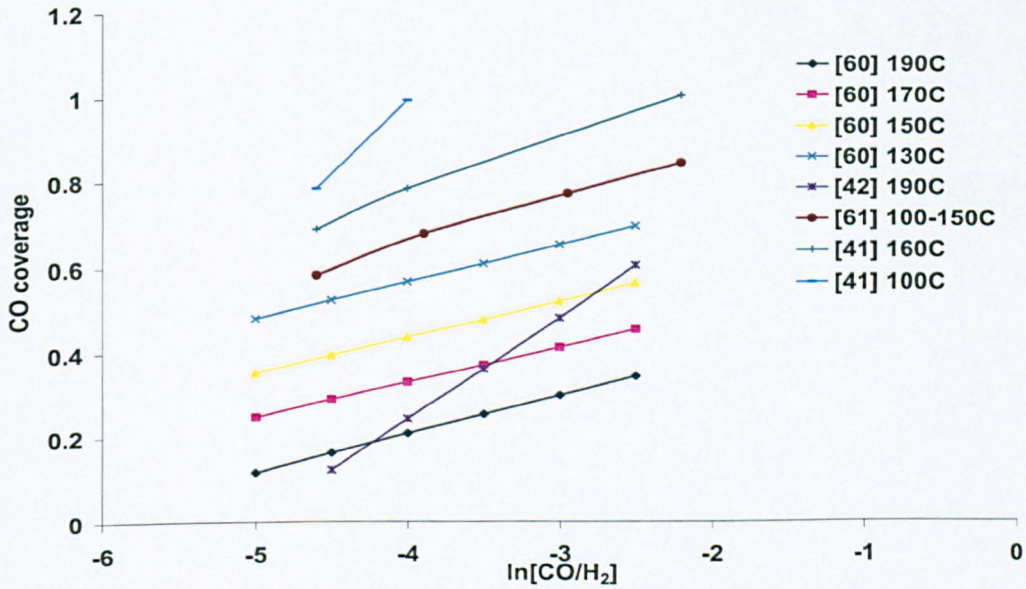

Figure 7-22. CO coverage on platinum surface from Ref [41, 42, 60, 61] in phosphoric acid.

In the case of carbon dioxide only its dilution effect was considered in the model; ignoring any effect of reduction of carbon dioxide to carbon monoxide by hydrogen at the studied temperature [62].

Under the circumstances of insufficient data on the effect of methane on the platinum surface in phosphoric acid, two cases were considered:

Case A: Sustersic et al [63] showed that methane adsorption on platinum surface started from a potential 0.2 V vs. NHE and reached a maximum adsorption peak at 0.25 V (vs. NHE). In HT-PEMFC the anode potential does not exceed 50 mV (even at high current densities of 1.5 A cm^{-2}) which is far below the minimum potential suggested for methane adsorption. Niedrach [64], found that methane had low adsorption on platinum (0.28 at STP) compared to that of other saturated hydrocarbons (moderate) except ethane, while unsaturated hydrocarbons exhibited very high adsorption; 0.79 (at STP) for propylene and 0.91 (at STP) for cyclopropane. This suggests

that consideration should be taken for non-saturated hydrocarbons in the reformate gas, and their concentration should be determined. (Case A)

Case B: Taylor and Brummer [65], studied methane adsorption in 12 M H_3PO_4 at 130 °C. Similarly, they found a maximum adsorption peak at 0.25 V vs. NHE, however, on the contrary, they observed methane adsorption at low potentials of 0.1 V and lower (vs. NHE) some 50% of that at 0.25 V. This suggests that methane adsorption might occur even at the low operating anode potentials.

Hsieh and Chen [66], studied methane oxidation on Pt in 1 M H_2SO_4. The rest potential was 100 mV vs. NHE, the exchange current density was 10^{-7} A cm^{-2} at 80 °C and 1 atm methane, and the activation energy was 125 kJ $mole^{-1}$. The activation energy was 3.5 larger than that of hydrogen oxidation and the exchange current density was six orders of magnitude lower than that of hydrogen oxidation. The rate of methane oxidation compared to hydrogen is negligible, so it can be treated as an inert species with only dilution/concentration effect (case A), or considering the worse case scenario as adsorption similar to that for CO (case B).

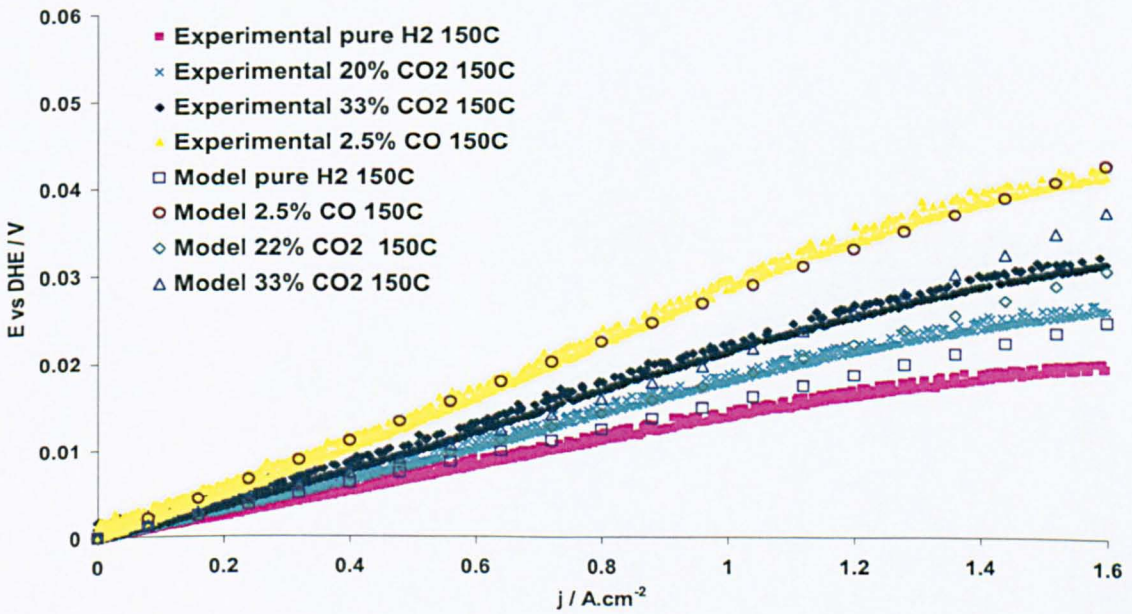

Figure 7-23. Experimental CO & CO_2 effects on anode performance at 150 °C with platinum (20% Pt/C) loading of 0.2 $mg_{Pt}.cm^{-2}$, compared to the model results.

7.10.1 Model Simulations for diesel reformate

A comparison between the model and experimental CO and CO_2 effects on the anode performance at 150 °C is shown in figure 7-23. The voltage drop at a current density of 1.5 A cm^{-2} was for both experimental and modelled data 8, 12 & 22 mV when switching from pure hydrogen to 20%, 33%vol CO_2 and 2.5%vol CO, respectively. This results in losses of power density of 12, 18 & 33 mW cm^{-2}, respectively. Very good agreement was observed (Fig. 7-23) between the experimental and the model data over the entire studied compositions. A small deviation was observed at high current densities where the experimental data approached a plateau (curve) whilst the model data continued in the expected, close to linear variation. This behaviour was also observed with pure hydrogen. Due to fast hydrogen oxidation kinetics and high hydrogen concentrations used, IR losses were the main contribution for anode losses at high current densities. Whilst no water flux through the membrane was considered in this model, the flux of gaseous water product from the cathode to the anode will occur at high current densities, driven by the large gradient in water content which in turn will cause the observed enhanced proton conductivity of the anode (anode feed -in this experimental case- had a very low humidity RH = 0.36% at 150 °C with humidifier temperature of ~16 °C). Water permeability of 1×10^{-14} to 3×10^{-14} cm^3(STP) m m^{-2} s^{-1} Pa^{-1} for phosphoric acid doped PBI membranes were reported [38] at elevated temperatures of 125-150 °C.

Figure 7-24 shows the simulated anode performance at 150 °C with various reformate compositions considering case A (concentration effect only for methane).
The following observations can be drawn:

- Methane has a worse dilution effect than CO_2, at the same concentration of 22%. An increase in anode potential in comparison to pure hydrogen of 11 mV was observed at 1.5 A cm^{-2} when using methane (a power density loss of 16.5 mW cm^{-2}) compared to that of 8 mV when using CO_2 (loss of 12 mW cm^{-2}).

- The addition of the separate dilution effect of inert species (CO_2, H_2O, etc..) with the poisoning and dilution effects of poisonous species (CO), does not add up to the simultaneous effects of a mixture of both species. This is explained by equations 70 &

72 [42, 60], where CO coverage is proportional to $\ln([CO]/[H_2])$, which means that any fall in hydrogen concentration, due to dilution by inert species, will lead to higher CO coverage at the same CO concentration and therefore enhance the poisoning effect.

- A 30 mV potential difference between pure hydrogen and the diesel reformate composition taken from [59] at a current density of 1.5 A cm^{-2} was obtained considering only the dilution effect for methane (case A); reflecting a fall in power density of 45 mW cm^{-2}.

- The potential difference between pure hydrogen and diesel reformate increases to 50 mV at the same current density, when adding 20% water to the gas stream (no information was available for water concentration in the reformate mixture). However, 20% water content should be reasonable for steam reforming case, which means a loss of 75 mW cm^{-2} in power density at 1.5 A cm^{-2}. Water dilution is significant as the hydrogen concentration falls from 75% to 55% leading to intensified CO poisoning effects, whilst initially increasing water concentration in the stream is thought to be beneficial in terms of proton conductivity enhancement. The maximum allowed water content in the gas steam should also be considered to avoid acid losses (wash-out) and corresponding losses of system overall conductivity. This was observed experimentally when operating HT-DMFC with a high water content gas feed (Chapter 5).

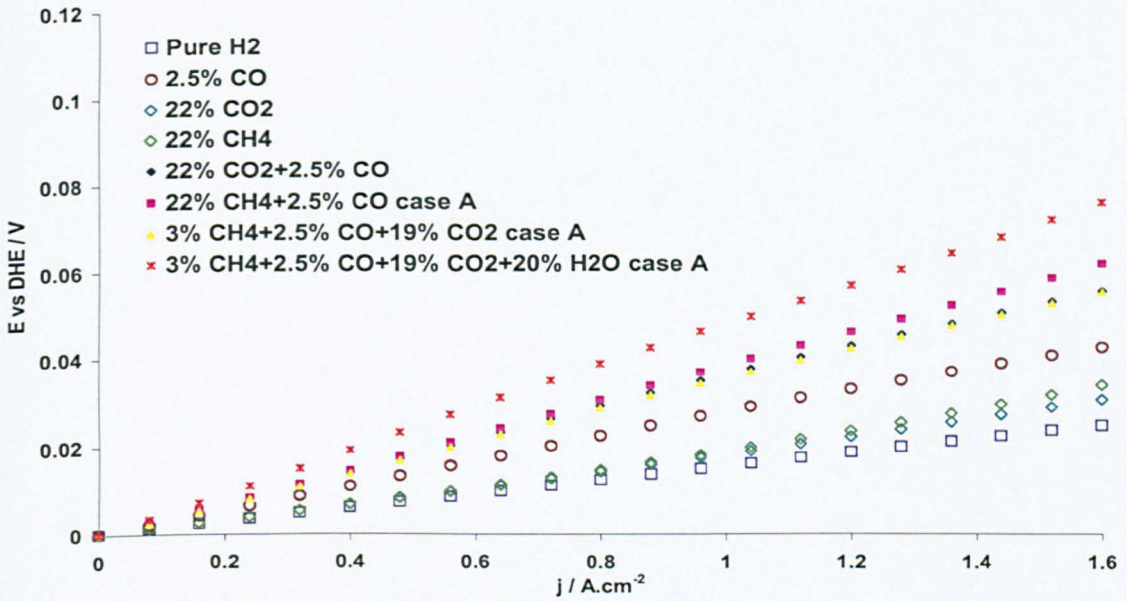

Figure 7-24. Modelled reformate composition effect on anode performance at 150 °C.

Figure 7-25 shows the modelling results for anode performance at 150 °C under various reformate compositions, considering case A & B simultaneously. The voltage loss compared to pure hydrogen increased from 30 to 35 mV when switching from case A to case B (methane treated similar to CO as poisoning species) with 5 % methane in the gas feed at 1.5 A cm^{-2}. The addition of 20 % water to the stream led to a voltage loss (compared to pure hydrogen) of 50 mV and 55 mV for case A and B, respectively. This means a power density loss of 75 to 82.5 mW cm^{-2}. Considering a system power density peak of 250-300 mW cm^{-2} when operating with air (atm), this would mean a loss of ca.30% of the generated power density.

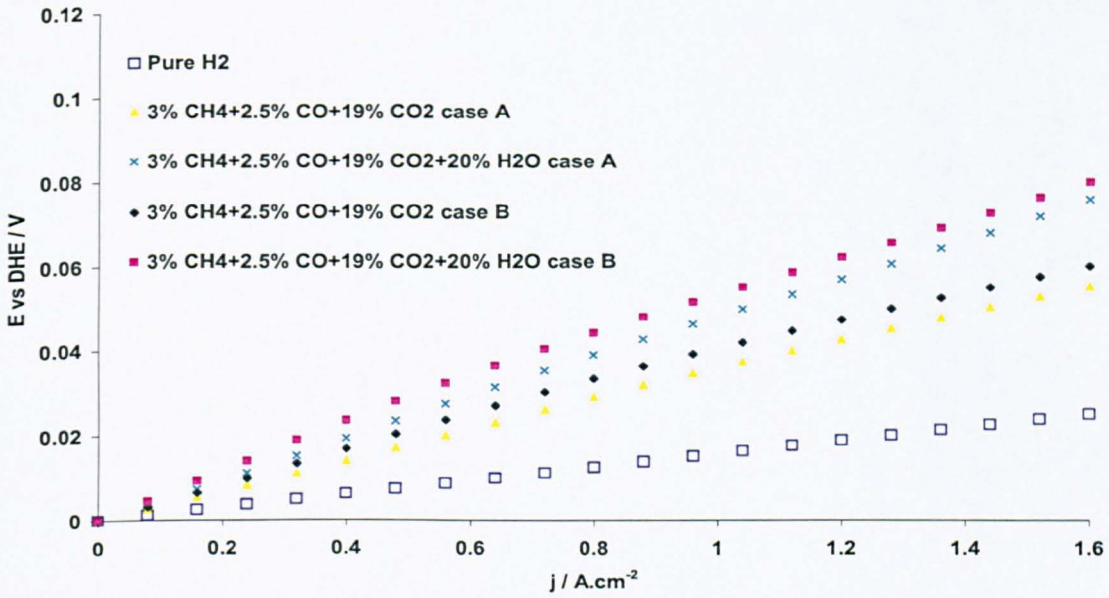

Figure 7-25. Effect of methane on anode potential modelled as inert species case A, and as poisoning species (CO) case B, with various reformate compositions at 150 °C.

7.11 Conclusions

A model of a high temperature fuel cell using PBI membranes has been developed using thermodynamics, transport and kinetic equations. The model considers mass transport through a thin film electrolyte as well as through the porous media. The incorporation of the thin film layer is crucial for model accuracy, particularly at high current densities and low oxygen concentrations (air).

Oxygen permeability through the thin electrolyte film varies for a given temperature depending on the equilibrium vapour pressure of the product water above the thin film and, correspondingly, the operating current density, due to variations in oxygen permeability with phosphoric acid concentration (electrolyte film).

The model showed very good agreement with experimental data under various operating conditions and oxygen concentrations. The model emphasises the importance and sensitivity of the electrolyte content on electrode performance; particularly on the cathode which was observed experimentally (Chapter 4).

Similarly, it was shown that the optimum content of electrolyte in the cathode is much lower than that in the anode and deviation from an optimum content has a severe impact on cathode performance, while electrolyte content at the anode has a less significant impact. This is caused by the higher hydrogen concentration in the anode feed compared to the air operating cathode, combined with a faster diffusion of hydrogen, compared to oxygen, in the thin film. These conclusions were also supported experimentally during electrode optimisation (Chapter 4).

The model is a good tool for optimisation of the electrode performance and the understanding of reasons behind performance limitations. For example, the model showed that acid doped PBI is not suitable as ionomer for the cathode catalyst layer, and that pristine phosphoric acid is preferred. Similarly, the anode can tolerate small quantities (loading) of PBI, however, excess PBI will lead to severe mass transport limitations.

The model was also used to predict cell performance under reformate operation. Good agreement was observed between the available experimental data on CO and CO_2 effects on the anode and model predications. A small content of poisoning species can be tolerated by the system due to the higher temperature operation. However, the dilution effect of inert species (CO_2, H_2O, etc.) when added to the gas stream will greatly intensify poisoning due to lower hydrogen concentration, and thus higher CO coverage at the same CO concentration.

The maximum allowed water content in the gas steam should be considered to avoid the dilution effect on hydrogen and corresponding poisoning effects. Possible acid losses (wash-out) and corresponding losses of the overall system conductivity might also occur. Reformate gas should ideally be cooled to temperatures below 100 °C (60-80 °C) to condense excess water and maintain only a small fraction of water beneficial for system conductivity.

7.12 References

1. Bernardi, D.M. and M.W. Verbugge, *A Mathematical Model of the Solid-Polymer-Electrolyte Fuel Cell.* J. Electrochem. Soc., 1992. **139**: p. 2477-249.
2. Mennola, T., M. Noponen, M. Aronniemi, T. Hottinen, M. Mikkola, O. Himanen, and P. Lund, *Mass transport in the cathode of a free-breathing polymer electrolyte membrane fuel cell* J. Appl. Electrochem., 2003. **33**: p. 979-987.
3. Hottinen, T., M. Noponen, T. Mennola, O. Himanen, M. Mikkola, and P. Lund, *Effect of ambient conditions on performance and current distribution of a polymer electrolyte membrane fuel cell* Journal of Applied Electrochemistry 2003. **33**: p. 265-271.
4. Guvelioglu, G.H. and H.G. Stenger, *Computational fluid dynamics modeling of polymer electrolyte membrane fuel cells.* Journal of Power Sources, 2005. **147**(1-2): p. 95-106.
5. Sun, Y.P. and K. Scott, *The Influence of Mass Transfer on a Porous Fuel Cell Electrode.* Fuel Cells, 2004. **4**: p. 30-38.
6. Mazumder, S. and J.V. Cole, *Rigorous 3-D Mathematical Modeling of PEM Fuel Cells, Part I. Model Predictions without Liquid Water Transport* J. Electrochem. Soc., 2003. **150**: p. A1503-A1509 .
7. Amphlett, J.C., R.M. Baumert, R.F. Mann, B.A. Peppley, P.R. Roberge, and T.J. Harris, *Performance Modeling of the Ballard Mark IV Solid Polymer Electrolyte Fuel Cell.* J. Electrochem. Soc., 1995. **142**: p. 1-8.
8. Noponen, M., E. Birgersson, J. Ihonen, M. Vynnycky, A. Lundblad, and G. Lindbergh, *A Two-Phase Non-Isothermal PEFC Model: Theory and Validation.* Fuel Cells, 2004. **4**: p. 365-377.
9. Birgersson, E., M. Noponen, and M. Vynnycky, *Analysis of a Two-Phase Non-Isothermal Model for a PEFC.* J. Electrochem. Soc., 2005. **152**: p. A1021-A1034.
10. Mazumder, S. and J.V. Cole, *Rigorous 3-D Mathematical Modeling of PEM Fuel Cells, Part II. Model Predictions with Liquid Water Transport* J. Electrochem. Soc., 2003. **150**: p. A1510-A1517.
11. Argyropoulos, P., K. Scott, and W.M. Taama, *One-dimensional thermal model for direct methanol fuel cell stacks: Part I. Model development.* Journal of Power Sources, 1999. **79**(2): p. 169-183.
12. Rao, R.M., D. Bhattacharyya, R. Rengaswamy, and S.R. Choudhury, *A two-dimensional steady state model including the effect of liquid water for a PEM fuel cell cathode.* Journal of Power Sources, 2007. **173**(1): p. 375-393.
13. Hu, M., X. Zhu, M. Wang, A. Gu, and L. Yu, *Three dimensional, two phase flow mathematical model for PEM fuel cell: Part II. Analysis and discussion of the internal transport mechanisms.* Energy Conversion and Management, 2004. **45**(11-12): p. 1883-1916.
14. Hu, M., A. Gu, M. Wang, X. Zhu, and L. Yu, *Three dimensional, two phase flow mathematical model for PEM fuel cell: Part I. Model development.* Energy Conversion and Management, 2004. **45**(11-12): p. 1861-1882.
15. Cheddie, D. and N. Munroe, *Parametric model of an intermediate temperature PEMFC.* Journal of Power Sources, 2006. **156**(2): p. 414-423.
16. Cheddie, D. and N. Munroe, *Mathematical model of a PEMFC using a PBI membrane.* Energy Conversion and Management, 2006. **47**(11-12): p. 1490-1504.

17. Cheddie, D.F. and N.D.H. Munroe, *Three dimensional modeling of high temperature PEM fuel cells.* Journal of Power Sources, 2006. **160**(1): p. 215-223.
18. Scott, K., S. Pilditch, and M. Mamlouk, *Modelling and experimental validation of a high temperature polymer electrolyte fuel cell.* Journal of Applied Electrochemistry, 2007. **37**: p. 1245-1259.
19. Hu, J., H. Zhang, J. Hu, Y. Zhai, and B. Yi, *Two dimensional modeling study of PBI/H3PO4 high temperature PEMFCs based on electrochemical methods.* Journal of Power Sources, 2006. **160**(2): p. 1026-1034.
20. Hu, J., H. Zhang, Y. Zhai, G. Liu, J. Hu, and B. Yi, *Performance degradation studies on PBI/H3PO4 high temperature PEMFC and one-dimensional numerical analysis.* Electrochimica Acta, 2006. **52**(2): p. 394-401.
21. Cutlip, M.B., S.C. Yang, and P. Stonehart, *Simulation and optimization of porous gas-diffusion electrodes used in hydrogen oxygen phosphoric acid fuel cells--II development of a detailed anode model.* Electrochimica Acta, 1991. **36**(3-4): p. 547-553.
22. Yang, S.C., M.B. Cutlip, and P. Stonehart, *Simulation and optimization of porous gas-diffusion electrodes used in hydrogen/oxygen phosphoric acid fuel cells--I. Application of cathode model simulation and optimization to PAFC cathode development.* Electrochimica Acta, 1990. **35**(5): p. 869-878.
23. Liu, Z.Y., J.S. Wainright, M.H. Litt, and R.F. Savinell, *Study of the oxygen reduction reaction (ORR) at Pt interfaced with phosphoric acid doped polybenzimidazole at elevated temperature and low relative humidity.* Electrochimica Acta, 2006. **51**(19): p. 3914-3923.
24. Liu, Z.Y., J.S. Wainright, and R.F. Savinell, *High-temperature polymer electrolytes for PEM fuel cells: study of the oxygen reduction reaction (ORR) at a Pt-polymer electrolyte interface.* Chemical Engineering Science, 2004. **59**(22-23): p. 4833-4838.
25. Appleby, A.J., *Evolution and reduction of oxygen on oxidized platinum in 85% orthophosphoric acid.* J. Electroanal. Chem. Interfacial Electrochem., 1970. **24**: p. 97.
26. Huang, J.C., R.K. Sen, and E. Yeager, *Oxygen Reduction on Platinum in 85% Orthophosphoric Acid.* J. Electrochem. Soc., 1979. **126**(5): p. 786-792.
27. Clouser, S.J., J.C. Huang, and E. Yeager, *Temperature dependance of the Tafel slope for oxygen reduction on platinum in concentrated phosphoric acid.* Journal of Applied Electrochemistry, 1993. **23**: p. 597-605.
28. Appleby, A.J., *Oxygen Reduction on Oxide-Free Platinum in 85% Orthophosphoric Acid: Temperature and Impurity Dependence.* J. Electrochem. Soc., 1970. **117**(3): p. 328-335.
29. Sugishima, N., J.T. Hinatsu, and F.R. Foulkes, *Phosphorous Acid Impurities in Phosphoric Acid Fuel Cell Electrolytes II. Effects on the Oxygen Reduction Reaction at Platinum Electrodes.* J. Electrochem. Soc., 1994 **141**(12): p. 3332-3335.
30. McBreen, J., W.E. O'Grady, and R. Richter, *A Rotating Disk Electrode Apparatus for the Study of Fuel Cell Reactions at Elevated Temperatures and Pressures.* J. Electrochem. Soc., 1984. **131**(5): p. 1215-1216.
31. Scharifker, B.R., P. Zelenay, and J.O.M. Bockris, *The Kinetics of Oxygen Reduction in Molten Phosphoric Acid at High Temperatures.* J. Electrochem. Soc., 1987. **134**: p. 2714-2725.

32. Korsgaard, A.R., R. Refshauge, M.P. Nielsen, M. Bang, and S.K. Kaer, *Experimental characterization and modeling of commercial polybenzimidazole-based MEA performance.* Journal of Power Sources, 2006. **162**(1): p. 239-245.
33. O'Grady, W.E., E.J. Taylor, and S. Srinivasan, *Electroreduction of Oxygen on Reduced Platinum in 85% Phosphoric acid.* J. Electroanal. Chem., 1982. **132**: p. 137-150.
34. HAMPSON, N.A. and A.J.S. McNEIL, *The Electrochemistry of Porous Electrodes: Flooded, Static (Natural) Electrodes*, in *Electrochemistry.* , D. Pletcher, Editor. 1983, Royal Society of Chemistry (RSC). London. p. 1-53.
35. *Recommended Reference Materials for the Realization of Physicochemical Properties*, ed. K.N. Marsh. 1987, Oxford: Blackwell.
36. Kenneth, W., *Advanced thermodynamics for engineers* . McGraw-Hill series in mechanical engineering ed. J.K. Wark. 1995, New York McGraw-Hill.
37. Yaws, C.L., *Yaws' Handbook of Thermodynamic and Physical Properties of Chemical Compounds.* http://www.knovel.com/knovel2/Toc.jsp?BookID=667&VerticalID=0. 2003: Knovel.
38. Weng, D., J.S. Wainright, U. Landau, and R.F. Savinell, *Electro-osmotic drag coefficient of water and methanol in polymer electrolytes at elevated temperatures.* Journal of the Electrochemical Society, 1996. **143**(4): p. 1260-1263.
39. *Smith son Ian steam tables.* 2006, Knovel (www.knovel.com).
40. Slattery, J.C. and R.B. Bird, *Calculation of the Diffusion Coefficient of Dilute Gases and of the Self-diffusion Coefficient of Dense Gases.* J. A.I.Ch.E, 1958. 4(2): p. 137-142.
41. Vogel, W., L. Lundquist, P. Ross, and P. Stonehart, *Reaction pathways and poisons--II : The rate controlling step for electrochemical oxidation of hydrogen on Pt in acid and poisoning of the reaction by CO.* Electrochimica Acta, 1975. **20**(1): p. 79-93.
42. Dhar, H.P., L.G. Christner, A.K. Kush, and H.C. Maru, *Performance Study of a Fuel Cell Pt-on-C Anode in Presence of CO and CO_2, and Calculation of Adsorption Parameters for CO Poisoning.* J. Electrochem. Soc., 1986. **133**(8): p. 1574-1582.
43. Klinedinst, K., J.A.S. Bett, J. MacDonald, and P. Stonehart, *Oxygen solubility and diffusivity in hot concentrated H_3PO_4.* J. Electroanalytical Chemistry and Interfacial Electrochemistry, 1974. **57**: p. 281-289.
44. Enayetullah, M.A., T.D. DeVilbiss, and J.O.M. Bockris, *Activation Parameters for Oxygen Reduction Kinetics in Trifluoromethane Sulfonic Acid Systems.* J. Electrochem. Soc. , 1989. **136**(11): p. 3369-3376.
45. Zelenay, O.P., B.R. Scharifker, J.O.M. Bockris, and D. Gervasio, *A Comparison of the Properties of CF_3SO_3H and H_3PO_4 in Relation to Fuel Cells.* J. Electrochem. Soc., 1986. **133**(11): p. 2262-2267.
46. Razaq, M., A. Razaq, E. Yeager, D.D. Desmarteau, and S. Singh, *Oxygen electroreduction in perfluorinated sulphonyl imides.* Journal of Applied Electrochemistry, 1987. **17**(5): p. 1057-1064.
47. MacDonald, D.I. and J.R. Boyack, *Density, Electrical Conductivity, and Vapor Pressure of Concentrated Phosphoric acid.* Journal of Chemical and Engineering Data, 1969. **14**(3): p. 380.
48. Appleby, A.J., *Oxygen Reduction on Active Platinum in 85% Orthophosphoric Acid.* J. Electrochem. Soc., 1970. **117**(5): p. 641-645.
49. Bockris, J.O.M. and A. Gochev, *Temperature dependence of the symmetry factor in electrode kinetics.* Journal of Electroanalytical Chemistry, 1986. **214**(1-2): p. 655-674.

50. E-TEK. *PRODUCT TECHNICAL INFORMATION* 2003 [cited; Available from: http://www.etek-inc.com/standard/product_NMC.php?prodid=59.
51. Barbir, F., *PEM Fuel Cells: Theory and Practice (Sustainable World Series)*. 2005: Elsevier Academic Press.
52. Kunz, H.R. and G.A. Gruver, *The Catalytic Activity of Platinum Supported on Carbon for Electrochemical Oxygen Reduction in Phosphoric Acid.* J. Electrochem. Soc., 1975. **122**(10): p. 1279-1287.
53. Souquet, J.-L., M. Duclot, and M. Levy, *Salt-polymer complexes: strong or weak electrolytes?* Solid State Ionics, 1996. **85**(1-4): p. 149-157.
54. Ma, Y.L., *The Fundamental Studies of Polybenzimidazole/Phosphoric Acid Polymer Electrolyte For Fuel Cells*. 2004, CASE WESTERN RESERVE UNIVERSITY.
55. Bouchet, R. and E. Siebert, *Proton conduction in acid doped polybenzimidazole.* Solid State Ionics, 1999. **118**(3-4): p. 287-299.
56. Bouchet, R., S. Miller, M. Duclot, and J.L. Souquet, *A thermodynamic approach to proton conductivity in acid-doped polybenzimidazole.* Solid State Ionics, 2001. **145**(1-4): p. 69-78.
57. Ma, Y.L., J.S. Wainright, M.H. Litt, and R.F. Savinell, *Conductivity of PBI membranes for high-temperature polymer electrolyte fuel cells.* Journal of the Electrochemical Society, 2004. **151**(1): p. A8-A16.
58. Angerstein-Kozlowska, H., B.E. Conway, B. Barnett, and J. Mozota, *The role of ion adsorption in surface oxide formation and reduction at noble metals: General features of the surface process.* Journal of Electroanalytical Chemistry, 1979. **100**(1-2): p. 417-446.
59. Hygear-The-Netherlands, *FURIM 30M interim report.* 2006, Further improvements and integration of high temperature PEM. www.furim.com.
60. Dhar, H.P., L.G. Christner, and A.K. Kush, *Nature of CO Adsorption during H2 Oxidation in Relation to Modeling for CO Poisoning of a Fuel Cell Anode* J. Electrochem. Soc., 1987. **134**(12): p. 3021-3026.
61. Kohlmayr, G. and P. Stonehart, *Adsorption kinetics for carbon monoxide on platinum in hot phosphoric acid.* Electrochimica Acta, 1973. **18**(2): p. 211-223.
62. Li, Q.F., R.H. He, J.A. Gao, J.O. Jensen, and N.J. Bjerrum, *The CO poisoning effect in PEMFCs operational at temperatures up to 200 degrees C.* Journal of the Electrochemical Society, 2003. **150**(12): p. A1599-A1605.
63. M. G. Sustersic, R. Cordova, W. E. Triaca, and A.J. Arvla, *The Electrosorption of Methane and Its Potentiodynamic Electrooxidation on Platinized Platinum.* J. Electrochem. Soc., 1980. **127**(6): p. 1242-1248.
64. Niedrach, L.W., *Galvanostatic and Volumetric Studies of Hydrocarbons Adsorbed on Fuel Cell Anodes.* J. Electrochem. Soc., 1964. **111**(12): p. 1309-1317.
65. Taylor, A.H. and S.B. Brummer, *The Adsorption and Oxidation of Hydrocarbons on Noble Metal Electrodes. VII. Oxidative Adsorption of Methane on Platinum Electrodes'.* J. Physical Chemistry, 1968. **72**: p. 2856-2862.
66. Hsieh, S.Y. and K.M. Chen, *Anodic Oxidation of Methane.* J. Electrochem. Soc. , 1977. **124**(8): p. 1171-1174.

8 Summary, Conclusions and Future Work

8.1 Summary and conclusion

Proton exchange membrane fuel cells (PEMFC) are currently based on Nafion® or similar membranes and operate at low temperatures of less than 80 °C. The main challenges for technology development are: (i) high materials cost (noble metal catalysts, polymer membrane, etc) (ii) complex system construction and operation with respect to water and thermal management; (iii) fuel supply, i.e. on-board storage and re-fuelling of hydrogen or reformer-purification units for hydrocarbons/alcohols (iv) low value of heat energy, low overall efficiency (~30 %) and limited co-generation of heat and power for stationary applications.

Sulfonated poly ether ether ketone (SPEEK) showed even a higher dependency on humidity in its conductivity than Nafion; the conductivity values were dependant on the sulfonation degree. For sulfonation degrees of 70 % and above, SPEEK become partially soluble in water and fully soluble in MEOH. At a sulfonation degree of 60 % the conductivity was one order of magnitude lower than that of PBI, even at high humidity (RH ~100%). Overall this makes SPEEK an unsuitable candidate for high temperature operation.

Phosphoric acid doped PBI offers good proton conductivity extending over a wide range of operating temperature up to 200 °C. This conductivity depends on relative humidity, temperature and acid doping level. For a doping level of 5.6 M H_3PO_4 per repeat PBI unit and low relative humidity (1-10%), the measured PBI conductivity varied between 0.02 to 0.06 S cm^{-1} at temperatures between 120 to 175 °C. Increased operating temperature above 175 °C and low relative humidity did not add significantly to the conductivity due to dimerisation of the phosphoric acid. PBI's conductivity improves with increasing humidity; however, this dependence is much smaller than that of Nafion, and becomes more significant at high temperatures. These characteristics make PBI the best choice membrane for anhydrous operation above 100 °C.

For oxygen reduction at platinum supported carbon in phosphoric acid doped PBI, the catalyst layer structure and composition play an important role in electrode performance. The acid doping

level in the catalyst layer affects the oxygen permeability; with a doping level of 6 PRU exhibiting the best oxygen permeability, of those studied. However an optimum doping level might lie in the range between 3 and 6 PRU which was not investigated. The optimum doping level depended on temperature and oxygen partial pressure, as both affect the permeability.

The kinetics of oxygen reduction in PBI doped phosphoric acid are similar to those of phosphoric acid at high doping levels. Doping level affected the activation energy of the reaction, transfer coefficient and exchange current density. Increased doping level increased the exchange current density although decreased α values. The transfer coefficient (α) for the ORR; depended on temperature. The dependency is explained by adsorption of impurities and thermodynamic effects. The influence of doping level on electrode kinetics depended on temperature and oxygen partial pressure and a compromise between exchange current density and transfer coefficient was realised. A high doping level was favourable at low temperatures, high oxygen concentrations or low operating overvoltages whilst low doping was favourable at high temperatures, low oxygen concentrations or high operating overvoltages.

Pristine PBI exhibits low hydrogen & oxygen permeability and therefore is a good candidate for the membrane material. This however makes PBI a less attractive candidate for ionomer material in the catalyst layer. PBI relies on phosphoric acid to provide its conductivity and oxygen permeability; in a similar manner to Nafion reliance on water; to provide its conductivity and oxygen permeability. Alternative structures based on PTFE and H_3PO_4 show advantages over PBI based electrodes due to higher oxygen permeability.

There was an optimum thickness for the catalyst layer that provided a balance between acid content in the catalyst layer (added or mobile from the membrane) and oxygen permeability from the flow channel. This optimum thickness was achieved using 40% to 50% Pt/C catalyst and it depended on the operating temperature and oxygen partial pressure. Lower oxygen concentrations required a thinner catalyst layer or higher Pt:C ratio. Electrodes fabricated from 60% Pt/C (thin catalyst layer) showed limited performance due to flooding from mobile H_3PO_4 acid from the membrane.

Pt binary alloys and particularly Pt-Co/C showed advantages over non-alloyed platinum as cathode catalysts, allowing lower platinum loading at the cathode of 0.2 mg_{Pt} cm^{-2}. However, such enhancement was subject to the operating temperature or more precisely the water activity. With high water content, Pt alloys suppress the initiation and extent of surface oxide formation on platinum surface and therefore offer enhanced oxygen adsorption. The fall in water activity at elevated temperatures (above 150 °C) resulted in an increase in ORR activity for Pt/C, due to a lowering of surface oxide formation; a corresponding effect with Pt alloys does not occur.

A vapour feed HT- DMFC was demonstrated with reasonable performance and high open circuit potential arising from low cross-over (permeability) of methanol through the membrane and high CO tolerance at the cathode at elevated temperatures. The cell suffered from high anode polarisation which resulted in significantly lower performance than that achievable with low temperature cells using Nafion as the membrane. In addition, acid wash out and therefore conductivity loss was a major limitation for HT-DMFC based on phosphoric acid doped PBI. Another major factor is the very poor methanol oxidation kinetics in a phosphoric acid environment. An improvement in performance may be possible by using a higher methanol concentration to enhance methanol oxidation, which may offset the detrimental effect of increased methanol crossover. In terms of methanol cross-over, PBI was an excellent barrier for methanol with permeability one order of magnitude lower than SPEEK and two orders of magnitude lower than Nafion.

Chronoamperometry measurements were performed in an attempt to obtain mass transport information for the studied electrodes. The current transient varied exponentially with time, with a time constant depending on L^2/D for finite length (L) diffusion. The transient time constant did not vary with oxygen partial pressure, and decreased with increased temperature as expected. However, there was a larger decrease in the time constant from temperatures of 120 to 150 °C in comparison to that from 150 to 175 °C. This was caused by phosphoric acid dehydration and consequently increased viscosity slowing down the solubility equilibrium and oxygen diffusion.

Whilst a temperature increase will lead to a decrease in oxygen solubility, it will also lead to an increase in diffusion. However the rate of increase in diffusion will fall as temperature increases due to dehydration and increase in viscosity. The solubility and diffusion at a given temperature also depends on water activity or in other words phosphoric acid concentration. Therefore, the product (D.C) can either increase, decrease or exhibit a maximum value with an increase in temperature.

The decrease in solubility with temperature counteracts the effect on the increase in kinetics with temperature; where both processes vary exponentially with temperature (heat of solution and activation energy). This was reflected by no observed increase in kinetics for PBI-free electrodes above 150 °C, and a slow enhancement in PBI based electrodes. In other words, at 150 °C fast oxygen diffusion in phosphoric acid (liquid) in comparison to PBI/H_3PO_4 (gel) gave rise to enhanced performance (solubility values are similar), whilst at 175 °C this enhancement was suppressed by a lower solubility and slower increase in diffusion due to increased viscosity of phosphoric acid caused by dehydration; effecting mainly PBI free electrodes.

Frequency response analysis was used to compare electrode performance in terms of kinetics, ohmic and mass transport losses. Simple equivalent circuit were used to fit the observed spectra. For polarisable electrodes under small to medium steady-state current operation, the model was capable of identifying electrodes with the best kinetic or mass transport behaviour and classifying behaviour in terms of relative performance. However, care must be taken in interoperating the spectra results at open circuit potentials or high steady-state currents. OCP is affected by cross-over rate and thermodynamic oxygen concentration effects (Nernst equation) and therefore will lead to smaller apparent charge transfer resistance. At high current densities the effect of the equivalent resistance, used to polarise the electrode to the desired steady-state current, dominates the observed impedance spectra and mask any useful information about electrode performance.

A model of a high temperature fuel cell using PBI membranes has been developed using thermodynamics, transport and kinetic equations. The model considers mass transport through a thin film electrolyte as well as through the porous media. The incorporation of the thin film layer

is crucial for model accuracy; particularly at high current densities and low oxygen concentrations (air). Oxygen permeability through the thin electrolyte film varies for a given temperature depending on the equilibrium vapour pressure of the product water above the thin film and, correspondingly, the operating current density, due to variations in oxygen permeability with phosphoric acid concentration (electrolyte film).

The model showed very good agreement with experimental data under various operating conditions and oxygen concentrations. The model emphasises the importance and sensitivity of the electrolyte content on electrode performance; particularly on the cathode; which was also observed experimentally. The model is a useful tool for optimisation of the electrode performance and helps in understanding the reasons behind performance limitations. For example, the model showed that acid doped PBI is not suitable as ionomer for the cathode catalyst layer, and that pristine phosphoric acid is preferred.

The model was also used to predict cell performance under reformate operation. Good agreement was observed between the available experimental data on CO and CO_2 effects on the anode and model predications. A small amount of poisoning species can be tolerated by the system due to the higher temperature operation. However, the dilution effect of inert species (CO_2, H_2O, etc.) when added to the gas stream will greatly intensify poisoning due to lower hydrogen concentration, and thus higher CO coverage at the same CO concentration.

The maximum allowed water content in the gas steam should be considered to avoid the dilution effect on hydrogen and corresponding poisoning effects. Possible acid losses (wash-out) and corresponding losses of the overall system conductivity might also occur. Reformate gas should ideally be cooled to temperatures below 100 °C (60-80 °C) to condense excess water and maintain only a small fraction of water that is beneficial for system conductivity.

8.2 Future work

The limited oxygen permeability and slow oxygen reduction kinetics in phosphoric acid (phosphates and impurities within adsorbs on platinum) is a major limitation for the performance of PBI based PEMFC electrodes. PBI is still an attractive material due to its relatively low cost ($70-100/lb), excellent oxidative and thermal stability, good mechanical flexibility at elevated temperature and basic properties (pK_a = 5.5). PBI basic properties allow it to be easily doped with strong acids to form single phase polymer electrolyte [1, 2]. Future work should consider alternative acid dopants (at least for electrodes ionomer) for PBI that provide better permeabilities and smaller adsorption on platinum. Fluorinated acids are one of the best candidates for these dopants, several suggestion are given below:

- Trifluoromethane sulfonic acid (TFMSA): measurements showed that TFMSA conductivity and proton activity is 100 times higher than that of phosphoric acid at the same temperature and concentration [3]. Its adsorption on platinum surface is much lower than phosphoric acid [4], and both oxygen solubility and diffusion is an order of magnitude higher than that in phosphoric acid under the same conditions [5].
  The only limitation of TFMSA is its low vapour pressure (boiling point of 162 °C). However, at low doping levels (two moles acid per mole PBI) no free acid will be present and such limitation will not be seen. The low doping level impact on conductivity will also be minimal due to the high conductivity of TFMSA.

- Perfluronated -organo sulfonic/phosphonic acids: Saffarian et al [6] observed an order of magnitude faster oxygen reduction rate in Bis(trifluoromethylsulfonyl)-Methane ($(CF_3SO_2)_2CH_2$) than that in phosphoric acid at similar conditions. However, $(CF_3SO_2)_2CH_2$ has a limited solubility of 1.15 M in water which restricts its use to low temperatures. Such a limitation could be overcome by forming acid-base complex (doping) with PBI. Burton et al [7, 8] also showed encouraging results for oxygen reduction in tetrafluoroethylene-1,2-bisphosphonic acid at 200 °C in comparison to phosphoric acid where he obtained a mass activity of 61 mA mg_{Pt}^{-1} at 0.7 V for the perfluronated-organo-phosphonic acid in comparison to 55 mA mg_{Pt}^{-1} for phosphoric acid.

The alternative dopants can also show enhancement for PBI based HT-DMFCs, in terms of improved methanol oxidation and lower acid wash-out rates (lower solubility in water).

The rate of improvements can be estimated using the built model by setting the appropriate parameters for the new electrolytes conductivity, volume fraction, oxygen solubility, exchange current density, etc .The model can be further developed by considering a one or two dimensional catalyst layer (instead of 0D macro-homogeneous model) in order to provide clearer current and oxygen concentration profiles in the catalyst layer. Further improvements include incorporation of water and hydrogen cross-over and non-isothermal operation.

8.3 References

1. Wang, J.T., R.F. Savinell, J. Wainright, M. Litt, and H. Yu, *A H-2/O-2 fuel cell using acid doped polybenzimidazole as polymer electrolyte.* Electrochimica Acta, 1996. **41**(2): p. 193-197.
2. Fontanella, J.J., M.C. Wintersgill, J.S. Wainright, R.F. Savinell, and M. Litt, *High pressure electrical conductivity studies of acid doped polybenzimidazole.* Electrochimica Acta, 1998. **43**(10-11): p. 1289-1294.
3. Bhardwaj, R.C., M.A. Enayetullah, and J.O.M. Bockris, *Proton Activities in Concentrated Phosphoric and Trifluoromethane Sulfonic Acid at Elevated Temperature in Relation to Acid Fuel Cells.* J. Electrochem. Soc., 1990. **137**(7): p. 2070-2076.
4. Zelenay, O.P., B.R. Scharifker, J.O.M. Bockris, and D. Gervasio, *A Comparison of the Properties of CF_3SO_3H and H_3PO_4 in Relation to Fuel Cells.* J. Electrochem. Soc., 1986. **133**(11): p. 2262-2267.
5. Appleby, A.J. and B.S. Baker, *Oxygen reduction on platinum in trifluoromethane sulfonic acid.* J. Electrochem. Soc., 1978. **125**(3): p. 404-406
6. Saffarian, H., P. Ross, F.E. Behr, and G.L. Gard, *Electrochemical Evaluation of Bis(trifluoromethylsulfonyl) Methane as a Fuel Cell Electrolyte.* J. Electrochem. Soc., 1990. **137**(5): p. 1345-1348.
7. Kanamura, K., A. Tanaka, D. Gervasio, V. Kennedy, R. Adzic, E.B. Yeager, D. Burton, and R. Guneralne, *Perfluoro-ethylene- 1,2-bis-phosphonic Acid Fuel Cell Electrolyte.* J. Electrochem. Soc., 1996. **143**(9): p. 2765-2770.
8. Burton, D.J., *Synthesis of novel fluorinated phosphonic acid electrolytes for phosphoric acid fuel cells. Final report, January 1, 1989-June 30, 1991*, in *See also PB90-207366. Sponsored by Gas Research Inst., Chicago, IL.* 1992: United States. p. Pages: (28 p).

9 Appendix A

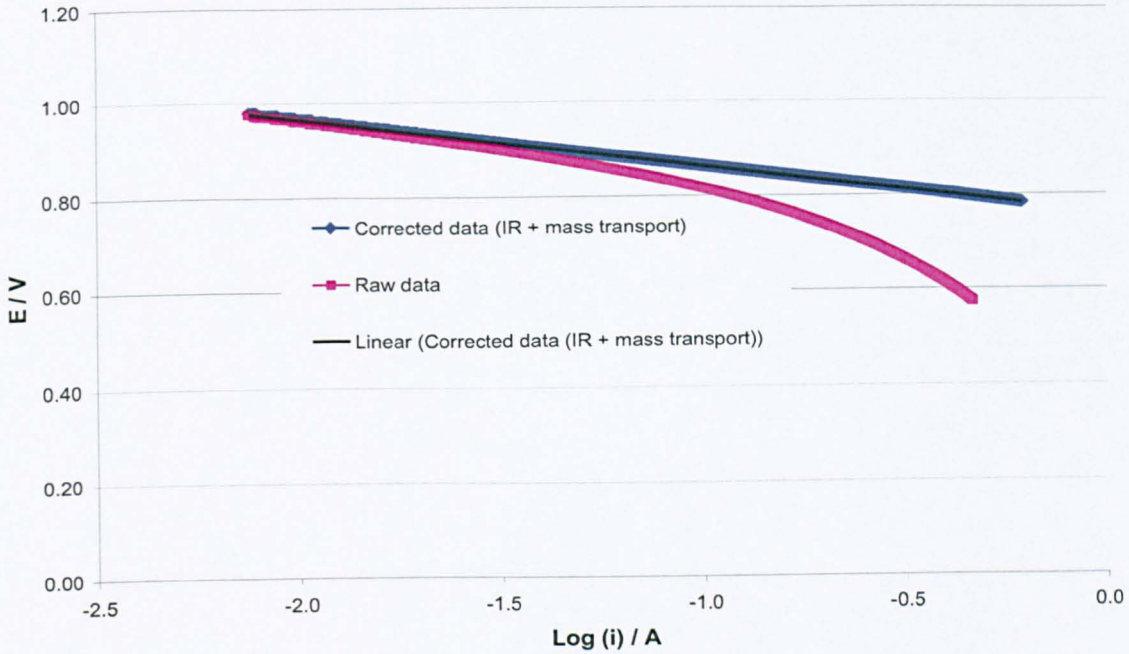

Figure 9-1. Tafel plot for raw and corrected data of 40% Pt/ C 3 PRU electrode at 140 °C (E vs. SHE).

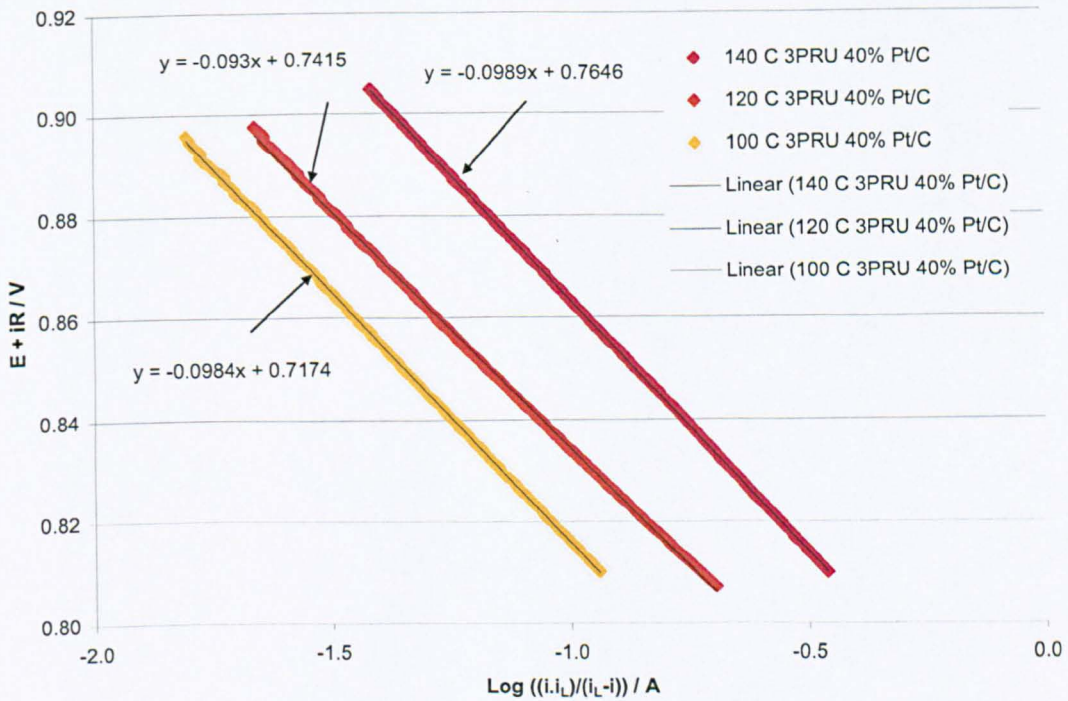

Figure 9-2. Corrected Tafel plots for 40% Pt/C 3PRU at temperatures of 100, 120 & 140 °C (E vs. SHE).

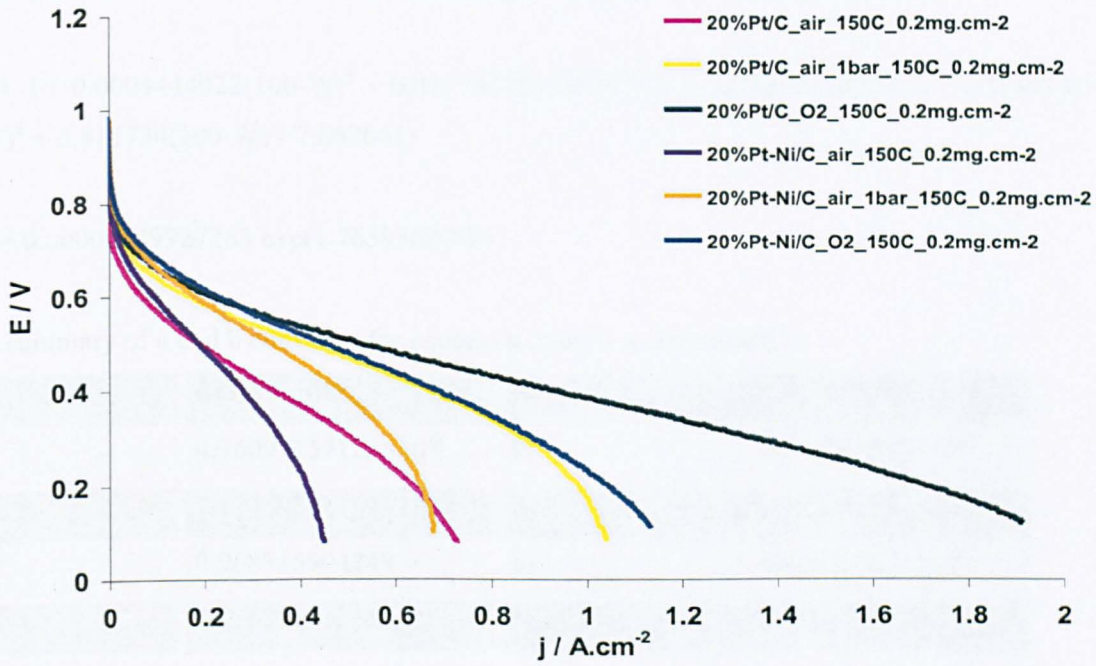

Figure 9-3. Compares cell performance under various oxygen concentrations at 120 °C of MEAs using 20% Pt-Ni/C (~17% Pt) & 20% Pt/C cathode electrodes utilising 0.2 mg_{Pt} cm^{-2} with 40% wt PTFE.

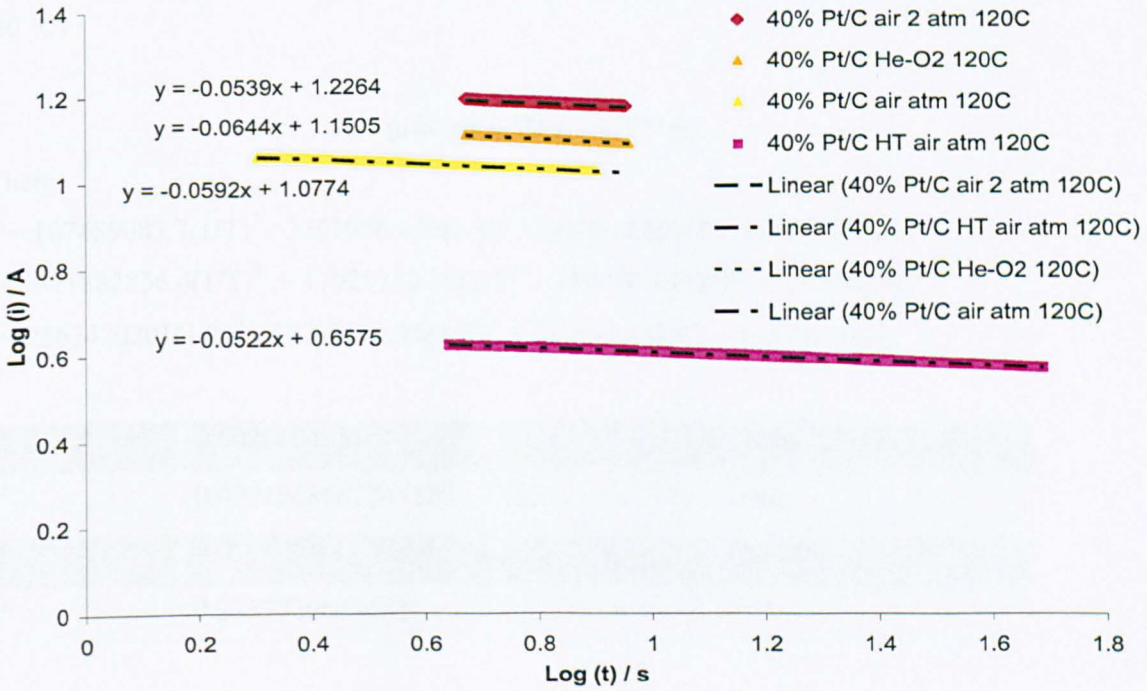

Figure 9-4. Log (i) vs. Log (t) transient at 120 °C for 40% Pt/C at various cathode's feed (fractal boundary).

The pre-exponential factors A&B in equation (47) and (48) are calculated using:

$B= 1/(0.0004444022(100-W)^5 - 0.01678248(100-W)^4 + 0.2476135(100-W)^3 - 1.714433(100-W)^2 + 5.815734(100-W) - 7.662641)$

$A= 0.00000249927283 \exp(1.76593087W)$

A summary of a and b constants for equations 53&54 is tabled below:

a_0	639.232305358	b_0	7.59437538894
a_1	$4.76099157122\times10^{-5}$	b_1	$2.79345043928\times10^{-7}$
a_2	$1.13460344152\times10^{-2}$	b_2	$6.74458517151\times10^{-5}$
a_3	0.968715904249	b_3	$5.7142688687\times10^{-3}$
a_4	33.2532981315	b_4	0.209801719227

To obtain X from log (P_{mmHg}) and 1/T $^oC^{-1}$ the following function was built (valid from 120 to 180 ^oC)

$$X = g_1(\log(P))\text{^}2+g_2\log(P)+g_3$$

Where:

$g_1 = 107489083.7(1/T)^3 - 3301976.439(1/T)^2 + 30786.6253/T - 99.97517454.$

$g_2= -571882856.4(1/T)^3 + 17025276.36(1/T)^2 - 159050.3432/T + 478.3506443.$

$g_3= 2563470201(1/T)^3 - 57770551.75(1/T)^2 + 427861.8321/T - 931.0823368.$

k_0^a	9.6082194551	k_0^b	26300
k_1^a	0.0001968662247125	k_1^b	0.62
k_2^a	-0.01322071446206	k_2^b	-39.7
k_3^a	0.2257720843463	k_3^b	527

10 Appendix B: List of Publications

Scientific Journals

1. Modelling and Experimental Validation of a High Temperature Polymer Electrolyte Fuel Cell.
   K. Scott, S. Pilditch and M. Mamlouk, J. Appl Electrochem, vol. 37, P.1245-1259 (2007).

2. High temperature polymer electrolyte membrane fuel cell.
   K. Scott, M. Mamlouk, J. Battery Bimonthly, vol. 36, 5, P.347 (2006).

International Conferences

Oral Presentation

3. M Mamlouk. 0 D Model of High Temperature PEMFC using Matlab / Simulink.
   Lecture in Newcastle's HT-PEMFC spring school, Newcastle, United Kingdom, March 2008.

4. M Mamlouk & K Scott. Studies of Phosphoric acid Polybenzimidazole based High Temperature PEMFC.
   Carisma Conference "Ionomer Membranes for Medium and High Temperature PEM Fuel Cells", Stuttgart, Germany, November 2007.

5. M Mamlouk & K Scott. Studies and Modelling of Phosphoric acid doped Polybenzimidazole for High Temperature PEMFC.
   Supergen meeting, Loughborough, United Kingdom, August 2007.

6. M Mamlouk. High temperature MEA development.
   36M meeting of Further improvement and system integration of HT-PEMFC, Svendborg, Denmark, March 2007.

7. M Mamlouk & K Scott. 0D Model for HT-PEMFC using Matlab/Simulink®.
   30M meeting of Further improvement and system integration of HT-PEMFC, Gothenburg, Sweden, October 2006.

8. M Mamlouk & K Scott. High temperature polymer electrolyte fuel cells. Modelling and experimental validation.
   Fuel cells science and technology, Turin, Italy, September 2006.

9. M Mamlouk, N Hidayati & K Scott. Performance of Direct Alcohol Fuel Cell Stack.
   57th Annual meeting of the International Society of Electrochemistry, Edinburgh, United Kingdom, September 2006.

10. M Mamlouk, N Hidayati & K Scott. Development of Direct alcohol-proton exchange membrane using alcohol tolerant cathodes.
    11th APCChE congress, Kuala Lumpur, Malaysia, August 2006.

11. M Mamlouk & K Scott. HT-PEMFC electrode optimisation.
    24M meeting of Further improvement and system integration of HT-PEMFC, Trondheim, Norway, April 2006.

12. M Mamlouk. High Temperature PEM fuel cell.
    2006 postgraduate student research conference, Newcastle, United Kingdom, March 2006.

13. M Mamlouk & K Scott. High Temperature Polymer Electrolyte Membrane Fuel cells.
    IEA Annex XVI Advanced Fuel Cells workshop, Loughborough, United Kingdom, November 2005.

14. M Mamlouk & K Scott. High Temperature Polymer Electrolyte Membrane Fuel cells.
    Symposium on High Temperature PEM Fuel Cells, Patras, Greece, September 2005.

15. M Mamlouk & K Scott. Sulfonated PEEK and composite membrane characterization.
    18M meeting of Further improvement and system integration of HT-PEMFC, Patras, Greece, September 2005.

16. M Mamlouk. High temperature polymer electrolyte membrane fuel cells.
    Star city science technology and research, Marie curie conferences, Sector B energy, Kalkar, Germany, June 2005.

17. M Mamlouk. High Temperature PEM fuel cell.
    2005 postgraduate student research seminar, Newcastle, United Kingdom, January 2005.

18. M Mamlouk & K Scott. HT Polymer Electrolyte Membrane Fuel cells.
    6M meeting of Further improvement and system integration of HT-PEMFC, Newcastle, United Kingdom, October 2004.

19. M Mamlouk & K Scott. High temperature polymer synthesis and characterization.
    6M meeting of Further improvement and system integration of HT-PEMFC, Newcastle, United Kingdom, October 2004.

Poster Presentation

20. Performance of Direct Alcohol Fuel Cell Stack.
    Fuel cells science and technology, Turin, Italy, September 2006.
21. Use of methanol tolerant cathode materials in direct alcohol fuel cell stack.
    Fuel cells science and technology, Turin, Italy, September 2006.
22. High temperature polymer electrolyte fuel cells. Modelling and experimental validation.
    57th Annual meeting of the International Society of Electrochemistry, Edinburgh, United Kingdom, September 2006.
23. Use of methanol tolerant cathode materials in direct alcohol fuel cell stack.
    57th Annual meeting of the International Society of Electrochemistry, Edinburgh, United Kingdom, September 2006.
24. High temperature polymer electrolyte fuel cells.
    2005 Fuel Cell Seminar, Palm Springs, USA, November 2005.
25. High temperature PEMFC's.
    7th European Symposium on Electrochemical Engineering, Toulouse, France, October 2005.
26. Polymer electrolyte fuel cells. Will higher temperatures and alternative fuels accelerate technology uptakes? World renewable energy congress, Aberdeen, United Kingdom, May 2005.

Others

27. K Scott and M Mamlouk. High temperature polymer membrane electrolyte fuel cells.
    Plenary Lecture 3rd Guangzhou Fuel Cell Conference, China, 21-23 June, 2006.

28. M Mamlouk, N Hidayati, G F Alvarez, M Q Li and K Scott. Catalytic activity of carbon supported platinum-based catalysts towards oxygen reduction at high temperatures Poster presented at Electrochem 2007, 3-4 September 2007, London.

29. T Sousa, M mamlouk and K Scott. 2-Dimensional modelling and experimental validation of a High Temperature PEM Fuel Cell. Progress in MEA components for Medium and High Temperature Polymer Electrolyte Fuel Cells" CARISMA 1st International Conference, 21 - 24 September 2008, Montpellier.

30. T Sousa, M mamlouk and K Scott. A non-isothermal PEMFC model related to High Temperature cell testing and analysis. Progress in MEA components for Medium and High Temperature Polymer Electrolyte Fuel Cells" CARISMA 1st International Conference, 21 - 24 September 2008, Montpellier.

31. M Mamlouk, N Hidayati and K Scott Progress in the understanding and performance of direct ethanol fuel cells. Progress in MEA components for Medium and High Temperature Polymer Electrolyte Fuel Cells" CARISMA 1st International Conference, 21 - 24 September 2008, Montpellier.

32. M Mamlouk and K Scott Material and electrode development for PBI based HT-PEMFC. Progress in MEA components for Medium and High Temperature Polymer Electrolyte Fuel Cells" CARISMA 1st International Conference, 21 - 24 September 2008, Montpellier.

33. T Sousa, M Mamlouk and K Scott. 2-Dimensional modelling and experimental validation of a High Temperature PEM Fuel Cell. Fuel Cells Science and Technology 2008, Scientific Advances in Fuel Cell Systems, 8 – 9 October 2008, Copenhagen.

34. T Sousa, M Mamlouk and K Scott. A non-isothermal PEMFC model related to High Temperature cell testing and analysis. Fuel Cells Science and Technology 2008, 8 – 9 October 2008, Copenhagen.